Heinrich Heine
Universität
Düsseldorf

Application of *C3*-methyltransferases for natural product synthesis

Inaugural dissertation

for the attainment of the title of doctor
in the Faculty of Mathematics and Natural Sciences
at the Heinrich Heine University Düsseldorf

presented by

Mona Haase
from Westerstede, Germany

Düsseldorf, September 2025

from the Institute of Bioorganic Chemistry

of the Heinrich Heine University Düsseldorf

Printed with the permission of the

Faculty of Mathematics and Natural Sciences of the

Heinrich Heine University Düsseldorf

Supervisor: Prof. Dr. Jörg Pietruszka

Co-supervisor: Prof. Dr. Holger Gohlke

Date of the oral examination: 08.09.2025

Parts of this work have already been published in specialised journals or presented at conferences. The present work contains results from the below listed thesis, which was supervised by the author and is identified by name at the appropriate places in the present dissertation.

B.Sc. Elias Leon Pfirmann (Heinrich Heine University Düsseldorf, Bachelor thesis), 2023; “Synthese des Pyrroloindol Motivs via C3-Methyltransferases“

Publications

First author publications included in this thesis (reprinted/reproduced with permission from the corresponding article. Copyright belongs to the publisher)

[1] M. Haase, B. David, B. Paschold, T. Classen, P. Schneider, N. Pozhydaieva, H. Gohlke, J. Pietruszka, *ACS Catal.* **2023**, *14*, 227-236; 'Application of the C3-Methyltransferase StspM1 for the Synthesis of the Natural Pyrroloindole Motif', 10.1021/acscatal.3c04952.

[2] D. A. Amariei[+], M. Haase[+], M. K. T. Klischan, M. Wäscher, J. Pietruszka, *ChemCatChem* **2024**, *16*, e202400052; 'High-Throughput Colorimetric Detection and Quantification of Indoles and Pyrroloindoles for Enzymatic Activity Determination', 10.1002/cctc.202400052.

[3] M. Haase, O. H. Weiergräber, B. David, E. L. Pfirmann, B. Paschold, H. Gohlke, J. Pietruszka, *Chem. Sci.* **2025**, *16*, 2041-6520; 'Characterization of a C-methyltransferase from Streptomyces griseoviridis – crystal structure, mechanism, and substrate scope', 10.1039/D4SC07300B.

[4] M. Schatton[+], M. Haase[+], J. Tenhaef, C. Gronkowsky, S. Noack, J. Pietruszka, *Chem. Eur. J.* **2025**, *31*, e202500740; 'Chemoenzymatic Total Synthesis of Lansai B', 10.1002/chem.202500740.

[5] M. Haase, O.H. Weiergräber, J. Pietruszka, *Prot. Sci*. **2025**; 34(9):e70254. 'Re-engineering a transferase scaffold for indole C3 methylation in diketopiperazines', 10.1002/pro.70254

[6] M. Haase, M. Schatton, C. Gronkowsky, J. Pietruszka, *to be submitted* **2025**; 'Anticancer activity of Lansai B and related diketopiperazines'.

[7] M. Haase, B. P. Paschold, J. Pietruszka, *to be submitted* **2025**; 'Biosynthesis of Lansai B'.

Contribution in these publications: Conceptualization, methodology, analysis, investigation, writing (original draft, review & editing), visualization, project administration.

[+] These authors contributed equally to this work, the order has been decided by flipping a coin

Publications not discussed in this thesis

[8] M. K. T. Klischan, F. Mazzone, L. Berning, J. Greb, M. Schlamkow, M. Haase, W. Frey, B. Stork, K. Pfeffer, J. Pietruszka, *ACS Omega* **2023**, *8*, 41816-41834; 'Modular Approach for the Synthesis and Bioactivity Profiling of 8,8′-Biflavones', 10.1021/acsomega.3c06503.

Contribution: Investigation, analysis

[9] B. P. N. Chapple, Lia, P. Schneider, B. Henßen, M. Haase, T. Classen, J. Pietruszka, *to be submitted* **2025**; 'Characterization of the N-Methyl Transferase SgPsmC and its Application in the Kinetic Resolution of Pyrroloindolines. '.

Contribution: Investigation

Conference contributions

CLIB-Competence Centre Biotechnology (CKB) Symposium

16.09.2021, Düsseldorf

Pitch Talk

“Towards a new era of biocatalytic methylation

- Application of C3-methyl transferases for natural product synthesis”

Mona Haase, Jörg Pietruszka

CLIB International Conference (CIC)

01.02.2022 – 02.02.2022, Düsseldorf

Pitch Talk in the Global Biobased Business Plan Competition (G-BiB)

about enzymcatalysed methylation

Mona Haase, Benjamin Chapple, Diana Amariei, Marcel Schatton

10th International Congress on Biocatalysis (BIOCAT)

28.08.2022 – 01.09.2022, Hamburg

Pitch Talk + Poster Presentation

“Application of C3-methyl transferases for natural product synthesis”

Mona Haase, Benoit David, Thomas Classen, Holger Gohlke, Jörg Pietruszka

25th Day of Organic Chemistry (TOCUS)

14.10.2022, Stuttgart

Oral presentation

“Application of C3-methyl transferases for natural product synthesis”

Mona Haase, Jörg Pietruszka

Symposium on Biological and Medicinal Chemistry

06.03.2023-08.03.2023, Bonn

Poster Presentation

“Selective Biocatalytic Methylation of Dipeptides as a Tool for Natural Product Synthesis”

Mona Haase, Benoit David, Holger Gohlke, Jörg Pietruszka

35. Irseer Naturstofftage

26.04.2023 - 28.04.2023, Kloster Irsee

Pitch Talk + Poster Presentation

“Investigations on the C3-Methyltransferase StspM1 and Its Application in Natural Product Synthesis”

Mona Haase, Benoit David, Beatrix Paschold, Thomas Classen, Holger Gohlke, Jörg Pietruszka

16th International Symposium on Biocatalysis and Biotransformations (BioTrans)

25.06.2023-29.06.2023, La Rochelle

Poster Presentation

“Application of the C3-Methyltransferase StspM1 as Catalyst for the Formation of the Pyrroloindole motive in Natural Product Synthesis”

Mona Haase, Benoit David, Thomas Classen, Holger Gohlke, Jörg Pietruszka

Poster Contribution

“Mirror, mirror on the wall: Application of an *N*-methyltransferase for preparative scale enzymatic kinetic resolution”

Benjamin P. Chapple, Pascal Schneider, Mona Haase, Jörg Pietruszka

22nd European Symposium on Organic Chemistry

09.07.2023-13.07.2023, Ghent (Belgium)

Poster Contribution

“Functionalization of Pyrroloindoles for Application in Methyltransferase Reactions”

M. Schatton, M. Haase, B. P. Chapple, D. Amariei, P. Schneider, J. Pietruszka

Florida Heterocyclic and Synthetic Conference

10.03.2024-13.03.2024, Gainesville (USA)

Poster Contribution

“Studies towards the Total Synthesis of Lansai B”

M. Schatton, M. Haase, C. Gronkowsky, L. Meerkatz, J. Pietruszka

NextGenBiocat 2024

20.05.24-23.05.24, Crete

Poster Contribution

“Investigation on Methyltransferase Secretion for Enhanced Natural Product Biosynthesis”

Lisa M. Böhmer, Mona Haase, Rebecca Hamel, Patrick Lenz, Karl-Erich Jaeger, Marco Oldiges, Jörg Pietruszka

Nord Bio II: Nordic midsummer symposium

13.06.2024-14.06.2024, Stockholm (Sweden)

Poster Presentation

“Investigations of the methyltransferase SgMT as a tool for the chemoenzymatic total synthesis of Lansai B”

Mona Haase, Benoit David, M. Schatton, Julia Tenheaf, O. Weiergräber, Holger Gohlke, Jörg Pietruszka

11th International Congress on Biocatalysis - Biocat2024

25.08.2024-29.08.2024, Hamburg

Poster Contribution

“Exploring Late-Stage Scaffold Construction in Chemoenzymatic Natural Product Synthesis“

Simon Przetak, Mona Haase, Thomas Classen, Jörg Pietruszka

23. Lecture Conference Orchem

Poster Contribution

09.09.2024-11.09.2024, Regensburg (Germany)

“Chemoenzymatic Total Synthesis of Lansai B”

M. Schatton, M. Haase, C. Gronkowsky, L. Meerkatz, J. Pietruszka

DECHEMA FORUM

11.09.2024-13.09.2024, Friedrichshafen

Pitch Talk + Poster Presentation

“Application of C3-methyl transferases for natural product synthesis“

Mona Haase, Benoit David, M. Schatton, O. Weiergräber, Holger Gohlke, Jörg Pietruszka

37. Irseer Naturstofftage

19.02.2025 - 21.02.2025, Kloster Irsee

Poster Contribution

“Precision in Complex Molecule Assembly: Advancing Alkylation Techniques with Prenyltransferases”

Simon Przetak, Mona Haase, Jörg Pietruszka

NextGenBiocat 2025

08.05.25-09.05.25, Milan (Italy)

Oral presentation

“Application of C3-methyl transferases for natural product synthesis“

Mona Haase, Benoit David, M. Schatton, O. Weiergräber, Holger Gohlke, Jörg Pietruszka

Oral presentation

“Biocatalytic tools for late-stage functionalization: advanced alkylation techniques with prenyltransferases“

Simon Przetak, Mona Haase, Jörg Pietruszka

Awards

Poster prices

At the 10th International Congress on Biocatalysis (BIOCAT) (28.08.2022 – 01.09.2022, Hamburg) for the poster with the title “Application of C3-methyl transferases for natural product synthesis” (Mona Haase, Benoit David, Beatrix Paschold, Thomas Classen, Holger Gohlke, Jörg Pietruszka)

At the 35. Irseer Naturstofftage (26.04.2023 - 28.04.2023, Kloster Irsee) for the poster with the title “Investigations on the C3-Methyltransferase StspM1 and Its Application in Natural Product Synthesis” (Mona Haase, Benoit David, Beatrix Paschold, Thomas Classen, Holger Gohlke, Jörg Pietruszka)

At the 23. Lecture Conference Orchem (09.09.2024-11.09.2024, Regensburg) for the poster with the title “Chemoenzymatic Total Synthesis of Lansai B” (M. Schatton, M. Haase, C. Gronkowsky, L. Meerkatz, J. Pietruszka)

At the 37. Irseer Naturstofftage (19.02.2025 - 21.02.2025, Kloster Irsee) for the poster with the title “Precision in Complex Molecule Assembly: Advancing Alkylation Techniques with Prenyltransferases” (Simon Przetak, Mona Haase, Jörg Pietruszka)

Other Awards

Second Place in the Global Biobased Business Plan Competition (G-BiB) with a project about enzymcatalysed methylation (Mona Haase, Benjamin Chapple, Diana Amariei, Marcel Schatton)

Second Place in the Jülich Innovation & Entrepreneurship Certificate (JUICE) Program with a project about enzymcatalysed methylation (Mona Haase, Benjamin Chapple, Diana Amariei, Lisa Böhmer)

FOREWORD

Diese Arbeit ist viel mehr als nur das Ergebnis wissenschaftlicher Forschung – sie ist das Produkt vieler Jahre des Lernens, Zweifelns, Wachsens und Durchhaltens. Sie wurde möglich durch Menschen, die an meiner Seite waren: die mich inspiriert, unterstützt, bestärkt – und manchmal einfach nur aufgefangen haben, wenn ich es gebraucht habe.

Ganz besonders widme ich diese Dissertation meinem Vater. Du konntest diesen Abschluss leider nicht mehr miterleben, aber in Gedanken warst du immer bei mir. Deine ruhige Art und dein Vertrauen in mich haben mich auf eine Weise getragen, die ich nie vergessen werde. Du fehlst.

1. LIST OF ABBREVIATIONS

Abs	Absorption
Amp	Ampicillin
ATP	Adenosintriphosphat
bp	Base pair
bw	Backwards (primer)
C	Cells (Cell pellet fraction)
CDPS	Cyclodipeptide synthase
CDS	Coding sequence
COSY	Correlation spectroscopy
cWW	Cyclo-Trp-Trp DKP
DAD	Diode array detector
DEPT	Distortionless enhancement by polarisation transfer
Dest.	Destilled
DKP	Diketopiperazine
dNTP	Deoxyribonucleoside triphosphates
DMAPP	Dimethylallyl pyrophosphate
DMAB	p-Dimethylaminobenzaldehyde
DMF	Dimethylformamide
DMSO	Dimethyl sulfoxide
DTT	1,4-Dithio-D-threitol
EC	Enzyme class
Equiv.	Molar equivalent
ES	Electrospray
ESI	Electron spray ionisation
EV	Empty vector
FT	Flow through (chromatography)
fw	Forward (Primer)
GC	Gas chromatography
HMBC	Heteronuclear multiple bond correlation
HMT	Halide methyltransferase
HPI	Hexapyrroloindole
HPLC	High performance liquid chromatography
HRMS	High-resolution mass spectrometry
HSQC	Heteronuclear single quantum coherence
IC	Inhibitory concentration
IMAC	Immobilised metal ion affinity chromatography
IPTG	Isopropyl-*β*-D-thiogalactopyranoside
IR	Infrared spectroscopy
Kan	Kanamycin
kb	Kilobase
kDa	Kilodalton
KP_i	Potassium phosphate buffer
LB	Lysogeny broth
LC	Liquid chromatography
Lys	Lysate
M (IR)	Medium signal
NCBI	National Centre for Biotechnology Information
Ni-NTA	Nickel (II) nitrilotriacetic acid
NMR	Nuclear magnetic resonance
OD	Optical density
MS	Mass sprectrometry
MTase	Methyltransferase
PDB	Protein data bank
PE	Petroleum ether
PEG	Polyethylene glycol
ppm	Parts per million
PTase	Prenyltransferase
Ref	Reference
rpm	revolutions per minute
RT	Room temperature
S (IR)	Strong signal
SAH	S-adenosylhomocysteine
SAM	S-adenosylmethionine
SAR	Structure-activity-relationship
SDS	Sodium dodecyl sulfate
Taq	Thermus aquaticus Polymerase
TB	Terrific broth
TEA	Triethylamine
Term	Terminator
TLC	Thin layer chromatography
THF	Tetrahydrofuran
t_R	Retention time
Tris	Tris(hydroxymethyl)aminomethane
T7P	T-7 Promotor
T7T	T-7 Terminator
Vs (IR)	Very strong signal
W (IR)	Weak signal

2. ABSTRACT

Natural products play a vital role in drug development, either directly as pharmaceuticals or as templates for designing target-specific therapeutics. The chemical synthesis of these compounds often presents significant challenges, requiring multiple reaction steps and hazardous reagents. One prominent structural motif found in numerous bioactive natural products is the hexahydropyrrolo[2,3-b]indole (HPI) framework. Its unique tricyclic structure and diverse biological activities have driven significant synthetic interest, yet traditional methods struggle to achieve stereoselectivity efficiently.

This thesis aims to develop a biocatalytic route for synthesising the HPI motif using methyltransferases (MTases), which catalyses *C3*-methylation of tryptophan-based cyclic dipeptides (DKPs). The MTase StspM1 from *Streptomyces sp.* HPH0547 was selected as the starting point for these studies: Optimised reaction conditions, enzyme immobilisation, and *S*-adenosyl methionine (SAM) cofactor recycling were investigated to create a scalable, efficient method. To broaden the understanding of their catalytic functions, homologs of StspM1 were explored, focusing on their structure and mechanism. This investigation was supported by two crystal structures obtained during the study. Computational docking and mutagenesis confirmed key residues critical for activity. Among these homologs, SgMT from *Streptomyces griseoviridis* was successfully integrated into the total synthesis of the natural product lansai B, demonstrating its synthetic utility.

The gene clusters linked to these *C3*-MTases involve additional enzymes contributing to the biosynthesis of lansai B, including a second MTase, a cyclodipeptide synthase (CDPS) and a prenyltransferase (PTase). The second MTase was confirmed to function as an *N*-MTase. The PTase was found to prenylate the *C5*-position, representing the final step in the biosynthesis of lansai B

This work advances biocatalytic strategies for synthesising complex natural product frameworks, offering new methodologies for pharmaceutical development.

3. INTRODUCTION

3.1 Introduction into natural products

Since the beginning of human history, nature has served as a source for the treatment of diseases.[1-3] For example, the Greek Hippocrates, the forefather of all medicine, already knew in the 4th century BC that an extract of willow bark relieved pain of all kinds. This knowledge was applied by various cultures without knowing the exact reason for the pain relieve.[4] In 1828, the pharmacologist Johann Andreas Buchner succeeded in isolating a compound from willow bark extracts called salicin (**1**) [Figure 1]. One year later, the French pharmacist Henri Leroux improved the process of salicin (**1**) extraction and isolated pure crystals of this natural product. Salicin (**1**) is a glycoside of salicylic alcohol, which is converted into salicylic acid in the body.[4-6] In 1874, Friedrich von Heyden produced salicylic acid on a large scale using the Kolbe-Schmitt reaction.[7] Salicylic acid became the first industrially produced and packaged medicine in the world, but its medical use was limited due to side effects. The breakthrough of this drug was achieved on August 10, 1897: the chemist Felix Hoffmann synthesised by-product-free p-acetylsalicylic acid from acetic anhydride and salicylic acid at Bayer's main factory in Elberfeld, which was pharmacologically evaluated by Heinrich Dreser.[8] Today, acetylsalicylic acid is a widely used analgesic and antipyretic agent and has been listed in 1977 on the World Health Organisation's (WHO) list of essential medicines: Its common name is Aspirin®.[9-11] Aspirin® was present in Edmund Hillary's first successful ascent of Mount Everest in 1953, it travelled to the moon as part of the Apollo 11 mission's hand luggage in 1969 and was the subject of the studies of the British pharmacologist John Vane, which was awarded the Nobel Prize in Medicine 1982.[6, 12, 13]

This success story serves as a prime example of the significance of natural products and their impact on the pharmaceutical industry. By its definition, natural products are organic compounds formed by a natural living system.[14] These sources of natural products reach from plants over bacteria and fungi to animals from all over the world.[2, 15-17] In organic chemistry, natural products are often classified as primary and secondary metabolites. Primary metabolites are essential components of basic metabolic pathways necessary for life. In contrast, secondary metabolites are not essential for survival. Secondary metabolites serve a wide variety of functions and are especially interesting in drug discovery because of their function on other organisms.[14]

The discovery of natural products is an ongoing field of research[18] and not always as lucky as in 1928, when the famous discovery of penicillin began with a mouldy bacterial culture: Alexander Fleming, who was studying *Staphylococcus* species at St. Mary's Hospital in London, inoculated an agar plate with Gram-positive bacteria before leaving for summer vacation. When he returned, he found that a mould had grown on the culture medium, preventing the bacteria from multiplying near the fungus (*Penicillium notatum*). Fleming named the bactericidal substance extracted from the culture medium penicillin G (**2**) [Figure 1]. [19]

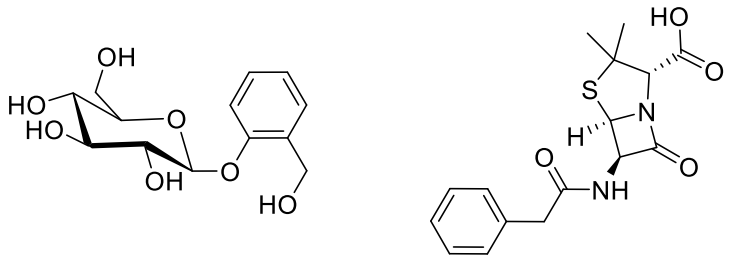

salicin (**1**) penicillin G (**2**)

Figure 1: Chemical structures of salicin (**1**) and penicillin G (**2**).

This finding of penicillin started the “Golden Era” of natural products, where many major pharmaceutical industries initiated natural product discovery programmes targeting not just antibacterial compounds, but focussing all kinds of diseases. However, in the 1990s and early 2000s, many of these companies discontinued their natural product discovery programmes due to the advances in chemistry and the rise of automated high throughput screening tools, which provided an efficient way to generate and test large numbers of new compounds to create large substance libraries. Traditional extract-based screening was considered less favourable due to the frequent re-discovery of known compounds and the extensive work on extraction and indentification.[2, 20, 21] In 1994 Corley and Durley estimated that it took on average 50.000 US Dollar and three months of work to isolate and identify natural products from its source at that time.[22]

The method for isolating new compounds from biological samples has remained relatively consistent over the past decades. But the introduction of advanced spectrometric technologies combined with established bioassays and database searching, has accelerated the identification process. The technique of identifying known compounds responsible for a crude extract's activity before proceeding with isolation is called dereplication.[2, 23, 24] In addition to the faster process of dereplication, the diversity regarding taxonomy and geography has changed. Marine-derived natural products have significantly expanded the scope of research in this field.[25, 26] Until 2023, 39.560 natural products have been identified from marine sources according to the database MarinLit.[27]

After identification of their biological activity, natural products usually need further optimisation to enhance their pharmacokinetics and pharmacodynamics.[28, 29] Multiple modification strategies have been developed to optimise natural products as drugs in the recent years. These strategies focus on raising the activity, improving solubility, increasing metabolic stability, modulating pharmacokinetic parameters and removing toxicity (side effects).[30] The pharmacokinetic parameters are summed up under the term ADME: Absorption, Distribution, Metabolism and Excretion. High-throughput ADME screening is a well-established technique in drug discovery that uses in vitro assays to investigate a compound's properties.[31] Another important guideline in drug development is Lipinski's Rule of Five. In the studies from 1997 by *Lipinski* and his co-workers, they analysed drug properties related to their permeability and solubility necessary for oral absorption by calculating properties of several thousand drugs. They found that having fewer than five hydrogen-bond donor groups and ten hydrogen-bond acceptor groups is advantageous. Additionally, the molecular weight (MWT) should not exceed 500 Da, and the calculated Log P should be less than 5.[32-34]

The discovery of new drugs from different sources gained a lot of attention in the past years: On the 31st December 2019, SARS-CoV-2 was identified in Wuhan City, China.[35] The resulting COVID-19 pandemic taught us that the fast development of drugs is essential in a global health crisis. In silico screenings were conducted using libraries of known natural products and synthetically derived compounds, evaluated based on their ligand efficiency.[36] The ligand efficiency of compounds measures the binding energy per unit mass of a molecule relative to its drug target making it a crucial factor in the early stages of lead optimisation.[30, 37] For this process, the target protein was modelled (or was based of the crystal structure) and the potential drugs were docked into the protein.[38-40] Docking allows for the discovery of new drugs by predicting how these ligands interact with targets at the molecular level. Techniques like this do shape the future of drug discovery more and more.[41-43]

3.2 Goal of the thesis

Natural products often function directly as pharmaceuticals due to their inherent biological activity or act as valuable starting points for target-oriented drug development. However, the natural sources of these compounds frequently yield insufficient quantities to meet the demands of the pharmaceutical industry, making alternative production methods essential. Depending on their chemical complexity, synthesising these compounds can be highly challenging, involving numerous reaction steps and the use of hazardous reagents.

An example of a structural motif commonly found in various natural products is the hexahydropyrrolo[2,3-b]indole (HPI) framework.[44-46] The unique tricyclic architecture of the HPI motif, combined with its diverse biological activities, has made this motif an attractive and highly sought-after target for synthesis. However, achieving the stereoselective synthesis of the HPI motif continues to pose a substantial challenge when using traditional organic synthesis approaches. [47-51]

The aim of this thesis is to develop a biocatalytic method for synthesising the HPI structural motif on a preparative scale using MTases. A key enzyme for this approach is the MTase StspM1 from *Streptomyces sp.* HPH0547, known for its ability to methylate the *C3*-position of L-tryptophan-based cyclic dipeptides **3**, thereby forming the HPI motif in the corresponding reaction product **4** [Figure 2]. To enable practical synthetic application, the reaction conditions must be optimised, and the enzyme should be made accessible in a user-friendly format, such as through immobilisation. Additionally, recycling the cofactor *S*-adenosyl methionine (SAM) offers the potential for improved atom economy and greater efficiency in the reaction.

The natural product aimed for in this thesis is lansai B (**5**), which is a diketopiperazine (DKP) featuring two HPI motifs [Figure 2]. Following the development of a robust biocatalytic methylation method, the goal is to integrate this reaction into the total synthesis of lansai B (**5**), demonstrating its practical utility and effectiveness.

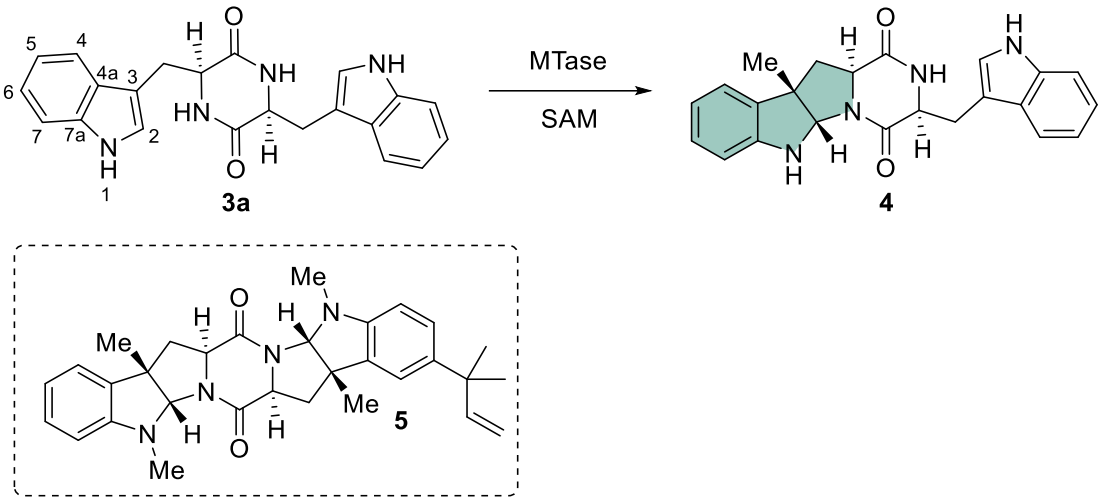

Figure 2: Reaction scheme of the biocatalytic methylation reaction with a MTase on a DKP product forming a HPI motif (green) and the chemical structure of lansai B (**5**, box).

To gain deeper insights into this class of enzymes, obtaining a crystal structure is highly desirable, particularly for studying the enzyme's catalytic mechanism. Additionally, exploring homologs of StspM1 shall broaden the enzyme panel and reveal potential structural and functional diversity. Since the original natural products resulting from biosynthetic pathways involving the investigated *C3*-MTases remain unknown, further investigation into other enzymes within the associated gene clusters are sought to provide valuable context and enhance our understanding of their biosynthetic roles.

4. STATE OF THE ART

4.1 Structural elements of lansai B like natural products

Lansai B (**5**) is a natural product first isolated from *Streptomyces* sp. SUC1, which is a bacterium on the aerial roots of *Ficus benjamina*. It is weakly active against the breast cancer cell line (IC_{50}=15 µg mL^{-1}).[52] Structurally, lansai B (**5**) features a ring system containing seven rings **6** that imparts rigidity, with the three-dimensional arrangement governed by stereochemical information at the ring junctions: The central DKP ring is fused to two HPI motifs with two methyl-groups on the *C3*-positions. These methyl groups are *trans*-configured with respect to the hydrogens on the DKP core, which are (*S*)-configured because of the origin of L-tryptophan as a natural building block. In addition to this central ring structure, lansai B (**5**) contains one branched prenyl-group at the *C5*-position of the HPI. Furthermore, both nitrogen atoms within the HPI motifs are methylated [Figure 3].[52, 53]

A structurally similar natural product is nocardioazine B (**7**). Nocardioazine B (**7**) was first isolated from a *Nocardiopsis sp.* (CMB-M0232) found in an Australian marine sediment.[54] In recent years, the absolute configuration of the stereogenic centres on the DKP core of nocardioazine has been debated. Based on the discovery of L-tryptophan derived precursor molecule **3** in the investigations of the biosynthesis and NMR spectral studies, the stereogenic centres at the DKP core were proposed to have an (*S*)-configuration.[54] The first attempt of a total synthesis of nocardioazine B (**7**) started with L-configurated tryptophans and revealed that the synthetic product's optical rotation was the opposite of that of the natural product.[55] Nocardioazine B (**7**), like lansai B (**5**), has a seven ring system with two HPI motifs attached to the DKP core. In comparison to lansai B (**5**), one *C3*-position is methylated, and the other *C3*-position is prenylated. The methyl-group is *cis*-configured, while the prenyl-group is *trans*-configured with respect to the hydrogen on the DKP core leading to a different 3D-strucuture compared to lansai B (**5**). Additionally, only the HPI nitrogen on the prenylated side of the molecule is methylated [Figure 3].

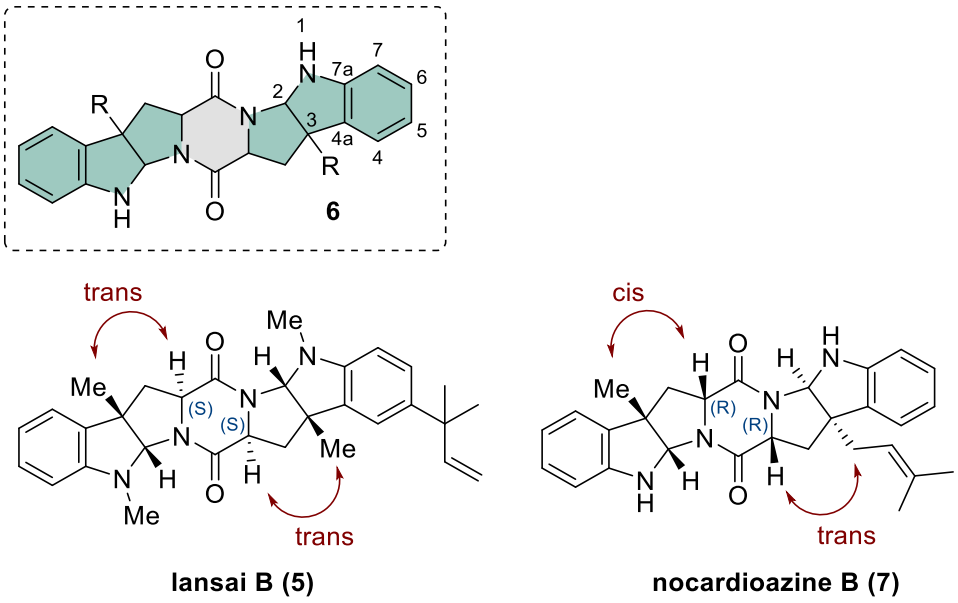

Figure 3: Structures of lansai B (**5**) (bottom left) and nocardioazine B (**7**) (bottom right). The general seven-ring structure of these molecules include the DKP ring (grey) and the two HPI rings (green).

The first and only total synthesis of lansai B (**5**) was published in 2014 [Figure 5]. The HPI structural motif is built via (3+2) cycloaddition of methyl 2-trifluoroacetamidoacrylate (**8**) and the indole **9** in 85% yield and 92% ee. The bottleneck of this synthesis route is the coupling of the two different HPIs **10** (R^1 = H or prenyl). A coupling of this orthogonally protected HPIs under various conditions did not lead to the DKP formation. Lansai B (**5**) was finally formed from the deprotected HPIs **11** and **12**, leading to the desired hetero dimer **5** in a yield of 38% (yields of the other homodimers **13** and **14** are each 20%) [Figure 4].[53]

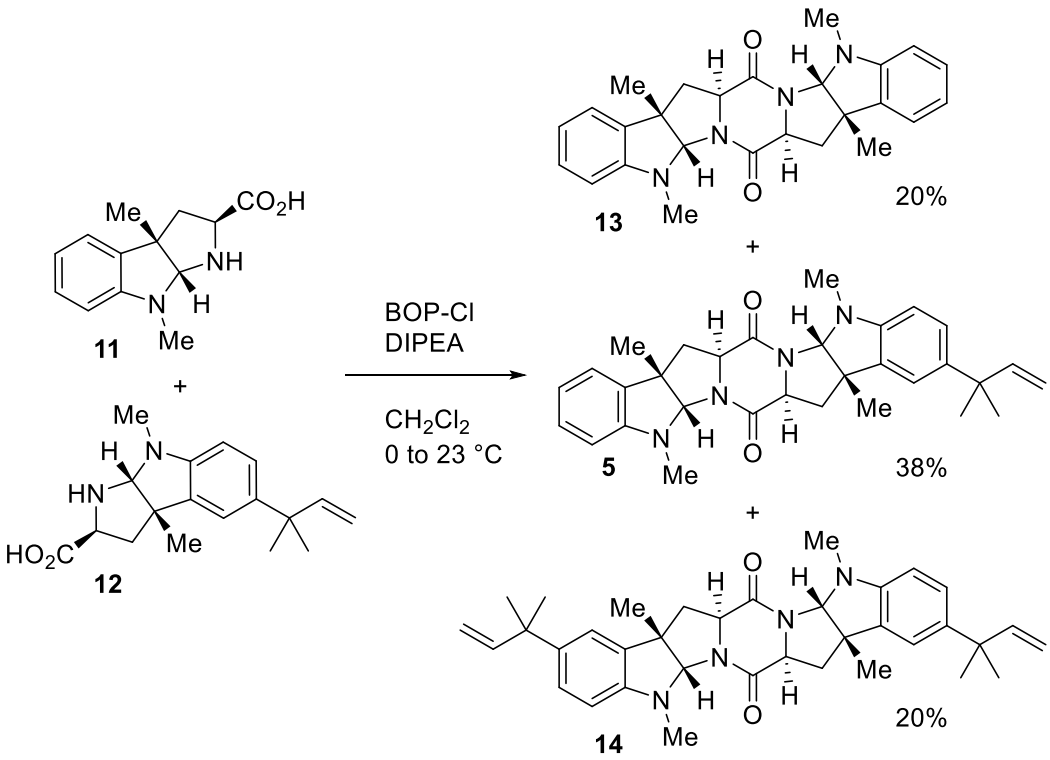

Figure 4: Final step of the total synthesis of lansai B (**5**).

In the first published synthesis route from 2012 and also in the latest total synthesis from 2022 of nocardioazine B (**7**), the methylated HPI structural motif is synthesised starting from protected L-tryptophan, which is brominated at the *C3*-position with NBS giving the HPI motif in the intermediate **15**. As a next step, an enolate formation was promoted under basic conditions, followed by the rapid intramolecular displacement of the bromide, resulting in the formation of a cyclopropylazetoindoline **16**. By treating this intermediate **16** with the Lewis acidic trimethylaluminium, a stereospecific cyclopropane ring opening occurred with a final *C3*-methylation step to form the methylated HPI **17**. In contrast to the challenging coupling of two protected *trans*-configured HPI as required in the synthesis of lansai B, the peptide bond formation of the *cis*- and *trans*-configured HPIs in nocardioazine B proceeded without difficulty. Wang and co-workers attribute this difference to the stereochemistry of the pyrroloindoline partners, which contributes to the efficiency of peptide bond formation.[55, 56] In 2018 another total synthesis of nocardioazine B (**7**) was published starting from a oxindole **18** to form the HPI motif in the building block **19** [Figure 5].[57] In nature, the HPI structural motifs in this natural product are formed via a PTase and a MTase.[58]

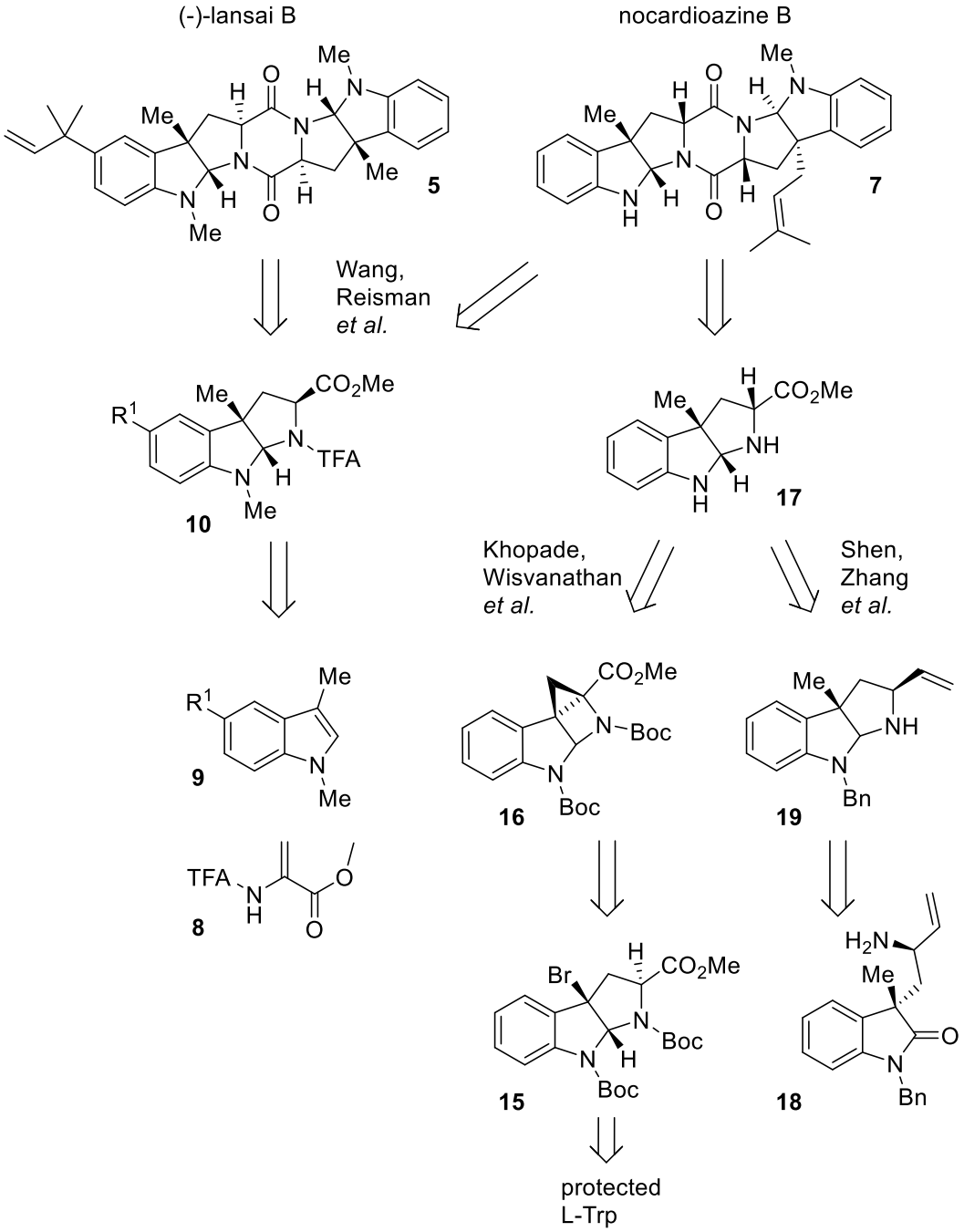

Figure 5: Retrosynthesis of nocardioazine B (**7**) and lansai B (**5**).

This chapter primarily focuses on the two central motifs found in lansai B-like natural products: the DKP core and the HPI motif. The DKP scaffold serves as a foundational structure in many natural products, offering rigidity and structural diversity that contribute to their biological activities.[45] The HPI motif, characterised by its tricyclic framework, plays a critical role in molecular recognition and binding interactions within biological systems.[47, 59]

4.1.1 Diketopiperazine natural products

A prominent class of natural products are the cyclic dipeptides containing the 2,5 DKP structural motif **20** [Figure 6]. DKPs are formed by the condensation of two *α*-amino acids building a six-membered ring with two amide bonds. Natural products containing the DKP motif have a wide range of biological activities making them an interesting target structure for drug discovery [Table 1].[45, 60, 61] Besides the application as therapeutics with antibacterial,[62] antifungal,[63, 64] anticancer,[65, 66] antiviral,[67, 68] and anti-inflammatory[69] activities, DKPs can be used as building blocks in material science. Due to their molecular self-assembly properties driven by their unique hydrogen bonding patterns, they form functional nano- and micro-architectures, which can be used for example as hydrogel or nanotube.[70-72]

The wide range of applications and especially the variety of bioactive properties is influenced by a lot of factors based on the structure: The diversity of the DKPs can be introduced to different positions on the core structure. Due to the peptide bonds in the six membered ring, the core of the structure is semirigid meaning the difference in energy between the planar and the boat form is rather low (1.3 – 1.7 kcal/mol).[73] Additionally, configuration plays an important role in bioactivity as the amino acids as building blocks for the DKP are chiral. The multiple H-bond acceptor and donor functionalities depending on the substituents enable a high affinity to a variety of receptors.[45]

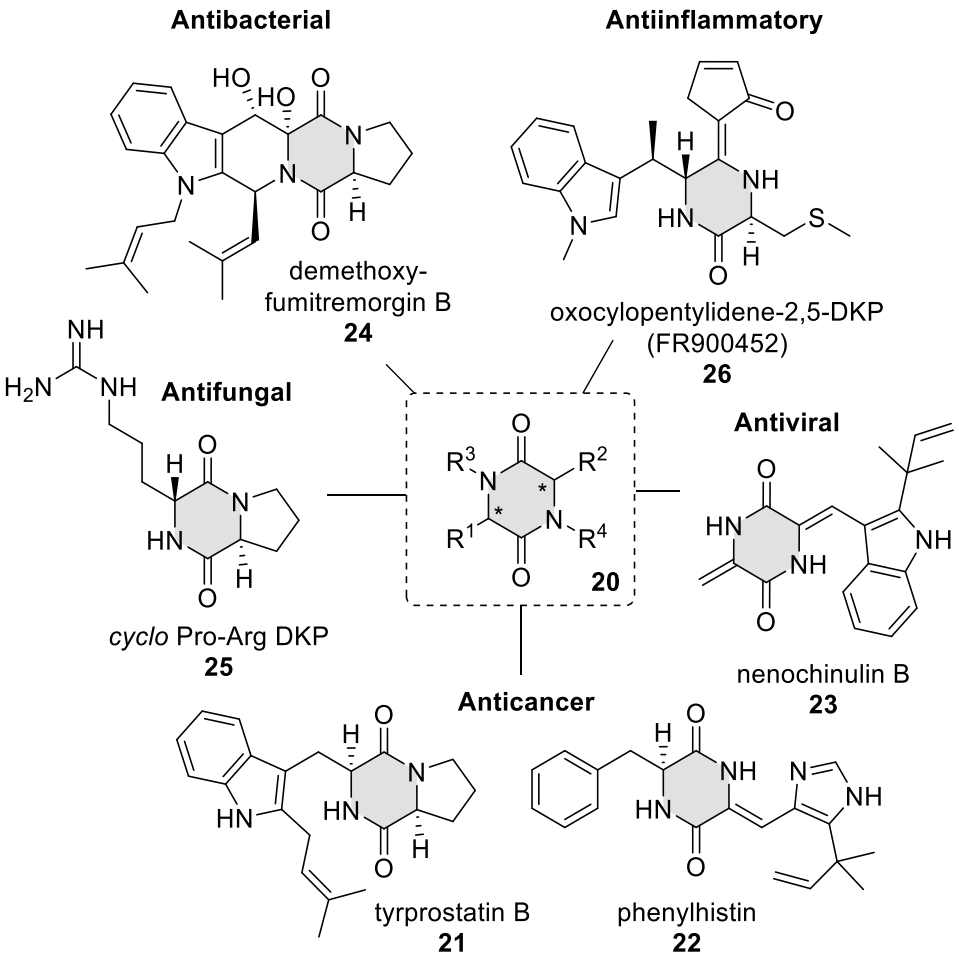

Figure 6. Chemical structures of natural products containing a DKP structural motif **20** (grey) organised by their biological activity.

Table 1: DKP-containing natural products and their biological activity.

Natural product	**Origin (organism)**	**Bioactivity**
Tryprostatin B **21**	*Aspergillus fumigatus*	Mammalian cell-cycle inhibitor[66, 74]
(−)-Phenylhistin **22**	*Aspergillus ustus*	Microtubule binding agent[75, 76]
Neoechinulin B **23**	*Eurotium rubrum* Hiji025	Antiviral effects against the hepatitis C virus[68]
Demethoxy-fumitremorgin B **24**	*Aspergillus fumigatus*	Antibacterial activity against multiple bacterial strains[77]
Cyclo (L-Arg-D-Pro) **25**	*Pseudomonas sp. IZ208*	Chitinase inhibitor[64]
Oxocylopentylidene-2,5-DKP derivative FR900452 **26**	*Streptomyces phaeofaciens*	Anti-inflammatory activity[78]

These examples represent only a small selection of the wide-ranging biological activities associated with the DKP core structural motif. This broad bioactivity combined with its structural adaptability and functional diversity makes it an interesting target for synthesis.

The first described syntheses of DKPs date back to the middle of the 19 century.[79-81] Since then, many different strategies have been developed to produce the DKP core structure **27**. From a retrosynthetic perspective, two main disconnections are the most favourable ones based on the DKP: The disconnection of the amide bond and the disconnection of the C-N bond. Additionally, the cleavage of the C-C bond is found in newer synthetic approaches [Figure 7].[45, 61, 82]

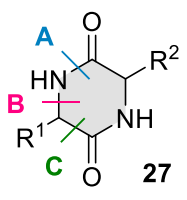

Figure 7: Possible retrosynthetic cuts (A,B and C) of the DKP structural motif.

The amid bound formation is the most commonly used way to create the DKP structure. Even though the dipeptide ester cyclisation to the DKP ring can occur spontaneously starting from a linear dipeptide **28** with an amine and an ester terminus, multiple reaction optimisations were carried out in the past to reduce racemisation and optimise the yield of the desired product.[45, 83-85] One example for a fast method is the microwave assisted DKP formation which is universally applicable to many dipeptides. By heating the dipeptide **28** in water as a solvent for 10 min in the microwave to 140 °C, the DKP **29** is formed without any epimerisation [Figure 8].[86]

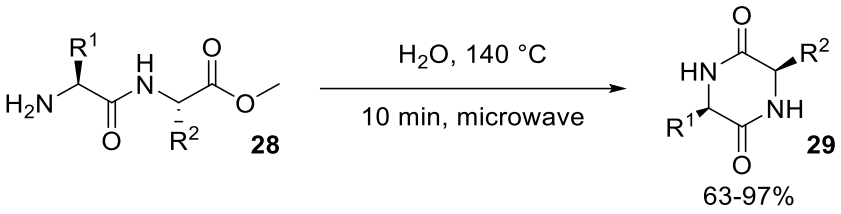

Figure 8: Synthesis of the DKP structural motif via a microwave assisted approach.

The linear dipeptide **30**, which serves as a substrate for this kind of reaction, is usually formed from two orthogonally protected amino acids **31** and **32** coupled by the standard peptide synthesis. This protected peptide **33** yields the final product **30** by deprotection of the amine [Figure 9A].[85, 87] Another approach to form a dipeptide is the Ugi-reaction [Figure 9B].[88] An amine **34**, aldehyde **35**, isonitrile **36** and acid **37** serve as substrates to form the coupled intermediate **38** and allow a huge chemical diversity of the corresponding product **39**.[89, 90]

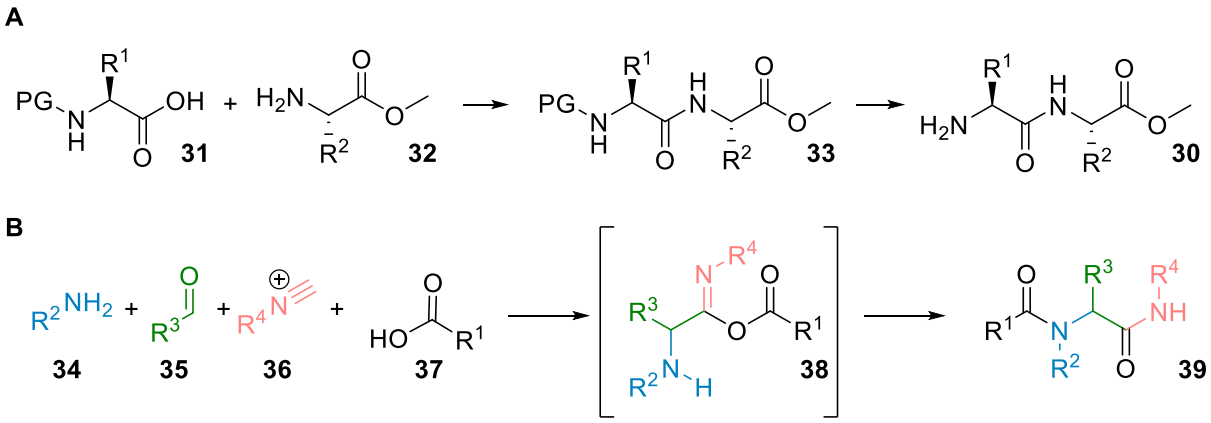

Figure 9: Synthesis of linear dipeptides. A: coupling of two orthogonal protected amino acids **31** and **32** forming the dipeptide **33** followed by the amine deprotection. B: Ugi-reaction of an amine **34**, aldehyde **35**, isonitrile **36** and an acid **37** to form the linear peptide **39**.

The *N*-alkylation is the second most used approach in organic chemistry to form the DKP structural motif. As an example, the ring-closure of two *α*-haloacetamides **40** in presence of a base leads to DKP ring formation in high yields. Still, this synthesis is only applicable for symmetric DKPs like compound **41** [Figure 10].[91]

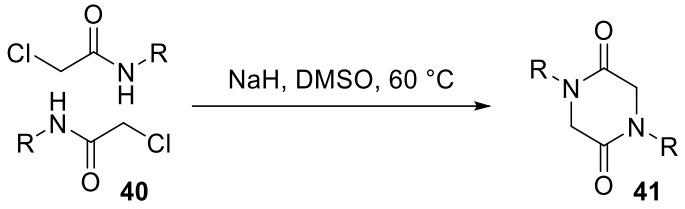

Figure 10: Synthesis of the DKP structural motif via ring-closure of two α-haloacetamides **40** under basic conditions.

The C-C bond formation to construct the DKP structural motif was for example utilised in the asymmetric synthesis of the ABC-ring system of the antitumour antibiotic MPC1001. The DKP unit was generated through a cyclisation process, where an enolate attacks the carbonyl of a phenyl carbamate **42** to form the DKP **43** [Figure 11].

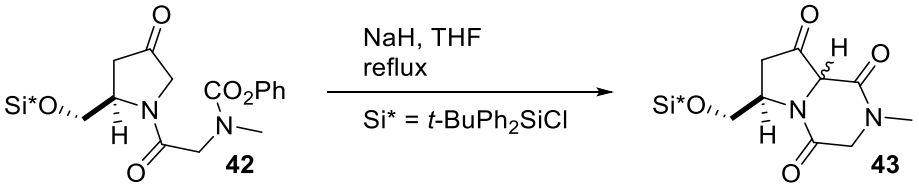

Figure 11: Synthesis of the DKP structural motif via C-C-bond formation.

4.1.2 HPI natural products

The HPI structural motif **44** is prevalent in multiple biologically active natural products.[44-46, 92] The rigid tricyclic structure promotes high affinities for various protein targets due to hydrophobic interactions.[45, 47, 93] HPI natural products can be categorised based on the substituent at the *C3*-position: substituent-free (R = H; Type A), hydroxylated (R = OH; Type B), alkylated (R = alkyl; Type C), arylated (R = Ar; Type D), and dimeric HPIs (Type E) [Figure 12].[59] Biochemically, various enzyme classes, such as monooxygenases,[77, 94-98] MTases,[87, 99, 100] and PTases,[101-103] are known to be involved in the biosynthesis of these natural products by catalysing an intramolecular cyclisation step of a substituted indole, leading to dearomatisation and the formation of HPI structural motif.[59]

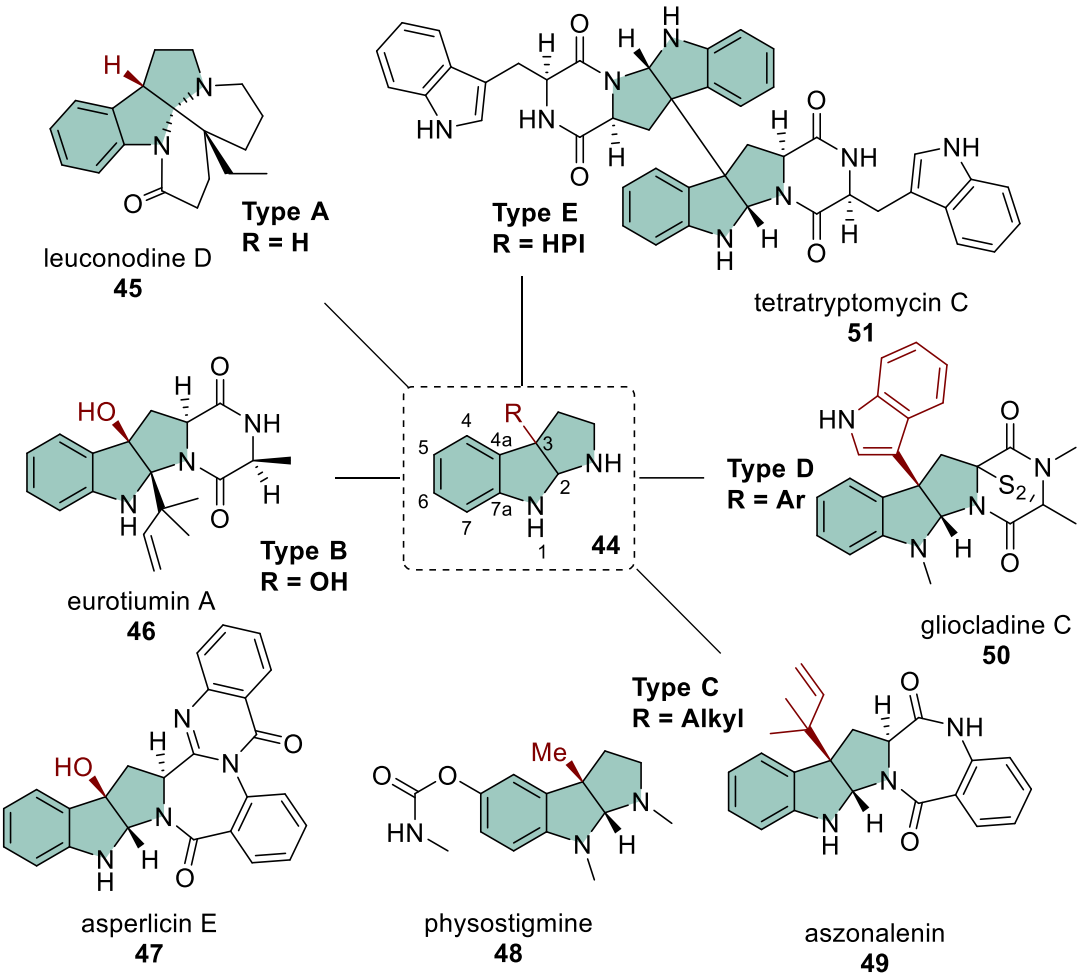

Figure 12. Chemical structures of natural products containing the HPI structural motif organised by their substituent at the *C3*-position: Substituent-free (R = H; Type A), hydroxylated (R = OH; Type B), alkylated (R = alkyl; Type C), arylated (R = Ar; Type D), and dimeric HPIs (Type E).

Natural products containing the HPI structural motif exibit various different biological activities [Figure 12]: leuconodine D (**45**) (Type A), isolated from the stem-bark extract of *Leuconotis griffithii*, shows cytotoxicity toward KB cells.[104] Eurotiumin A (**46**), isolated from the fungus *Eurotium* sp. SCSIO F452, and asperlicin E (**47**), isolated from the fungus *Aspergillus alliaceus,* contain a hydroxy-group at the *C3*-position (Type B).[105, 106] Asperlicin E (**47**) is known to be an cholecystokinin antagonist.[106] Alkylation often influence the biological activity of compounds due to an increased lipophilicity and membrane permeability.[107, 108] The *C3*-alkylated HPI containing natural products (Type C) contain mostly either an methyl- or a prenylgroup. Physostigmin (**48**), isolated from the seeds of *Physostigma venenosum,* is methylated at the *C3*-position and is a known acetylcholinesterase inhibitor.[109, 110] Aszonalenin (**49**), isolated from *Neosartorya fischeri,* is a prenylated HPI natural product active as *α*-glucosidase inhibitor.[111, 112] Gliocladines C (**50**) (Type D), isolated from *Gliocladium roseum*, shows nematicidal activity against *Caenorhabditis elegans* and *Panagrellus redivivus*.[113] *C3*-dimeric HPI natural products (Type E) contain two HPI cores connected by a *C3*–*C3* linkage. For example, linkage in tetratryptomycin (**51**) is created by the P450 TtpB1.[114] Dimeric HPI natural products and their derivatives exhibit various biological activities such as anticancer or antimicrobial activities.[59, 115]

The interesting molecular tricyclic structures of the HPI motif, along with the various biological activities, have made these compounds highly desirable targets for synthesis. This has led to extensive research efforts within the synthetic community over the past few decades. Still, achieving the stereoselective synthesis of HPI structural motif remains challenging with traditional organic synthesis methods.[47-51] Four main strategies have been developed to achieve the formation of the HPI motif **52** [Figure 13].[47]

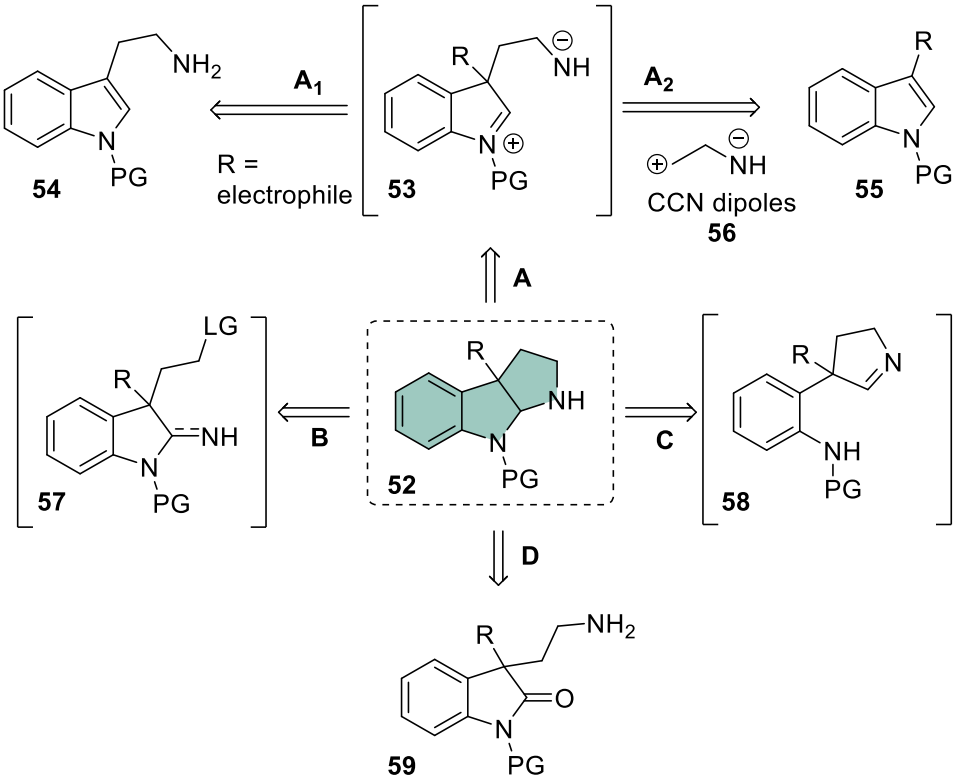

Figure 13: Retrosynthetic routes towards the HPI structural motif **52**. A: indole-based strategy via cyclisation (A1) or cycloaddition (A2), B: non-indole-based cyclisation strategy, C: aniline-based strategy, D: oxoindole-based strategy.

Path A, starting from an existing indole core **53**, includes a cyclisation (A1) and a cycloaddition (A2) approach: Emulating nature, current synthetic strategies emphasise a catalytic asymmetric dearomatisation reaction of indoles to produce HPIs starting from tryptophan or tryptamine **54** (path A1). In this approach, an asymmetric *C3*-functionalisation with an electrophile leads to the subsequent cyclisation towards the HPI structural motif.[51, 116, 117] For the alternative catalytic asymmetric dearomative [3+2] cycloaddition (path A2), the indole **55** reacts with a CCN 1,3-dipole **56** forming the same intermediate **53**.[49, 118, 119] Path B involves a different cyclisation strategy involving the intermediate **57**, which is not necessarily derived from an indole.[120] In path C, the middle ring of the HPI structural motif is formed last from the aniline intermediate **58**.[121, 122] In addition to these paths, the HPI motif can be formed from chiral 3,3-disubstituted oxindoles **59** via reductive cyclisation (path D).[48, 123, 124]

As described before, biological activities of pyrroloindolines are greatly influenced by the different moieties attached at the *C3*-position.[47, 59] Therefore, the synthetic flexibility to introduce a variety of substituents at the *C3*-carbon is a very important field of research.

Focussing in *C3*-alkylation, Stark's research group explored selective prenylation of a tryptophan derivative **60**. By using [Pd(PPh$_3$)$_4$] as a catalyst without a ligand and the prenyl donor **61**, they obtained linear prenylated products **62** and **63** in a 1:1 ratio. However, when [Ir(COD)Cl]$_2$ was used with a phosphoramidite ligand (**64**, L4), branched prenylation products **65** and **66** were obtained. By switching the configuration of the ligand, they were able to generate the corresponding isomers with a high selectivity. Notably, their studies also included reversed prenylation on a DKP-based substrate, demonstrating the applicability of this approach for such desired substrates [Figure 14].[125]

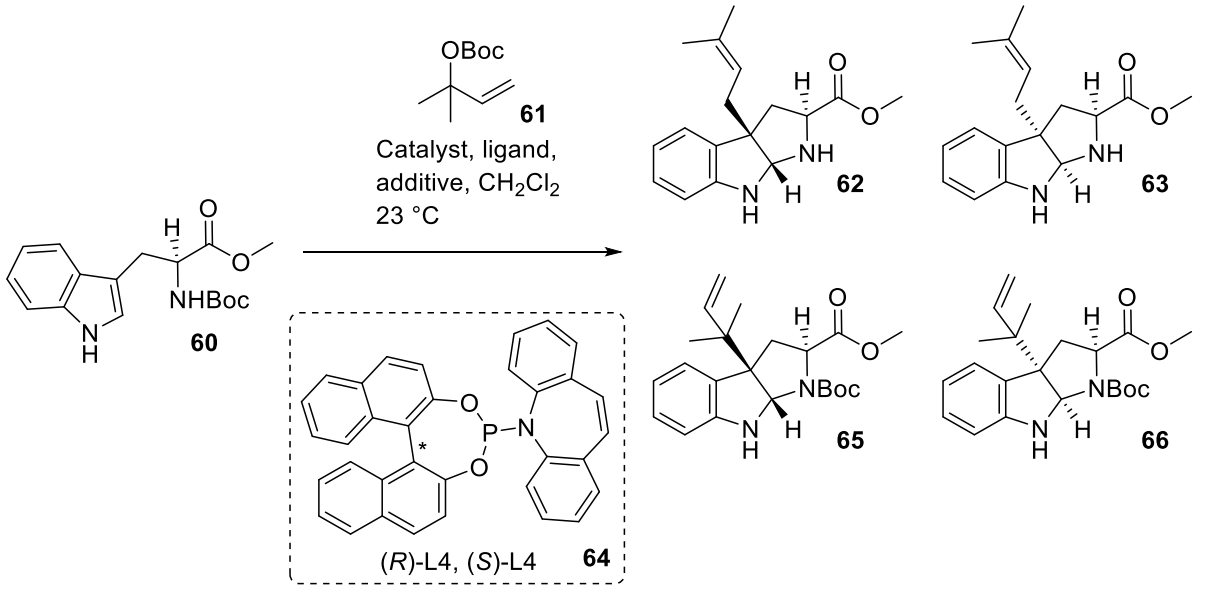

Catalyst and ligand	Additive	Branched/linear	*Trans*/*cis*	Yield [%]
[Pd(PPh$_3$)$_4$]	Et$_3$B, DBU	<1:20	1:1	87
[Ir(COD)Cl]$_2$, (*R*)-L4[a]	Ph$_3$B, TBD[b]	>20:1	>20:1	83
[Ir(COD)Cl]$_2$, (*S*)-L4[a]	Ph$_3$B, TBD[b]	>20:1	<1:20[c]	n.d.

Figure 14: Chemical prenylation reactions of protected L-Trp **60** forming different isomers based on the catalytic system. [a] [Ir(COD)Cl]2 (2.5 mol%), L4 (5 mol%), 1-benzyl-3-methylimidazolium chloride (5 mol%). [b] Base (10 mol%). [c] Determined by ^{1}H NMR spectroscopy of the crude reaction mixtures. DBU=1,8-diazabicyclo[5.4.0]undec-7-ene, TBD=1,5,7-triazabicyclo[4.4. 0]dec-5-ene

One of the most difficult substituents to introduce in a stereoselective manner is the methyl group. As *C3*-methylated natural products like physostigmine (**48**) are known for their biological activity since the end of the 19th century,[126] many strategies have been developed to synthesise them. In 1935, the first total synthesis of physostigmine (**48**) was published: The HPI motif was formed via path D with the oxindole **67** as starting material. Resolution of the racemic mixture of intermediate **68** was accomplished by crystallization, employing D-camphorsulfonic acid and D-tartaric acid as chiral resolving agents. The (*S)*-amine **69** was reduced to form the HPI precursor **70**, which was converted into physostigmine **48** in two steps [Figure 15].[127]

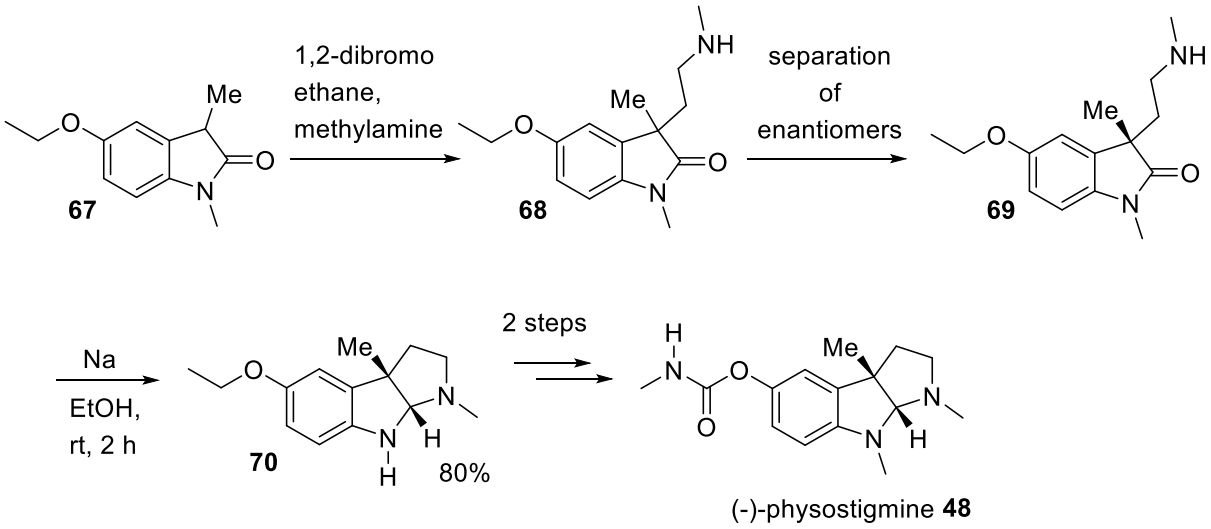

Figure 15: Oxoindole based (path D) synthesis of physostigmine (**48**).

Over the past decades, considerable effort has been devoted to the synthesis of chiral 3,3′-disubstituted oxindoles, which serve as key precursors to the HPI motif [Figure 16].[51, 128-131] For example, in 1993 Overman and co-workers reported a catalytic asymmetric Heck cyclization of (Z)-2-methyl-2-butenanilide (**71**), delivering the corresponding oxindole aldehyde **72** in 84 % yield with 95 % *ee*.[132] Additionally, transition-metal-catalyzed asymmetric allylic alkylation (AAA) strategies have been developed to access the 3,3-disubstituted oxindoles. In 2006, Trost and co-workers introduced the first molybdenum-catalyzed asymmetric allylation protocol for the stereoselective installation of the quaternary *C3* center in the oxindole substrate **73** with the ligand **74**, affording allylated product **75**.[133] More recently, in 2020, a nickel-catalyzed cycloisomerization reaction with ligand **76** of the substrate **77** was used to form the desired configuration at the *C3*-position of the corresponding product **78** [Figure 16].[134, 135]

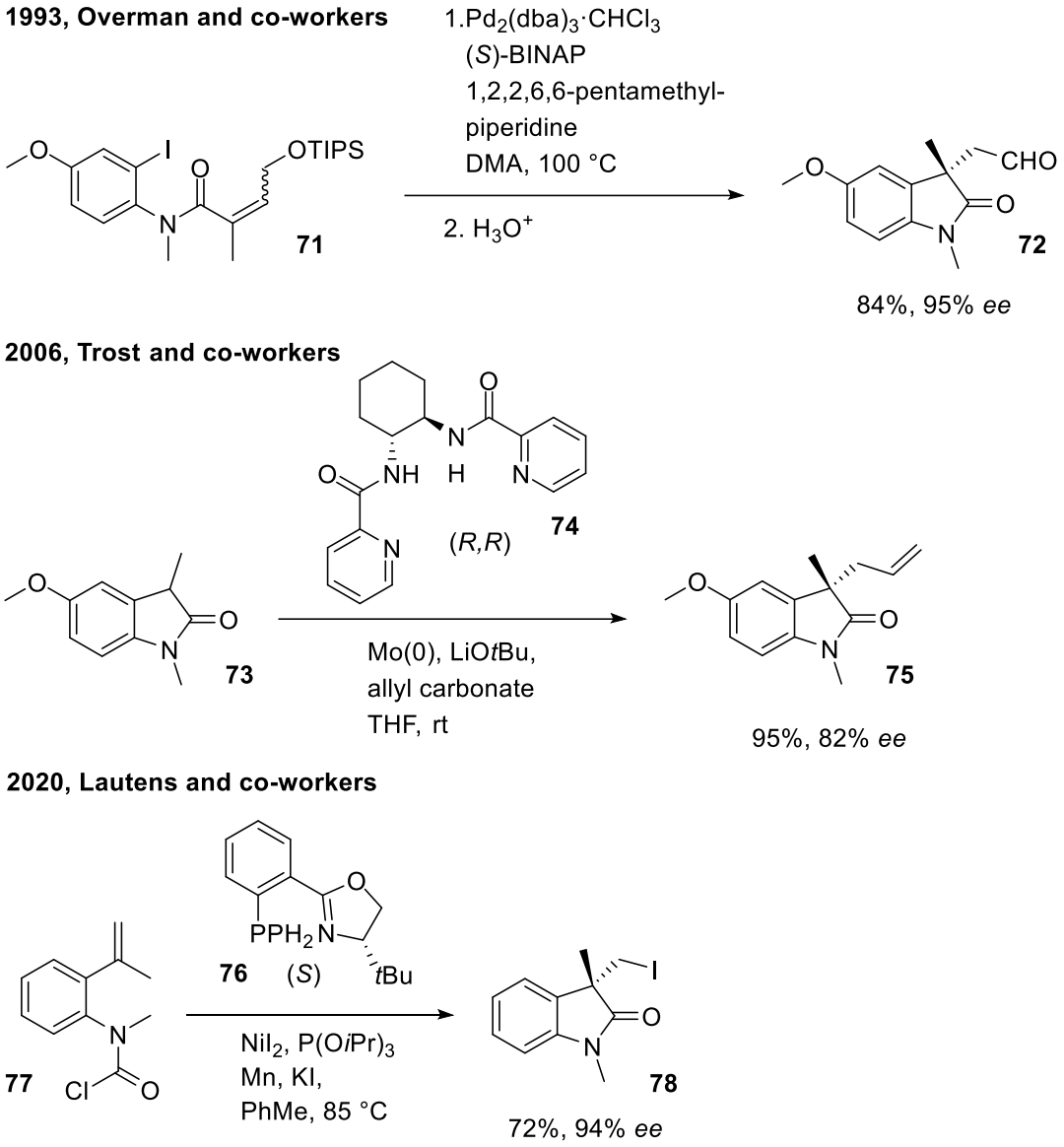

Figure 16: Synthesis of 3,3′-disubstituted oxindoles as precursor for the HPI formation by Overman[132], Trost[133] and Lautens[135] and co-workers.

An alternative biomimetic approach towards the HPI (path A1) was published in 2017, where a direct *C3*-methylation of the indole **79** was used to synthesise the HPI precursor **80** of the racemic physostigmine analogue esermethol (**81**).[136] In this reaction, methyl iodide functions as the methylating agent, targeting the *C3*-position and inducing the spontaneous formation of the HPI motif in a not stereoselective manner [Figure 17]. Despite extensive efforts to develop an efficient methylation protocol, the *C3*-methylated HPI scaffold still presents significant challenges in achieving the required stereoselectivity.

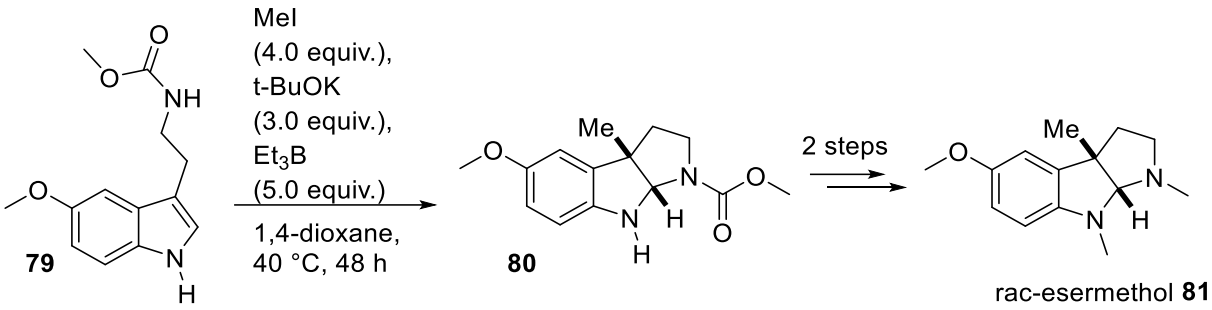

Figure 17: Indole based (path A1) synthesis of esermethol (**81**).

4.2 Biosynthesis of lansai B-like natural products

As previously described, lansai B (**5**) and nocardioazine B (**7**) both feature a seven-ring system composed of a central DKP core flanked by HPI motifs on either side [Figure 3]. Despite their structural resemblance, these compounds exhibit notable differences in their configuration, as well as distinct methylation and prenylation patterns. However, it is likely that their biosynthesis involves the same class of enzymes. In 2023, the biosynthetic pathway of nocardioazine B (**7**) was investigated, revealing the gene cluster and characterizing the enzymes involved: A cyclodipeptide synthase (CDPS) nozA or ncdA, an isomerase NozR, a PTase NozPT and a bifunctional MTase NozMT.[58] The CDPS acting on two molecules of L-tryptophanyl-tRNA (**82**) forms the DKP structural motif **3a** by condensing the two tryptophans carried by each tRNA. The CDPS genes involved in the biosynthesis of nocardioazine B (**7**) are located in a gene cluster (nozA/ncdA) separate from the noz2 cluster encoding the MTase NozMT. As the configuration in the DKP ring of nocardioazine is (1*R*,4*R*), an isomerase NozR is required for inverting the configuration at these stereogenic centres to form intermediate **3b**. Next, a PTase NozPT is prenylating one indole moiety of the substrate on the *C3*-position, forming the first HPI **83**. The *N*-methylation of the prenylated HPI towards the intermediate **84** as well as the subsequent *C3*-methylation of the other (non-prenylated) indole of the DKP are catalysed by the same MTase NozMT, yielding nocardioazine B (**7**) [Figure 18].

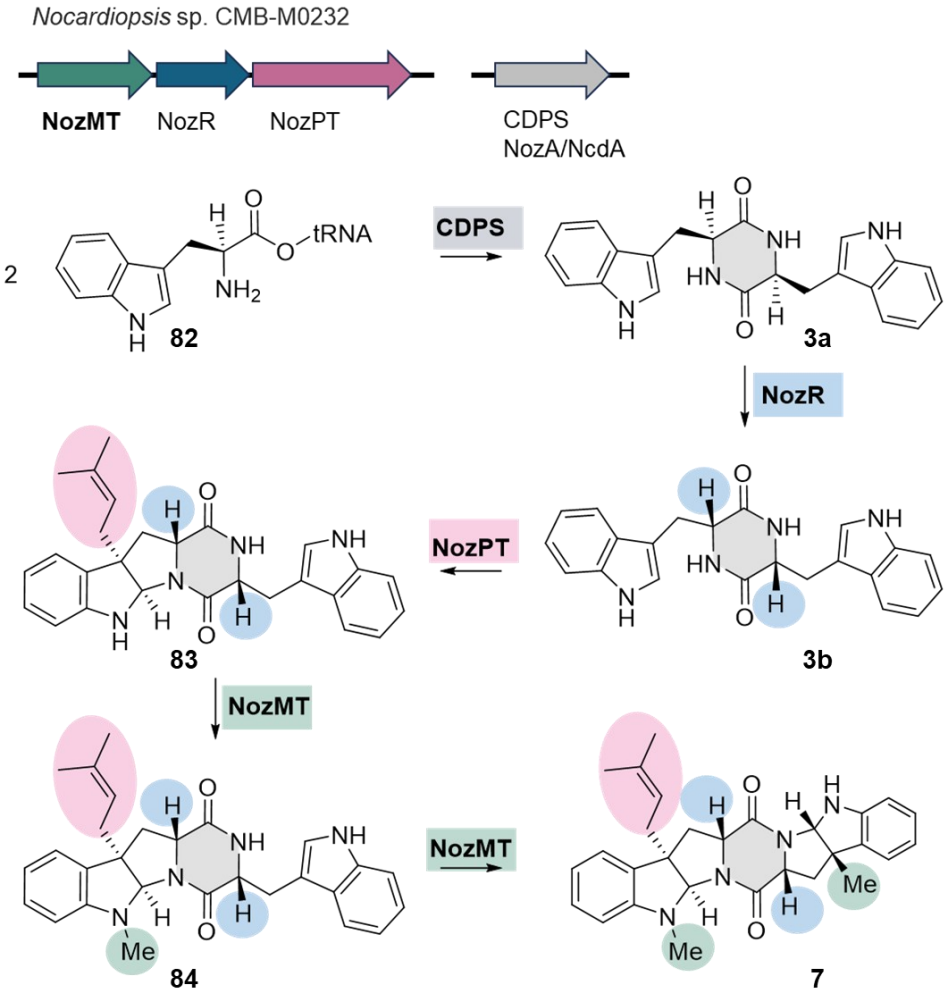

Figure 18: Gene cluster of nocardioazine B (**7**). The MTase is highlighted in green, the PTase in pink, the isomerase in blue and the CDPS in grey. The structural elements created by these enzymes are highlighted in the corresponding colour in the molecule.

The biosynthesis of lansai B (**5**) was unknown until recently[a], but based on its structural features, an enzyme forming the DKP core, like the CDPS in the biosynthesis of nocardioazine B (**7**), a PTase and a MTase are necessary to achieve all individual structural motifs [Figure 19]. This chapter focuses on analyzing these enzyme classes, with particular emphasis on the MTases.

[a] During the finalization process of this dissertation, a biosynthetic pathway for lansai B in *Streptomyces albus* J1074 was proposed by Duan *et al.[137] H. Duan, M. Zhang, Z. Chen, X. Wang, F. Xiao, W. Li, Bioorg. Chem.* ***2025****, 160, 108448; 'Unveiling a pyrroloindoline diketopiperazine biosynthetic pathway featuring a phytoene-synthase-like family prenyltransferase with distinct regioselectivity', 10.1016/j.bioorg.2025.108448.*, which aligns with the results presented in Chapter 5.7. and will be discussed in the context of our own results presented.

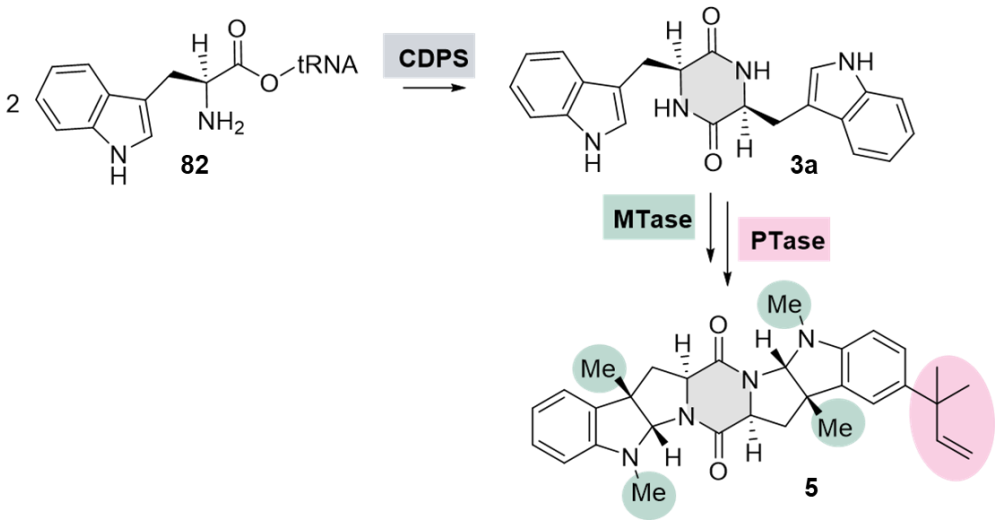

Figure 19: Potential biosynthesis of lansai B: An CDPS forms the cWW **3a** as initial step. A MTase and a PTase are involved to modify the cWW **3a** towards lansai B (**5**).

4.2.1 DKP-formation: Cyclodipeptide synthases

In nature, the formation of the DKP motif occurs via enzymatic pathways and nonenzymatic pathways. For example, the histidine-proline DKP cHP **85** is formed by a non- enzymatic process as a metabolite of the hypothalamic tyrotropin-releasing hormone [Figure 20]. The cyclic form was proven to have a higher stability against peptidases than the linear form.[138-140] Two enzyme families, the non-ribosomal peptide synthetases (NRPSs) and the CDPSs, have been identified as catalysts for the DKP structural motif. NRPSs are large (>100 kDa) multimodular enzymes, which are able to synthesise structurally and functionally diverse peptides from free amino acids.[141, 142]

In contrast to the well-studied NRPSs, CDPS are small (~30 kDa) enzymes, which have been reported first in 2009:[143] The albonoursin (**86**) biosynthesis pathway was the first DKP biosynthetic pathway discovered to involve a CDPS enzyme.[143, 144] Albonoursin (**86**), an antibacterial DKP produced by *Streptomyces noursei*, is derived from the precursor *cyclo* (L-Phe-L-Leu) cFL **87** [Figure 20].[145] In this study, scientists uncovered that the CDPS AlbC uses tRNA-bound amino acids as substrates for the formation of the DKP structural motif. Following its synthesis by AlbC, the cFL cyclodipeptide **87** undergoes further modification by a cyclodipeptide oxidase, which catalyses the *α*,*β*-dehydrogenation of the amino acid side chains, converting cFL **87** into the final product, albonoursin (**86**).[143] As AlbC was the first identified CDPS, the numbering of the amino acids for sequence alignment with other CDPSs refers to the AlbC sequence.

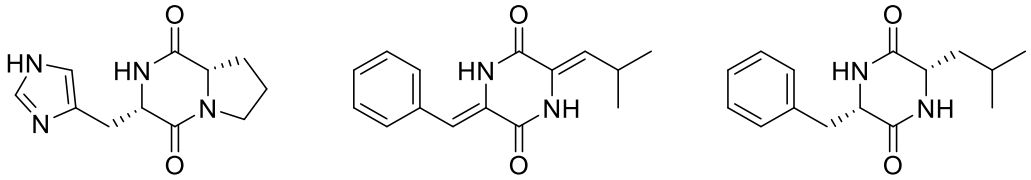

Figure 20: Structures of cHP **85** and the natural product albonoursin (**85**) and its pre-cursor molecule cFL-DKP **87**.

AlbC and other CDPS enzymes were crystallised to gain insights into their catalytic site architecture and underlying mechanisms.[146-149] Despite sharing only about 27% sequence identity, the structures of AlbC and other crystallised CDPSs (Rv2275 and YvmC-Blic) exhibit a high degree of structural alignment. Each enzyme has a compact *α*/*β* fold, featuring a central *β*-sheet composed of five parallel *β* strands flanked by *α*-helices. The overall structure includes a Rossmann-fold domain, followed by a helical region of three helices.[146]

CDPS enzymes utilise a ping-pong-type catalytic mechanism, initiating with the binding of the first aminoacyl-tRNA (aa-tRNA), which is transferred to a conserved serine residue **88** (Ser37), forming an aminoacyl-enzyme intermediate.[146] In 2014, further investigations into this mechanism revealed insights through the first crystal structure of a CDPS (AlbC) complexed with an intermediate cFF-analogue and site-directed mutagenesis [Figure 21].

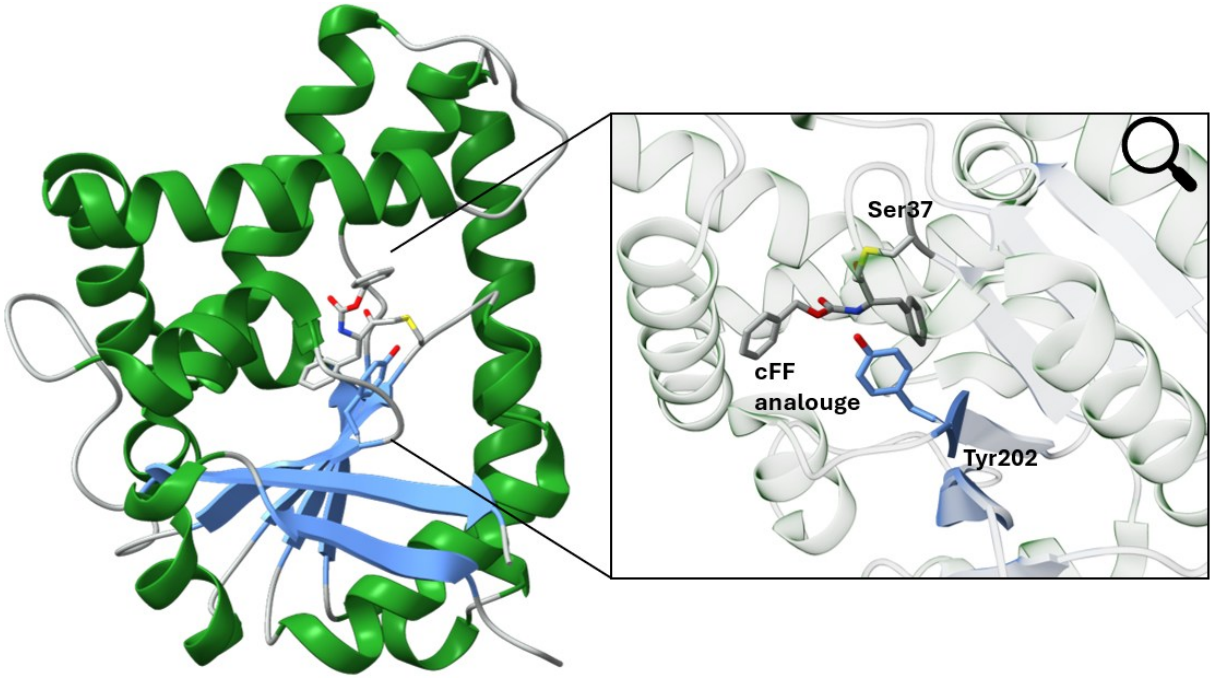

Figure 21: Crystal structure of AlbC bound with a cFF analog (PDB id: 4Q24). The catalytic side with the amino acids Ser37 and Y202 is highlighted.

This study demonstrated that a second phenylalanine **89** binds to the first phenylalanine, which remains attached to the serine in the intermediate **90**, forming a dipeptidyl enzyme **91**. In the final step, a tyrosine residue (Tyr202) deprotonates the primary ammonium group of the second phenylalanine in intermediate **91**, creating a nucleophile that attacks the enzyme ester bond, leading to the formation of the cyclodipeptide product **92** [Figure 22].[150]

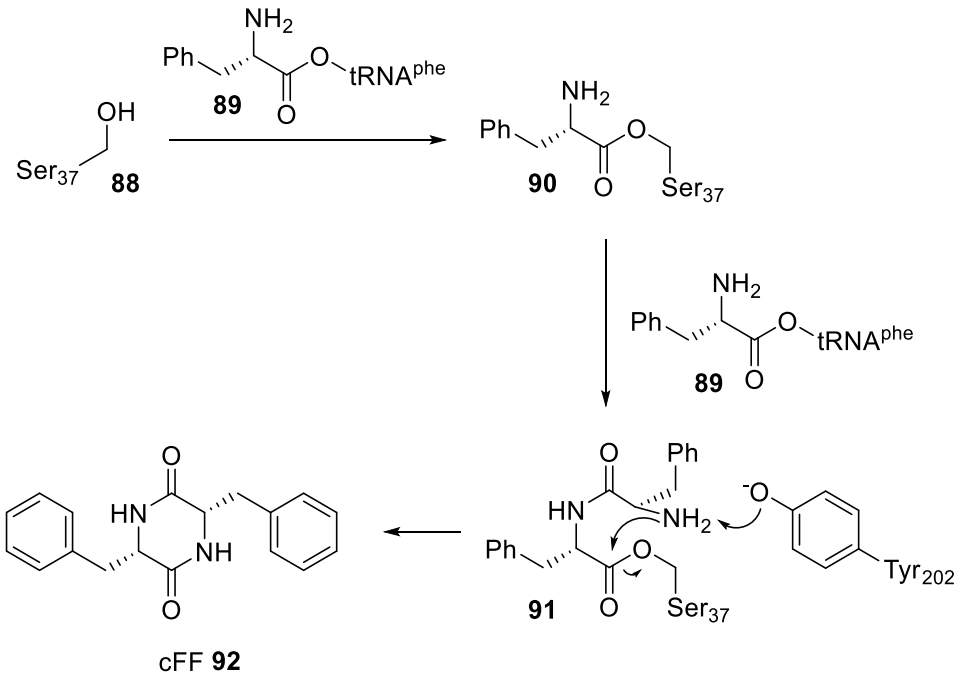

Figure 22: Mechanism of AlbC creating the cFF DKP **92**.

The highly conserved catalytic residue Y202 plays a key role in a hydrogen bond network with residues N40 and H203 in AlbC, ensuring the precise positioning of the loops that contain the catalytic residues. In 2015, a study of 51 CDPSs revealed that about half of the enzymes possess the 'N40, H203' pair, while others have an 'X40, P203' pair, where 'X' represents a non-conserved residue leading to the classification of CDPSs into two subfamilies: 'NYH' and 'XYP,' based on the 'X40, Y202, X203' sequence pattern.[151]

The two aminoacyl-tRNAs bind to separate pockets within the enzyme. The first aminoacyl-tRNA attaches to pocket P1, where its aminoacyl group interacts with basic residues located on a helix structure. The second aminoacyl-tRNA binds to pocket P2, where its tRNA moiety interacts with a flexible loop. Pocket P1 is characterised by eight specific residues (33, 35, 65, 67, 119, 185, 186, 200), while P2 is defined by seven residues (152, 155, 156, 159, 204, 206, 207) [Figure 23]. Since these residue positions are conserved across CDPSs and their chemical properties correlate with the specific aminoacyl groups they recognise, these consensus motifs can be used alongside phylogenetic data to predict the main products of uncharacterised CDPSs.[151, 152]

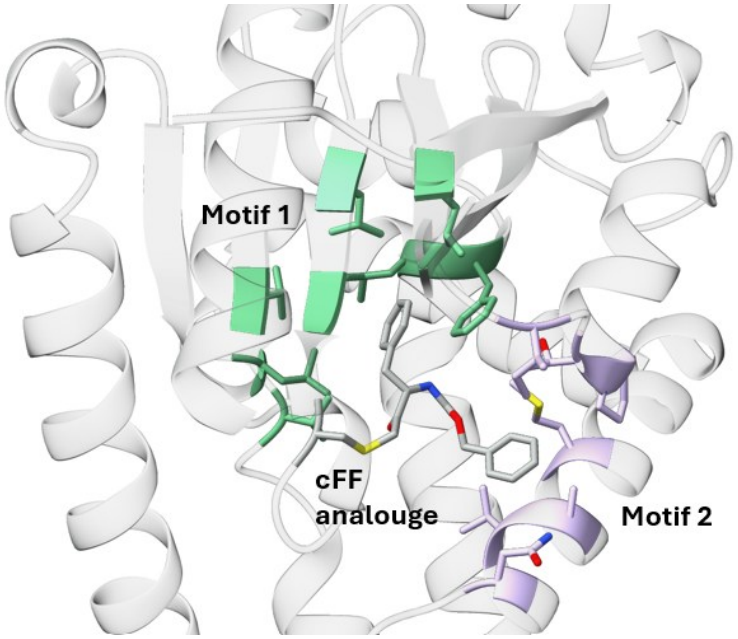

Figure 23: Crystal structure of AlbC bound with an cFF analog. The consensus motifs are highlighted in green (P1) and violet (P2).

The formation of cyclodipeptides frequently represents the initial step in creating more complex DKPs, which are produced after further modification reactions.[87, 153, 154] The most common DKP natural products are derived from the amino acids tryptophan and proline.[45] When proline is part of cyclic dipeptides, the six-membered DKP ring fuses with a five-membered imposing rigid constraints.[155-157] In the case of tryptophan-based DKPs, further processing often occurs, for example by forming the HPI ring systems which also increases rigidity.[53, 59]

4.2.2 Methylation: SAM dependent Methyltransferases

Methylation is a fundamental reaction in all living organisms, essential for various biological processes like the methylation of biopolymers like nucleic acids[158, 159] and proteins[160, 161] or for cell signaling.[162, 163] *S*-adenosyl-L-methionine (**93**, SAM) dependent MTases are the focus of numerous recent studies due to their diverse applications and significance in biomedical research.[164, 165] SAM-dependent MTases catalyse the methylation of a substrate (Nu) with SAM (**93**) as methyl source forming *S*-adenosyl homocysteine (**94**, SAH) [Figure 24].

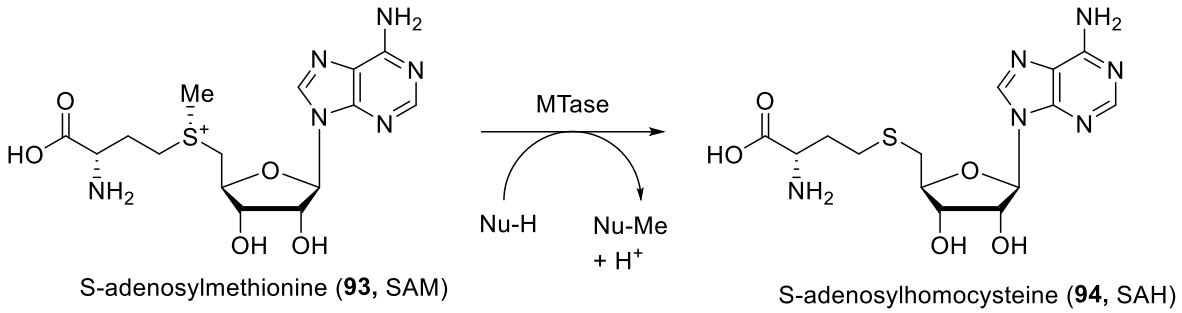

Figure 24: General reaction scheme for a SAM-dependent MTase: The methyl group is transferred from SAM (**93**) to the substrate (Nu) with SAH (**94**) as byproduct.

SAM-dependent natural product MTases are structurally diverse and are often involved in the secondary metabolism, where the methylation of various substrates often affects the biological activities of the resulting natural product.[165] The methyl acceptor atom on the substrate usually is oxygen (54%), nitrogen (23%), carbon (18%) or sulphur (3%).[164, 165] The ability of these enzymes to selectively methylate various substrates offers significant potential for therapeutic interventions and biocatalytic applications.

4.2.2.1 Pharmacological reasons for methylation

Having a look at the top 200 small molecule drugs by retail sales in 2022, three-quarter are methylated.[166] Wermuth stresses in the book “The Practice of Medicinal Chemistry” the importance of methyl groups for drug development:

“The methyl group, so often considered as chemically inert, is able to alter deeply the pharmacological properties of a molecule.”[167]

The reasons for this are diverse: the addition of methyl groups generally increases the lipophilicity of a compound, enhancing its solubility in biomembranes. These biomembranes act as barriers for the passage of compounds from the gastrointestinal tract to the bloodstream and target tissues, so increased lipophilicity can improve bioavailability.[167-170] In some other cases, methylation can also boost water solubility, which is crucial for extremely nonpolar molecules. For instance, methylation can alter the shape of a molecule, making it more globular, which is energetically favoured due to entropic effects. As an example, neopentanol (**95**), which has a more globular structure, is more soluble in water than pentan-2-ol (**96**) or n-pentanol (**97**) [Figure 25].[167, 171] In addition to this effect, methylation can increase the water solubility by hindering various intermolecular interactions.[167, 172]

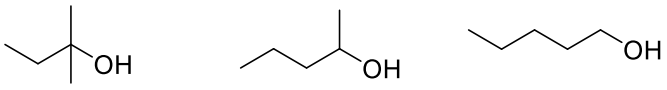

95 12.2 g/100 g H_2O | **96** 5 g/100 g H_2O | **97** 2.4 g/100 g H_2O

Figure 25: Chemical structures of pentan-1-ol (**97**), pentan-2-ol (**96**) and 2-methyl-butan-2-ol (**95**) and the solubility of these alcohols in water (g/g).

Another aspect of the influence of methyl groups for the biological activities of compounds are conformational effects.[167] The steric hindrance from an attached methyl group can impact ligand-receptor interactions. For example, methylation of the p38*α* MAP kinase inhibitor **98** with a biphenyl core structure resulted in a 200-fold increase in its inhibitory activity. This enhancement is due to the conformational preorganisation of the methylated molecule **99**.[173] The ortho-substitution of the biphenyl system changes the interphenyl dihedral angle from 30–40° to approximately 55° [Figure 26].[174] This adjusted conformation is similar to the conformation of the inhibitor within the enzyme, thereby improving its activity.[173]

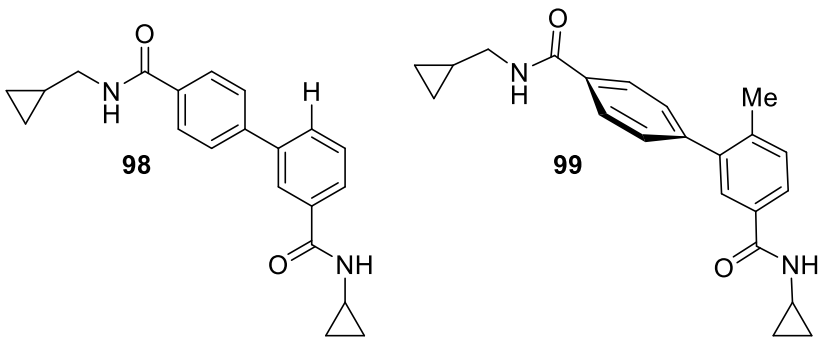

Figure 26. Chemical structures of the p38α MAP kinase inhibitor **99** and its demethylated precursor molecule **98**. The ortho-methylation on the biphenyl causes a conformational change.

A similar conformational effect of ortho-methylation can be observed in the antiarrhythmic drug lidocaine (**100**). Lidocaine's structure is derived from the natural product cocaine (**101**), an alkaloid found in coca leaves.[175, 176] Through molecular simplification in multiple steps, eucaine (**102**) and procainamide (**103**) were developed.[177] The final step, ortho-methylation, induces a conformational twist in the molecule [Figure 27]. This change, along with the steric hindrance of the methyl groups, protects lidocaine from amidases that could hydrolyze the amide bond at the centre of the molecule.[172, 178]

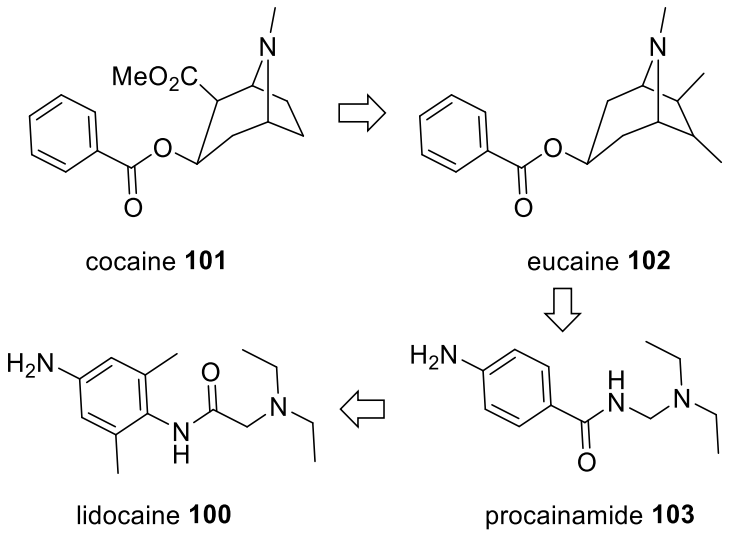

Figure 27. Development of lidocaine (**100**) starting from the natural product cocaine (**101**).

The half-life of a drug is a crucial factor for its effectiveness. In the case of lidocaine (**100**), methylation extended its half-life, but an excessively long half-life can be problematic due to drug accumulation and persistent side effects.[172] Celecoxib (**104**), used to treat degenerative joint diseases and chronic polyarthritis due to its inhibitory effect on cyclooxygenase 2 (COX-2), was developed from a fluorinated analog **105**.[179] The predecessor drug had a half-life of 117 hours, leading to accumulation of the drug causing side effects. In contrast, the methylated celecoxib (**104**) has a half-life of 12 hours, as it is metabolised by cytochrome P450 on the methylated position to a hydroxylated analogue **106**, which is only a weak inhibitor of the target protein and can be even further metabolised [Figure 28].[179-181]

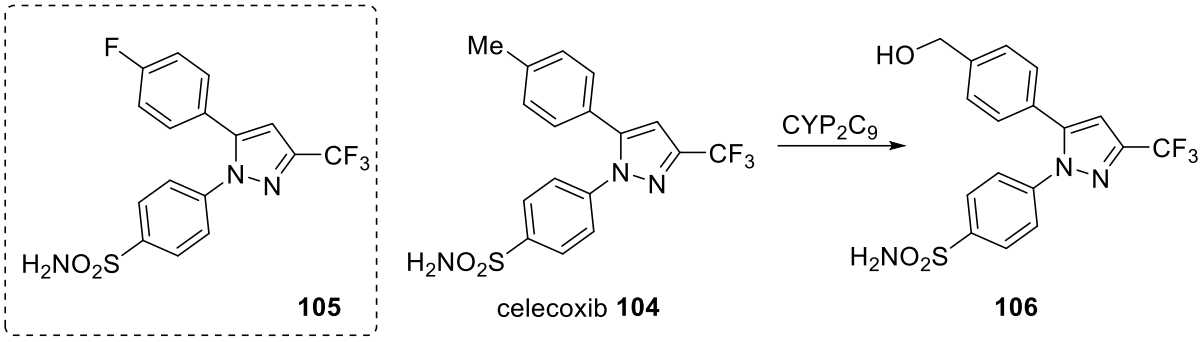

Figure 28. Chemical structures of celecoxib (**104**) and its fluorinated predecessor molecule **105**. Celecoxib (**104**) can be oxidised via a P450 (CYP_2C_9).

All these described effects are part of the "magic methyl effect." Some of these parameters can be predicted and calculated, others are individual and not transferable to other structures. Because of this magic methyl effect, the process of identifying advantageous methylation positions in a molecule is a known practice in the pharmaceutical industry.[182, 183]

One of the most prominent examples of the "magic methyl effect" is morphine (**107**). Morphine (**107**) is an analgesic that acts as an antagonist of opioid receptors in the central nervous system.[184] Removing the nitrogen's methyl group yields normorphine (**108**), which has reduced activity compared to morphine (**107**). The decreased lipophilicity hinders its ability to cross the blood-brain barrier.[185-187] Codeine (**109**) has an additional methyl group at the phenolic position of morphine (**107**). Since the hydroxyl group at this position is crucial for hydrogen bond interactions with the receptor site, methylation decreases the activity in this case.[185, 188] However, methylating the other hydroxyl group does not impact receptor binding but does increase the drug's lipophilicity. As a result, heterocodeine's (**110**) activity is significantly higher than that of morphine (**107**) [Figure 29][172, 189, 190]

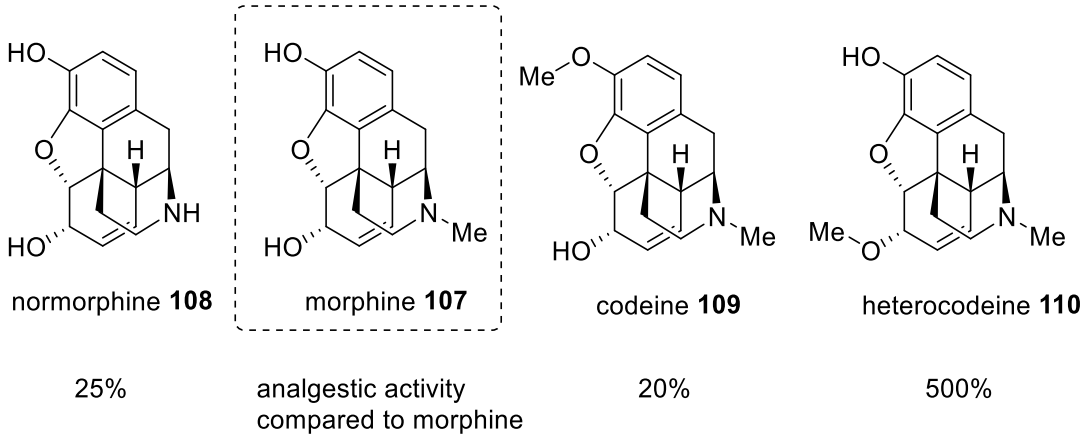

Figure 29. Chemical structures of normorphine (**108**), morphine (**107**), codeine (**109**) and heterocodein (**110**). Their analgesic activity is given in percentage compared to morphine.[167]

4.2.2.2 Structure of methyltransferases

MTases are categorised into five main classes based on their structural characteristics:[191]

The largest group, Class I, features a Rossmann-like superfold [Figure 30] and performs methylation via an S_N2-type mechanism with high selectivity.[192] The *α*/*β*-class Rossmann fold is one of the most common structural motives in enzymes.[193] It consists of six to seven *β*-strands connected via hydrogen bonds, which are intercalated by *α*-helices. In MTases, the last *β*-strand is oriented in antiparallel with respect to the others six strands.[194] The binding position of SAM (**93**) is located along the *C*-terminal end of the core *β*-sheet (strain 1-III), where SAM (**93**) is bound due to a network of hydrogen bonds and van der Waals interactions. Three motifs are important for the binding: Motif I [(V/I/L) (L/V) D/E (V/I) G (G/C) G (T/P) G] contains the GxGxG sequence being in contact with the carboxypropyl portion of SAM (**93**), the acidic residue in Motif II [(P/G) (Q/T) (F/Y/A) D A (I/V/Y) (F/I) (C/V/L)] forms hydrogen bonds with the ribosyl part of the cofactor and the motif III [L L (R/K) P G G (R/I/L) (L/I) (L/F/I/V) (I/L)] is located on the adenin-moiety.[165, 195-198]

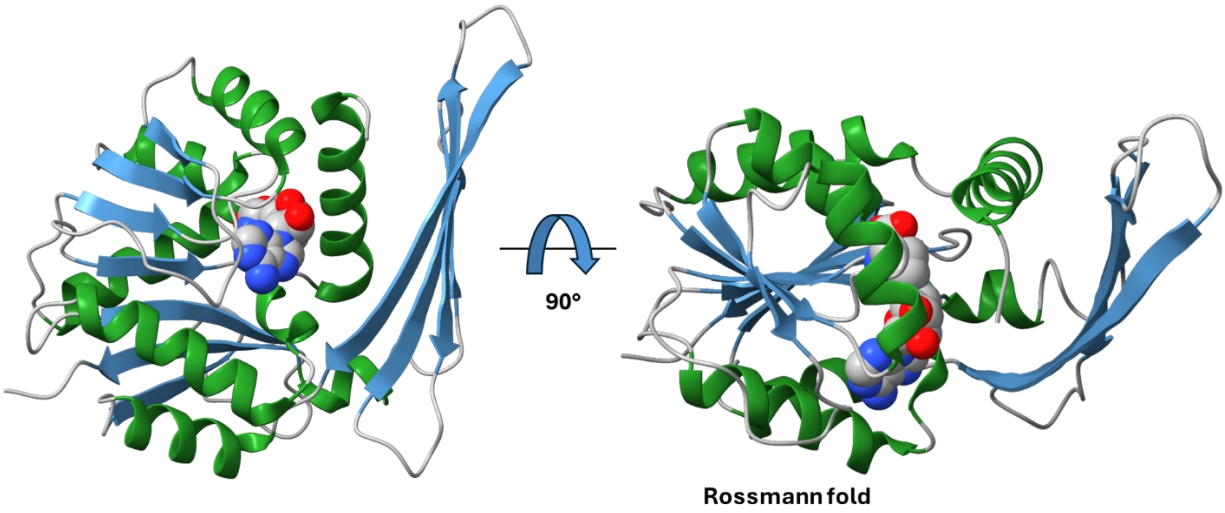

Figure 30: C-MTase PsmD from *Streptomyces griseofuscus* with bound cofactor (PDB: 7ZKG). Helices are marked in green, β-strands in blue. The cofactor SAM (**93**) is shown in grey.

Class II MTases form a domain within methionine synthase responsible for oxidizing cobalamin.[199] Structurally, they feature a long antiparallel *β*-sheet surrounded by *α*-helices, giving the enzyme its characteristic C-shape. SAM (**93**) binds in a shallow surface groove near the conserved RXXxGY motif.[200] Class III MTases are dimeric enzymes, with SAM (**93**) binding in a deep pocket between the two domains. Each domain consists of a central *β*-sheet surrounded by *α*-helices. These MTases primarily methylate tetrapyrroles, which are bound in a groove along the *N*-terminal domain.[201, 202] Class IV MTases belong to the SPOUT enzyme superfamily, named after the RNA MTases SpoU and TrmD.[203] They methylate post-transcriptional RNAs and rRNAs. Structurally, they are composed of a 6-strand parallel *β*-sheet flanked by *α*-helices. A unique knot structure at the *C*-terminus is necessary for SAM binding.[204, 205] Lastly, Class V MTases are the SET domain proteins (suppressor of variegation, enhancer of zeste, and trithorax). These MTases methylate proteins, such as lysines in histones. Their structure consists of twisted *β*-sheets surrounded by of four *α*-helices. SAM (**93**) binds near a knot formed by the loop preceding the *C*-terminal helix, within a channel at the protein's surface [Figure 31].[206, 207]

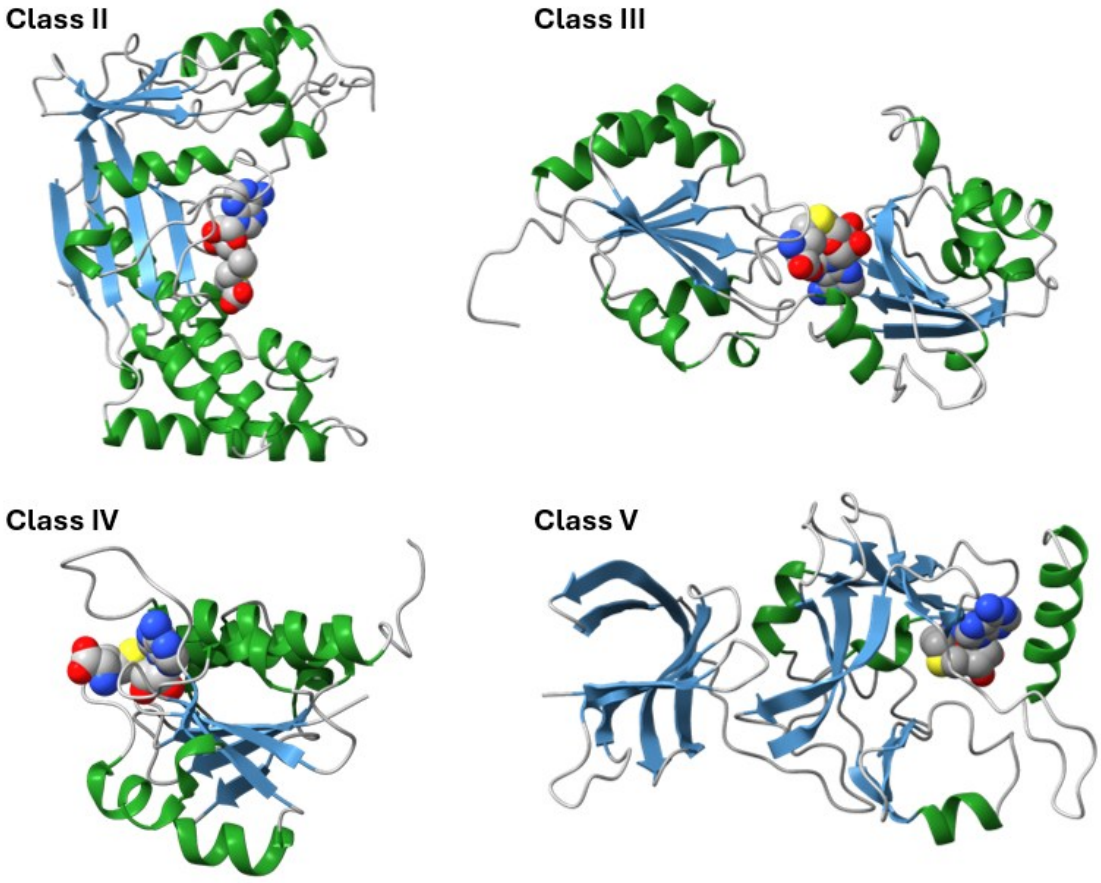

Figure 31: Crystal structure of MTases of class II - V. Helices are marked in green, β-strands in blue. The cofactor SAM (**93**) is shown in grey. Class II: Methionine synthase (activation domain) (PDB: 1MSK); Class III: Cobalamin biosynthetic enzyme, cobalt precorrin-4 MTase (PDB: 1CBF); Class IV: YibK from *Haemophilus influenzae* (HI0766): a MTase with a cofactor bound at a site formed by a knot (PDB: 1MXI); Class V: Ternary complex of the human histone MTase SET7/9 (PDB: 1O9S)

4.2.2.3 *N*-Methyltransferases

Methyltransferases can also be classified based on the atom that serves as the methyl acceptor. Nitrogen-MTases (NMT) are found in metabolic pathways in plants, bacteria, yeast, and animals.[165] Natural product NMTs are known for their large substrate scope reaching from peptides,[208] primary amines[209] to a variety of heterocycles.[165] Especially the *N*-methylation of heterocycles is a large field of research, because nitrogen-containing heterocycles are among the most common structural motifs in pharmaceuticals. In fact, 59% of all small-molecule drugs approved by the U.S. FDA contain at least one nitrogen heterocycle.

The most common heterocycle is piperidine (**111**), followed by pyridine (**112**) and piperazine (**113**). The top ten also include cephem (**114**), pyrrolidine (**115**), thiazole (**116**), imidazole (**117**), penam (**118**), indole (**119**) and tetrazole (**120**) [Figure 32A, ordered by relative frequency].[210-212] As an example, ondansetron (**121**), a selective serotonin 5-HT3 receptor antagonist, contains a methylated indole structure and an imidazole ring.[213] The cholinesterase inhibitor pyridostigmine (**122**) contains a methylated pyridine ring.[214, 215] Sildenafil (**123**), known as Viagra®, includes both a methylated piperazine and a methylated imidazole ring in its structure.[216] The psychopharmacological agent asenapine (**124**) has a methylated pyrrolidine ring [Figure 32B].[210, 217]

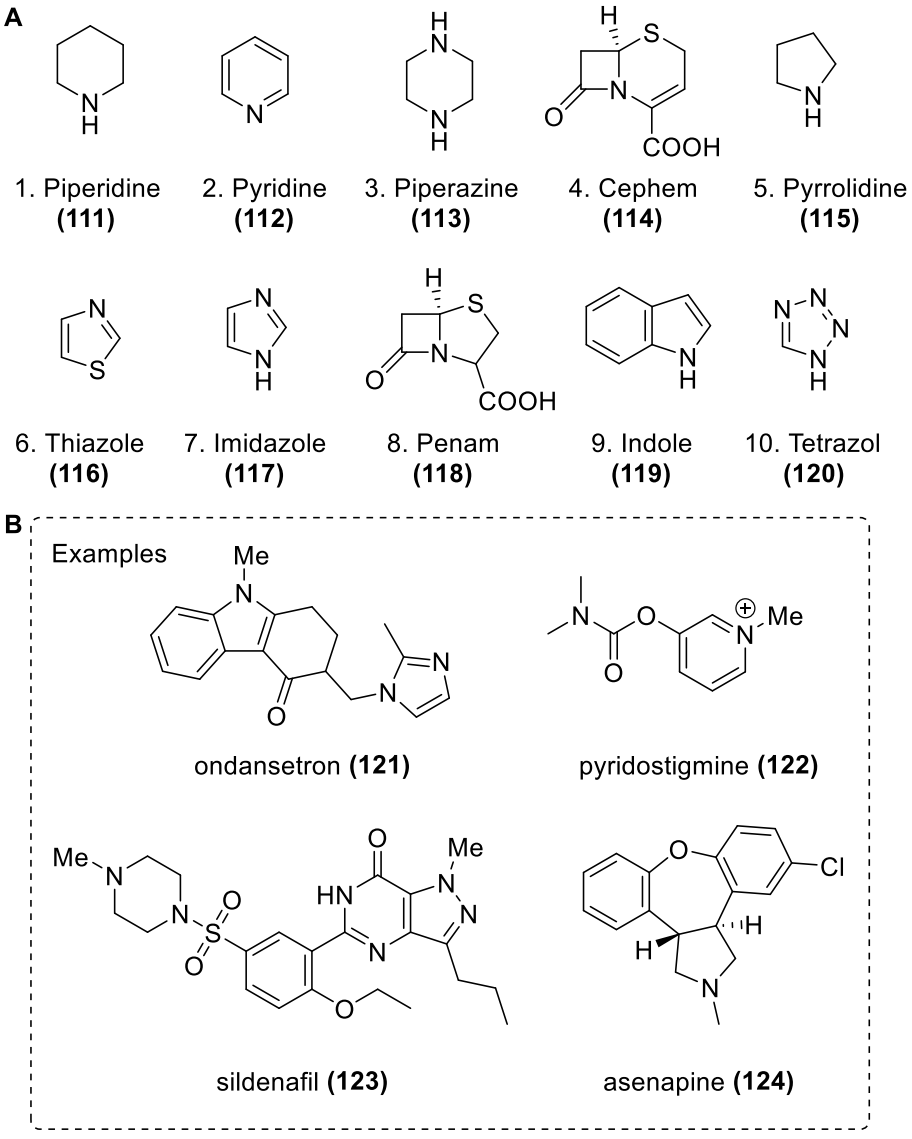

Figure 32: A: Top ten nitrogen containing heterocycles present small-molecule drugs approved by the U.S. FDA; B: Ondansetron (**121**), pyridostigmine (**122**), sildenafil (**123**), asenapine (**124**).

N-methylation with conventional organic chemistry methods poses challenges in terms of regioselectivity.[218, 219] To address this, Hammer and his team investigated the biocatalytic *N*-methylation of unsaturated heterocycles in studies published in 2020 and 2022.[220, 221] Initially, they focused on the selective alkylation of pyrazoles **125**. Since no natural pyrazole *N*-MTase is known, they selected a nicotinamide *N*-MTase (NMT), a phenylethanolamine *N*-MTase, and a histamine *N*-MTase known for their broad substrate scope. Using the computational enzyme library design tool FuncLib,[222] they engineered 50 variants of these enzymes, which were tested with different pyrazole substrates for methylation towards the regioisomers **126** and **127**.[220] In the follow-up study two years later, they expanded the enzyme and substrate scope, testing imidazoles **128**+**129,** indazoles **130**+**131,** benzimidazoles **132**-**135** and benzotriazoles **136**+**137** in addition to the pyrazoles **125**. This created enzyme library allowed for the selective methylation of *N*-heterocycles with a high regioselectivity up to >99% and a yield up to 99% on a preparative scale [Figure 33].[221]

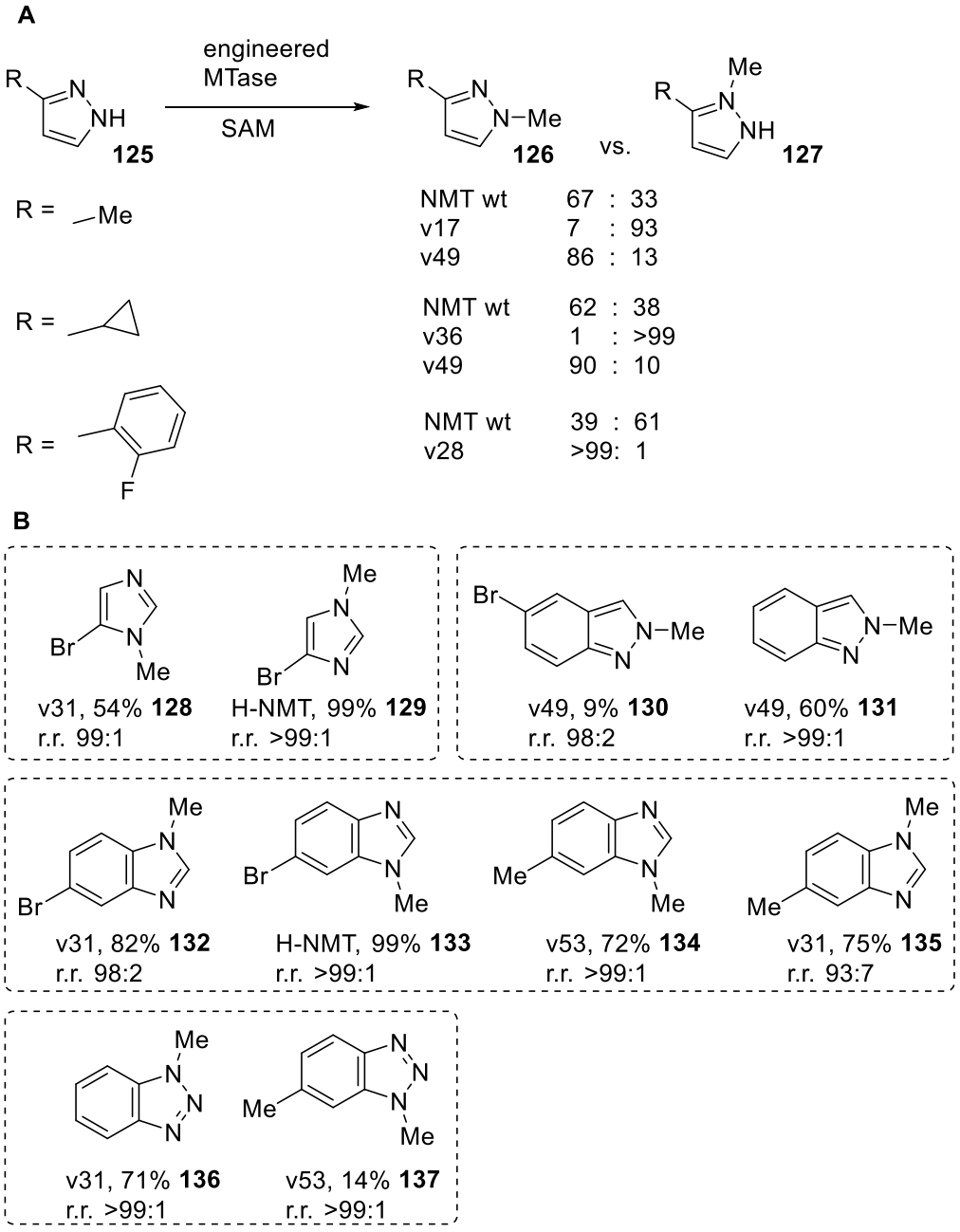

Figure 33: Biocatalytic formation of *N*-heterocycles. A: Selective methylation of pyrazoles **125** with engineered MTases (wild type + variants v17, v49, v36 and v28); B: Methylated benzimidazoles **132**-**135**, benzotriazoles **130**+**131**, imidazoles **128**+**129**, indazoles **136**+**137** and pyrazoles **126**+**127** methylated by MTases.

4.2.2.3.1 Pyrroloindole *N*-methyltransferases

Several MTases have been reported in the literature to methylate the nitrogen atom within the HPI structural motif, including NozMT, SazB-MT, DmtM2, and PsmC. These enzymes play crucial roles in the biosynthesis of their bioactive natural products. These MTases exhibit varying substrate specificities, which contribute to their diverse catalytic activities and potential applications in drug development.

NozMT is involved in the biosynthesis of nocardioazine B (**7**) and acts post *C3*-prenylation with the PTase using dimethylallyl diphosphate (DMAPP) as cofactor to catalyse the nitrogen methylation on the prenylated side and the *C3*-methylation on the other side of the DKP substrate [Figure 34].[58]

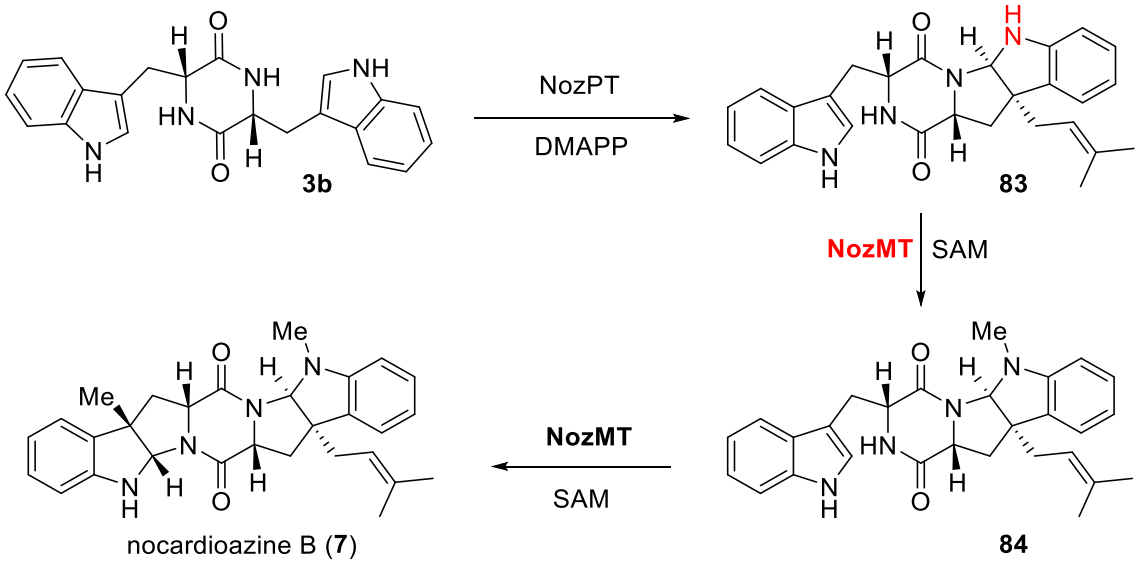

Figure 34: Biosynthesis of nocardioazine B (**7**). NozMT serves as a bifunctional enzyme methylating the *C3* position and the N1-position.

SazB-MT is the methyltransferase domain of the bifunctional enzyme SazB, which also includes a prenyltransferase domain, SazB-PT. SazB-MT methylates the *N1*-HPI motif created by SazB-PT via *C3*-prenylation in the precursor **138** for the natural product streptoazine C (**139**) [Figure 35].[223]

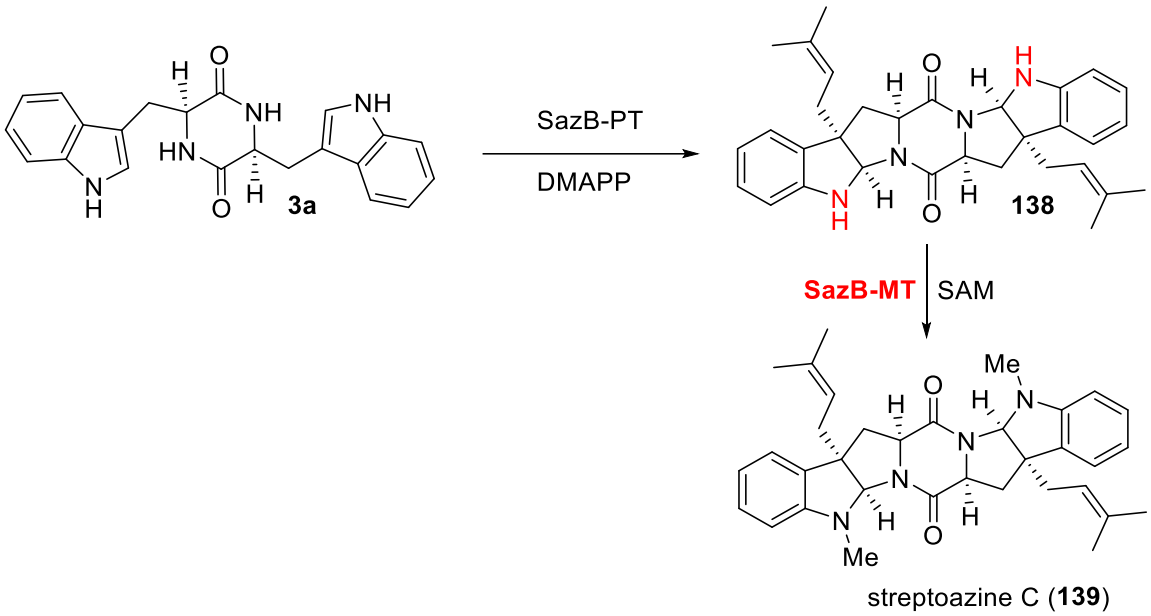

Figure 35: Biosynthesis of streptoazine C (**139**). SazB-MT serves as *N*-MTase methylating and the N1-position as final step.

DmtM2 is involved in the biosynthesis of different drimentines. Starting from the cWV DKP **140**, this substrate is further modified by a PTase DmtC1, which farnesylates at the *C3*-position forming the HPI motif and a terpene cyclase. The DmtM2 MTase methylates the *N1*-position of the HPI in the intermediates **141**-**143**. This reaction proceeds at various stages in the biosynthesis proving its broad substrate acceptance and the formation of a variety of products **144**-**146** [Figure 36].[224]

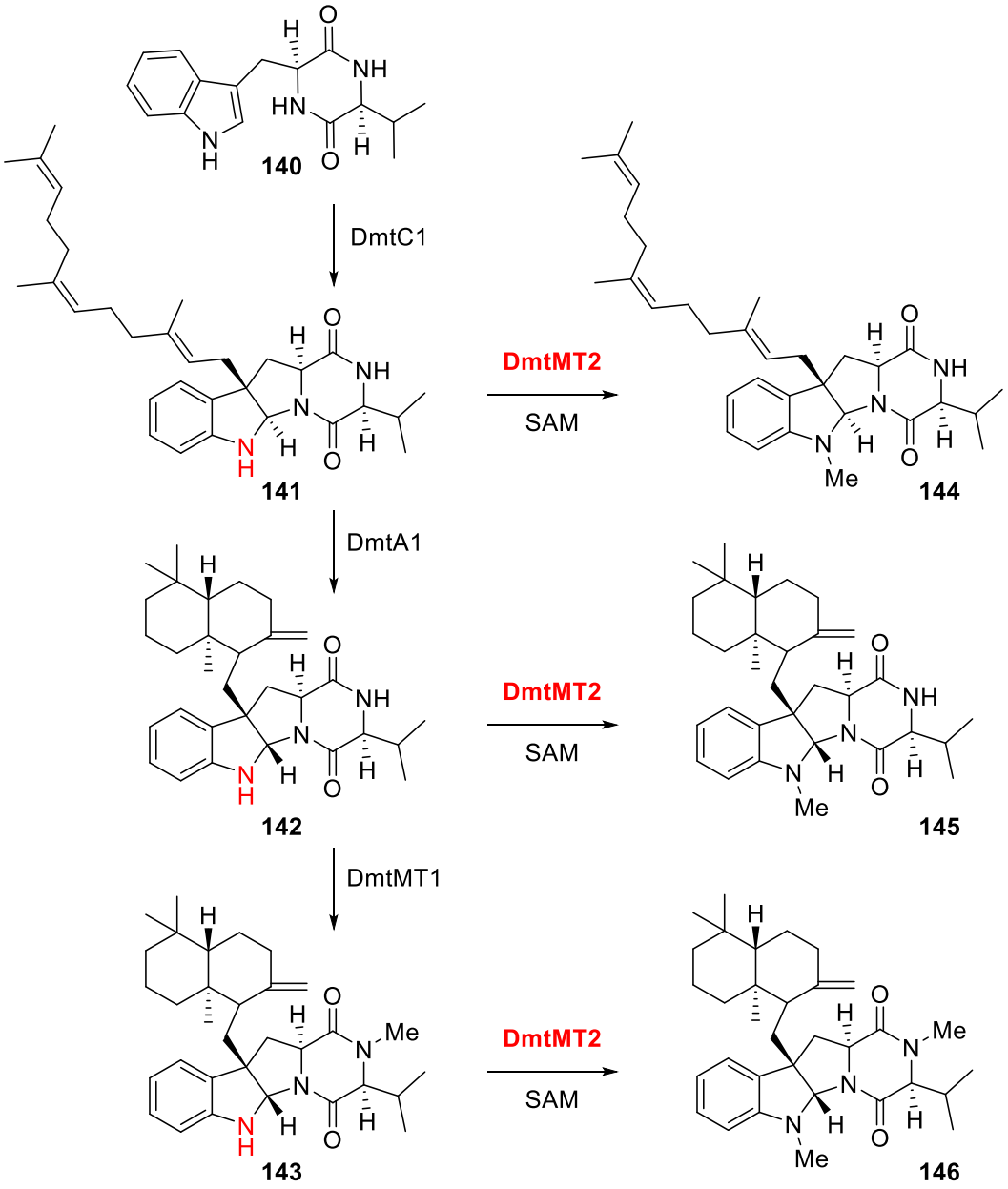

Figure 36: Biosynthesis of various drimentines **144-146**. DmtMT2 serves as a *N*-MTase methylating the *N1*-position at different stages within the biosynthesis. DmtA2 is a terpene cyclase, DmtC1 a PTase and DmtMT1 a MTase.

PsmC plays a role in the biosynthesis of physostigmine (**48**). The Trp derivative **147** is processed by four enzymes (PsmA, PsmE, PsmF, and PsmH) to produce the precursor **148**, which undergoes *C3*-methylation by PsmD. PsmC introduces a methyl group to the nitrogen atom in the HPI **149**. Following deacetylation of this compound **150** by PsmB, PsmC further *N*-methylates the resulting intermediate **151**, ultimately leading to the formation of physostigmine (**48**). [Figure 37].[225]

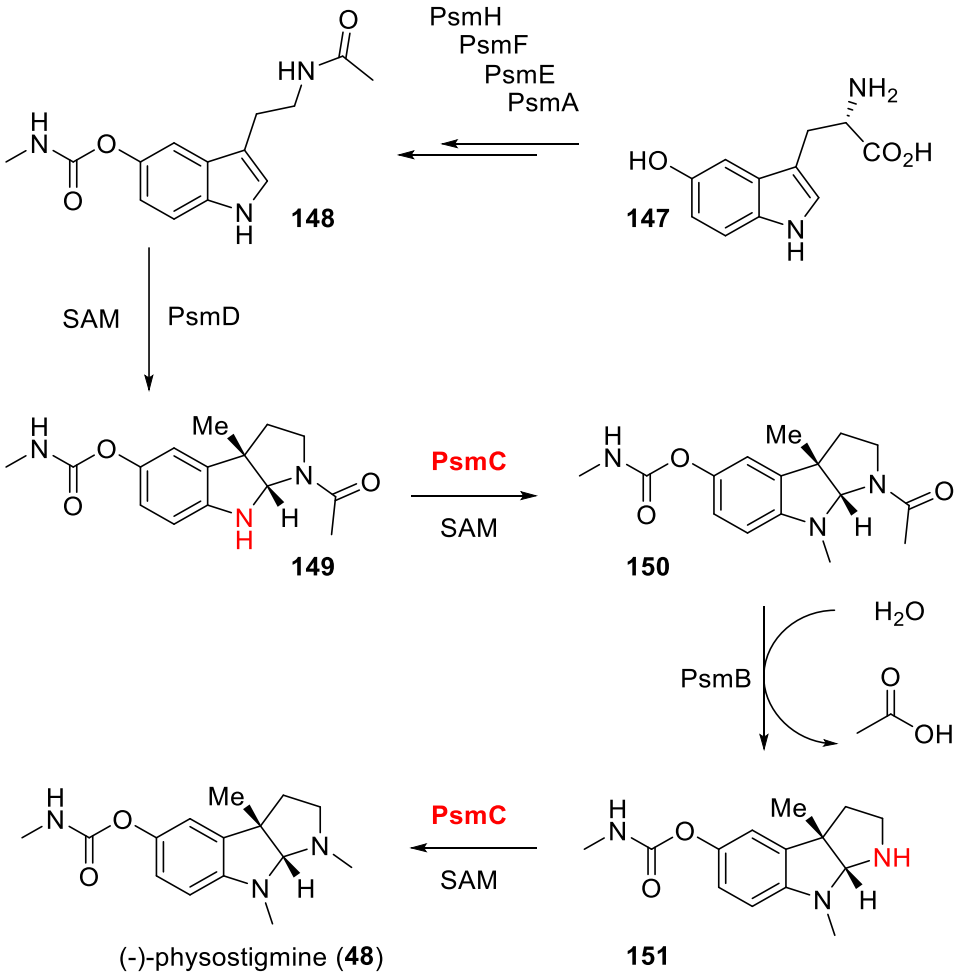

Figure 37: Biosynthesis of physostigmine (**48**). PsmC serves as a *N*-MTase for both nitrogen atoms in the HPI motif.

These *N*-MTases participate in distinct biosynthetic pathways. However, research on these enzymes remains limited, leaving many aspects of their structure, function, and potential applications unexplored.

4.2.2.4 *C*-Methyltransferases

Carbon-MTases are less common than Nitrogen-MTases, being predominantly found in bacteria and plants rather than in eukaryotic systems.[164, 165, 226]

However, their use remains highly valuable, especially in the organic synthesis of small molecules. One prominent class of small molecule C-MTases can enantioselectively methylate the *β*-position of *α*-ketoacids **152** and **153** forming the methylated products **154** and **155**. Subsequent conversion with aminotransferases produces non-proteinogenic *β*-methyl-*α*-amino acids **156** and **157**, which serve as valuable building blocks for the total synthesis of pharmaceuticals [Figure 38].[227-229]

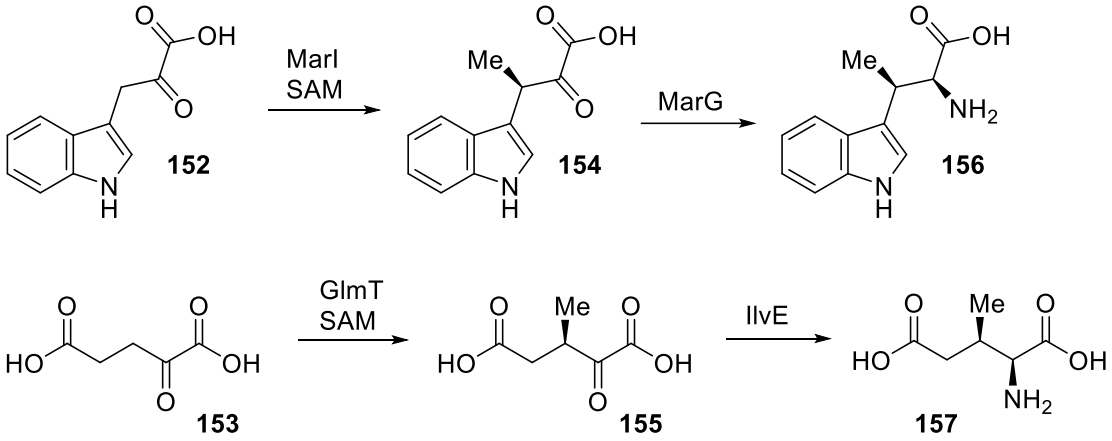

Figure 38: Formation of non-proteinogenic β-methyl-α-amino acids **156** and **157**: C-MTases (MarI, GlmT) enantioselectively methylate the β-position of α-ketoacids **152** and **153** prior to the conversion with aminotransferases (MarG,IlvE).

The mechanism of C-MTases is based on a S_N2-like displacement of the methyl group of SAM (**93**) by nucleophilic attack of the substrate, but the details vary from enzyme to enzyme. More and more crystal structures and mechanistic studies are helping to understand the similarities and differences within this specific class of enzymes.[99, 230-233]

The mechanism of two C-MTases is discussed exemplary:

The Friedel-Crafts alkylation of coumarin **158** and naphthalene **159** substrates catalysed by the C-MTases CouO and NovO towards the methylated products **160** and **161** has been extensively studied in recent years. Based on the crystal structure of CouO in complex with SAH (**94**) and molecular docking studies, the catalytic residues were identified. Site-directed mutagenesis revealed that a histidine is necessary to activate the coumarin **158** before the nucleophilic attack of the SAM (**93**) proceeds [Figure 39].[230, 234]

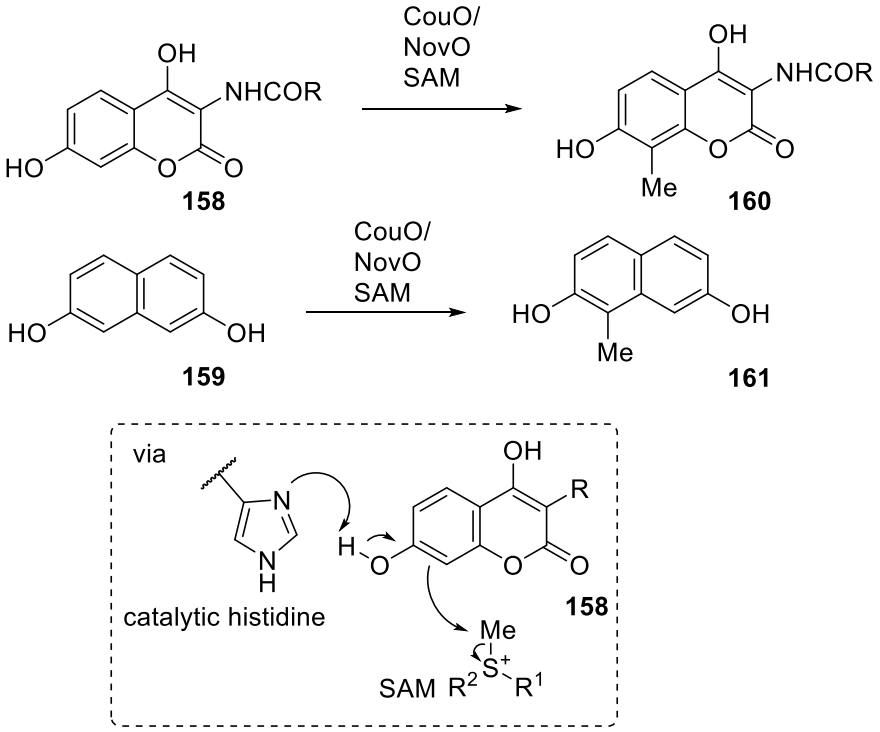

Figure 39: The Friedel-Crafts methylation of coumarin **158** and naphthalene **159** substrates catalysed by the C-MTases CouO and NovO. A catalytic histidine activates the coumarin **158** by deprotonation prior to the nucleophilic attack on the SAM (**93**).

The C-MTase SibL from *Streptosporangium sibiricum* is a class I C-MTase containing a Rossman fold domain. The crystal structure of this enzyme along with mutagenesis studies propose a two-step catalytic mechanism to catalyze the methylation of 3-hydroxykynurenine (**162**) yielding the methylated product **163**. The proposed mechanism involves a tyrosine clamp of two tyrosine residues that activate the substrate **162** and are necessary for hydrogen transfers within the active site with the intermediate **164** [Figure 40].[231]

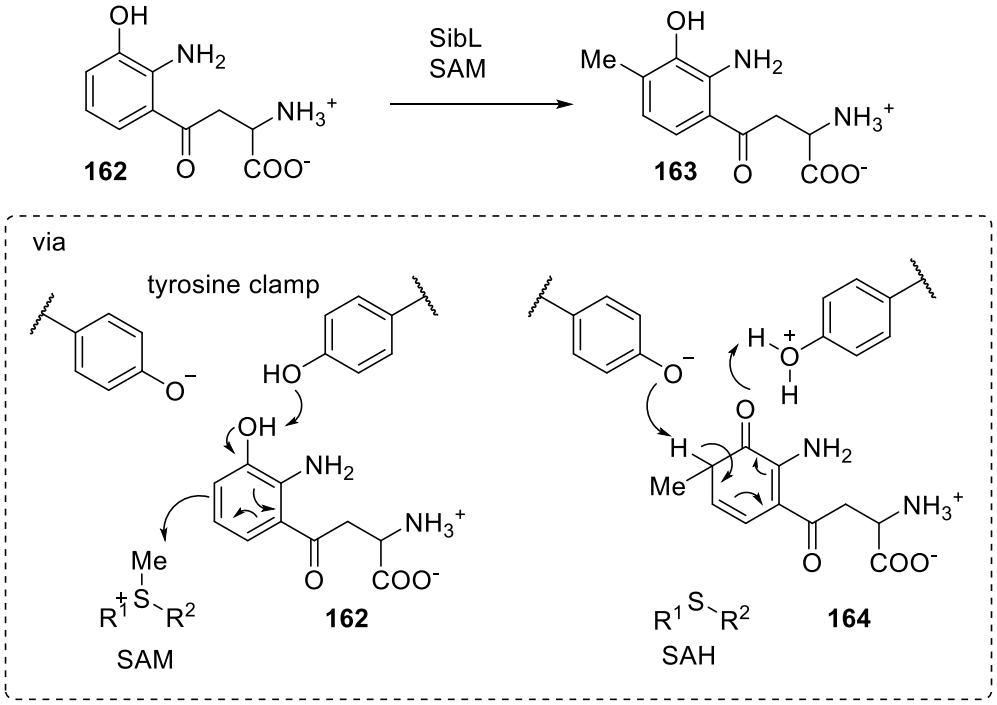

Figure 40: Methylation of 3-hydroxykynurenine (**162**) by the MTase SibL. A tyrosine clamp activates the substrate **162** via hydrogen transfers within the active site.

4.2.2.4.1 Indole *C3*-methyltransferases

As described previously, C-MTases are also involved in the formation of HPI motif containing natural products. A key example of such an enzyme is PsmD, which participates in the biosynthesis of physostigmine (**48**).[99, 110] PsmD is a class I C-indole MTase, which methylates at the *C3*-position of the indole substrate **148** forming a reactive intermediate **165**, which cyclises to the HPI. Detailed studies, including crystallisation and alanine scanning mutagenesis, have revealed important insights into the catalytic site of PsmD. The mechanism of this enzyme involves a catalytic triad including a tyrosine, histidine and glutamate [Figure 41].[99]

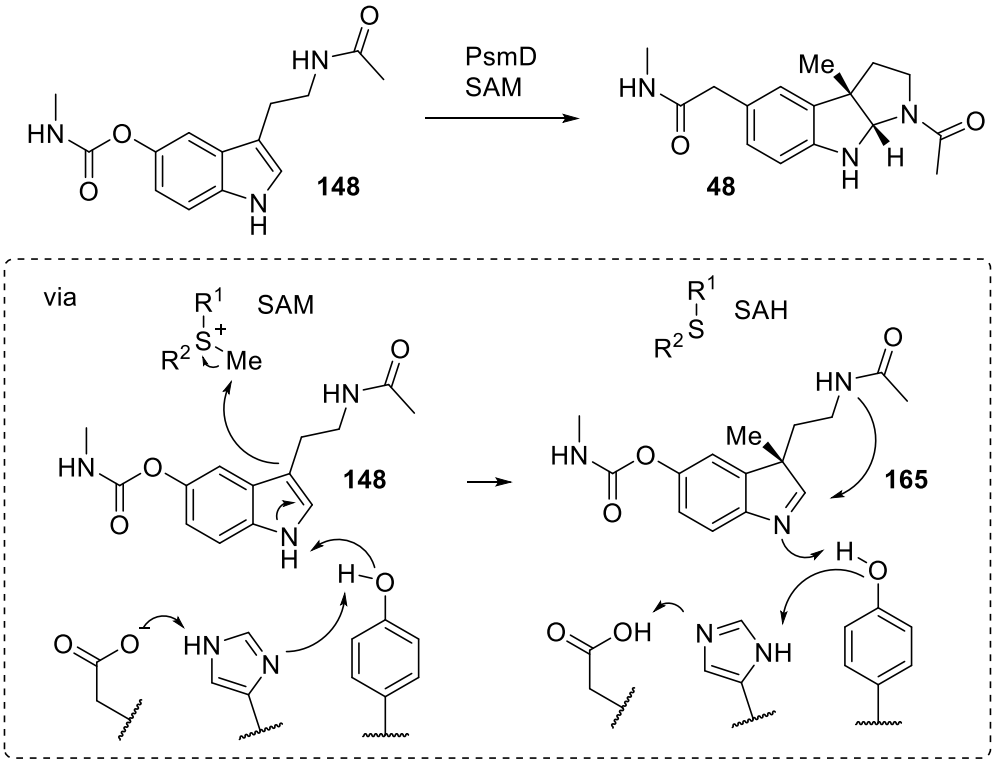

Figure 41: Methylation of a physostigmine precursor molecule **148** by the MTase PsmD. A catalytic triade of a tyrosine, histidine and glutamate activates the substrate by deprotonation.

PsmD is the most extensively studied *C3*-indole MTase, with only two additional MTases identified so far methylating a DKP based substrate.[58, 87, 235]

The first study involving a *C3*-MTase with a DKP substrate was published in 2015. This study involved a bioinformatic analysis of the genome of *Nocardiopsis sp.* CMB-M0232 to explore the potential biosynthesis of nocardioazine A and B. The nocardioazine biosynthetic pathway is distributed over multiple genomic loci. The *Nocardiopsis sp.* CMB-M0232 strain was cultivated, and the resulting alkaloids were analysed using mass spectroscopy and HPLC, comparing them with chemically synthesised standards. The observed intermediates suggest a biosynthetic pathway, where the LL-cWW **3a** is formed via a cyclodipeptidase NozA prior to conversion into a DD-cWW **3b** by an isomerase (the LL/DD nomenclature derives from the stereochemical configuration of the amino acid building blocks). The *C3*-methylation by NozB occurs according to this study before *C3*-prenylation and *N*-methylation forming intermediate **166**. The exact order of *C3*-prenylation and *N*-methylation remained uncertain, as intermediates **83** and **167** for both steps were identified [Figure 42]. NozB was not isolated or tested with specific substrates separately in this study.[87]

Eight years later, the same gene cluster of *Nocardiopsis* sp. CMB-M0232 was investigated further in detail. The MTase NozMT (earlier called NozB) was isolated and tested with various unsubstituted cWW isomers, showing no conversion. Instead, NozMT catalyses *C3*- and *N*-methylation post *C3*-prenylation by the PTase NozPT [Figure 18]. This result contradicts previous findings, as the formed intermediates were not detected in the alkaloid profile of the *Nocardiopsis* sp. extracts.[58, 87]

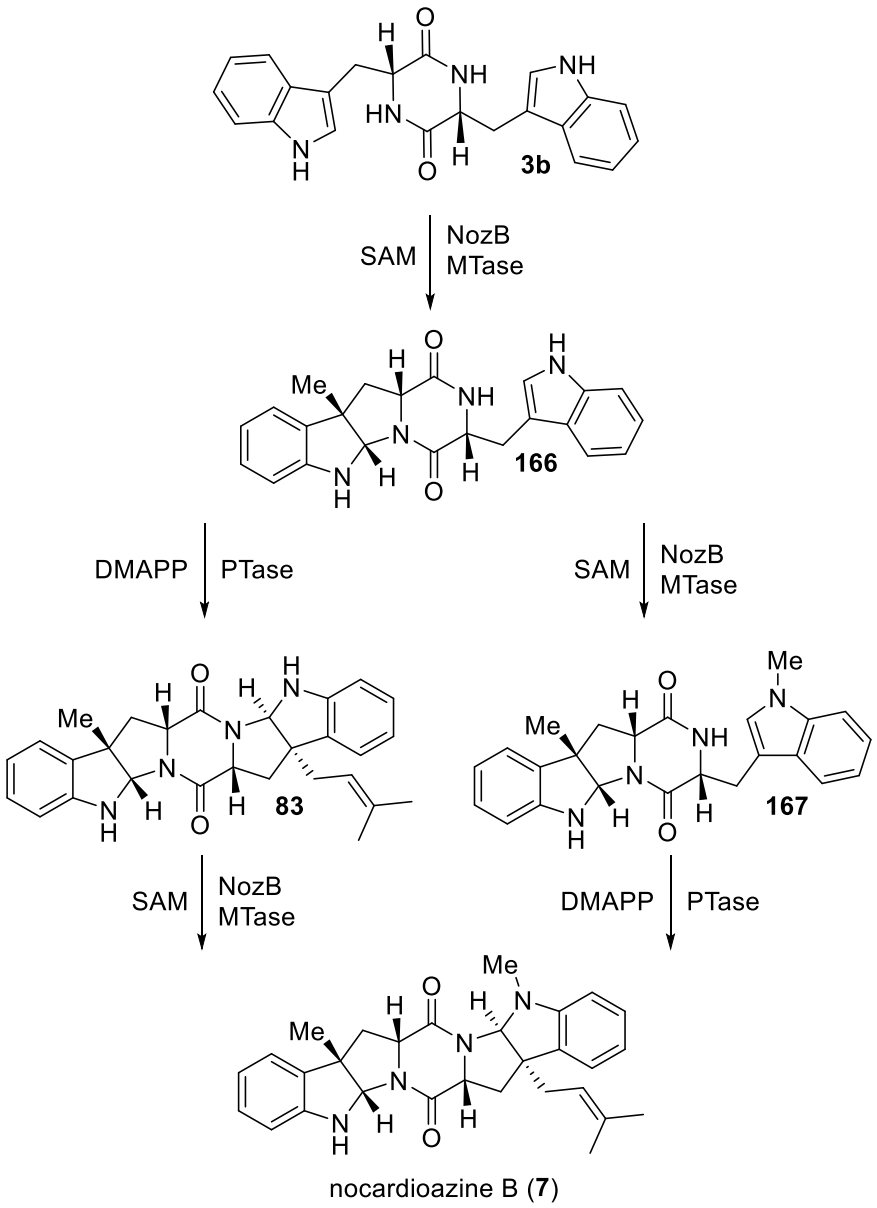

Figure 42: Potential biosynthesis of nocardioazine B (**7**) proposed in 2015 including a MTase NozB methylating the *C3* position of the DD-cWW **3b** on one side of the molecule. The order of *N*-methylation and prenylation remained unclear.

In 2019, another *C3*-MTase, StspM1, was studied. StspM1 shares 43.23% sequence homology with NozMT and is part of a gene cluster that includes a CDPS, a PTase (StspPT), and another MTase (StspM2). StspM1 was found to methylate the LL-cWW **3a** substrate, forming the HPI structural motif on one side of the DKP **168a**. Based on these findings, the authors proposed a biosynthesis pathway where prenylation towards intermediate **169** and *N*-methylation occur after *C3*-methylation, resulting in a nocardioazine B isomer **170** [Figure 43].[235] Since this potential nocardioazine B isomer has never been isolated from nature, the proposed biosynthesis remains completely speculative.

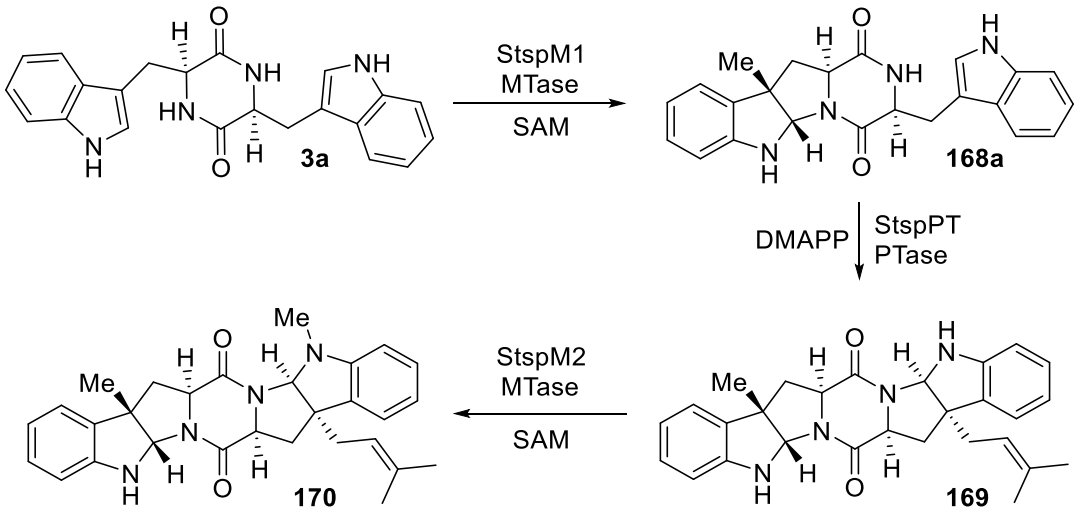

Figure 43: Proposed biosynthesis of a nocardioazine B isomer **170**. The MTase StspM1 methylated the LL-cWW **3a** to form the HPI motif on one side of the molecule prior to *C3* prenylation by a PTase StspPT and *N*-methylation by StspM2.

4.2.2.5 Solving the bottleneck of SAM availability

Most MTases require SAM (**93**) as a cofactor, which is expensive when purchased in pure form from commercial suppliers.[236] Furthermore, with SAM (**93**) having a molecular weight of nearly 400 g/mol, its stoichiometric use as a methyl donor results in poor atom economy. To make MTases viable for preparative synthesis, effective cosubstrate supply or recycling systems are essential. In recent years, the demand for reliable methods to facilitate the *in situ* generation of SAM (**93**) has increased. This has led to the exploration of various (chemo-) enzymatic solutions differing in their underlying strategy.[237-239]

In nature, SAM (**93**) is formed from adenosine triphosphate (ATP, **171**) and L-methionine (**172**), which are separately regenerated from the SAH cleavage products ribosyl-adenosine (**173**) and L-homocysteine (**174**).[240-242] Inspired by this natural process, Andexer and coworkers implemented a biomimetic approach for the SAM (**93**) formation in 2017 focussing on the regeneration of the building block ATP (**171**): The consumed SAM (**93**) is converted into SAH (**94**), which is then cleaved into ribosyl-adenine **173** and homocysteine (**174**) by a SAH-hydrolase (SAHH). Subsequently, ATP (**171**) is regenerated through three phosphorylation steps catalysed by an adenosine kinase (ADK) and two polyphosphate kinases (PPK2) I & II. Finally, a methionine adenosyltransferase (MAT) catalyses the formation of SAM (**93**) from the regenerated ATP (**171**) and additional supplied methionine (**172**) [Figure 44].[238]

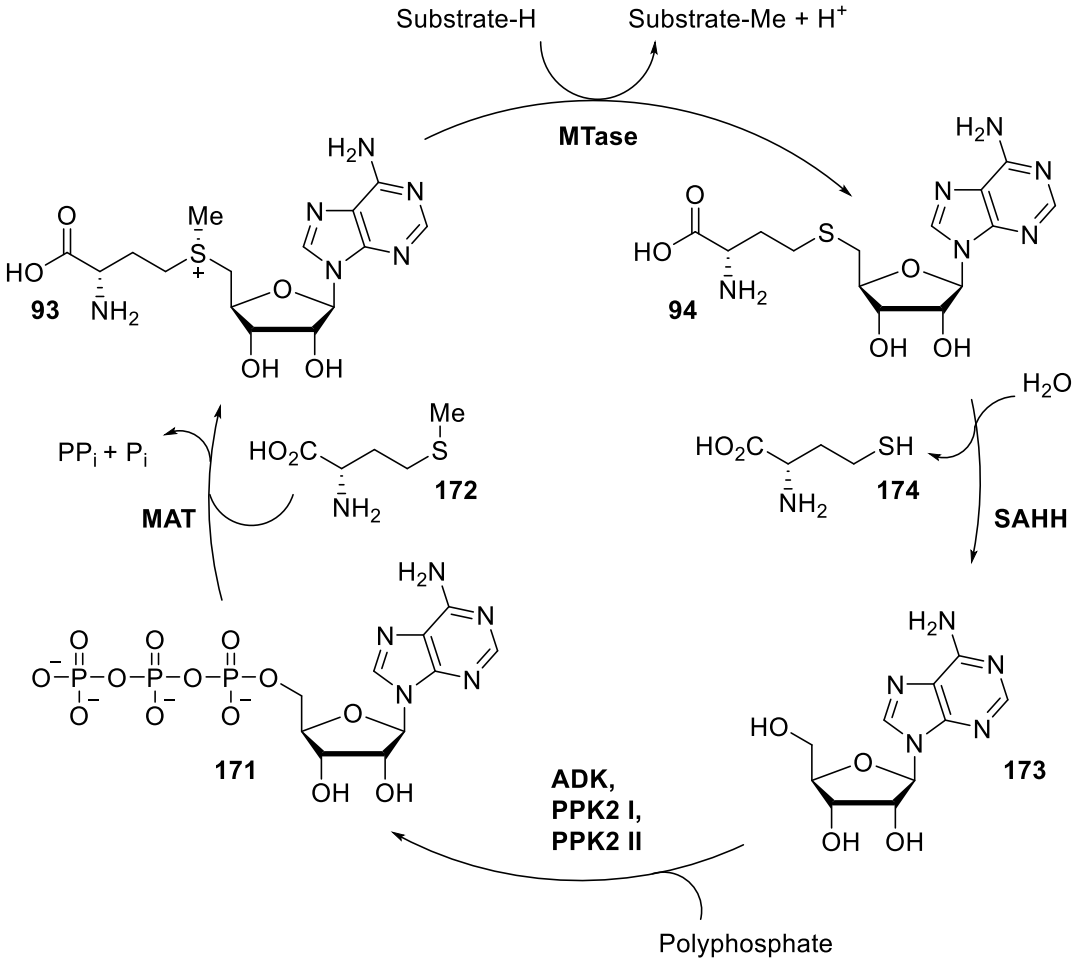

Figure 44: Catalytic cycle of biomimetic SAM (**93**) regeneration.

This system, along with a simplified linear version containing only MAT and SAH hydrolase, has been integrated into various MTase systems.[237, 238, 243, 244] A bottleneck of this system is the number of achievable regeneration cycles, which is caused by the instability of SAM (**93**) and SAH (**94**). One non-enzymatic degradation of SAM (**93**) is the process of depurination, where the SAM (**93**) is degraded into adenine (**175**) and *S*-ribosylmethionine (**176**) [Figure 45A].[245] To address this, SAM isosteres **177** with different purine and pyrimidine nucleobases **178-180** were progressively incorporated into the regeneration cycle [Figure 45B]. Stability studies conducted at 37 °C and pH 8.0 with the purified 7dzSAM isostere confirmed its enhanced resistance to depurination (7dzSAM $t_1/_2$ = 1243 min; SAM $t_1/_2$ = 942 min).[245] Although this approach effectively prevented the non-enzymatic depurination of SAM (**93**), it led to a reduction in the efficiency of the coupled reaction, as not all enzymes in the regeneration system were equally compatible with the nucleoside isosteres.[246]

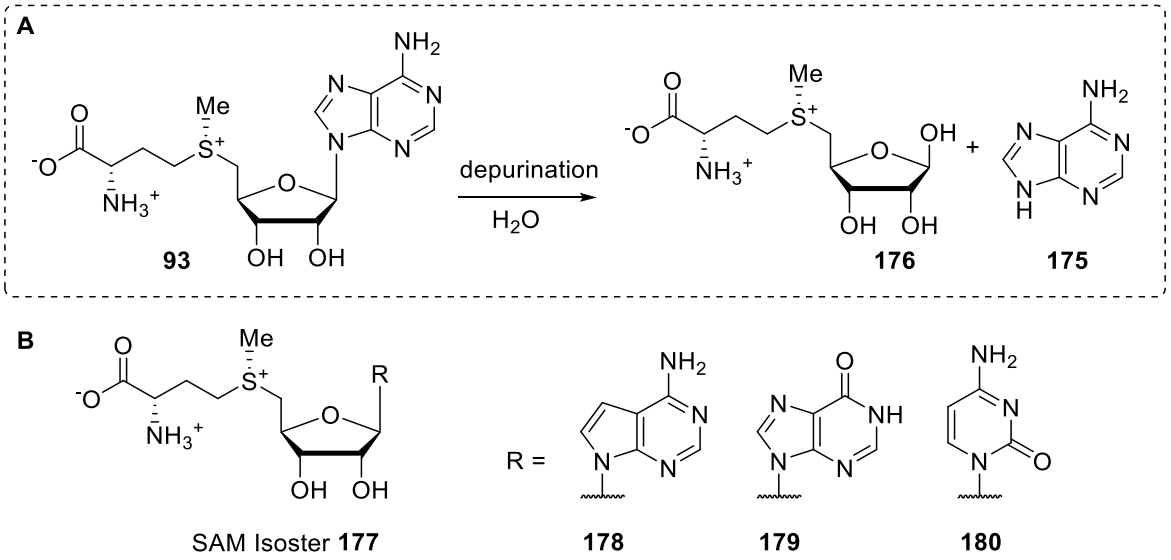

Figure 45: Depurination of SAM (**93**). SAM isosteres **177** with different adenine surrogates were synthesised to inhibit the depurination process.

An alternative linear approach uses a chlorinase (SalL) or fluorinase (FDAS), which catalyse the formation of SAM (**93**) from methionine (**172**) and 5'-chloro/fluoro-5'-deoxyadenosine (**181**) (CIDA) [Figure 46].[247-249] For example, the chlorinase SalL from the marine bacterium *Salinispora tropica* was utilised for tandem chemo-enzymatic methylation of the antibiotic teicoplanin. The produced SAM (**93**) from L-Met (**172**) and CIDA (**181**) can be directly used as a methyl donor for methyltransferase-catalysed reactions without the need for purification.[248]

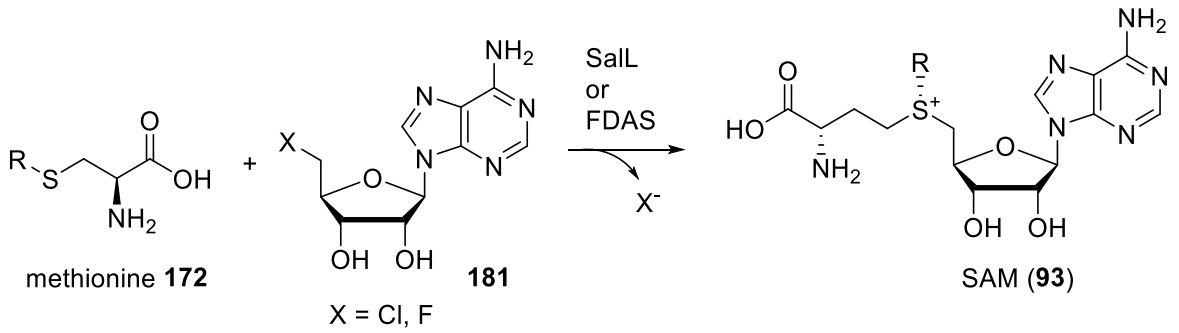

Figure 46: Linear SAM (**93**) formation via chlorinase (SalL) or fluorinase (FDAS) catalyzing the formation of SAM (**93**) from methionine (**172**) and 5' chloro/fluoro-5'-deoxyadenosine (**181**).

In 2019, Liao and Seebeck developed a new SAM recycling system that does not require expensive additional substrates. In this system, the SAH (**94**) produced during the MTase reaction is recycled by a halide MTase (HMT), which re-methylates SAH (**94**) using methyl iodide as the substrate forming SAM (**93**) and iodid [Figure 47]. To prevent the biocatalytic degradation of SAH (**94**), a SAH nucleosidase-deficient strain of *E. coli* was engineered. This system utilises only catalytic amounts of SAM/SAH and was tested for over 500 turnovers.[239] This publication marked a significant milestone in the field of MTases, as it facilitated the preparative use of this enzyme class.[239, 250] This SAM recycling system was used by multiple researchers for different MTase reactions showing its broader applicability.[110, 251-253]

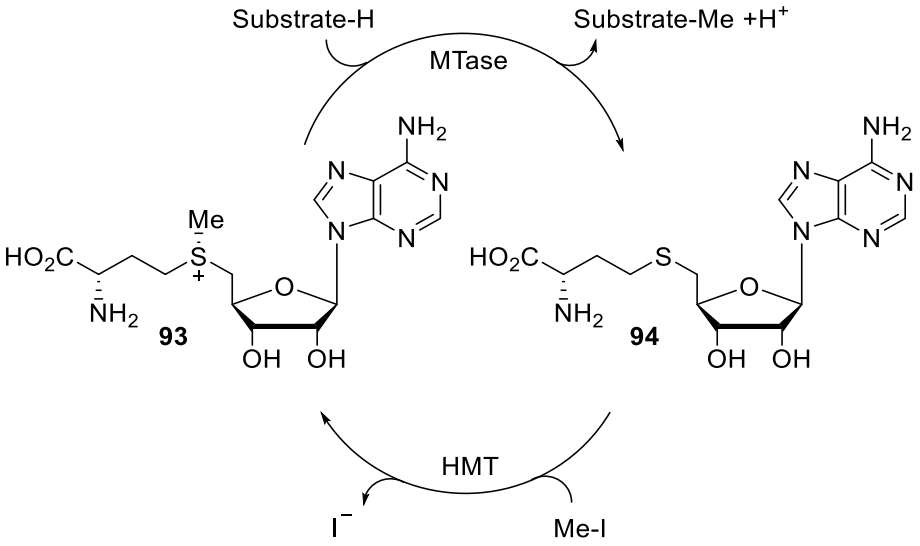

Figure 47: SAM recycling system based on a HMT: SAH (**94**) is methylated by an HMT, which uses methyl iodide as methyl source to form SAM (**93**).

A disadvantage of the HMT-based SAM recycling system is the use of volatile methyl iodide as a methyl source. In 2022, Seebeck and his team developed a SAM regeneration system using methyl p-toluenesulfonate as an alternative methyl donor: They tested 14 enzymes from the thiopurine MTase (TPMT) family for their ability to utilise various methyl donors, including dimethyl sulfate (**182**, DMS), methyl methanesulfonate (**183**, MeOMs), methyl p-toluenesulfonate (**184**, MeOTs), and methyl 4-nitrobenzenesulfonate (**185**, MeONs) [Figure 48]. The TPMTs showed varying activity depending on the substrate for the methylation of SAH (**94**). One of the most effective enzymes for this recycling system, a MTase from *Ustilago maydis* (Uma), was successfully combined with different secondary MTases, highlighting the potential of this improved SAM recycling system.[254]

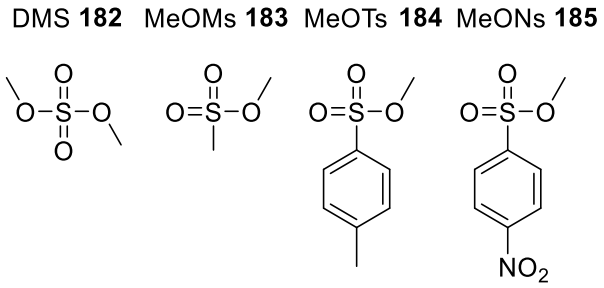

Figure 48: Chemical structures of dimethyl sulfate (**182**), methyl methanesulfonate (**183**), methyl p-toluenesulfonate (**184**) and methyl 4-nitrobenzenesulfonate (**185**).

4.2.2.6 Beyond methylation

In recent years, these systems have been further investigated for the production of SAM analogs.[255-258] These analogs enable MTases to transfer groups beyond “methyl”, thereby expanding their applicability for synthesising various compounds.[259]

Studies from 2014 suggest that sulfonium-to-selenonium substitution in SAM (**93**) can enhance the compatibility with certain MTases to accept less reactive SAM analogs.[258] In the same year, a large platform for the synthesis of SAM/SeAM analogs **186** was created by synthesising methionine/se-methionine analogues **187** converting them with different MATs [Figure 49A].[260] MATs have in general a rather broad substrate spectrum for SAM analogs compared to HMTs. For example, the MAT from *Sulfolobus solfataricus* produces a large variety of SAM analogs from methionine analogues **187** and ATP (**171**) without further enzyme enegeering.[261]

The HMT from *Chloracidobacterium thermophilum* (Ct-HMT), which was the first enzyme used in Seebeck's SAM recycling system, does only accept a few alkyl halides (R-X) besides methyl iodide also with a low activity. To overcome this limitation, researchers expanded the list of characterised HMT enzymes through homology-based searches and engineered HMTs to produce SAM analogues **188**. In 2020, Bornscheuer's research group generated HMT variants based on a halide MTase from *Arabidopsis thaliana* using directed evolution. These optimised variants exhibited a broader alkyl halide substrate spectrum and higher enzyme activity compared to Ct-HMT [Figure 49B].[256] In 2021, Hammer's team further expanded the list of HMT enzymes and created substrate profiles for each enzyme.[255]

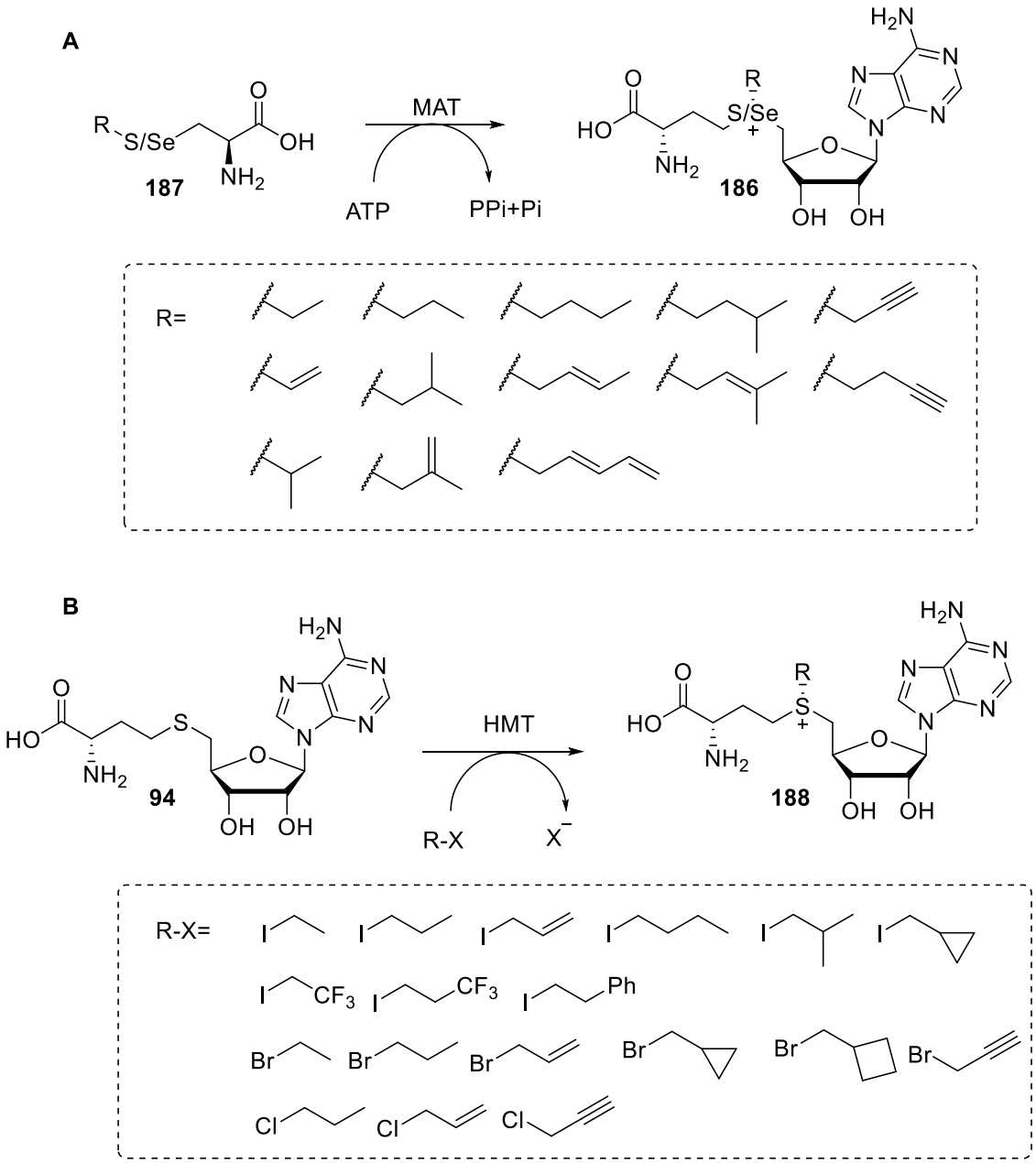

Figure 49: Synthesis of SAM analogs containing different alkyl chains. A: Methionine/se-methionine variants are converted by a MAT towards SAM/SeAM analogs **186**. B: HMTs are used for creating SAM analogs **188** from different alkyl halides.

In addition to investigating the transfer of various alkyl groups, Seebeck's research group turned its attention to fluoromethylation.[262] Organofluorine compounds play a crucial role in a wide array of fields, including pharmaceuticals, agrochemicals and polymers. The unique advantages of incorporating fluorine, such as increased stability and hydrophobicity, have been well-known for years. Fluorine substitution can also alter the conformational behaviour of organic molecules, making it a valuable tool for enhancing the efficacy of therapeutic compounds.[263, 264]

In 2021, a HMT was employed to synthesise *S*-adenosyl-*S*-(fluoromethyl)-L-homocysteine (fluorinated SAM, **189**) [Figure 50A] from SAH (**94**) and fluoroiodomethane. The compatibility of this fluorinated SAM analogue **189** was evaluated across various MTases, leading to the production of fluorinated products. However, the enzyme cascade for fluoromethylation was not universally successful, primarily due to the instability of fluorinated SAM **189** in combination with the lower turnover frequencies of the MTases. The fluorinated SAM **189** could not be isolated.[262]

Two years later in 2023, Wang *et al.* successfully synthesised fluorinated SAM **189** and confirmed its rapid decomposition in buffer at pH 8, with a half-life of less than one hour.[265] SAM's decomposition is next to the depurination additionally driven by an intramolecular attack by the carboxylate group on Cγ-Met, leading to the formation of 5′-methylthioadenosine (**190**, MTA) and L-homoserine lactone (**191**, HSL) [Figure 50B].[266] The electron-withdrawing effect of the CH_2F group further increases the electron deficiency of the sulfonium group, thereby accelerating F-SAM's decomposition. To address this issue, an analogue of fluorinated SAM **192** (dcSAM) without the carboxy group was synthesised [Figure 50A], significantly improving its stability by preventing the intramolecular formation of a five-membered ring. Under the same conditions, fluorinated dcSAM **192** exhibited a half-life exceeding 24 hours. This fluorinated dcSAM **192** was then tested with various MTases proving its applicability as cofactor analogue. The dcSAH was additionally tested as a substrate for a HMT enabling the cofactor recycling system with this more stable analog.[265]

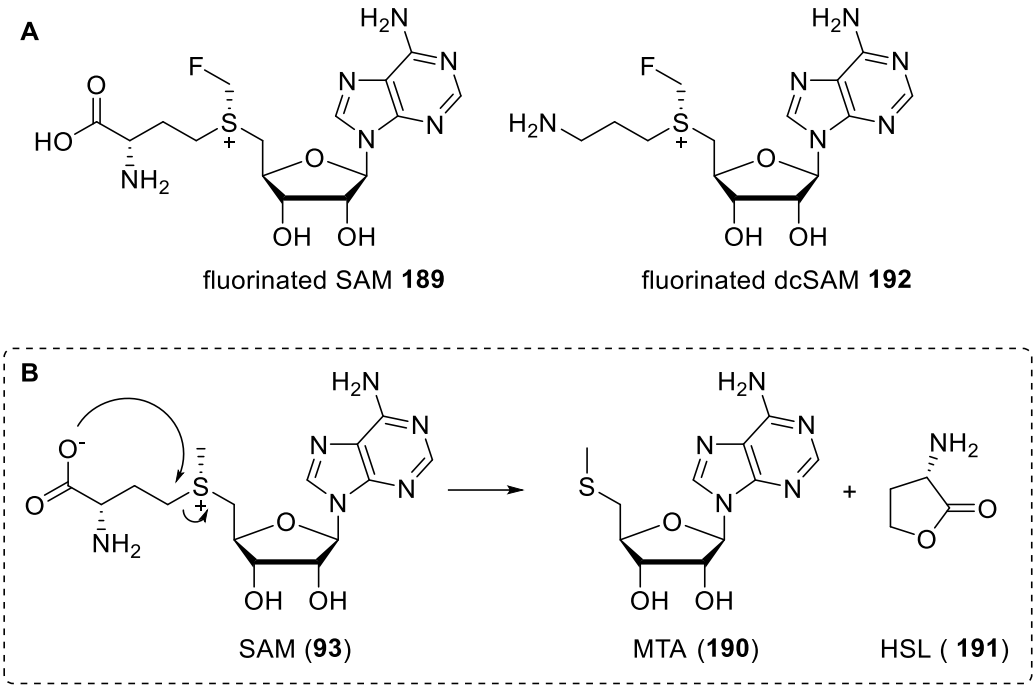

Figure 50: Chemical structures of fluorinated SAM **189** and fluorinated dcSAM **192**. SAM (**93**) degrades into of 5′-methylthioadenosine (**190**) and L-homoserine lactone (**191**) due to the carboxy-group of the methionine.

4.2.3 Prenylation: Aromatic Prenyltransferases

Biocatalytic alkylations can also be catalysed by PTases: PTases transfer isoprenyl moieties to various acceptor molecules, using different isoprenyl pyrophosphates as cosubstrates. These cosubstrates vary in the length of their alkyl chains like dimethylallyl diphosphate (**193**, DMAPP; C5), geranyl diphosphate (**194**, GPP; C10), and farnesyl diphosphate (**195**, FPP; C15) [Figure 51A].[267]

Isoprenylation can enhance the lipophilicity and the binding affinity to target proteins, thereby directly influencing biological activity.[268-270] For example, prenylating naringenin to form 8-prenylnaringenin (**196**) enables the molecule to interact with a hydrophobic pocket in estrogen receptors, resulting in stronger estrogenic activity.[268] In case of the chalcone **197**, prenylation and geranylation leads to an increased cytotoxic activity against the human tumour cell line K562 [Figure 51B].[271]

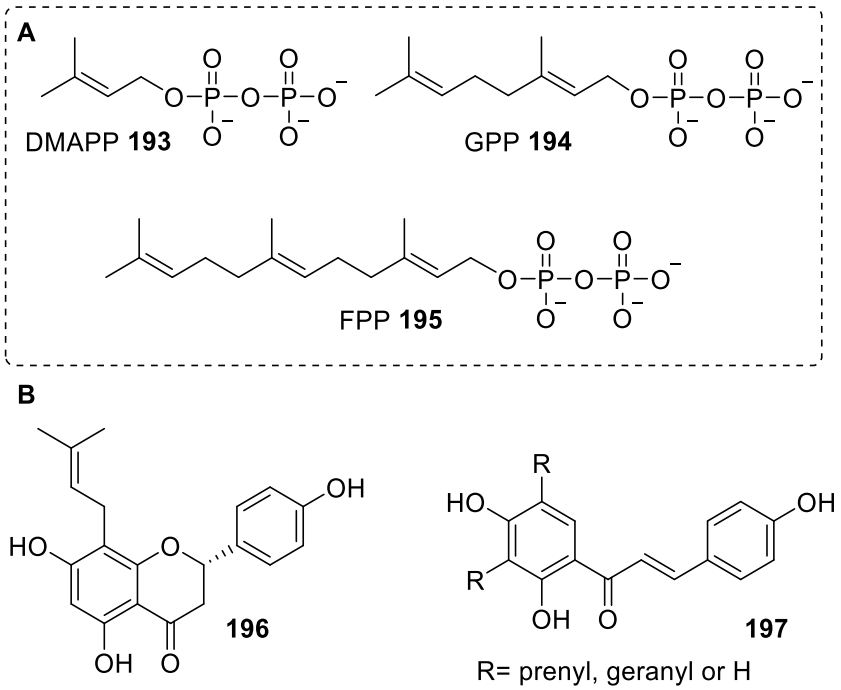

Figure 51: Cosubstrates of iso-PTase: dimethylallyl diphosphate (**193**), geranyl diphosphate (**194**) and farnesyl diphosphate (**195**). Chemical structures of 8-prenylnaringenin (**196**) and a chalcone **197** as examples for prenylated drugs.

The *C*-prenylation of natural products like these aromatic molecules is catalysed by a specific class of PTases. These aromatic PTases specifically catalyze the transfer to aromatic substrates, leading to a diverse array of primary and secondary metabolites in plants, fungi, and bacteria. They are categorised into four major groups based on their structural properties.[272, 273]

4.2.3.1 Structure of Aromatic Prenyltransferases

The first group, UbiA-like PTases, comprises membrane-embedded enzymes, which are often involved in the primary metabolism. They play a crucial role in synthesising ubiquinones, hemes, vitamin E, and various structural lipids, making these compounds soluble in biomembranes.[274, 275] UbiA is involved in the biosynthesis of ubiquinon geranylating the *meta*-position of 4-hydroxy benzoic acid (**198**) forming the corresponding product **199**.[276] The first crystal structure of these enzymes was solved in 2014, revealing that the UbiA homolog contains nine transmembrane helices forming a U-shaped architecture with a large central cavity. This cavity is sealed by a cap domain containing Asp-rich motifs [Figure 52].[277]

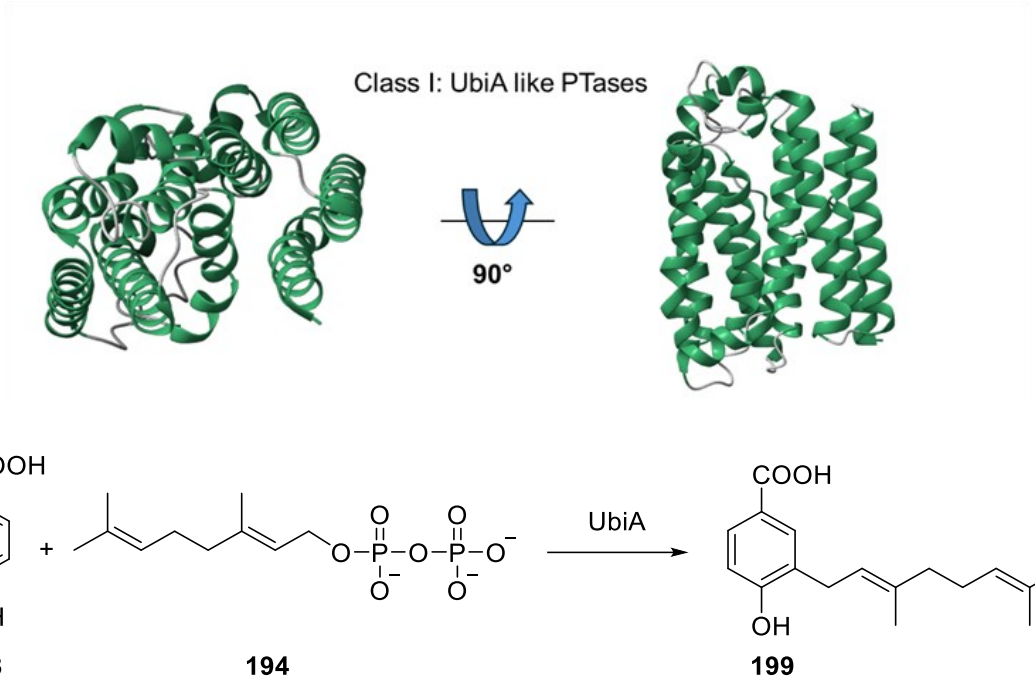

Figure 52: Crystal structure of a UbiA homolog from Aeropyrum pernix K1 (PDB: 4OD4). Geranylating of the meta-position of 4-hydroxy benzoic acid (**198**) catalysed by UbiA.

The second and third group both belong to the ABBA-superfamily: the CloQ/NphB-like and the dimethylallyl tryptophan synthase (DMATS)-like PTases.[278]

CloQ, identified as a PTase that prenylates at *C3* of 4-hydroxyphenylpyruvate (**200**) (4HPP) forming the prenylated product **201** [Figure 53], is involved in the biosynthesis of the antibiotic clorobiocin produced by *Streptomyces roseochromogenes*.[279] CloQ is soluble and lacks sequence similarity, including the characteristic DDXXD motif, compared to known class I PTases.[280] NphB from *Streptomyces* sp. strain CL190 was identified through its sequence similarity to CloQ. For structural insights into this class of enzymes, the homologue PTase Orf2 was crystallised and revealed a novel *β*/*α* fold with antiparallel strands in an *α*-*β*-*β*-*α* architecture.[281] This barrel structure and large central cavity are the reason for the enzyme's promiscuity towards various aromatic substrates [Figure 53].[272, 273]

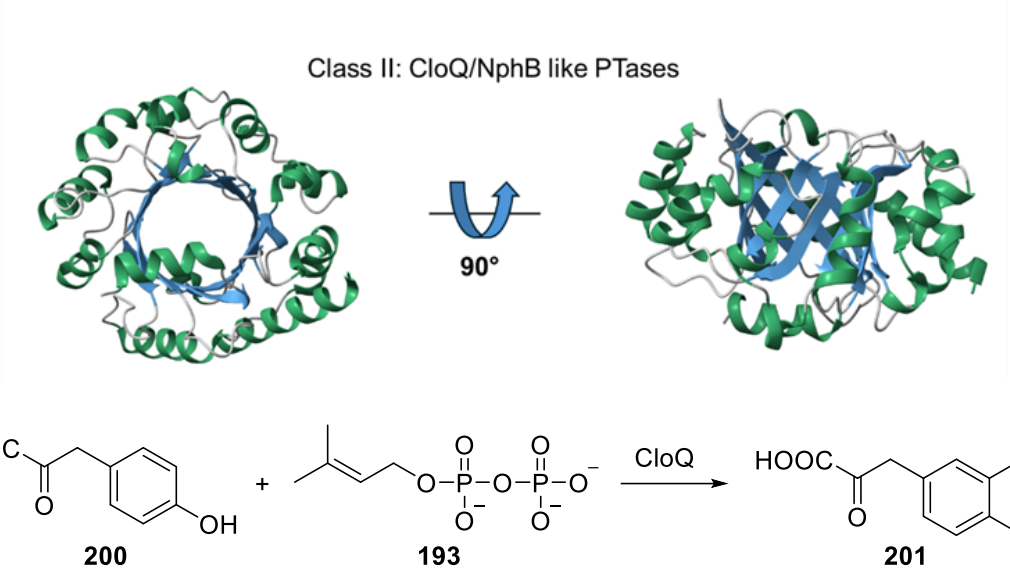

Figure 53: Co-crystal structure of Orf2 an aromatic prenyl transferase from Streptomyces sp. strain CL190 complexed with GPP (PDPB: 1ZCW). Prenylation of the *C3* position of 4-hydroxyphenylpyruvate (**200**) catalysed by CloQ.

The first identified dimethylallyl tryptophan synthase (DMAT) was DmaW from *Aspergillus fumigatus*, which catalyses the prenylation of L-tryptophan (**202**) at the C-4 position of the indole ring yielding the prenylated product **203** [Figure 54A]. This soluble enzyme contains a (N/D)DXXD motif.[282-284] Over the past decade, numerous PTases with significant sequence homology have been identified, forming the DMATS superfamily. Between 2009 and 2023, 12 crystal structures of this enzyme class were solved, revealing the characteristic *α-β-β-α* architecture. These enzymes predominantly accept DMAPP (**193**) as the prenyl donor and catalyze prenylation at aromatic substrates **204** in either a regular/linear or branched manner towards the corresponding regioisomers **205** and **206** via the cationic intermediated **207** and **208** [Figure 54B].[285, 286]

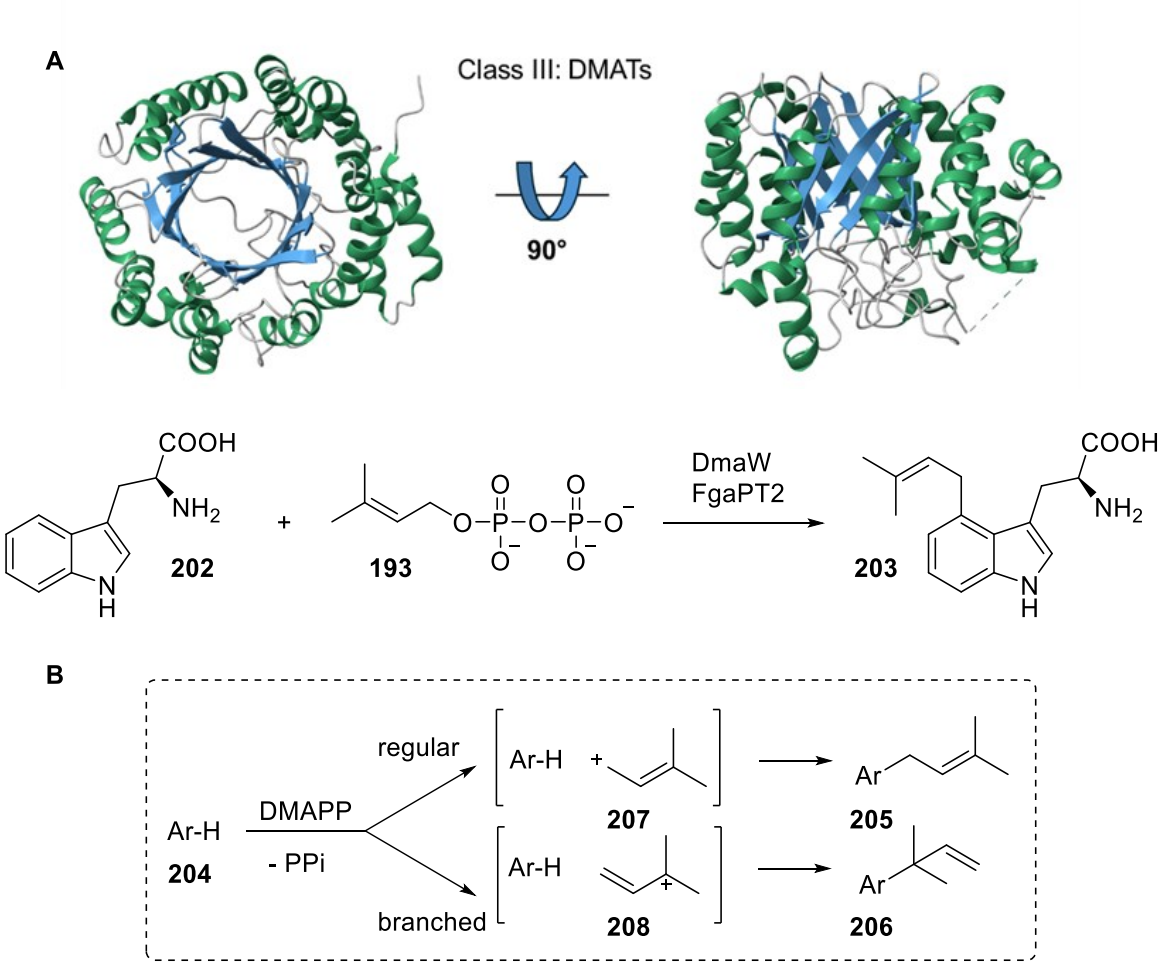

Figure 54: A: Crystal structure of the dimethylallyl tryptophan synthase FgaPT2 from Aspergillus fumigatus (PDB: 3I4Z). Prenylation of tryptophan (**202**) by DmaW or FgaPT2 at the C4 position. B: Reaction schemes for a linear and reversed prenylation on an aromatic substrate catalysed by a DMAT.

The fourth group consists of squalene synthase (SQS)-like PTases, which have not been extensively studied. The crystal structure of the SQS-like PTase LvqB4 from *Streptomyces viridochromogenes* 2942-SVS3 in complex with a cofactor analogue shows a structure similar to SQS, with the prenyl donor and acceptor stacking interactions resembling those of known aromatic PTs.[287] LvqB4 is homologous to CqsB4 from *Streptomyces exfoliatus* 2419-SVT2, which is involved in the biosynthesis prenylating the carbazole substrate **209** to form carquinostatin A (**210**).[288] However, LvqB4 uses a different cosubstrate, cyclolavandulyl diphosphate (**211**, CLPP), yielding a different reaction product **212**. LvqB4's structure mainly comprises 12 *α*-helices that form a large cavity surrounded by these helices, with two aspartate-rich motifs located on the upper side of the cavity [Figure 55].[287]

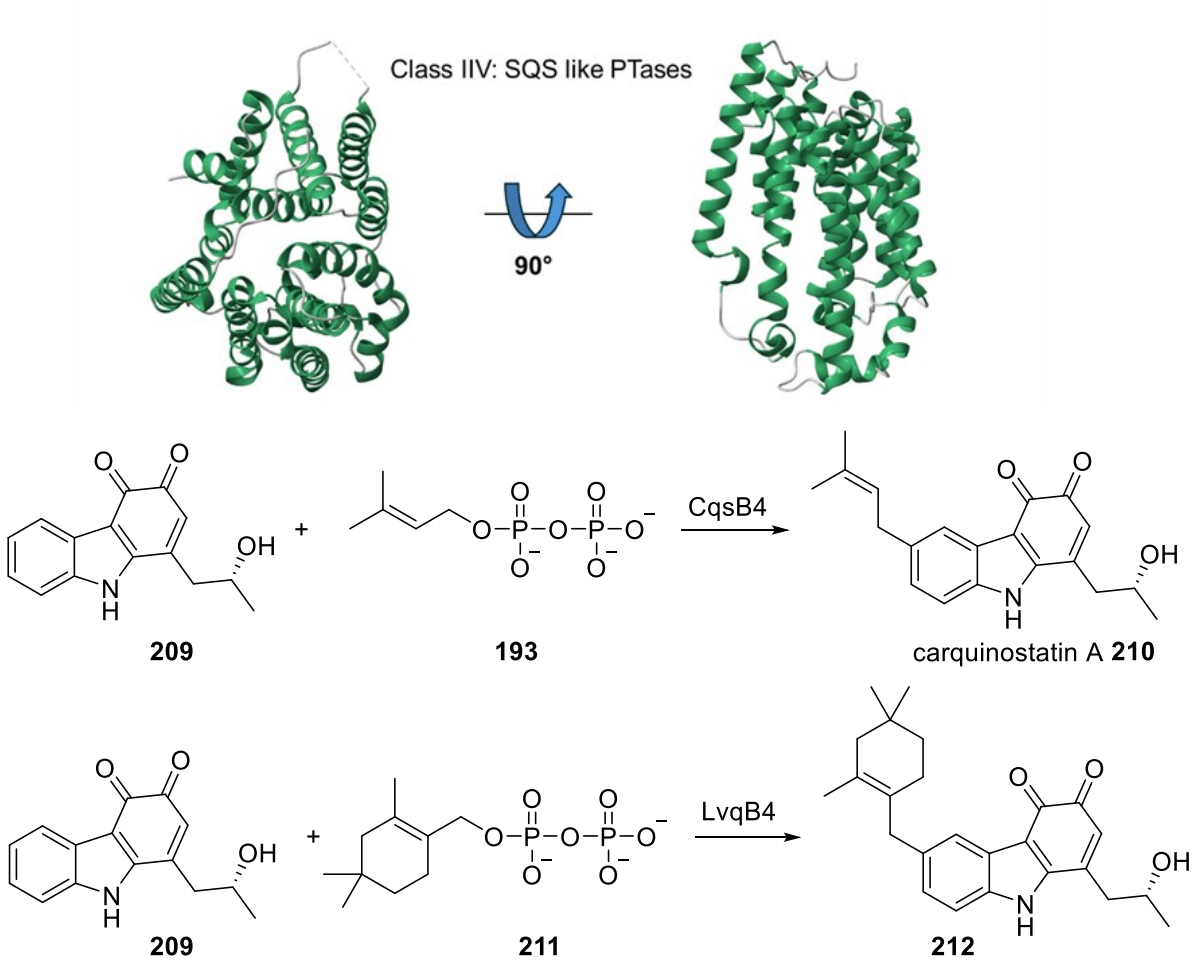

Figure 55: Crystal structure of the carbazole PTase LvqB4 (PDB: 7VWS). Prenylation of a carbazole substrate by CqsB4 or LvqB4.

4.2.3.1.1 Trp-Diketopiperazine prenyltransferases

Most Trp-DKP PTases are classified under class III PTases. These DKP-DMATs feature a relatively hydrophobic and more spacious active site compared to Trp-DMATs, with the size of the binding pocket playing a critical role in determining the substrate scope.[286, 289] For example, the binding pocket of FtmPT1 from *Aspergillus fumigatus*, prenylating a cWP DKP **213**, has a solvent-accessible volume of about 1600 Å³, while the binding pocket of PTases prenylating cWW substrates **3a**, like CdpNPT from the same organism, is approximately 500 Å³ larger [Figure 56].

As a result, CdpNPT is capable of prenylating a way wider range of substrates.[290, 291] Although substrate binding interactions in DKP-DMATs are typically conserved, relying mainly on hydrophobic interactions and hydrogen bonds with the substrate's heteroatoms, these enzymes display unique regioselectivities and prenylation types. These differences arise not only from the overall size of the binding pocket but also from its rigidity and the orientation of the indole moiety within the pocket.[286, 292-294] For example, FtmPT1 catalyses prenylation in the regular/linear manner to form the *C2*-prenylated product **214**.[290, 295] CdpNTP catalyses linear *N*-prenylation yielding the *N*-methylated cWW **215**.[296] AnaPT and CdpC3PT from *Neosartorya fischeri* catalyse reverse prenylation at the *C3*-position of the indole of cWA **216** forming the HPI structural motifs in the diastereomers **217** and **218** [Figure 56].[293]

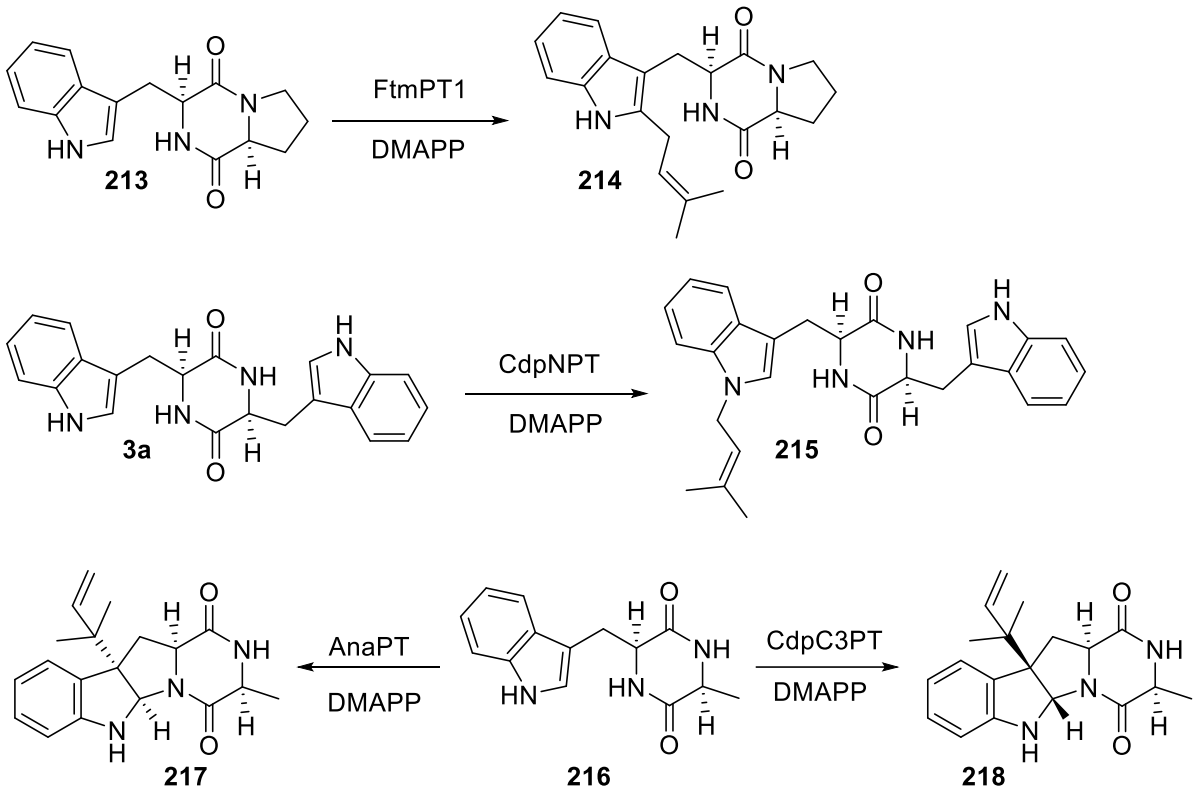

Figure 56: Prenylation of DKP substrates by DMATS: FtmPT1 catalysis C2 prenylation, CdpNPT and CTrpPT catalyse *N*-prenylation. AnaPT and CdpC3PT catalyse *C3* prenylation in a reverse manner forming different isomers.

Although Trp-PTases are known to catalyze prenylation at every position on the indole ring,[297] DKP PTases primarily target the nitrogen atom or the *C2* and *C3* positions like shown in the previous examples.[285, 297] CTrpPT from *Aspergillus oryzae* and CdpC7PT from *Aspergillus terreus* are the only cyclic dipeptide PTase known to catalyze prenylation on the *C7* position,[296, 298] whereas FgaPT2 from *Aspergillus fumigatus* and CpaD from *Aspergillus oryzae* prenylated the *C4* position of the Trp containing DKP **219** [Figure 57].[102, 299, 300]

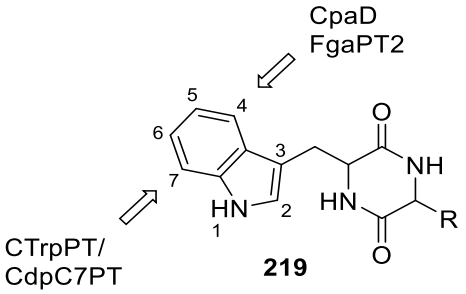

Figure 57: Prenylation of the benzene ring of DKPs. CpaD and FgaPT2 prenylate at the *C4* position, CtrpPT and CdpC7PT at the *C7* position.

EchPT2 from *Aspergillus ruber* is the only known PTase that catalyses prenylation at the *C5* position of the indole ring in a DKP, producing compound **220**. This reaction takes place on the cWA substrate **216** only after the *C2* position has been prenylated by the PTase EchPT1 from the same organism, leading to the formation of the intermediate **221**. [Figure 58].[301]

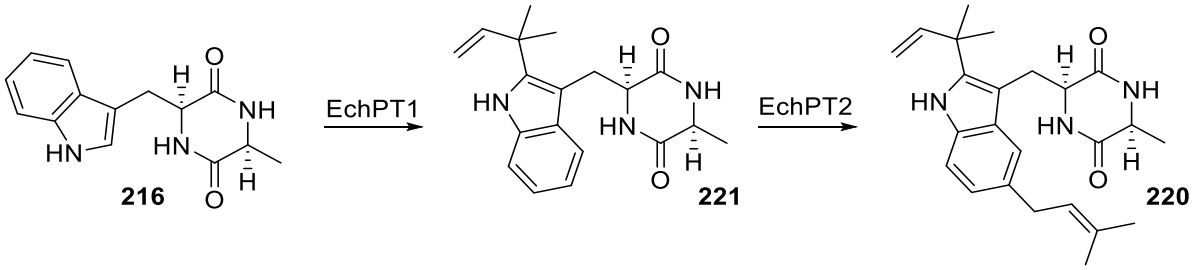

Figure 58: Prenylation of cWA. EchPT1 catalyses C2-prenylation, EchPT2 *C5*-prenylation.

In recent years, a few SQS-like PTases have been identified that accept DKP substrates. In 2018, genome mining of marine *Streptomyces* strains uncovered a three-gene locus in *Streptomyces youssoufiensis* OUC6819, which includes a new PTase, DmtC1. This enzyme uses geranyl pyrophosphate to isoprenylate the *C3*-position of the cWP substrate **213** forming the corresponding HPI **222** [Figure 59]. Phylogenetic analysis indicated that DmtC1 clusters with squalene synthases rather than with typical indole PTs.[302] Another example from 2021 involves genome mining of *Streptomyces leeuwenhoekii* NRRL B-24963, which revealed a two-gene locus with a PTase SazB fused with a MTase. SazB prenylates the *C3*-position of the cWW **3a** forming the HPI motif in compound **223**.[223] Similar to this enzyme, the PTase GczB from *Streptomyces griseocarneus* 132 prenylates the same substrate, but leading to the diastereo-complementary product **224** [Figure 59].[303]

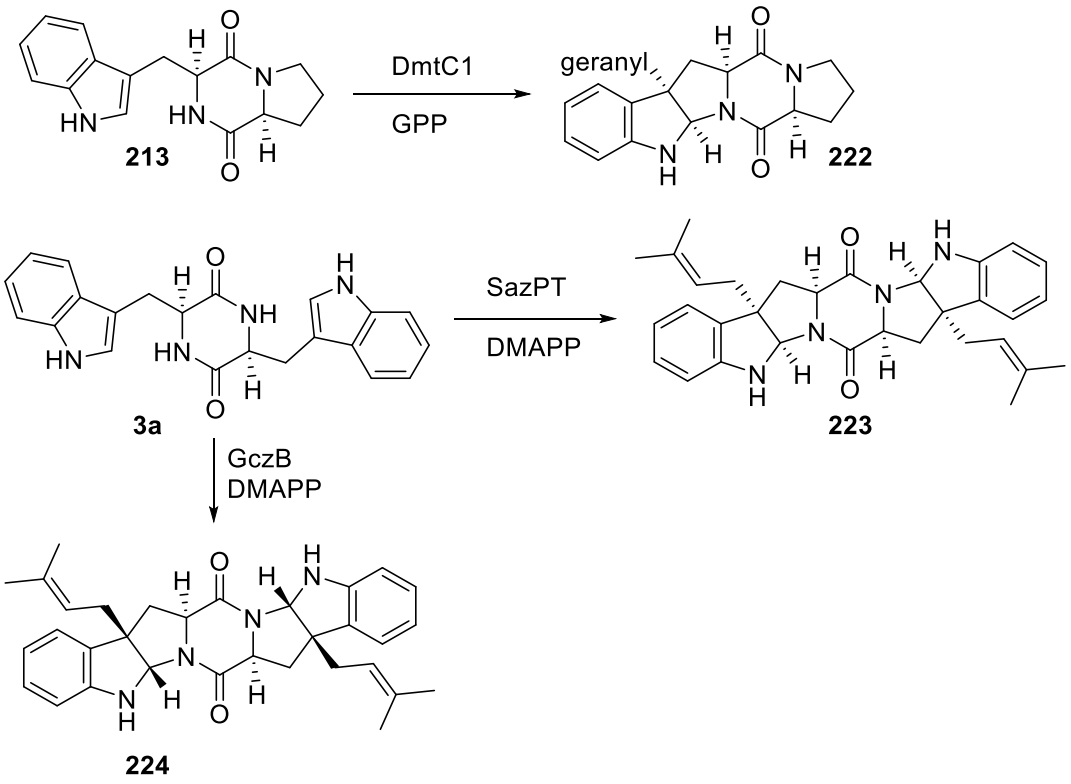

Figure 59: Prenylation by SQS like PTases. DmtC1 catalyses *C3*-gernylation, SazPT *C3*-prenylation.

5. RESULTS

5.1. Pyrroloindole based assay

As previously described, the HPI motif is a common building block in biologically active natural products.[44-46] The stereoselective synthesis of this motif, however, remains a significant challenge using traditional organic methods.[47] Therefore, enzymes involved in the formation of HPI-based compounds are increasingly studied. These biocatalytic reactions often feature an intramolecular cyclisation of a substituted indole **225**, leading to dearomatisation and the formation of the HPI scaffold **226**.[59, 99] Several enzyme classes have been identified to produce HPIs, including cytochromes P450,[77, 97, 98] monooxygenases,[94-96] MTases,[87, 99, 100] and PTases,[101-103] which catalyze the addition of various functional groups, such as hydroxyl, methyl, or prenyl groups [Figure 60].

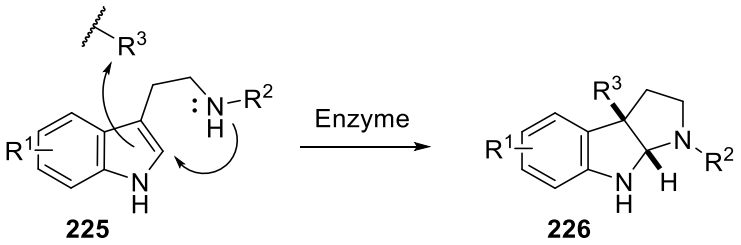

Figure 60: Reaction scheme of an enzymatic HPI formation from an indole substrate **225**.

Nevertheless, enzyme optimisation, often via enzyme engineering and directed evolution, is frequently required to meet industrial demands on a catalyst. This optimisation is key for enhancing enzyme properties like selectivity, stability, and activity. Robust high-throughput screening strategies are essential for generating large enzyme libraries and optimizing biocatalytic processes for drug and natural product synthesis.[304-306]

As part of this thesis, a specialised assay was established to quantify the formation of the HPI reaction product. The inspiration for this HPI product based assay is driven by a common staining solution in organic chemistry: The cerium molybdate stain (CAM stain, also known as Hanessian's stain or Moly-Dip) is commonly used in thin-layer chromatography (TLC) for detecting a wide range of compounds, including aromatic alcohols, alkaloids, and lipids.[110, 307-309] The staining solution contains cerium sulfate, ammonium molybdate, and sulphuric acid. Its mechanism of action involves the reduction of Mo(VI) to a lower oxidation state, producing molybdenum blue-like structures that result in visible colour changes. The Ce(IV) from cerium sulfate acts as a potent one-electron oxidant.[310, 311] Traditionally, CAM stain is employed for the qualitative detection of compounds, but recent applications have shown its utility in the semi-quantitative analysis of lipids on high-performance TLC plates.[308]

5.1.1 Assay development

To develop an assay suitable for enzymes that form HPIs from indole substrates, a suitable indole/HPI compound pair is required to ensure that the assay specifically detects the enzymatic product. Melatonin (**227**) and its *C3*-methylated derivative **228** were selected as model compounds for this purpose due to their availability and ease of modification. The *C3*-methylation of melatonin was achieved using iodomethane as the methylating agent under basic conditions, with triethyl borane added to prevent *N*-methylation. The reaction yielded the *C3*-methylated HPI melatonin derivative **228** in a good yield of 76% [Figure 61].

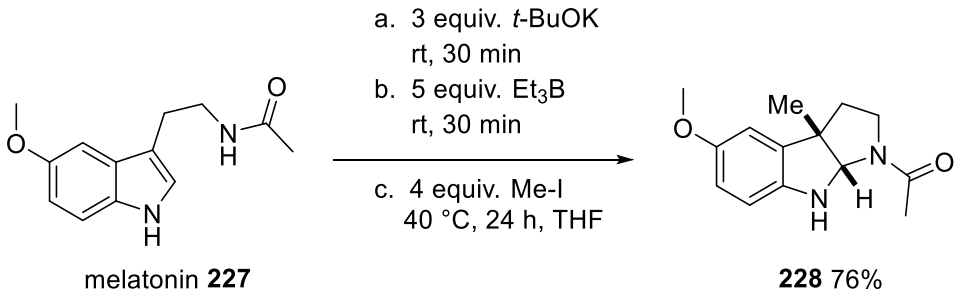

Figure 61: Synthesis of *C3*-methylated melatonin **228**.

As previously mentioned, the HPI assay based on the principle of the CAM stain: Normally, a TLC plate is dipped into the CAM staining solution, and upon heating, blue spots develop against a yellow background due to the reduction of the stain's components and the formation of molybdenum blue-like compounds as described before. When this stain is applied to a TLC plate containing both indole and HPI compounds, the HPI spot becomes colourful without heating, while the indole spot remains colourless. This observation inspired the development of a microtiter plate absorbance assay for enzymes involved in HPI formation.

In a first attempt, 5 vol% CAM stain were added to a 1 mM solution of melatonin **227** and *C3*-methylated melatonin **228** (in 50 mM KPi buffer, pH 7.5) in a 96-well plate. Only the solution containing the HPI gradually developed a blue colour, further supporting its potential as a tool for monitoring HPI-forming enzymes. After 20 min, the absorption spectrum was measured giving an absorption maximum of 608 nm for the *C3*-methylated melatonin [Figure 62].

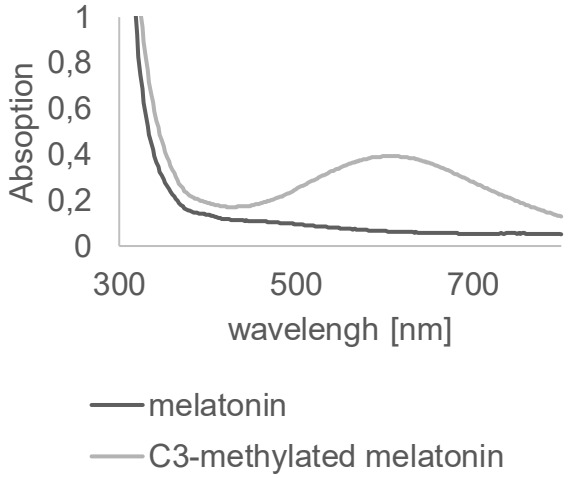

Figure 62: Absorption spectra of 1 mM solutions of melatonin (**227**) and methylated melatonin **228** after treatment with 5 vol% CAM stain and incubation for 20 minutes.

The assay was optimised by adjusting both the incubation time and the volume of CAM staining solution. To determine the optimal incubation time, the reaction was repeated under the same conditions, while measuring the absorbance at different time points. The maximal absorbance of 0.5 was reached after 30 minutes. For optimizing the CAM stain volume, the absorbance was recorded after 30 minutes after adding different amounts of the staining solution. The maximum absorbance was observed with the addition of 3-5% (v/v) CAM stain. Adding more than 5% led to the formation of a precipitate, which interfered with absorbance measurements [Figure 63].

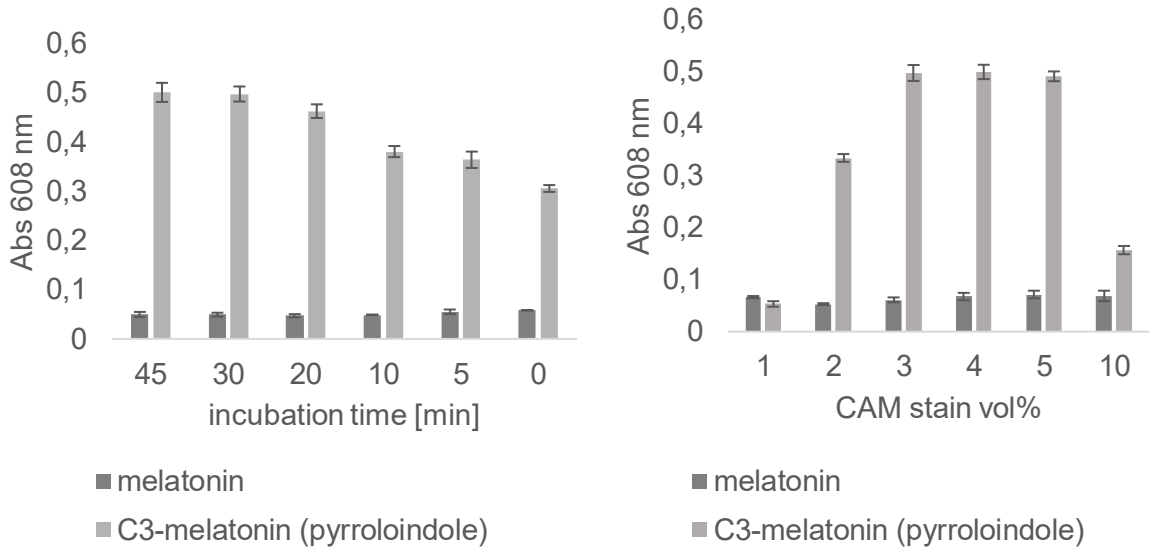

Figure 63: Absorption at 608 nm of a 1 mM solution of melatonin (**227**) and methylated melatonin **228** after treatment with 5 vol% CAM stain and different incubation times (left). Absorption at 608 nm of a 1 mM solution of melatonin (**227**) and methylated melatonin **228** after treatment with different concentrations of the CAM stain and incubation for 30 min (right).

To determine which component of the cerium molybdate (CAM) stain is responsible for the blue colouration, the individual components of the stain were added separately to a solution of *C3*-methylated melatonin **228**. The CAM stain is composed of 25 mM cerium(IV) sulfate (Cer), 15 mM phosphomolybdic acid (PMA), and 1 M sulphuric acid (A) in water. Each component was added in proportions equivalent to the amount present in a 3% (v/v) CAM solution. The most intense colour change was observed when cerium sulfate and sulphuric acid were combined. The PMA and the complete CAM stain produced a light blue/violet colour after incubation with the HPI substrate. In the CAM stain, the blue colour typically arises from the reduction of Mo(VI) to a lower oxidation state, resulting in molybdenum blue-like pigments.[310, 312] Ascorbic acid, a known reducing agent, was tested as a positive control to verify this mechanism using the individual components of the CAM stain. Only the solutions containing PMA exhibited the characteristic blue colour. However, the colour formation observed in the HPI-containing solution, when treated with acid and cerium sulfate, cannot be attributed to the formation of these molybdenum blue pigments, indicating a different underlying mechanism [Figure 64].

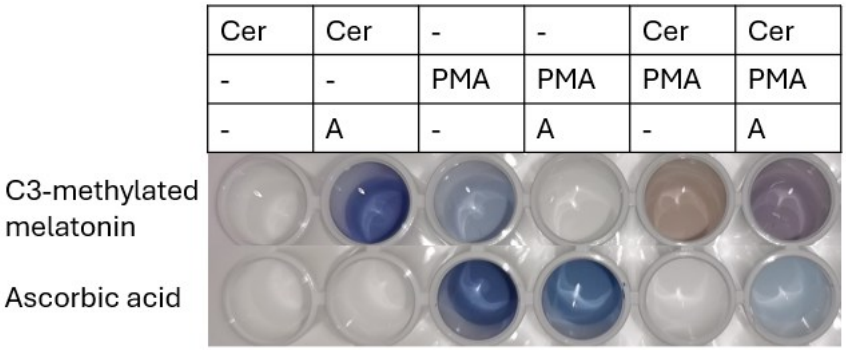

Figure 64: Screening of CAM stain components. 1 mM solution of *C3*-methylated melatonin **228** or ascorbic acid after treated with CAM stain components and incubation for 30 min. The CAM stain is composed of 25 mM cerium(IV) sulfate (Cer), 15 mM phosphomolybdic acid (PMA), and 1 M sulphuric acid (A) in water. Each component was added in proportions equivalent to the amount present in a 3% (v/v) CAM solution.

To compare the CAM stain with the newly developed acidic cerium sulfate stain, a dilution series of the model substrate, *C3*-methylated melatonin **228** in KPi buffer, was prepared. Each dilution was treated under the same optimised conditions: 3% v/v staining solution and 30-minute incubation. With the CAM stain, precipitation occurred at HPI concentrations below 0.5 mM, resulting in diminished colour intensity. In contrast, the acidic cerium sulfate stain did not produce any precipitation even at lower HPI concentrations, making it more effective for detecting these compounds at lower levels.

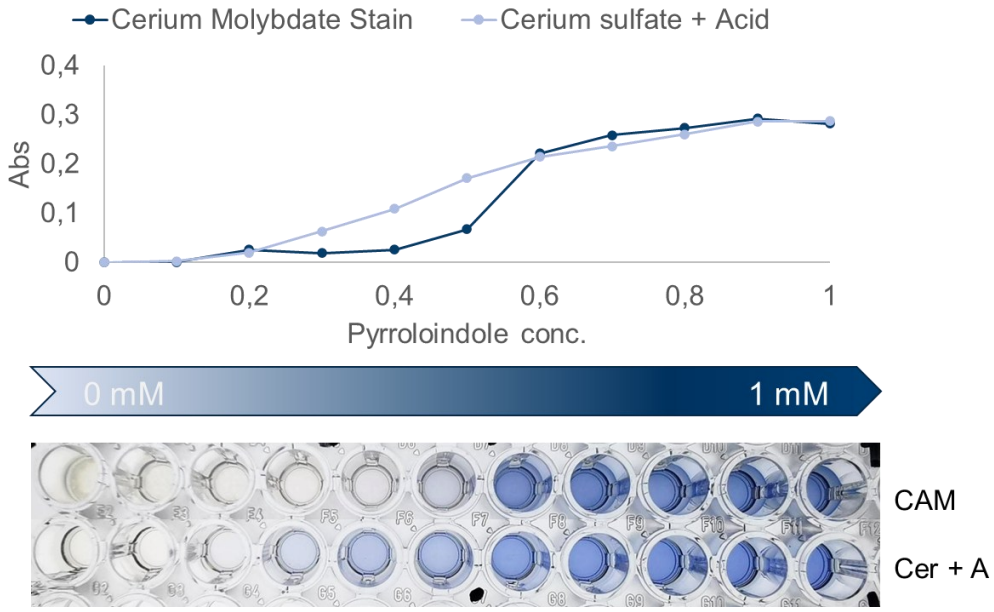

Figure 65: Dilution row of *C3*-methylated melatonin **228** (0-1 mM, 200 µL) after adding the staining solutions (3 Vol% CAM or acidic cerium sulfate solution) and incubation for 30 min. The absorption was measured at 608 nm after centrifuging the solution and pipetting 100 µL in a new plate.

Since cerium sulfate and sulphuric acid appeared to be crucial for the colouration of the HPI-containing solution, these components were selected for individual optimisation. Either the sulphuric acid or the cerium sulfate concentration was varied, while keeping the other component stable (same amount like in the starting condition: 3 vol% acidic cerium sulfate solution). The optimisation was conducted at two HPI **228** concentrations (0.25 mM and 0.75 mM) to assess both low and high concentrations in KPi buffer (50 mM, pH 7.5) in a total volume of 200 µL. At concentration of 0.25 mM of the HPI **228**, the highest absorption was observed with 0.02 M acid and 0.5 mM cerium sulfate. For the concentration of 0.75 mM of the *C3*-methylated melatonin **228**, optimal absorption required higher amounts: 0.03 M acid and 1.25 mM cerium sulfate. In an additional experiment, the incubation temperatures were varied (20 °C, 35 °C, and 50 °C) revealing the highest absorption when incubating 35 °C, even though the temperature has only little impact [Figure S 3].

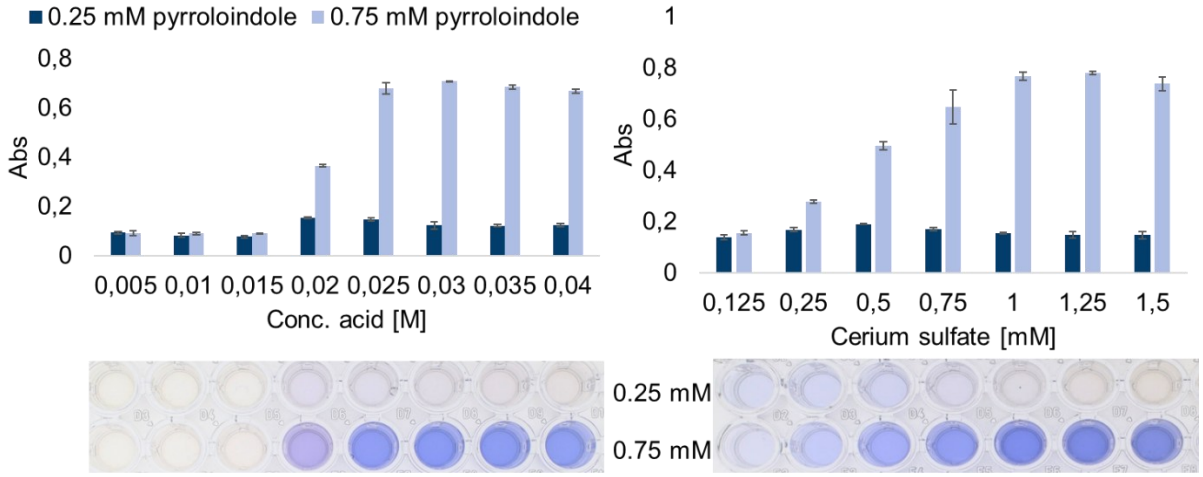

Figure 66 Optimisation of the HPI assay. Single parameter optimisation of acid concentration or cerium sulfate concentration for 0.25 mM and 0.75 mM of the HPI **228**.

To account for potential interactions between parameters, a design of experiment was conducted using sulphuric acid and cerium sulfate concentrations as variables, with absorption as the response measure. The findings confirmed the results from the single parameter optimisation for the higher HPI concentration. For the lower concentration, the acid concentration was optimised to 22.5 mM, while the cerium sulfate concentration was maintained at 0.5 mM [Table S 1, Table S 2].

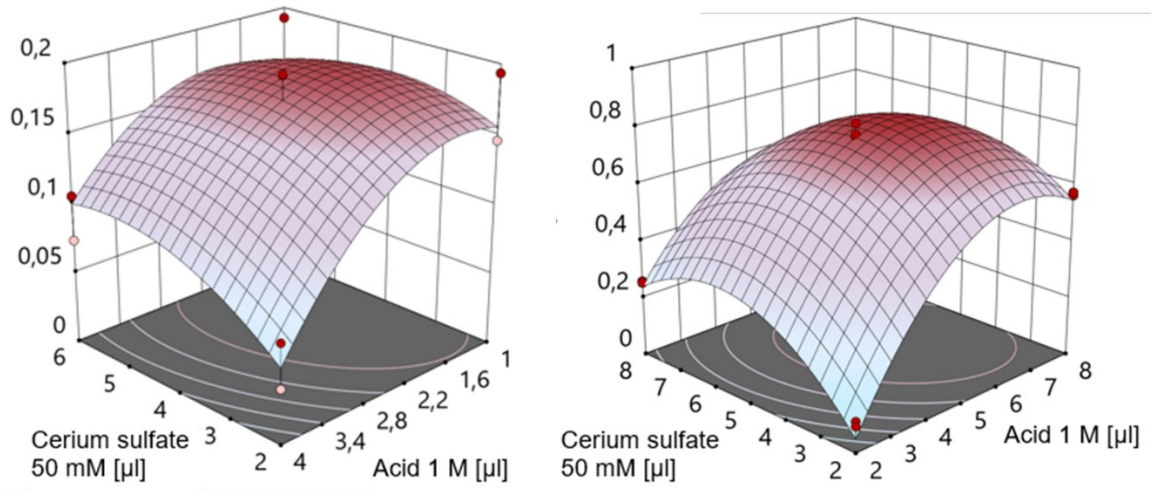

Figure 67: Result of the design of experiment approach varying the acid and cerium sulfate concentration for 0.25 mM and 0.75 mM of the *C3*-methylated melatonin **228**.

Using the newly optimised conditions, the linear range for each concentration was determined. The optimised parameters for low HPI concentrations exhibited a linear range from 0.1 to 0.4 mM, while the conditions for high HPI concentrations showed a linear range from 0.5 mM to 1 mM.

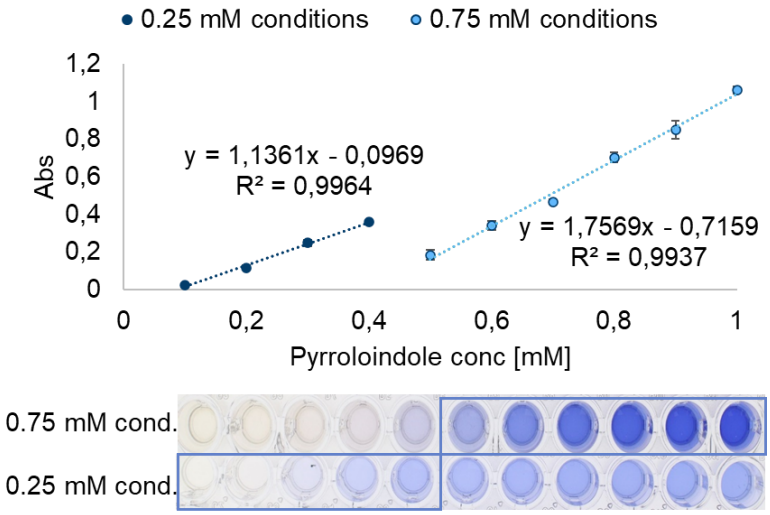

Figure 68: Calibration of the *C3* methylated melatonin **228** under optimised conditions for low and high concentrations.

5.1.2 Substrate scope

In the class of HPI natural products, *C3*-hydroxylated (class B) and *C3*-alkylated (class C) derivatives are widely found and display a variety of biologically significant properties. To demonstrate the utility of the developed assay for enzymes transferring these groups to form the HPI motif, the model substrate melatonin (**227**) was modified respectively: The melatonin was selectively modified at the *C3*-position by methylation, prenylation, and hydroxylation. The prenylation was accomplished using prenylbromide as alkylating agent yielding the *C3*-prenylated melatonin **229**. The *C3*-hydroxylated melatonin **230** was synthesised via a four-step process: the indole *N1*-nitrogen of melatonin (**227**) was first protected with a tert-butyloxycarbonyl (Boc) group, resulting in the Boc-protected melatonin **231**. The HPI motif in the intermediate **232** was formed by adding potassium bromide and Oxone® in equimolar amounts to the protected melatonin **231** in acetonitrile for 4h at room temperature. After the deprotection of the nitrogen under acidic conditions towards intermediate **232**, the bromine was substituted by the hydroxy group by the reaction with silver sulfate in water and acetonitrile yielding the protected *C3*-hydroxylated melatonin **233**. An overall yield of 49% was achieved for these four reactions [Figure 69].

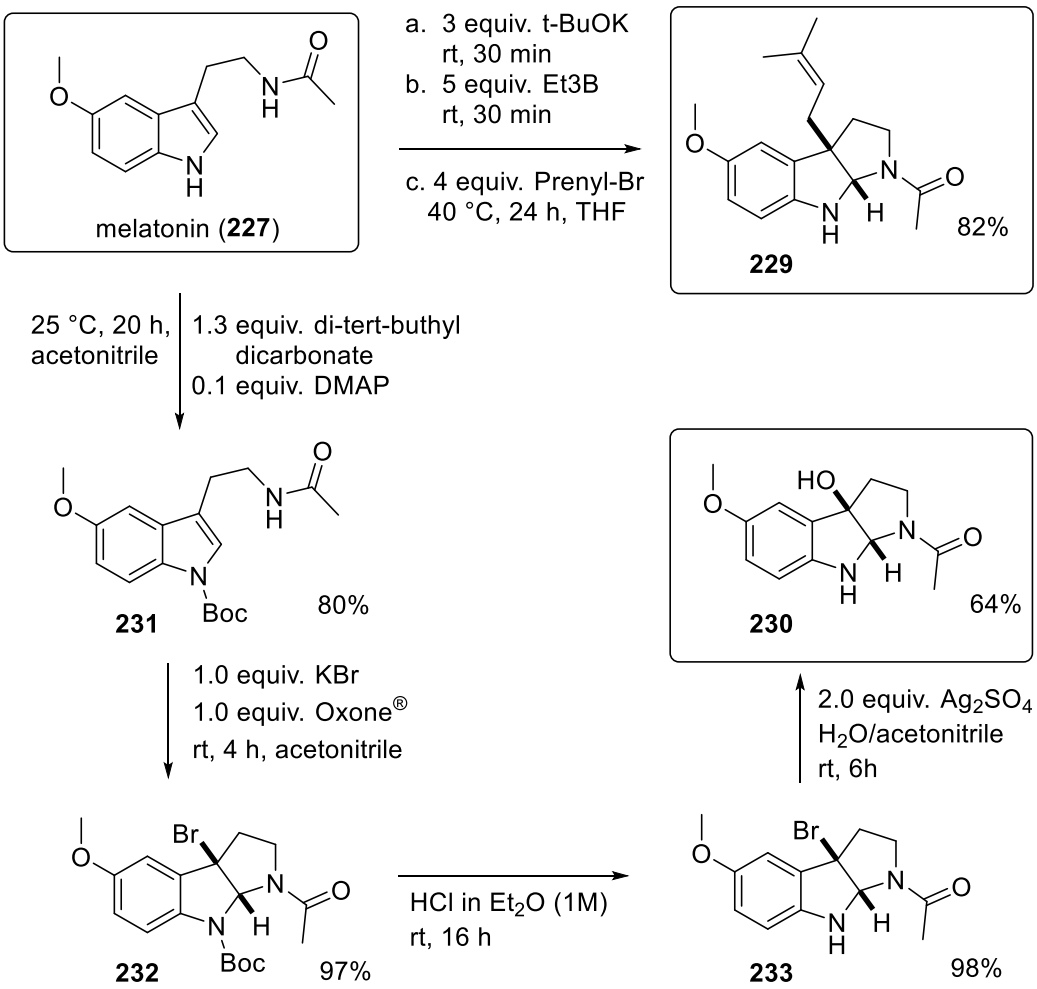

Figure 69: Synthesis of *C3*-prenylated **229** and *C3*-hydroxylated melatonin **230**.

To test the applicability of the developed assay for these substrates, each derivative was prepared in a 1 mM solution in KPi buffer (50 mM, pH 7.5) and tested under the optimised conditions. The substituted derivatives exhibited absorption maxima between 595 nm and 615 nm, indicating that the colourimetric assay is not reliant on specific substituents at the *C3*-position. Therefore, the HPI assay is not only suitable for methyltransferases but also holds potential for use with cytochromes P450, monooxygenases, prenyltransferases, and other enzymes involved in HPI motif formation, although additional research is needed to confirm its broader applicability.

Additionally, various natural products and derivatives were tested to extend the substrate scope like esermethol (**81**), phenserine (**234**), eseroline (**235**), rivastigmine (**236**) and physostigmine (**48**). Only those containing a HPI motif displayed colour (absorption maxima between 455 and 475 nm) after treatment with the staining solution. Additionally, physostigmine precursor analogues **148**+**149** and **237**-**239** (provided by Diana Amariei and Pascal Schneider), which differ in their *C5*-position and nitrogen substituents in the HPI ring, showed absorption maxima ranging from 560 nm to 570 nm. The dipeptide **3a**, which is a core structure for many HPI-containing natural products, was also tested. A vibrant red precipitate formed after adding the staining solution to the HPI containing DKP **240**. Interestingly, when the experiment was repeated using ten times the amount of sulphuric acid, no precipitate formed indicating a better solubility, resulting in a high measurable absorption at 475 nm. This molecule, containing two HPI motifs, exhibited an absorption more than double that of the other tested compounds [Figure 70].

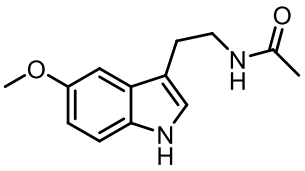

melatonin (**227**)

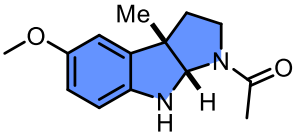

228 610 nm

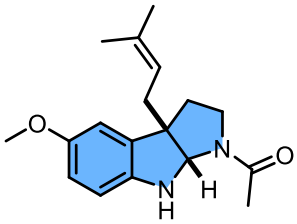

229 615 nm

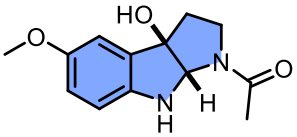

230 595 nm

Melatonin derivatives

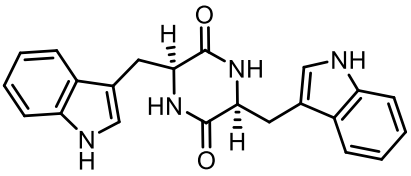

3a

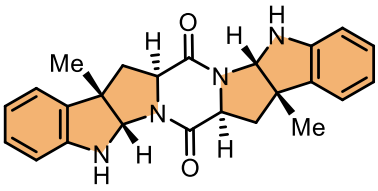

240 475 nm

Dipeptides

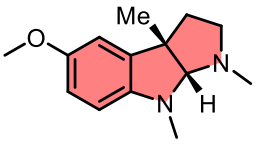

esermethol (**81**)

475 nm

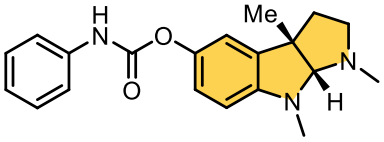

phenserine (**234**)

465 nm

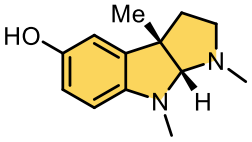

eseroline (**235**)

465 nm

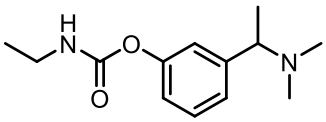

rivastigmine (**236**)

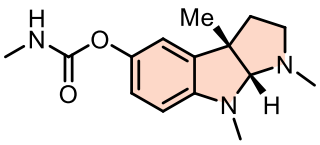

physostigmine (**48**)

455 nm

Natural products

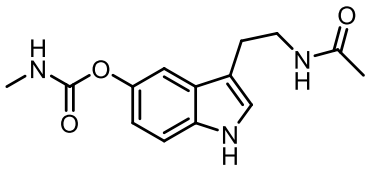

148

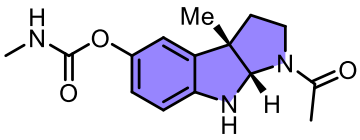

149 570 nm

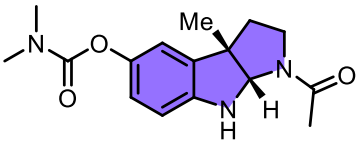

237 270 nm

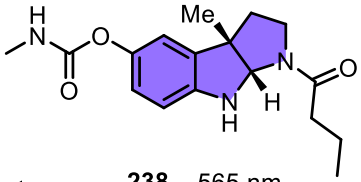

238 565 nm

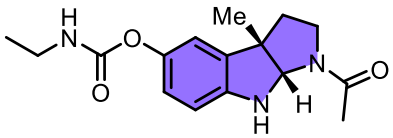

239 560 nm

PsmD products

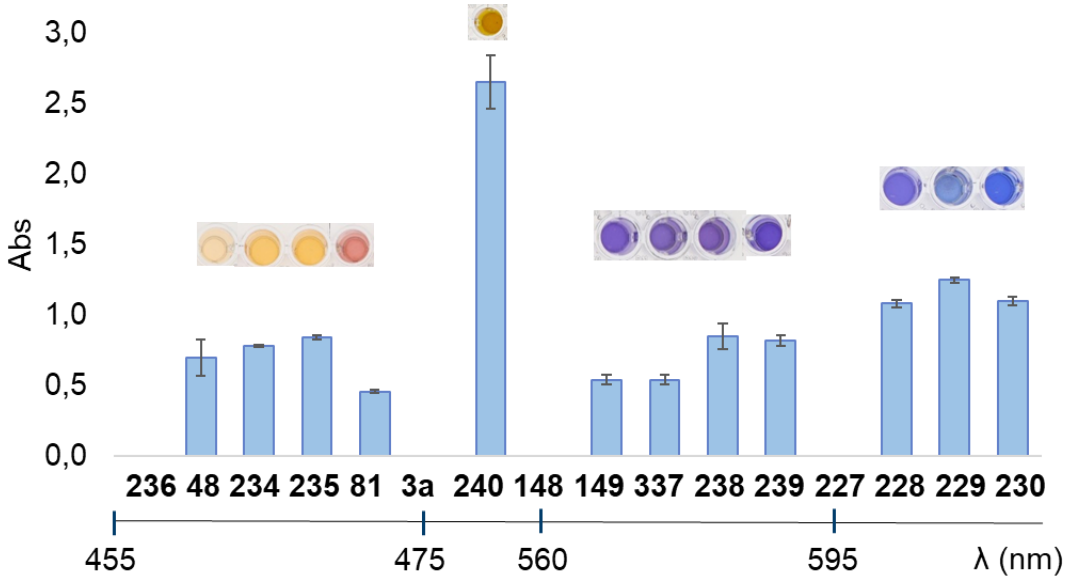

Figure 70: Application of the HPI assay for the melatonin derivatives, physostigmine analogs, a dipeptide, and other natural products. The ring filled colour indicates the colour after applying the assay to the corresponding compound. The absorption was measured at the absorption maximum.

As cerium-based staining solutions rely usually on redox mechanisms, the redox properties of the tested compounds were analysed. To determine their oxidation potential, an ABTS-based method was employed. In this approach, a pre-generated ABTS•+ radical cation reacts with the antioxidant, causing the characteristic absorption peak at 734 nm to disappear.[313] This change in absorbance was compared to a standard (ascorbic acid) to calculate the relative oxidation potential of each compound. Results showed that the HPI form of melatonin, the physostigmine analogs, and the dipeptide exhibited significantly higher oxidation potentials compared to their non-cyclised indole forms. Additionally, the reduction potential of melatonin derivatives was assessed using cyclic voltammetry with the equipment of the working group of Prof. Dr. Constantin Czekelius. Melatonin's reduction potential was measured at 0.98 V, consistent with values reported in the literature.[314] The *C3*-substituted derivatives showed lower reduction potentials, around 0.6 V [Figure 71].

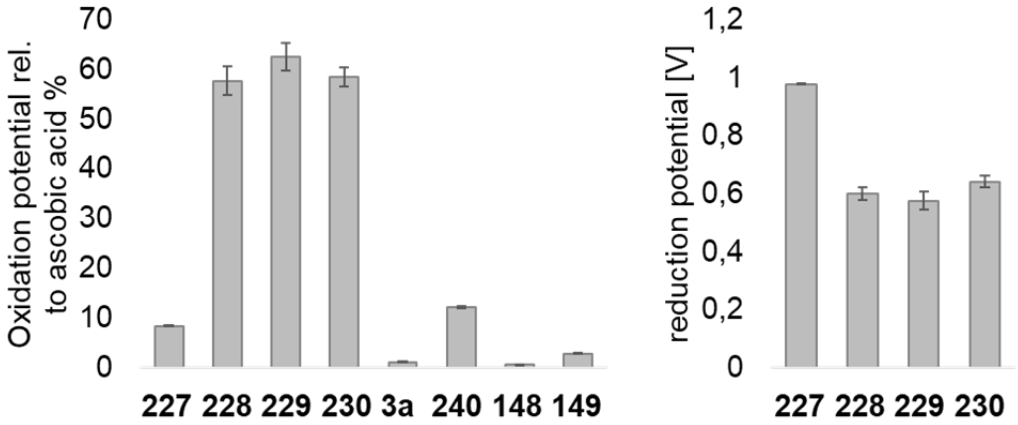

Figure 71: Oxidation potential measured with the ABTS assay (left) and reduction potential measured with cyclic voltammetry of selected compounds (right).

In a similar experiment, solutions of *C3*-substituted HPI melatonin derivatives were electrochemically oxidised using a carbon felt anode and Ag/AgCl cathode at 0.1 A and 15 V. Gradually, the solutions turned blue. Absorbance measurements revealed an absorption profile with a peak at approximately 608 nm, confirming the characteristic colour formation. This suggests that the colour formation is due to the oxidation of the *C3*-substituted HPI melatonin derivative itself, triggered by the cerium sulfate. However, the coloured compound could not be isolated or crystallised, preventing further structural elucidation [Figure 72].

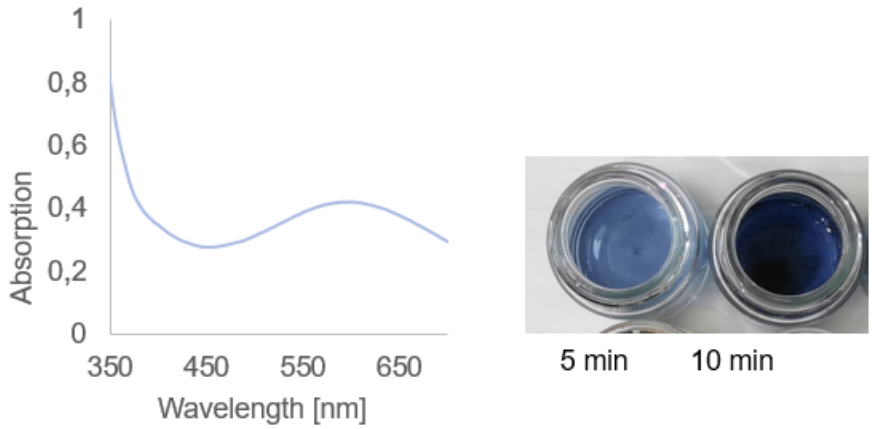

Figure 72: Absorption spectrum of a solution of 1 mM *C3*-methalted melatonin in 50 mM KPi buffer and 0.03 M sulphuric acid after 5 min at 0.1 A and 15 V. Picture of the same solution after 5 and 10 min.

5.1.3 Application for Methyltransferases

The assay was applied to determine the activity of the *C3*-indole MTase PsmD from *Streptomyces albulus* (PsmD_Sa), an enzyme involved in the biosynthesis of the acetylcholinesterase (AChE) inhibitor physostigmine (**48**). The enzyme was provided by Diana Amariei. A dilution series of the *C3*-methylated product **149** was used as a calibration curve to quantify the product concentration during the enzymatic reaction [Figure S 5]. The reaction was stopped at various time points by addition of TFA, and the samples were directly analysed using the assay. The product concentration was plotted against time, allowing for the calculation of the specific activity of PsmD_Sa. Using the HPI assay, the specific activity was determined to be 0.047 ± 0.006 U/mg [Figure 73]. A comparison with RP-HPLC measurements provided a similar specific activity of 0.046 ± 0.003 U/mg.

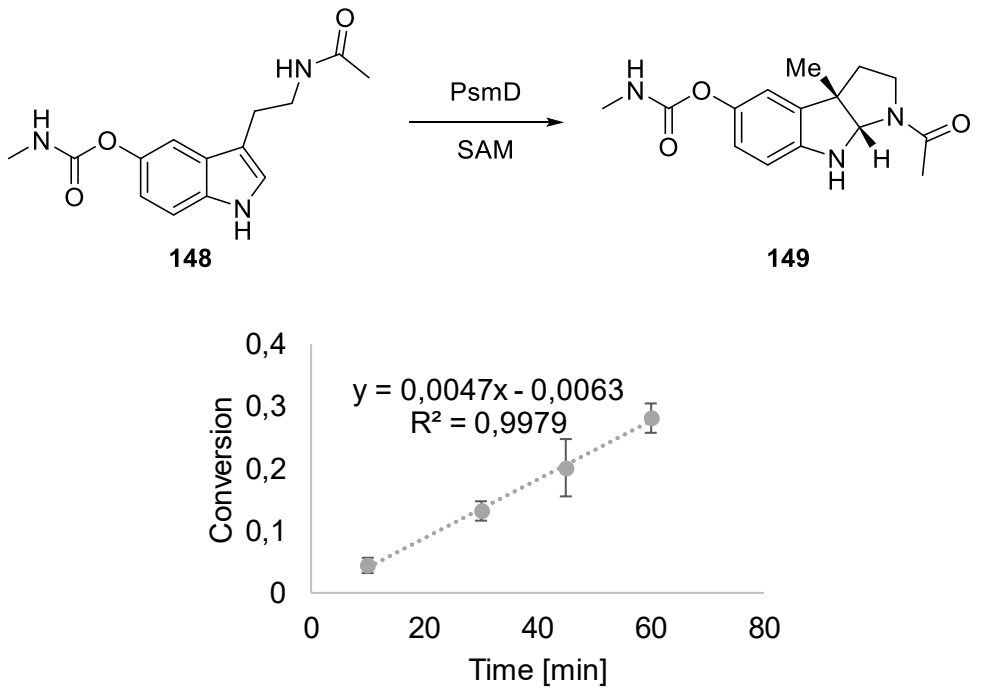

Figure 73: Reaction scheme of the reaction catalysed by PsmD_Sa in the presence of the SAM cofactor. The conversion was calculated at different time points during the reaction catalysed by isolated PsmD_Sa. The slope corresponds to comparable activity.

To demonstrate proof of concept for high-throughput screening applications, the HPI assays were tested to monitor reaction conversions using whole cells containing the biocatalyst. Wild-type PsmD_Sa and its mutants R85A and E35A were expressed in *E. coli*, and the harvested cells were resuspended in a reaction mixture containing compound **148** and supplemented with SAM (**93**). *E. coli* cells carrying an empty pET21a(+) vector served as a negative control. After 16 hours of incubation, the reactions were quenched, and cell debris was removed by centrifugation. The enzymatic reaction was performed by Diana Amariei. The resulting supernatant was subjected to the HPI assay, following standard protocols. For validation purposes, conversion was also assessed via RP-HPLC.

The results from the HPI assay showed significant influence from the background signal in the reactions containing cells, leading to discrepancies from the HPLC results, particularly at lower conversion rates. However, at higher conversions, the trend was consistent, although the absolute conversion values varied. Thus, under these conditions, the HPI assay can be effectively used for qualitative screening, but not for precise quantitative analysis when not working with purified enzyme.

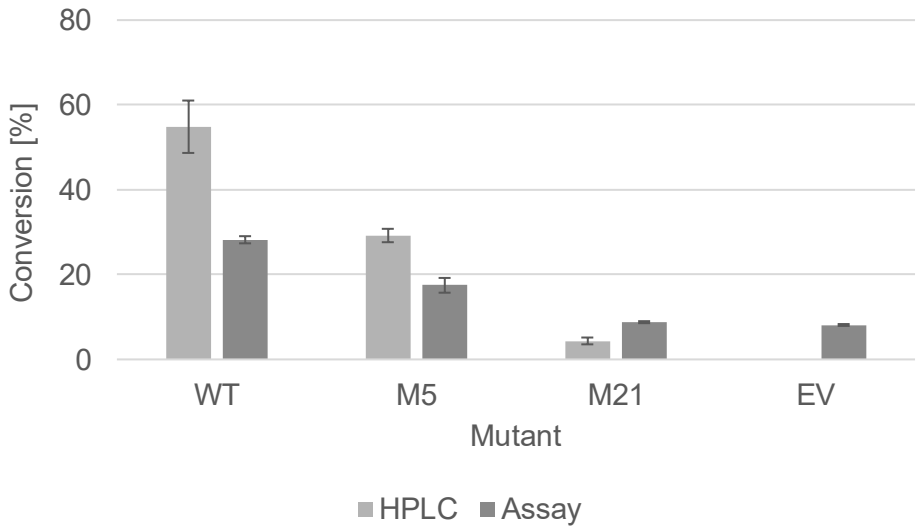

Figure 74: Conversion of **148** to **149** for the tested mutants, determined from the supernatant using the HPI assay (orange) and RP-HPLC (grey).

The assay, however, is not limited to these specific reactions and can be broadly applied to quantify substituted indoles and HPIs. For instance, *C3*-hydroxyl melatonin **230**, an oxidised melatonin metabolite with a HPI structure, serves as a biomarker for oxidative stress.[315, 316] The assay has the potential to be applied for detecting similar compounds across various fields. Its flexibility allows it to be adapted for diverse applications, making it useful in enzymatic activity studies, drug discovery, or high-throughput screening in biosynthetic research.

In this chapter, a high-throughput assay was established for detecting pyrroloindoles using the cerium molybdate (CAM) stain. The method selectively identifies HPIs but not indoles, making it suitable for monitoring enzymes such as P450s, monooxygenases, methyltransferases, and prenyltransferases that generate HPIs via indole cyclisation. Using melatonin and its *C3*-methylated derivative as model compounds, the assay was simplified to an acidic cerium sulfate system and optimized *via* a design of experiment approach. It reliably detects a broad range of *C3*-substituted HPIs and natural products, regardless of substituents. The assay successfully quantified the activity of the methyltransferase PsmD, giving results consistent with HPLC measurements, and demonstrated potential for high-throughput screening.

5.2 DKP *C3*-indole methyltransferases

C3-MTases play a role in the biosynthesis of some interesting natural products containing the HPI motif. One objective of this thesis is to explore their potential as biocatalysts for the stereoselective synthesis of this structural motif, highlighting their synthetic utility. A prominent example is the MTase from *Streptomyces griseofuscus* PsmD, which is involved in the production of physostigmine.[99, 110] PsmD is the most extensively studied *C3*-indole MTase, with only two additional MTases identified so far, which both methylate a DKP based substrate: the MTase from *Nocardiopsis* sp. CMB-M0232 NozMT and the MTase from *Streptomyces* sp. HPH0547 StspM1.[58, 87, 235] The MTase NozMT catalyses *C3* and *N*-methylation within the biosynthesis pathway of nocardioazine B (**7**).[58, 87] The *C3*-MTase StspM1 was found to methylate the LL-cWW substrate **3a** forming the HPI structural motif on one side of the DKP.[235] Furthermore, a homolog of NozMT, named NozB-CYIM, has been identified in *Nocardiopsis chromatogenes* YIM 90109. However, its biochemical properties and functional characterisation remain unexplored.[87]

In this study, StspM1 was used as a reference for a homology search as this enzyme accepts the DKP substrate without further modifications. This search revealed three potential homologs based on sequence similarity: SgMT from *Streptomyces griseoviridis*, SeMT from *Saccharopolyspora erythraea*, and SaMT from *Streptomyces albus*. Furthermore, two homologs of NozB-CYIM were identified by homology search on this uncharacterised enzyme: MtMT from *Marinactinospora thermotolerans* and ThMT from *Thermobifida halotolerans*. These enzymes (StspM1, SgMT, SeMT, SaMT, NozB-CYIM, MtMT, and ThMT) were analysed for similarities in their sequences and their structures [Table 2].

Table 2: Origin organism and gene bank entry number of the MTases NozMT, NozB-CYIM, ThMT, MtMT, StspM1, SgMT, SeMT and SaMT.

Enzyme	Organism	Gene bank entry
NozMT	*Nocardiopsis sp. CMB-M0232*	UYF26243.1
NozB-CYIM	*Nocardiopsis chromatogenes*	WP_026123683.1
ThMT	*Thermobifida halotolerans*	WP_068687933.1
MtMT	*Marinactinospora thermotolerans*	WP_078762832
StspM1	*Streptomyces sp. HPH0547*	QEI59523.1
SgMT	*Streptomyces griseoviridis*	WP_189425200.1
SeMT	*Saccharopolyspora erythraea*	WP_009942263.1
SaMT	*Streptomyces albus*	WP_205630362.1

5.2.1 Sequence and structural comparison

The sequences of the new MTases SgMT, SeMT, SaMT, MtMT, and ThMT were compared to those of the literature known MTases PsmD, NozMT, StspM1, and NozB-CYIM. Based on sequence similarity, the enzymes can be classified into two groups. The first group, consisting of NozMT, StspM1, SgMT, SeMT, and SaMT, shows 37% to 45% sequence identity with the well-studied PsmD. The second group includes NozB-CYIM and its homologs, MtMT and ThMT, which exhibit lower similarity to PsmD (around 20%). Among StspM1 and its homologs, sequence similarity varies: SaMTs sequence is 98% identical to the sequence of StspM1, SgMT 79%, and SeMT 56%. SaMT has the highest similarity but is shorter by 21 amino acids at the *N*-terminus. The sequences of the group two MTases NozB-CYIM, ThMT, and MtMT are over 80% identical (85.19% between ThMT and MtMT) [Table 3].

Table 3: Sequence identity of literature known MTases with the analysed enzymes.

Enzyme	Sequence identity with			
	PsmD	NozMT	StspM1	NozB-CYIM
NozMT	37,26	-	43,61	20,60
StspM1	39,69	43,61	-	22,39
SgMT	40,23	44,53	79,18	20,90
SeMT	44,40	43,56	56,39	21,11
SaMT	38,59	43,67	97,59	22,39
NozB-CYIM	18,46	20,60	22,39	-
ThMT	21,54	20,10	21,89	80,99

The literature known and characterised *C3*-MTases NozMT and StspM1 belong to class I MTases, characterised by a Rossmann-like superfold.[58, 99] This domain typically consists of six to seven *β*-strands connected by hydrogen bonds, interspersed with *α*-helices. In MTases, the final *β*-strand is oriented antiparallel to the other six strands.[194] The structures of NozMT, StspM1, and its homologs SgMT, SeMT, and SaMT as well as NozB-CYIM and its homologs ThMT and MtMT were analysed for their overall structural features. Structural models were generated using RobettaFold from the BakerLab.[317]

The group one MTases display a high degree of structural similarity, featuring the typical Rossmann fold and a *β*-cap domain, both of which have also been described for PsmD [Figure 75A]. The generated models generally have high structural confidence, with low estimated errors for most amino acid positions. However, larger errors were noted at the *N*-terminus and in loop regions around amino acids 170 and 210 [Figure 75B].

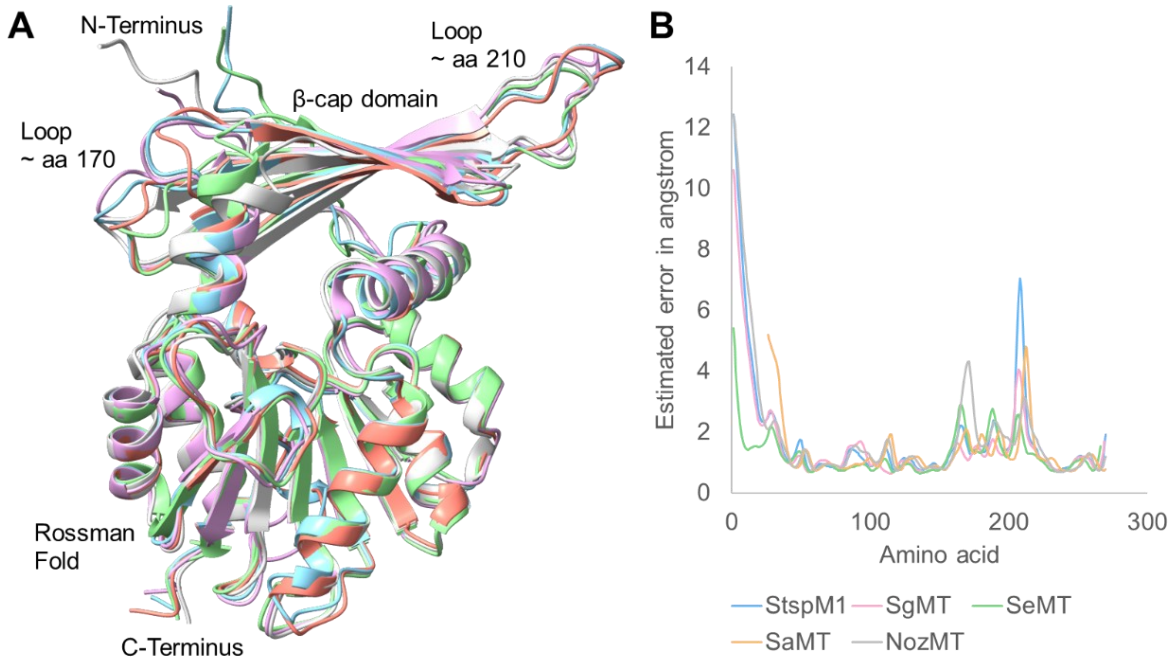

Figure 75: A: Structures of StspM1 (blue), SgMT (pink), SeMT (green), SaMT (orange) and NozMT (grey) generated using RobettaFold. B: Structural confidence of the created structures: Estimated errors in angstrom for each amino acid position of the modelled enzyme.

Similarly, the group two MTases exhibit strong structural similarity to one another containing the Rossman fold [Figure 76A]. Higher estimated errors were observed at the *C*-terminus and in loop regions around amino acids 140, 190, and 210, compared to the rest of the enzyme [Figure 76B].

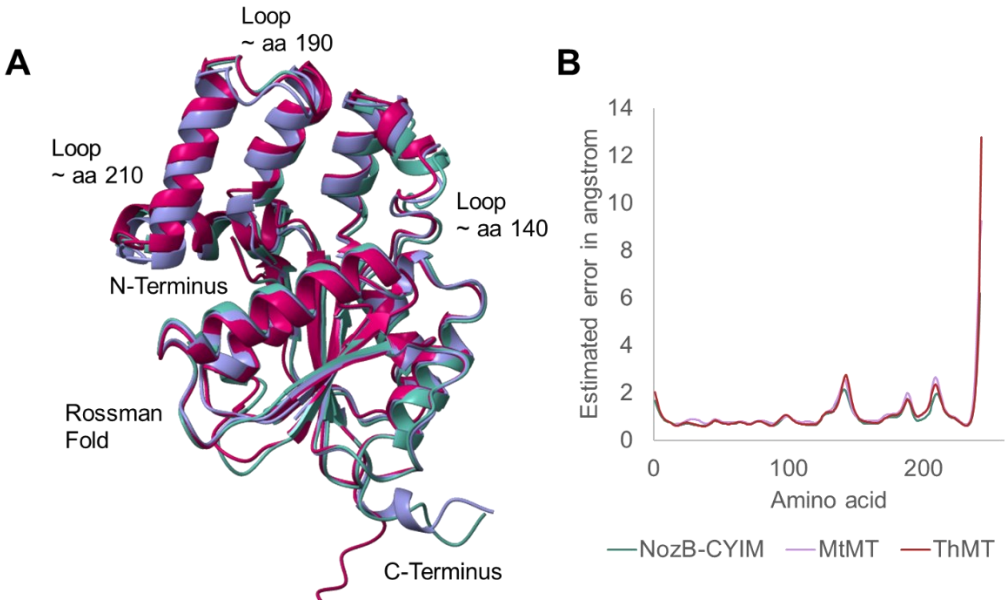

Figure 76: Structures of NozB-CYIM (green), MtMT (violet) and ThMT (red) generated using RobettaFold. B: Structural confidence of the created structures: Estimated errors in angstrom for each amino acid position of the modelled enzyme.

When comparing the group one and group two MTases, both share the characteristic Rossmann fold. However, the most significant difference is observed between amino acids 175 to 225 in NozMT (exemplary for group one) and NozB-CYIM (exemplary for group two) and the corresponding regions in their homologs. In the group one MTases, this region forms a *β*-cap domain, whereas in the group two MTases, the cap domain is composed of *α*-helices. Additionally, the positioning of these cap domains differs relative to the active site in each group [Figure 77].

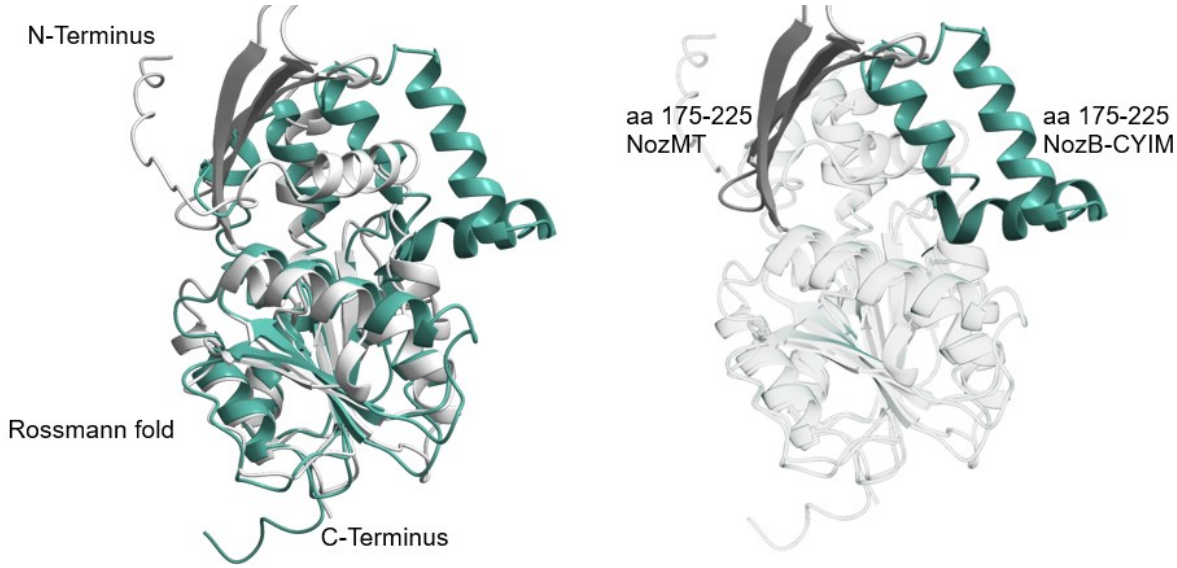

Figure 77: Structures of NozMT (grey) and NozB-CYIM (green) as representants of group one and two MTases aligned. The cap domains are highlighted showing a different secondary structure and positioning.

To identify the active site of a MTase, the SAM binding site can be located. In MTases, the SAM binding position is found along the *C*-terminal end of the core *β*-sheet (strand I-III), where SAM (**93**) is stabilised by a network of hydrogen bonds and van der Waals interactions. The SAM-binding motif is typically characterised by the sequence [(V/I/L) (L/V) D/E (V/I) G (G/C) G (T/P) G], which interacts with the carboxypropyl group of SAM (**93**). Identifying this motif in unknown enzymes can provide an initial indication of MTase activity.[165, 195-198]

StspM1 and its homologs SgMT, SeMT, and SaMT as well as NozMT, NozB-CYIM, and its homologs ThMT and MtMT were analysed for the presence of the SAM-binding motif. In all these MTases, the core SAM-binding motif was identified, with only minor amino acid variations [Table 4, Figure 78]. For instance, in the group one MTases, the first glycine in the GxG/CxG motif is replaced by cysteine, resulting in a CxGxG sequence. Despite this variation, NozMT and StspM1 have been shown to be active, indicating that this difference does not hinder SAM binding.[58, 235]

Table 4: SAM binding motif identified in the listed MTases.

MOTIF	**V/I/L**	**L/V**	**D/E**	**V/I**	**G**	**G/C**	**G**	**T/P**	**G**
NozMT	V	I	E	L	C	C	G	T	G
NozB-CYIM	V	L	D	L	G	C	G	G	G
ThMT	V	L	D	L	G	C	G	G	G
MtMT	M	L	D	L	G	C	G	G	G
StspM1	V	L	E	I	C	C	G	T	G
SgMT	V	L	E	I	C	C	G	T	G
SeMT	V	L	E	I	C	C	G	T	G
SaMT	V	L	E	I	C	C	G	T	G

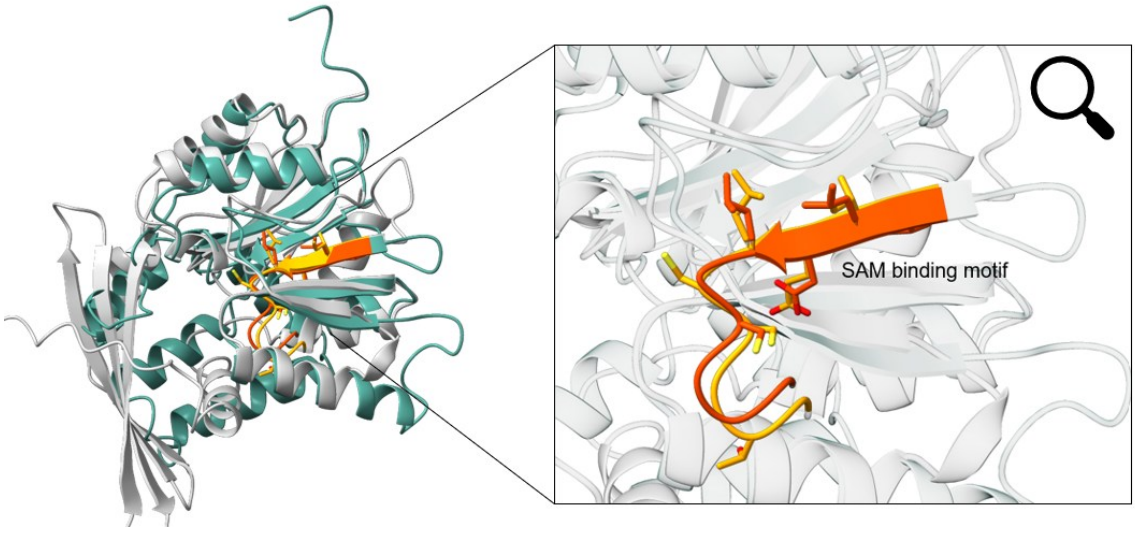

Figure 78: Structures of NozMT (grey) and NozB-CYIM (grey) as representatives of group one and two MTases aligned. The SAM binding motif of NozMT is highlighted in yellow, the binding motif of NozB-CYIM in orange.

The active site differs in size between the two groups due to the variation in their cap domains. Group one MTases have a *β*-cap domain along with an *N*-terminal helix ("lid") that covers the active site. In contrast, the *α*-cap domain in group two MTases is positioned differently, resulting in a more open active site [Figure 79].

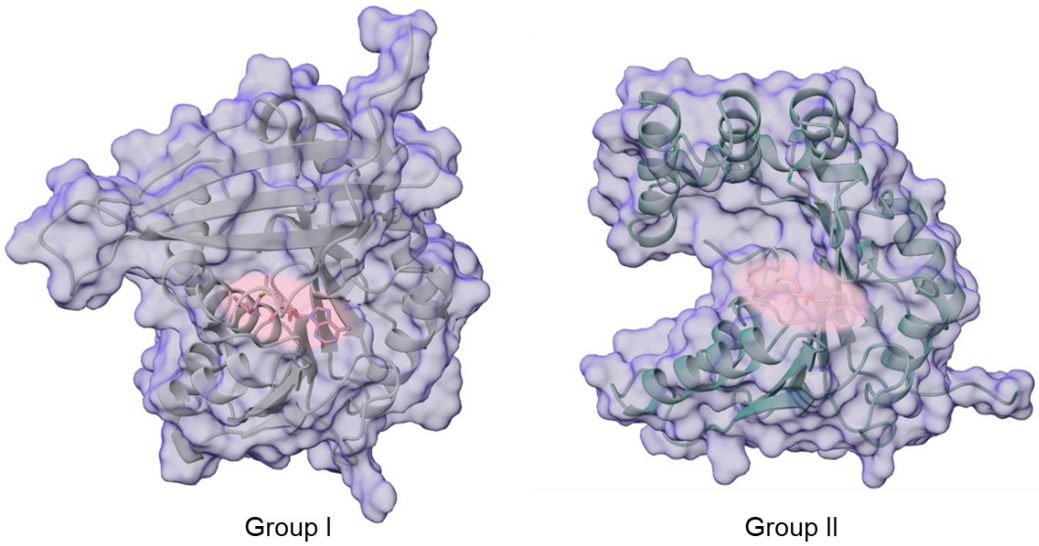

Figure 79: Structures of NozMT (grey, left) and NozB-CYIM (green, right) as representants of group one and two MTases displayed with the protein surface and the active site with SAM (**93**) (pink).

The active site of a *C3*-MTase was analysed in literature on PsmD: A comprehensive study, which included crystallisation and alanine scanning mutagenesis, provided significant insights into its catalytic site. The enzyme's mechanism involves a catalytic triad composed of tyrosine, histidine, and glutamate [Figure 41].[99] The MTases from both group one and group two were analysed for the presence of this catalytic triad. Group one MTases possess this triad in the equivalent positions, although in StspM1, SgMT, and SaMT, the glutamate found in PsmD is replaced by aspartate. SeMT and NozMT retain the glutamate [Figure 80]. Since the histidine and aspartate residues are located in the *β*-cap domain, group two MTases do not contain these residues. The tyrosine of the catalytic triade is replaced by a histidine in all the enzymes from group two [Figure S 8].

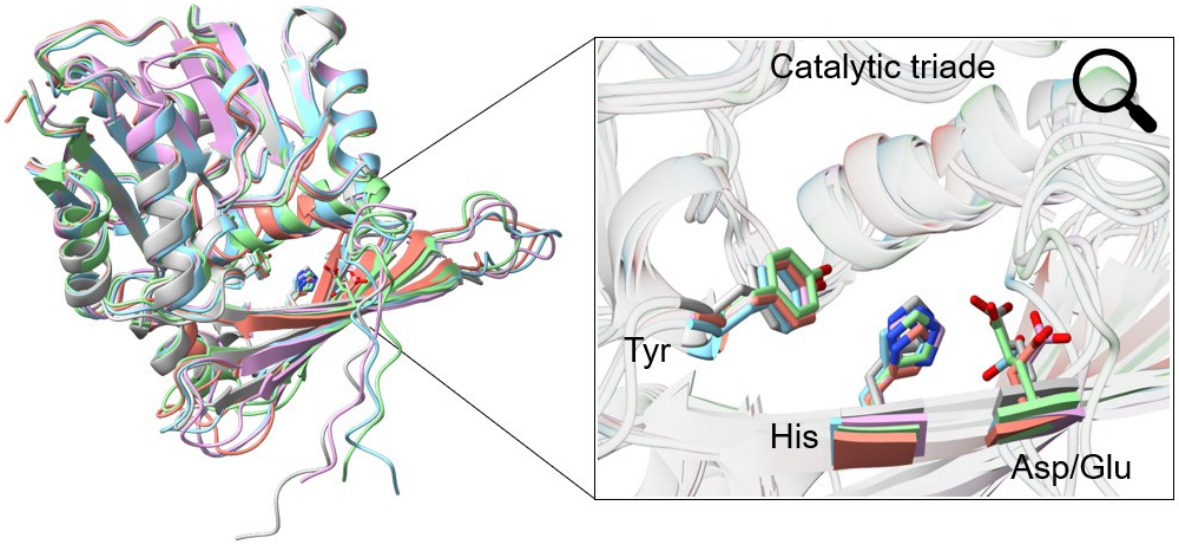

Figure 80: Structures of StspM1 (blue), SgMT (pink), SeMT (green), SaMT (orange) and NozMT (grey) generated using RobettaFold. The active site is zoomed in showing the catalytic triade containing a Tyr, His and Asp/Glu depending on the enzyme.

As the goal of this thesis is to utilise *C3*-MTases for the synthesis of natural products with a DKP core (Iansai B), the initial analysis suggests focusing on group one MTases: Within this group, both StspM1 and NozMT have been shown to accept derivatives of the cWW DKP [Figure 18, Figure 19]. Since Iansai B **5** is based on an LL-cWW **3a** structure, StspM1 appears to be a promising candidate, as it accepts this substrate, though it is only known to methylate one side of the DKP. Therefore, StspM1 and its homologs SgMT, SeMT, and SaMT will be focused within this study.

5.2.2 Substrate synthesis

Since StspM1 and NozMT are known to accept DKP substrates, a range of DKP-containing and structurally related compounds were synthesised to evaluate the substrate specificity of selected MTases. The main substrate for StspM1 is LL-cWW **3a**, but no other stereoisomers have been explored yet. The aromatic side chain on the second tryptophan residue in 2,5-DKP may be important for StspM1 activity, as it could play a role in substrate recognition and configuration.[235] Therefore, all stereoisomers of cWW **3a-c**, cWY **241a-d**, cWF **242a-d**, and cWH **243a-d** were selected as the primary substrate set. To investigate whether the aromatic side chain is essential, a second set of substrates—cWA **216**, cWV **244**, and cWL **245**—was chosen, varying the side chain length of the second amino acid. Lastly, two benzodiazepine-2,5-dione substrates **246**a+b were selected, which features a seven-membered ring as the central motif while maintaining aromaticity on both sides of the molecule [Figure 81]. Noteworthy, prenylation of this substrate at the *C3*-position results in the formation of the natural product aszonalenin (**49**) [Figure 12].[318] The synthesis of these substrates was carried out with help of students from the "Naturstoffsynthese" practical course, namely A. Wassing, S. Malaczynski, S. Dewi, A. Apostolidis, S. Przetak, N. Hassani, and E. Pfirmann during his bachelor thesis.

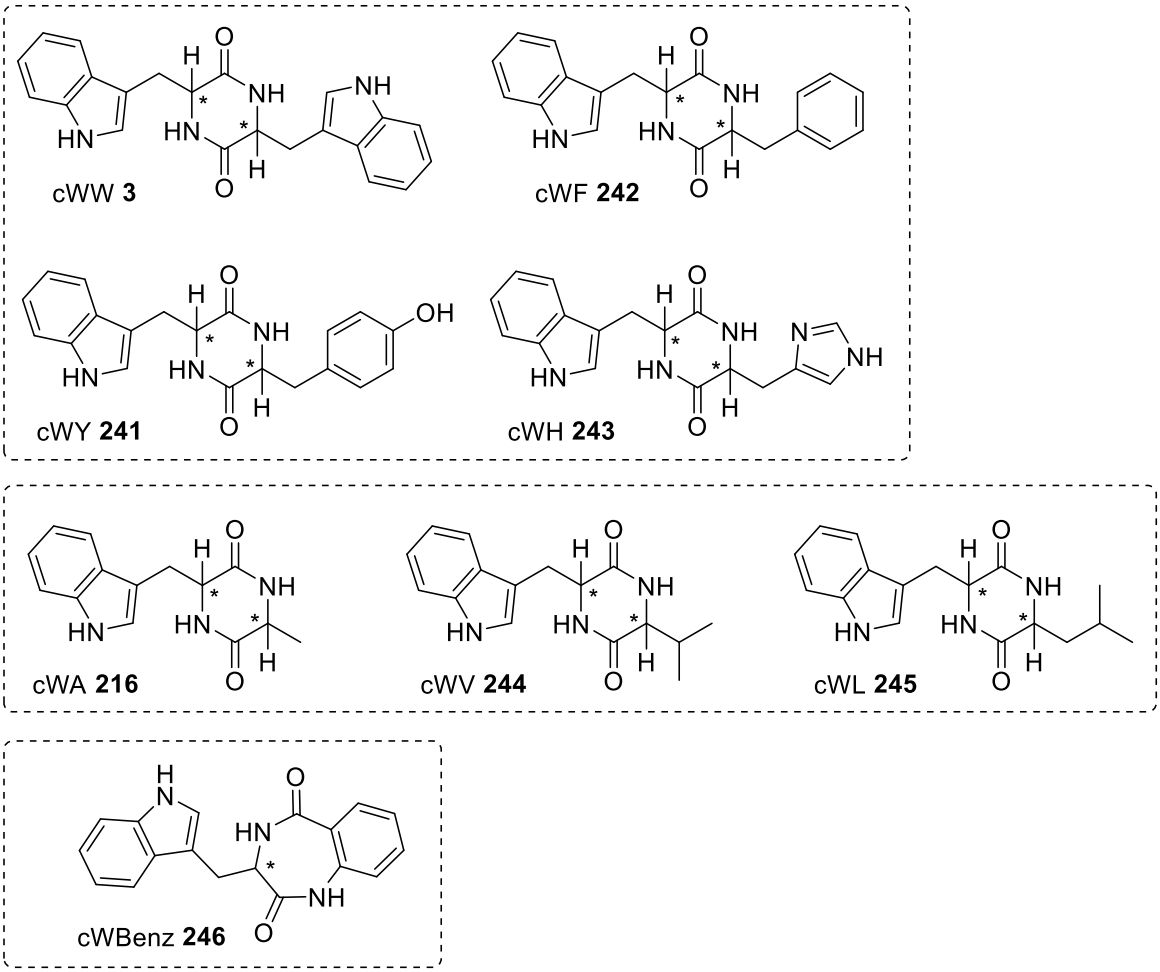

Figure 81: Set of compounds which have been synthesised as substrates for the methylation reaction with the MTases. For cWW **3**, cWF **242**, cWY **241** and cWH **243** all different isomers (**a-d**) have been synthesised, for cWA **216**, cWL **244** and cWV **245** only L-amino acids were used. The cWBenz **246** were synthesised as both enantiomers.

The synthesis of the DKP substrates involved three reaction steps. First, Cbz-protected tryptophan **247** was coupled with an orthogonally protected methyl ester amino acid **248**. Bis-(2-oxo-3-oxazolidinyl)phosphinic chloride (BOP-Cl) was used as the coupling agent, except for the cWH substrates **243**, where ethylcarbodiimide hydrochloride (EDC-HCl) was employed under different conditions due to lack of conversion. After deprotecting the amino group using Pd/C and hydrogen generated from ammonium formate of the dipeptide **249**, the final step involved cyclizing the DKP ring by adding a solution of ammonia in methanol to the amine **250** and applying heating for 3 h. Each final DKP product **251** was purified via column chromatography [Figure 82]. The yields of the DKP products were determined for the three steps [Table 5].

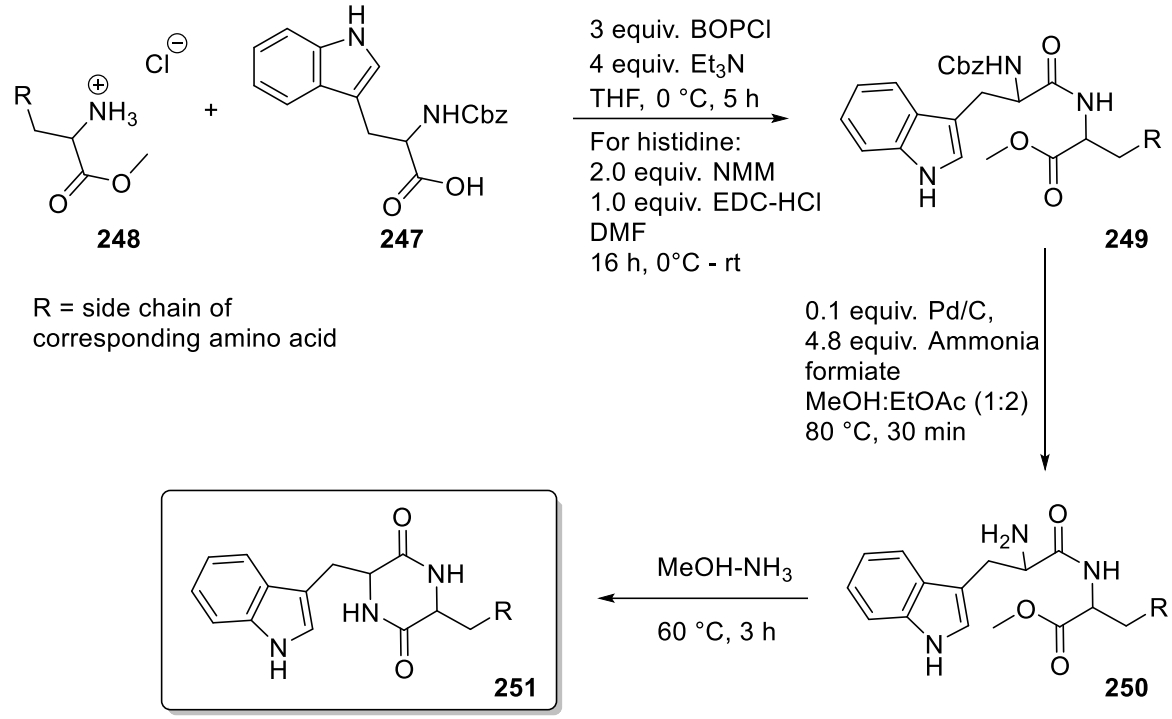

Figure 82: Synthesis scheme for the synthesis of the DKP substrates.

The synthesis of the benzodiazepine-2,5-dione substrates **246** were completed in two steps, starting with tryptophan **202** and isatoic anhydride **252** [Figure 83]. First, triethylamine was added as a base together with water and the reaction was stirred for 5 hours at room temperature. After removing the water as solvent under reduced pressure, acetic acid was added, and the mixture was refluxed for 5 hours. The final product was purified by recrystallisation [Table 5].

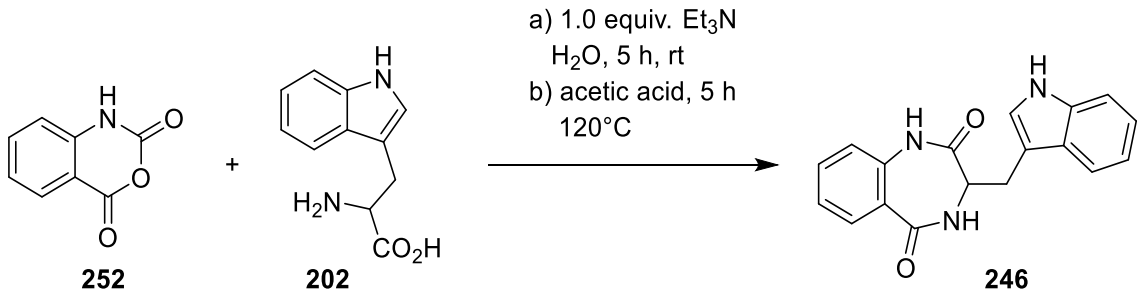

Figure 83: Reaction scheme for the synthesis of the benzodiazepine-2,5-dione substrates **246**.

Table 5: Yields and scale of the synthesised DKP substrates. The L/D nomenclature derives from the stereochemical configuration of the amino acids used as starting material.

DKP	*Stereo-information*	*No.*	*Final yield [%]*	*Scale of final product [mmol]*	*Scale of final product [mg]*
cWW	LL	**3a**	91	1.11	409
	DD	**3b**	90	1.38	514
	LD	**3c**	85	0.8	298
cWY	LL	**241a**	71	1.21	423
	DD	**241b**	89	1.21	424
	LD	**241c**	85	1.19	415
	DL	**241d**	55	0.98	343
cWF	LL	**242a**	91	1.35	449
	DD	**242b**	90	1.34	447
	LD	**242c**	75	1.20	401
	DL	**242d**	74	0.98	328
cWH	LL	**243a**	57	0.99	320
	DD	**243b**	35	0.59	190
	LD	**243c**	46	0.55	178
	DL	**243d**	41	0.51	165
cWA	LL	**216**	62	1.53	393
cWV	LL	**244**	80	0.77	220
cWL	LL	**245**	77	0.87	260
cWBenz	L	**246a**	31	0.76	231
	D	**246b**	33	0.78	249

This chapter gives an introduction into the C3-MTases investigated in this thesis. **NozMT** from *Nocardiopsis sp. CMB-M0232* and **StspM1** from *Streptomyces sp. HPH0547* are literature known DKP C3-MTases. **NozB-CYIM** from *Nocardiopsis chromatogenes* was mentioned in literature as a potential homologous catalyst to NozMT. Using StspM1 as a reference, a homology search identified additional potential C3-MTases, including **SgMT** from *Streptomyces griseoviridis*, **SeMT** from *Saccharopolyspora erythraea*, and **SaMT** from *Streptomyces albus*. Homologs of NozB-CYIM include **MtMT** from *Marinactinospora thermotolerans* and **ThMT** from *Thermobifida halotolerans*. These enzymes were analyzed for sequence and structural similarities, revealing two distinct groups:

1. **Group One:** NozMT, StspM1, SgMT, SeMT, and SaMT
2. **Group Two:** NozB-CYIM, MtMT, and ThMT

Structural models generated with RobettaFold revealed that group one MTases share structural similarities, including the Rossmann fold and a *β*-cap domain, while group two MTases display α-cap domains, contributing to differences in active site configuration. The SAM-binding motifs in all analyzed MTases are conserved, with minor variations. Group one MTases possess a catalytic triad (tyrosine, histidine, and glutamate/aspartate), while group two MTases lack this specific configuration.

Various DKP substrates were synthesized including all stereoisomers of cWW **3**, cWY **241**, cWF **242**, and cWH **243**, as well as the L- amino acid based cWA **216**, cWV **244**, and cWL **245** to explore the role of aromatic side chains in substrate recognition. Additionally, two benzodiazepine-2,5-dione substrates **246** were synthesized.

5.3 StspM1

The indole *C3*-MTase from *Streptomyces sp.* HPH0547 is the first identified enzyme capable of converting the LL-cWW **3a** as a substrate. It catalyses the indole *C3*-methylation in this DKP substrate, resulting in a mono-methylated HPI product. While previous studies have explored the enzyme's pH and temperature optima, its natural substrate and precise role in the biosynthesis of HPI-containing natural products remains unclear. Li *et al.* proposed a potential biosynthetic pathway in *Streptomyces sp.* HPH0547, suggesting the (*S*)-isomer of nocardioazine B (**7**) as the pathway's final product [Figure 43].[235] However, naturally occurring nocardioazine B (**7**) is now recognised to contain D-tryptophan amino acids.[55] This discrepancy underlines the importance of investigating the enzyme's acceptance of DD-cWW **3b** as a substrate in further studies. The gene of StspM1 was synthetically constructed in a pET28a(+) vector (GenScript, USA) by Pascal Schneider during his doctoral thesis and cloned into a pET21a(+) expression vector with a *C*-terminal His6-tag by Nadiia Pozhydaieva during her master thesis.

5.3.1 Characterisation

The MTase StspM1 was heterologously expressed in *E. coli* BL21 Gold (DE3). After cell lysis, the enzyme was purified via nickel NTA affinity chromatography according to the protocol of Nadiia Pozhydaieva using a washing buffer containing 100 mM imidazole and a elution buffer containing 250 mM imidazole.[319] The molecular weight of StspM1, including the *C*-terminal His-tag, is calculated to be 30.9 kDa. A distinct band at approximately 30 kDa is observed at the SDS-gel electrophoresis of the lysate-, washing- and elution fractions collected during the purification process [Figure 84].

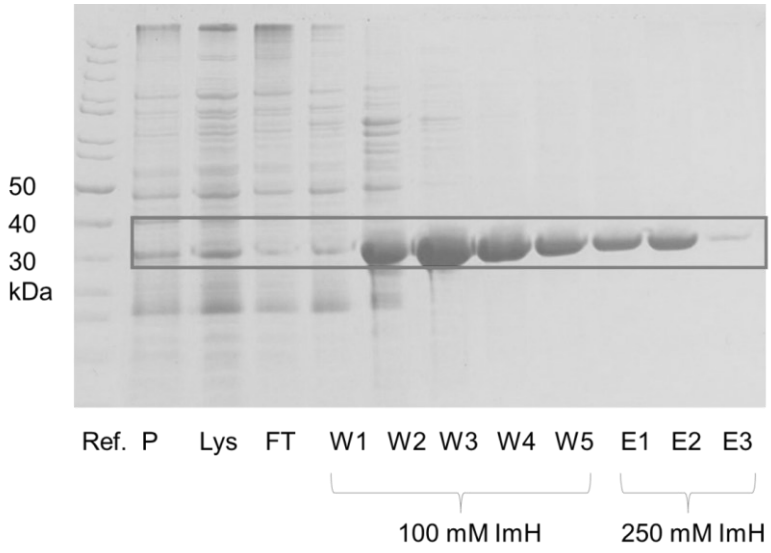

Figure 84: SDS-Gel of the purification of StspM1 according to the protocol of Nadiia Pozhydaieva. Ref. = Unstained protein Standard, P = pellet, Lys = lysate, FT = flow through, W = wash (100 mM ImH), E = elution (250 mM ImH). The band at 30 kDa is highlighted.

In the initial purification attempt using a washing buffer with 100 mM imidazole and an elution buffer containing 250 mM imidazole, a significant portion of the protein was lost in the washing fraction. To optimise the process, a linear imidazole gradient was applied using an ÄKTA system, with protein elution monitored by absorbance at 280 nm [Figure 85A]. During the gradient, unbound protein was observed to elute in the early fractions with no imidazole, and a second peak appeared in fractions 5 to 8 (ca. 80 mM imidazole), corresponding to impurities as confirmed by SDS-gel. The target protein, StspM1, eluted in fractions 9 to 14 (ca. 160 mM imidazole), displaying a strong band at approximately 30 kDa on the gel [Figure 85B]. Based on these observations, an optimised purification protocol was developed. A washing buffer with 80 mM imidazole was selected to elute the impurities, and an elution buffer with 160 mM imidazole was chosen to efficiently release StspM1.

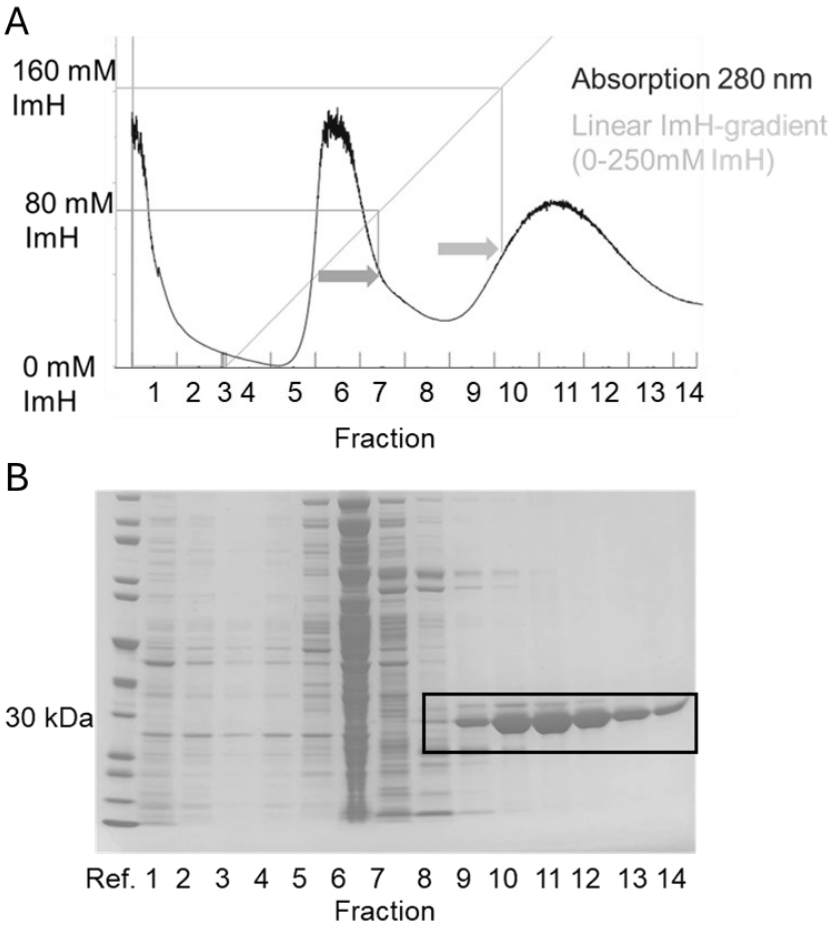

Figure 85: Optimisation of the purification process via Ni-NTA of StspM1. A: Chromatogram of the purification with the Äkta: A linear imidazole gradient was applied. The absorption at 280 nm was measured during the process. B: Corresponding SDS-Gel to the purification.

Using this updated imidazole concentrations, the purification process involved washing with five column volumes of the 80 mM imidazole buffer (fractions W1-W5) followed by elution with three column volumes of 160 mM imidazole buffer (E1-E3). The SDS-gel analysis of the elution fractions confirmed the high purity of StspM1, with no visible contaminating proteins [Figure 86]. The optimised protocol significantly improved the enzyme yield, achieving 1.6 mg of StspM1 per gram of wet cell weight, representing a 240% increase compared to the initial method.

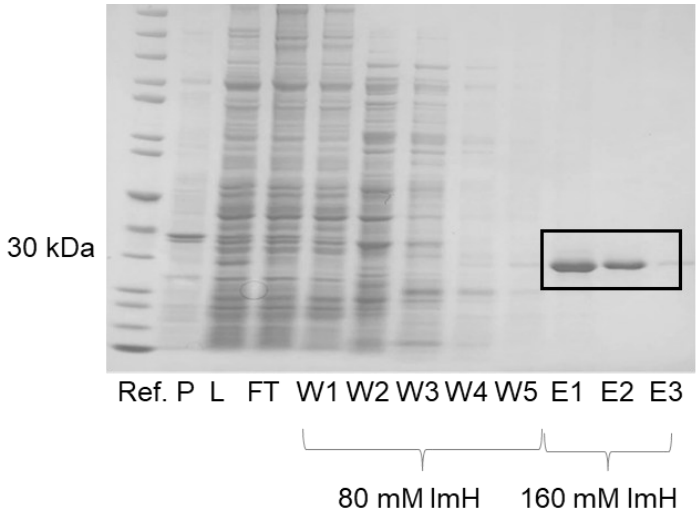

Figure 86: SDS-Gel of the optimised purification process of StspM1: The washing buffer contained 80 mM ImH, the elution buffer 160 mM ImH.

After the purification via IMAC, the oligomerisation state of StspM1 was assessed using size-exclusion chromatography. The calibration for the analytic size exclusion chromatography was performed using a gel filtration marker kit including blue dextran, *α*-amylase, cytochrome C, alcohol dehydrogenase, BSA, and carbonic anhydrase [Figure S 9, Table S 3]. StspM1 eluted at an elution volume of 78.4 mL, which corresponds to an experimentally determined molecular weight of 70.5 kDa, which differed from the predicted weight based on the sequence (61.8 kDa). This discrepancy can be attributed to the dimer's non-ideal globular shape, a phenomenon also reported for the homologous MTase PsmD.[99] Additionally, a dimeric structure was supported by predictions from GalaxyHomomer[320], which is a bioinformatics tool used for protein structure and oligomeric state prediction, by Benoit David. The *β*-cap domain, containing solvent-exposed apolar amino acids, likely facilitates dimerisation through interactions mediated by this region [Figure 87].

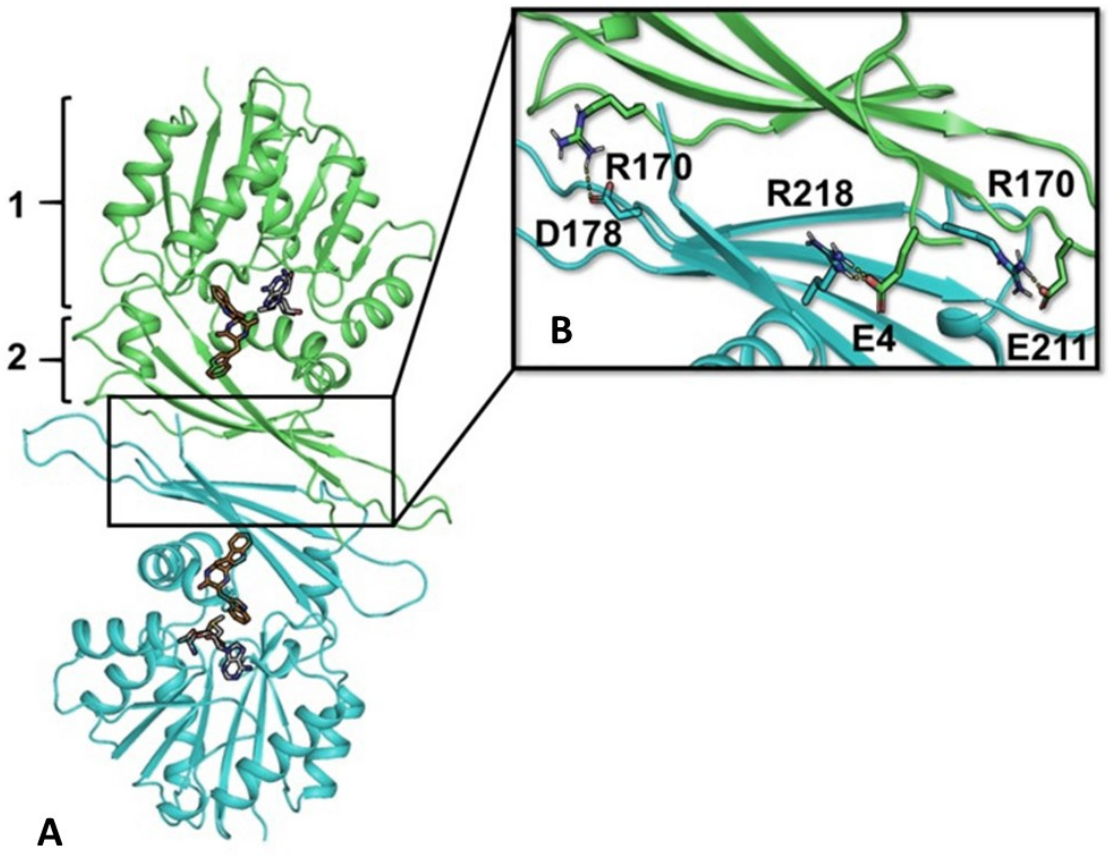

Figure 87: A: Dimeric model of StspM1 in complex with LL-cWW **3a** and SAM (**93**). B: Predicted dimerisation interface: 1 and 2 highlight the parts of the 3D structure corresponding to the Rossmann fold and the β-cap domain, respectively. Figure by Benoit David.

As previously stated, StspM1 is known to catalyze the indole *C3*-methylation of LL-cWW **3a**, producing a mono-methylated HPI product **168a**.[235] For comparison, a chemically synthesised reference product was prepared through methylation using a base, triethyl borane and methyl iodide as the methylating agent [Figure 88].[136] The lack of stereoselectivity in this chemical synthesis resulted in the formation of two single methylated diastereomers **253**, requiring separation via column chromatography. This process yielded the individual isomers in low amounts. In addition to the desired mono-methylated product **253**, methylation on both sides of the substrate was also observed forming the dimethylated products **254**. A HPLC method was developed to effectively separate the diastereomers and to serve as a standard for evaluating the biocatalytic methylation products with the help of Birgit Henßen [Figure 88].

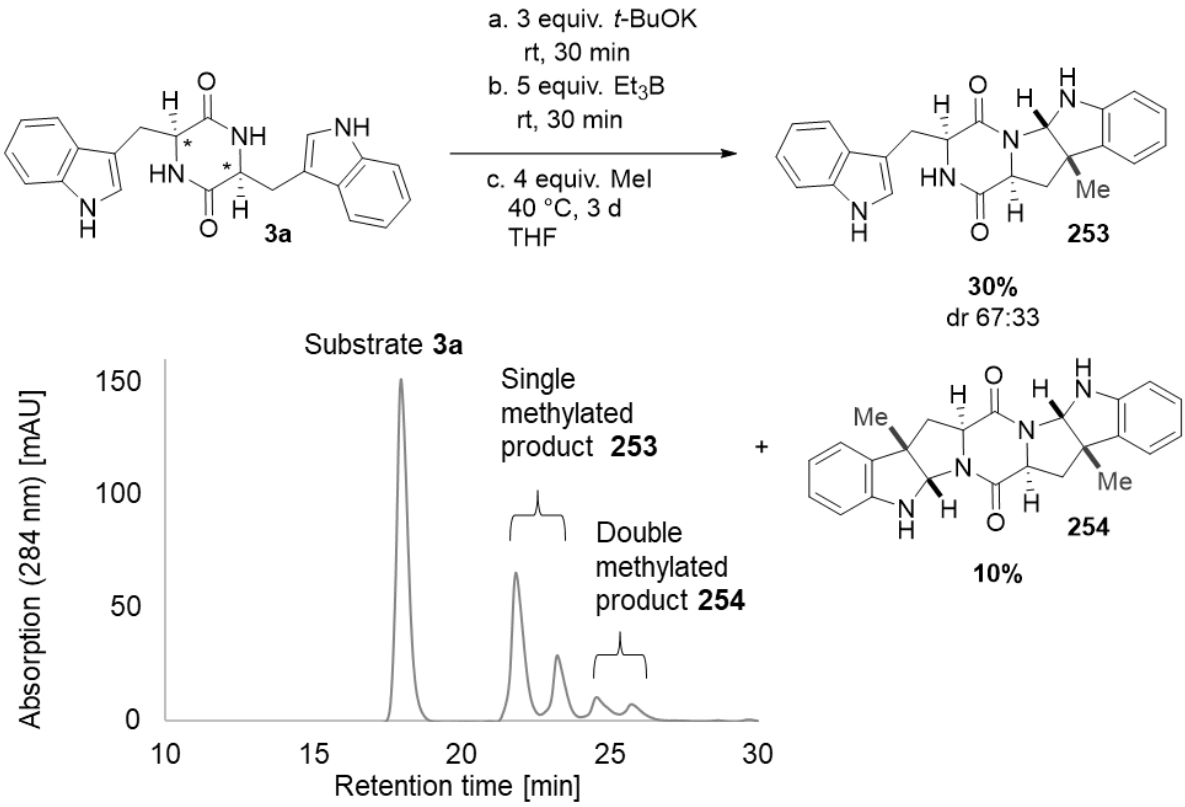

Figure 88: Chemical methylation reaction using *t*-BuOK, triethylborane and methyl iodide as the methylating agent. The substrate and products were submitted to RV-HPLC (hyperclone column, gradient of water and acetonitrile) eluting at different time points visible by absorption measurement at 284 nm.

In an initial attempt, the enzymatic reaction was repeated with the LL-cWW **3a**, its isomers DD-cWW **3c** as well as LD-cWW **3c** under the same conditions as previously published by Li *et al.* (pH 7.5, 50 mM TRIS, 100 mM NaCl, 1 mM SAM (**93**), 1 mM cWW **3**, 40 µM StspM1, 30 °C, 120 min).[235] The methylation reaction proceeded at a rate ten times slower than reported. More surprisingly, the enzyme StspM1 not only catalysed single methylation, but also exhibited double methylation for the LL-cWW **3a** to form the product **240**. In comparison, DD-cWW **3b** was only converted to the single-methylated product, and LD-cWW **3c** did not show any conversion under the tested conditions [Table S 4, Figure 89A]. To determine the relative configuration of the newly formed stereogenic centres in methylated LL-cWW **3a** and DD-cWW **3b**, ROESY NMR spectra were recorded to identify spatially adjacent protons. For single-methylated DD-cWW **168b**, a correlation between 3-Me and 11-H was observed, confirming a relative configuration in which the 11-H proton and 3-Me methyl group are on the same side of the molecule (*cis*) [Figure 246, Figure 89B]. In contrast, no correlation was observed between 3-Me and 11-H in methylated LL-cWW **168a** (*trans*) [Figure 245, Figure 89B].

The absolute configuration of the newly formed stereogenic centres in both isomers aligns with those found in nocardioazine B (**7**) and lansai B (**5**).[53] Regarding selectivity, StspM1 demonstrated exceptional diastereoselectivity (dr >99:1) as a catalyst for synthesising the HPI structural motif found in these natural compounds. For comparison, the recently studied MTase NozMT from *Nocardiopsis sp.* CMB-M0232, which is involved in the biosynthesis of nocardioazine B (**7**), does not accept any of the cWW-substrates **3a-c**.[58]

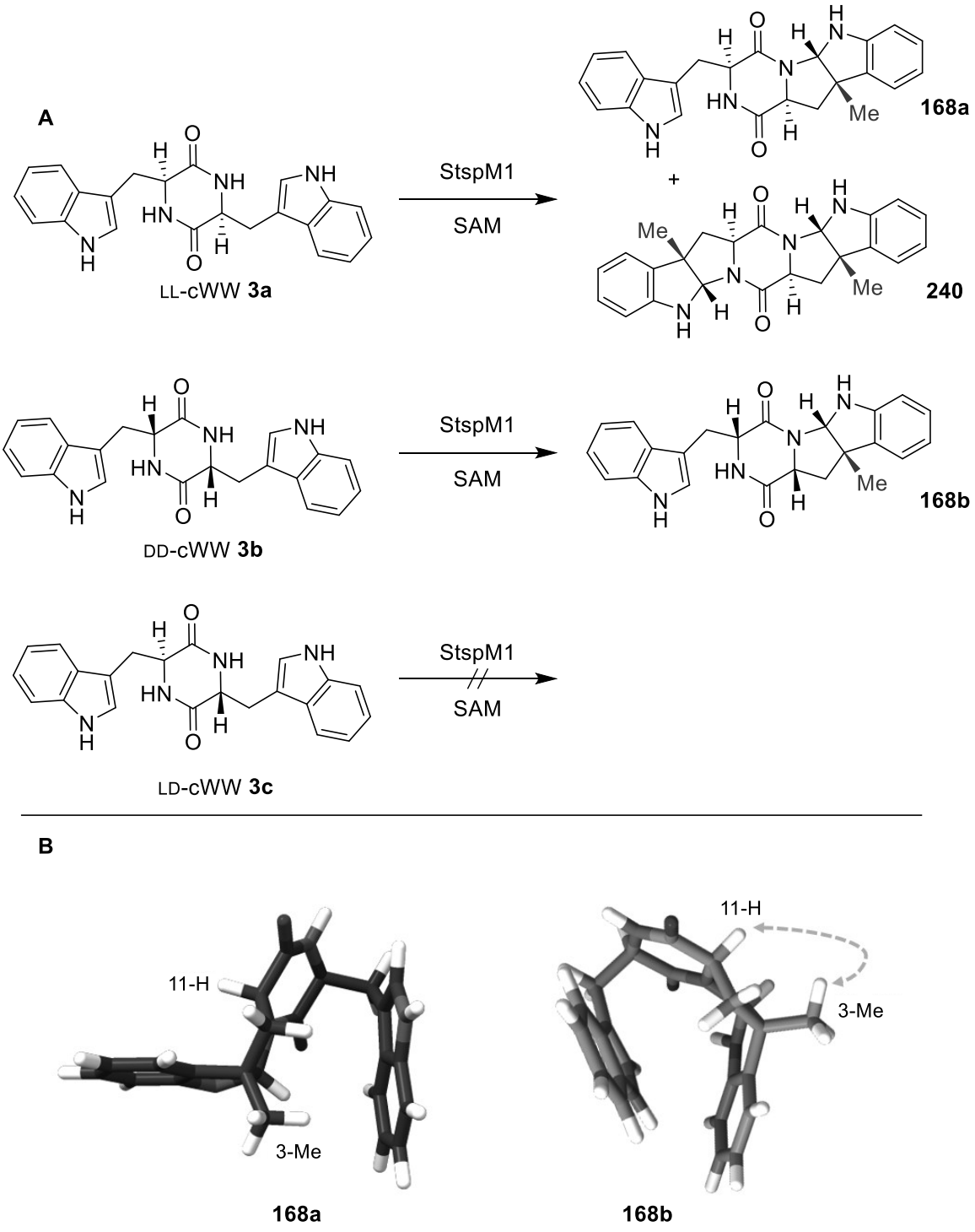

Figure 89: A: Substrate acceptance (cWW isomers **3**) of the MTase StspM1. B: DFT-structures (r2SCAN-D4/def2-TZVP/C-PCM(H2O)) of single methylated LL-cWW **168a** (left) and DD-cWW **168b** (right) created by Sebastian Myllek. ROESY correlation was only observed between 11-H and 3-Me in the single methylated DD-cWW **168b**.

To further investigate these findings and compare the enzyme's performance with both enantiomeric cWW substrates **3a** and **3b**, 3D Michaelis-Menten kinetic (MMK) analyses were conducted to determine the kinetic parameters of StspM1 for each substrate [Figure 90, Figure 91]. During the experiments, the concentration of either SAM (**93**) or the respective cWW substrate **3** was fixed at 50 µM, while the other substrate was varied across a range of 0.2–200 µM. Reactions were carried out in a 96-well plate using an enzyme concentration of 1.5 µM. Substrate conversion rates were determined using the commercially available MTase Glo Assay (Promega), a bioluminescence-based method that detects the formation of SAH and, therefore, measures SAM (**93**) consumption during the MTase reaction [Figure S 1].

By plotting the reaction rate against substrate concentrations, a K_m value of 3.86 µM was determined for LL-cWW **3a**, while its enantiomer DD-cWW **3b** exhibited a K_m value of 14.75 µM, indicating a higher substrate affinity of the enzyme for LL-cWW **3a** [Table 6].

Table 6: Kinetic parameters of LL-cWW **3a** (left) and DD-cWW **3b** (right) for the biocatalysed methylation using SAM (**93**) as a cofactor.

	LL- cWW 3a	**DD- cWW 3b**
K_m (cWW) [µM]	3.86 ± 0.28	14.75 ± 1.90
K_m (SAM) [µM]	10.39 ± 0.79	12.31 ± 1.59
K_{cat} [s^{-1}]	0.0036	0.0011
V_{max} [µM/min]	0.32 ± 0.01	0.10 ± 0.004
R^2	0.986	0.987

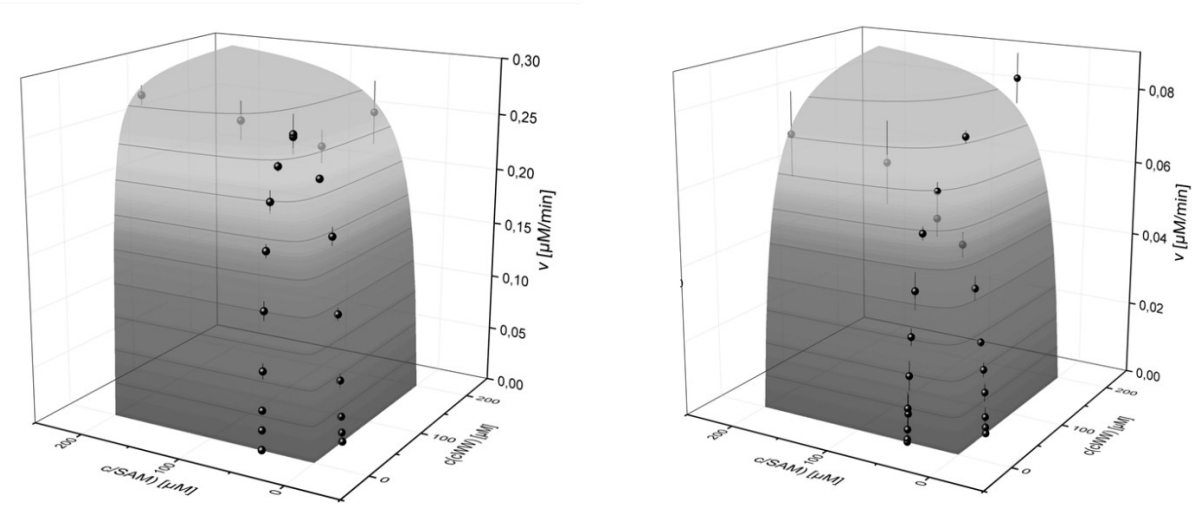

Figure 90: Michaelis Menten kinetics of LL-cWW **3a** (left) and DD-cWW **3b** (right) for the biocatalysed methylation using SAM (**93**) as a cofactor.

Furthermore, the K_m value for the second methylation step of LL-cWW **168a** was measured at 33.43 µM, which is approximately 10 times higher than the K_m for the initial mono-methylation. For the second methylation reaction, in addition to the MMK model, a McMurray model was applied to account for potential substrate inhibition by SAM (**93**). Both models yielded comparable values for the kinetic parameters and demonstrated a strong correlation with the experimental data, as reflected by high R^2 values [Table 7].

Table 7: kinetic parameters for the *C3*-methylation using the single methylation LL-cWW **168a** as substrate for the second methylation step. Two models were picked: MMK (left) and Mc Murray (right).

	Singe methylated LL-cWW 168a - MMK	**Single methylated LL-cWW 168a – Mc Murray**
K_m (cWW)	33.43 ±3.38	32.45 ±2.83
K_m (SAM)	3.20± 0.34	4.20± 0.46
v_{max}	0.14 ±0.01	0.16 ±0.01
K_{cat} [s^{-1}]	0.0016	0,0016
R^2	0.974	0.981
Ki (SAM)	-	612.15 ±160.01

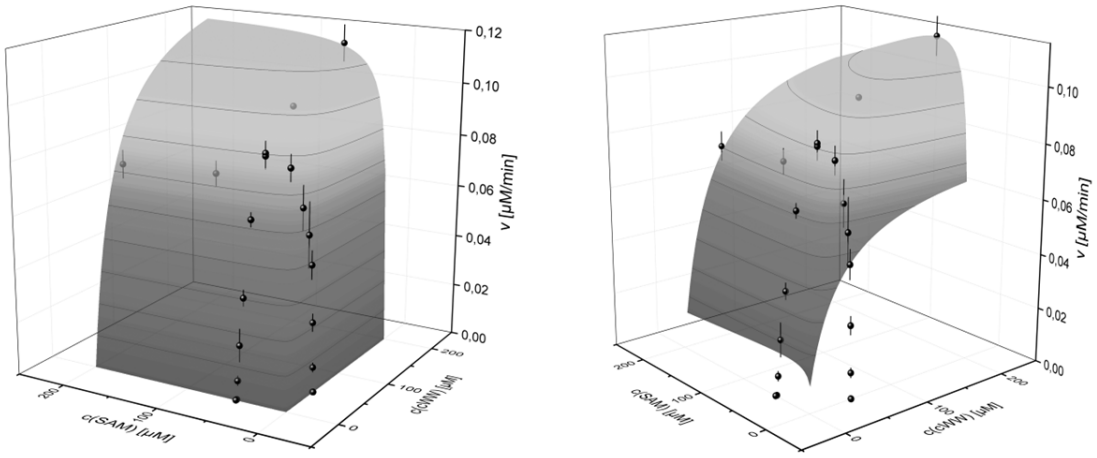

Figure 91: Michaelis Menten kinetics for the *C3*-methylation using the single methylation LL-cWW **168a** as substrate for the second methylation step. Two models were picked: MMK (left) and Mc Murray (right).

In addition to the well-characterised cWW substrates **3a** and **3b**, various other DKP derivatives containing different amino acids on the second side of the molecule, as well as benzodiazepine-2,5-dione substrates **246a** and **246b**, were tested for conversion using the MTase Glo Assay. Among the tested compounds, minimal conversion was observed only for LD-cWW **3**c, LL-cWF **242**a, and LL-cWL **245**, apart from the known substrates LL-cWW **3a** and DD-cWW **3b**. These results highlight the high specificity of the MTase StspM1 for its substrates.

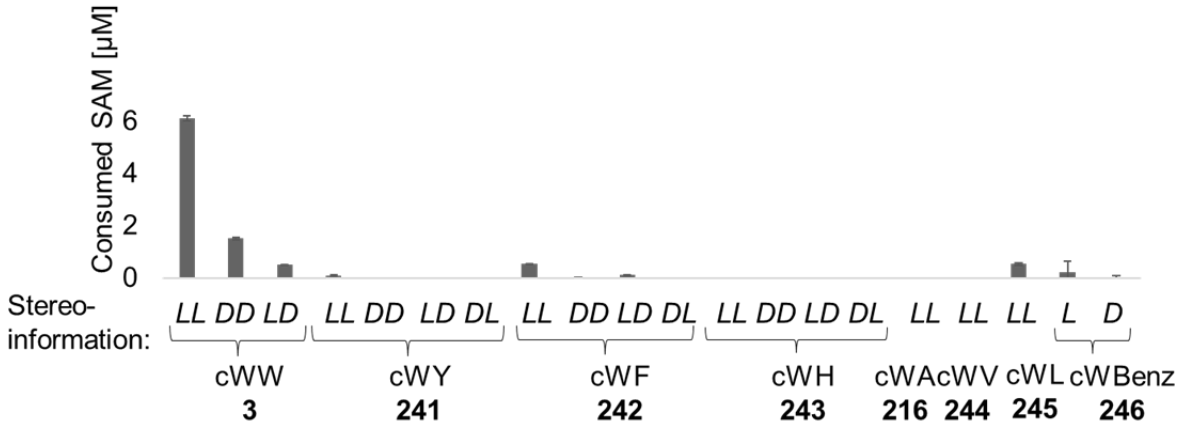

Figure 92: Substrate scope of StspM1. The activity of the MTase was determined via the MTase Glo Assay, which detects the consumption of SAM (**93**). The substrates are numbered, with letters indicating stereoisomers (a, LL; b, DD; c, LD; d, DL). The first stereodescriptor refers to the tryptophan and the second stereodescriptor to the respective second amino acid residue.

5.3.2 Binding mode of cWW substrates

To understand the relationship between substrate stereoselectivity of the cWW isomers **3** and the reactivity in this reaction at the molecular level, a 3D model of the protein in complex with SAM (**93**) and each tested cWW **3** was generated for use in subsequent molecular dynamics (MD) simulations by Benoit David.[321-324]

In the biocatalytic methylation reaction of the cWW substrate **3**, the methyl group from the cofactor SAM (**93**) is transferred to the *C3* position of the indole ring in cWW **3**, generating an electron deficiency on the indole nitrogen and forming a highly reactive imine intermediate **255**. Subsequently, the nucleophilic nitrogen of the DKP ring attacks the C2 position of the indole, resulting in the formation of the desired methylated product. StspM1 features a catalytic triad comprising residues Y127, D219, and H223 supporting this mechanism, similar to the triad in PsmD [Figure 93, Figure 94].[99]

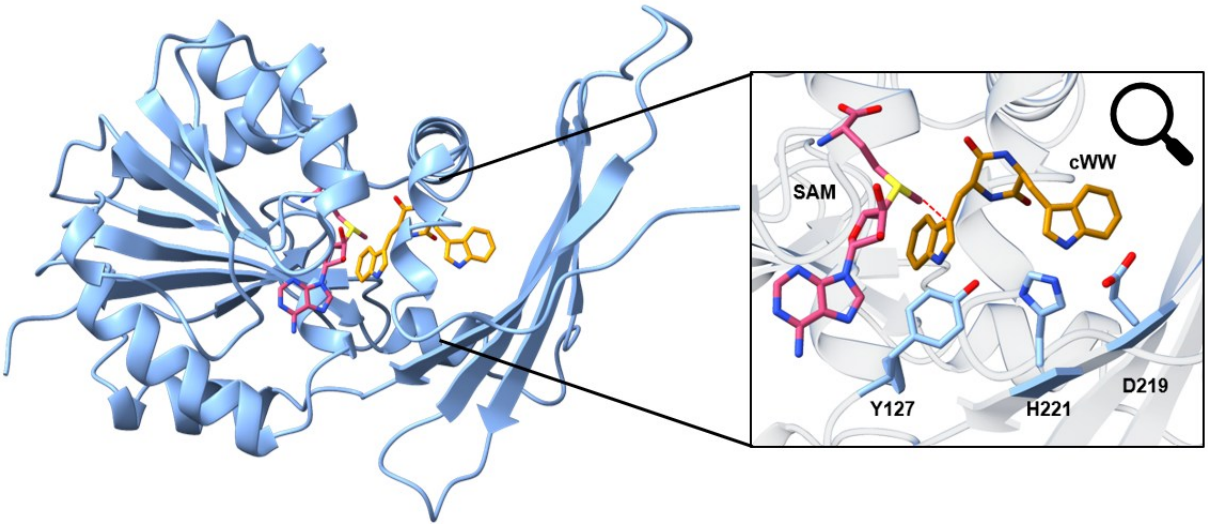

Figure 93: 3D model structure of StspM1 with SAM (**93**, pink) and the LL-cWW **3a** substrate (orange). The active site is zoomed in showing the catalytic triade containing of Y127, H221 and D219.

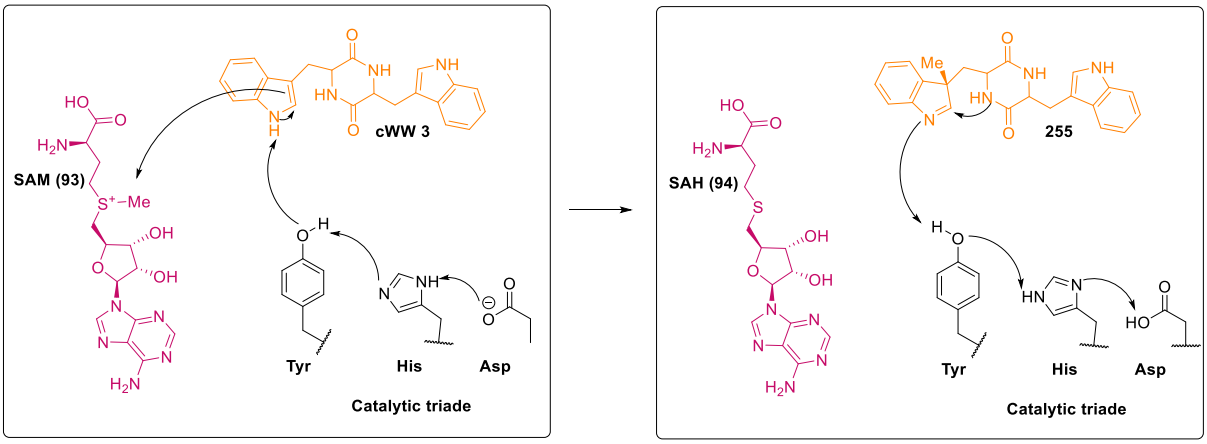

Figure 94: Mechanism for the methylation of cWW **3** with a MTase. The methyl group from SAM (**93**, red) is transferred to the *C3*-position of the indole ring of the cWW **3** (orange) forming the HPI structural motive as the final step. The catalytic triade contains a Tyr, His and Asp.

Molecular modelling demonstrates that the configuration of cWW **3** plays a critical role in determining their preferred conformations within the enzyme's binding pocket. Using MD simulations, the important geometric factors were established to identify conformations of cWW **3** that are conducive to an S_N2 methyl transfer mechanism: the distance $C3_{SAM}$–$C7_{indole}$, the angle $S1_{SAM}$–$C3_{SAM}$–$N7_{indole}$ [Figure 95A], the angle $C3_{SAM}$–$C7_{indole}$–$N9_{indole}$ [Figure 95B], and the distance between the two atoms involved in HPI cyclisation [Figure 95C]. These criteria allowed for the characterisation of reactive conformations, providing insights into the structural requirements for successful catalysis.

In addition to these geometric criteria based on the cWW **3** and SAM (**93**) substrates themselves, the positioning of residue Y127 and the residue Y223 play a critical role in catalysis through polar interactions with the substrate's reactive indole group. To validate the significance of these residues, Y127 was mutated to alanine or phenylalanine using degenerate primers [Figure S 12, Figure S 13]. The Y127A mutant replaces tyrosine with a small, non-aromatic alanine residue to evaluate the significance of aromaticity at this position. In comparison, the Y127F mutant substitutes tyrosine with phenylalanine, retaining the aromatic ring but lacking the hydroxyl group, to investigate the specific functional role of the hydroxyl group in the proposed catalytic mechanism. Both mutations resulted in complete loss of enzyme activity, confirming the essential role of the phenolic function of this residue for catalysis. The Y223F mutant, genetically constructed by GenScript, was found to be inactive, confirming the importance of the phenolic function of Y223 similar to Y127. These polar interactions of Y127 and Y223 were in addition to previously described criteria used to explain the differences in reactivity among the cWW isomers **3a-c** [Figure 95D].

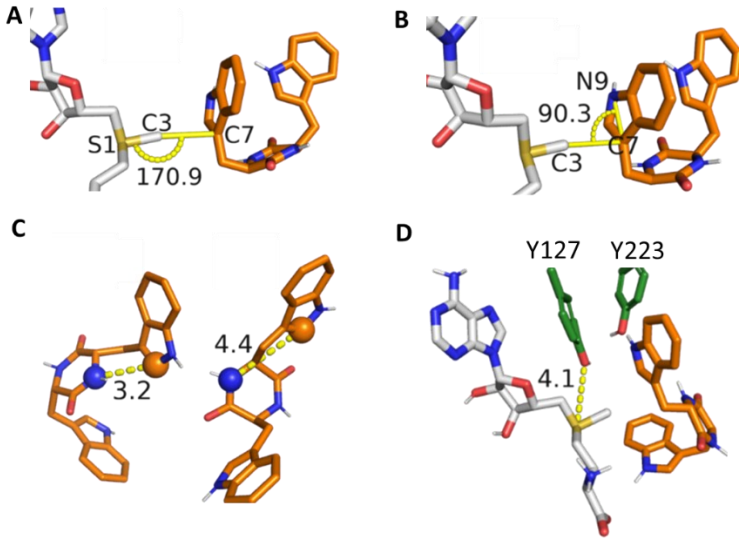

Figure 95: Geometry criteria chosen for the definition of reactive conformations. Examples of DD-cWW **3b** conformations (orange) showing acceptable values for the distance $C3_{SAM}$–$C7_{indole}$ and the angle $S1_{SAM}$–$C3_{SAM}$–$N7_{indole}$ and the angle $C3_{SAM}$–$C7_{indole}$–$N9_{indole}$ (B). The distances between the Y127 hydroxyl group and the sulphur atom of the SAM (**93**) cofactor are shown by dashed lines with their corresponding value. C: Examples of compatible and incompatible distances (dashed lines) between the two atoms involved in HPI cyclisation. D: Orientation of the Y127 and Y223 side chain suitable for catalysis. Modified figure by Benoit David.

Among the tested cWW substrates, the unmethylated LL-cWW **3a** displayed the highest conformational flexibility within the binding pocket. Despite this flexibility, only one reactive conformation [Figure 96A] was identified twice during the MD simulation trajectory. In this conformation, the reactive indole group forms a hydrogen bond with the side chain of Y127, indicating a potential catalytic interaction.

The unmethylated DD-cWW **3b** adopted two types of reactive conformations, observed in 19 frames out of approximately 137,000 frames from the MD trajectory. Four of these conformations exhibited an envelope-like geometry [Figure 96B,C], while the remaining conformers adopted a boat-like structure [Figure 96D]. The *DD* configuration facilitates close proximity between the two indole moieties, stabilizing the boat-like conformations [Figure S 22]. However, hydrogen bonding between the reactive indole and the Y127 or Y223 side chains was observed only in the envelope-like conformations. In contrast, the boat-like conformations lacked any interaction with catalytic residues and are therefore unlikely to be catalytically relevant.

The unmethylated LD-cWW **3c** did not form any reactive conformations, consistent with experimental findings indicating that this substrate is nearly inactive. Only a single conformation [Figure 96E] meeting two of the four geometric criteria ($C3_{SAM}$–$C7_{indole}$, the angle $C3_{SAM}$–$C7_{indole}$–$N9_{indole}$) was identified, further corroborating its lack of catalytic activity.

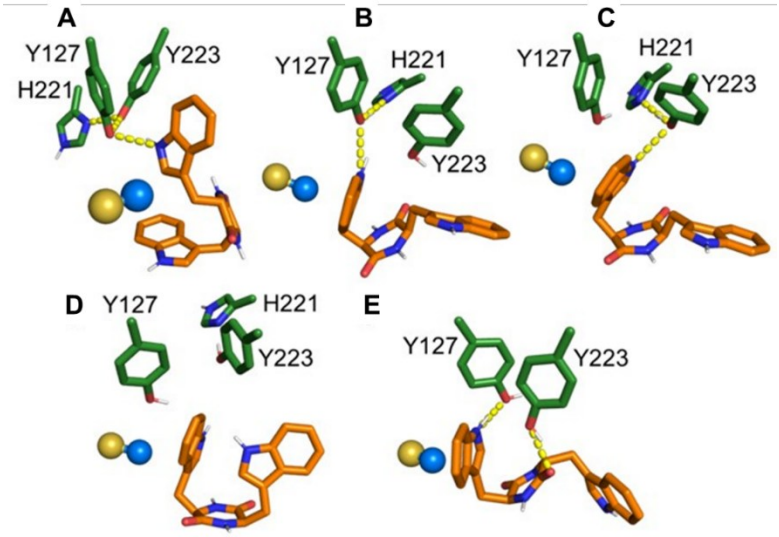

Figure 96: Binding modes of the reactive conformations of the unmethylated LL-cWW **3a** (A) and unmethylated DD-cWW **3b** (B, C, D). E: Unreactive conformation of the unmethylated LD-cWW **3c**. Selected binding pocket residues (green), SAM (**93**) sulphur and methyl group (golden and blue spheres), and cWW substrates (orange) are shown. Polar interactions: yellow dashed lines. Figure by Benoit David.

Experimental data demonstrate that the singly methylated LL-cWW **168a** product can act as a secondary substrate, accepting an additional methyl group on its second reactive indole. This substrate adopts reactive conformations in 12 frames of the MD simulation trajectory. While Y223 predominantly interacts with the DKP moiety during most of the simulation, a hydrogen bond between the reactive indole and the hydroxyl group of Y223 is observed in 5 frames. In QM-optimised geometries, the reactive indole forms a hydrogen bond with the Y127 side chain in 3 of these 5 frames. In contrast, the singly methylated DD-cWW **168b** substrate is experimentally inactive. Despite forming reactive conformations in 18 frames of the MD trajectory, the reactive indole in these conformations does not establish hydrogen bonds with either Y127 or Y223 [Figure 97]. This lack of interaction with these critical catalytic residues may account for the substrate's inactivity.

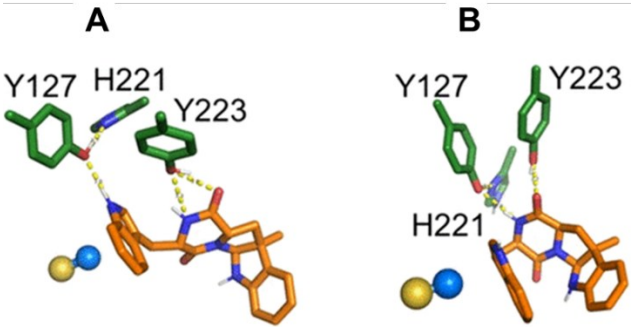

Figure 97: Binding modes of the reactive conformations of the single-methylated LL-cWW **168a** (A) and DD-cWW **168b** (B) substrates for the second methylation reaction. The legend is identical to Figure 96. Figure by Benoit David.

5.3.3 Integration of the SAM-recycling System

The synthetic application of the MTase reaction can be limited by the stoichiometric requirement for the cofactor SAM (**93**). This challenge can be addressed using a SAM recycling system, based on the halide MTase from *Chloracidobacterium thermophilum* (CtHMT), as described by Seebeck *et al.*[239] The CtHMT regenerates SAM (**93**) by transferring a methyl group from methyl iodide to SAH (**94**), which is then used as methyl source during the methylation reaction catalysed by StspM1 [Figure 98].

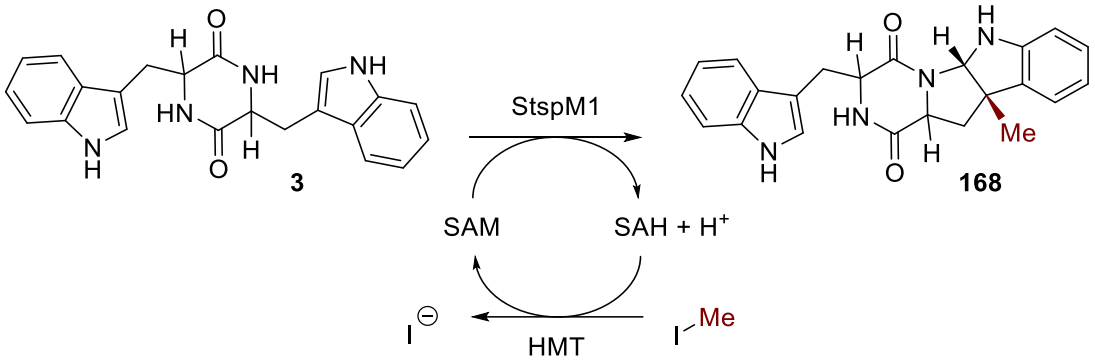

Figure 98: SAM recycling system using a HMT and methyl iodide as methyl source.

In addition, using lysates instead of purified enzymes offers several advantages for enhancing the synthetic utility of the reaction. Lysates eliminate the need for time-intensive and costly protein purification and negate the requirement for additional SAH or SAM cofactors due to the sufficient SAM (**93**) present in lysed cells when using the recycling system.

In an initial test with the LL-cWW **3a** substrate, 20 Vol% HMT and 80 Vol% StspM1 lysates were used. Although both enzymes perform optimally at elevated temperatures, the reaction temperature was capped at 40 °C to prevent methyl iodide evaporation, as its boiling point is 42 °C. To counteract potential evaporation, an excess of ten equivalents methyl iodide was included in the reaction. Relative conversions were monitored via HPLC by measuring absorbance at 284 nm at 0.5, 3, and 24 hours of incubation [Table S 5]. Full conversion to the double methylated product was detectet after 24 h. The reduced peak area of the methylated products compared to the substrate can be attributed to their lower extinction coefficients. During the formation of the HPI motif from the indole motif, the aromatic system is reduced, resulting in decreased absorption at 284 nm. The extinction coefficient of the cWW substrate **3**a is 8607 M^{-1} cm^{-1}, while the single-methylated product **168** exhibits a lower value of 4460 M^{-1} cm^{-1}, and the double-methylated product **240** is even lower at 2270 M^{-1} cm^{-1} [Figure S 15]. Therefore, calibration curves for both the substrate and the products were established for further analysis and quantification [Figure S 11].

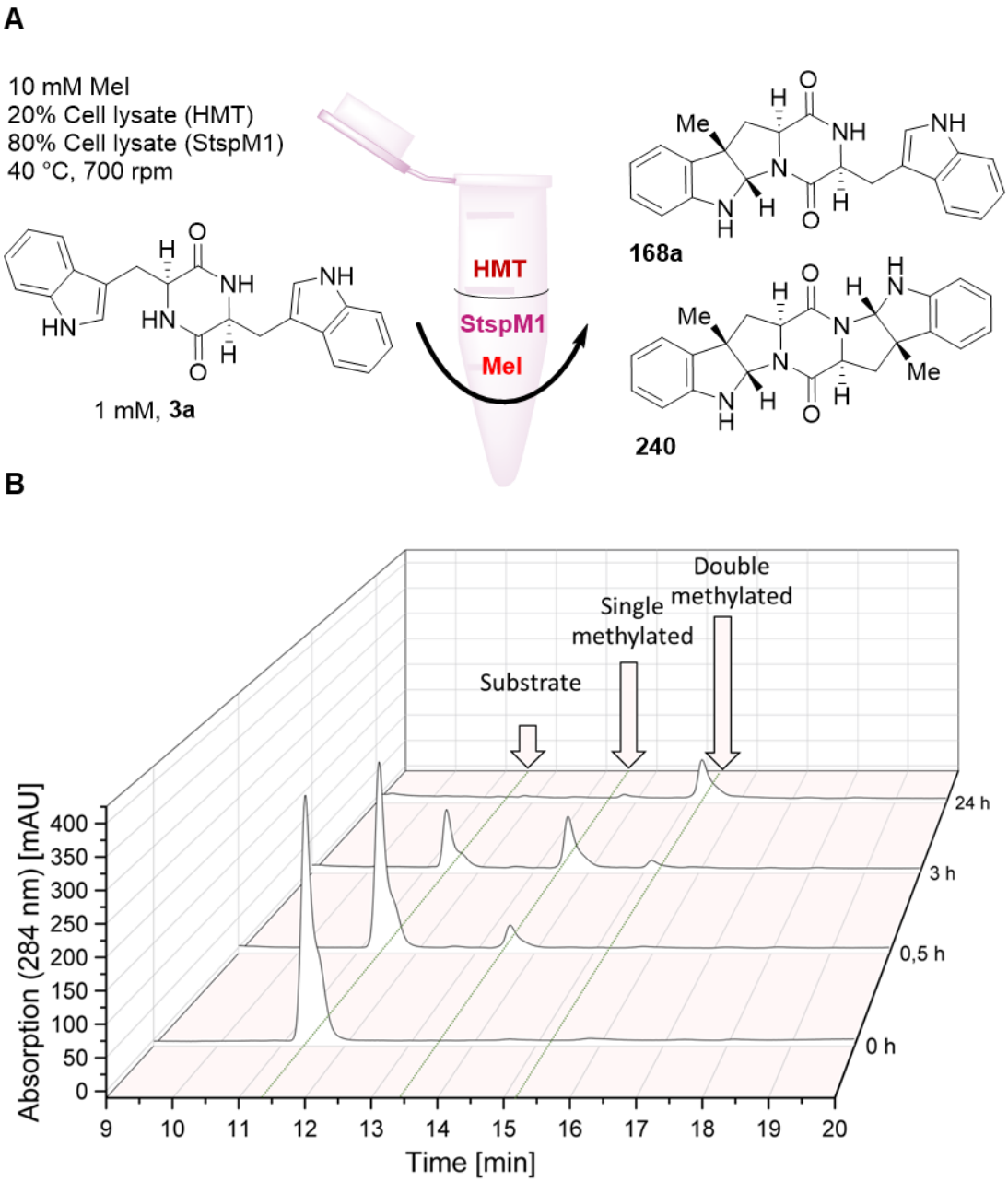

Figure 99: A: Biocatalytic methylation of LL-cWW **3a** with StspM1 using a SAM recycling system. B: Chromatograms of the time-dependent (0, 0.5, 3, 24 h) conversion of LL-cWW **3a** to its single methylated product **168a** and double methylated product **240** by measuring the absorption at 284 nm and retention times with RV-HPLC (hyperclone column, gradient of water and acetonitrile).

To enhance the system's efficiency for preparative-scale applications and reduce the required amounts of catalysts, a response-surface design-of-experiment (DoE) approach was implemented. This method involved systematically varying the concentrations of methyl iodide, StspM1 lysate, and CtHMT lysate as independent variables. Conversion rates were measured via HPLC after 24 hours for each experimental condition. In total, 34 individual experiments were conducted [Table S 6]. The conversion of LL-cWW **3a** after 24 hours was modeled using a hypersurface representation in a 3D diagram. Analysis of the DoE results indicated that the conversion rate was predominantly influenced by the amount of CtHMT lysate in the reaction mixture. To achieve maximal conversion after 24 hours with minimal StspM1 lysate, optimal conditions were determined as a v/v ratio of 34% StspM1 lysate, 16% CtHMT lysate, and 12 equivalents of methyl iodide [Table S 7]. To validate these findings, an additional experiment was conducted under these optimised conditions, resulting in the anticipated substrate conversion of 93 ± 4% [Table S 8].

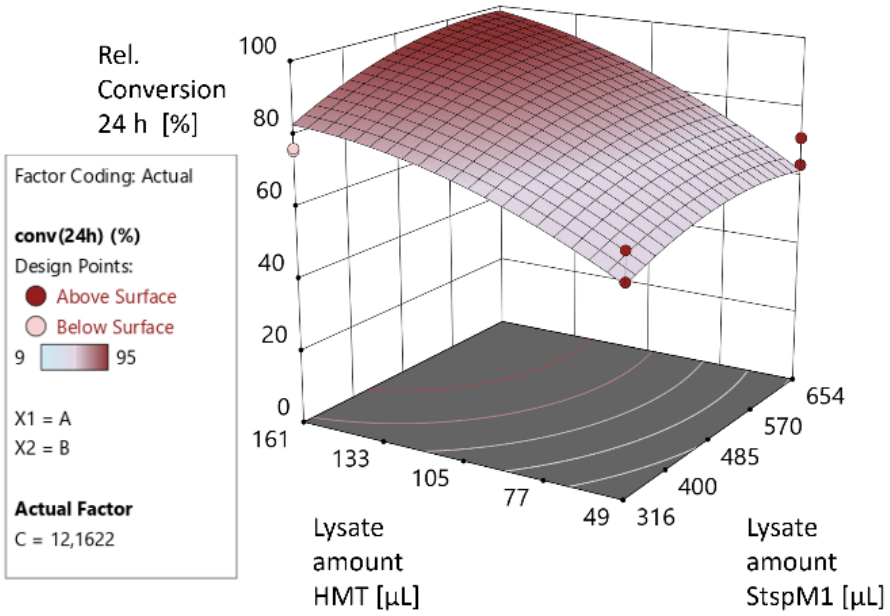

Figure 100: Result of the design of experiment approach. The conversion after 24 h of the LL-cWW **3a** is modelled by the hypersurface in the 3D diagram.

5.2.4 Preparative scale reaction

Under these optimised conditions, a preparative-scale experiment was conducted using 50 mg of substrate. After 24 hours, a conversion rate of 90% was achieved (HPLC result), consistent with the results of analytical-scale reactions. The product mixture contained 46% mono-methylated **168a** and 44% di-methylated **240** products. Following workup, a combined yield of 36% was obtained, comprising 19% mono-methylated **168a** and 17% di-methylated **240** products. This workup involved quenching residual methyl iodide with sodium hydroxide and precipitating proteins in the lysate using ammonium sulfate. However, during extraction with ethyl acetate, residual proteins aggregated, forming an inseparable interphase. This led to product losses of up to 60%.

To address this issue, the enzymes StspM1 and CtHMT were immobilised on Ni-NTA agarose beads. The immobilisation process involved incubating the enzyme-containing lysate with pre-washed beads for 1 hour under gentle inversion. Afterwards, unbound proteins were removed by collecting the flow-through, and the beads were washed with a washing buffer before being used in the reaction as immobilised enzyme. SDS-PAGE analysis confirmed that the entire amount of StspM1 was successfully bound to the beads. For CtHMT, a small amount of protein was lost during the washing step. Nonetheless, most of the enzyme remained attached to the beads [Figure S 16].

A comparison of enzymatic activity between lysates and immobilised enzymes revealed that immobilised StspM1 exhibited fourfold lower activity than the lysate, while immobilised CtHMT showed twofold lower activity. Since immobilisation can enhance enzyme stability, activity measurements were repeated after 24 hours of incubation under the same conditions as the preparative-scale experiment [Figure S 17, Figure S 18]. The activity of CtHMT decreased similarly in both lysate and immobilised forms after 24 hours (lysate: 11%, immobilised: 10%). In contrast, immobilised StspM1 showed only a slight decrease in activity (13%) over the same period, whereas lysate-based StspM1 activity dropped significantly, by 66% [Figure 101]. These findings demonstrate that immobilisation notably stabilises StspM1, improving its performance over extended reaction times.

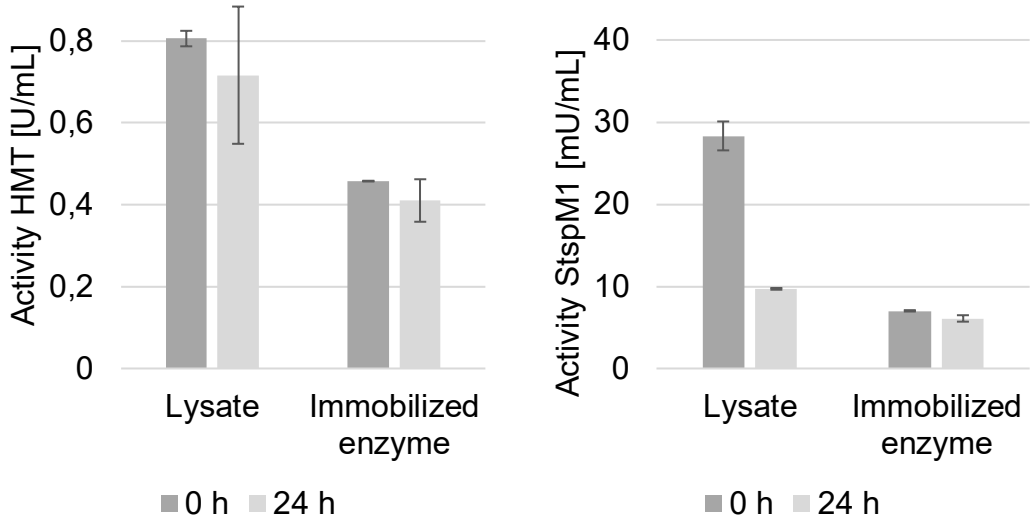

Figure 101: Activity of HMT (left) and StspM1 (right) in the lysate and the immobilised form before (0 h) and after (24 h) incubation at 40 °C.

When using immobilised enzymes instead of lysates, the separate addition of SAH/SAM is necessary since the cofactors are no longer supplied by the lysates themselves. Various concentrations of SAH were tested to identify the optimal amount, using the same conditions established in the design-of-experiment approach. After 24 hours, conversions close to the expected 90% were achieved with 0.1 or 0.05 equivalents of SAH, whereas lower concentrations resulted in reduced conversions

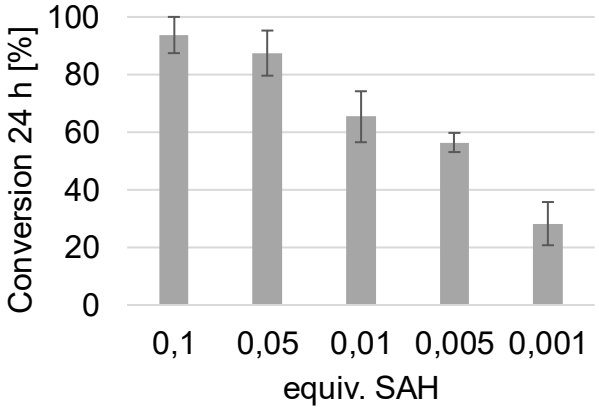

Figure 102: Conversion after 24 h of the methylation reaction of LL-cWW **3a** under in vitro assay conditions with immobilised enzymes and different concentrations of SAH.

A preparative-scale experiment using 50 mg of substrate was repeated under identical conditions, but with immobilised enzymes and the addition of 0.1 equivalents of SAH. After 24 hours, a conversion rate of 97% was achieved (20% mono-methylated product **168a** and 78% double-methylated product **240**). The reaction was quenched with ammonium thiosulfate, followed by filtration to remove the Ni-NTA beads, and the products were extracted with ethyl acetate. The reaction yielded 89% of the products, consisting of 20% mono-methylated **168a** and 69% double-methylated **240** compounds. Compared to the lysate-based reaction, the workup required less solvent, and the isolated yield improved. With the increased stability of immobilised StspM1, the incubation period was extended to 48 hours to favour the formation of the double-methylated product. Conversion rates were monitored at various time points [Figure S 19]. After 48 hours, no further substrate conversion was observed, resulting in a final conversion of 91% of the cWW **3a** substrate to the symmetric double-methylated product **240**. The overall yield was 89% [

Figure 103]. To test the applicability of this method, DD-cWW **3b** was used as a substrate. Given the lower conversion rates previously observed for this substrate, double the enzyme amounts were employed compared to LL-cWW **3a**. The reaction was stopped after three days, yielding a conversion rate of 63% and a final yield of 61% of the single-methylated product **168b** [Figure S 20].

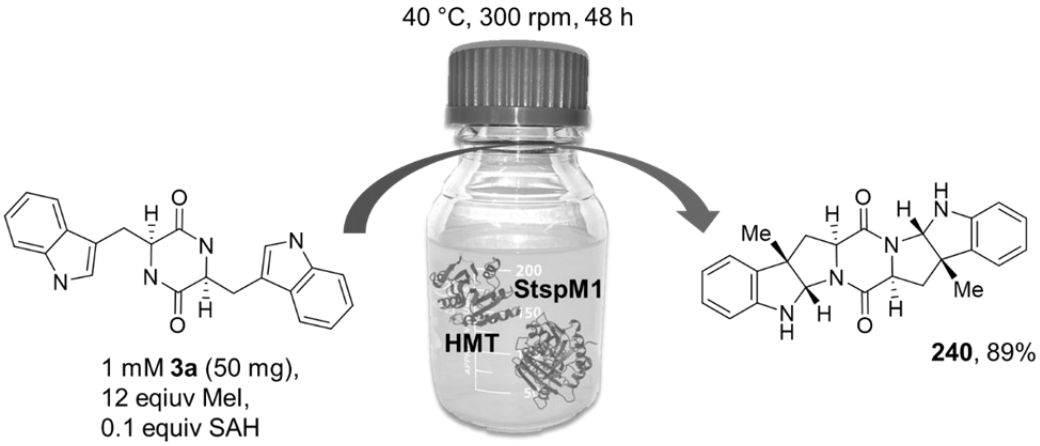

Figure 103: Set-up of the preparative enzymatic methylation of LL-cWW **3a** as a substrate leading to a yield of 89% of the double methylated product **240**.

This chapter demonstrates the use of the methyltransferase StspM1 for synthesising the pyrroloindole structural motif in diketopiperazines. Unlike conventional organic synthesis, this enzymatic reaction operates under mild conditions, achieving excellent conversion rates and diastereoselectivity. Various stereoisomers of cWW were evaluated as substrates, resulting in either single- or double-methylation depending on the configuration of the DKP core. Computational simulations, including classical and quantum mechanics (QM) analyses, were performed to explain the substrate stereoselectivity observed experimentally. To enhance the synthetic utility of StspM1, a SAM cofactor recycling system was implemented using a halide methyltransferase. The reaction was optimized through a design-of-experiment approach, and the performance of lysates and immobilized enzymes was compared at a preparative scale. This optimized protocol integrates SAM recycling and enzyme immobilization, enabling efficient enzymatic methylation of cWW substrates on a preparative scale with high yields. The new setup simplifies reaction workup and improves catalyst stability, offering a robust method for scalable production.

5.4 SgMT

The MTase SgMT from *Streptomyces griseoviridis* was identified through a homology search based on StspM1 and shares 79% sequence identity with this enzyme. To date, SgMT has not been reported or studied in the literature, leaving its biosynthetic role and natural substrate unknown. However, analysis of its sequence reveals the presence of a SAM-binding motif and a catalytic triad similar to those found in StspM1, suggesting that SgMT possesses the essential features required for methyl transfer catalysis [Table 4].

The gene encoding SgMT with an *N*-terminal His-tag was synthesised and cloned into a pET28a(+) expression vector by GenScript. To further investigate the enzyme's functional properties, Beatrix Paschold conducted cloning experiments to relocate the His-tag from the *N*-terminus to the *C*-terminus and produce an additional variant.

5.4.1 Characterisation

The enzyme with the *N*- and *C*-terminal His-Tag was heterologously expressed in *Escherichia coli* BL21 (DE3) and purified using Ni-NTA column chromatography. The molecular weight of SgMT, including a His-tags, is calculated to be 31 kDa. The purification of the *N*-terminal His-tagged SgMT was carried out by Elias Pfirmann during his bachelor thesis according to the established protocol of StspM1 with an additional washing step with 40 mM ImH. A distinct band at approximately 30 kDa is observed at the SDS-PAGE in the second washing and elution fraction. The enzyme in the elution fraction was very pure enabling the option for protein crystallisation [Figure 104]. As a lot of pure protein was already eluted in the washing fraction with 80 mM imidazole during the purification process, this washing step was thus left out in further purifications. The *C*-terminal His-tagged SgMT was purified with this shortened protocol [Figure S 21]. This process yielded approximately 40 milligrams of protein per gram of wet cell mass, which is 25 times higher than the yield achieved with the analogous MTase StspM1. These results highlight SgMT's robust expression and excellent solubility, making it a promising candidate for synthetic applications.

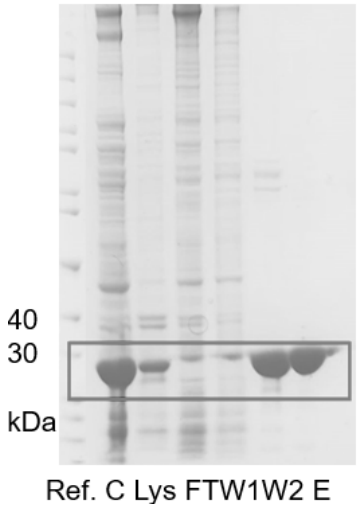

Figure 104: SDS-PAGE of the purification of *N*-terminal His-tagged SgMT. Ref. = Unstained Protein Standard, P = pellet, Lys = lysate, FT = flow through, W = wash (40 mM or 80 mM ImH), E = elution (160 mM ImH). The band at 30 kDa is highlighted.

Due to its high sequence similarity to StspM1, the LL-cWW **3a** substrate was selected to characterise SgMT [Figure 105A]. Enzymatic activity was assessed using the MTase Glo Assay, which measures SAM (**93**) consumption via luminescence. As described, SgMT was expressed and purified with a *C*- or *N*-terminal His-tag. The *N*-terminal His-tagged version contains a thrombin cleavage side, which was used to remove the *N*-terminal His-Tag after the purification. Activity measurements of the *N*-terminally tagged and the untagged variant as well as the *C*-terminally tagged enzyme revealed reduced activity for the *N*-terminally tagged enzyme compared to the other variants [Figure 105D]. The *N*-terminal His-tag might restrict the movement of the *N*-terminal lid region, which is thought to be critical for catalysis in the homologous MTase PsmD.[99]

The *C*-terminal His-tagged SgMT was further characterise, as this variant is readily accessible in a purified form and its His-tag does not affect enzymatic activity: Temperature screening experiments revealed maximum activity at 45 °C across a range of 22–50 °C [Figure 105B]. For pH optimisation, substrate conversion was analysed via HPLC using citrate-phosphate buffers (pH 5.5–8) and Tris buffers (pH 7.6–8.6) [Figure 105C]. The highest conversions occurred between pH 7.5 and 8.2. These conditions align closely with the optima for StspM1 (45 °C, pH 6–8) and PsmD (45 °C, pH 6–9). Kinetic parameters for LL-cWW **3a** showed a K_m of 10.53 ± 2.01 µM, a v_{max} of 0.44 ± 0.03 µM/min, and a k_{cat} of 0.0025 s^{-1}, slightly lower than StspM1's k_{cat} of 0.0036 s^{-1} under identical conditions [Figure 105D].

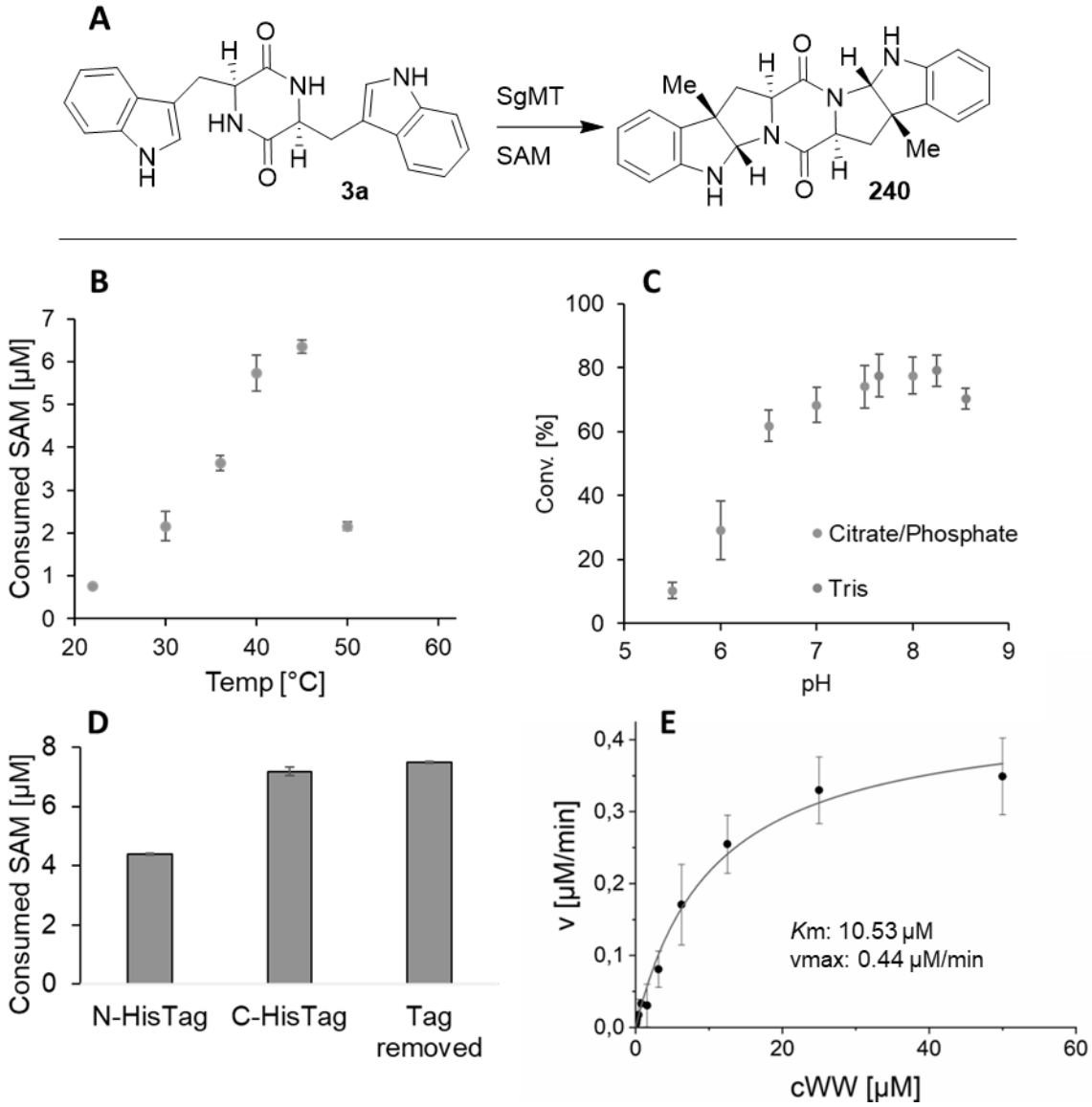

Figure 105: *C3*-Methylation of LL-cWW **3a** catalysed by SgMT [A]. Biochemical characterisation of SgMT: Temperature screen [B], pH screen [C], influence of the His-Tag on the enzyme activity [D] and a Michaelis Menten kinetic [E]. The activity in B, D and E were determined with the MTase Glo Assay, C via HPLC.

In addition to the LL-cWW **3a** substrate, a variety of DKP derivatives with amino acids different than solely tryptophane, as well as benzodiazepine-2,5-dione derivatives, were tested using the MTase Glo Assay [Figure 106]. Among the substrates, LL-cWW **3a** exhibited the highest enzymatic activity, while its isomer DD-cWW **3b** was also accepted but with significantly reduced activity. Analytical-scale reactions confirmed these findings, with retention times matching those products previously reported for StspM1 via HPLC. Product characterisation revealed that LL-cWW **3a** underwent methylation on both indole moieties, whereas DD-cWW **3b** was only singly methylated. These results align with the MTase Glo Assay, which detected conversion for singly methylated LL-cWW **3a** but not for singly methylated DD-cWW **3b**. Additional substrates, including LD-cWW **3c**, LL-cWF **242a**, LD-cWF **242c**, LL-cWY **241a**, LL-cWL **245**, and benzodiazepine-2,5-dione derivatives **246a** and **246b**, were also converted, though with low enzyme activity. Overall, the substrate profile of SgMT closely resembles that of StspM1 [Figure 106, Figure 92].

Finally, the doubly *C3*-methylated LL-cWW **240** was tested to evaluate whether SgMT could catalyze further *N*-methylation of the HPI ring, as observed with the bifunctional enzyme NozMT. However, no additional conversion was detected, indicating that SgMT does not exhibit the same bifunctional activity [Figure 106].

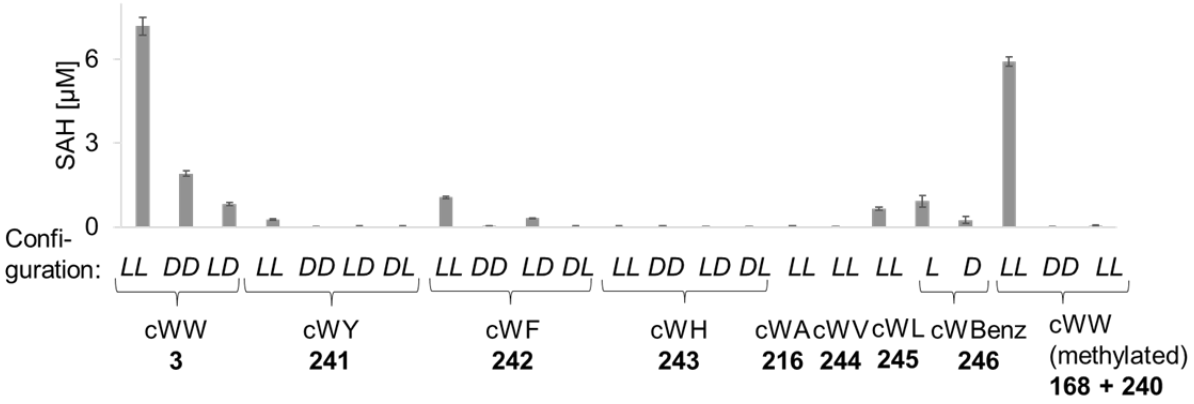

Figure 106: Substrate scope of SgMT. The activity of the MTase was determined via the MTase Glo Assay. The first stereodescriptor refers to the tryptophan and the second stereodescriptor to the respective second amino acid residue.

SgMT was additionally used in a preparative scale reaction (100 mg scale) as immobilised enzyme on Ni-NTA agarose beads for the conversion of the LL-cWW **3a**. 34 Vol% SgMT lysate were used in a reaction with 3 mM SAM (**93**) and 1 mM cWW **3a** for 48 h at 40°C yielding 89% of the double methylated product **240**, similar to StspM1.

5.4.2 Crystallisation and X-ray structure

To gain deeper insights into the structural and catalytic features of SgMT, the protein was crystallised in the presence of its cofactor, specifically the non-methylated form, SAH (**94**). Crystallisation trials were conducted using commercially available screening kits and the vapor diffusion method in a sitting-drop setup. Initial crystals were observed under multiple conditions, which were further refined through matrix optimisation and additive screening.

The crystals used for high-quality diffraction and structural determination were grown in a reservoir solution containing sodium citrate (pH 5.6), isopropanol, PEG 4000, glycerol, and hexaammine cobalt(III) chloride as an additive [Figure 107]. This optimised condition yielded diffraction-quality crystals suitable for structural analysis. The three-dimensional structure of SgMT was resolved via X-ray crystallography (PDB: 9GDJ) by Oliver Weiergräber. The crystals belong to the space group $P4_12_12$ and contain three protein chains within the asymmetric unit [Table S 9].

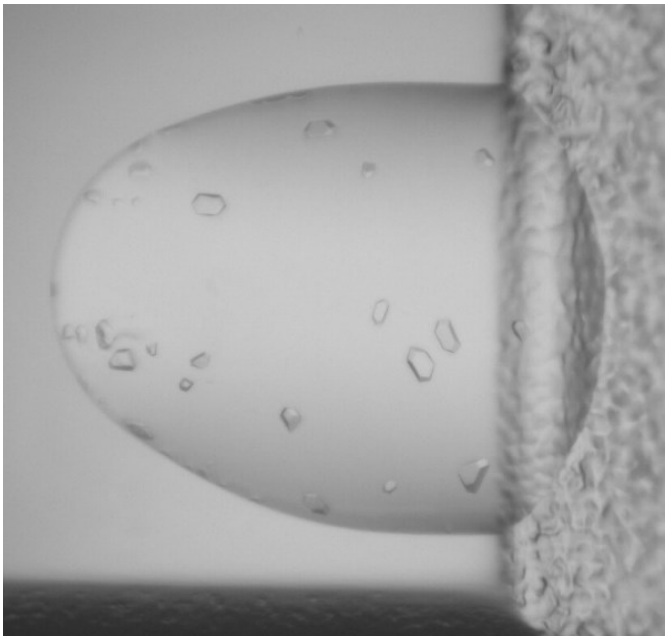

Figure 107: Picture of the protein crystals of SgMT in the droplet containing the crystallisation buffer and the reservoir solution (sodium citrate pH 5.6, isopropanol, PEG 4000, glycerol, and hexaammine cobalt(III) chloride as an additive).

Structurally, SgMT exhibits a strong resemblance to the *C3*-MTase PsmD from *Streptomyces griseofuscus*. Its main domain adopts a Rossmann-type *α*/*β* fold with the cofactor at the base of a large solvent-filled cavity. The structural similarity to PsmD extends to the quaternary arrangement, where two cap domains associate face-to-face at a right angle, forming a dimeric interface. Within the asymmetric unit, two of the three chains form a non-crystallographic dimer, while the third chain establishes a comparable interaction with a symmetry-equivalent partner. Although the overall structure of SgMT resembles the closed conformation observed for PsmD, the distal regions of the two enzymes differ significantly in both sequence and conformation. Functionally, the Ω-loop (lid) of PsmD, formed by residues 2–14, corresponds to the shorter extended segment 7–9 in SgMT. In PsmD, the side chain of M2 and a bent R86 conformation shield the SAH adenine moiety from solvent, whereas in SgMT, this role is fulfiled by the straight conformation of R81 [Figure 108]. The absence of electron density for residues preceding T7 in SgMT suggests that this region is disordered.

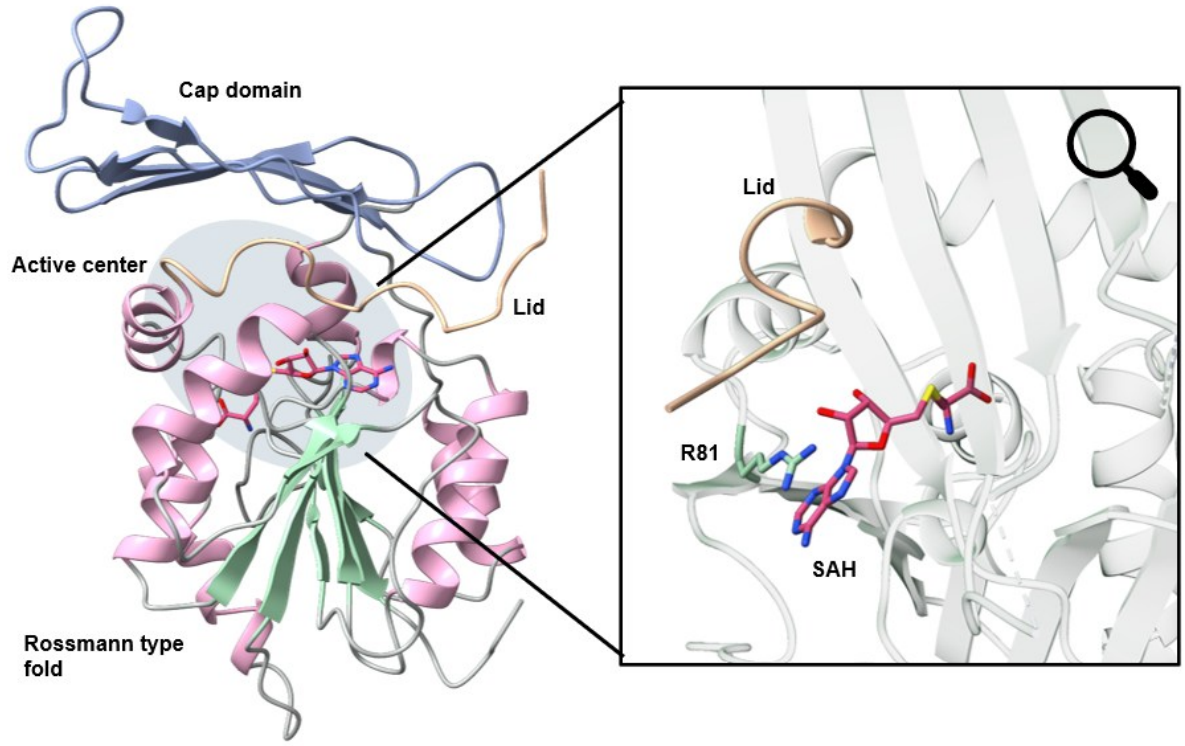

Figure 108: Crystal structure of SgMT (PDB: 9GDJ). The Rossmann fold is displayed with α-helices and β-strands coloured pink and green, respectively. The cap domain is shown in blue, the lid in light orange. SAH (**94**) is highlighted in dark pink. The active site is zoomed in showing the lid and R81 covering the SAH (**94**).

5.4.3 Mechanistic studies

The structural analysis of SgMT reveals a catalytic triad comprising Y126, H220, and D218 [Figure 109], analogous to the catalytic triad identified in PsmD and suggested for StspM1. This structural similarity suggests that SgMT operates through a similar mechanistic paradigm. To test this hypothesis, site-directed mutagenesis was performed on these residues, and the impact on enzymatic activity was assessed. Substitution of Y126 with either alanine or phenylalanine resulted in a complete loss of activity, demonstrating the necessity of a phenolic moiety. This finding is consistent with the results obtained for StspM1. In addition, replacing H220 with alanine abolished activity, proving its proposed role as a proton acceptor from the adjacent tyrosine. At position 218, the substitution of aspartic acid with glutamic acid or alanine retained partial activity [Figure 109]. This indicates that D218 has limited functional significance on its own, but that full activity relies on the accurate positioning of the acidic group, which the longer side chain of glutamic acid cannot provide. These results strongly support the hypothesis that SgMT employs a proton relay system similar to PsmD. This mechanism, driven by catalytic tyrosine activation, appears to be a conserved feature among related MTases, including StspM1 and SgMT.

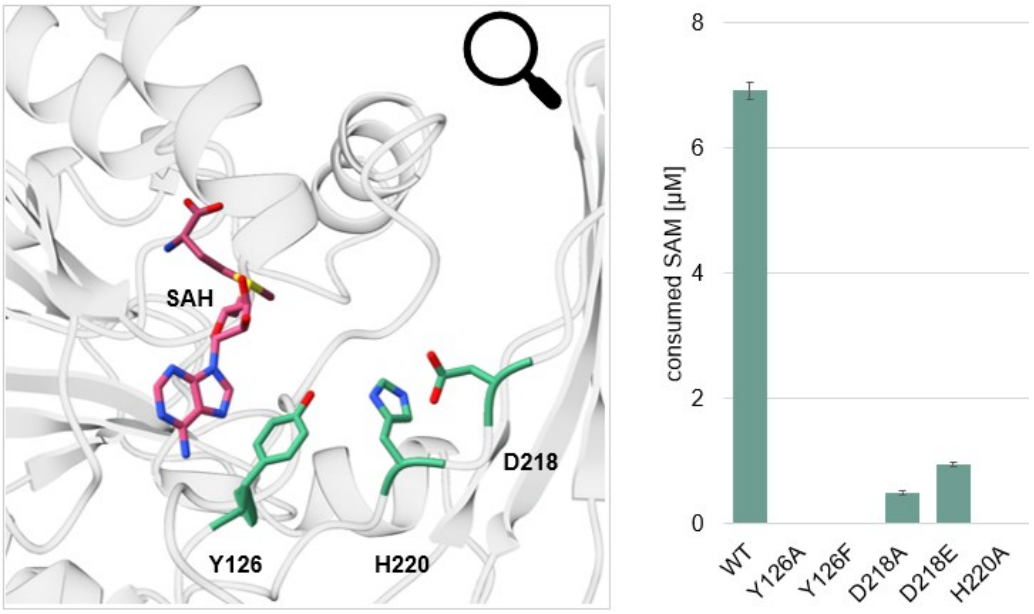

Figure 109: Crystal structure of SgMT (PDB: 9GDJ). The catalytic triad (Y126, H220, and D218) is shown in green, the cofactor in dark pink (left). Results of the mutagenesis study probing the catalytic residues of SgMT. Enzyme activities were measured with the MTase Glo Assay (right).

To elucidate the binding mode of the LL-cWW **3a** substrate in relation to SgMT's catalytic residues, docking studies were performed by Benoit David. MD simulations of the SgMT dimer with the docked substrate and SAM (**93**) cofactor, were conducted to explore substrate conformational dynamics and interactions with surrounding residues. Substrate conformations compatible with catalysis were identified based on five geometric criteria previously established for StspM1.

While most LL-cWW **3a** substrate binding poses adopted geometries suitable for the methyl transfer step, only a small fraction met all five criteria, aligning with both catalytic steps: methyl transfer and subsequent HPI cyclisation. Specifically, only 13 snapshots from the total MD trajectory (comprising 103197 snapshots) fulfiled these stringent geometric requirements, highlighting the challenge in achieving the precise alignment necessary for the full catalytic mechanism. The simulations revealed that the hydroxyl groups of Y126 and Y222 establish polar interactions with the reactive indole nitrogen of the substrate, similar to StspM1. A hydrogen bond between the hydroxyl group of Y126 and the indole nitrogen was observed in six snapshots [Figure 110].

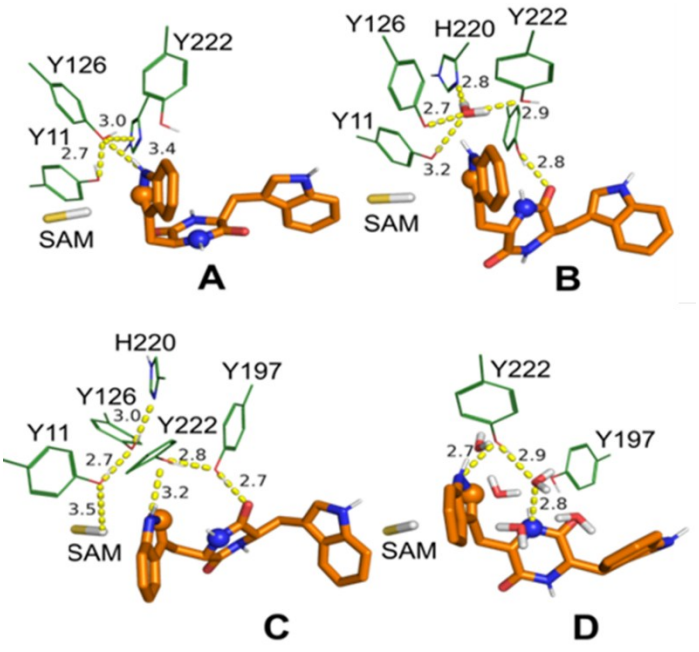

Figure 110: Putative LL-cWW **3a** catalytic conformations extracted from MD simulations. Grey sticks: reactive methyl group of SAM (**93**), Orange sticks: LL-cWW **3a**, Green lines: selected residues. Dashed lines: relevant hydrogen bond interactions and distances (in Å). As spheres: DKP nitrogen (blue sphere) and indole carbon (orange sphere) involved in HPI cyclisation. In A: conformation suitable for methyl transfer but not for HPI cyclisation as the DKP nitrogen and indole carbon involved are too far from one another. In B, C, D: conformations suitable for both methyl transfer and pyrroloindole cyclisation. Figure by Benoit David.

StspM1s residue Y223, the residue equivalent to SgMTs Y222, plays a catalytic role by forming a hydrogen bond with the reactive indole nitrogen of the substrate. This was demonstrated by the Y223F mutation, which confirmed the essential role of the phenolic group in catalysis, as the mutant exhibited no activity. However, in SgMT, the analogous Y222F mutation only slightly reduced activity compared to the wild-type enzyme [Figure 111]. The data suggests that while the hydroxyl group of Y222 is not essential for catalysis, the inactivity of the Y222A mutant confirms the importance of an aromatic ring at this position. In simulations, the Y222 side chain formed more hydrogen bonds with the reactive indole nitrogen of the substrate than Y126 [Figure S 22], consistent with similar observations in StspM1. However, the relatively high activity of the Y222F mutant suggests these hydrogen bonds are not critical for catalysis. Instead, the aromatic ring of Y222 likely plays a structural role, helping to correctly orient Y126 for catalysis, as suggested by the inactivity of the Y222A mutant and the close spatial relationship between Y222 and Y126.

Unlike StspM1, SgMT additionally features a network of five tyrosine residues oriented toward the reaction centre. To evaluate their significance, these tyrosines were individually mutated to alanine and phenylalanine. All alanine mutants completely lost activity, highlighting the essential positions of these residues. Phenylalanine mutants retained reduced activity [Figure 111]. This suggests that while the aromatic scaffold of the tyrosines is important, their hydroxyl groups are not essential for the catalytic function as already explained in detail for Y222.

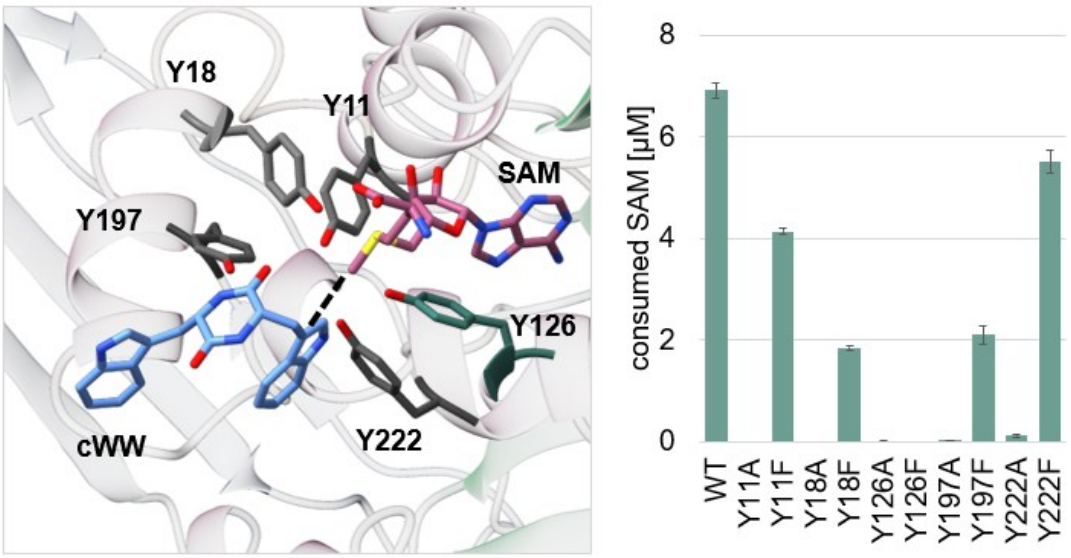

Figure 111: Tyrosine network in SgMT. A: Tyrosines Y11, Y18, Y126, Y197, and Y222 are shown in grey, the cofactor in dark pink and the docked substrate **3a** in blue. The dashed line connects the SAM (**93**) methyl group to the reactive indole moiety (left). Results of the mutagenesis study probing the tyrosine network of SgMT. Enzyme activities were measured with the MTase Glo Assay (right).

5.4.4 Integration of the biocatalytic methylation in the total synthesis of lansai B

Lansai B (**5**) features a central DKP motif with two HPI groups attached.[53] Its configuration at the *C3*-positions aligns with the product produced by the reaction of LL-cWW **3a** with the MTase SgMT. While SgMT was tested on a range of DKPs composed of tryptophan and different natural amino acids, all tested substrates were smaller in size than the cWW **3**. Given that lansai B (**5**) includes a prenyl group at the 5-position, the substrate scope had to be expanded to include substituted non-canonical amino acids. For the methyl transfer to occur with an enzyme like SgMT, several structural criteria must be met as described before. Modifications to the substrate, such as the desired adding of substituents, can significantly impact the enzyme's activity by disrupting these parameters, highlighting the enzyme's specificity.

Thus, halogen substituents were chosen for the investigations due to their small size, while they later on can be utilised in cross-coupling reactions to synthesise the desired target structure. 5-Brominated and chlorinated tryptophans **256**, readily available from commercial sources as racemic mixtures, were used as starting materials for the synthesis. The synthetic procedure followed a previously established protocol, with the modification of using a Boc-protecting group instead of a Cbz-protection group at the L-tryptophan as second substrate **257**. The resulting diastereomers (substituted LL- and LD-cWW **258a** and **258c**) were then separated by column chromatography. Subsequently, the brominated LL-cWW **258a** was reacted in a Suzuki-Miyaura cross-coupling reaction with prenyl pinacolborane (**260**) to yield 5-prenyl LL-cWW **261a**. Two catalyst-ligand systems were tested, showing that SPhos/SPhos Pd G4 **262** acts superior to *NOM-Phos*/Allyl-Pd-Cl **263**. The described syntheses were performed by Marcel Schatton [Figure 112].[325]

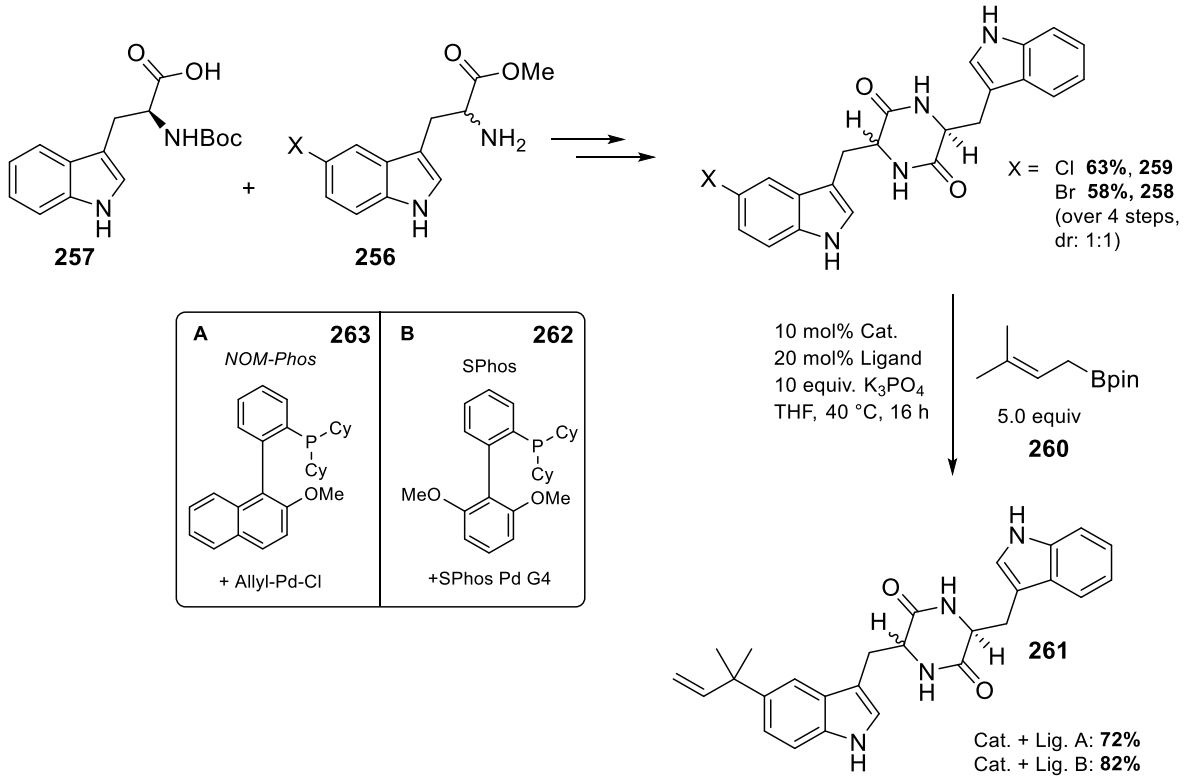

Figure 112: Synthesis of 5-substituted cyclic Trp-Trp-DKPs starting form racemic 5-chloro and 5-bromo-tryptophan **256**.

The *C5*-Cl-, *C5*-Br-, and *C5*-prenyl substituted LL-cWWs **259a, 258a** and **261a** were tested as substrates for the activity in the MTase reaction with SgMT using the bioluminescence-based MTase Glo Assay to form the corresponding single or double methylated products **264-266** and **267-269**. The substituted cWWs exhibited reduced enzyme activity compared to the unsubstituted variant: The halogenated cWWs **259a** and **258a** retained 22.3% (R = Br) and 24.4% (R = Cl) of the activity, while the prenylated cWW **261a** displayed significantly lower activity, at just 4.3% [Figure 113]. These findings highlight that the size of the substituent and its electronic properties play a critical role in influencing the enzyme's conversion efficiency.

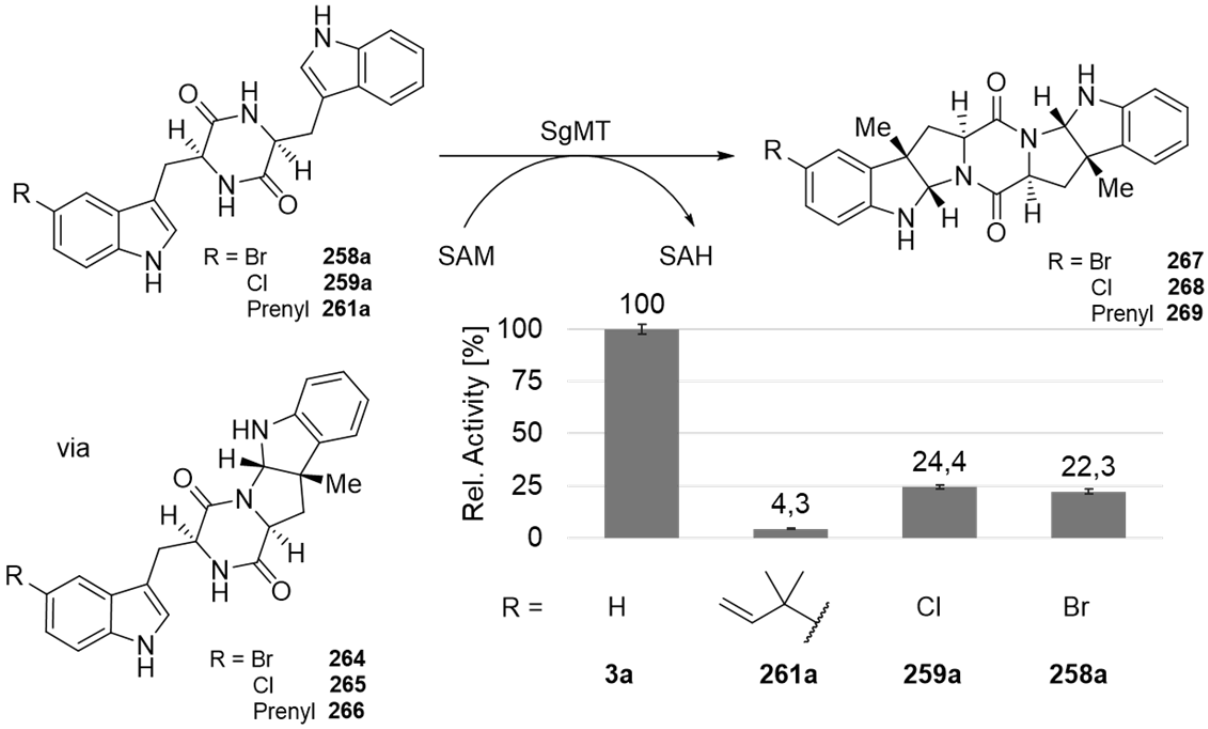

Figure 113: Relative activity of SgMT for the synthesised functionalised DKPs in comparison to the unsubstituted substrate measured with the MTase Glo Assay.

Since the conversion rates for halogenated substrates are higher than for the already prenylated substrate, a late-stage prenylation after the MTase-catalysed reaction was chosen as synthesis route potentially allowing for higher overall yields. Among the halogenated substrates, *C5*-Br cWW **258a** was chosen for further investigation with SgMT, as the established prenylation conditions could not be directly applied to the chlorinated DKP due to its lower reactivity.

To enhance the enzyme's activity towards the 5-Br cWW **258a**, a mutagenesis study was conducted modifying the active site. The process involved several methodical steps [Figure 114]. The automated library screening was conducted on the AutoBioTech platform in collaboration with Julia Tenhaef, who developed the technical scripts for the robotic systems and assisted with device operation and handling.[326]

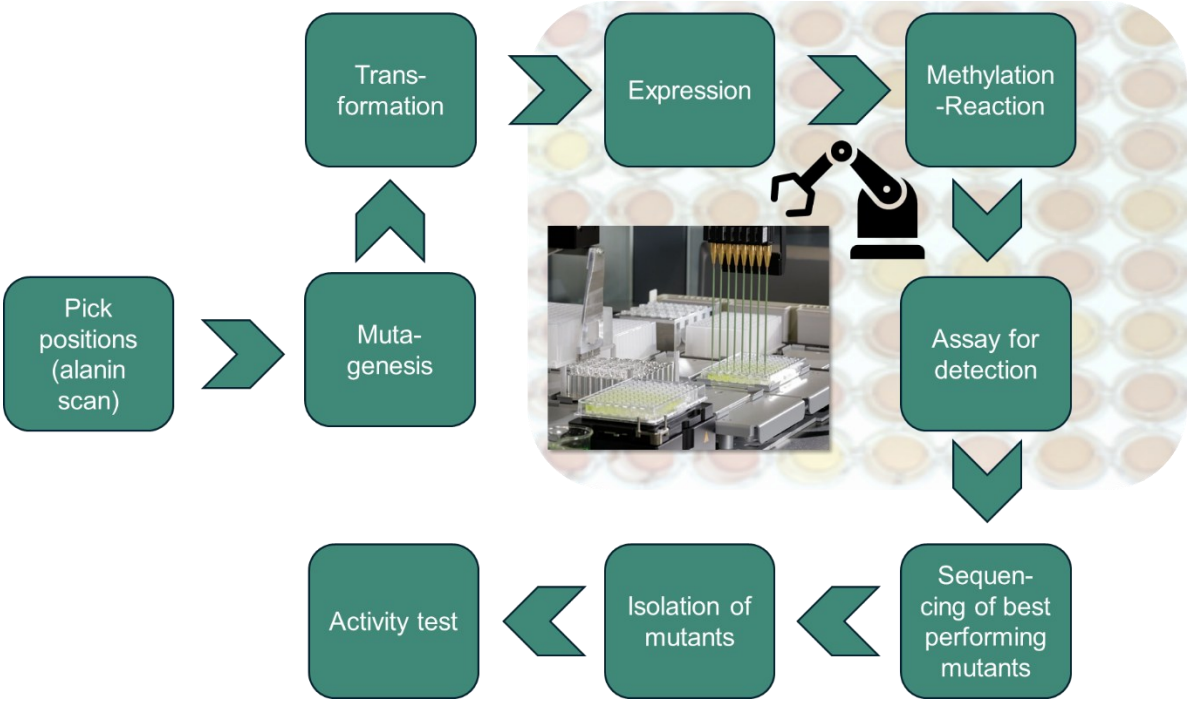

Figure 114: Setup of the mutagenesis process using the AutoBioTech platform. The mutagenesis approach to optimise SgMT activity involves several key steps.

An alanine scan was used to identify positions within the active site that are not essential for enzyme activity but provide opportunities for modification. Seven residues (L21, W24, N125, D152, W182, F184, M195) near the cWW binding site were investigated to identify candidates for mutagenesis experiments. Three positions were prioritised: one on the catalytic side of the cWW **3a** (N125) and two on the outer side of the binding site (W182 and F184). The alanine scan showed that mutating N125 and F184 did not completely abolish enzymatic activity, indicating that modifications at these positions would not directly inactivate the enzyme. W182, located in the outer binding region near the indole substituent, occupies most of the space in this area. As a preliminary experiment, W182 was mutated to phenylalanine, which retained residual activity, suggesting it as a promising target for further optimisation [Figure 115].

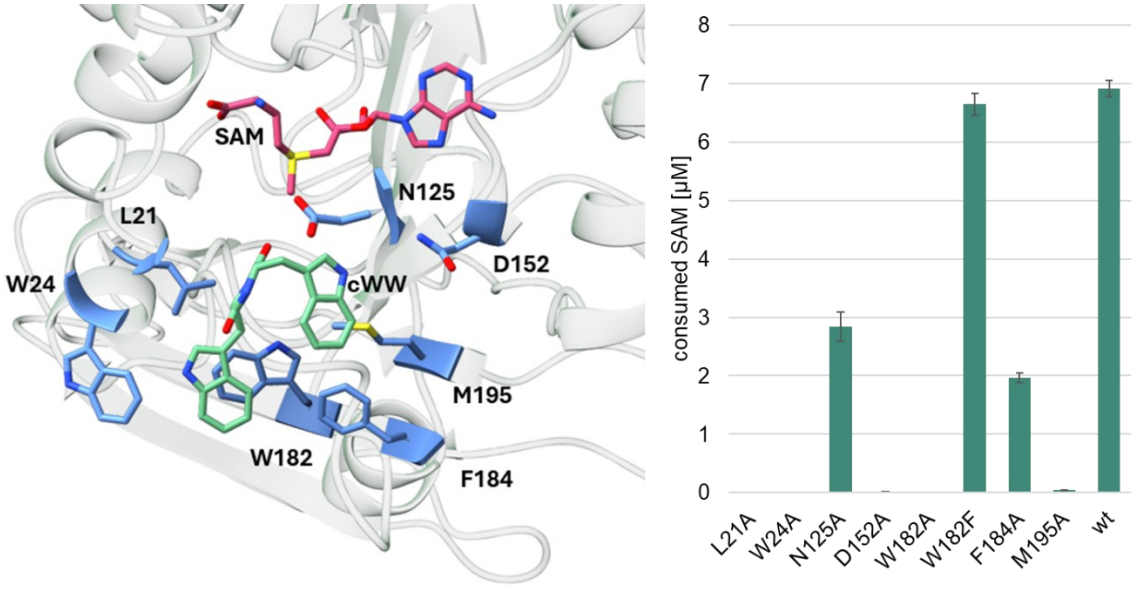

Figure 115: Left: Catalytic side of SgMT with SAM (**93**, dark pink), the cWW **3a** (green) and the amino acids tested in the alanine scan (blue). Right: Activity of SgMT variants for the cWW **3a** substrate measured with the MTase Glo Assay.

These positions were targeted for mutation using the 22c trick,[327] an approach that minimises codon redundancy and reduces the size of mutant libraries, resulting in the creation of a comprehensive plasmid library containing all possible variant sequences. This library was used to transform *E. coli* BL21 (DE3), generating a diverse pool of mutants. From this pool, 66 individual clones were selected, cultivated under controlled conditions, and harvested for analysis (wells A1-B9). As a positive control, wild-type SgMT was cultured under identical conditions (wells C9, D9), while an empty vector served as the negative control (wells E9, F9).

Each clone was incubated with substrates, *C5*-Br cWW **258a** and SAM (**93**), in a reaction buffer for a 7-hour reaction period. Mutant activity was evaluated using a colourimetric indole detection assay, which quantifies the unreacted substrate by forming a coloured solution [Figure S 23]. Consequently, a lower absorbance value indicates a higher conversion of substrate.[328, 329] For positions W182 and N125, none of the mutants demonstrated higher conversion rates than the wild-type enzyme [Table S 11, Table S 12]. The most promising results emerged from the F184 mutant library [Table 8]. Among the five mutants with the highest conversion in the preliminary experiment (mutants A1, A3, A5, H5 and F8), sequencing revealed that four corresponded to the F184L mutation, while one was identified as F184A. Both amino acids, leucin and alanine, are smaller in size than phenylalanine and could therefore be beneficial for the enlarged *C5*-Br cWW **258a**.

Table 8: Results of the mutagenesis study for position F184. The indole assay was used to form the coloured product, which was measured via absorption at 540 nm.

<>	1	2	3	4	5	6	7	8	9
A	0,160	0,221	0,154	0,288	0,164	0,193	0,177	0,172	0,232
B	0,700	0,234	0,199	0,166	0,204	0,240	0,208	0,233	0,259
C	0,326	0,248	0,271	0,252	0,217	0,255	0,283	0,237	0,174
D	0,278	0,232	0,249	0,223	0,293	0,275	0,259	0,233	0,173
E	0,276	0,223	0,256	0,173	0,194	0,208	0,244	0,215	0,263
F	0,206	0,177	0,259	0,217	0,251	0,275	0,204	0,164	0,282
G	0,285	0,240	0,182	0,222	0,228	0,230	0,241	0,235	
H	0,188	0,232	0,230	0,218	0,161	0,276	0,256	0,219	

The mutants F184L and F184A were purified, and their activity was assessed using the Glo Assay as previously described. The substrates tested included *C5*-Br cWW **258a** and its singly *C3*-methylated derivative **264**. Among the mutants, only F184L exhibited improved conversion for *C5*-Br cWW **258a**, achieving a 12% increase compared to the wild-type enzyme. However, this mutant showed reduced activity (-26%) for the second methylation step compared to the wild type. For the complete synthesis of lansai B (**5**), which requires methylation on both sides, the wild-type enzyme thus remained the best choice. Nonetheless, the expanded alanine scan and mutagenesis study provided valuable insights into the active site architecture of SgMT.

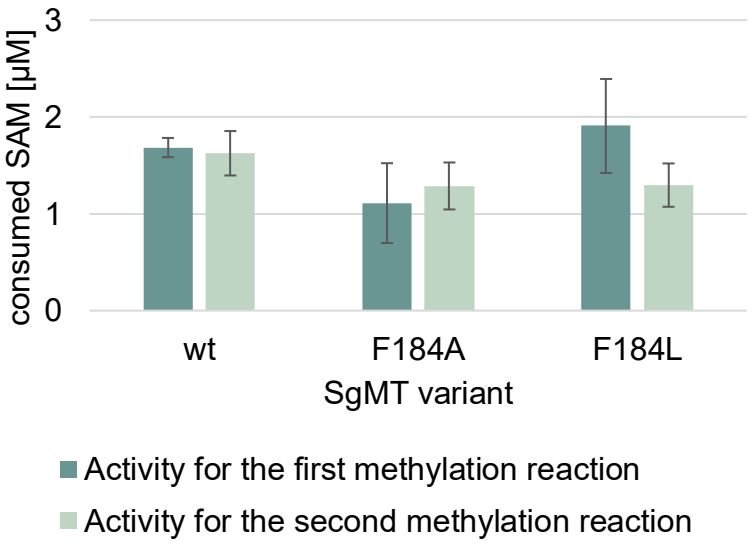

Figure 116: Activity of SgMT variants against the *C5*-Br-cWW substrate **258a** (dark green) and the single methylated 5-Bromo-cWW intermediate **264** (light green) measured with the MTase Glo Assay.

To optimise the methylation reaction of *C5*-Br cWW **258a** using SgMT, the optimal enzyme amount was determined. SgMT was immobilised directly from the lysate using Ni-NTA agarose beads as described for StspM1. Small-scale reactions were performed with varying amounts of SgMT-containing cell lysate (10–100 Vol%). After 20 hours of reaction time, the reactions were stopped, and samples were analysed using two independent assays. The first assay, detecting indoles, measured the remaining substrate, while the second assay, detecting HPIs, measured the product formed after two methylations. The HPI detection assay uses cerium sulfate under acidic conditions for product quantification [see chapter 5.6 for details]. Both assays provided complementary results based on absorbance measurements of the assay-generated products. The findings revealed that a 70 Vol% immobilised SgMT lysate was sufficient for optimal conversion.

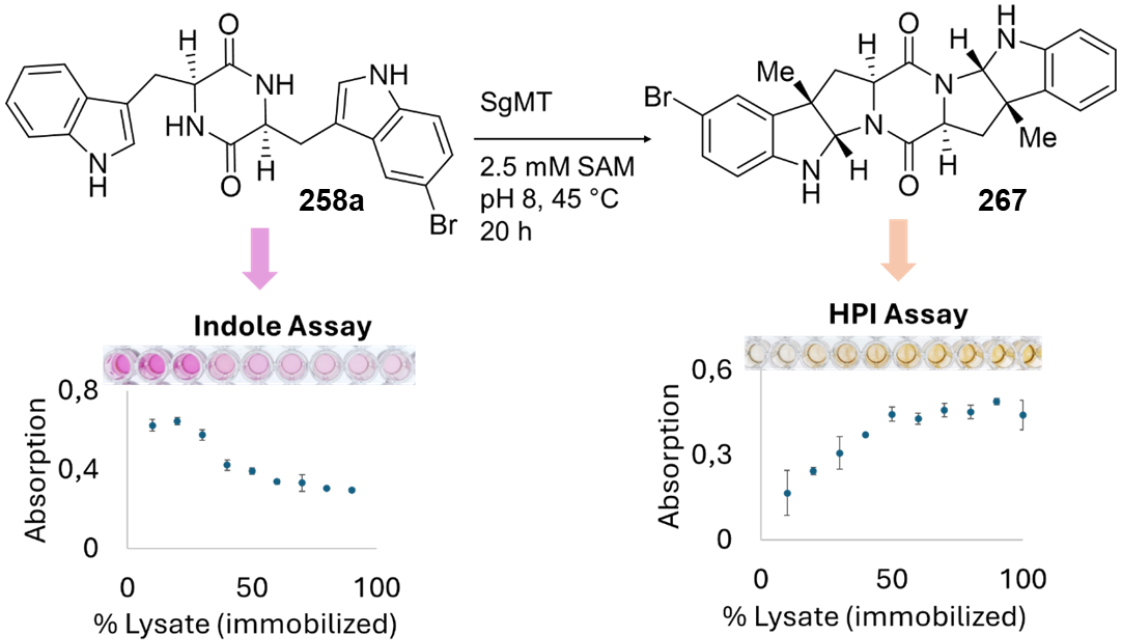

Figure 117: Optimisation of the biocatalytic methylation reaction of SgMT with the *C5*-Br cWW **258a**. Two assays were used to detect the substate (indole assay, left) and the product **267** (HPI assay, right) in parallel via absorption. The amount of immobilised lysate of SgMT cells was varied.

After refining the enzymatic key step of the synthesis using *C5*-Br LL-cWW **258a** as substrate, Marcel Schatton further optimised the synthesis of this substrate, developing a more sustainable approach from readily available building blocks. Collaborating with Catharina Gronkowsky, they employed a variant of the tryptophan synthase from *Pyrococcus furiosus*, an enzyme that had been extensively studied and bio-engineered by Francis Arnold and her coworkers.[330, 331] This enzyme efficiently catalyses the conversion of serine and indole into tryptophan. By applying this method, 5-bromoindole (**270**) was converted to enantiomerically pure *C5*-Br L-tryptophan (**271**) in 96% yield. The resulting tryptophan **271** was then used as the substrate for synthesising the corresponding DKP **258a**, yielding 72% over four steps. For the MTase reaction, 50 mg of substrate were processed under optimised conditions (70 Vol% immobilised SgMT lysate, 3 mM SAM (**93**), pH 8, 40 °C, 1 day). After extraction, 79% of the doubly methylated product was successfully obtained.

The prenylation step was carried out by Marcel Schatton under the same conditions as previously described, yielding 78% of the prenylated product **269** when using the naphthyl-ligand. For the final step, a combination of Meerwein's salt **272** and a proton sponge **273** as the base was identified as the best approach. With the need for large quantities of reagents, since the reaction tended to stop after a certain period, the use of 12 equivalents of base and 9.0 equivalents of Meerwein's salt ultimately provided lansai B (**5**) in an 80% yield [Figure 118].[325]

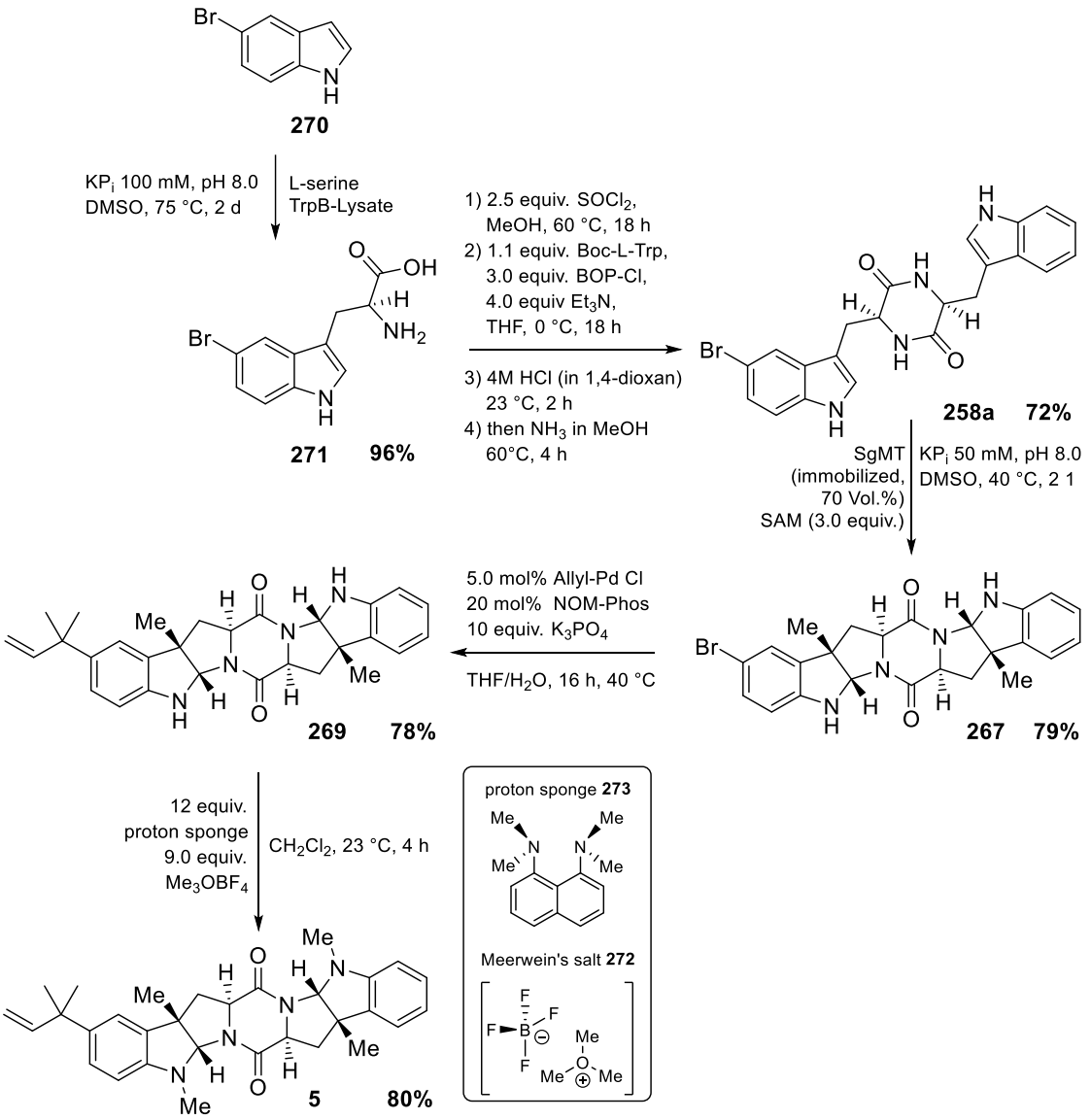

Figure 118: Enantioselective total synthesis of lansai B (**5**) employing two chemoenzymatic steps starting from the small building block bromo-indole.

5.4.5 Lansai B derivatives

To expand the substrate scope of SgMT, various substituted cWW derivatives were synthesised by targeting each position (4-7) of the indole ring using the tryptophan synthase described in the previous chapter. The corresponding halogenated tryptophans were coupled to either unsubstituted or halogenated tryptophans, resulting in eight distinct products **258a** and **274-280**. The synthesis of these compounds was carried out by Marcel Schatton and Catharina Gronkowsky.

These derivatives were tested for acceptance by SgMT using the Glo Assay from Promega. The single brominated substrates **258a** and **274-276** showed reduced activity compared to the unsubstituted cWW **3a**, with the 5-Br cWW **258a**—previously used in the total synthesis of lansai B—being the least accepted. Among the double halogenated substrates, only the 5,5'-Br cWW **278** showed similar activity to the 5-Br cWW **258a**. The 7,7'-Br cWW **280** exhibited only slight activity, while the other two double-substituted derivatives **277** and **279** were not accepted by the enzyme [Figure 119].

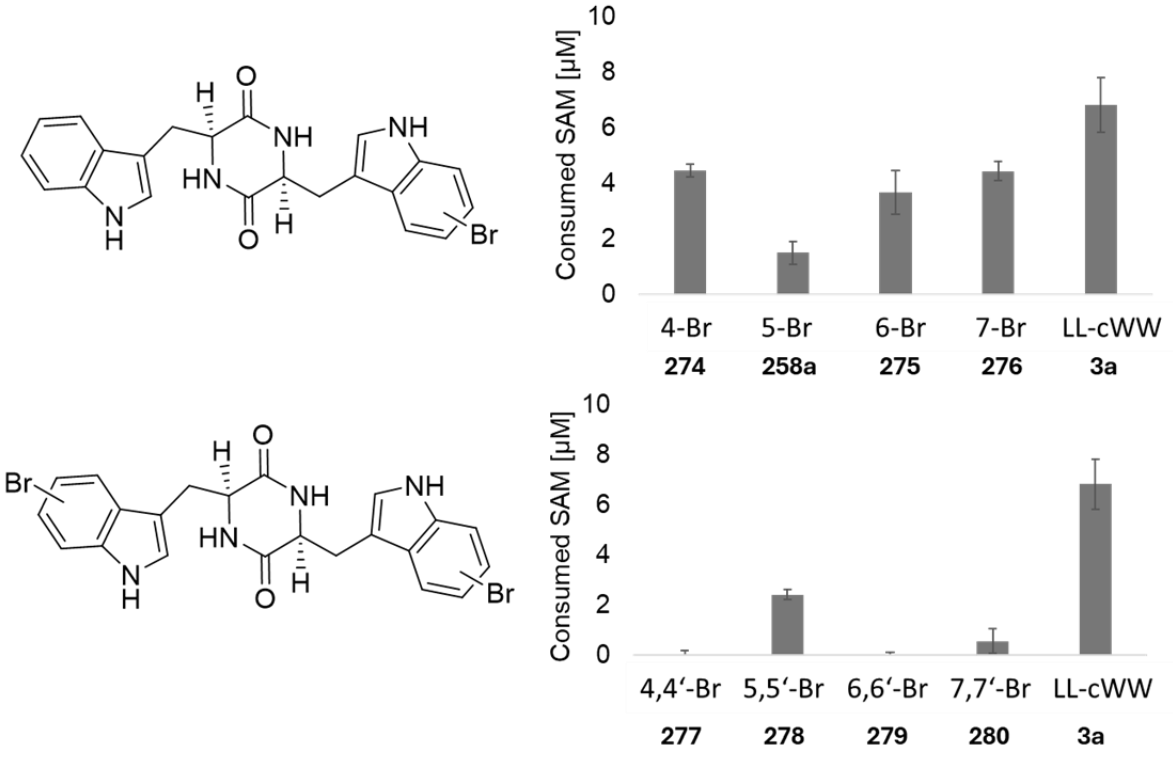

Figure 119: Activity of SgMT for the synthesised functionalised DKPs in comparison to the unsubstituted substrate measured with the MTase Glo Assay.

However, as the Glo Assay only measures SAM (**93**) consumption and does not differentiate between products, further analysis was required to determine the methylation status of the products. To complement the substrate acceptance analysis, additional small-scale reactions were performed with the corresponding brominated substrate, SAM (**93**) and SgMT lysate in KPi buffer (50 mM, pH 8) at 40 °C overnight.

These reactions were monitored at various time points via TLC, with plates analysed under UV light and stained using cerium molybdate stain. This staining solution is known to specifically colour HPIs, particularly those with an attached DKP in red. This characteristic was previously observed for both unsubstituted cWW **3a** and 5-Br cWW **258a** during the total synthesis of lansai B (**5**) and serves only an initial qualitative reaction control. This first analysis revealed that all single-halogenated substrates displayed conversion. For 6-Br cWW **275**, only a single product spot was visible, likely corresponding to the singly methylated product. In contrast, for 4-Br and 7-Br cWW **274** and **276**, an additional faint second spot appeared alongside the intense spot, suggesting a second methylation reaction. Among the double-halogenated substrates, only 5,5'-Br cWW **278** and 7,7'-Br cWW **280** were converted. The 5,5'-Br cWW **278** showed two product spots, while the 7,7'-Br cWW **280** displayed only one [Figure 120]. These findings align with the Glo Assay results, which also indicated conversion for these specific substrates.

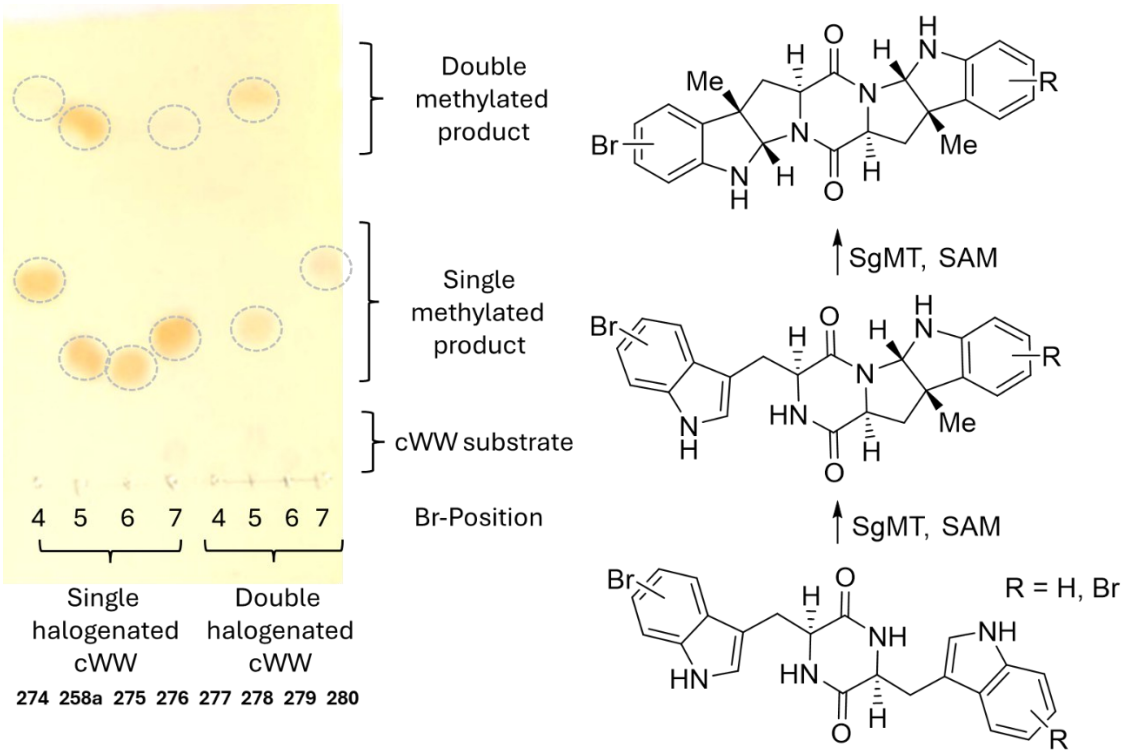

Figure 120: TLC (ethyl acetate as eluent) stained with cerium molybdate stain for detection of the HPI containing products. Small-scale reactions were performed with the corresponding brominated substrate, SAM (**93**) and SgMT lysate in KPi buffer (50 mM, pH 8) at 40°C overnight.

To verify whether the singly halogenated 4-Br and 7-Br cWW **274** and **276**, as well as the double-halogenated 5,5'-Br cWW **278**, underwent double methylation like indicated on the TLC, large-scale reactions were conducted under optimised conditions established for 5-Br cWW **258a** during the total synthesis of lansai B.

- For 4-Br cWW **274**, the reaction yielded 29% single methylated and 52% double methylated product **281** and **282** (100 mg scale).
- For 7-Br cWW **276**, the reaction predominantly resulted in the single methylated product **283**, with a yield of 73%, alongside a minor yield (3%) of the double methylated product **284** (100 mg scale).
- The reaction with 5,5'-Br cWW **278** was carried out on a 10 mg scale, yielding 54% single methylated and 25% double methylated products **285** and **286**.

These larger-scale reactions confirmed the formation of both single and double methylated products for certain substrates, highlighting SgMT's selective activity on halogenated cWW derivatives.

Given the lower conversion rates observed for the 4-, 6- and 7-Br cWW **274, 274** and **276** substrates towards the double methylated product compared to 5-Br cWW **258a**, a mutagenesis approach was implemented. The same mutant libraries targeting positions N125, W182, and F184 were utilised, following the strategy established for 5-Br cWW **258a**. After cultivation, the mutant containing cells were harvested, and reaction mixtures containing buffer, SAM (**93**) and the corresponding Br-cWW substrates were added. The mutant activity was measured using a colourimetric indole assay, as previously described. Automated library screening was carried out using the AutoBioTech platform in collaboration with Julia Tenhaef.

As with 5-Br cWW **258a**, the F184 mutant library yielded the most promising results. Sequencing of the top-performing mutants from the preliminary experiment revealed substitutions with nonpolar amino acids (alanine, valine, leucine), polar residues (cysteine, threonine), and an aromatic amino acid (tyrosine). These variants showed potential across all substrates tested, though specific activity levels varied [Table S 16, Table S 17, Table S 18]. Subsequently, these mutants were expressed, purified, and evaluated for activity with the brominated cWW substrates **274**-**276** using the Glo Assay, with wild-type activity set as the standard. Among the tested mutants, the leucine variant consistently demonstrated the highest activity. However, the activity of the leucine mutant was still comparable to that of the wild type, indicating limited improvement. To check if potentially more double methylated product was formed, the mutants were tested in small-scale reactions evaluated via TLC. However, these qualitative experiments revealed no improvement compared to the wild type [Figure S 24].

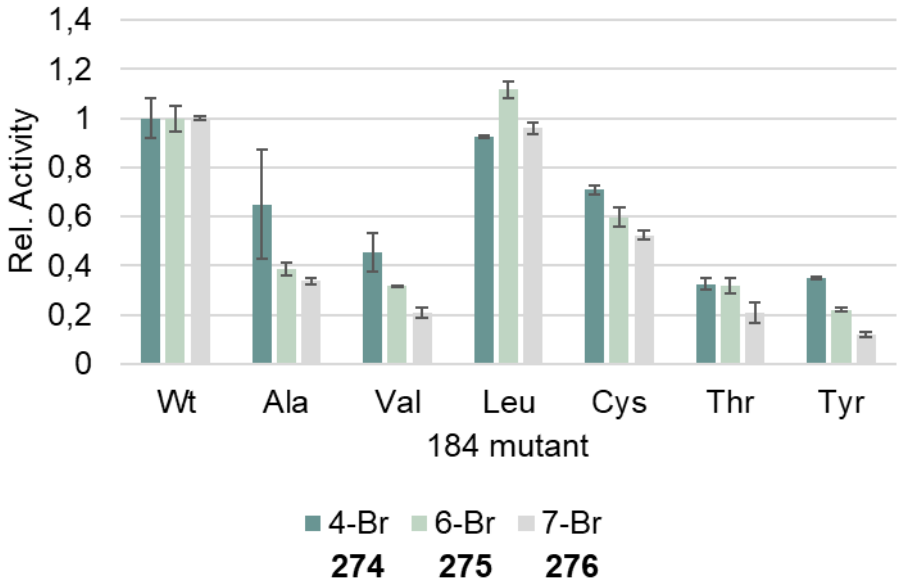

Figure 121: Activity of the mutants F184A, F184L, F184V, F184C, F184T, F184Y and the wild type for the functionalised Br-cWWs **274-276** measured with the MTase Glo Assay.

The W182 and N125 mutant libraries either displayed reduced activity or yielded similar results to the wild type [Table S 13, Table S 14, Table S 15, Table S 19, Table S 20, Table S 21]. In the N125 library, the best-performing hits consistently exhibited the N125S substitution across all substrates. This mutant was tested in small-scale reactions. However, these experiments revealed no improvement compared to the wild type, with even less double methylation observed [Figure S 25]. As a result, the N125S mutant was not isolated or subjected to further investigation.With the picked positions, the activity of the SgMT enzyme was not improved towards the brominated cWWs **274-276** trough mutagenesis.

This chapter presents an in-depth investigation of the methyltransferase SgMT. The enzyme's biochemical properties, including its optimal pH and temperature, were characterized, and its kinetic parameters were determined. The substrate scope was explored by testing various DKPs with amino acid variations and related compounds. Structural insights were gained through a detailed analysis of the enzyme's X-Ray structure, which revealed the presence of a catalytic triad and a tyrosine network. The catalytic importance of specific residues was confirmed via mutagenesis. Computational simulations provided additional understanding of substrate positioning within the active site and interactions with key catalytic residues.

SgMT was further utilized in the total synthesis of lansai B (**5**), where the enzyme-catalyzed C3-methylation formed the pyrroloindole motif. This key step is part of an eight-step synthesis starting from 5-bromoindole. The methylation reaction, performed with 5-Br cWW as the substrate, was optimized for efficiency. Additionally, the substrate range of SgMT was expanded by testing seven more halogenated DKPs, which could lead to lansai B derivatives.

To enhance activity towards these larger substrates, an iterative saturation mutagenesis strategy was employed. This process integrated a modular automated system for mutant library expression, enzymatic reactions, and activity screening, utilizing a robotic platform. However, no improved variants were obtained.

5.5 SeMT and SaMT

The MTases SeMT from *Saccharopolyspora erythraea* and SaMT from *Streptomyces albulus* were identified via a homology search based on StspM1. These enzymes share 56% and 98% sequence identity with StspM1, and 57% and 79% with SgMT. SeMT and SaMT have not yet been characterised, leaving their biosynthetic roles and natural substrates unknown. Especially, the gene encoding SeMT is not situated within the conventional gene cluster that includes a cyclic dipeptide synthase, PTase, and additional MTase like for SgMT, StspM1 and SaMT [Chapter 5.5]. This indicates that SeMT may be involved in a currently unidentified biosynthetic pathway.

The genes encoding SeMT and SaMT were synthesised and cloned into a pET28a(+) expression vector by GenScript with an *N*-terminal His-tag. Beatrix Paschold performed cloning experiments to additionally relocate the His-tag to the *C*-terminus.

5.5.1 Expression and initial testing of SaMT and SeMT

The genes of SaMT and SeMT, each featuring an *N*-terminal His-tag, were heterologously expressed in *Escherichia coli* BL21 (DE3) and purified using Ni-NTA resin. The molecular weights of SeMT and SaMT are calculated as 30.8 kDa and 28.5 kDa, respectively, with SaMT being shorter by 21 amino acids at the *N*-terminus. Elias Pfirmann conducted the purification as part of his bachelor's thesis, following the established protocol for StspM1 with an additional washing step using 40 mM ImH, which was beneficial in case of the purification of SgMT. SDS-PAGE analysis revealed a distinct band at approximately 30 kDa in the washing fraction W2 and the elution fraction [Figure 122]. The high purity of the eluted enzyme makes it suitable for protein crystallisation.

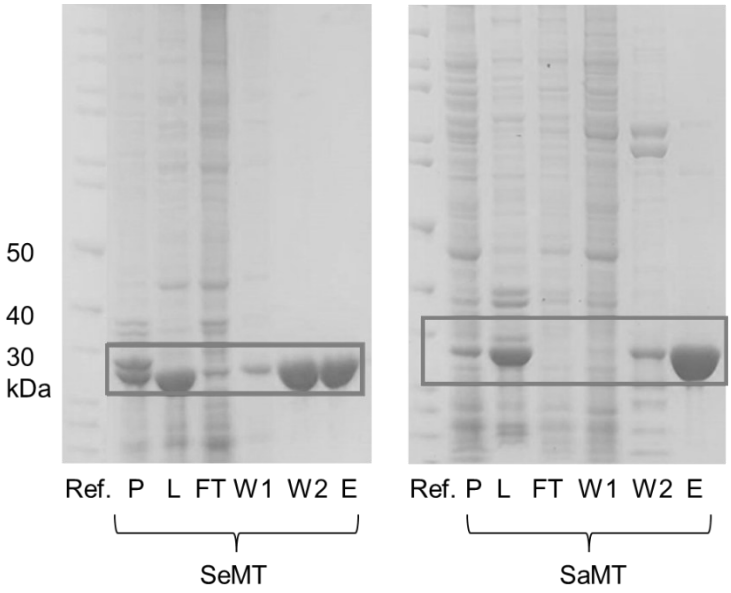

Figure 122: SDS-PAGE of the purification of *N*-terminal His-tagged SeMT and SaMT. Ref. = Unstained Protein Standard, P = pellet, Lys = lysate, FT = flow through, W = wash (40 mM or 80 mM ImH), E = elution (160 mM ImH). The band at 30 kDa is highlighted.

Enzymatic activity was measured using the MTase Glo Assay for LL-cWW **3a** and DD-cWW **3b** under the optimal conditions for SgMT. For comparison, the activity of SgMT was also assessed. SaMT exhibited no activity, while SeMT displayed residual activity [Figure 123].

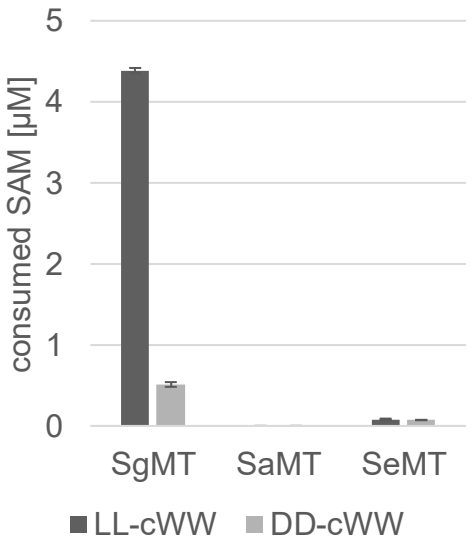

Figure 123: Activity of SaMT, SeMT and SgMT with the LL- and DD-cWW **3a** and **3b** substrates under optimised conditions for SgMT measured with the Glo Assay.

5.5.2 Restoring activity of SaMT

As demonstrated for SgMT, the *N*-terminal His-tag decreased enzyme activity. Therefore, the enzymes with a *C*-terminal His-tag were used in subsequent experiments. The SaMT with a *C*-terminal His-tag was expressed and purified on a small scale and tested under the same conditions as the *N*-terminal His-tagged version [Figure S 26]. However, the enzyme showed no activity towards the LL-cWW **3a** [Figure 125]. SaMT is highly similar to StspM1, with the primary difference being a truncated *N*-terminus, shorter by 21 amino acids. Among the missing 21 amino acids are the residues Y11 and Y18 of SgMT, which have already been shown to affect enzymatic activity when mutated. To determine whether this truncation was responsible for the inactivity, Beatrix Paschold cloned the missing segment from SgMT to the SaMT enzyme [Figure 124]. The elongated enzyme was then expressed and purified on a small scale for further testing [Figure S 26].

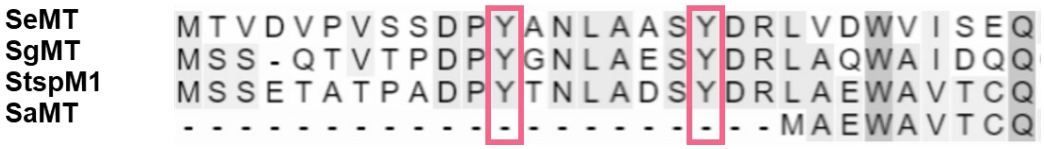

Figure 124: Comparison of the *N*-terminal sequences of SeMT, SgMT, StspM1 and SaMT with Y11 and Y18 highlighted in pink.

The elongated SaMT was tested for activity and displayed similar levels of activity in comparison to SgMT, successfully restoring its enzymatic function [Figure 125]. These experiments further highlight the critical role of the *N*-terminal amino acids in catalysis. Since the elongated enzyme does not exhibit enhanced activity compared to SgMT and its catalytic site is nearly identical to that of StspM1, no further investigation of this enzyme was pursued in this thesis.

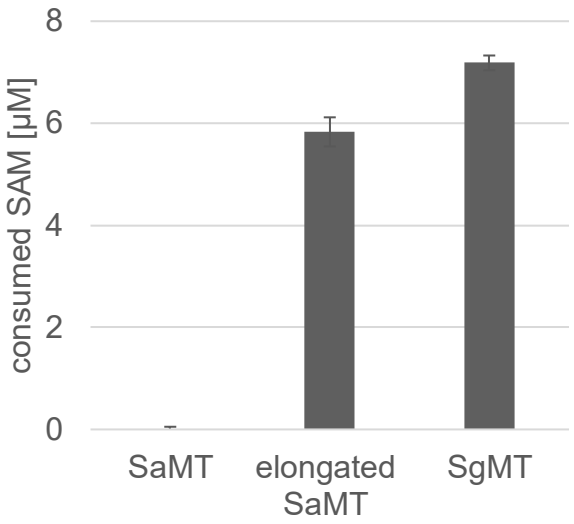

Figure 125: Activity of the truncated SaMT, the elongated SaMT and SgMT with the LL-cWW substrate **3a** under optimised conditions for SgMT measured with the Glo Assay.

5.5.3 Crystal structure of SeMT

The SeMT with a *C*-terminal His-tag was expressed and purified using Ni-NTA chromatography, adhering to the established protocol. Unlike the enzyme with a *N*-terminally His-tag, which predominantly eluted in the W2 washing step with 80 mM imidazole, the version with a *C*-terminal His-tag primarily eluted when the imidazole concentration was increased to 160 mM. This difference can be attributed to the position of the His-tag, with the *C*-terminal tag potentially being more accessible, allowing for stronger binding to the column. The purification yielded 7.13 mg of protein per gram of wet cells, which is 4.5 times higher than the yield for StspM1 but 5.5 times lower than that for SgMT.

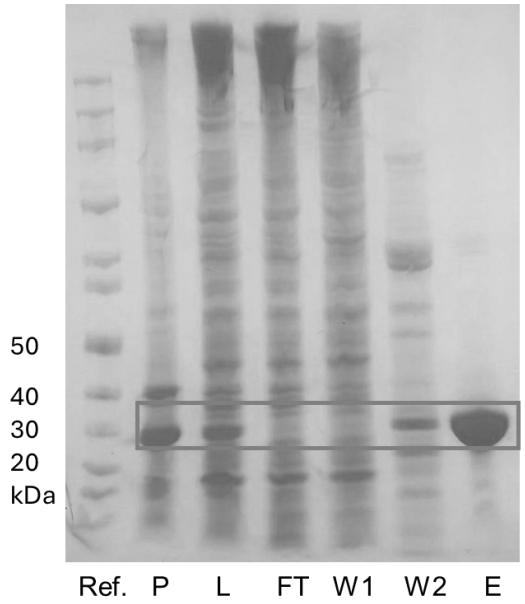

Figure 126: SDS-PAGE of the purification of C-terminal His-tagged SeMT. Ref. = Unstained Protein Standard, P = pellet, Lys = lysate, FT = flow through, W = wash (40 mM or 80 mM ImH), E = elution (160 mM ImH). The band at 30 kDa is highlighted.

The highly purified wild-type SeMT was crystallised with SAH (**94**) using the sitting-drop vapour diffusion method and standard commercial screening kits. Initial crystals were obtained from reservoir solutions containing either ammonium sulfate or a combination of lithium sulfate and ammonium sulfate in sodium citrate buffer (pH 5.6). These conditions were further optimised through matrix screening and the use of additives. The diffraction-quality crystals used for structural determination were grown in a solution of lithium sulfate, ammonium sulfate in sodium citrate buffer (pH 5.6), supplemented with 1,6-diaminohexane. SeMT crystallised in the orthorhombic space group C2221, with two protomer copies present in the asymmetric unit.

As predicted from the sequence similarity, SeMT displays a structural framework similar to the indole *C3*-methyltransferases SgMT and PsmD. Consistent with earlier observations for these enzymes, the dimeric form of SeMT is believed to represent its biologically relevant state. The proposed catalytic site is positioned at the interface between a Rossmann-type *α*/*β* domain and the *β* cap domain. The demethylated cofactor SAH (**94**) is bound within a pocket nearly identical to those observed in related enzymes. Key structural elements are preserved, including the distinctive tyrosine side chains (Y12, Y19, Y126) that shield the cofactor, and the catalytic histidine-acidic residue pair (H218, E216) believed to play a role in the methyl transfer process [Figure 127]. This high level of conservation in critical catalytic features strongly indicates that SeMT is an active enzyme, although its natural substrate remains unknown.

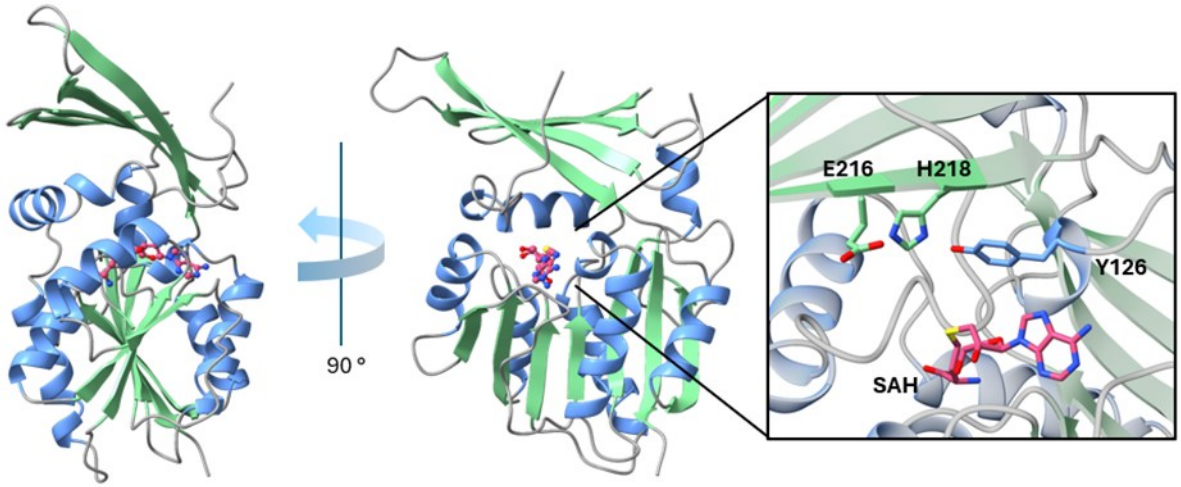

Figure 127: X-ray structure of SeMT with SAH (**94**, pink). The active site with the catalytic triade (E216, H218 and Y126) is highlighted.

5.5.4 Restoring activity of SeMT

Although the catalytic cavity of SeMT is comparable to that of SgMT in size (417 Å³ vs. 378 Å³, averaged across the A–B dimer) and shares general features like hydrophobic and aromatic regions, notable differences exist in the size and polarity of specific residues within the substrate-binding site. To determine whether these differences affect the enzyme's activity and substrate range, SeMT was tested with seven different DKP substrates, LL-configurated cWW **3a**, cWF **242a**, cWY **241a**, cWH **243a**, cWL **245**, cWV **244** and cWA **216**, using the Glo Assay under SgMT's optimal conditions. Among these, only the cWW substrate **3a** exhibited residual activity, which remained nearly 80 times lower than that of SgMT [Figure 128].

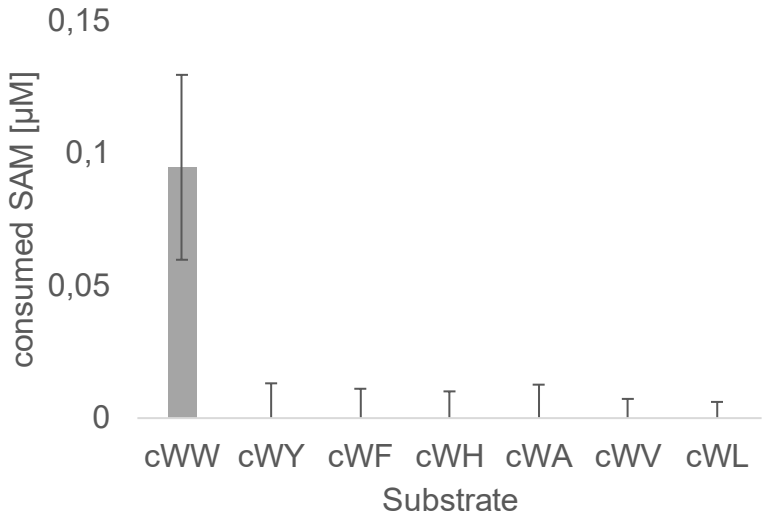

Figure 128: Activity of the SeMT with a C-terminal His-tag against the LL-configurated cWW **3a**, cWF **242a**, cWY **241a**, cWH **243a**, cWL **245**, cWV **244** and cWA **216** substrates under optimised conditions for SgMT measured with the Glo Assay.

A detailed comparison of the sequences and structures of SeMT, StspM1, and SgMT reveals several notable differences in their active sites: Nine specific residues, identified based on their homology in StspM1 and SgMT and proximity to the active site, were selected for mutational analysis [Figure S 27, Figure 129, Table 9]. The aim was to modify SeMT's active site to mimic SgMT's, potentially restoring activity. The key residues mainly surround the proposed cWW binding site, except for G131, which aligns with a glutamine in StspM1 and SgMT. G131 is located in the first turn of helix *α*D at the base of the cofactor binding cleft. Although it doesn't directly interact with SAM (**93**), its side chain likely influences the solvation around the cofactor's adenine group. The V23A and V26A mutations create additional space in the active site through steric adjustments. Similarly, V195M and H197Y affect steric factors while introducing additionally altered polar interactions. These four positions are located near the DKP ring, rather than the indole ring that is subject to methylation. In contrast, mutations T125N and N122G are closer to the methylation site. Residues Y154F and F220Y alter the orientation of the hydroxyl group within the active site. Notably, in StspM1, F220 corresponds to Y223, a residue critical for enzymatic activity as it may form a hydrogen bond with the indole nitrogen of the substrate. In SgMT, the homologous residue Y222 is proposed to align Y126, a key member of the catalytic triad.

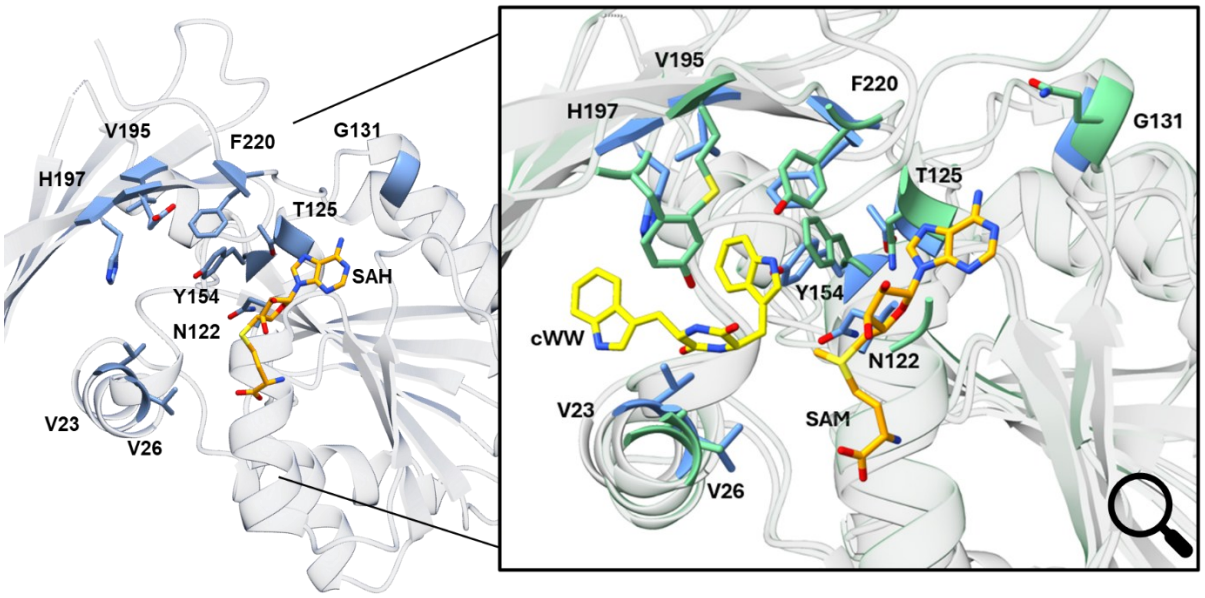

Figure 129: X-ray structure of SeMT with the nine mutation positions highlighted in blue. Zoomed picture: active side of SeMT (blue) and SgMT (green) containing the amino acid residues of the nine positions aligned. SAM/SAH (X-Ray) highlighted in orange, the cWW **3a** (docked position in SgMT) in yellow.

Table 9: Nine mutations to adjust the active site of SeMT towards SgMT/StspM1 and their potential function.

No	Mutation	Location / Function
1	**V23A**	Substrate cavity
2	**V26A**	Substrate cavity
3	**N122G**	Active site
4	**T125N**	Active site
5	**G131Q**	SAM binding site
6	**Y154F**	Tyrosine network / Active site
7	**V195M**	Substrate cavity
8	**H197Y**	Substrate cavity
9	**F220Y**	Tyrosine network / Active site

However, testing the resulting 9x mutant with the cWW substrate **3a** under standard conditions (Glo Assay, 45 °C, 15 min, 10 µM enzyme) did not yield any significant increase in activity. A key distinction in SeMT's catalytic triad is the presence of a glutamate residue where SgMT and StspM1 have an aspartate. While both amino acids share carboxylic acid functionality, the longer side chain of glutamate may affect enzymatic efficiency. Previous experiments have shown that mutating the aspartate in SgMT to glutamate significantly reduces activity. In the *C3*-MTase PsmD from *Streptomyces griseofuscus*, replacing its natural glutamate with aspartate caused a substantial activity drop.[99] Recognizing the significance of this residue, the glutamate in SeMT was substituted with aspartate as a tenth mutation. The resulting 10x mutant displayed activity 33 times higher than the wild-type enzyme [Figure 130].

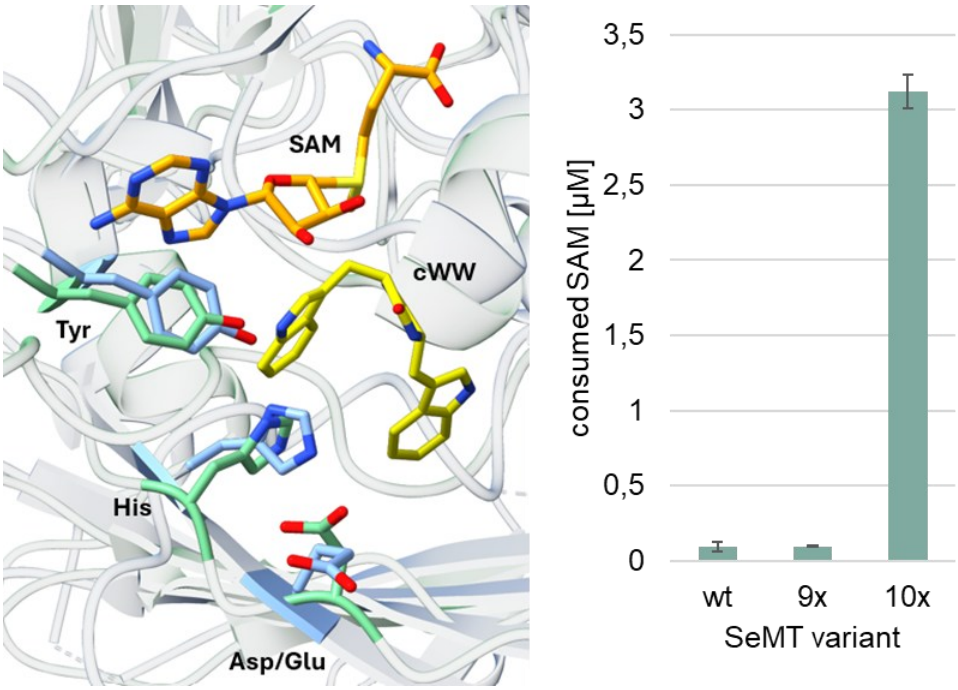

Figure 130: X-ray structure of the active side of SeMT (blue) and SgMT (green) containing the amino acid residues of the catalytic triade. SAM/SAH (X-Ray) is highlighted in orange, the cWW **3a** (docked position in SgMT) in yellow. The activity of the SeMT wt the 9x mutant and the 10x mutant with the additional E216D mutation was measured with the MTase Glo Assay for the cWW substrate **3a** under SgMT's optimal conditions.

The active 10x mutant of SeMT underwent further characterisation. The pH optimum was determined using HPLC, while substrate scope and temperature screening were assessed with the Glo Assay from Promega, using an enzyme concentration of 10 µM [Figure 131]. SeMT displayed a similar pH optimum to SgMT at pH 8, but had a distinctly different temperature optimum. The highest conversion for SeMT occurred at 25 °C, whereas SgMT and StspM1 exhibited optimal activity at 45 °C. Based on these results, subsequent experiments with SeMT were conducted under optimal conditions of pH 8 and 25 °C. The substrate acceptance profile of SeMT closely resembled that of SgMT and StspM1.

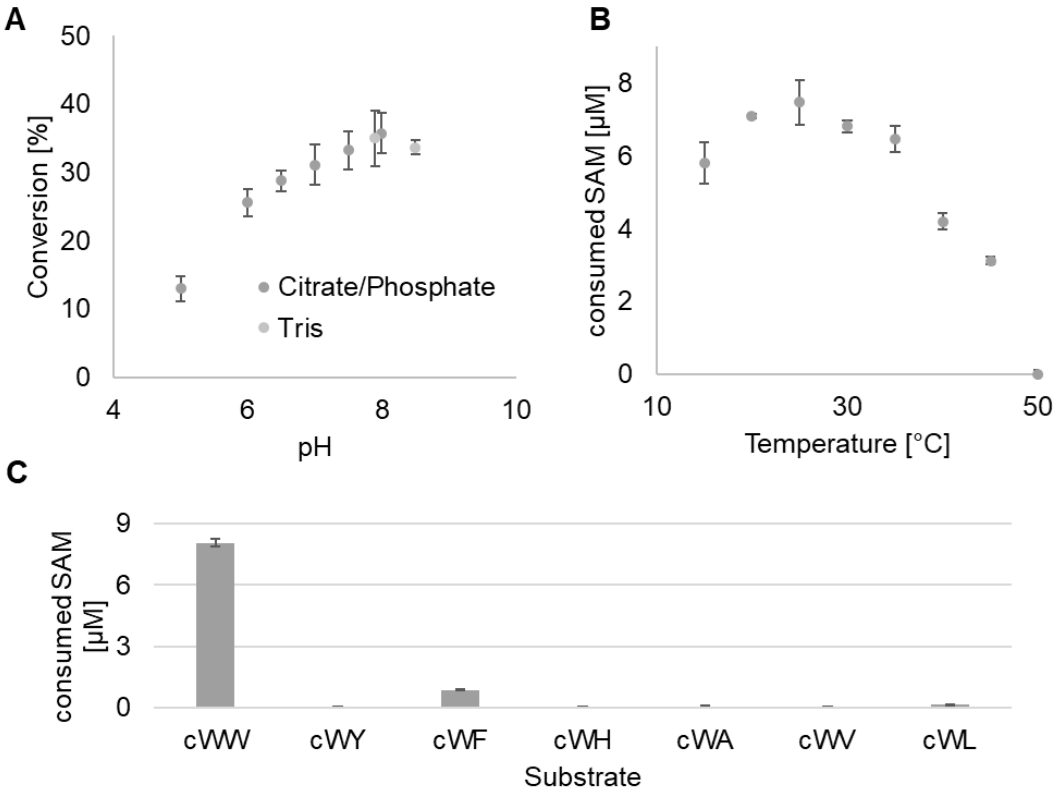

Figure 131: Biochemical characterisation of the SeMT 10x mutant. A: pH profile measured via HPLC. B: Temperature profile measured with the Glo Assay. C: substrate scope measured with the Glo Assay.

To investigate the significance of individual mutations within the 10x mutant, each mutation was reverted to its wild-type form one at a time. Due to their proximity, the V23+V26, N122+T125, and V195+H197 mutations were reverted in pairs, while other mutations were tested individually. These enzyme variants were expressed and purified in small scale [Figure S 28] Enzyme activity was measured using the Glo Assay with the cWW substrate **3a** at 25 °C and an enzyme concentration of 10 µM. Under these conditions, the wild-type enzyme exhibited negligible activity, while all mutants retained measurable activity [Figure 132]. Notably, the 9x mutant, which retained the wild-type glutamate in the catalytic triad, showed activity at 25 °C despite being inactive at 45 °C in earlier experiments.

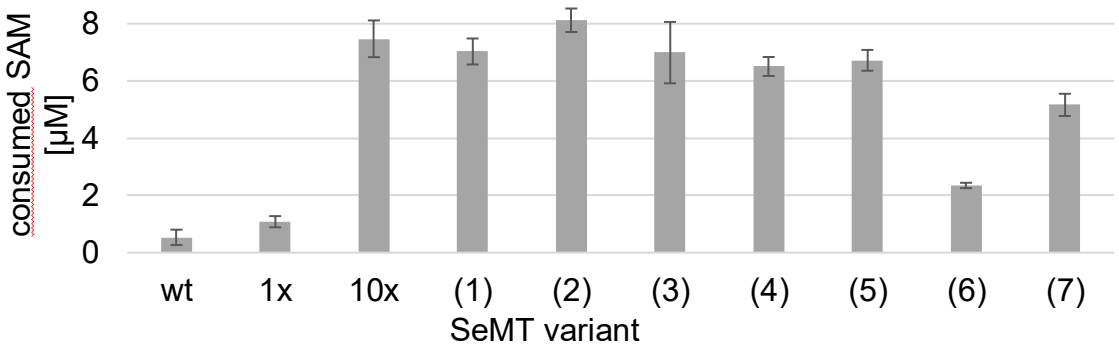

Figure 132: Activities of different SeMT variants measured with the Glo Assay using cWW as substrate. The 10x mutant contains all ten mutations from Table 9. The 1x mutant contains only the E216D mutation. The other variants are based on the 10x mutant, with the annotated mutations being reversed towards the wild type leading to 9x or 8x mutants. (1): V23A+V26A, (2): N122G+T125N, (3): G131Q, (4): Y154F, (5): V195M+V195Y, (6): E216D, (7): F220Y.

Both SeMT variants (9x and 10x mutant) exhibited a temperature optimum of 25 °C, while the overall activity of the 10x mutant is approximately three times higher. Additionally, a single mutant of SeMT with only the E216D substitution was generated and tested under the same conditions. However, this mutant showed minimal activity, emphasizing that the other nine mutations are critical for restoring SeMT activity toward the cWW substrate **3a**. In Addition to the investigations on SeMT, the wild-type SgMT (D218), and a SgMT mutant containing glutamate (E218) were tested at 3 µM enzyme concentration using the Glo Assay. For SgMT, the D218E substitution altered its temperature profile by shifting its optimum from 45 °C to 25 °C, but the overall activity decreased [Figure 133B].

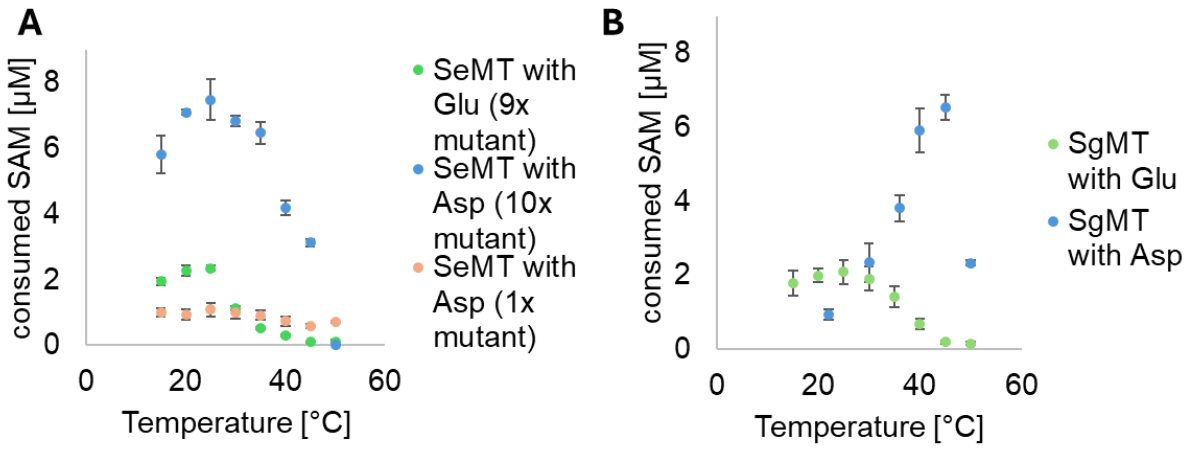

Figure 133: Temperature activity profiles of SeMT and SgMT measured with the Glo Assay. The SeMT enzyme concentration was set at 10 µM, the SgMT variants 3 µM. A. The 9x mutant (green) contains the nine mutations, the 10x mutant (blue) contains additionally the E216D mutation. The single mutant (orange) is based on the wild type with only the E216D mutation. B: SgMT wild type (blue) and a single mutant D218E (blue).

The crystal structures of PsmD, SgMT, and SeMT reveal insights into how D-E mutations affect the activity of these methyltransferases. In SeMT, the *N*-terminal extension of the Rossmann fold helps enclose the catalytic cavity. This segment includes a flexible "lid" that likely regulates access to the active site during catalysis. Unlike SgMT, SeMT's lid forms a 90-degree bend at S9, positioning the *N*-terminus towards the *β*-cap domain. This conformation, consistently observed in crystal structures, is stabilised by hydrophobic interactions and hydrogen bonds, notably involving E216, which bridges S8 and N14 [Figure 134]. In SgMT, the equivalent D218 lacks this stabilizing interaction with S8, leading to a more flexible *N*-terminus. These structural differences suggest that in SeMT, the stabilised lid limits access to the tested substrates, while the E216D mutation might loosen these restraints, enabling substrate entry. Conversely, in SgMT, introducing a glutamate (D218E) may stabilise the lid similarly to SeMT, restricting substrate access and reducing activity. As observed, the D218E mutation in SgMT shifts its temperature optimum, potentially due to differences in side chain flexibility between aspartic and glutamic acid, affecting enzyme dynamics and catalytic efficiency at higher temperatures.

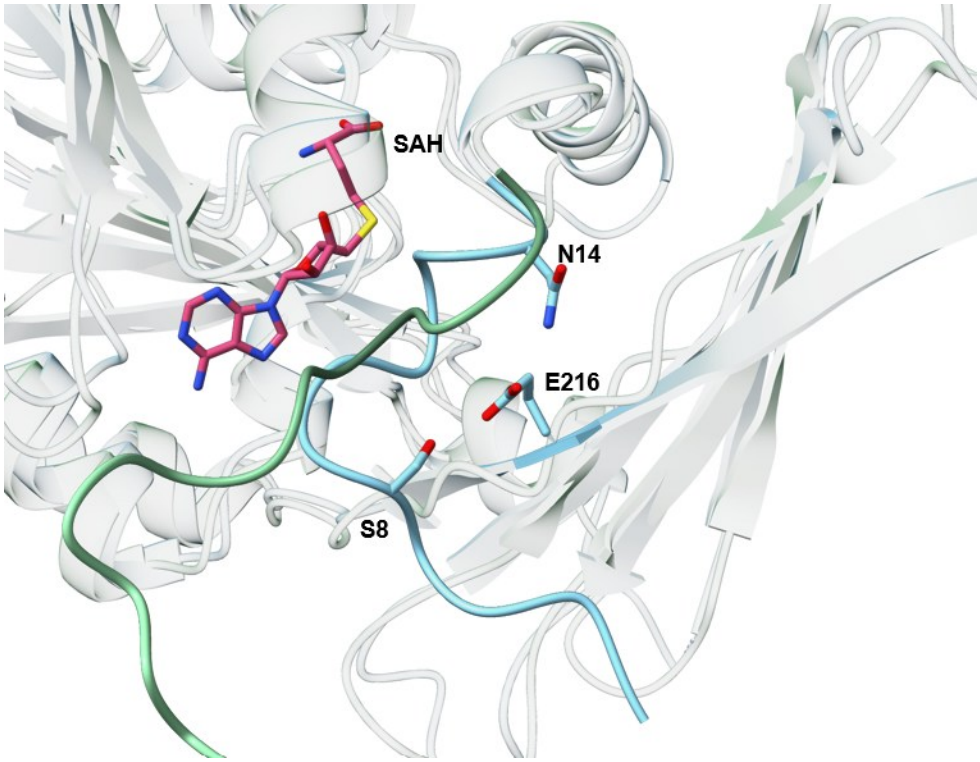

Figure 134: X-ray structure of SeMT (blue) and SgMT (green). SAH (**94**) is highlighted in dark pink. For SeMT, the residues E216, N14 an S8 are highlighted, which influence the positioning of the lid region.

Despite the restoration of SeMT activity through the introduction of ten mutations, its overall performance at 25 °C remains threefold lower than SgMT's activity at its optimal temperature of 45 °C. Notably, SgMT's MTase activity drops at temperatures below its optimum. Thus, the 10x mutant of SeMT and the D218E single mutant of SgMT could serve as promising catalysts for reactions requiring temperatures below 30 °C. This temperature-dependent activity profile suggests that these enzyme variants may offer unique advantages for applications in low-temperature biocatalysis, expanding the practical usability of MTases in temperature-sensitive reactions.

In this chapter, the methyltransferases SaMT and SeMT were investigated. Initial experiments revealed that SaMT exhibited no enzymatic activity, while SeMT demonstrated only residual activity towards the LL-cWW substrate.

The activity of SaMT was restored by extending its N-terminus with a segment from the SgMT sequence. The modified SaMT achieved a conversion rate comparable to StspM1 and SgMT but was not further studied due to the neglectable advantages expected in comparison to StspM1.

For SeMT, activity was restored through an intensive mutagenesis study. X-ray crystallography provided a three-dimensional structure of SeMT, offering valuable insights into its catalytic centre. Efforts to enhance SeMT activity included introducing nine mutations into its active site to resemble the active sites of SgMT and StspM1. However, the 9x mutant did not exhibit significant activity. A critical tenth mutation within the catalytic triad (E216D) was identified as essential for restoring enzymatic function. This new SeMT variant underwent further characterization, including determination of its optimal pH, temperature profile, and substrate scope. Additionally, the tenth mutation was found to influence the temperature activity profile of its structurally related homolog, SgMT.

5.6. NozB-CYIM

The MTase NozMT, originating from a gene cluster in *Nocardiopsis sp.* CMB-M0232, is known to catalyze both *C3* and *N*-methylation steps in the biosynthesis of nocardioazine B.[58, 87] Within the study published in 2015, a homolog of NozMT, referred to as NozB-CYIM, has been identified from *Nocardiopsis chromatogenes* YIM 90109 (WP_026123683).[87] This enzyme, however, remains uncharacterised and shares only 21% sequence identity with NozMT. Notably, its active site architecture differs significantly from the previously analysed MTase. The cap domain is composed of alpha helices that are arranged differently, resulting in a more open active site. Investigating this enzyme could potentially reveal variations in substrate specificity and broaden the understanding of its catalytic capabilities. The gene of NozB-CYIM was ordered by Pascal Schneider and cloned into a pET21a(+) expression vector with a *C*-terminal His-tag by Nadiia Pozhydaieva during her master thesis.

5.6.1 NozB-CYIM expression study

In her master's thesis, Nadiia Pozhydaieva reported challenges in obtaining the target protein in a pure form. While the protein was expressed in high quantities, the purification process yielded only minimal protein concentrations, as noted in her documentation. However, no optimisation was undertaken for this enzyme during her research.[319]

As an initial experiment in this study, the enzyme was produced in *E. coli* BL21 Gold (DE3) and purified using the protocol described in Pozhydaieva's thesis. The molecular weight of NozB-CYIM, including the *C*-terminal His-tag, was calculated to be 28.7 kDa. On SDS-Gel, a distinct band around 30 kDa was observed in the pellet fraction [Figure 135]. Since no corresponding protein band appeared in the lysate or subsequent fractions, it was concluded that the enzyme is insoluble under these conditions.

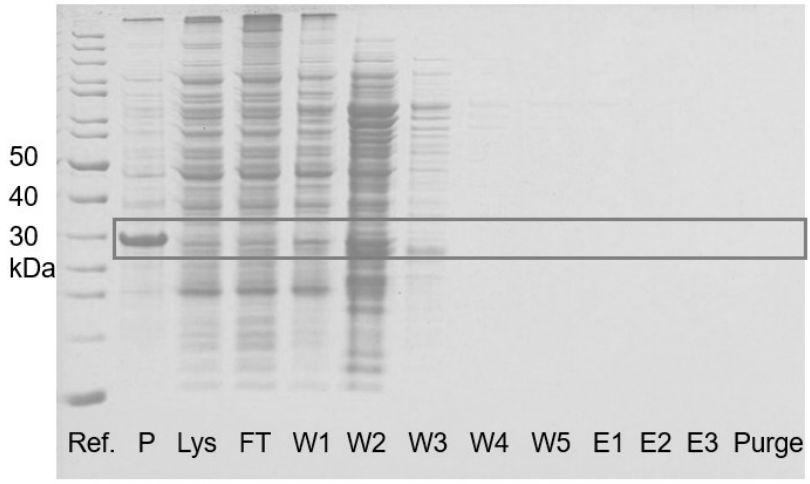

Figure 135: SDS-PAGE of the purification of NozB-CYIM according to the protocol of Nadiia Pozhydaieva. Ref. = Unstained Protein Standard, P = pellet, Lys = lysate, FT = flow through, W = wash (100 mM ImH), E = elution (250 mM ImH). The band at 30 kDa is highlighted.

To address the observed insolubility of NozB-CYIM under the initial expression conditions, an optimisation of expression parameters was conducted. Expression temperatures were varied to 15 °C, 20 °C, and 25 °C, while maintaining the IPTG induction concentration at 100 µM. Additionally, the effect of varying IPTG concentrations (50 µM and 100 µM) at a constant expression temperature of 20 °C was evaluated. Following cell lysis, the solubility of the expressed protein was assessed by analysing both the lysate (L) and pellet fractions (P) as well as the cells prior lysis (C) via SDS-PAGE. However, none of these modifications resulted in a measurable improvement in the solubility of NozB-CYIM as the lysate fractions remained without the band at 30 kDa [Figure 136].

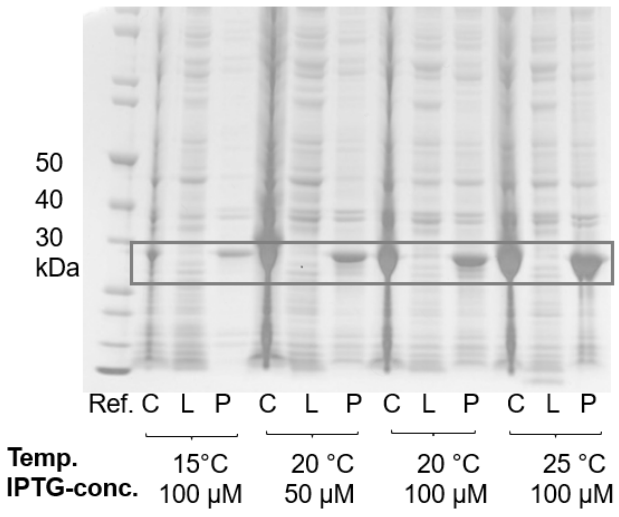

Figure 136: SDS-PAGE of the expression screening of NozB-CYIM. Ref. = Unstained Protein Standard, P = pellet, L = lysate, c = cells (160 mM ImH). The band at 30 kDa is highlighted.

Since the solubility of NozB-CYIM did not improve under the initial conditions, the *E. coli* Arctic Express strain was employed for further optimisation. This strain, derived from *E. coli* BL21-Gold, is equipped with chaperonins designed to enhance protein folding and solubility. For expression, the main culture was induced with IPTG at an OD_{600} of 0.5 following a 20-minute cold shock on ice. The culture was then incubated at 15 °C for two days. The enzyme was subsequently purified using Ni-NTA chromatography. SDS-PAGE analysis revealed an additional overexpressed band at ~60 kDa, corresponding to the Cpn60 chaperonin protein expressed by the Arctic Express strain (molecular weight ~57 kDa). While partial solubility of NozB-CYIM was achieved under these conditions, the enzyme could not be isolated effectively due to co-elution with Cpn60 during the purification process [Figure 137].

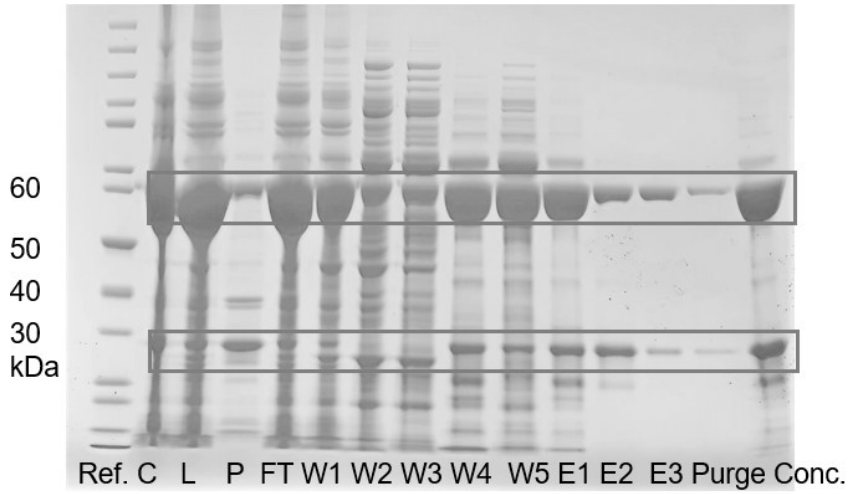

Figure 137: SDS-PAGE of the purification of NozB-CYIM from E.coli arctic express according to the protocol of Nadiia Pozhydaieva. Ref. = Unstained Protein Standard, P = pellet, Lys = lysate, FT = flow through, W = wash (100 mM ImH), E = elution (250 mM ImH). The band at 30 kDa and 60 kDa are highlighted.

The concentrated protein fraction was evaluated for its enzymatic activity in a conversion test using the LL-cWW substrate **3a**. A total of 50 µg of protein was tested under the same standard in-vitro assay conditions. However, no substrate conversion was detected with the HPLC. Additionally, whole-cell experiments were conducted using *E. coli* BL21 Gold and *E. coli* Arctic Express cells (200 mg wet cells per 1 mL reaction solution) as well as the lysates (25 Vol%) and cell pellets (25% w/v) after cell lysis. Still, no conversion of the substrate was observed in any of the experiments.

5.6.2 Homologues of NozB-CYIM: ThMT and MtMT

Due to the insolubility of NozB-CYIM, two homologous enzymes were selected for a further investigation: ThMT from *Thermobifida halotolerans* and MtMT from *Marinactinospora thermotolerans*. These homologs share over 80% sequence identity with NozB-CYIM and an 85.19% sequence identity between each other.

The genes encoding ThMT and MtMT were synthesised with an *N*-terminal His-tag and cloned into the pET28a(+) plasmid by GenScript. Transformation of the plasmids into *E. coli* BL21(DE3) Gold was achieved using the heat-shock method. The enzymes were expressed under standard conditions, and cell disruption was performed via ultrasonic lysis. SDS-PAGE analysis confirmed that both MtMT and ThMT were expressed as soluble proteins, in contrast to the insoluble behaviour of their homolog NozB-CYIM. Further analysis of these enzymes was conducted by Elias Pfirmann as part of his bachelor's thesis. The MTases were purified using Ni-NTA affinity chromatography. Despite the protein loss in the pellet fraction, attributed to inefficient cell lysis, relatively pure protein was successfully isolated from the lysate [Figure 138].

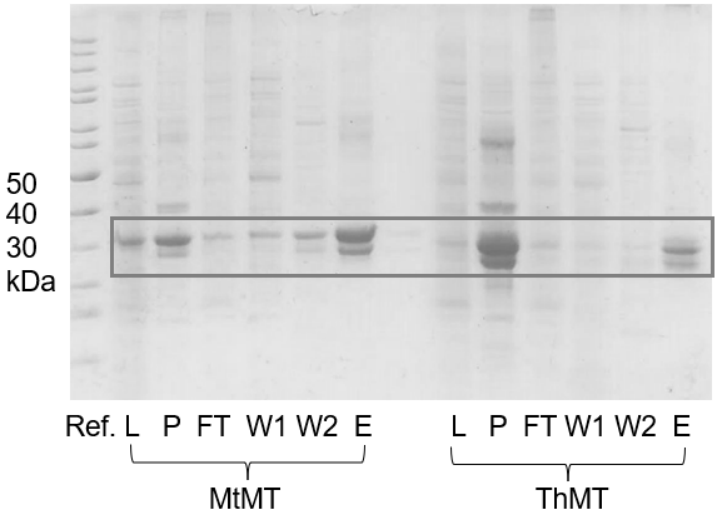

Figure 138: SDS-PAGE of the purification of *N*-terminal His-tagged MtMT and ThMT. Ref. = Unstained Protein Standard, P = pellet, Lys = lysate, FT = flow through, W = wash (40 mM or 80 mM ImH), E = elution (160 mM ImH). The band at 30 kDa is highlighted.

The semi-purified MtMT and ThMT were evaluated for their activity using LL-cWW **3a** and DD-cWW **3b** by Elias Pfirmann. The MTase Glo Assay from Promega was employed, with enzyme concentrations maintained at 40 µM and substrate **3** and SAM (**93**) concentrations at 25 µM. Reactions were conducted at 45 °C. Both enzymes exhibited comparably low activity towards the tested substrates [Figure 139].

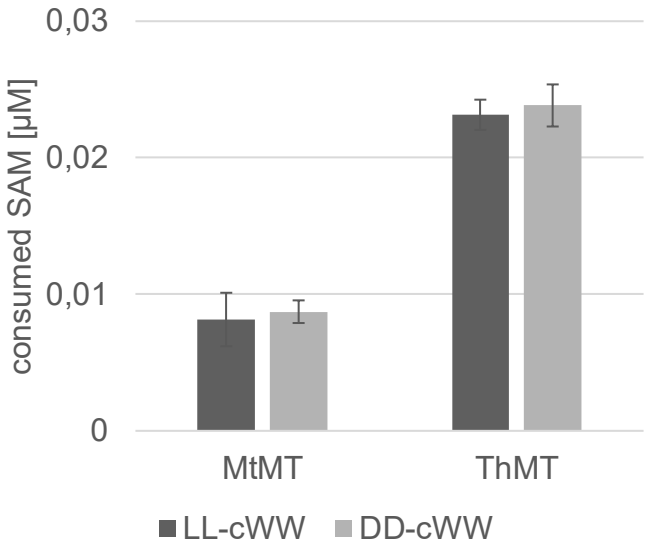

Figure 139: Activity of MtMT and ThMT with four different substrates measured by the Glo Assay.

In conclusion, the MTases ThMT and MtMT, unlike the insoluble NozB-CYIM, demonstrated solubility under the tested conditions. However, their activity with the tested substrates was extremely low. Given that their active sites differ significantly from those of previously characterised MTases, a broader substrate screening is necessary and could be complemented by docking studies for further insights. Additionally, the reaction conditions have not yet been optimised.

Since both enzymes originate from extremophilic organisms—ThMT from *Thermobifida halotolerans* and MtMT from *Marinactinospora thermotolerans*—reaction conditions may have a significant impact on their activity. *Thermobifida halotolerans* was isolated from a salt mine sample in Yunnan Province, while *Marinactinospora thermotolerans* was sourced from deep-sea marine sediment in the South China Sea.[332, 333] These origins suggest that higher salt concentrations or altered temperatures could enhance enzyme activity. Numerous examples of enzymes derived from these organisms highlight their notable salt tolerance and thermostability.[334-337]

NozB-CYIM is a homolog of NozMT, involved in the biosynthesis of nocardioazine B. Initial expression of NozB-CYIM in *E. coli* BL21 Gold (DE3) resulted in insoluble protein. Despite optimization efforts, including varying expression temperatures and IPTG concentrations, no improvement in solubility was observed. Switching to the *E. coli* Arctic Express strain allowed partial solubility, but the enzyme co-eluted with the Cpn60 chaperonin during purification, hindering isolation. Activity assays using LL-cWW substrate showed no conversion. To explore alternative enzymes, two homologs—ThMT from *Thermobifida halotolerans* and MtMT from *Marinactinospora thermotolerans*—were expressed. These enzymes, with over 80% sequence identity to NozB-CYIM, were soluble and purified successfully. Activity assays only showed residual activity for both ThMT and MtMT with various substrates. Further optimization is needed to enhance activity and explore the substrate specificity.

5.7. Studies towards the biosynthesis of lansai B like natural products

Lansai B (**5**) and nocardioazine B (**7**) both contain a seven-ring system, characterised by a central DKP core flanked by HPI motifs on either side. Despite their structural similarities, these compounds differ significantly in absolute and relative configuration as well as methylation and prenylation patterns. Nevertheless, the biosynthesis of both molecules likely involves the same class of enzymes. In 2023, the biosynthetic pathway of nocardioazine B (**7**) was investigated, revealing the gene cluster and characterizing the enzymes involved: A CDPS nozA or ncdA, an isomerase NozR, a PTase NozPT and a bifunctional MTase NozMT [Figure 18, Figure 140].[58]

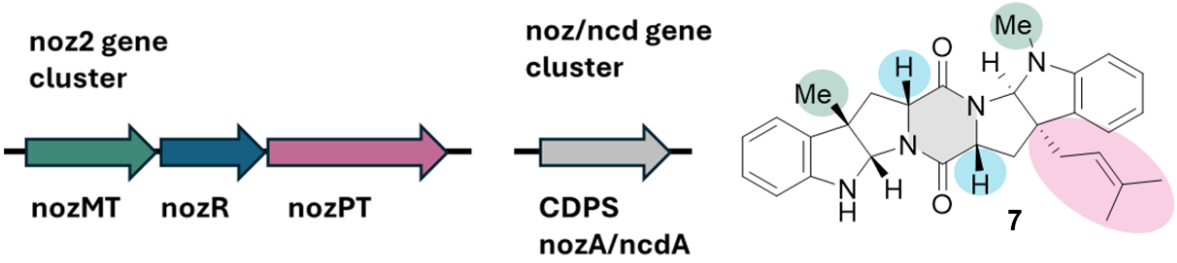

Figure 140: Gene cluster of nocardioazine B (**7**). The MTase is associated with green, the PTase with pink, the isomerase with blue and the CDPS with grey. The structural elements created by these enzymes are highlighted in the corresponding colour in the molecule.

As outlined earlier, the MTases StspM1 and SgMT catalyze methylation at the *C3*-position of the cWW substrate **3a**, a key step in the biosynthesis of lansai B-like natural products. StspM1 is involved in a gene cluster, which has been described previously.[235] This gene cluster involves next to StspM1 (green) a CDPS (grey), a PTase (pink) and another MTase (green), which functions are unknown, yet. SgMT, identified through homology with StspM1, is associated with a similar gene cluster containing the same enzyme classes but arranged in a different sequence [Figure 141]. Notably, no isomerase analogous to NozR were detected in either gene cluster or throughout the genomes of the producing organisms.

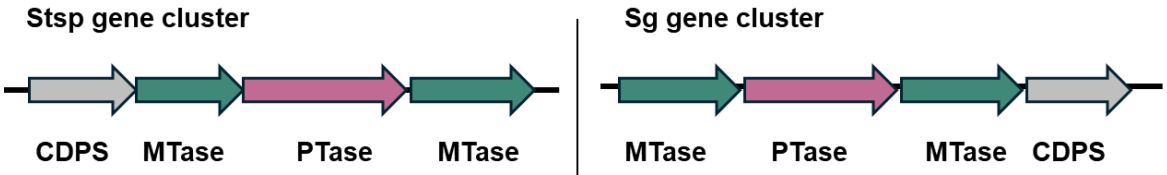

Enzyme	Gene bank entry
CDPS	EPD89497.1
StspM1	EPD89498.1
StspPT	EPD89499.1
StspM2	EPD89500.1

Enzyme	Gene bank entry
MTase	GGT26780.1
PTase	GGT26785.1
MTase	GGT26788.1
CDPS	GGT26792.1

Figure 141: Gene clusters in *Streptomyces sp.* HPH0547 and *Streptomyces griseoviridis*, which could be involved in the formation of lansai B like natural products.

The enzymes within the Stsp and Sg gene clusters could, in principle, facilitate the formation of a natural product like lansai B. The CDPS (grey) could generate the DKP motif from l-tryptophanyl-tRNA 82. This intermediate could then undergo methylation by the *C3*-MTase (StspM1 or SgMT), leading to the formation of HPI motifs. An additional MTase is required for N-methylation, and the PTase could catalyze the prenylation at the *C5* position of one of the two HPI motifs (indicated in pink) [Figure 142].

In this chapter, the CDPS, the second MTase, and the PTase from the Sg and Stsp gene clusters are examined in detail to deduce the natural product linked to these gene clusters. Finally, *Streptomyces griseoviridis* was cultivated, and the resulting extracts were analysed for the presence of lansai B and its potential biosynthetic intermediates.

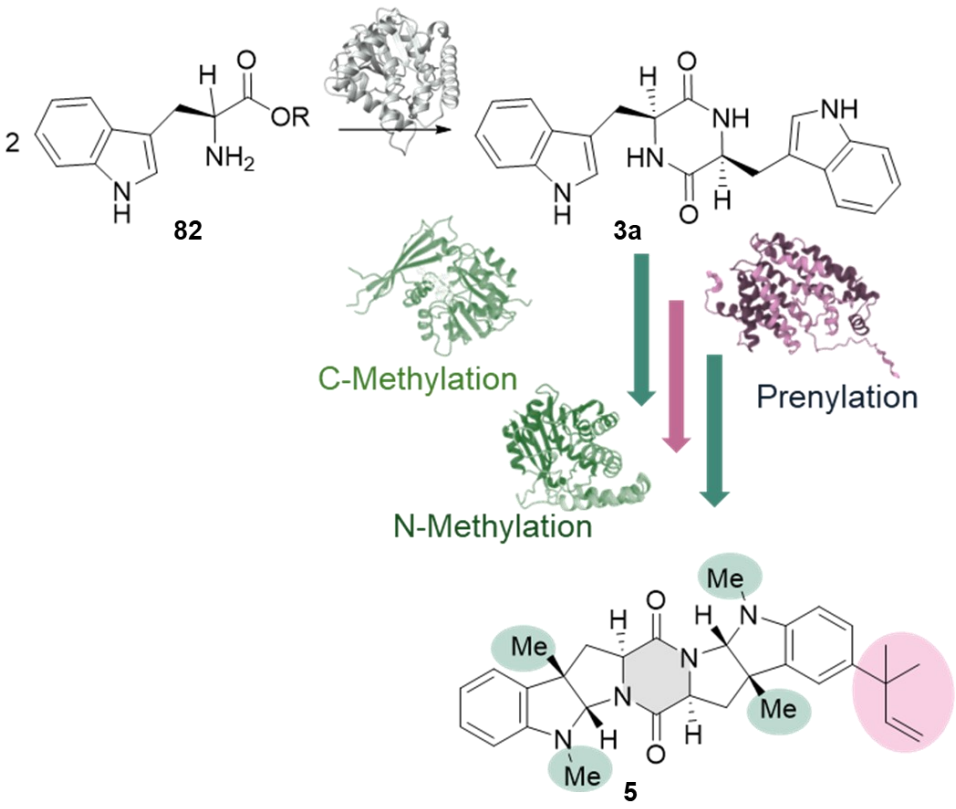

Figure 142: Potential biosynthesis of lansai B: An enzyme forms the cWW DKP **3a** as initial step. A *C3*-MTase, an *N*-MTase and a PTase are involved to modify the cWW **3a** towards lansai B (**5**).

5.7.1 Cyclodipeptide synthase

The gene clusters containing the *C3*-MTases SgMT and StspM1 include a gene coding for a CDPS. CDPS enzymes are relatively small (around 30 kDa) and catalyze the formation of the DKP core using tRNA-bound amino acids as substrates. The first CDPS identified was AlbC, and its amino acid sequence serves as a reference for numbering in sequence alignments with other CDPS enzymes as in this thesis.[149]

The sequences of SgCDPS (GenBank: GGT26792.1) and StspCDPS (GenBank: EPD89497.1) were compared with that of AlbC (GenBank: AAN07909.1). The StspCDPS gene is truncated at the *N*-terminus as the annotated protein lacks the first 61 amino acids compared to AlbC. This truncated part includes the critical catalytic residue Ser37 (AlbC), where the substrate binds to the enzyme. Analysis of the surrounding genomic region suggests that the start codon may be incorrectly annotated in the GenBank entry, and the correct start codon aligns with position 19 relative to AlbC. Both SgCDPS and the non-truncated StspCDPS contain the key catalytic residues Ser37 and Tyr202. CDPS enzymes are categorised into two subfamilies, 'NYH' and 'XYP,' based on the 'X40, Y202, X203' sequence motif.[151] Both SgCDPS and StspCDPS belong to the more common NYH subfamily as they contain the specific asparagine, tyrosine and histidine. StspCDPS (not truncated) and SgCDPS share 67.6% sequence identity with each other, and 29.9% and 26.9% identity with AlbC, respectively.

The structures of SgCDPS and the non-truncated StspCDPS were modelled using Robetta fold. Like AlbC, these CDPS enzymes exhibit a compact *α*/*β* fold, with a central *β*-sheet consisting of five parallel *β* strands flanked by *α* helices. Both structures feature a Rossmann-fold domain followed by a helical region composed of three helices. SgCDPS differs from AlbC by having two additional *β* strands at its *N*-terminus, extending the central *β*-sheet. Notably, the crystal structure of AlbC starts at Asp10, therefore the amino acids preceding this position are undefined. The *C*-terminus of SgCDPS is elongated compared to AlbC with nine extra amino acids. StspCDPS (not truncated) begins at residue 18 compared to AlbC, just before the start of the central *β*-sheet, and has a significantly elongated *C*-terminus by 50 amino acids [Figure 143]. The estimated structural errors in Ångström for both models are low for the first 210 amino acids, the highest error rates occur at the *C*-termini [Figure S 30]. This region, starting immediately after the Rossmann-fold, is not part of the conserved structure observed in the AlbC crystal structure.

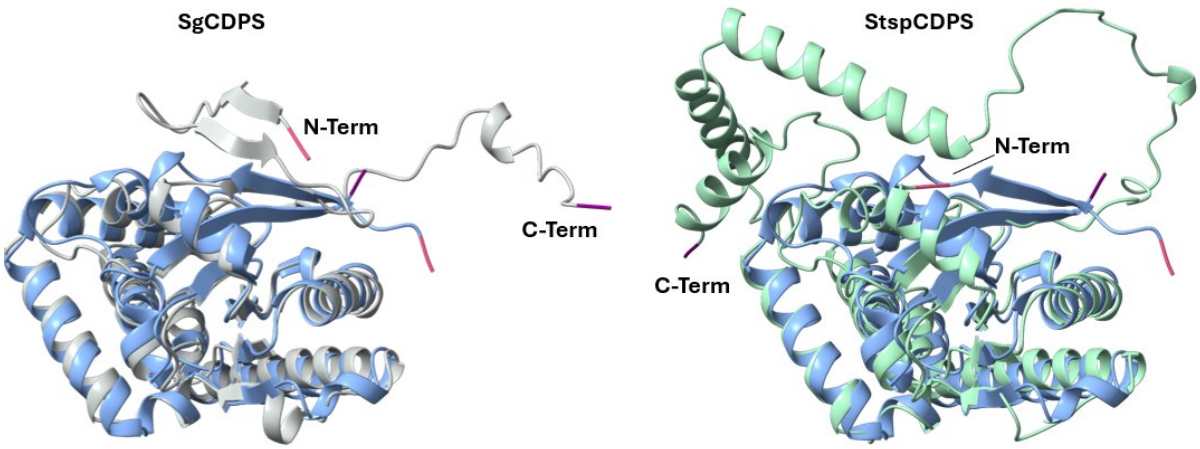

Figure 143: Comparison of AlbC (blue) and SgCDPS (grey, left) and StspCDPS (green, right). The C-termini are marked in violet, the *N*-termini in pink.

The two aminoacyl-tRNAs bind to distinct pockets within the CDPS enzyme, allowing predictions about the potential DKP product based on specific residues. Pocket P1 is defined by eight key residues (33, 35, 65, 67, 119, 185, 186, 200), while pocket P2 is composed of seven residues (152, 155, 156, 159, 204, 206, 207).[151, 152] SgCDPS is annotated as a cyclo(L-leucyl-L-leucyl) synthase in the gene data bank but given that the *C3*-MTase SgMT from the same gene cluster methylates at an indole *C3*-position, it is suspected that SgCDPS produces a tryptophane containing DKP. The specific residues of the two binding pockets P1 and P2 for recognition of the aminoacyl-tRNAs were extracted of the protein sequence of SgCDPS and StspCDPS. These consensus sequences were compared with the consensus sequences of analysed and characterised CDPS [Figure 144]. In 2018, Gondry et al. extended the number of experimentally characterised CDPSs to about 100, improving the predictive model of CDPS specificity.[152] This data served as base for the consensus sequence comparison. SgCDPS and StspCDPS share highly similar consensus sequences, with only two differences out of 15 residues: position 65 in P1 (V/I) and position 155 in P2 (V/T).

StspCDPS aligns with the known cWW-producing CDPSs, while the valine at position 155 of SgCDPS was not previously linked to cWW formation. However, position 155 is considered degenerate and not critical for tryptophanyl-tRNA **82** recognition. This conclusion is reinforced by the fact that the CDPSs involved in the nocardioazine B (**7**) pathway (NozA and NcdA) also possess a serine at this position, another residue not common among known cWW-accepting CDPSs. Comparisons with cLL-accepting CDPSs reveal significant differences in their consensus sequences compared to SgCDPS. Although SgCDPS is annotated as a cyclo(L-leucyl-L-leucyl) synthase, the sequence analysis suggests that this annotation is incorrect, and SgCDPS likely belongs to the class of cWW-forming CDPSs.

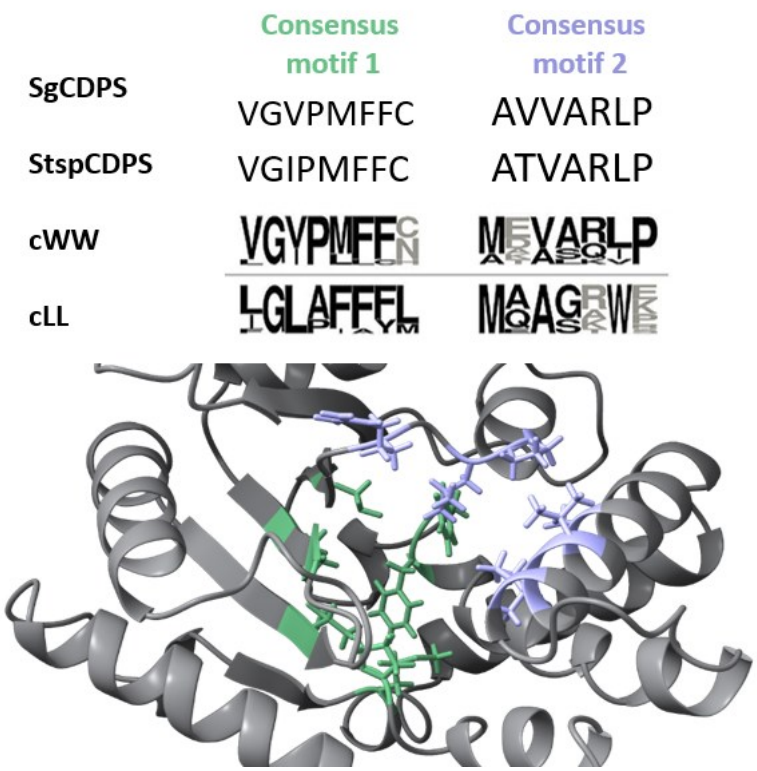

Figure 144: Consensus sequences of SgCDPS and StspCDPS compared with consensus sequences of cWW **3** and cLL accepting CDPS (degenerated positions are highlighted in grey). Structure of SgCDPS with consensus motif 1 in green and consensus motif 2 in violet.

5.7.2 *N*-Methyltransferase

Both gene clusters contain another gene encoding a MTase in addition to the *C3*-MTases. The functions of SgMT2 (GenBank: GGT26780.1) and StspM2 (GenBank: EPD89500.1) have not been described in the literature. SgMT2 and StspM2 share a 79.2% sequence identity with each other but only 24.3% and 27.0% identity with their respective *C3*-MTases, SgMT and StspM1. The structures of both enzymes were modelled using RobettaFold. The estimated error in Ångström is relatively low, except for the *N*-terminus and two loop regions around residues 145 and 185. Structurally, both enzymes exhibit a similar Rossmann-fold, consisting of seven *β*-strands interspersed with *α*-helices, with the final *β*-strand oriented antiparallel to the other six [Figure 145]. This core domain is similar to that of the *C3*-MTases SgMT and StspM1.

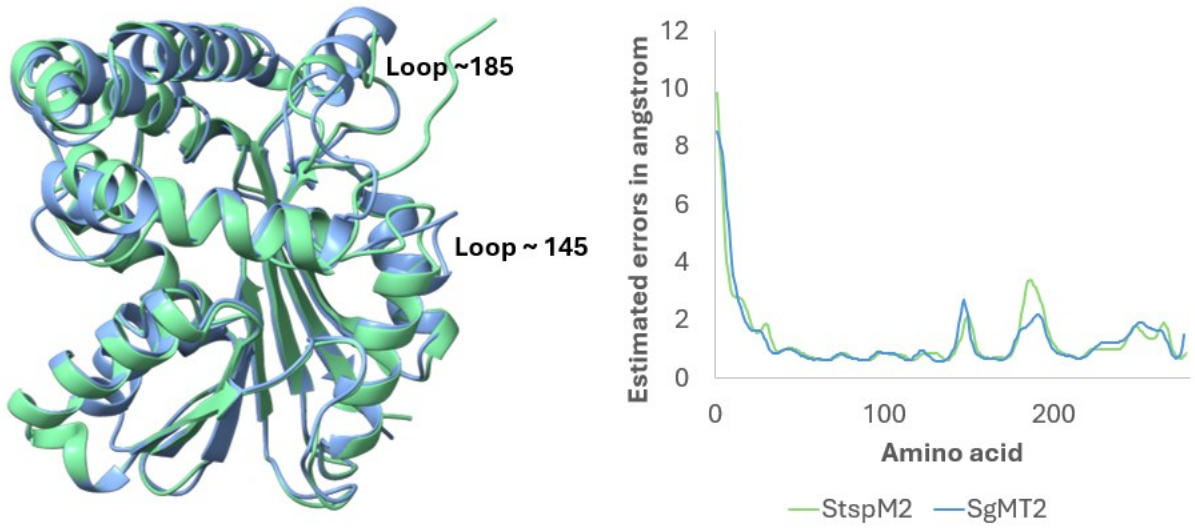

Figure 145: Modelled structures of StspM2 (green) and SgMT2 (blue). Estimated errors in Ångström for each residue in the structural models of StspM2 and SgMT2.

The main difference between these MTases and the *C3*-MTases is the cap-domain: in SgMT2 and StspM2, the cap-domain is composed of three *α*-helices, while in SgMT and StspM1, it is formed by four antiparallel *β*-strands. This *α*-helix cap is positioned in the same area as the *β*-cap [Figure 146]. The *α*-helix cap of the MTases NozB-CYIM and its homologs ThMT and MtMT is differently positioned and therefore not directly comparable.

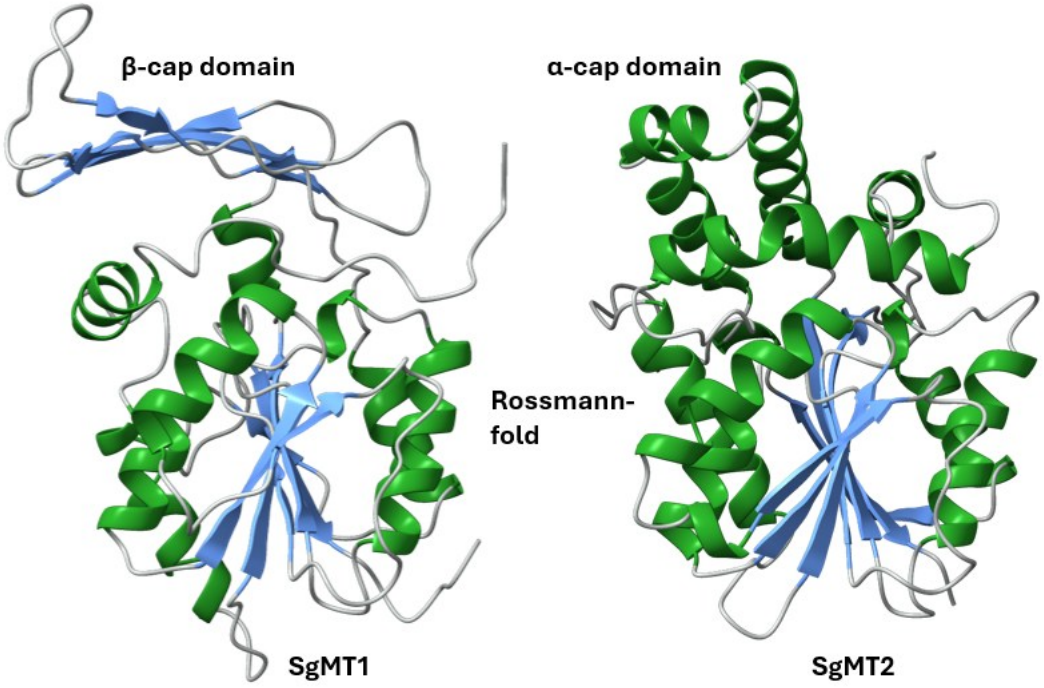

Figure 146: Crystal structure of SgMT (left) and modelled structure of SgMT2 (right). Helices are marked in green, β-strands in blue.

In MTases, the cofactor SAM (**93**) is typically bound along the *C*-terminal end of the core *β*-sheet through a network of hydrogen bonds and van der Waals interactions. To identify potential MTases bioinformatically, the SAM-binding motif is analysed. This motif, characterised by the sequence [(V/I/L) (L/V) D/E (V/I) G (G/C) G (T/P) G] interacts with the carboxypropyl group of SAM (**93**). Both StspM2 and SgMT2 contain this SAM-binding motif, indicating their likely role as MTases [Figure 147].

MOTIF1	V/I/L	L/V	D/E	V/I	G	G/C	G	T/P	G
STSPM2	L	L	D	I	G	C	G	A	G
SGMT2	L	L	D	I	G	C	G	T	G

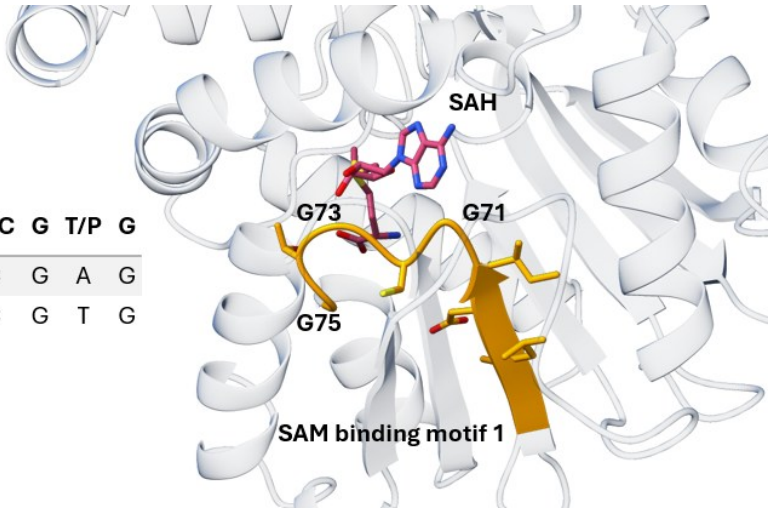

Figure 147: Comparison of StspM2 and SgMT2 regarding the SAM binding motif. The SAM binding motif is highlighted in the structure of StspM2 (orange). SAH (**94**, extracted from the crystal structure of SgMT) is marked in pink.

To investigate their precise function, the genes encoding StspM2 and SgM2 were cloned with a *C*-terminal His-Tag into a pET28a(+) plasmid by GenScript. *E. coli* BL21(DE3) Gold was transformed with these plasmids using a heat-shock method. Both enzymes were produced under standard conditions and purified using a Ni-NTA column following the protocol established for StspM1. StspM2 and SgMT2 each have an approximate molecular weight of ~29.5 kDa. SDS-PAGE analysis revealed that StspM2 was expressed at a higher level than SgMT2. However, the prominent band observed in the pellet fraction for StspM2 suggests that a significant portion of the protein is insoluble. Both proteins eluted at an imidazole concentration of 250 mM but in low amounts and not completely pure [Figure 148].

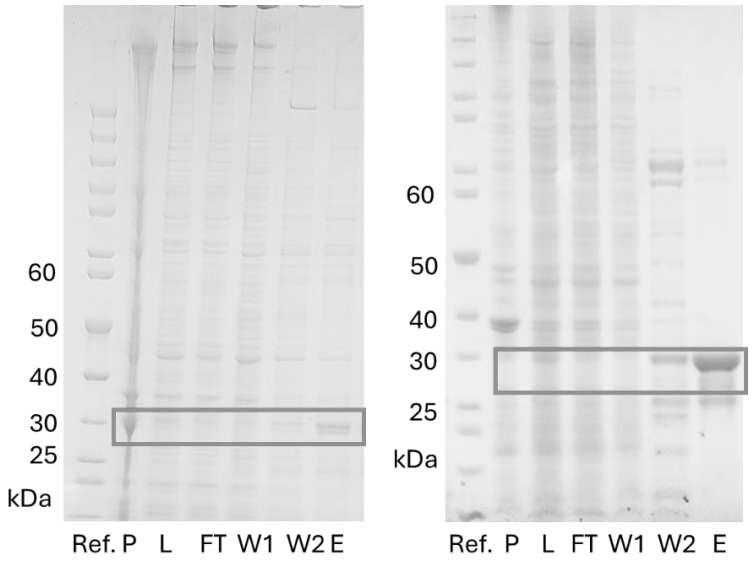

Figure 148: SDS Gel of the purification of StspM2 (left) and SgMT2 (right) using a Ni-NTA column. Ref. = Unstained Protein Standard, P = pellet, Lys = lysate, FT = flow through, W = wash (40 mM or 80 mM ImH), E = elution (250 mM ImH). The band at 30 kDa is highlighted.

Since StspM2 exhibited a higher expression rate but was partially insoluble, an optimisation of expression conditions was conducted. The expression temperature was varied to 15, 20, and 25 °C while maintaining the IPTG induction concentration at 100 µM. Additionally, IPTG concentrations were tested at 50, 100, and 1000 µM, with the temperature held constant at 20 °C. After cell lysis, both the lysate and pellet fractions were analysed using SDS-PAGE, but no significant differences in expression levels and protein solubility were observed [Figure S 31].

As the solubility of the enzyme did not improve under these conditions, the *E. coli* Arctic Express strain was selected for further experimentation. Competent *E. coli* Arctic Express cells were transformed with the plasmid containing StspM2. For protein expression, the main culture was incubated at 37 °C in either LB or TB media. Once an OD600 of 0.4 was reached, the cells were placed on ice for 20 minutes before being induced with 1 mM IPTG and incubated at 15 °C for two days. Following cell lysis, both the lysate and pellet fractions were analysed using SDS-PAGE, but the main protein remained in the insoluble pellet fraction [Figure S 32].

The expression could not be optimised with these experiments, but some soluble protein was obtained under standard conditions. This semi-purified StspM2 was used for an initial activity assay with LL-cWW **3a** and the double *C3*-methylated cWW **240** as substrates. The activity test was performed using Promega's MTase Glo Assay. Enzyme concentration was maintained at 3 µM, while substrate and SAM (**93**) concentrations were set to 25 µM. The reaction was conducted at 45 °C. The enzyme showed the highest activity with the double *C3*-methylated cWW **240**, while the non-*C3*-methylated substrate **3a** was only weakly accepted [Figure 149].

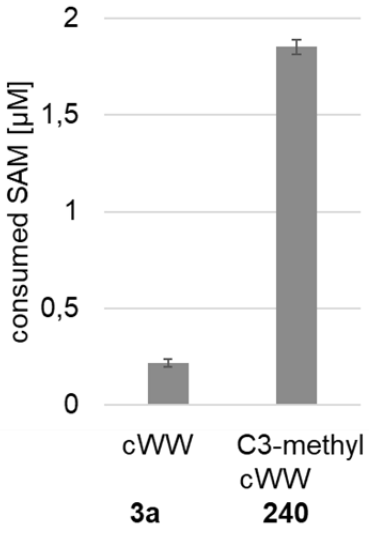

Figure 149: Activity test of StspM2 with the cWW **3a** and the double *C3* methylated cWW **240**. The MTase Glo Assay was used, which measures the formation of SAH.

The Glo Assay only detects the formation of SAH and does not provide insights into the specific products generated or the type of methylation performed by the enzyme. To further investigate this, a preparative-scale reaction using the double *C3*-methylated LL-cWW **240** was performed with 25 mg of substrate in 70 mL of pure lysate. After 40 hours at 40 °C with 4 mM SAM (**93**), a yield of 79% of the *N*-methylated product **287** was achieved following an extensive work-up with several extraction steps [Figure 150]. SgMT2 was also tested on small scale, yielding the same product as StspM2. Therefore, both enzymes are identified as *N*-MTases that can methylate the nitrogen in the HPI motif.

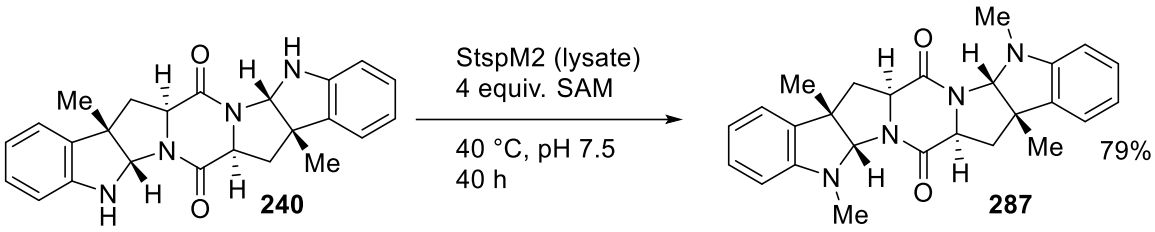

Figure 150: Preparative methylation with StspM2 (25 mg).

StspM2 was further characterised for its temperature optimum using the MTase Glo Assay from Promega. The temperature was varied between 25 °C and 50 °C, while maintaining an enzyme concentration of 10 mM and substrate **240** and SAM (**93**) concentrations at 25 µM. The results indicate that StspM2 exhibits a temperature optimum of 30 °C.

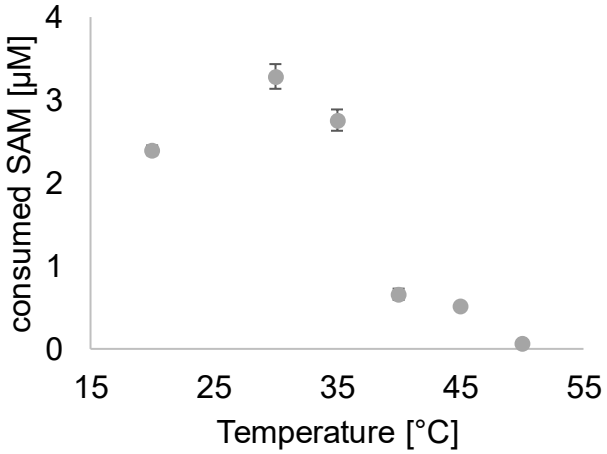

Figure 151: Temperature screening of StspM2 using the MTase Glo Assay with enzyme concentration fixed at 10 mM.

The conversion rate at 30 °C is more than five times higher than at 40 °C, the temperature used for the preparative reaction. These findings underscore the enzyme's potential for synthetic applications, as the lysate amount could potentially be reduced while still achieving high conversion rates. This is particularly notable compared to the challenges faced in the chemical methylation performed by Marcel Schatton during the total synthesis of lansai B (**5**): the HPI DKP showed minimal reactivity in nucleophilic substitution with methyl iodide, even with a strong base like potassium tert-butoxide. Attempts to use elevated temperatures under Eschweiler-Clarke conditions with microwave heating resulted in decomposition. Ultimately, the combination of high quantities of Meerwein's salt **272** and proton sponge **273** as a base was identified as optimal for the final methylation step.[325] The enzymatic *N*-methylation could be an alternative reaction as this reaction proceeds under mild conditions.

SgMT2 and StspM2 were further analysed and compared to other MTases known to methylate nitrogen within a HPI structural motif, including NozMT, SazB-MT, DmtM2, and PsmC [see Chapter 4.2.2.3.1]. The structures of NozMT, SazB-MT, and DmtM2 were modelled using RobettaFold from the Baker Lab, while the structure of PsmC is an unpublished crystal structure by Benjamin Chapple and Oliver Weiergräber. Both NozMT and PsmC feature a *β*-cap domain, similar to various known HPI *C3*-MTases such as PsmD, StspM1, and SgMT. Sequence alignment of these MTases with SgMT2 and StspM2 reveals around 20% sequence identity for both enzymes. In comparison, SazB-MT and DmtMT2 share around 30 % sequence identity with SgMT2 and StspM2. They both possess an *α*-cap domain, which was also found in SgMT2 and StspM2 [Figure 152].

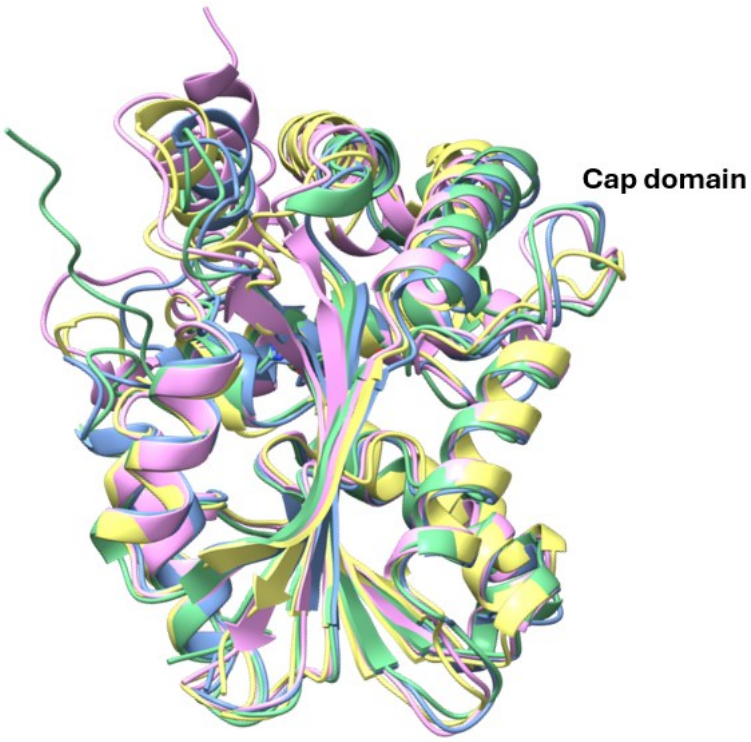

Figure 152: Modelled structures of SgMT2 (blue), StspM2 (green), SazB-MT (yellow) and DmtMT2 (pink).

The beta-cap domain HPI-MTases (C- and *N*-MTases) contain a catalytic triad consisting of aspartate or glutamate, histidine, and tyrosine. The *α*-cap domain HPI-MTases have not yet been studied in terms of their mechanism. These enzymes cannot form the typical triad with tyrosine, histidine, and aspartate at the same position, as the histidine and aspartate residues are located in the *β*-cap domain [Figure 153]. In these *α*-cap enzymes, the catalytic tyrosine is replaced by histidine (H143 in SgMT2 and H145 in StspM2), which may still fulfil a catalytic role despite the absence of the conventional triad at this position. The *α*-cap domain HPI-MTases SazB-MT and DmtMT2 have a relatively high substrate promiscuity compared to other HPI MTases which could be influenced by these differences in the architecture of the active site.

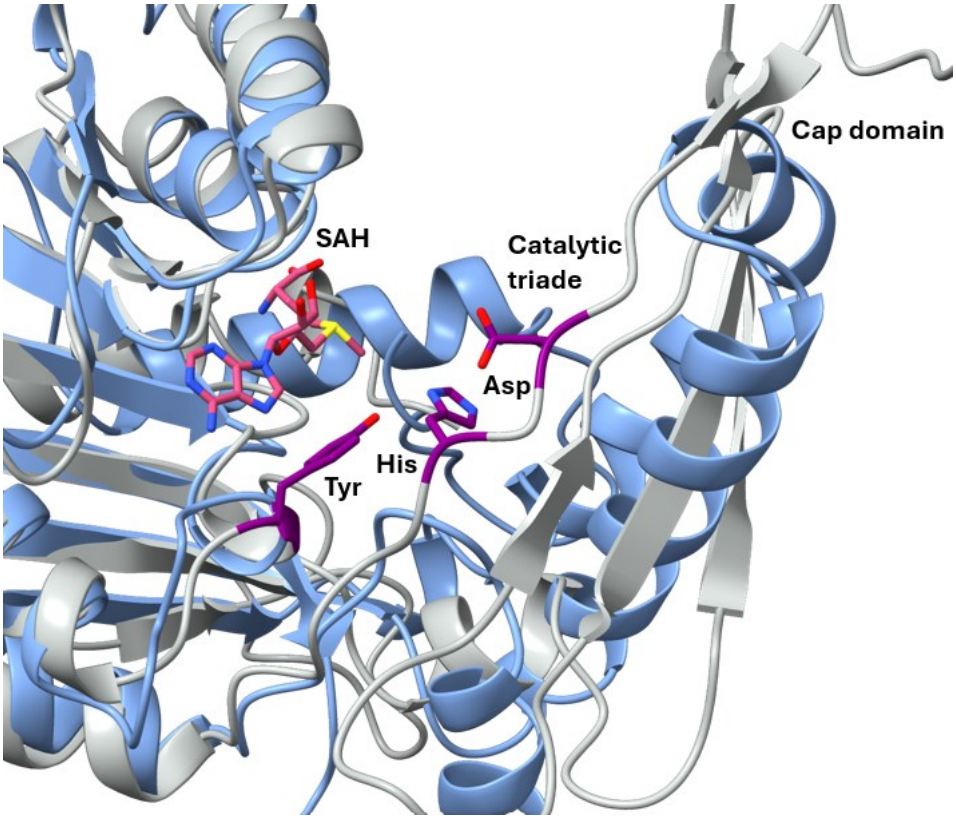

Figure 153: SgMT (grey) and SgMT2 (blue) structures without the amino acids 1-30. The catalytic triade in SgMT is highlighted in violet. SgMT2 lacks this triade at this position due to structural differences in the cap domain.

5.7.3 Prenyltransferase

The Stsp and Sg gene clusters also contain a gene encoding a "phytoene synthase". Sequence alignment with known type IV PTases reveals approximately 30% sequence identity with carbazole PTases such as LvqB4 and NzsG.[287, 338] The sequence similarity is nearly 40% with PTases known to accept DKP substrates, like SazPT and NozPT, which prenylate the cWW DKP **3a** at the *C3* position of the indole.[58, 223] StspPT and SgPT exhibit a high degree of similarity, sharing 71.3% sequence identity with each other [Table 10].

Table 10: Sequence comparison of LvqB4, NzsG, SazPT, NozPT, StspPT and SgPT.

	StspPT	**SgPT**
LvqB4	28.53%	29.32%
NzsG	27.61%	30.25%
SazPT	40.62%	41.80%
NozPT	40.67%	42.46%
StspPT	-	71.30%
SgPT	71.30%	-

To investigate the structures of StspPT and SgPT, as well as NozPT and SazPT for comparison, these enzymes were modelled using RobettaFold from the Baker Lab. All four enzymes exhibit very similar three-dimensional structures, characterised by eleven main alpha-helices (labelled A-K). The structures of StspPT and SgPT are extremely similar, with the exception of the disordered *C*-terminus. The active site of SQS-like PTases is located centrally within the enzyme, positioned between helices B, C, G, H, and J. The estimated error for the modelled structures is notably high from position 290 to the *C*-terminus, with the last helix (K) and the disordered *C*-terminus exhibiting the highest errors. Additional higher errors are observed in loop regions, particularly around amino acid position 100 [Figure 154, Figure 155].

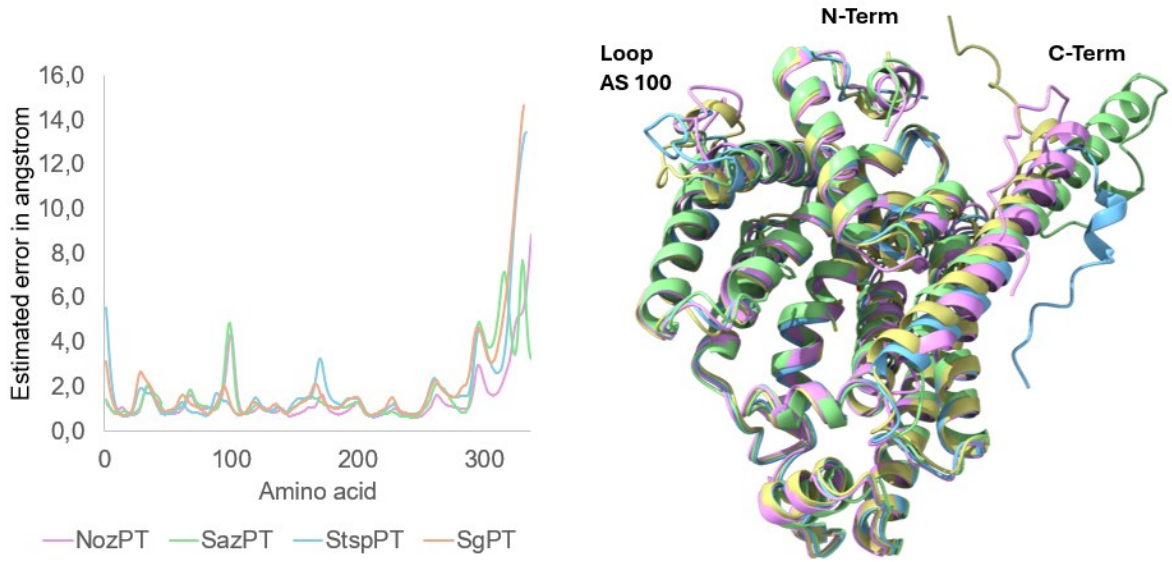

Figure 154: Structure evaluation of StspPT (blue), SgPT (yellow), NozPT (pink) and SazB (green). Aliment of the structures of these enzymes.

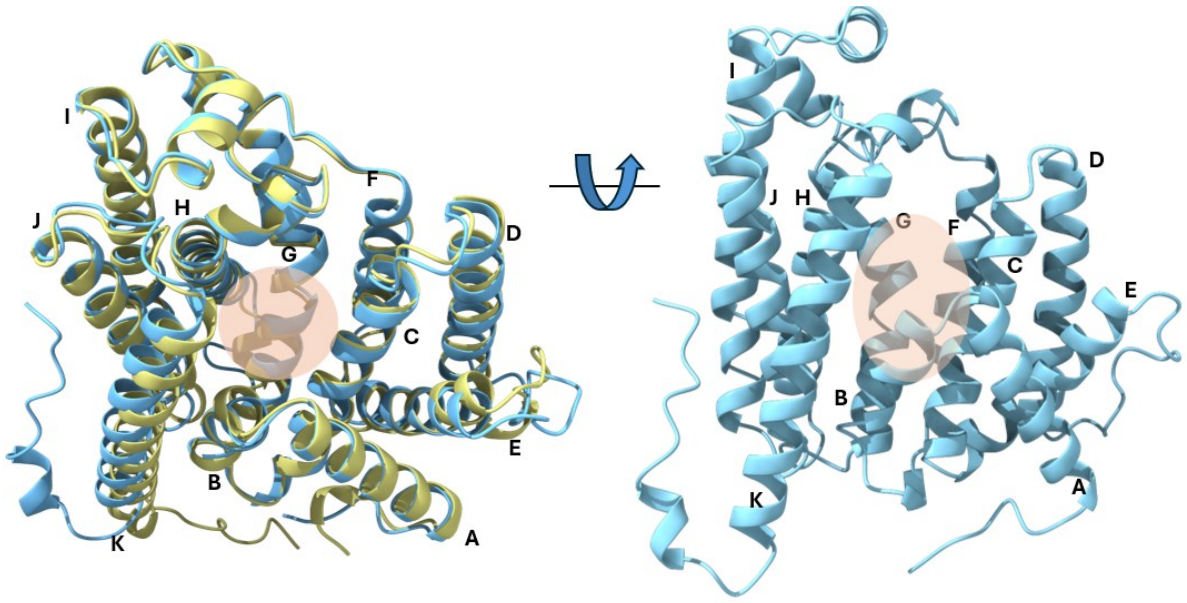

Figure 155: Alignment of StspPT (blue) and SgPT (yellow) with helix numbering. The active site is highlighted in light orange. StspPT is shown from two perspectives.

To enhance the localisation and visualisation of the active site, the structure of StspPT was aligned with that of LvqB4, a carbazole PTase. LvqB4 was crystallised in a ternary complex that includes the enzyme, the carbazole substrate, and (*S*)-citronellyl diphosphate (**288**, CPP). CPP serves as a geranyl diphosphate (GPP) analog **289**; its lack of a double bond between the *C2* and *C3* atoms prevents the formation of an allylic cation at the *C1* atom leading to its inactivity [Figure 156]. Additionally, two magnesium ions were identified within the ligand-binding cavity of the LvqB4 structure.

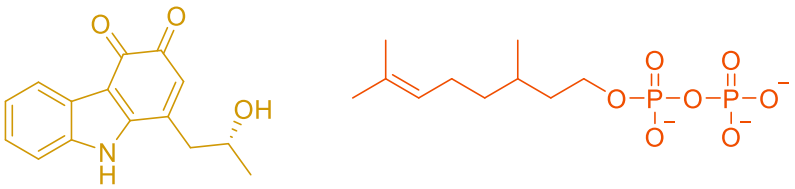

carbazole substrate **288** (*S*)-citronellyl diphosphate **289**

Figure 156: substrates found in the LvqB4 crystal structure.

The two aspartate-rich motifs, which are highly conserved in SQSs, are located on the upper side of the StspPT cavity at positions identical to those in LvqB4. The first aspartate-rich motif ($D^{55}XXXD^{59}$) is found in helix C, while the second motif ($D^{190}XXD^{194}$) is located in helix H. Additionally, helix C contains two residues critical for cofactor acceptance. Smaller amino acids like alanine and isoleucine suggest the presence of a larger cofactor like in LvqB4, in contrast to cytosine and phenylalanine in NzsG, which is known to accommodate the smallest cofactor, DMAPP. Both StspPT and SgPT feature isoleucine and glutamine at this position, while NozPT and SazPT contain phenylalanine/leucine and threonine, respectively [Figure 157].

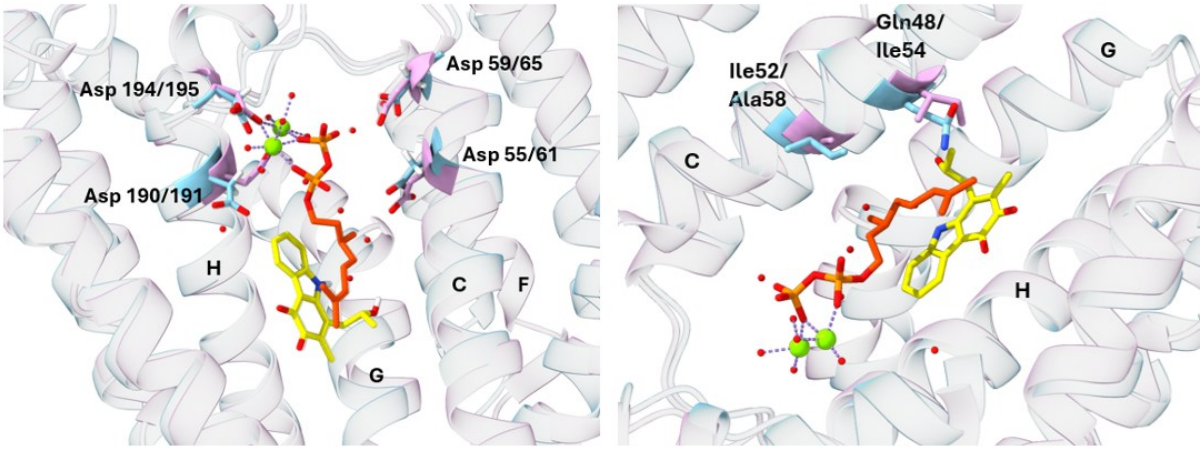

Figure 157: Comparison of SgPT (blue) with the crystal structure of LvqB4 including the substrates **288** and **289** (light pink). The aspartate rich motives (left) and the cofactor binding motif (right) are highlighted.

The gene for StspPT was obtained with a *C*-terminal His-Tag on a pET28a(+) plasmid by GenScript. *E. coli* BL21(DE3) Gold was transformed with the plasmid via heat shock. The enzyme was produced under standard conditions and the lysate was applied to a Ni-NTA column for enzyme purification. StspPT has a molecular weight of approximately 37.7 kDa. An intense band around 40 kDa is visible on the SDS gel in the insoluble pellet fraction, but no overexpressed protein is detected in any other fraction at the expected size [Figure 158].

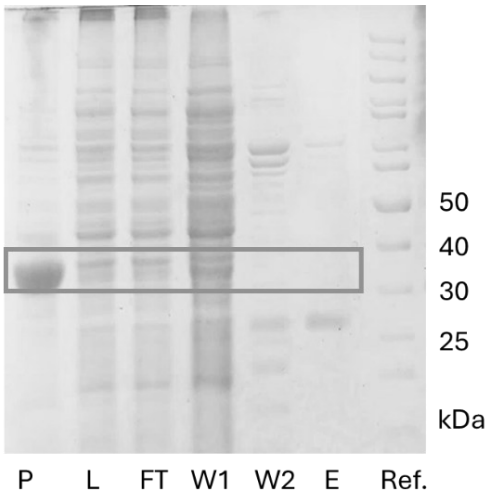

Figure 158: SDS-gel of the purification of StspPT (38 kDa) using a Ni-NTA column. Ref. = Unstained Protein Standard, P = pellet, Lys = lysate, FT = flow through, W = wash (40 mM or 80 mM ImH), E = elution (250 mM ImH). The band at 35 kDa is highlighted.

An expression screening was conducted to enhance the solubility of the PTase StspPT. Initially, the expression temperature was varied among 15, 20, and 25 °C while maintaining an IPTG induction concentration of 100 µM. Additionally, the IPTG concentration was tested at 50, 100, and 1000 µM with the temperature kept constant at 20 °C. After lysis, both the lysate and pellet fractions were analysed using SDS-PAGE, showing no improvement compared to the initial conditions [Figure S 35].

Additives can be added during the cell lysis to enhance protein solubility: Given that the PTase has a magnesium-binding site, magnesium chloride was selected as the first additive, as it could help stabilise the enzyme during the stress induced by cell lysis. The PTase StspPT is classified as a member of the fourth group of PTases, the squalene synthase (SQS)-like PTases. The squalene synthase is anchored to the membrane by a short *C*-terminal membrane-spanning domain.[339] Even though StspPTs structure differs at the *C*-terminus indicating no membrane anchor [Figure S 36]. A typical additive to increase the solubility of these enzymes, 3-[(3-**ch**olamidopropyl)dimethyl**a**mmonio]-1-**p**ropane**s**ulfonate (**290**, CHAPS), was chosen as second additive within this screening.[340] Trehalose (**291**) was chosen as the third additive in this screening process. A study conducted in 2011 evaluated 144 different additive conditions across 41 recombinant proteins and identified trehalose as the most effective additive for improving the solubility of the majority of the proteins tested.[341] During the cell lysis either 0.75 mM trehalose, 5 mM $MgCl_2$ or 1% w/v CHAPS were added to the lysis buffer. However, the intensity of the band at 40 kDa in the soluble fraction did not increase with any of the additives, indicating that none were effective in enhancing protein solubility [Figure S 37].

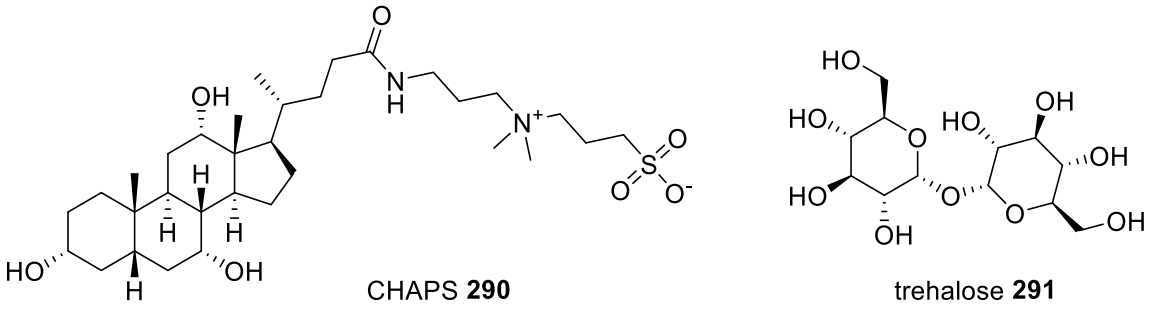

Figure 159: Structures of CHAPS (**290**) and trehalose (**291**).

As the expression of soluble protein was still not improved, the *E. coli* Arctic Express strain was chosen as this strain was developed to increase protein solubility of recombinant proteins. For expression, the main culture was incubated at 37 °C in either LB or TB media with antibiotics or without antibiotics. After reaching an OD600nm of 0.4, the cells were incubated for 20 min on ice before inducing with 1 mM IPTG and incubating at 15 °C for two days. The cells were lysed and the lysate and pellet were applied on an SDS gel. The main protein was still in the insoluble pellet fraction [Figure S 38].

None of the techniques applied—such as altering expression conditions (temperature, IPTG concentration), changing the expression strain, or incorporating additives—resulted in improved protein solubility. The structural characteristics of PTase were therefore investigated in more detail and the genetic construct (enzyme + potential tags) itself was reconsidered.

The *C*-terminus of StspPT (amino acids 291–331, K-helix) is notably more basic than the rest of the enzyme, containing a high number of arginines. In this 42-amino-acid sequence, there are no negatively charged residues (aspartate or glutamate), while there are 13 positively charged residues (arginine and lysine). In contrast, the rest of the protein (amino acids 1–290) exhibits a more balanced distribution of acidic and basic residues, with a ratio of 46 acidic to 39 basic residues [Figure S 39]. In 1993, researchers studied a yeast farnesyl-diphosphate synthase and found that introducing a negatively charged -EEF sequence to its positively charged *C*-terminus reduced enzyme activity by a factor of 12. They proposed that the charged tail plays a crucial role in cofactor binding.[342] StspPT features a His-Tag at its *C*-terminus, which could potentially affect both the enzyme's activity and its proper folding if the charged terminus needs to be oriented in a specific way. To investigate this, the His-Tag was moved to the *N*-terminus (cloning for this switch was conducted by Beatrix Paschold). The new construct with the *N*-terminal His-Tag was then expressed in *E. coli* BL21 (DE3) Gold. While this modification did lead to an increase in the overexpression of the PTase, the protein remained in the insoluble fraction [Figure S 40, Figure 160].

Another approach to enhance enzyme solubility is the use of solubility fusion tags. These tags are attached to the insoluble protein of interest, thereby improving its solubility.[343] This technique was also used for different SQS like PTases: The PTase DmtC1 shares 33% sequence identity with StspPT. DmtC1 catalyses the farnesylation of the *C3*-position of a cWP DKP forming a HPI structural motif. This enzyme was fused to the 109aa Trx•Tag™ thioredoxin protein tag by Beatrix Paschold to increase the protein solubility.[302] The thioredoxin protein Tag has robust folding characteristics serving as a covalently joined molecular chaperon.[344] StspPT was therefore fused to the Trx-tag and expressed under the same conditions as DmtC1, in LB medium induced at an OD600 of approximately 0.6 with a final IPTG concentration of 0.05 mM, followed by cultivation for 16 hours at 16 °C. The lysis was conducted using the same buffer (0.05 M Tris-HCl, 0.5 M NaCl, pH 7.5). The molecular weight of StspPT with the Trx-tag is 54.6 kDa; however, the protein still remained in the insoluble fraction [Figure 160, Figure S 41]. Since the theoretical isoelectric point of the new construct (StspPT+Trx-Tag) is 7.66 and the pH of the buffer used in literature conditions is 7.5, the lysis was repeated at various pH levels ranging from 6.5 to 8.5 to minimise the potential pH caused aggregation. However, no noticeable differences in enzyme solubility were observed [Figure S 42].

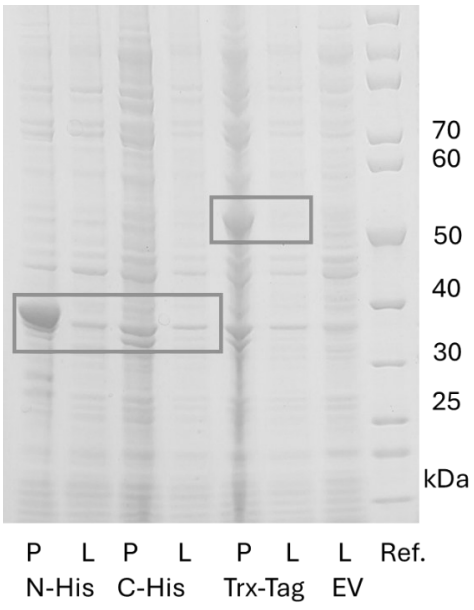

Figure 160: SDS-gel of StspPT (38 kDa) with a *N*-terminal and C-terminal His-Tag or with a Trx-Tag. Ref. = Unstained Protein Standard, P = pellet, L = lysate. The band at 35 kDa is highlighted.

Lysates and insoluble fractions from *N*- and *C*-terminal His-tagged StspPT, Trx-tagged StspPT, as well as from cells carrying the empty vector, were used for activity assays. The lysate and the resuspended insoluble cell pellets were incubated with 1 mM *C3*- and *N*-methylated substrate and 2 mM DMAPP at 30 °C while shaking at 700 rpm in KPi buffer (pH 8) with 2.5 mM $MgCl_2$. The samples were analysed by LC-MS, where no substrate conversion was observed in all cases [Figure 162].

To determine whether the insolubility and inactivity was a specific issue with StspPT, SgPT, the homolog of StspPT, was obtained with an *N*-terminal His-Tag on a pET28a(+) plasmid by GenScript. *E. coli* BL21(DE3) Gold was transformed with the plasmid using a heat shock method. The cells were cultivated overnight at 15 °C for expression of the desired protein. SgPT has a molecular weight of approximately 40 kDa. Similar to StspPT, SgPT was found to be mainly insoluble [Figure 161]

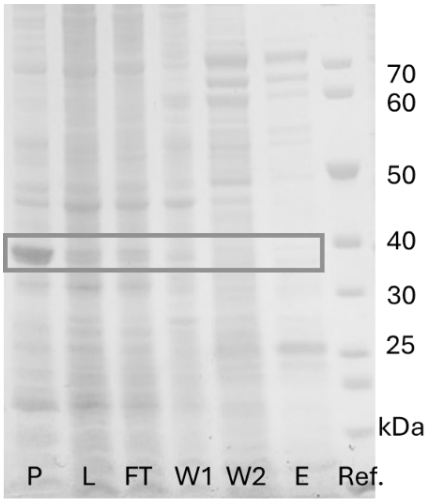

Figure 161: SDS-gel of the purification of SgPT (38 kDa) using a Ni-NTA column. Ref. = Unstained Protein Standard, P = pellet, Lys = lysate, FT = flow through, W = wash (40 mM or 80 mM ImH), E = elution (160 mM ImH). The band at 35 kDa is highlighted.

The activity test for SgPT was repeated under the previously described conditions. In both the lysate and the insoluble fraction, a product was observed with a retention time of 23.8 minutes on LC-MS, consistent with lansai B [Figure 162]. The detected mass of 497 m/z and the corresponding UV spectrum further confirmed the formation of lansai B in the reaction [Figure S 43, Figure S 44]. These results demonstrate that SgPT is an active enzyme, although its solubility and catalytic efficiency still leave room for improvement.

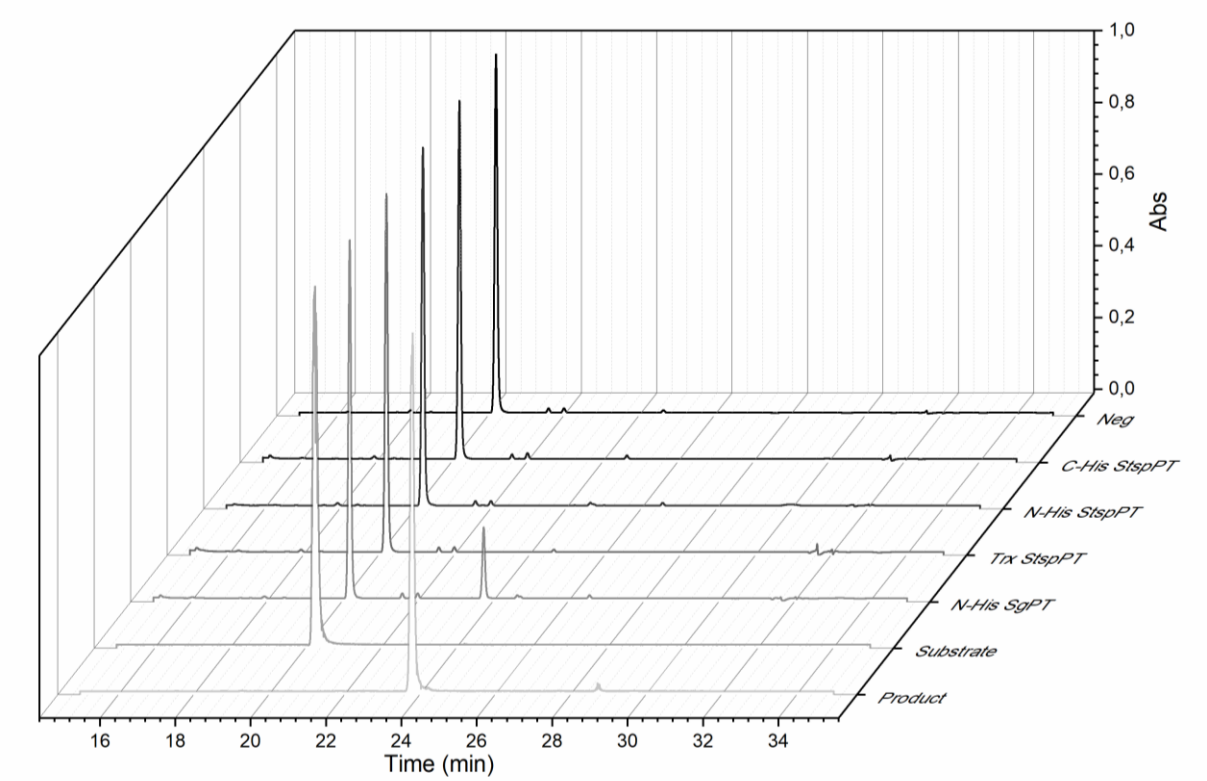

Figure 162: LC-MS chromatograms of the prenylation reaction using variants of StspPT and SgMT with the *C3*- and *N*-methylated cWW **287** as substrate. The retention time of the substrate is 20.2 min and of lansai b, the prenylated product, 23.8 min.

5.7.4 Proposed Biosynthesis

The enzymes in the gene clusters of Sg and Stsp were investigated in detail. Both strains belong to the *Streptomyces* genus, which is the original source of lansai B (**5**), a natural product first isolated from *Streptomyces sp. SUC1*.[52] These gene clusters encompass all necessary genes for the enzymes potentially involved in the biosynthesis of lansai B (**5**).

The initial step in the biosynthesis of lansai B (**5**) would involve an enzyme to form a cWW DKP **3.** Both SgCDPS and StspCDPS possess recognition sites for tRNA-bound tryptophan substrates **82** and are therefore theoretically able to synthesise the cWW DKP **3a**. This cWW **3a** would be further altered by the methyl- and PTases.

StspM1 and SgMT were tested for their ability to convert the *N1*-methylated cWW **292**, as well as *C5*-prenylated cWW **261a**. The *N1*-methylated cWW **292** was not converted, the *C5*-prenylated cWW **261a** was accepted by SgMT and StspM1, but more than four times less than the unprenylated cWW **3a** [Figure 163]. These results implicate, that the *C3*-methylating could be the second step in the potential biosynthesis of lansai B (**5**).

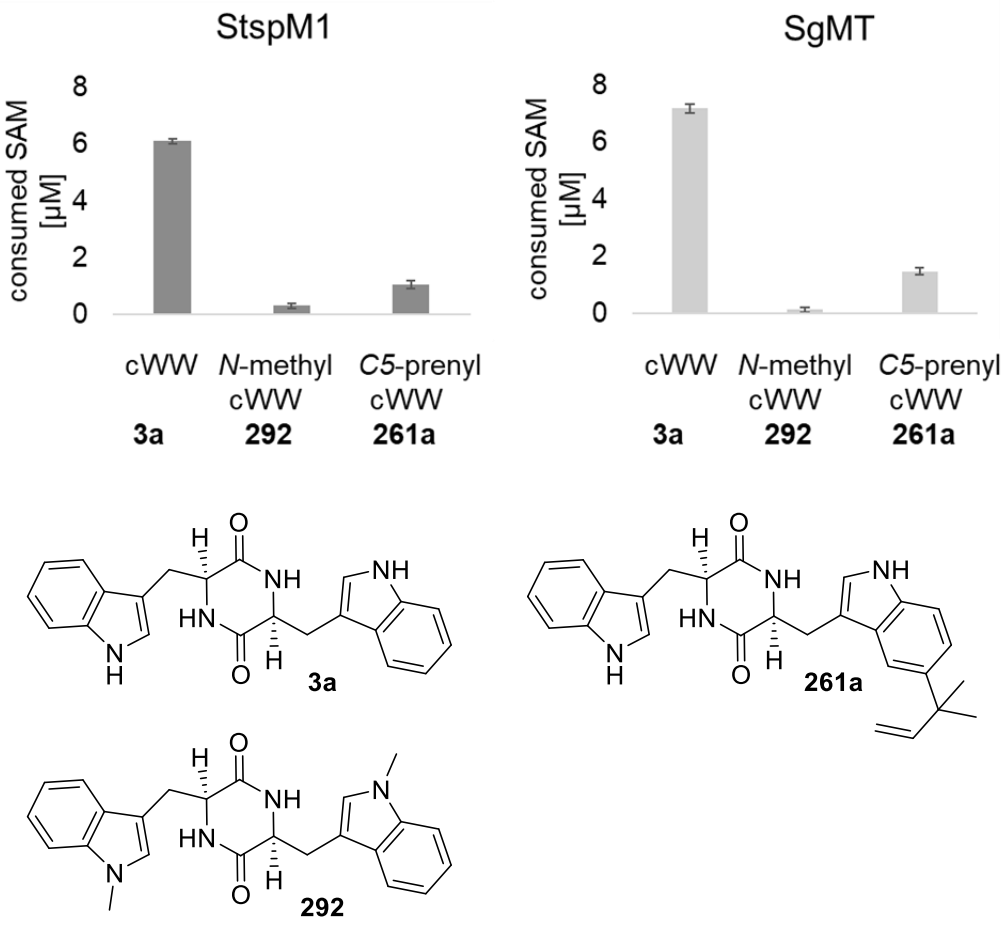

Figure 163: Activity test of StspM1 and SgMT with the cWW **3a** and the double *N*-methylated and the *C5*-prenylated cWW **292** and **261a**. The MTase Glo Assay from Promega was used for detection of the formed SAH.

The *N*-MTases StspM2 and SgMT2 were evaluated for their ability to accept various potential intermediates in the biosynthesis pathway, including cWW **3a**, *C3*-methylated cWW **240**, *C5*-prenylated cWW **261a**, and *C5*-prenylated plus doubly *C3*-methylated cWW **269**. The activity of StspM2 was determined with the MTase Glo-assay, whereas the conversions of SgMT were measured via LC-MS. Among these substrates, the double *C3*-methylated cWW **240** showed the highest acceptance. The presence of an additional prenyl group on the same substrate at the *C5* position reduced the conversion rates. Substrates that were not *C3*-methylated were accepted only marginally [Figure 164, Figure S 34]. These findings suggest that *N*-methylation may represent the third step in the potential biosynthesis of lansai B (**5**).

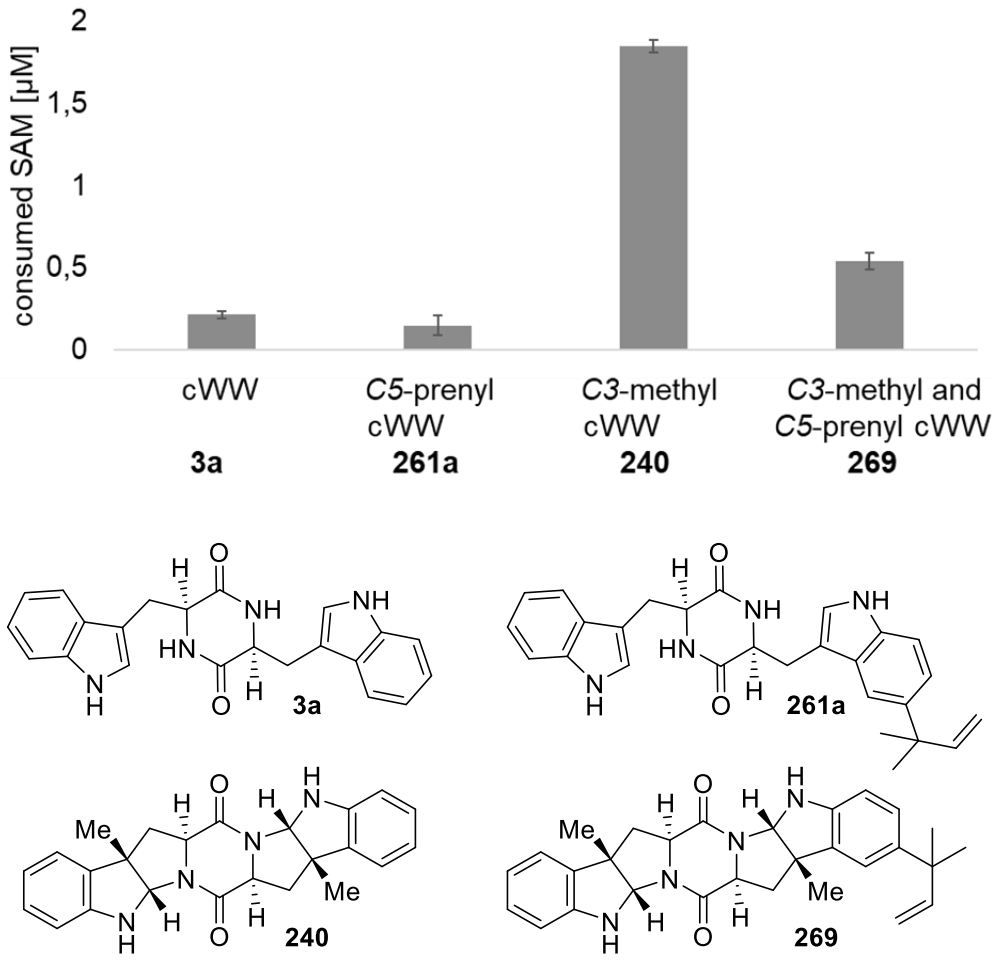

Figure 164: Activity test of StspM2 with the cWW **3a**, the double *C3*-methylated **240**, the *C5*-prenylated cWW **261a** and the double *C3*-methylated+*C5*-prenylated cWW **269**. The MTase Glo Assay was used for detection of the formed SAH.

The prenyltransferases StspPT and SgPT represent the final enzymes encoded within the analyzed gene cluster. Both enzymes were evaluated for their ability to convert the *C3*- and *N*-methylated cWW substrate. Only SgPT showed activity towards the *C3*- and *N*-methylated cWW **287**, catalyzing the formation of Lansai B, thereby confirming prenylation at the *C5*-position of the indole ring.

To determine whether this reaction constitutes the final step in the biosynthetic pathway—or whether SgPT is also capable of prenylating on earlier intermediates—its activity was further tested with unmethylated cWW **3a**, *C3*-methylated cWW **240**, and *N*-methylated cWW **292** [Figure 165]. No conversion was observed by LC-MS in any of these cases towards the desired product [Figure S 45]. These results indicate that only the fully methylated cWW is accepted by SgPT.

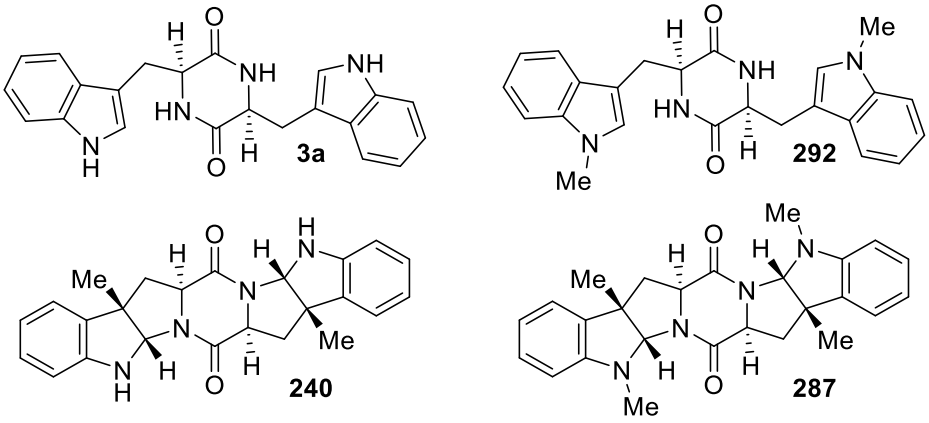

Figure 165: Substrates tested with the SgPT.

For *Streptomyces griseoviridis*, all genes encoding the enzymes SgCDPS, SgMT, SgMT2, and SgPT were analyzed. While SgCDPS was evaluated theoretically, the enzymes SgMT, SgMT2, and SgPT were heterologously expressed and tested with various substrates representing potential intermediates in the biosynthetic pathway. Based on the obtained results, the most likely biosynthetic sequence begins with the cyclodipeptide synthase (CDPS), followed by *C3*-methylation by SgMT, *N*-methylation by SgMT2, and finally *C5*-prenylation catalyzed by SgPT [Figure 166].

A similar pattern was observed for the gene cluster from *Streptomyces sp. HPH0547*: the CDPS and methyltransferases exhibited comparable activities. However, the prenyltransferase StspPT showed no detectable activity under the tested conditions. Despite this, the high degree of structural similarity in the active site compared to SgPT suggests a shared substrate scope and potential functional equivalence.

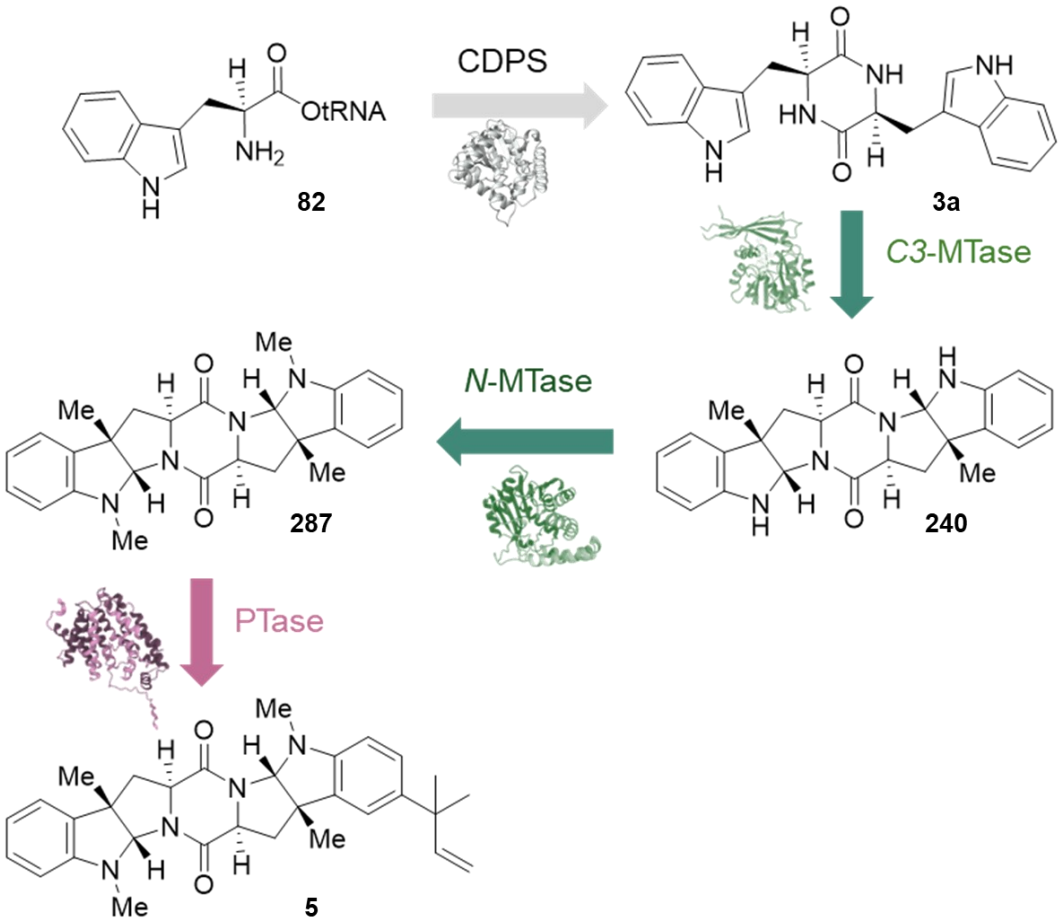

Figure 166: Potential biosynthesis of lansai B (**5**).

This biosynthetic pathway was independently elucidated in parallel to this work by Duan *et al.* in a different *Streptomyces* species. In their study, the enzymes encoded by the lan biosynthetic gene cluster were heterologously expressed, including LanA—a bifunctional CDPS-methyltransferase fusion protein—as well as the *N*-methyltransferase LanC and the prenyltransferase LanB. Through a combination of gene inactivation experiments and biochemical assays, the authors proposed a biosynthetic sequence that supports the same order of enzymatic transformations described in this thesis. Notably, in contrast to the findings presented here, LanB was found to catalyze both *C5* reverse and *C7* linear prenylation towards the products **269** and **293** and exhibited activity even prior to the *N*-methylation step [Figure 167].[137] This broader substrate flexibility was not observed for SgPT in *the in vitro* assays conducted in this work, where no conversion was detected for the non-*N*-methylated intermediate **240** and only a single product, corresponding in retention time and mass to lansai B (**5**), was formed from the fully methylated precursor **287**.

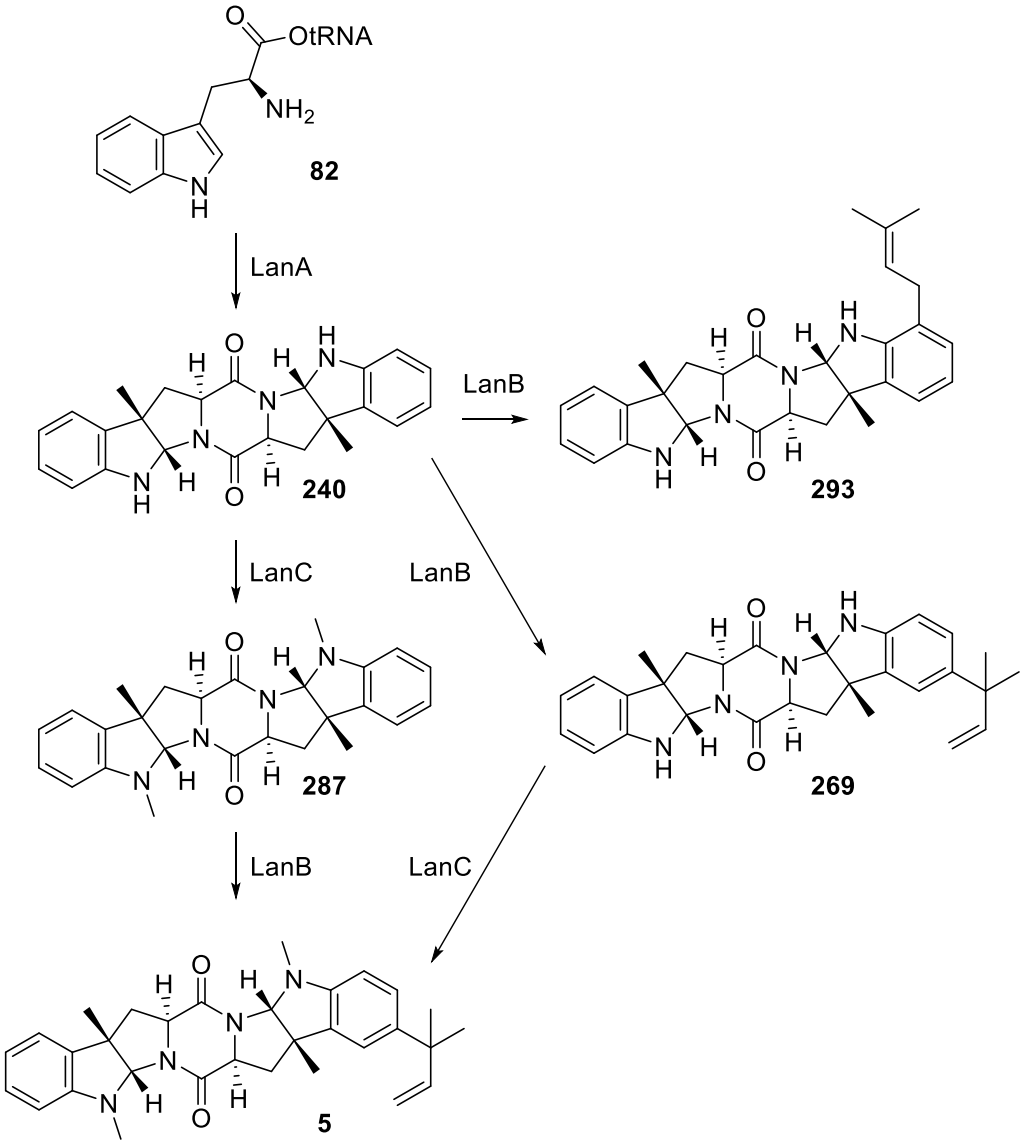

Figure 167: Potential biosynthesis of lansai B by Duan et al.[137]

The prenylation conditions applied for LanB (pH 7.5, 28 °C) are comparable to those used in this study (pH 8.0, 30 °C), suggesting that differences in enzymatic activity are unlikely to be solely attributed to variations in reaction parameters. Nevertheless, the published conditions should be evaluated experimentally for SgPT and StspPT.

The amino acid sequence of the PTase from *Streptomyces albus* shares over 99% identity with StspPT, while showing only 72% similarity to SgPT. In the present study, StspPT activity could not be confirmed, potentially due to challenges related to protein solubility. Similarly, Duan *et al.* reported initial difficulties in expressing LanB in soluble form, which were eventually overcome by utilizing the inducible *tsr* promoter in *Streptomyces coelicolor* M1146.[137] Adopting these expression conditions may represent a promising strategy for achieving soluble expression of StspPT.

The active sites of LanB, StspPT and SgPT exhibit a high degree of structural similarity. The catalytic center was inferred based on the conserved magnesium-binding motif and by comparison with the crystal structure of LvqB4 complexed with its cofactor analog, (*S*)-citronellyl diphosphate, and its carbazole substrate. The putative substrate-binding pocket is primarily enclosed by helices H, G, and J. Among these helices, only a few residues projecting into the binding cavity differ between the enzymes—specifically Ile160/Leu161, Ala186/Gln187, and Leu272/Met273 (SgPT/LanB) [Figure 168]. Targeted site-directed mutagenesis of these positions could provide insights into their roles in determining regioselectivity.

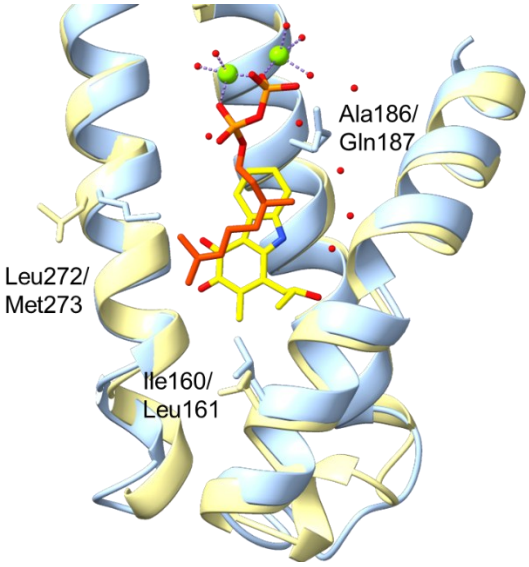

Figure 168: Structure (helices H,G and J) of LanB (light yellow) and SgPT (blue). To highlight the cofactor binding side, the crystal structure of LvqB4 with its cofactor analog (*S*)-citronellyl diphosphate (orange), the carbazole substrate (yellow) and Mg (green) were aligned.

5.7.5 Extraction of lansai B from *Streptomyces griseoviridis*

The analysed gene clusters belong to *Streptomyces* strains. The natural product lansai B (**5**) was isolated from *Streptomyces* sp. SUC1, which is a bacterium on the aerial roots of *Ficus benjamina*.[52] The extraction of natural products from *streptomyces* strains is a common method for identifying new compounds in drug discovery.[345, 346]

The strain *Streptomyces griseoviridis* was cultivated for 14 days on plates [Figure 169] and the produced natural products were extracted. The extract was applied to a silica column to remove the main impurities before the fractions (three fractions, eluted with ethyl acetate) were analysed via LC-MS.

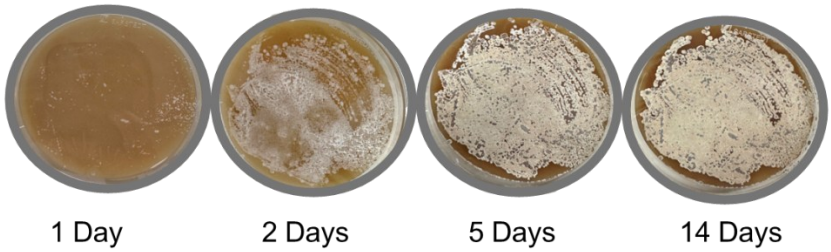

Figure 169: *Streptomyces griseoviridis* grown on agar plates (Medium 65) for 14 days.

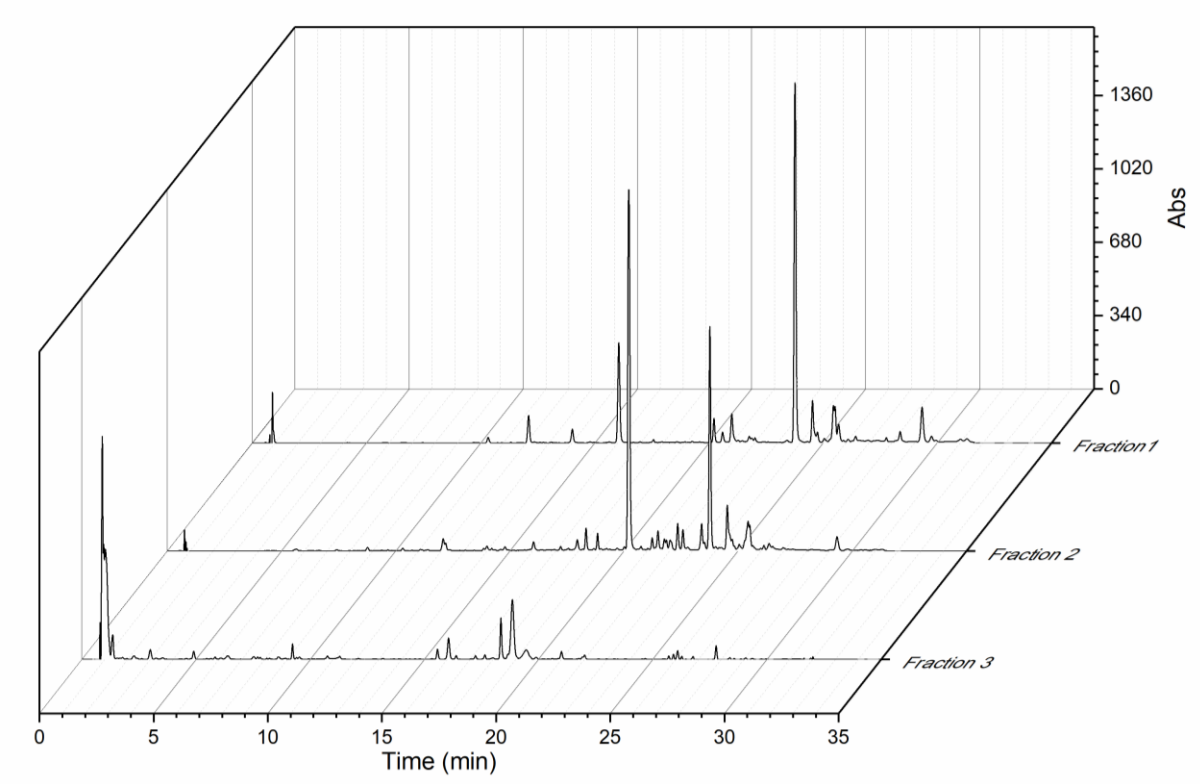

Figure 170. LC-MS spectra (absorption at 205 nm) of the fractions 1-3 of the extract of *Streptomyces griseoviridis.*

All fractions were screened by LC-MS for the expected biosynthetic intermediates—namely, cWW **3a** (m/z 373), the *C3*-methylated cWW **240** (m/z 401), the *C3*- and *N*-methylated cWW **287** (m/z 429) and lansai B **5** (m/z 497). Retention times were compared with synthesised reference standards.

Fractions 1 and 2 primarily contained the *C3*- and *N*-methylated cWW **287** (429 m/z) and lansai B **5** (497 m/z). Fraction 3, which eluted last, additionally showed peaks corresponding to the more polar intermediates cWW **3a** (373 m/z) and the *C3*-methylated cWW **240** (401 m/z) [Figure 171]. Detection of alternative intermediates, that would only accumulate under an alternative biosynthetic sequence were not detected. [Figure S 48].

As further confirmation of the presence of lansai B **5** in the extract, both the UV–Vis spectra and MS fragmentation patterns of the compound found in the extract matched those of the synthesised reference compound [Figure S 46, Figure S 47].

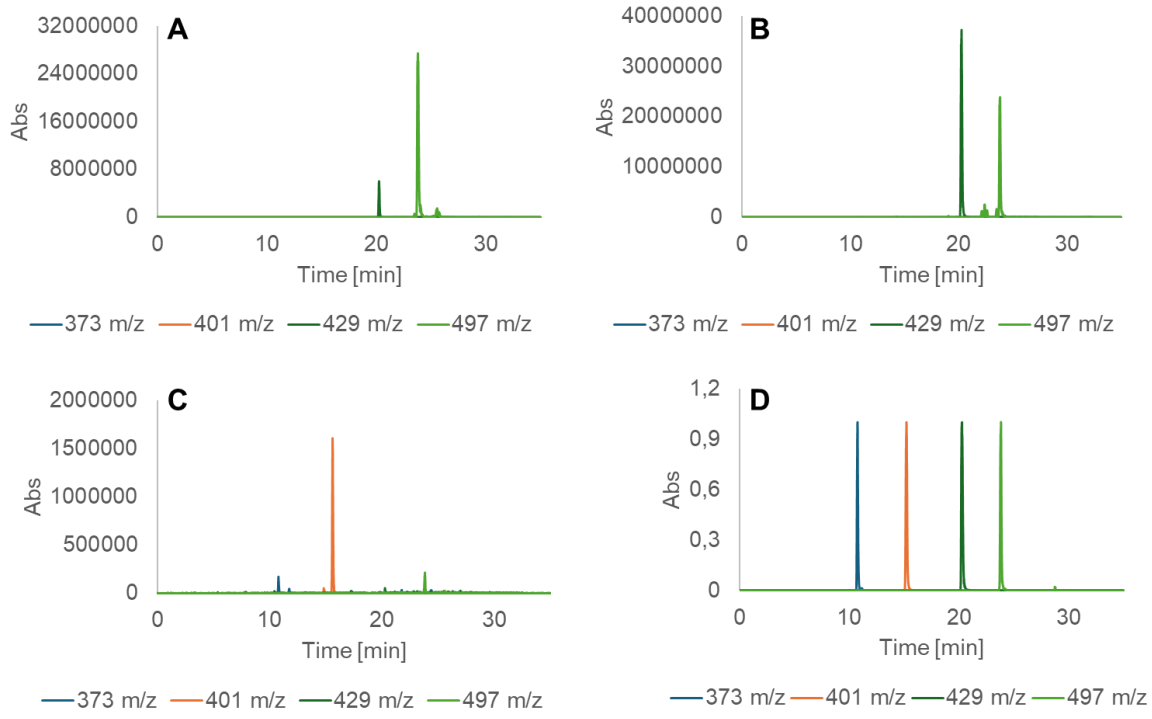

Figure 171: LC-MS traces for the expected biosynthetic intermediates—cWW **3a** (m/z 373), the *C3*-methylated cWW **240** (m/z 401), the *C3*- and *N*-methylated cWW **287** (m/z 429) and lansai B **5** (m/z 497) in the fraction 1 [A], fraction 2 [B] and fraction 3 [C]. D: LC-MS traces for the chemical synthesised references.

The presence of the cWW **3a**, the *C3*-methylated cWW **240**, the *C3*- and *N*-methylated cWW **297** and lansai B (**5**), as well as the absence of any other potential intermediates in the extract of *Streptomyces griseoviridis* further support the in this thesis proposed biosynthetic pathway [Figure 166]. Notably, in contrast to the findings reported by Duan *et al*., no intermediate corresponding to an m/z of 469—consistent with a dimethylated and prenylated (either C5- or C7-substituted) derivative—was detected in any of the extracts.[137]

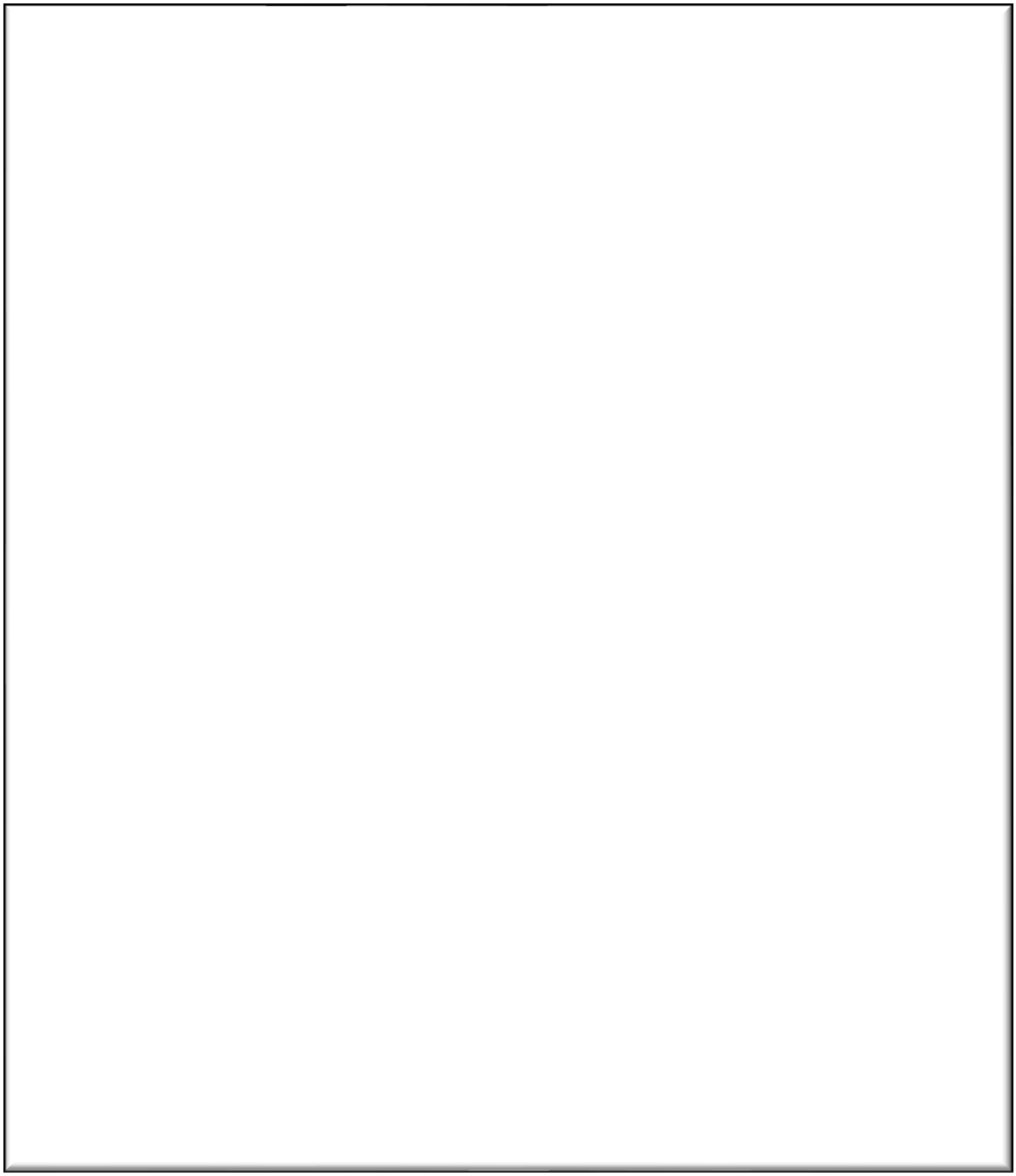

6. OUTLOOK

6.1. *C3*-Methyltransferases

Within this thesis, five potential *C3*-MTases have been studied in varying levels of depth, focusing particularly on StspM1 and SgMT. Both enzymes were extensively investigated for their mechanisms, substrate binding and substrate scope, and were applied on a semi-preparative scale, demonstrating their utility as catalysts beyond analytical studies.

SgMT was subjected to mutagenesis to enhance its activity towards brominated LL-cWW derivatives, though improvements in double methylation activity were not achieved. Mutagenesis targeted three residues (N125, F184, W182) identified via alanine scanning. Expanding residue selection through substrate-specific docking studies could better pinpoint key interactions within the active site. Comparative analysis of binding sites between SgMT, StspM1, and PsmD by Benoit David revealed that altering a few different residues could improve SgMT's activity for DKP substrates beyond cWW **3**. For example, per-residue MM-GBSA calculations highlight Q29 as stabilizing the indole side chain through hydrogen bonding. Substituting Q29 with F or W may improve binding of smaller substrate homologs by improving their packing in the binding site. Additionally, replacing F158 with Y could enable additional hydrogen bonding for substrates like cWH [Figure 172]. The structural similarities between SgMT and StspM1 suggest that these modifications could also enhance StspM1. Site-directed mutagenesis can implement these specific changes, while a combinatorial approach, altering multiple residues simultaneously, could serve as a broader alternative strategy for optimizing substrate compatibility.

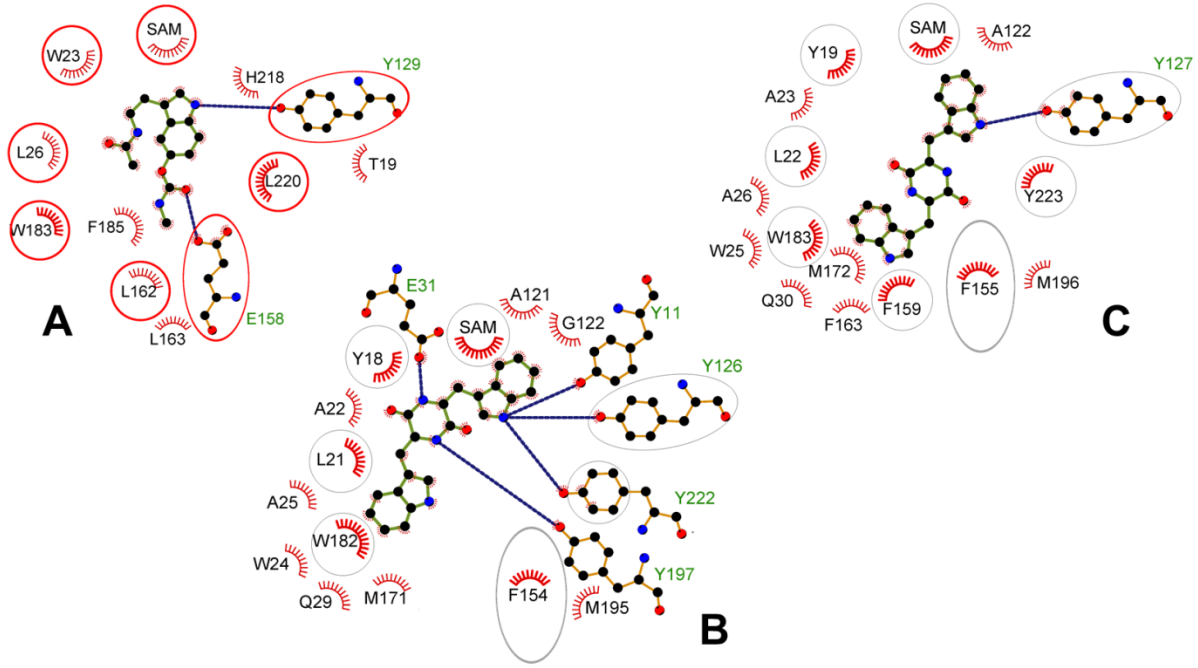

Figure 172: Substrate binding sites in PsmD (A), SgMT (B), and StspM1 (C). The 2D sketches were drawn using LigPlus, considering only binding residues within 4 Å from the bound substrate. Polar interactions are shown as a blue dashed line. Spatially equivalent positions in all three 3D structures are circled in red (PsmD) and grey (SgMT/StspM1). Figure by Benoit David.

The MTase SeMT exhibits structural differences from StspM1 and SgMT. Insights into its catalytic mechanism were gained through its crystal structure and mutagenesis studies, identifying key amino acids required for converting the cWW substrate **3**. However, the enzyme's natural substrate remains unidentified. To address this, a detailed analysis of the active site combined with modelling potential substrates within this environment is essential. These candidate substrates would then be chemically synthesised and tested for conversion by SeMT, with further modifications performed based on the results. If a suitable substrate is identified, the wild-type SeMT would undergo renewed biochemical characterisation to determine its optimal pH and temperature conditions. Additionally, since the natural product associated with SeMT's biosynthetic pathway in its native strain is unknown, cultivating and extracting this strain may lead to the discovery of a novel natural product. This process could provide valuable insights into SeMT's physiological role and expand its potential applications.

The MTase NozB-CYIM and its homologs, ThMT and MtMT, were evaluated with only a limited set of substrates under standard conditions. Given the distinct origins of ThMT and MtMT, exploring alternative reaction conditions would be valuable, as these enzymes may exhibit unique optimal parameters. The significant differences in their active sites suggest that their natural substrates might also differ structurally. A similar approach to that proposed for SeMT could be employed to identify their natural substrates. This would involve active site analysis, modelling potential substrates, chemical synthesis, and testing for catalytic activity. Currently, knowledge about these enzymes is limited, as no crystal structures or reports of successful catalytic activity have been documented. Further investigation is essential to elucidate their biochemical properties and substrate specificities.

6.1.1. More than methylation?

As discussed in the state-of-the-art chapter, MTases have been explored for transferring groups larger than methyl, requiring SAM derivatives that can be synthesised through various pathways.[255-259] One extensively studied approach involves the SAM recycling system introduced in 2019, which employs a HMT to generate SAM derivatives from SAH (**94**) using different alkylation agents. This system operates with catalytic amounts of SAH (**94**) and demonstrates over 500 turnovers.[239] However, the HMT from *Chloracidobacterium thermophilum*, initially utilised in Seebeck's SAM recycling system, exhibits limited activity and substrate flexibility, accepting only a few alkyl halides beyond methyl iodide. To address this limitation, researchers have broadened the repertoire of HMT enzymes through homology-based searches and engineering efforts to produce diverse SAM analogs.[256] In 2021, Hammer and colleagues expanded this catalogue further, creating substrate profiles for multiple HMTs. Notably, this study identified the HMT from *Aspergillus clavatus* (AcHMT), which demonstrated compatibility with various alkyl donors.[255] The gene encoding AcHMT was ordered and expressed by Benjamin Chapple.

The purified AcHMT was evaluated in initial alkylation tests using SgMT as alkyltransferase under the following conditions:[347] 100 µM HMT was incubated in KPi buffer (50 mM, pH 7.5), supplemented with 7 mM SAH (**94**) and 70 mM of the respective alkyl donor. The alkyl donors tested included methyl iodide, ethyl iodide, prenyl bromide, and allyl iodide. After 2 hours at 35 °C, the reaction solution was transferred at a ratio of 1:4 to a second mixture containing 100 µM SgMT and 1 mM cWW **3a**. This second reaction was incubated overnight and analysed via TLC and LC-MS. It is important to note that no standards for the reaction products were synthesised; thus, the results are based solely on the relative peak areas of the corresponding signals. Actual conversion rates may vary, as the extinction coefficients of the products could differ significantly, as demonstrated for the methylated products [Figure S 15].

Methylation, used as a positive control, demonstrated successful conversion, validating the effectiveness of the system. In contrast, a negative control without HMT showed no conversion, confirming the enzyme's essential role in the reaction. Ethyl iodide as an alkyl donor resulted in no detectable ethylation, with only the starting material observed via LC-MS. Prenyl bromide yielded low relative conversion to a single prenylated cWW product, identified with an m/z of 441. Allylation using allyl iodide showed higher relative conversions, producing a single allylated product (m/z 413) and a double allylated product (m/z 453) [Table S 25, Table 11]. However, it remains unclear whether allylation occurred twice at the *C3* position or if an initial *C3*-allylation was followed by *N*-allylation on the HPI. The publication introducing the HMT states a higher non enzymatic background alkylation using allyl iodide because of its high reactivity.[255] As allylation and prenylation are feasible, the lack of conversion with the ethyl donor can be concluded to be caused not by steric hindrance but rather the generally lower electrophilicity and thus reactivity of the resulting ethyl-SAM (SAE) derivative.

Table 11: LC-MS result of the alkylation experiments using the AcHMT and SgMT with methyl iodide, ethyl iodide, prenyl bromide, and allyl iodide as alkylation agents. The relative peak areas are given in percent for the LL-cWW substrate, the single alkylated product and the double alkylated product.

	RELATIVE PEAK AREAS [%]			
ALKYL-DONOR	Methyl	Ethyl	Allyl	Prenyl
SUBSTRATE	39	100	68	97
SINGLE ALKYLATED PRODUCT	58	-	26	3
DOUBLE ALKYLATED PRODUCT	3	-	6	-

The allylation reaction was repeated under direct recycling system conditions, where HMT and SgMT were added at a concentration of 100 µM directly to a solution containing 1 mM cWW **3a**, 1 mM SAH (**94**), and 10 mM allyl iodide. These reactions were only monitored using TLC, which indicated nearly complete substrate conversion overnight at 35 °C. A negative control without HMT showed no formed reaction product [Figure S 58].

To confirm the allylation positions, the reaction should be scaled up to a preparative level. For this purpose, purified or immobilised enzymes should be employed to minimise background methylation caused by SAM (**93**) in the lysate. The allylated reaction product could then be utilised as a precursor for further modifications and the synthesis of various natural product derivatives.

6.1.2 Perspectives for total synthesis

In this thesis, the *C3*-MTase SgMT was successfully integrated into the total synthesis of lansai B (**5**), demonstrating the utility of this enzymatic method for complex molecule construction. Beyond lansai B (**5**), other DKPs containing HPI motifs, such as nocardioazine B (**7**), also represent interesting targets due to their biological activities.[45] Nocardioazine B (**7**), derived from D-tryptophan, features (*R*)-configured stereogenic centres at the DKP core, with the *C3*-methyl group in an *cis* configuration and the *C3*-prenyl group in an *trans* configuration relative to these stereogenic centres.[55]

MTases such as StspM1 and SgMT have been demonstrated to catalyze the methylation of the DKP substrate DD-cWW **3b** with the correct configuration consistent with the natural product nocardioazine B (**7**). To optimise the methylation of DD-cWW **3b** using SgMT, the enzyme amount was systematically varied. SgMT was immobilised directly from the lysate using Ni-NTA agarose beads, following a procedure established for StspM1. Small-scale reactions were conducted with SgMT-containing cell lysate at concentrations ranging from 10% to 100% (v/v). After 20 h, the reactions were terminated, and product formation was analysed using two complementary assays. The first assay quantified remaining substrate by detecting indoles, while the second assay measured the HPI product formed during methylation. Both assays, based on absorbance measurements of assay-generated products, demonstrated that increasing the amount of immobilised SgMT lysate beyond 90% (v/v) did not significantly enhance conversion efficiency [Figure 173].

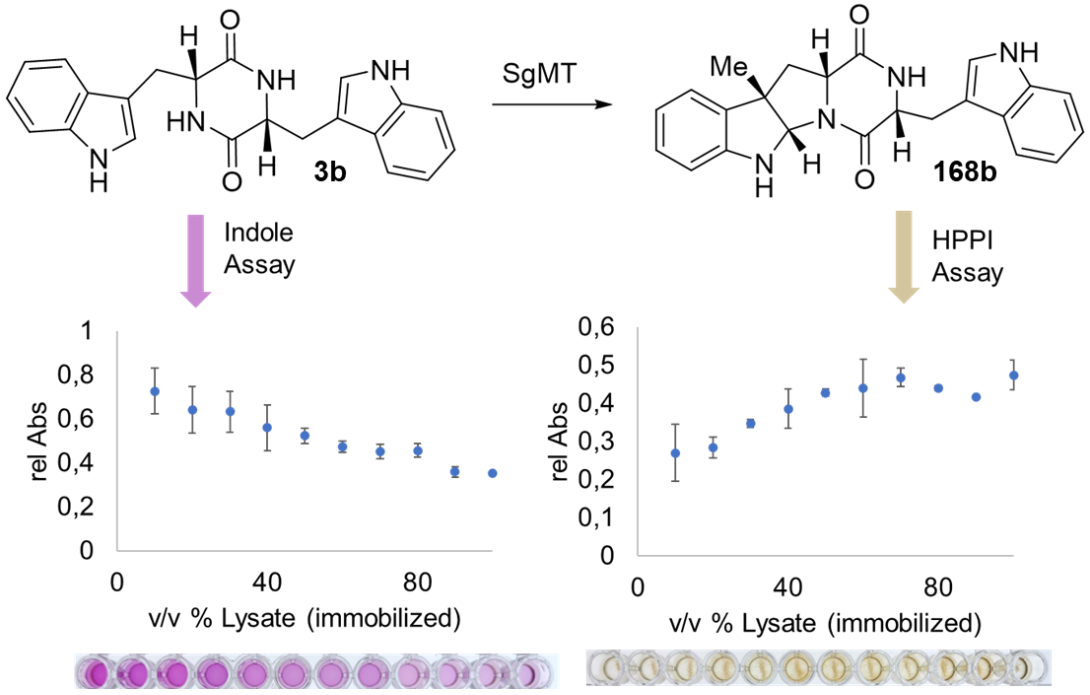

Figure 173: Optimisation of the biocatalytic methylation reaction of SgMT with the DD-cWW **3b**. Two assays were used to detect the substate (indole assay,[328, 347] left) and the product (HPPI assay, right) in parallel via absorption. The amount of immobilised lysate of SgMT cells was varied.

Therefore, the reaction was next carried out in a 50 mg scale with 90 vol% lysate, yielding 93% of the methylated product. Notably, methylation occurred exclusively on one side of the molecule as previously described. This single methylated product could serve as a starting point for further modification towards the synthesis of nocardioazine B (**7**) and derivatives.

A key structural distinction between nocardioazine B (**7**) and lansai B (**5**), beyond differences in configuration and prenylation position, is that nocardioazine B (**7**) features *N*-methylation on only one HPI nitrogen. The nitrogen on the methylated side remains unmethylated, enabling further reactions to produce nocardioazine A. With regards to the total synthesis, this selective *N*-methylation cannot be achieved as the final step using conventional organic chemistry methods due to lack of selectivity. In the singly *C3*-methylated DD-cWW **3b** intermediate, which results from the biocatalytic methylation, one side of the molecule contains the HPI motif while the other side remains an indole. Given the higher nucleophile of the HPI nitrogen compared to the indole nitrogen, this HPI nitrogen could be selectively protected at this stage of synthesis, for instance, yielding the Boc-protected intermediate **294**. Following this, the prenyl group could be introduced chemically, as previously reported to form the second HPI motif in compound **295**.[56] After prenylation, the nitrogen on the newly formed HPI could be methylated. In the final step, the protecting group would be removed from the intermediate **296**, yielding nocardioazine B (**7**) [Figure 174].

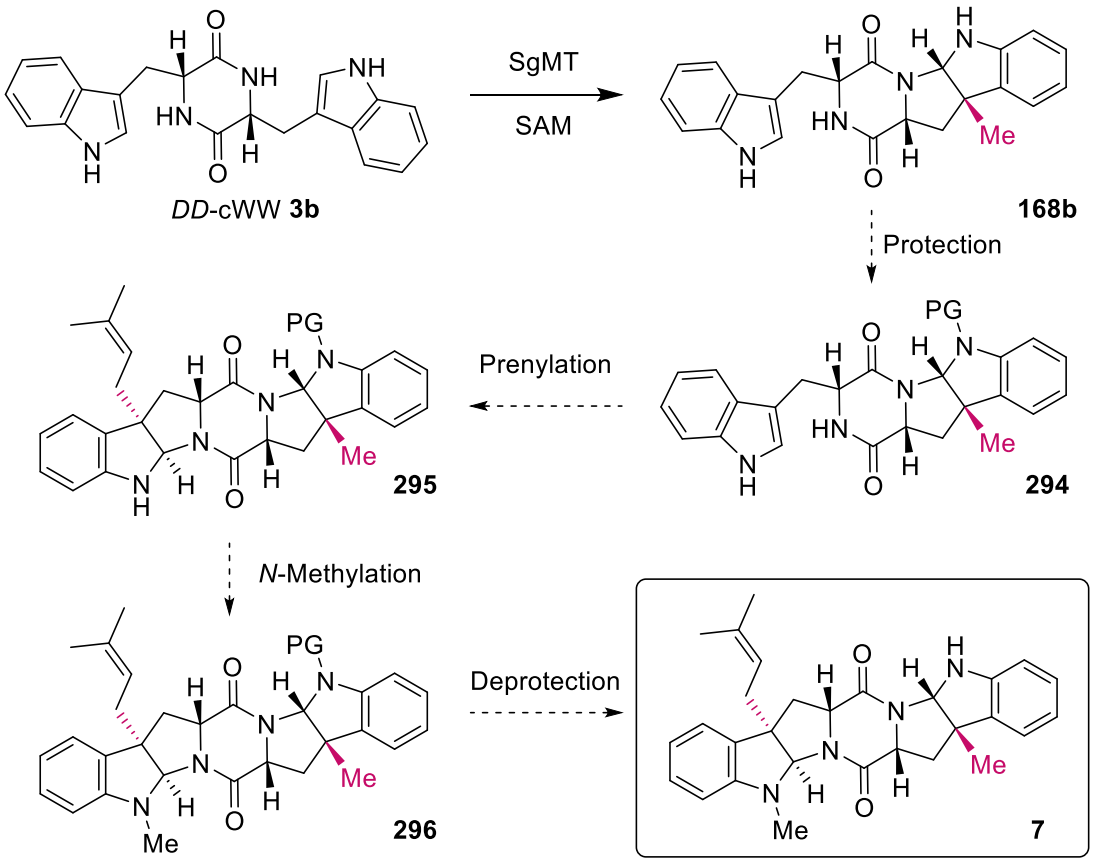

Figure 174: Strategy for the chemoenzymatic synthesis of nocardioazine B (**7**) starting from DD-cWW **3b**.

Using DD-cWW **3b** as a key intermediate, the prenylation can be modified to create different derivatives of nocardioazine B (**7**). By altering the configuration of the prenylated carbon *C3*, it is possible to generate a diastereomer **297** of nocardioazine B (**7**). Additionally, the introduction of a branched prenyl group is an opportunity to further expand the library of derivatives like **298** and **299** Natural products with similar structures, such as aszonalenin (**49**) and roquefortine D (**300**), also contain branched *C3*-prenyl groups, which have been shown to exhibit interesting biological activities [Figure 175]. [45, 112, 348]

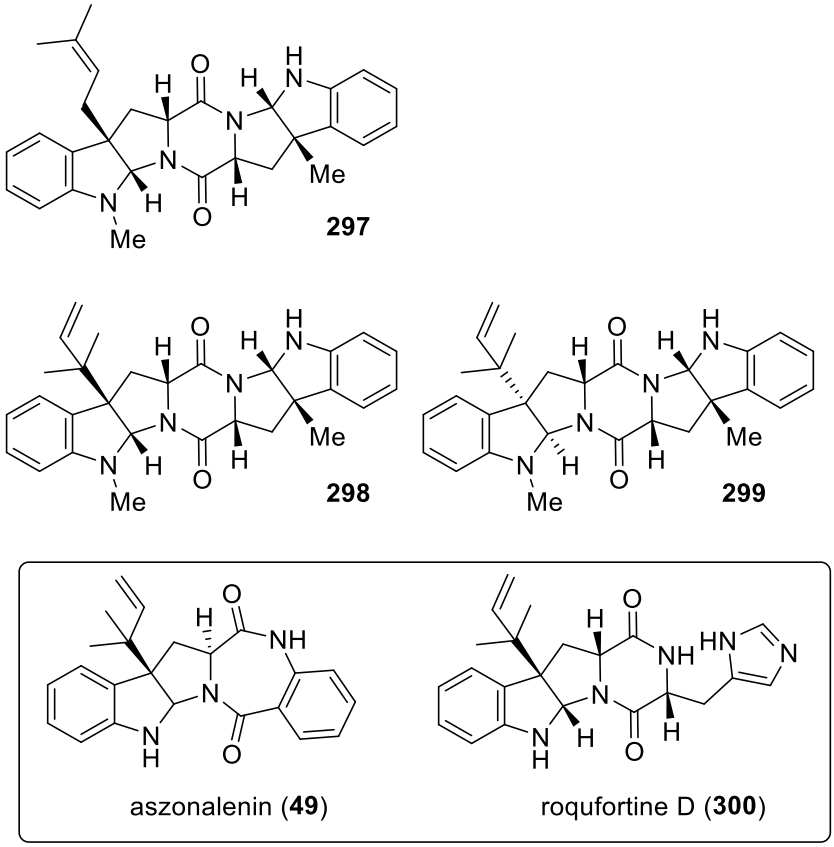

Figure 175: Potential derivatives of nocardioazine B (**7)** including its diastereomer and two constitution isomers with branched prenyl groups. Branched prenyl groups are also present in natural products like aszonalenin (**49**) and roquefortine D (**300**).

In contrast to chemical *C3*-methylation, there are studies available in literature that focus on selective *C3*-prenylation. In 2016, Stark and co-workers reported the selective prenylation method. Using $[Ir(COD)Cl]_2$ with a phosphoramidite ligand afforded branched prenylated products of tryptophan derivatives and DKP-based compounds [Figure 14, chapter 4.1.4]. By inverting the ligand's stereochemistry, they selectively accessed the complementary isomers. [125]

The selective linear prenylation was investigated two years later a similar tryptophane based substrate scope. In this study, $[Pd(prenyl)Cl]_2$ (5 mol%) was used as a catalyst along with a chiral phosphoramidite ligand **301** (allylphos, 5 mol%) and Cs_2CO_3 (150 mol%) to selectively achieve the desired linear prenylated products. This strategy was applied to both protected L- and D-tryptophan **302** and **303**, resulting in the formation of *trans*- and *cis*-configured products **304** and **305**, respectively [Figure 176].[349] For the D-tryptophan based nocardioazine B (**7**), an *trans*-configuration of the prenylgroup towards this stereogenic centre is required. To achieve this, the enantiomer of the allylphos ligand **301** used in this publication is needed. In 2022, the reaction was successfully performed on the protected D-tryptophan substrate **303**, achieving the correct configuration with an 83% yield. This demonstrates the viability of the selective linear prenylation approach for the total synthesis of nocardioazine B (**7**). Notably, the study of 2022 highlights the significance of the unmethylated indole nitrogen in enabling successful prenylation.[56] This further supports the proposed synthetic route for nocardioazine B (**7**).

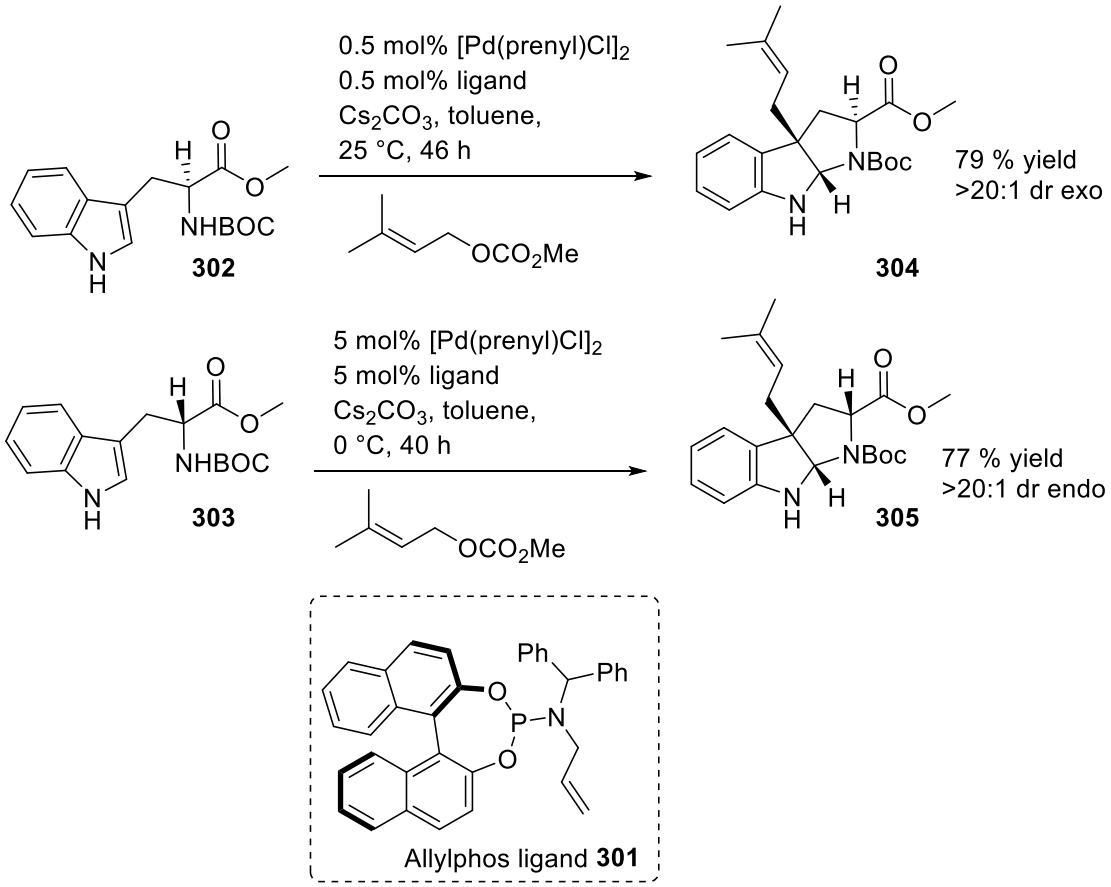

Figure 176:Chemical prenylation reactions of protected L-Trp and D-Trp **203** and **303** forming the *trans* and *cis* isomeric products using a Pd-catalysis and the allylphos ligand **301**.

In addition to the proposed chemical prenylation reactions, biocatalytic prenylation could be performed using PTases as previously described: The PTase SazB prenylates linear the *C3*-position of the LL-cWW **3a**, forming the HPI motif.[223] Similar to this enzyme, the PTase GczB prenylates linear the same substrate, but diastereo-complementary [Figure 59, chapter 4.2.3.1.1].[303] AnaPT and CdpC3PT catalyse reverse prenylation at the *C3*-position on DKP substrates [Figure 56, chapter 4.2.3.1.1].[293] Still, none of these enzymes have been tested for the single methylated DD-cWW **168b** so far. In addition to biocatalytic prenylation, alternative *N*-MTases could be explored to eliminate the need for protection groups, assuming they exhibit selective methylation of only the prenylated side of the molecule. The *N*-MTase from the nocardioazine B (**7**) biosynthetic gene cluster specifically methylates the *C3*-prenylated DD-cWW **83** before performing *C3*-methylation [Figure 34, chapter 4.2.2.3.1]. As the *C3*-methylated side is not further methylated, this enzyme could potentially be utilised for a selective late-stage *N*-methylation in the synthesis of nocardioazine B (**7**).[58]

To further expand the scope of nocardioazine derivatives, the LL-cWW **3a** could serve as a starting point. However, both StspM1 and SgMT methylate LL-cWW **3a** on both sides, eliminating the potential for selective *C3*-prenylation. During efforts to identify a mutant more efficient at methylating brominated substrate for the total synthesis of lansai B, the F184L variant demonstrated a 12% increase in efficiency for the first methylation step but exhibited a 26% decrease in activity for the second methylation reaction [Figure 116]. This observation suggests that further research could potentially identify a variant that predominantly performs only single *C3*-methylation. The mutant libraries created in earlier studies were not screened with this objective in mind. Future screening could focus on the unsubstituted cWW **3a** and the single methylated LL-cWW **168a** as substrates. The ideal mutant would retain activity towards the cWW **3a** substrate but display reduced or no activity towards the single *C3*-methylated cWW **168a**.

Beyond nocardioazine B (**7**), numerous DKP-based natural products feature HPI motifs, which could potentially be synthesised enzymatically.[59] Many of these compounds include a prenyl group at the *C3*-position.[45] As previously discussed: if SgMT can catalyze allylation, the resulting allylated product **306** could serve as precursor for further chemical modifications. For instance, in the total synthesis of nocardioazine B (**7**), a cross-metathesis reaction with 2-methyl-2-butene (**307**) converted an allyl group into a linear prenyl group with an 83% yield.[53] This strategy could open pathways to synthesise additional natural products and their derivatives using MTases. For example, starting with LL-cWW **3a**, SgMT could potentially allylate both *C3*-positions. A subsequent cross-metathesis, similar to the one employed in literature, could yield the natural product griseocazine B (**308**).[303] Following an additional *N*-methylation step, a diastereomer of streptoazine C (**139**) might be obtained [Figure 177].[223]

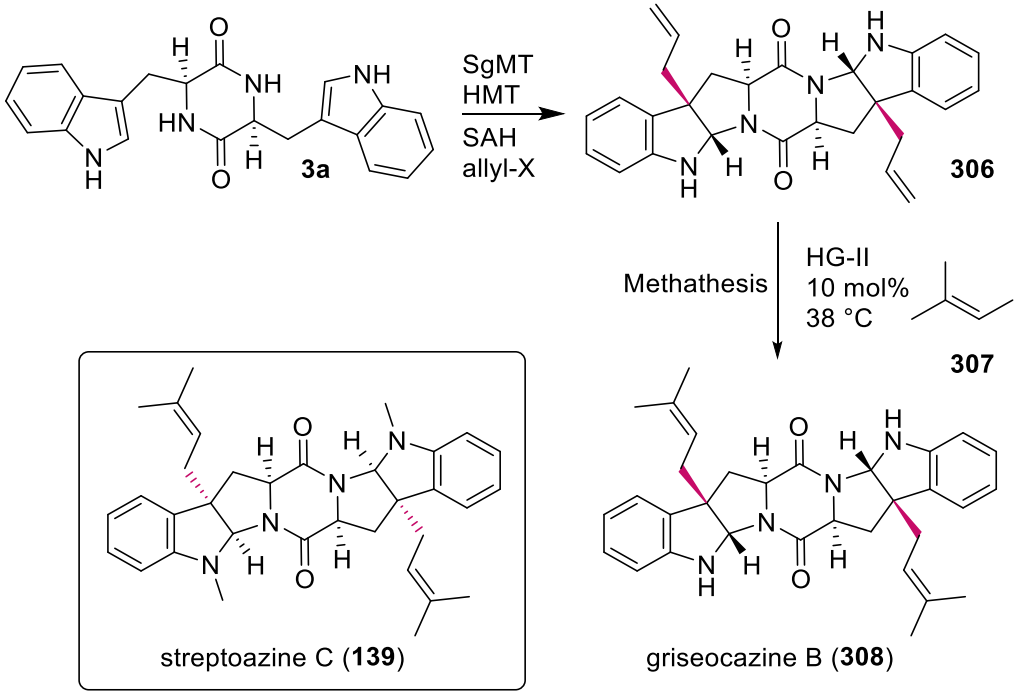

Figure 177: Strategy to for the total synthesis of further natural products and derivatives using the MTase SgMT in an allylation reaction as key step. Further modification via methathesis using the Hoveyda-Grubbs II catalyst could lead to natural product derivatives of streptoazine B (**139**) and griseocazine B (**308**).

The potential to employ metathesis expands the opportunities for structural modifications of these molecules, particularly of their three-dimensional structure. All these HPI cWW natural products feature a seven-ring system that imparts rigidity, with the three-dimensional arrangement governed by stereochemical information at the ring junctions. To better visualise their 3D conformations, simplified structures of lansai B and nocardioazine B **240** and **309** were generated. The DFT (Density Functional Theory) calculations were performed by Sebastian Myllek and Moritz Klischan. The computational method used is r2SCAN-D4/def2-TZVP/C-PCM(H2O), where r2SCAN is the DFT functional, D4 accounts for dispersion corrections, def2-TZVP is the chosen basis set, and C-PCM models solvation. The calculated 3D orientations differ: The lansai B (**5**) analog adopts a "W"-shaped structure, while nocardioazine B (**7**) analog assumes an "S"-shaped conformation [Figure 178].

In nocardioazine A (**310**), the HPI nitrogen on the methylated side is linked to the *C3*-carbon of the opposite side through a four-carbon chain containing an additional methyl group and an epoxide functional group. These atoms are relatively close to each other due to the "S"-shaped conformation of the precursor molecule nocardioazine B (**7**). Conversely, in a lansai B-like natural product, these atoms are oriented away from each other, making such a connection challenging to achieve. Instead, the "W"-shaped conformation positions the two *C3*-carbons of each side in the same direction. If the MTase SgMT can allylate both sides of the LL-cWW **3a**, an intramolecular metathesis reaction could potentially create a linker between the two sides of the molecule.

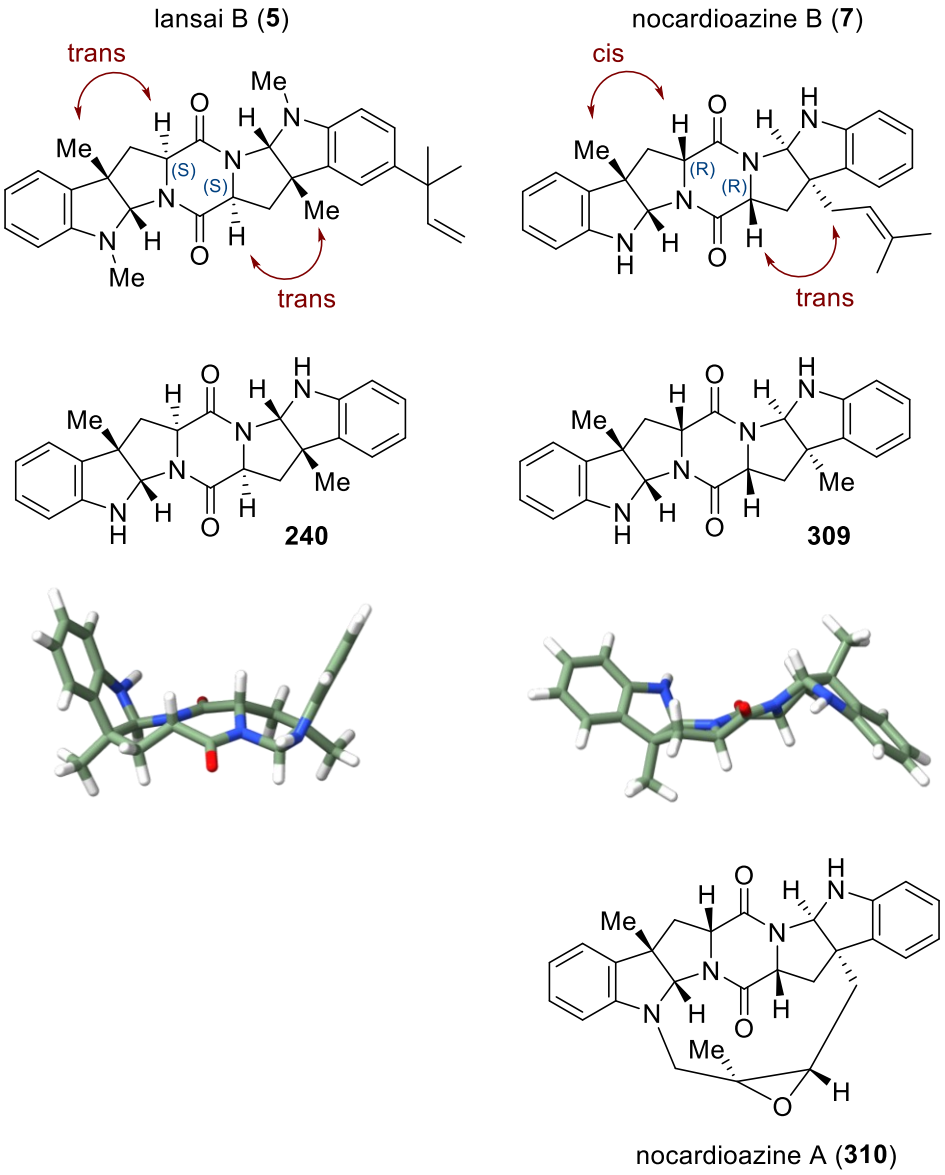

Figure 178: Structures of lansai B (**5**, left) and nocardioazine B (**7,** right). The structures were simplified and DFT calculations result in the 3D structures of the simplified analogues (by Sebastian Myllek and Moritz Klischan). Nocardioazine A displays a connection between one of the *C3*-position and the HPI nitrogen of the other side of the molecule.

6.2 Bioactivity of the synthesised compounds

The bioactivity of several cWW-based HPI natural products has been previously explored: lansai B (**5**) exhibited weak activity against the BC cell line (IC50 = 15 µg mL^{-1}),[52] while nocardioazine A demonstrated non-cytotoxic inhibition of the membrane efflux pump P-glycoprotein, effectively reversing doxorubicin resistance in multidrug-resistant colon cancer cells.[54] Various griseocazines displayed strong neuroprotective activity, protecting HT22 cells from excitotoxicity across a broad therapeutic range (1–77 µM).[303] However, the current dataset remains limited and primarily focuses on the natural products themselves. Further investigation into their bioactivity, including studies on derivatives, is therefore necessary.

In an initial attempt to evaluate the bioactivity for some of the synthesised molecules within this thesis, cell viability assays using PrestoBlue™ were conducted by the institute of Nicole Teusch. PrestoBlue™ contains resazurin, a non-fluorescent blue dye that is reduced to resorufin, a fluorescent, pink- coloured product in metabolically active cells. This reduction is primarily driven by mitochondrial activity, serving as an indicator of viable, healthy cells.[350]

Initially, two cell lines were tested: the leukaemia cell line HL60 and the lymphoma B cell line Ramos. A total of 54,000 cells per well were seeded into a microtitre plate. Following a four-hour incubation period, the cells were treated with a 100 µM concentration of the respective compound (corresponding amount of DMSO as negative control) for three days. With the applied assay, a reduction in fluorescence indicates decreased cell viability, reflecting cytotoxic activity. As substrates, lansai B (**5**) and the DKP-intermediates towards lansai B were tested.

For both tested cell lines, the unmethylated 5-Br cWW **258a** exhibited higher cytotoxicity than the subsequent *C3*-methylated intermediate **267**. Substitution of the bromine atom with a prenyl group in compound **269** led to a further increase in cytotoxicity. In the case of the HL-60 cell line, the introduction of an additional *N*-methyl group enhanced the bioactivity even further. In contrast, final *N*-methylation towards lansai B (**5**) resulted in reduced cytotoxicity against the Ramos cell line.

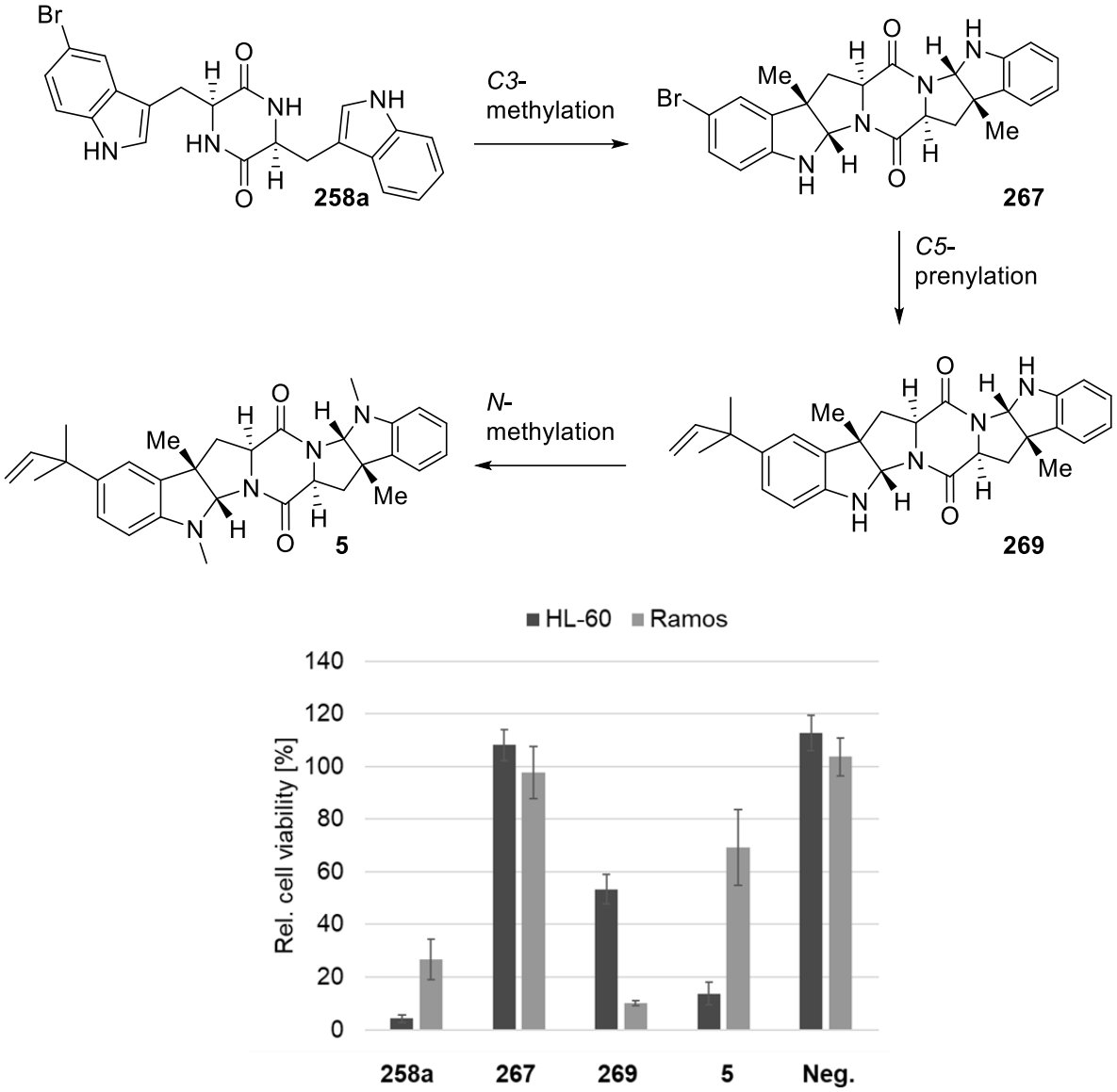

Figure 179: Cell viability of Ramos and HL-60 cells (bottom) after incubation with the lansai B derivatives which were obtained during the total synthesis of lansai B (top).

As the unmethylated 5-Br cWW exhibited strong effects on the cell viability of both cell lines, further brominated DKPs were investigated. The position of the bromine atom was varied (C4–C7), and symmetric dibrominated DKPs were additionally tested. Given that prenylation had proven advantageous for bioactivity in the previous evaluation of the lansai intermediates, the unmethylated 5-prenyl cWW was also subjected to evaluation. As a result, the dibrominated DKPs demonstrated higher bioactivity compared to the singly halogenated compounds. Bromination at positions C4 and C5 generally resulted in increased cytotoxicity of the corresponding compounds. The bioactivity of 5-prenyl cWW was comparable to that of 5-Br cWW.

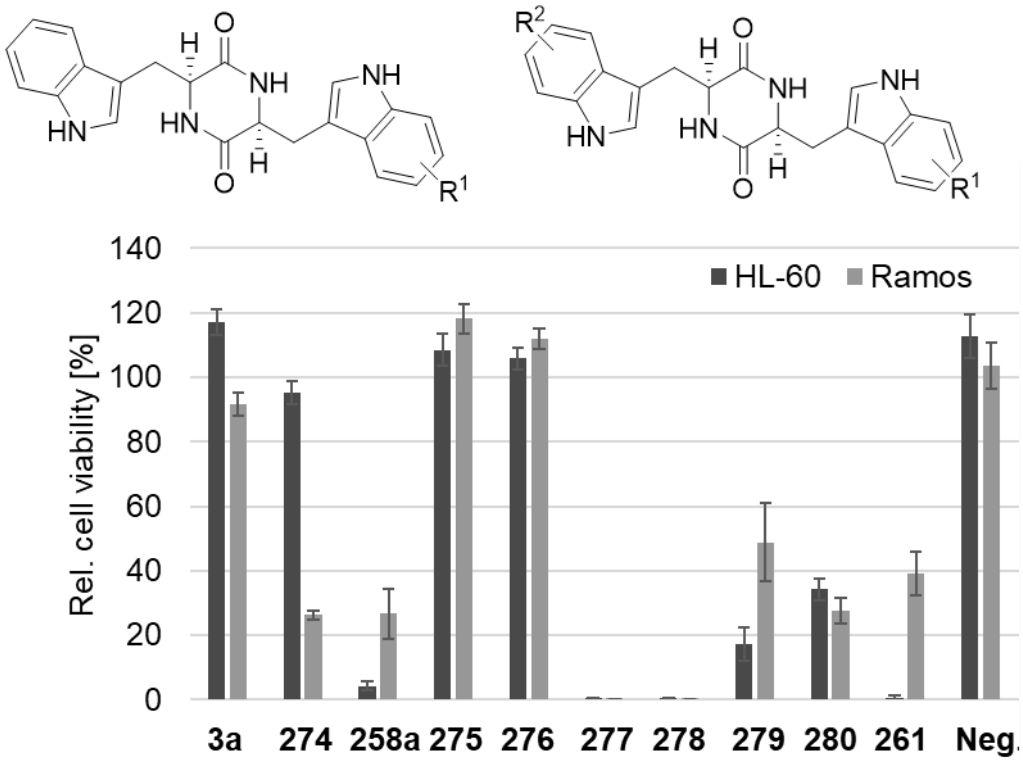

Pos. R^1+R^2	-	4	5	6	7	4	5	6	7	5
R^1	H	Br	Br	Br	Br	Br	Br	Br	Br	Pr
R^2	H	H	H	H	H	Br	Br	Br	Br	H

Figure 180: Cell viability of Ramos and HL-60 cells after incubation with the brominated and prenylated cWW derivatives.

The influence of *C3*-methylation and pyrroloindole formation was investigated for the 4-, 5-, and 7-Br cWW derivatives. The 6-Br cWW was not examined, as the methyltransferase SgMT catalyses *C3*-methylation on only one side of the molecule. Consequently, the cytotoxicity of the unmethylated (motif A), singly methylated (motif B), and doubly methylated Br-cWWs (motif C) was compared. A general trend was observed, indicating that the pyrroloindole-containing molecules exhibited lower cytotoxicity than the corresponding uncyclised indole compounds.

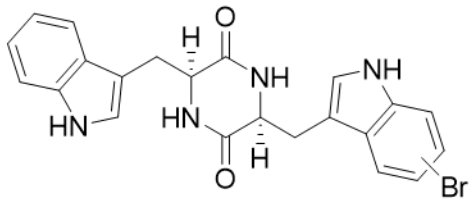

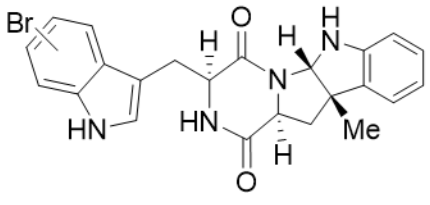

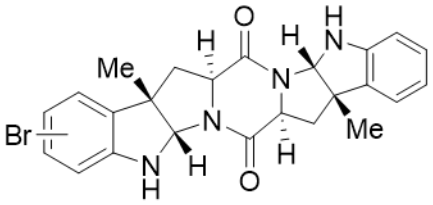

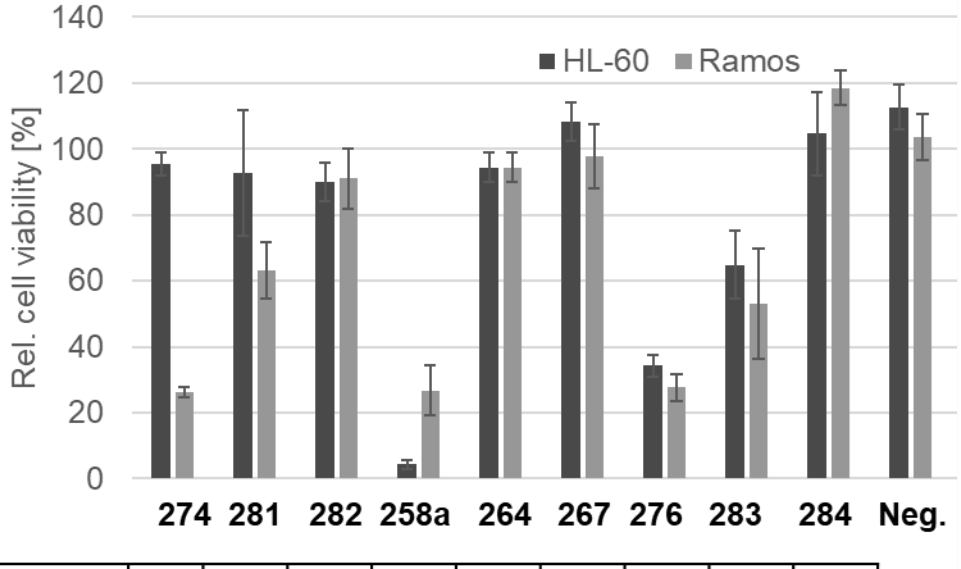

Pos. Br	4	4	4	5	5	5	7	7	7
Motif	A	B	C	A	B	C	A	B	C

Figure 181: Cell viability of Ramos and HL-60 cells after incubation with the brominated cWW derivatives after single and double *C3*-methylation.

These results highlight the potential bioactivity of the synthesised cWW substrates. In these initial tests, the cells were treated with a 100 µM concentration of the respective compounds. To obtain more detailed insights, IC_{50} values should be determined. In particular, the singly brominated cWW **258a**, the singly prenylated cWW **261**, and the doubly brominated cWWs **277** and **278** warrant further investigation, as they exhibited the highest cytotoxicity against both cell lines. The 4-Br cWW is also of interest, as it demonstrated selective activity against the Ramos cell line while showing no effect on the viability of the HL-60 cells.

The incorporation of halogens into drug structures is a well-established and widely utilised modification in medicinal chemistry. While fluorine and chlorine are more commonly employed, bromine is less frequently encountered. Still, bromine is also present in several approved drugs currently used in pharmacological applications. The presence of bromine can enhance various properties of drug candidates, such as metabolic stability, elimination kinetics, membrane permeability, and bioavailability. However, the specific effects of bromination must be assessed on a case-by-case basis.[351-353] Expanding the scope of tested substrates could include the incorporation of other halogens, such as chlorine or fluorine, into the cWW core structure. Additionally, asymmetric compounds or substrates with multiple halogen substitutions could be developed. Notably, C4- and *C5*-halogenated cWW derivatives are of particular interest due to their demonstrated high bioactivity in the first tests. Further modifications, such as altering the configuration of tryptophan, could enhance the diversity of derivatives and aid in identifying an optimal drug candidate.

The central DKP core structure could also be modified. For instance, dragmacidin (**311**), a natural product derived from the deep-water marine sponge *Dragmacidon sp.*, features a piperazine ring fused with two substituted indole rings. This compound exhibits bioactivity, inhibiting leukemic murine cells P388 (IC50 = 15 µg/mL) and showing in vivo cytotoxic effects against A-549 lung cells, HCT-8 colon cells, and MDMB breast cancer cells (IC50 = 1–10 µg/mL).[354-356] Notably, dragmacidin B (**312**) is derived from an *N*-methylated DKP **313** containing two *C5*-brominated indoles, a structure closely resembling the brominated cWW derivatives tested in this study [Figure 182].

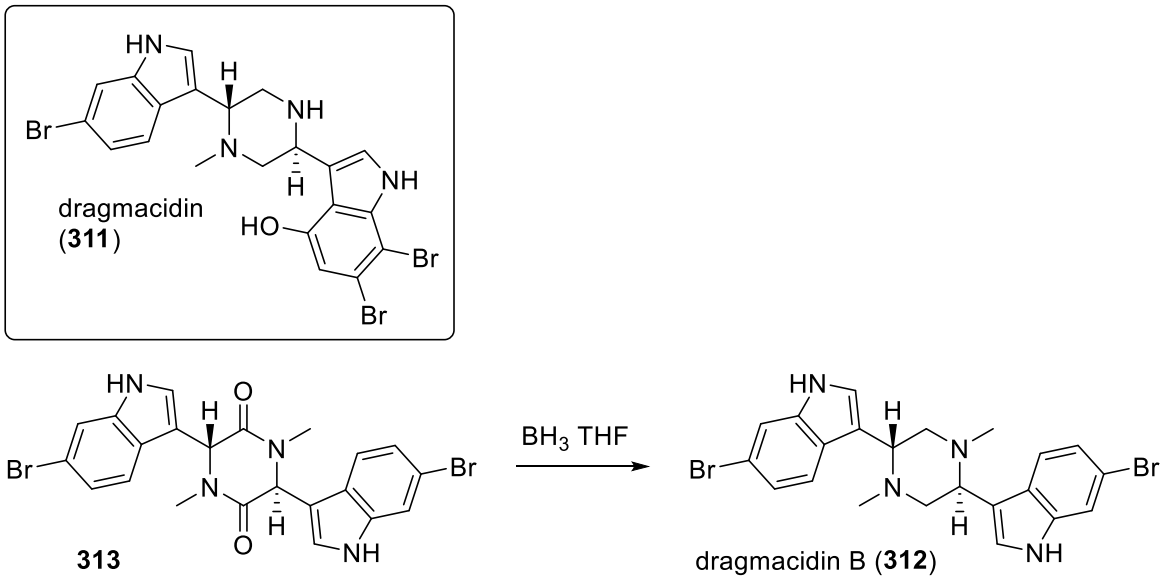

Figure 182: Chemical structure of dragmacidin (**312**) and its synthesis starting from a DKP substrate **313**.

A more detailed investigation into the bioactivity of this class of compounds, including their specific binding targets, is essential. Inspired by the natural product nocardioazine A, known for inhibiting the P-gp efflux pump in cancer cells, a study from 2024 examined 34 derivatives of *C3*-substituted cWWs **314** targeting a similar structure. Using bat cells as a model to identify effective ABCB1 inhibitors for human P-gp efflux pump modulation, compound **315** emerged as a lead ABCB1 inhibitor. This compound contains a single HPI motif, while nocardioazine A features two. However, only mono-substituted *C3*-DKPs were evaluated in the 2024 study.[357] The compounds synthesised in this thesis share structural similarity with the bioactive molecules recently investigated and present an opportunity to expand the substrate scope for identifying novel therapeutic agents. A valuable starting point for assessing their bioactivity regarding these targets would be molecular docking studies. Performing docking analysis with the human ABCB1 protein structure could offer preliminary insights into their potential activity.[357, 358] In the 2024 study, the compound **315**, which demonstrated the highest inhibitory potency against ABCB1, showed the highest binding complementarity within the access tunnel of the target protein indicated by the largest docking score [Figure 183].[357]

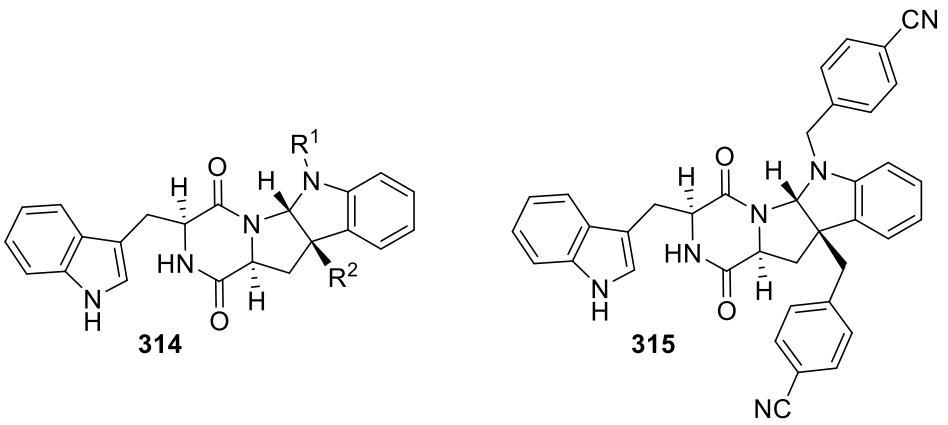

Figure 183: General structure of the tested derivatives of the LL-cWW **314**. The residues varied between the 34 tested derivatives. the compound **315** demonstrated the highest inhibitory potency against ABCB1.

6.3. Biosynthesis analysis

The gene clusters in *Streptomyces griseoviridis* and *Streptomyces* sp HPH0547 have been analysed. Both gene clusters contain a gene for a CDPS, a gene for a PTase and two genes coding for different MTases. The CDPSs were analysed on a theoretical level by identifying the consensus motifs for substrate binding. SgCDPS and StspCDPS are most likely to produce the cWW **3a**. The *C3*-MTases SgMT1 and StspM1 were analysed in detail (previous chapter). The MTases SgMT2 and StspM2 were identified as *N*-MTases which methylate the *N1*-position of the HPI motif. The PTases SgPT and StspPT were analysed on a theoretical basis. Only SgPT showed activity proving its ability to prenylate the *C5*-position of the *C3*- and *N*-methylated cWW **287** forming lansai B (**5**). To validate this biosynthetic sequence, the metabolites— cWW **3a**, *C3*-methylated cWW **240**, *C3*- and *N*-methylated cWW **287** and lansai B (**5**)—were extracted from *Streptomyces griseoviridis* and their identities confirmed by comparison with synthetic standards via LC-MS.

6.3.1 *N*-Methyltransferase

The structures of StspM2 and SgMT2 have been modelled, and the SAM binding sides were identified. The architecture of these enzymes was analysed and compared to known HPI MTases highlighting the *α*-cap domain. SgMT2 and StspM2 were successfully expressed and purified. StspM2 was used in a preparative reaction (25 mg) to identify the position of the enzymatic methylation: a *N1*-methylation. The substrate scope with potential intermediates of the lansai B (**5**) biosynthesis was investigated. Additionally, the temperature optimum StspM2 was determined at 30 °C.

StspM2 and SgMT2 should be further characterised regarding their pH optima and the temperature optimum of SgMT2. The kinetic parameters should be determined for a comparison with different other *N*-MTases. The expression of StspM2 is higher than for SgMT2, but a lot of the enzyme forms inclusion bodies leading to insoluble protein. If these MTases would be used as catalysts for natural product synthesis in larger scale, the amount of functional catalyst per gram scale is very important. To improve expression, further optimisation should be explored, such as testing different strains, incorporating additives, or utilizing a solubility tag, similar to the expression screening performed for StspPT. In the context of synthetic utility, the immobilisation of these enzymes could be considered as it simplifies the handling and decreases the amount of solvent necessary for the extraction.

SgMT2 and StspM2 are *N*-MTases that possess an *α*-cap domain similar to these of SazB-MT and DmtMT2. There is no crystal structure available for this kind of HPI MTases, which could give insides into the exact structure. As SgMT2 and StspM2 are soluble enzymes, which can be easily purified via Ni-NTA chromatography, they could be crystallised to determine the X-ray structure. Additionally, as SgMT2 and StspM2 are *N*-MTases, the position of the DKP substrate within the active side has not been investigated yet. A docking study would clarify the position and help with understanding the mechanism of this enzymes, as they do not contain the catalytic triade at the same position as other HPI MTases (PsmD, PsmC, SgMT, StspM1).

In SgMT2 and StspM2, the catalytic tyrosine present in *C3*-methyltransferases is replaced by a histidine residue (H145/H143). Additional to this residue, an aspartate (D139/D141) and a tyrosine (Y14/16) are in the direct environment [Figure 184]. Their catalytic function could be proven by mutating them to an alanine (phenylalanine for tyrosine) and testing the activity of the mutants (alanine scan). These residues are also present in SazB-MT and DmtMT2 indicating their importance for activity.

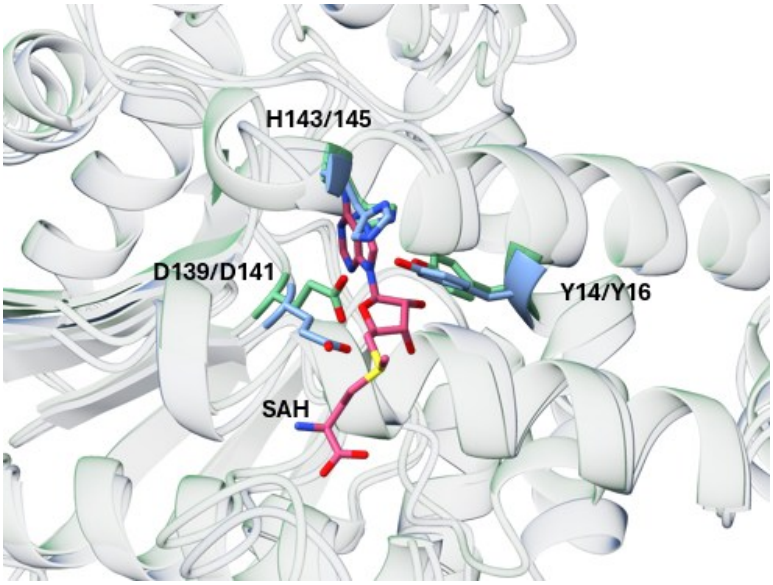

Figure 184: Structure of SgMT2 and StspM2. The potential catalytic residues are highlighted in blue (SgMT2) and green (StspM2). The SAH (**94**, pink) was extracted from the crystal structure of SgMT.

SazB-MT and DmtMT2 have a relatively high substrate promiscuity compared to other HPI MTases. The substrate scope of SgMT2 and StspM2 has not been investigated yet. The natural substrate of SgMT2 and StspM2 is the already *C3*-methylated cWW **240**, which is very rigid due to the seven-rings-structure. The less rigid single *C3*-methylated cWW **168** as intermediate should be tested to investigate, if the 3D seven-rings-structure is crucial. If not, different other DKP **316**, which contain the *C3*-methylated tryptophan on one side and a different amino acid on the other side would be interesting to investigate to explore the substrate scope. One interesting example of this substrate scope would be the *C3*-methylated cWP **317** as the proline builds a five membered ring to extend the ridged HPI-DKP ring system.

Additionally, the substrates **149** and **151** of the known *N*-HPI-MTase PsmC should be tested for acceptance. Another interesting substrate class are the *C3*-prenylated cWW natural products derived from streptoazine (**139**). The natural substrate of SazB-MT and derivatives **293, 294, 318** and **319** with branched prenyl groups can be synthesised chemically as previously described or biochemically with different PTases.[59, 294, 359] Especially the compounds **224** and **319** are promising, as the prenyl groups point in the same reaction as the methyl groups in the natural substrate [Figure 185].

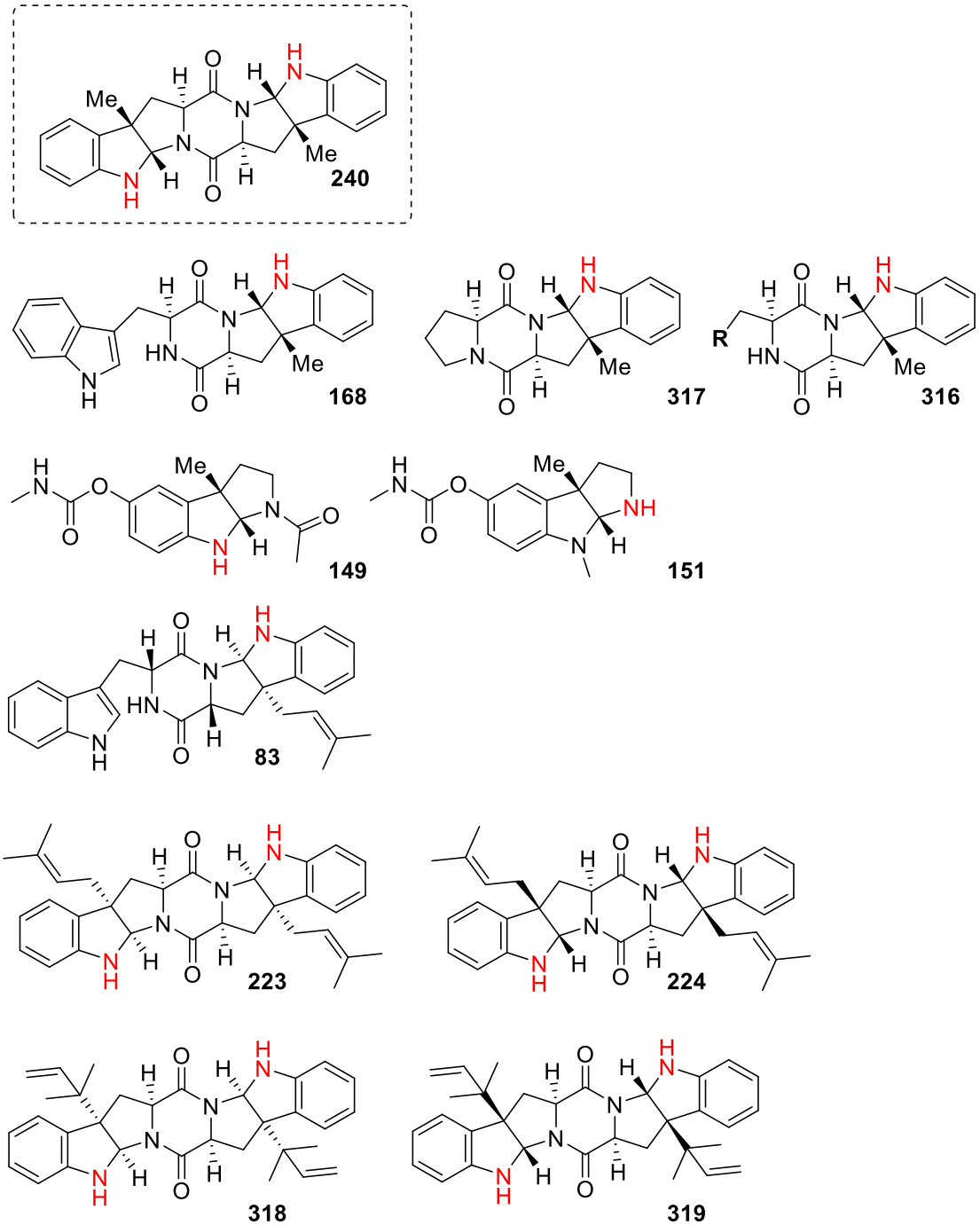

Figure 185: Potential substrate scope of SgMT2 and StspM2.

6.3.2 Prenyltransferase

The prenyltransferases SgPT and StspPT were theoretically analysed and heterologous expressed. Despite numerous efforts, the solubility of theses enzymes remained low.

In a parallel study, Duan *et al*. reported similar difficulties in achieving soluble expression of LanB, a homolog of StspPT. These challenges were overcome by employing the inducible *tsr* promoter system in *Streptomyces coelicolor* M1146, enabling successful protein production.[137] Given the high sequence similarity between LanB and StspPT, implementation of this expression strategy may represent a promising approach to obtain soluble and active StspPT for further biochemical characterization.

The use of a Trx-tag, which had been employed to enhance the solubility of the structurally similar PTase DmtC1 reported in the literature, did not result in improved solubility. Exploring alternative solubility tags may be beneficial. For instance, the structurally related PTase NzsG contains an *N*-terminal small ubiquitin-like modifier (SUMO) tag to enhance its solubility.[360, 361] Solubility tags are typically positioned at the *N*-terminus, as they are expressed first, aiding the proper folding of the target protein and enhancing its solubility. The PTase SazB is fused to an *N*-MTase from the same gene cluster at its *C*-terminus.[103] Therefore, attaching a solubility tag or fusing the corresponding *N*-MTase to the *C*-terminus could potentially enhance the solubility of StspPT or SgPT as well.

If solubility cannot be improved during protein expression, the insoluble protein can be unfolded and subsequently refolded. Various strategies and methods are available for this process. Typically, inclusion bodies are solubilised using high concentrations of denaturants like urea or guanidine hydrochloride.[362, 363] In an initial attempt, the Trx-tagged StspPT protein was resolubilised by resuspending the insoluble pellet fraction in lysis buffer containing 8 M urea. Successful resolubilisation was confirmed via SDS-PAGE [Figure 186]. The supernatant was then diluted to a final urea concentration of 0.4 M to promote protein refolding. However, the protein precipitated again during this process and could not be refolded into a soluble form. Alternative methods, such as dialysis or gel filtration, could be employed to gradually reduce the denaturant concentration allowing renaturation. Additionally, incorporating additives during the refolding process may enhance the solubility.[362, 363]

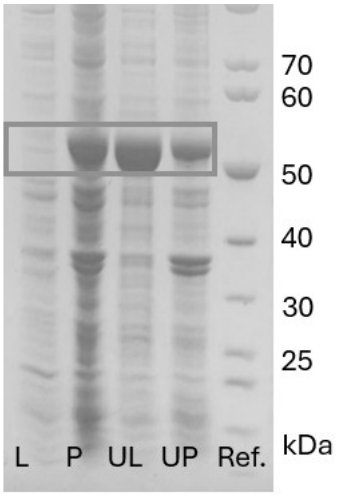

Figure 186: SDS-gel of StspPT with the solubility Trx-Tag (55 kDa). After cell lysis, both the lysate (L) and pellet fraction (P) were applied to the gel. The pellet was resolubilised by resuspending it in lysis buffer containing 8 M urea. After centrifugation the Urea containing supernatant (UL) and the pellet (UP) were applied to the SDS-gel.

Despite their limited solubility, SgPT catalyzes the *C5*-prenylation of the *C3*- and *N*-methylated cWW substrate **287** to produce lansai B (**5**). Because reaction parameters were not optimized, systematic biochemical characterization (including determination of pH and temperature optima, as well variation of the DMAPP and $MgCl_2$ concentrations) could enhance the enzyme activity.

In contrast, none of the StspPT constructs exhibited detectable activity under the conditions tested. Given the high degree of active-site homology between StspPT and LanB, StspPT is likely capable of the same transformation. Computational docking simulations could be used to validate this hypothesis and to map the substrate-binding interactions within StspPT. Cultivation of *Streptomyces* sp. HPH0547 and subsequent metabolomic profiling of pathway intermediates would provide *in vivo* evidence for the involved enzymes and therefore for the activity of StspPT.

7. EXPERIMENTAL PART

7.1 Biological and general methods

7.1.1 Protein sequence and vectors

The gene sequence for the MTases SgMT, SeMT, SaMT, ThMT and MtMT were codon harmonised and synthetically constructed with a *N*-terminal His-Tag in a pET28a(+) vector (GenScript, USA). Beatrix Paschold conducted cloning experiments to relocate the His-tag from the *N*-terminus to the *C*-terminus. The variants of the alanine scan for SgMT and the 9xmutant of SeMT were directly ordered with the *C*-terminal His-Tag. The gene sequences of StspM1 and NozB-CYIM were synthetically constructed in a pET21a(+) vector (GenScript, USA) by Pascal Schneider.

7.1.2 Bacterial strains and media

E. coli BL21(DE3), *E. coli* BL21(DE3) or *E. coli* Arctic Express (DE3) were selected for cultivation and protein expression. For pre cultures, LB (lysogeny broth) liquid medium (10 $g \cdot L^{-1}$ tryptone, 5 $g \cdot L^{-1}$ yeast extract, 2 $g \cdot L^{-1}$ sodium chloride) and for main cultures TB (terrific broth) liquid medium (Carl Roth, Karlsruhe, Germany: 12 $g \cdot L^{-1}$ casein, 24 $g \cdot L^{-1}$ yeast extract, 12.54 $g \cdot L^{-1}$ K_2HPO_4, 2.3 $g \cdot L^{-1}$ KH_2PO_4, 4 $mL \cdot L^{-1}$ glycerol) with the antibiotic (final concentration of 100 $\mu g \cdot mL^{-1}$) was used. The culture media were prepared with distilled water and sterilised by autoclaving.

7.1.3 Transformation

Competent *E. coli* cells were transformed by heat shock with the desired plasmid. For this, 100 ng plasmid DNA was added to 100 µL of competent cells and incubated for 30 min on ice. After incubation, the cells were heated in a water bath at 42 °C for 90 seconds. 700 µL LB medium was added and the cells were inverted with an overhead shaker at 37 °C for 1 hour. The transformed cells were centrifuged at 2000 rpm for two minutes to harvest a cell pellet. The cell pellet was resuspended in 100 µL LB medium and cultured on LB medium agar plates with kanamycin at 37 °C overnight.

7.1.4 Protein expression

As a preculture, 5 mL of LB medium with kanamycin was inoculated with a colony from the transformed cells and incubated at 37 °C for 16 hours. The preculture was used to inoculate the main culture (500 mL TB medium) at a dilution of 1:100. The main culture was incubated at 37 °C and 130 rpm until an OD600nm of 0.5 was reached. The protein expression was induced by adding the inducer IPTG (final concentration of 100 µM). After incubation at the desired temperature for 20 h, the cells were harvested by centrifugation at 7000 g for 35 minutes at 4 °C. The cell pellet was stored at -20 °C until further use. As standard conditions, the protein expression was induced with 100 mM IPTG before incubation over night at 25 °C. For *E. coli* Arctic Express (DE3), the protein expression was started after incubating the culture for 20 min on ice at a temperature of 15 °C for two days.

7.1.5 Enzyme purification (large scale, protocol by Nadiia Pozhydaieva)[319]

The cells were resuspended at a concentration of 0.2 g/mL in KPi buffer (50 KPi, pH 7.5) and lysed by sonication with an ultrasonic cell disruptor (Branson Sonifier II "Modell W-250", Heinemann) two times for 10 min (amplitude of 35–40%). After centrifugation at 7000 rpm for 30 min, the lysate was loaded on a Ni-NTA affinity chromatography column (5 mL HiTrap HP column, Bio-Rad) with a flow rate of 3 mL/min. A washing step was performed by washing the column with 25 mL in 5 x 5 mL fractions serving as W1-W5 with 50 mM KPi (100 mM ImH, pH 7.5). The enzyme was eluted with 15 mL (in 3 x 5 mL fractions, E1-E3) of the elution buffer (50 mM KPi, 250 mM ImH, pH 7.5). To exchange the buffer and concentrate the protein, protein concentrators (Vivaspin 20, 10000 MWCO PES, Sartorius Stedim Biotech) were used. The concentrated protein solution in KPi buffer (50 mM, pH 8) was frozen in liquid nitrogen and kept at −20 °C until usage.

7.1.6 Enzyme purification (large scale, optimised)

The cells were resuspended at a concentration of 0.2 g/mL in KPi buffer (50 KPi, pH 7.5) and lysed by sonication with an ultrasonic cell disruptor (Branson Sonifier II "Modell W-250", Heinemann) two times for 10 min (amplitude of 35–40%). After centrifugation at 7000 rpm for 30 min, the lysate was loaded on a Ni-NTA affinity chromatography column (5 mL HiTrap HP column, Bio-Rad) with a flow rate of 3 mL/min. An optional washing step was performed by washing the column with 15 mL 50 mM KPi (40 mM ImH, pH 7.5). A second washing step was performed by washing the column with 15 mL 50 mM KPi (80 mM ImH, pH 7.5). The enzyme was eluted with 15 mL of the elution buffer (50 mM KPi, 160 mM ImH, pH 7.5). To exchange the buffer and concentrate the protein, protein concentrators (Vivaspin 20, 10000 MWCO PES, Sartorius Stedim Biotech) were used. The concentrated protein solution in KPi buffer (50 mM, pH 8) was frozen in liquid nitrogen and kept at −20 °C until usage.

7.1.7 Enzyme purification (small scale)

200 mg cells were resuspended in 1 mL KPi buffer (50 KPi, pH 8) and lysed by glass bead (0.2 mm) cell disruption for 10 min and 30 Hz with a swing mill (Retsch, Type MM400). After centrifugation at 7000 rpm for 30 min, the lysate was added to 100 µL washed Ni-NTA agarose beads and incubated for 40 min by slowly inverting on ice. A washing step was performed by washing the beads with 1 mL 50 mM KPi (40 mM ImH, pH 7.5). The enzyme was eluted with 500 µL of the elution buffer (50 mM KPi, 250 mM ImH, pH 7.5). To exchange the buffer and concentrate the protein, centrifugal concentrators (Vivaspin 500, 10000 MWCO PES, Sartorius Stedim Biotech) were used. The concentrated protein solution in KPi buffer (50 mM, pH 8) was frozen in liquid nitrogen and kept at −20 °C until usage.

7.1.8 Size exclusion chromatography

Size Exclusion chromatography was performed on a Superdex™ G200 HiLoad 16/600 column (Cytiva) at 25 °C and a flow rate of 0.75 mL/min using an ÄKTA Purifier device. The Calibration for the analytic Size Exclusion chromatography was performed using a gel filtration marker kit for protein molecular weights 12000-200000 Da (Sigma) including blue dextran, *α*-amylase, cytochrome C, alcohol dehydrogenase, BSA, and carbonic anhydrase with KPi buffer (10 mM, 150 mM NaCl, pH = 7.5) as mobile phase.

7.1.9 General procedure for MTase glo assay

The commercially available MTase Glo Assay was used to determine the activity of the MTase according to the manufacturer's protocol. The luminescence was measured using a plate reader (Infinite plate reader, Tecan). Every reaction was carried out as triplicate in a 96-well plate (Nunc™ 96-well plates (Nunclon®; Polystyrene, flat bottom, white). The reactions were performed with a final concentration of 25 µM SAM (**93**) and the additional substrate at the desired temperature. The reactions were stopped after five, ten, or 15 min and ended by adding 0.5 % TFA. For the usual activity measurements, a reaction time of 15 min was chosen (temperature optimum, substrate screen, variants comparison). The enzyme concentration varied depending on the enzyme, usually 3 µM for StspM1, SgMT and SaMT and 10 µM for SeMT and 40 µM for ThMT and MtMT, if not stated otherwise. The kinetic parameters were determined using the Michaelis-Menten equation and calculated with the software Origin Pro 2017G (OriginLab Corporation, Northampton, MA, USA).

7.1.10 *In-vitro* assay for MTases

The substrates were dissolved in DMSO (100 mM). The reactions were performed with in 50 mM KPi buffer (pH 7.5 for all MTases except for SgMT at pH 8) with an end concentration of 1 mM substrate and 3 mM SAM (**93**) at 40 °C (C-MTases) or 30 °C (*N*-MTases) and 700 rpm if not stated otherwise. The experiments were performed either with pure enzyme, lysate or whole cells. As standard conditions, 50 µg pure enzyme, 34 Vol% lysate or 20% W/V of whole cells are used if not stated otherwise. For reaction with the coupled recycling system, the desired amounts of MTase lysate and HMT lysate were added plus the desired amount of MeI (1 M stock solution in DMSO). The lysate was produced by sonication of the cells in lysis buffer (0.2 g/mL) with an ultrasonic cell disruptor (Branson Sonifier II "Modell W-250", Heinemann) for 10 min and an amplitude of 35–40%. The reactions were stopped by addition of 20 % acetonitrile or 0.5 % TFA and analysed by RP-HPLC (Jasco HPLC).

For the literature repetition, the conditions varied: 50 mM Tris (pH 7.5, 100 mM NaCl), 1 mM SAM (**93**), 1 mM cWW **3**, 40 µM StspM1, 120 min, 30 °C. These conditions were varied in an initial optimised experiment: pH 7.5, 50 mM KPi, 1 mM SAM (**93**), 1 mM cWW **3**, 40 µM stspM1, 120 min, 40 °C.

7.1.11 *In-vitro* assay for PTases

The substrates were dissolved in DMSO (100 mM). The reactions were performed with in 50 mM KPi buffer (pH 8 + 2.5 mM $MgCl_2$) with an end concentration of 1 mM substrate and 2 mM DMAPP at the 30 °C temperature and 700 rpm if not stated otherwise. The experiments were performed either lysate or resuspended pellet. The lysate was produced by sonication of the cells in lysis buffer (0.2 g/mL) with an ultrasonic cell disruptor (Branson Sonifier II "Modell W-250", Heinemann) for 10 min and an amplitude of 35–40%. The reactions were stopped by addition 1% TFA.

7.1.12 pH optimum determination

SgMT: A reaction mixture was prepared by combining 1 mM cWW substrate **3a**, 1 mM SAM (**93**), and 50 µg of enzyme in reaction buffer to a final volume of 100 µL. The mixture was incubated at 45 °C with shaking at 300 rpm for 1 hours and 30 minutes. The reaction was then quenched by adding TFA to a final concentration of 1%. Conversion rates were analysed using HPLC. RP-HPLC was performed using a Jasco HPLC system

SeMT: A reaction mixture was prepared by combining 1 mM cWW substrate **3a**, 1 mM SAM (**93**), and 50 µg of enzyme in reaction buffer to a final volume of 100 µL. The mixture was incubated at 30 °C with shaking at 300 rpm for 4 hours and 45 minutes. The reaction was then quenched by adding TFA to a final concentration of 1%. Conversion rates were analysed using HPLC. RP-HPLC was performed using a Jasco HPLC system

7.1.13 HPLC method

To compare the retention times of the products with the references, the following HPLC-method was used:[100]

RP-HPLC: Jasco HPLC (pump: PU-4180, thermostat: CO-2060Plus, autosampler: AS-4050)
Stationary Phase: hyperclone column (5µ ODS C18, 125*4 mm, 120 Å, Fa. Phenomenex); mobile phase A: Acetonitrile + 0.1% formic acid (v/v) and B: water + 0.1% formic acid (v/v) Gradient: 0-2 min: 10:90 (A:B), 2-15 min: 10% A to 50% A, 15-25 min: 50% A to 95% A, 25-30 min: 95:5 (A:B), 30-35 min: 10:90 (A:B).
Flow rate: 0.8 mL/min
Column temperature: 25 °C
Detection wavelength: 284 nm

7.1.14 HMT activity

For measuring the HMT lysate activity a total volume of 1 mL in 1.5 mL Eppendorf tubes was chosen. SAH (**94**) and MeI as substrates were dissolved in DMSO. The reactions were performed in KPi buffer (pH 7.5, 50 mM) with an end concentration of 1 mM SAH (**94**) and 10 mM MeI at 40 °C and 700 rpm. The desired amount of HMT lysate (1% - 3%) were added additional to the substrates. The lysate was produced by sonication of the cells in lysis buffer (0.2 g/mL) with an ultrasonic cell disruptor (Branson Sonifier II "Modell W-250", Heinemann) for 10 min and an amplitude of 35–40%. The reactions were stopped by addition of 0.5% TFA after 3, 6, and 9 min and analysed by RP-HPLC (Jasco HPLC). As stationary phase, the hyperclone column (5µ ODS C18, 125*4 mm, 120 Å, Fa. Phenomenex) was used. As mobile phase A: Acetonitrile and B: 10 mM NaH_2PO_4 buffer (5 mM heptane sulfonic acid, pH 3.5) were used with the following gradient: 0-5 min: 5:95 (A:B), 5-20 min: 20:80 (A:B), 20-24 min: 80:20 (A:B), 24-35 min: 95:5 (A:B), 30-35 min: 10:90 (A:B). Flow rate was set to 0.8 mL/min and the column temperature was kept at 25 °C. As detection wavelength, 260 nm was chosen. 30 µL of each sample were injected.

7.1.15 Design of experiment (StspM1+HMT)

A response surface design of experiment approach was chosen with the methyl iodide concentration, the StspM1 lysate amount, and the CtHMT lysate as factors and the conversion after 24 h as response. The Design Expert 12 (12.0.7.0) was used to create the conditions. Two additional negative controls were measured. The reactions were carried out randomised under the in vitro assay conditions.

7.1.16 His-Tag removal

Thrombin from bovine plasma ordered from Sigma-Aldrich was used to cleave the His tag. The reaction was carried out in buffer (KPi buffer 10 mM with 140 mM NaCl, 2.7 mM KCl, pH 7) with 50 U thrombin per mg enzyme overnight at 16 °C and 700 rpm.

7.1.17 Enzymatic preparative scale reaction with immobilised enzyme

The cell pellet was lysed in reaction buffer (50 mM KPi, pH 7.5) at a concentration of 1 g/5 mL. The lysate was prepared by sonicating the cells in lysis buffer using an ultrasonic cell disruptor (Branson Sonifier II "Model W-250", Heinemann) for 10 minutes at 35–40% amplitude, performed twice. After centrifugation (4°C, 10,000 × rcf, 20 minutes), the supernatant was collected as the lysate. The lysate was then incubated with washed Protino® Ni-NTA agarose suspension (1:10 concentration) at 4°C for 40 minutes on an end-over-end shaker. After removing the supernatant, the washing solution (50 mM KPi, pH 7.5, 40 or 80 mM ImH) was added and incubated for 10 minutes at 4°C on an end-over-end shaker. The supernatant was discarded, and the immobilised enzyme was washed twice with reaction buffer (50 mM KPi, pH 7.5) to remove any residual imidazole. The enzyme-bound Ni-NTA material was transferred into a glass bottle. The cWW substrate **3** was dissolved in DMSO and added to the reaction mixture, along with SAM disulfate tosylate **93**. The reaction was carried out in KPi buffer (50 mM, pH 7.5) at a final concentration of 1 mM cWW substrate, at 40°C and 300 rpm. After 48 hours, the reaction was stopped by removing the Ni-NTA material via filtration. The product was extracted with ethyl acetate (three times), the organic phase was dried with $MgSO_4$, and concentrated under reduced pressure. The final products were purified via column chromatography (using ethyl acetate).

7.1.18 Immobilisation protocol (small scale)

0.2 mL of the homogeneous suspension of Ni-NTA Agarose were transferred in a 2 mL Eppendorf tube. The resin was settled by gravity and the supernatant was removed. 1 mL lysis buffer were added and gently resuspended. The supernatant was removed after settling down. 2 mL cleared lysate were added to the equilibrated Ni-NTA Agarose resin and incubated at 4 °C for 40 min on an end-over-end shaker. The superintend was removed and 1 mL washing solution (lysis buffer + 80 mM ImH (StspM1 or 40 mM ImH (HMT)) were added and incubated at 4 °C for 10 min on an end-over-end shaker. After removing the supernatant, 2 mL lysis buffer were added again and the mixture was ready to use.

7.1.19 Extinction coefficient determination

The absorption was measured with the Nanodrop 2000c (Thermo Scientific) in a concentration range from 0.2 mM to 1 mM in water: acetonitrile in a 4:1 ratio in duplicates. The path length of the system is 0.1 cm.

7.1.20 SgMT and SeMT crystallisation

The SgMT protein was crystallised using the vapour diffusion method in sitting-drop geometry, using robotic systems Freedom Evo (Tecan; Männedorf, Switzerland) and Mosquito LCP (SPT Labtech; Melbourn, United Kingdom) with commercially available screening sets. Protein crystals were observed for several conditions, several of which were subjected to matrix optimisation and additive screening. The diffraction-quality sample used for structure determination in this study was obtained with a reservoir solution containing 85.5 mM sodium citrate pH 5.6, 17.1% (v/v) isopropanol, 17.1% (w/v) PEG 4000, 4.5% (v/v) glycerol, 10 mM hexammine cobalt(III) chloride and a protein solution containing 8.4 mg/ml SgMT with 2.2 mM SAH (**94**) and 2 mM LL-cWW **3a**. Prior to cryocooling, the crystal was shortly incubated in reservoir solution supplemented with 12% (v/v) glycerol.

Wild-type SeMT was crystallised using the sitting-drop vapour diffusion method, using robotic systems Freedom Evo (Tecan; Männedorf, Switzerland) and Mosquito LCP (SPT Labtech; Melbourn, United Kingdom) with commercially available screening sets. Initial protein crystals were observed with reservoir solutions containing either 2.0 M ammonium sulfate, or 1.0 M lithium sulfate, 0.5 M ammonium sulfate, 0.1 M sodium citrate pH 5.6, which were subjected to matrix optimisation and additive screening. The diffraction-quality sample used for structure determination in this study was obtained with 0.9 M lithium sulfate, 0.45 M ammonium sulfate, 0.09 M sodium citrate pH 5.6, and 3% (w/v) 1,6-diaminohexane in the reservoir and a sample containing 8.2 mg/ml SeMT and 2 mM SAH (**94**) in 10 mM Tris-HCl pH 7.0, 100 mM NaCl and 4% (v/v) DMSO. While harvesting the crystal, it was shortly submerged in perfluoropolyether (Hampton Research; Aliso Viejo, USA) for cryoprotection.

7.1.21 Mutagenesis

Libraries: Amino acids at selected positions were modified using iterative saturation mutagenesis. Mutant libraries were created by applying the 22c-trick, which minimises codon redundancy and reduces library size. Degenerate primer mixtures were utilised in a whole-plasmid amplification PCR approach, with the intended mutation introduced at the centre of the forward primer.

Single mutation: The intended mutation was introduced at the centre of the forward primer. The codon with the least base changes was picked compared to the original codon of interest.

After amplification, PCR products were digested with DpnI at 37 °C for 1 hour and analysed on a 1% agarose gel (45 minutes at 100V) using Midori Green staining. The gel-purified products were ligated with T4 DNA ligase, using 6% (v/v) PEG 4000 to enhance efficiency. For transformation, 20 µL of the ligated product was added to chemically competent *E. coli* DH5*α* cells, which were heat-shocked to facilitate plasmid uptake. Plasmid isolation was performed with an Innuprep plasmid isolation kit (Analytik Jena), and sequencing confirmed successful introduction of the desired mutations.

Component	**Volume (µL)**
5X PrimeSTAr GXL Buffer	10
dNTP (2.5 mM)	4
Primer fw (10 µM)	1.5
Primer rev (10 µM)	1.5
Template vector (10 ng/µL)	0.7
PrimeSTAR polymerase	1
ddH2O	31.3
TOTAL	50

Step	Temperature (°C)	Time	Cycles
1	98	30 s	
2	98	10 s	17X
3	Touchdown	15 s	
4	68	3 min	
5	98	10 s	25X
6	55	15 s	
7	68	3 min	
8	68	5 min	
9	4	storage	

7.1.22 Reaction optimisation for the 5-Br cWW and the DD-cWW

A reaction mixture was prepared with 1 mM cWW, 2.5 mM SAM (**93**), and 10–100% lysate (v/v) od SgMT in KPi buffer (50 mM, pH 8) in a total volume of 500 µL. The mixture was incubated at 45 °C with shaking at 700 rpm for 20 hours. To stop the reaction, TFA was added to a final concentration of 0.5% (v/v). A 50 µL aliquot of each sample was subsequently analysed following the different assay procedures.

7.1.23 HPI Assay (short protocol)

A 50 µL aliquot of the analyte aqueous solution was pipetted into a 96-well clear microtiter plate. To this, 30 µL of 1 M H_2SO_4 was added, mixed thoroughly, and incubated for 10 minutes. Then, 2.5 µL of a 50 mM cerium sulfate solution (in water with 0.5% v/v H_2SO_4) was added, and the mixture was well-mixed. Absorbance was measured at 470 nm using a Tecan® plate reader.

7.1.24 Indole Assay (short protocol)

A 50 µL aliquot of the analyte aqueous solution was pipetted into a clear 96-well microtiter plate. To this, 50 µL of concentrated H_2SO_4 (98%) was added, and the mixture was incubated at room temperature for 10 minutes. Then, 50 µL of a 300 mM of p-dimethylaminobenzaldehyde solution in isopropanol was added and mixed thoroughly. The reaction mixture was then exposed to 405 nm LED light for 10 minutes. Following the exposure, absorbance was measured at 560 nm using a Tecan® plate reader.

7.1.25 Automated Screening Process

For the automated library screening the previously described AutoBioTech platform as well as an OT-2 liquid handler (Opentrons, USA) were used.[326]

Per library, 66 colonies were picked using a Tecan Fluent (Tecan, Switzerland) with integrated colony picker (Pickolo, SciRobotics, Israel) to inoculate 900 µL LB media in a square well deep well plate (sqDWP). 10 µL of cryo-cultures of an pET21a empty vector as well as pET21a(+) with PsmD wild type were additionally carried on each plate as negative and positive control. After 16 hours at 800 rpm and 37°C, 10 µL of these pre-cultures were used to inoculate four main cultures per variant in four fresh sqDWPs with 900 µL TB auto-induction media.

After 24 hours incubation at 37°C and 800 rpm, the cells were separated via centrifugation (5 minutes at 3500 rpm), the supernatant was removed and cells resuspended in 200 µL freshly prepared reaction mixture containing 1 mM of the four respective substrates and 4 mM SAM (**93**) in KPi buffer (50 mM, pH 8). The reaction was performed at 40°C for 7 hours, without shaking. Afterwards, the reaction was quenched and residual cells and enzyme was precipitated using 20 µL 5% TFA followed by a centrifugation step. 100 µL of the supernatant was transferred to a fresh micro titer plate (MTP) and stored at -20°C until further use.

For determination of the enzymatic activity, first 50 µL of the supernatant were mixed with 50 µL conc. H_2S0_4 and incubated for 30 minutes at room temperature. Afterwards, 100 µL mixture were transferred to a fresh MTP, 50 µL pDMAB (300 mM in isopropanol) were added followed by 10 minutes of UV-light exposure (405 nm LED light). Finally, the absorbance at 540 nm was determined in a plate photometer.

7.1.26 Alkylation experiments

AcHMT (100 µM final concentration) was added to KPi buffer (50 mM, pH 7.5), supplemented with 7 mM SAH (**94**) and 70 mM of the respective alkyl donor in a 100 µL scale. The alkyl donors tested included methyl iodide, ethyl iodide, prenyl bromide, and allyl iodide. After 2 hours of incubation at 35 °C, 25 µL of the reaction solution was transferred to a secondary mixture (100 µL) containing 100 µM SgMT and 1 mM cWW **3a**, following a protocol established by Diana Amariei. This reaction was incubated overnight at 700 rpm and 35 °C and analysed via TLC and LC-MS.

The allylation reaction was repeated under direct recycling system conditions, where HMT and SgMT were added at a concentration of 100 µM directly to a solution containing 1 mM cWW **3a**, 1 mM SAH (**95**), and 10 mM allyl iodide in KPi buffer (50 mM, pH 7.5). This reaction was incubated overnight at 700 rpm and 35 °C and analysed via TLC.

7.1.27 Resolubilisation of StspPT

1 g of cells were resuspended in 10 mL of 50 mM KPi buffer containing 2.5 mM $MgCl_2$, pH 7. Cell lysis was performed using an ultrasonic cell disruptor (Branson Sonifier II, Model W-250, Heinemann) for 10 minutes at 35–40% amplitude, repeated twice. The lysate was centrifuged at 4°C, 10,000 × rcf for 20 minutes. The resulting pellet, containing inclusion bodies, was resuspended in 1 mL of the same buffer supplemented with 8 M urea and incubated for 1 hour at 25°C to solubilise the protein. A 500 µL aliquot of this solution was gradually diluted with 10 mL of buffer lacking detergent to initiate protein refolding. However, the protein precipitated again, and the mixture was centrifuged at 4 °C, 10,000 × rcf for 20 minutes. The supernatant was concentrated, and protein concentration was measured using a NanoDrop spectrophotometer, but no detectable protein was found.

7.1.28 Cerium Molybdate stain investigations

For the CAM stain 25 g phosphomolybdic acid and 10 g cerium sulfate hydrate were diluted in 940 ml water with 60 ml sulphuric acid.

In a first attempt, 5 Vol% CAM stain (10 µL) were added to 190 µL of a 1 mM solution of melatonin and *C3*-methylated melatonin **228** (in 50 mM KPi buffer, pH 7.5) in a 96-well plate. After 20 min, the absorption was measured at 608 nm.

For the determination of the optimal incubation time, this experiment was repeated, while measuring the absorbance at different time points (5, 10, 20, 30 and 45 min) at 608 nm. For optimizing the CAM stain volume, the absorbance was recorded after 30 minutes after adding different amounts of the staining solution (1, 2, 3, 4, 5 and 10 Vol%).

To determine which component of the CAM stain is responsible for the blue colouration, the individual components of the stain were tested separately. The CAM stain is composed of 25 mM cerium(IV) sulfate (Cer), 15 mM phosphomolybdic acid (PMA), and 1 M sulphuric acid (A) in water. Each component was added in proportions equivalent to the amount present in a 3% (v/v) CAM solution to a 0.5 mM solution of *C3*-methylated melatonin **228** (in 50 mM KPi buffer, pH 7.5) or ascorbic acid.

7.1.29 Single parameter Optimisation (HPI assay)

The single parameter optimisation was carried out for a mixtures of 0.25 mM *C3*-methylated melatonin **228** and 0.75 mM melatonin **227** *vice versa*. 185 µl of the mixture was added to a 96-well plate (Greiner, F-Bottom, clear). The corresponding amount of sulphuric acid (1 M) and cerium sulfate solution in water (50 mM) were added and mixed thoroughly. The cerium sulfate solutions were prepared by dissolving the cerium sulfate in water containing 0.09 M sulphuric acid, due to insolubility issues. After 60 min at the corresponding temperature, the absorption was measured at 608 nm. As parameters, the sulphuric acid concentration, the cerium sulfate concentration and the temperature were chosen. The concentration of acid was kept stable at 0.025 M, the cerium sulfate concentration at 0.75 mM and the temperature at 20 °C in the corresponding experiments. The reactions were carried out in triplicates. In an additional experiment, the incubation temperatures was varied (20 °C, 35 °C, and 50 °C), while keeping the other parameters stable.

7.1.30 Design of experiment (HPI assay)

The DoE was carried out for a mixtures of 0.25 mM *C3*-methylated melatonin **228** and 0.75 mM melatonin **227** and *vice versa*. 190 µl of the mixture was added to a 96-well plate (Greiner, F-Bottom, clear). The corresponding amount of sulphuric acid (1 M) and cerium sulfate solution (50 mM) were added and mixed thoroughly (total volume of 200 µl). After 60 min at 35 °C, the absorption was measured at 608 nm. As parameters, the sulphuric acid concentration and the cerium sulfate concentration were chosen. For 0.25 mM *C3*-methylated melatonin **228** a range of 0.25 Mm to 1 mM cerium sulfate and 0.01 M to 0.03 M Acid were tested, for 0.75 mM *C3*-methylated melatonin a range of 0.5 mM to 2 mM and 0.01 M to 0.04 M respectively.

7.1.30 Calibration of the HPI assay

For the calibration of the HPI products under optimised small concentration conditions and optimised high concentration conditions a concentration range of 0 mM to 1 mM of HPI product was chosen. 22.5 mM acid and 0.5 mM cerium sulfate were used for the optimised small concentration conditions, 30 mM acid and 1.25 mM cerium sulfate for the optimised high concentration conditions. The mixture of the HPI product and the corresponding substrate was added to a 96-well plate (Greiner, F-Bottom, clear). The corresponding amount of sulphuric acid (1 M) and cerium sulfate solution (50 mM) were added and mixed thoroughly (total volume of 200 µl). After 60 min at 35 °C, the absorption was measured at 608 nm.

7.1.31 ABTS-Assay

The ABTS de colourisation assay was performed with ascorbic acid as reference antioxidant.[313] APS was added to a 7 mM solution of ABTS in ultrapure water to a final APS concentration of 2.45 mM. The mixture was incubated for 20 h over night in the dark resulting in a dark green solution. This solution was diluted until the absorbance at 734 nm of 200 µl in a 96-well plate (Greiner, F-Bottom, clear) was 0.7. As an antioxidant reference, ascorbic acid was prepared in a dilution row between 0 and 400 mM in DMSO in triplicates. 10 µl of these solutions were added to 190 µl of ABTS solution and mixed via pipetting. After 5 minutes at room temperature, the absorbance was measured at 734 nm. The de colourisation was calculated and plotted against the concentration of ascorbic acid giving a calibration for further samples.

The samples were diluted to various concentration in DMSO. 10 µl of these solutions were added to 190 µl of ABTS solution and mixed via pipetting. After 5 minutes at room temperature, the absorbance was measured at 734 nm. If the decolourisation was out of the range of the calibration, the experiment was repeated with an adjusted concentration of sample.

7.1.32 Cyclic voltammetry

The cyclic voltrammetric measurements were carried out with a potentiostat (PGSTAT204, Metrohm Autolab B.V. (voltage 100-240 V; 75 A, 50/60 Hz, Fuse 3.5 A/T). A platinum electrode was used as a counter electrode, a carbon electrode as a working electrode and an Ag/AgCl as reference electrode with an inner filling of a KCl solution (3 M). A 0.1 M KPF_6 solution was used as electrolyte. Scan rate was 50 mV/s. The software NOVA 2.1 (Metrohm Autolab B.V.) was used to record the cyclic voltammograms. In a similar experiment, solutions of *C3*-substituted HPI melatonin derivatives were electrochemically oxidised using a carbon felt anode and Ag/AgCl cathode at 0.1 A and 15 V using the same devices. The absorbance of the solution was measured after 5 min.

7.1.33 Enzyme expression and purification od PsmD

Purification of PsmD_*Sa* carrying *C*-terminal His6-tag was performed by Ni-NTA affinity chromatography. The protein was expressed in *E.coli* BL21 Gold using TB medium and 100 µM ampicillin at 37 °C. At OD_{600} of 0.5, the expression was induced with 100 µM IPTG and then the cultures incubated at 25 °C for 24 h. The cells were resuspended in lysis buffer (50 mM KPi, pH 7.5) to the final concentration of 0.5 mg/mL. The cell lysis was achieved by sonication (Branson Sonifier II "ModellW-250", Heinemann). The cell debris was removed by centrifugation (10000 rpm, 4 °C, 30 min), and the supernatant filtered through a 0.22 µM syringe filter. For purification, a 5 mL Ni-NTA column (Superflow Cartridge, QIAGEN GmbH, Hilden, Germany) was used. The column was equilibrated with three CV of equilibration buffer (50 mM KPi, 500 mM NaCl, pH 7.5). After the cell lysate was loaded on the column, the resin was washed with 5 CV of washing buffer (50 mM KPi, 500 mM NaCl, 100 mM imidazole, pH 7.5), after which the target protein was eluted with 3 CV of elution buffer (50 mM KPi, 500 mM NaCl, 250 mM imidazole, pH 7.5). The eluted protein was concentrated using Vivaspin® 20 centrifugal concentrators (MWCO 10 kDa, Sartorius, Germany). The protein solution was washed three times with 20 mL of lysis buffer. The purified protein was flash-frozen in liquid nitrogen and stored at −20 °C for further use.

7.1.34 PsmD activity evaluation using the HPI assay

A reaction mixture containing 1 mM **148**, 2 mM SAM (**93**) and 100 µg/mL isolated PsmD from *S. albulus* in KPi buffer (50 mM, pH 7.5) was incubated at 35 °C and 700 rpm. At different time points, samples were taken and the reaction was quenched with TFA (final concentration 0.5% v/v). Each sample was then analysed using each of the optimised assay procedures. The substrate concentration was plotted against time and the slope was used to calculate enzymatic activity.

7.1.35 PsmD mutant screening in whole cells

E.coli cells expressing PsmD WT, R85A and E35A as well as cells containing the empty pET21a(+) vector were resuspended in 500 µL reaction mixture containing 1 mM **148** and 2 mM SAM (**93**) in KPi buffer (50 mM, pH 7.5). A final OD_{600} of 6 was used in all cases. The mixtures were incubated at 35 °C and 700 rpm for 16 h. Afterwards, the cells were separated from the mixture by centrifugation at 15000 rpm for 15 min. 50 µL (indole assay) or 200 µL (HPI assay) supernatant were then used in the respective optimised assay procedure. 200 µL of the supernatant were filtered and analysed using RP-HPLC.

7.1.36 HPLC analysis of PsmD catalysed reaction

All enzymatic reactions were analysed by reverse-phase HPLC. The measurements were performed using a Jasco X-LC series device, equipped with a diode array; separation was achieved on a HyperClone 5µm ODS 120 Å (4 x 250 mm) C18 column. Distilled water and acetonitrile were used as eluents, using the following gradient sequence: min 0.00: 10% acetonitrile, 90% water; min 10.00: 20% acetonitrile, 80% water; min 12.00 20% acetonitrile, 80% water. The column was maintained at 40 °C during measurements. The injection volume was 30 µL and the flowrate was set at 1 mL/min.

7.1.37 Cultivation and extraction of *Streptomyces griseoviridis*

Streptomyces griseoviridis (DSM 40229, freeze-dried) was obtained from DSMZ. Spores were rehydrated and inoculated into 15 mL of Medium 65 (glucose 4 g L^{-1}, yeast extract 4 g L^{-1}, malt extract 10 g L^{-1}, pH 7.2) and incubated at 28 °C with shaking (120 rpm) for 4 days. A 100 µL aliquot of this preculture was spread onto each of 80 agar plates containing Medium 65 supplemented with $CaCO_3$ (2 g L^{-1}) and agar (20 g L^{-1}). Plates were incubated at 28 °C for 14 days.

Biomass was harvested by scraping the colony surface and extracted three times with 150 mL portions of ethyl acetate. Following filtration, the combined organic extracts were dried over $MgSO_4$, filtered, and solvent removed under reduced pressure. The crude extract was fractionated by silica gel column chromatography using ethyl acetate as eluent. Three fractions were collected, the solvent removed, resolubilized in acetonitrile and analysed by LC–MS.

7.1.38 LC-MS method

LC-MS: UltiMate 3000 Series (Column Compartment: TCC-3000SD, Pump: LPG-3400SD, Autosampler: WPS-3000TSL Analytical, DAD: DAD-3000; Vanquish ISQ Family Series, Mass Spectrometer: ISQEM)

Stationary Phase: hyperclone column (5µ ODS C18, 125*4 mm, 120 Å, Fa. Phenomenex); mobile phase A: Acetonitrile + 1% formic acid (v/v) and B: water + 1% formic acid (v/v) Gradient: 0-2 min: 10:90 (A:B), 2-15 min: 10% A to 50% A, 15-25 min: 50% A to 95% A, 25-30 min: 95:5 (A:B), 30-35 min: 10:90 (A:B).
Flow rate: 0.8 mL/min
Column temperature: 25 °C
Detection wavelength: 205 nm

7.2 Chemical methods

7.2.1 General information

For reactions under inert conditions, flame-dried glassware was used and an inert atmosphere (N_2 or Ar gas) was applied. Thin layer chromatography was performed with TLC-foil Polygram SilG/UV254 by Macherey-Nagel as a stationary phase and ethyl acetate as a mobile phase. A cerium-molybdate-solution [10 g $Ce(SO_4)_2 \cdot 4\ H_2O$, 25 g phosphomolybdic acid, 60 mL conc. H_2SO_4, 940 mL H_2O] was used for staining of the TLC plates. Preparative column chromatography was performed using silica gel (0.040−0.063 mm) from Merck as the stationary phase and ethyl acetate as the mobile phase. ^1H, ^{13}C, and 2D NMR (COSY, HSQC, HMBC) spectra were measured with a Bruker Avance DRX 600 NMR. The optical rotation was measured using a JASCO P-2000 polarimeter. IR spectra were measured with a PerkinElmer SpectrumTwo spectrometer. High-resolution ESI mass spectra were measured using an MDS SCIEXQ Model Trap 4000 mass spectrometer (HHU Centre of Molecular and Structural Analytics at the Heinrich-Heine-Universität Düsseldorf)

7.2.2 Diketopiperazine synthesis

The benzyl chloroformate-protected L-tryptophan **247** (1.0 equiv.) and methyl-protected corresponding amino acid **248** (1.0 equiv.) were dissolved in dry THF (0.25 mmol·mL^{-1}) at 0 °C. After Bis(2-oxo-3-oxazolidinyl)phosphinic chloride (BOP-Cl) (3.0 equiv.) was added, the reaction was stirred for 3 h at 0 °C and allowed to warm up to 21 °C over night. 20 mL water were added and the product was extracted with ethyl acetate (3 x 20 mL). The organic phases were washed with brine and dried over $MgSO_4$. The solvent was removed under reduced pressure. The crude product was filtered over silica with ethyl acetate and used without further purification for the next reaction step.

To deprotect the amine, the crude products **249** were dissolved in MeOH/ethyl acetate (1:2) (0.05 mmol·mL^{-1}) under nitrogen atmosphere. After adding ammonium formate (4.8 equiv.) and 10% Pd/C (0.1 equiv.), the reaction mixture was stirred for 30 minutes under reflux conditions. Ther Pd/C residue was filtered off and the solvent was removed under reduced pressure. The crude product **250** was used without further purification for the next step by dissolving it in 7 N methanolic ammonia (0.05 mmol·mL^{-1}). The reaction was stirred at 60 °C for 4 h. The solvent was removed under reduced pressure. The final product **251** was purified using column chromatography with ethyl acetate as solvent.

For the tryptophan-histidine DKPs, a different coupling reaction was chosen.[364] The methyl-protected histidine (1.0 equiv.) was dissolved in dry DMF (0.5 mmol·mL^{-1}) with the benzyl chloroformate-protected *L*-tryptophan **247**. *N*-methyl morpholine (2.0 equiv.) was added at 0 °C. EDC-HCl (1.0 equiv.) was added portion-wise and the reaction was stirred at 0 °C for 3 h and additional 16 h at 21 °C. The residue was taken up in ethyl acetate and washed with $NaHCO_3$ solution and water. The organic phases were dried over $MgSO_4$ before removing the solvent under reduced pressure. The crude product was filtered over silica with ethyl acetate and used without further purification for the next reaction step.[100]

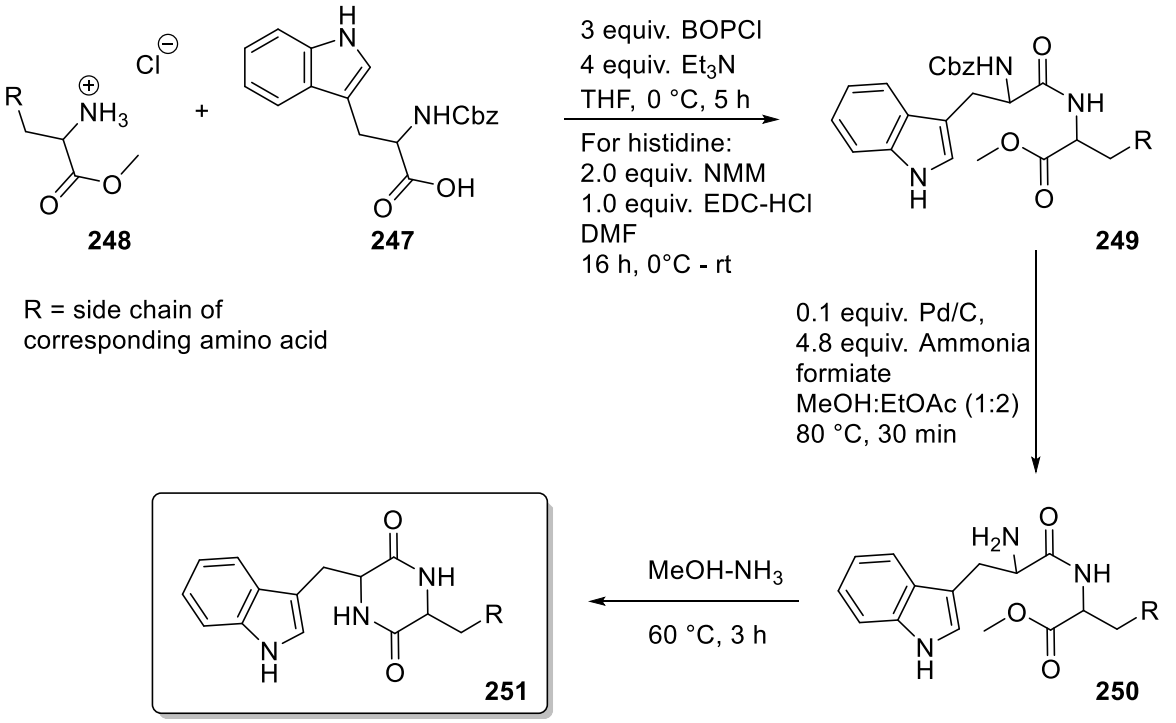

Figure 187: Synthesis of the DKP substrates.

7.2.2.1 cWW

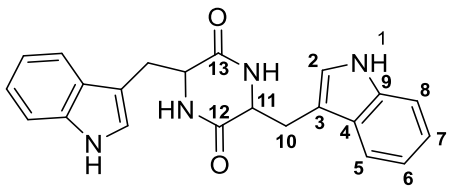

LL-cWW **3a**

The product was obtained in a 91% yield (1.11 mmol, 408 mg) using the established DKP synthesis protocol.

^{1}H NMR (600 MHz, MeOD) δ [ppm] = [ppm] = 7.47 (d, $^{3}J_{8,7}$ = 8.0 Hz, 2H, 8-H), 7.32 (d, $^{3}J_{5,6}$ = 8.1 Hz, 2H, 5-H), 7.11 (dd, $^{3}J_{7,8}$ = 8.1, $^{3}J_{7,6}$ =6.9 Hz, 2H, 7-H), 7.03 (dd, $^{3}J_{6,7}$ = 8.0, $^{3}J_{6,5}$ = 7.0 Hz, 2H, 6-H), 6.49 (s, 2H, 2-H), 4.06 (dd, $^{3}J_{11,10a}$ = 3.8 Hz, $^{3}J_{11,10b}$ = 7.2 Hz, 2H, 11-H), 2.94 (dd, $^{3}J_{10a,10b}$ = 14.8, $^{3}J_{10a,11}$ = 3.8 Hz, 2H, 10-H_a), 2.19 (dd, $^{3}J_{10b,10a}$ = 14.8, $^{3}J_{10b,11}$ = 7.3 Hz, 2H, 10-H_b).

^{13}C NMR (151 MHz, MeOD) δ [ppm] = [ppm] = 169.71 (C-12), 138.05 (C-9), 128.61 (C-4), 125.90 (C-2), 122.52 (C-7), 120.07 (C-6), 119.68 (C-8), 112.41 (C-5), 109.45 (C-3), 56.86 (C-11), 31.39 (C-10).

IR: IR (ATR): ṽ [cm^{-1}] = 3266 (s), 3053 (vw), 2926 (w), 1704 (m), 1664 (vs), 1457 (s), 1360 (m), 1325 (m), 1230 (m), 1011 (w), 743 (s), 535 (vw).

MS: MS (ESI, 60 eV): m/z (%) = 373.17 (80) [M^{+}]

Optical rotation: $[\alpha]_D^{25}$ = *-77 (c* 0.4*, DMSO);* Literature: -52 (*c* 0.05, MeOH)[87]

Melting point: 254.3 °C; Literature: 242 °C[87]

DD-cWW **3b**

The product was obtained in a 90% yield (1.38 mmol, 514 mg) using the established DKP synthesis protocol.

^{1}H NMR (600 MHz, MeOD) δ [ppm] = 7.45 (d, $^{3}J_{8,7}$ = 8.0 Hz, 2H, 8-H), 7.30 (d, $^{3}J_{5,6}$ = 8.1 Hz, 2H, 5-H), 7.09 (dd, $^{3}J_{7,8}$ = 8.1, $^{3}J_{7,6}$ 7.0 Hz, 2H, 7-H), 7.01 (dd, $^{3}J_{6,5}$ = 8.0, $^{3}J_{6,7}$ = 7.0 Hz, 2H, 6-H), 6.46 (s, 2H, 2-H), 4.05 (dd, $^{3}J_{11,10b}$ = 7.0, $^{3}J_{11,10a}$ = 3.8 Hz, 2H, 11-H), 2.92 (dd, $^{3}J_{10a,11}$ = 14.4, $^{3}J_{10a,10b}$ = 3.8 Hz, 2H, 10-H_a), 2.17 (dd, $^{3}J_{10b,11}$ = 14.4, $^{3}J_{10b,10a}$ = 7.2 Hz, 2H, 10-H_b).

^{13}C NMR (151 MHz, MeOD) δ [ppm] = 169.73 (C-12), 138.09 (C-9), 128.64 (C-4), 125.90 (C-2), 122.54 (C-7), 120.09 (C-6), 119.69 (C-8), 112.42 (C-5), 109.50 (C-3), 56.91 (C-11), 31.40 (C-10).

IR: IR (ATR): ṽ [cm^{-1}] = 3266 (vs), 2923 (w), 1703 (m), 1663 (vs), 1457 (s), 1359 (s), 1325 (s), 1229 (m), 1091 (m), 1011 (w), 743 (vs), 524 (vw).

MS: MS (ESI, 60 eV): m/z (%) = 373.17 (80) [M$^+$]

Optical rotation: $[\alpha]_D^{25}$ = *66 (c 0.3, DMSO);* Literature: 52 (*c* 0.05, MeOH)[87]

Melting point: 249.0 °C; Literature: 242 °C[87]

LD-cWW **3c**

The product was obtained in a 85% yield (0.8 mmol, 298 mg) using the established DKP synthesis protocol.

^{1}H NMR (600 MHz, MeOD) δ [ppm] = 7.43 (d, $^3J_{8,7}$ = 8.0 Hz, 2H, 8-H), 7.28 (d, $^3J_{5,6}$ = 8.2 Hz, 2H, 5-H), 7.07 (dd, $^3J_{7,6}$ = 8.2 Hz, $^3J_{7,8}$ = 7.0 Hz, 2H, 7-H), 6.99 (t, $^3J_{6,5}$ = 8.0 Hz, $^3J_{6,7}$ = 7.0 Hz, 2H, 6-H), 6.44 (s, 2H, 2-H), 4.03 (dd, $^3J_{11,10}$ = 7.1 Hz, 2H, 11-H), 2.90 (dd, $^3J_{10a,11}$ = 14.4, 2H, 10-H$_a$), 2.14 (dd, $^3J_{10b,11}$ = 14.4 Hz, 2H, 10-H$_b$).

^{13}C NMR (151 MHz, MeOD) δ [ppm] = 169.72 (C-12), 138.08 (C-9), 128.63 (C-4), 125.90 (C-2), 122.53 (C-7), 120.09 (C-6), 119.69 (C-8), 112.42 (C-5), 109.50 (C-3), 56.90 (C-11), 31.40 (C-10).

IR: IR (ATR): ṽ [cm^{-1}] = 3304 (s), 3055 (vw), 2927 (w), 1670 (vs), 1459 (m), 1363 (w), 1318 (m), 1229 (w), 1088 (w), 1012 (vw), 744 (s)

MS: MS (ESI, 60 eV): m/z (%) = 373.17 (80) [M$^+$]

Melting point: 239.7 °C

7.2.2.2 cWF

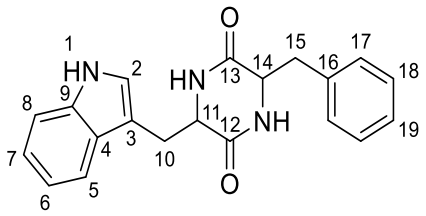

LL-cWF **242a**

The product was obtained in a 91% yield (1.35 mmol, 449 mg) using the established DKP synthesis protocol.

^{1}H NMR (600 MHz, DMSO-d6) δ [ppm] = 10.76 (s, 1H, NH), 7.79 (s, 1H, NH), 7.56 (s, 1H, NH), 7.35 (d, $^{3}J_{5,6}$ = 7.9 Hz, 1H, 5-H), 7.19 (d, $^{3}J_{8,7}$ = 8.1 Hz, 1H, 8-H), 7.07 – 6.98 (m, 3H, H-18 + H-19), 6.93 (dd, $^{3}J_{6,5+7}$ = 7.5 Hz, 1H, 6-H), 6.85 (t, $^{3}J_{7,6+8}$ = 7.5 Hz, 1H, 7-H), 6.83 (s, 1H, 2-H), 6.58 – 6.53 (m, 2H, 17-H), 3.87 – 3.82 (m, 1H, 11-H), 3.73 – 3.69 (m, 1H, 14-H), 2.67 (dd, $^{3}J_{10b,10a}$ = 14.5 Hz, $^{3}J_{10b,11}$ =4.4 Hz, 1H, 10-H_b), 2.39 (dd, $^{3}J_{10a,10b}$ = 14.5 Hz, $^{3}J_{10a,11}$ = 5.8 Hz, 1H, 10-H_a), 2.31 (dd, $^{3}J_{15,15a}$ = 13.5 Hz, $^{3}J_{15b,14}$ = 4.7 Hz, 1H, 15-H_b), 1.68 (dd, $^{3}J_{15a,15b}$ = 13.5 Hz, $^{3}J_{15a,14}$ = 7.2 Hz, 1H, 15-H_a).

^{13}C NMR (151 MHz, DMSO-d6) δ [ppm] = 167.00 (C-12), 166.38 (C-13), 136.57 (C-16), 136.16 (C-4), 129.81 (C-17), 128.18 (C-18), 127.63 (C-9), 126.53 (C-19), 124.57 (C-2), 121.06 (C-6), 118.89 (C-5), 118.60 (C-7), 111.47 (C-8), 108.87 (C-3), 55.73 (C-14), 55.38 (C-11), 39.91 (C-15), 29.79 (C-10).

IR: IR (ATR): $\tilde{\nu}$ [cm^{-1}] = 3424 (vw), 3324 (m), 2970 (m), 2920 (m), 1739 (s), 1667 (vs). 1457 (s), 1369 (s), 1217 (s), 1092 (w), 744 (s), 699 (m)

MS: MS (ESI, 60 eV): m/z (%) = 334.16 (80) [M^{+}]

Optical rotation: $[\alpha]_D^{25}$ = *-94 (c 0.23, DMSO)*

Melting point: 278.6 °C; Literature: 284 °C[86]

DD-cWF **242b**

The product was obtained in a 90% yield (1.34 mmol, 447 mg) using the established DKP synthesis protocol.

^{1}H NMR (600 MHz, DMSO-d6) δ [ppm] = 10.76 (s, 1H, NH), 7.79 (s, 1H, NH), 7.57 (s, 1H, NH), 7.35 (d, $^{3}J_{5,6}$ = 7.9 Hz, 1H, 5-H), 7.19 (d, $^{3}J_{8,7}$ = 8.1 Hz, 1H, 8-H), 7.07 – 6.99 (m, 3H, H-18 + H-19), 6.94 (dd, $^{3}J_{6,5+7}$ = 7.5 Hz, 1H, 6-H), 6.85 (dd, $^{3}J_{7,6+8}$ = 7.5 Hz, 1H, 7-H), 6.83 (s, 1H, 2-H), 6.56 (d,$^{3}J_{17,18}$ = 7.0 Hz, 2H, 17-H), 3.87 – 3.82 (m, 1H, 11-H), 3.74 – 3.69 (m, 1H, 14-H), 2.67 (dd, $^{3}J_{10b,10a}$ = 14.5 Hz, $^{3}J_{10b,11}$ =4.5 Hz, 1H, 10-H_b), 2.39 (2.41 – 2.38 (m, 1H, 10-H_a), 2.31 (dd, $^{3}J_{15,15a}$ = 13.5 Hz, $^{3}J_{15b,14}$ = 4.7 Hz, 1H, 15-H_b), 1.68 (dd, $^{3}J_{15a,15b}$ = 13.4 Hz, $^{3}J_{15a,14}$ = 7.1 Hz, 1H, 15-H_a).

^{13}C NMR (151 MHz, DMSO-d6) δ [ppm] = 166.99 (C-12), 166.37 (C-13), 136.57 (C-16), 136.15 (C-4), 129.81 (C-17), 128.17 (C-18), 127.62 (C-9), 126.56 (C-19), 124.56 (C-2), 121.05 (C-6), 118.88 (C-5), 118.59 (C-7), 111.47 (C-8), 108.86 (C-3), 55.72 (C-14), 55.37 (C-11), 39.91 (C-15), 29.79 (C-10).

IR: IR (ATR): ṽ [cm^{-1}] = 3452 (vw), 3313 (vw), 3025 (w), 2970 (m), 1738 (vs), 1674 (m), 1447 (m), 1366 (s), 1217 (s), 893 (vw), 528 (m)

MS: MS (ESI, 60 eV): m/z (%) = 334.16 (80) [M^{+}]

Optical rotation: $[\alpha]_D^{25}$ = *86 (c 0.17, DMSO)*

Melting point: 284.7 °C

LD-cWF **242c**

The product was obtained in a 75% yield (1.20 mmol, 401 mg) using the established DKP synthesis protocol.

^{1}H NMR (600 MHz, DMSO-d6) δ [ppm] = 10.73 (s, 1H, NH), 7.82 – 7.78 (m, 2H, NH), 7.38 (d, $^{3}J_{5,6}$ = 7.9 Hz, 1H, 5-H), 7.17 (d, $^{3}J_{8,7}$ = 8.1 Hz, 1H, 8-H), 7.12 – 7.02 (m, 3H, H-18 + H-19), 6.98 – 6.94 (m, 2H, 17-H), 6.90 (dd, $^{3}J_{6,5+7}$ = 7.6 Hz, 1H, 6-H), 6.88 – 6.85 (m, 1H, 2-H), 6.80 (dd, $^{3}J_{7,6+8}$ = 7.4 Hz, 1H, 7-H), 3.27 – 3.22 (m, 2H, 14-H + 11-H), 2.99 (dd, $^{3}J_{10b,10a}$ = 14.6 Hz, $^{3}J_{10b,11}$ =4.1 Hz, 1H, 10-H_b), 2.83 (dd, $^{3}J_{15b,15a}$ = 13.7 Hz, $^{3}J_{15b,14}$ = 3.9 Hz, 1H, 15-H_b), 2.74 (dd, $^{3}J_{10a,16b}$ = 14.6 Hz, $^{3}J_{10a,11}$ =4.6 Hz, 1H, 10-H_a), 2.56 (dd, $^{3}J_{15a,15b}$ = 13.7 Hz, $^{3}J_{15a,14}$ = 4.9 Hz, 1H, 15-H_a).

^{13}C NMR (151 MHz, DMSO-d6) δ [ppm] = 167.85 (C-12), 167.06 (C-13), 136.08 (C-16), 135.95 (C-4), 130.19 (C-17), 128.09 (C-18), 127.69 (C-9), 126.73 (C-19), 124.68 (C-2), 120.98 (C-6), 118.99 (C-5), 118.51 (C-7), 111.26 (C-8), 108.36 (C-3), 54.77 (C-14), 54.69 (C-11), 37.77 (C-15), 28.45 (C-10).

IR: IR (ATR): ṽ [cm^{-1}] = 3324(w), 3197 (w), 3031 (m), 2970 (m), 1738 (s), 1671 (vs), 1452 (s), 1365 (s), 1217 (s), 1098 (w), 749 (w), 519 (w)

MS: MS (ESI, 60 eV): m/z (%) = 334.16 (80) [M$^+$]

Optical rotation: $[\alpha]_D^{25}$ = *-12,4 (c 0.21, DMSO);* Literature: -4 (*c* 0.12, MeOH)[365]

Melting point: 251.5 °C

DL-cWF **242d**

The product was obtained in a 74% yield (0.98 mmol, 328 mg) using the established DKP synthesis protocol.

^{1}H NMR (600 MHz, DMSO-d6) δ [ppm] = 10.87 (s, 1H, NH), 7.96 – 7.92 (m, 2H, NH), 7.51 (d, $^3J_{5,6}$ = 7.9 Hz, 1H, 5-H), 7.30 (d, $^3J_{8,7}$ = 8.1 Hz, 1H, 8-H), 7.25 – 7.13 (m, 3H, H-18 + H-19), 7.11 – 7.07 (m, 2H, 17-H), 7.03 (dd, $^3J_{6,5+7}$ = 7.6 Hz, 1H, 6-H), 7.00 – 6.99 (m, 1H, 2-H), 6.92 (dd, $^3J_{7,6+8}$ = 7.5 Hz, 1H, 7-H), 3.41 – 3.34 (m, 2H, 14-H + 11-H), 3.12 (dd, $^3J_{10b,10a}$ = 14.6 Hz, $^3J_{10b,11}$ =4.1 Hz, 1H, 10-H$_b$), 2.96 (dd, $^3J_{15b,15a}$ = 13.7 Hz, $^3J_{15b,14}$ = 3.8 Hz, 1H, 15-H$_b$), 2.85 (dd, $^3J_{10a,16b}$ = 14.6 Hz, $^3J_{10a,11}$ =4.6 Hz, 1H, 10-H$_a$), 2.68 (dd, $^3J_{15a,15b}$ = 13.7 Hz, $^3J_{15a,14}$ = 4.9 Hz, 1H, 15-H$_a$).

^{13}C NMR (151 MHz, DMSO-d6) δ [ppm] = 167.65 (C-12), 166.87 (C-13), 136.04 (C-16), 135.84 (C-4), 130.09 (C-17), 127.95 (C-18), 127.60 (C-9), 126.57 (C-19), 124.55 (C-2), 120.81 (C-6), 118.89 (C-5), 118.35 (C-7), 111.13 (C-8), 108.28 (C-3), 54.65 (C-14), 54.65 (C-11), 37.64 (C-15), 28.35 (C-10).

IR: IR (ATR): ṽ [cm^{-1}] = 3258 (m), 3031 (m), 2970 (m), 2920 (m), 2859 (vw), 1738 (vs), 1668 (vs), 1452 (m), 1365 (s), 1217 (s), 1092 (w), 744 (w), 705 (w), 528 (w)

MS: MS (ESI, 60 eV): m/z (%) = 334.16 (80) [M$^+$]

Optical rotation: $[\alpha]_D^{25}$ = *4 (c 0.57, DMSO)*

Melting point: 241.2 °C

The analytical data are consistent with the literature.[365]

7.2.2.3 cWY

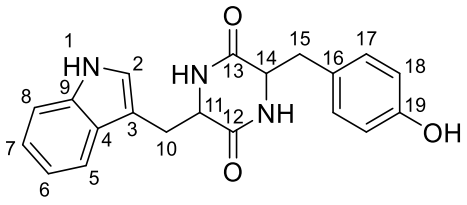

LL-cWY **241a**

The product was obtained in a 71% yield (1.21 mmol, 423 mg) using the established DKP synthesis protocol.

^{1}H NMR (600 MHz, DMSO-d6) δ [ppm] = 10.76 (s, 1H, NH), 7.70 (s, 1H, NH), 7.49 (s, 1H, NH), 7.34 (d, $^{3}J_{5,6}$ = 7.9 Hz, 1H, 5-H), 7.18 (d, $^{3}J_{8,7}$ = 8.1 Hz, 1H, 8-H), 6.93 (dd, $^{3}J_{6,5+7}$ = 7.5 Hz, 1H, 6-H), 6.87 – 6.81 (m, 2H, 2-H + 7-H), 6.44 (d, $^{3}J_{18,17}$ = 8.3 Hz, 2H, H-18), 6.37 (d, $^{3}J_{17,18}$ = 8.3 Hz, 2H, 17-H), 3.83 – 3.78 (m, 1H, 11-H), 3.66 – 3.61 (m, 1H, 14-H), 3.03 (s, 1H, OH), 2.66 (dd, $^{3}J_{10b,10a}$ = 14.4 Hz, $^{3}J_{10b,11}$ =4.4 Hz 1H, 10-H_b), 2.31 (dd, $^{3}J_{15,15a}$ = 14.4 Hz, $^{3}J_{15b,14}$ = 6.3 Hz, 1H, 15-H_b), 2.27 (dd, $^{3}J_{10a,10b}$ = 13.6 Hz, $^{3}J_{10a,11}$ = 4.6 Hz, 1H, 10-H_a), 1.63 (dd, $^{3}J_{15a,15b}$ = 13.5 Hz, $^{3}J_{15a,14}$ = 7.1 Hz, 1H, 15-H_a).

^{13}C NMR (151 MHz, DMSO-d6) δ [ppm] = 166.95 (C-12), 166.46 (C-13), 156.07 (C-19), 136.18 (C-4), 130.82 (C-17), 127.58 (C-9), 126.50 (C-16), 124.52 (C-2), 121.04 (C-6), 118.85 (C-5), 118.58 (C-7), 115.03 (C-18), 111.46 (C-8), 108.96 (C-3), 55.99 (C-14), 55.35 (C-11), 19.91 (C-15), 30.04 (C-10).

IR: IR (ATR): ṽ [cm^{-1}] = 3313 (m), 3202 (m), 3056 (w), 2926 (vw), 1671 (vs), 1619 (vw), 1516 (m), 1457 (s), 1358 (vw), 1232 (m), 1104 (w), 821 (w), 745 (m)

MS: MS (ESI, 60 eV): m/z (%) = 350.15 (80) [M^{+}]

Optical rotation: $[\alpha]_D^{25}$ = *-106 (c 0.29, DMSO);* Literature: -118 (*c* 0.02, MeOH)[366]

Melting point: 271.3 °C; Literature: 265.6 °C[366]

DD-cWY **241b**

The product was obtained in a 89% yield (1.21 mmol, 424 mg) using the established DKP synthesis protocol.

^{1}H NMR (600 MHz, DMSO-d6) δ [ppm] = 10.75 (s, 1H, NH), 7.69 (s, 1H, NH), 7.49 (s, 1H, NH), 7.34 (d, $^{3}J_{5,6}$ = 7.9 Hz, 1H, 5-H), 7.18 (d, $^{3}J_{8,7}$ = 8.1 Hz, 1H, 8-H), 6.93 (dd, $^{3}J_{6,5+7}$ = 7.5 Hz, 1H, 6-H), 6.87 – 6.81 (m, 2H, 2-H + 7-H), 6.44 (d, $^{3}J_{18,17}$ = 8.1 Hz, 2H, H-18), 6.37 (d, $^{3}J_{17,18}$ = 8.1 Hz, 2H, 17-H), 3.83 – 3.78 (m, 1H, 11-H), 3.66 – 3.61 (m, 1H, 14-H), 3.03 (s, 1H, 1H), 2.66 (dd, $^{3}J_{10b,10a}$ = 14.5 Hz, $^{3}J_{10b,11}$ =4.4 Hz 1H, 10-H_b), 2.31 (dd, $^{3}J_{15,15a}$ = 14.4 Hz, $^{3}J_{15b,14}$ = 6.3 Hz, 1H, 15-H_b), 2.27 (dd, $^{3}J_{10a,10b}$ = 13.6 Hz, $^{3}J_{10a,11}$ = 4.6 Hz, 1H, 10-H_a), 1.62 (dd, $^{3}J_{15a,15b}$ = 13.6 Hz, $^{3}J_{15a,14}$ = 7.1 Hz, 1H 15-H_a).

^{13}C NMR (151 MHz, DMSO-d6) δ [ppm] = 166.96 (C-12), 166.47 (C-13), 156.08 (C-19), 136.19 (C-4), 130.83 (C-17), 127.59 (C-9), 126.50 (C-16), 124.53 (C-2), 121.04 (C-6), 118.86 (C-5), 118.58 (C-7), 115.03 (C-18), 111.46 (C-8), 108.96 (C-3), 55.99 (C-14), 55.35 (C-11), 39.93 (C-15), 30.04 (C-10).

IR: IR (ATR): ṽ [cm^{-1}] = 3300 (m), 3208 (w), 3092 (w), 2926 (vw), 1704 (s), 1681 (vs), 1613 (w), 1519 (m), 1467 (m), 1358 (m), 1331 (m), 1233 (s), 1104 (m), 777 (w), 733 (s)

MS: MS (ESI, 60 eV): m/z (%) = 350.15 (80) [M^{+}]

Optical rotation: $[\alpha]_D^{25}$ = *102 (c 0.22, DMSO)*

Melting point: 267.3 °C

LD-cWY **241c**

The product was obtained in a 85% yield (1.19 mmol, 415 mg) using the established DKP synthesis protocol.

^{1}H NMR (600 MHz, DMSO-d6) δ [ppm] = 7.46 (d, $^{3}J_{5,6}$ = 8.0 Hz, 1H, 5-H), 7.28 (d, $^{3}J_{8,7}$ = 8.1 Hz, 1H, 8-H), 7.07 – 7.01 (m, 1H, 6-H), 6.98 (s, 1H, 2-H), 6.97 – 6.92 (m, 1H, 7-H), 6.87 – 6.82 (m, 2H, 17-H), 6.64 – 6.58 (m, 2H, H-18), 3.47 (t, *J* = 4.6 Hz, 1H, 11-H), 3.35 – 3.33 (m, 1H, 14-H), 3.23 – 3.18 (m, 1H, 10-H_b), 3.02 (dd, $^{3}J_{10a,10b}$ = 14.8 Hz, $^{3}J_{10a,11}$ = 4.4 Hz, 1H, 10-H_a), 2.90 (dd, $^{3}J_{15,15a}$ = 14.2 Hz, $^{3}J_{15b,14}$ = 4.2 Hz, 1H, 15-H_b), 2.66 (dd, $^{3}J_{15a,15b}$ = 14.1 Hz, $^{3}J_{15a,14}$ = 4.6 Hz, 1H 15-H_a).

^{13}C NMR (151 MHz, MeOD) δ [ppm] = 170.70 (C-12), 170.04 (C-13), 157.78 (C-19), 137.95 (C-4), 132.26 (C-17), 128.76 (C-9), 126.88 (C-16), 125.77 (C-2), 122.50 (C-6), 120.07 (C-5), 119.78 (C-7), 116.16 (C-18), 112.15 (C-8), 109.09 (C-3), 56.77 (C-14), 56.29 (C-11), 38.84 (C-15), 30.24 (C-10).

IR: IR (ATR): ṽ [cm^{-1}] = 3319 (s), 3191 (m), 3047 (w), 2926 (vw), 1671 (vs), 1613 (w), 1516 (m), 1330 (m), 1231 (s), 1103 (w), 827 (w), 745 (m)

MS: MS (ESI, 60 eV): m/z (%) = 350.15 (80) [M$^+$]

Optical rotation: $[\alpha]_D^{25}$ = *-21 (c 0.41, DMSO)*

Melting point: 237.5 °C

DL-cWY **241c**

The product was obtained in a 55% yield (0.98 mmol, 343 mg) using the established DKP synthesis protocol.

1H NMR (600 MHz, MeOD) δ [ppm] = 7.47 (d, $^3J_{5,6}$ = 8.0 Hz, 1H, 5-H), 7.29 (d, $^3J_{8,7}$ = 8.1 Hz, 1H, 8-H), 7.07 – 7.03 (m, 1H, 6-H), 6.99 (s, 1H, 2-H), 6.98 – 6.95 (m, 1H, 7-H), 6.88 – 6.83 (m, 2H, 17-H), 6.64 – 6.57 (m, 2H, H-18), 3.50 – 3.45 (m, 1H, 11-H), 3.35 – 3.33 (m, 1H, 14-H), 3.21 (dd, $^3J_{10b,10a}$ = 14.8 Hz, $^3J_{10b,11}$ = 4.8 Hz 1H, 10-H$_b$), 3.02 (dd, $^3J_{10a,10b}$ = 14.8 Hz, $^3J_{10a,11}$ = 4.4 Hz, 1H, 10-H$_a$), 2.91 (dd, $^3J_{15,15a}$ = 14.1 Hz, $^3J_{15b,14}$ = 4.2 Hz, 1H, 15-H$_b$), 2.66 (dd, $^3J_{15a,15b}$ = 14.1 Hz, $^3J_{15a,14}$ = 4.6 Hz, 1H 15-H$_a$).

^{13}C NMR (151 MHz, MeOD) δ [ppm] = 170.71 (C-12), 170.04 (C-13), 157.77 (C-19), 137.98 (C-4), 132.22 (C-17), 128.76 (C-9), 126.94 (C-16), 125.76 (C-2), 122.52 (C-6), 120.09 (C-5), 119.76 (C-7), 116.22 (C-18), 112.17 (C-8), 109.15 (C-3), 56.80 (C-14), 56.29 (C-11), 38.89 (C-15), 30.26 (C-10).

IR: IR (ATR): ṽ [cm-1] = 3324 (m), 3196 (m), 3056 (m), 2915 (w), 1670 (vs), 1615 (w), 1516 (m), 1467 (s), 1103 (w), 1015 (vw), 827 (w), 745 (m)

MS: MS (ESI, 60 eV): m/z (%) = 350.15 (80) [M+]

Optical rotation: $[\alpha]_D^{25}$ = 7 (c 5.4, DMSO)

Melting point: 234.9 °C

7.2.2.4 cWH

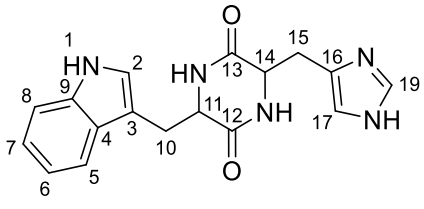

LL-cWH **243a**

The product was obtained in a 57% yield (0.99 mmol, 320 mg) using the established DKP synthesis protocol.

^{1}H NMR (600 MHz, MeOD) δ [ppm] = 8.26 (s, 1H, NH), 8.01 (s, 1H, H-19), 7.61 (d, $^{3}J_{5,6}$ = 7.9 Hz, 1H, 5-H), 7.34 (d, $^{3}J_{8,7}$ = 8.1 Hz, 1H, 8-H), 7.13 (dd, $^{3}J_{6,5+7}$ = 7.5 Hz, 1H, 6-H), 7.08 (s, 1H, 2-H), 7.04 (dd, $^{3}J_{7,6+8}$ = 7.4 Hz, 1H, 7-H), 5.62 – 5.59 (m, 1H, 17-H), 4.26 – 4.21 (m, 1H, 11-H), 3.83 – 3.78 (m, 1H, 14-H), 3.36 (dd, $^{3}J_{10b,10a}$ = 14.8 Hz, $^{3}J_{10b,11}$ = 3.7 Hz, 1H, 10-H_b), 3.05 (dd, $^{3}J_{10a,10b}$ = 14.7 Hz, $^{3}J_{10a,11}$ = 4.5 Hz, 1H, 10-H_a), 2.32 (dd, $^{3}J_{15b,15a}$ = 14.5 Hz, $^{3}J_{15b,14}$ = 4.3 Hz, 1H, 15-H_b), 0.99 (dd, $^{3}J_{15a,15b}$ = 14.5 Hz, $^{3}J_{15a,14}$ = 10.0 Hz, 1H, 15-H_a).

^{13}C NMR (151 MHz, MeOD) δ [ppm] = 169.78 (C-13), 168.58 (C-12), 137.83 (C-4), 135.76 (C-19), 131.16 (C-16), 129.28 (C-9), 126.40 (C-2), 122.72 (C-6), 120.42 (C-5), 120.34 (C-7), 118.91 (C-17), 112.64 (C-8), 109.59 (C-3), 57.33 (C-11), 55.30 (C-14), 31.79 (C-15), 30.73 (C-10).

IR: IR (ATR): ṽ [cm-1] = 3214 (m), 3134 (m), 3059 (w), 2926 (w), 2870 (w), 1667 (vs), 1584 (s), 1457 (s), 1340 (s), 1225 (m), 1094 (m), 747 (s), 633 (w)

MS: MS (ESI, 60 eV): m/z (%) = 324.15 (80) [M+]

Optical rotation: $[\alpha]_D^{25}$ = -72 (*c* 0.22, DMSO); Literature: −42 (*c* 4.06, H_2O)[367]

Melting point: 304.2 °C

DD-cWH **243b**

The product was obtained in a 35% yield (0.59 mmol, 190 mg) using the established DKP synthesis protocol.

^{1}H NMR (600 MHz, MeOD) δ [ppm] = 7.58 (d, $^{3}J_{5,6}$ = 8.0 Hz, 1H, 5-H), 7.44 – 7.41 (m, 1H, H-19), 7.32 (d, $^{3}J_{8,7}$ = 8.1 Hz, 1H, 8-H), 7.09 (dd, $^{3}J_{6,5+7}$ = 8.2 Hz, 1H, 6-H), 7.05 (s, 1H, 2-H), 7.00 (dd, $^{3}J_{7,6+8}$ = 7.4 Hz, 1H, 7-H), 5.75 (s, 1H, 17-H), 4.21 – 4.16 (m, 1H, 11-H), 3.86 – 3.80 (m, 1H, 14-H), 3.20 (dd, $^{3}J_{10b,10a}$ = 14.7 Hz, $^{3}J_{10b,11}$ = 4.5 Hz, 1H, 10-H_b), 3.04 (dd, $^{3}J_{10a,10b}$ = 14.7 Hz, $^{3}J_{10a,11}$ = 4.5 Hz, 1H, 10-H_a), 2.43 – 2.37 (m, 1H, 15-H_b), 1.02 (dd, $^{3}J_{15a,15b}$ = 14.3 Hz, $^{3}J_{15a,14}$ = 9.9 Hz, 1H, 15-H_a).

^{13}C NMR (151 MHz, MeOD) δ [ppm] = 169.73 (C-13), 169.23 (C-12), 137.88 (C-4), 136.52 (C-19), 132.6 (C-16), 129.18 (C-9), 126.14 (C-2), 122.65 (C-6), 120.27 (C-5), 120.27 (C-7), 117.81 (C-17), 112.65 (C-8), 109.52 (C-3), 57.25 (C-11), 55.93 (C-14), 31.12 (C-15), 30.92 (C-10).

IR: IR (ATR): ṽ [cm-1] = 3220 (m), 3021 (m), 2971 (m), 1738 (vs), 1667 (vs), 1589 (m), 1456 (s), 1362 (vs), 1224 (vs), 1091 (w), 743 (m=, 533 (vw)

MS: MS (ESI, 60 eV): m/z (%) = 324.15 (80) [M+]

Optical rotation: $[\alpha]_D^{25}$ = 79 (*c* 0.3, DMSO); Literature: 35 (*c* 2.56, H_2O)[367]

Melting point: 301.3 °C

LD-cWH **243c**

The product was obtained in a 46% yield (0.55 mmol, 178 mg) using the established DKP synthesis protocol.

^{1}H NMR (600 MHz, MeOD) δ [ppm] = 7.51 (d, $^{3}J_{5,6}$ = 8.0 Hz, 1H, 5-H), 7.48 (s, 1H, H-19), 7.26 (d, $^{3}J_{8,7}$ = 8.1 Hz, 1H, 8-H), 7.02 (dd, $^{3}J_{6,5+7}$ = 7.6 Hz, 1H, 6-H), 6.99 (s, 1H, 2-H), 6.93 (dd, $^{3}J_{7,6+8}$ = 7.4 Hz, 1H, 7-H), 6.59 (s, 1H, 17-H), 3.90 (t, $^{3}J_{11,10}$ = 4.5 Hz, 1H, 11-H), 3.34 – 3.29 (m, 1H, 10-H_b), 3.06 (dd, $^{3}J_{10a,10b}$ = 14.8 Hz, $^{3}J_{10a,11}$ =4.4 Hz, 1H, 10-H_a), 3.04 – 3.00 (m, 1H, 14-H), 2.84 (dd, $^{3}J_{15b,15a}$ = 15.2 Hz, $^{3}J_{15b,14}$ = 5.5 Hz, 1H, 15-H_b), 2.74 (dd, $^{3}J_{15a,15b}$ = 15.2 Hz, $^{3}J_{15a,14}$ = 4.4 Hz, 1H, 15-H_a).

^{13}C NMR (151 MHz, MeOD) δ [ppm] = 170.90 (C-12), 169.86 (C-13), 137.96 (C-4), 136.24 (C-19), 128.78 (C-9), 125.91 (C-2), 122.57 (C-6), 120.15 (C-7), 119.71 (C-5), 119.21 (C-17), 112.24 (C-8), 109.18 (C-3), 57.22 (C-11), 55.23 (C-14), 30.81 (C-10), 30.69 (C-15).

IR: IR (ATR): ṽ [cm-1] = 3225 (s), 2920 (m), 2848 (w), 1740 (m), 1667 (vs), 1585 (m), 1452 (s), 1364 (s), 1225 (m), 1092 (w), 749 (m), 622 (vw)

MS: MS (ESI, 60 eV): m/z (%) = 324.15 (80) [M+]

Optical rotation: $[\alpha]_D^{25}$ = - 6 (*c* 0.98, DMSO); Literature: −17 (*c* 4.84, H_2O)[367]

Melting point: 212.7 °C

DL-cWH **243d**

The product was obtained in a 41% yield (0.51 mmol, 165 mg) using the established DKP synthesis protocol.

^{1}H NMR (600 MHz, MeOD) δ [ppm] = 7.53 (d, $^3J_{5,6}$ = 8.0 Hz, 1H, 5-H), 7.51 (s, 1H, H-19), 7.29 (d, $^3J_{8,7}$ = 8.1 Hz, 1H, 8-H), 7.04 (dd, $^3J_{6,5+7}$ = 7.6 Hz, 1H, 6-H), 7.01 (s, 1H, 2-H), 6.96 (dd, $^3J_{7,6+8}$ = 7.4 Hz, 1H, 7-H), 6.61 (s, 1H, 17-H), 3.92 (t, $^3J_{11,10}$ = 4.4 Hz, 1H, 11-H), 3.36 – 3.32 (m, 1H, 10-H_b), 3.09 (dd, $^3J_{10a,10b}$ = 14.8 Hz, $^3J_{10a,11}$ =4.4 Hz, 1H, 10-H_a), 3.06 – 3.01 (m, 1H, 14-H), 2.86 (dd, $^3J_{15b,15a}$ = 15.2 Hz, $^3J_{15b,14}$ = 5.5 Hz, 1H, 15-H_b), 2.76 (dd, $^3J_{15a,15b}$ = 15.2 Hz, $^3J_{15a,14}$ = 4.4 Hz, 1H, 15-H_a).

^{13}C NMR (151 MHz, MeOD) δ [ppm] = 170.92, (C-12), 169.86 (C-13), 137.98 (C-4), 136.23 (C-19), 128.79 (C-9), 125.93 (C-2), 122.58 (C-6), 120.15 (C-7), 119.71 (C-5), 119.19 (C-17), 112.23 (C-8), 109.17 (C-3), 57.24 (C-11), 55.23 (C-14), 30.83 (C-10), 30.68 (C-15).

IR: IR (ATR): ṽ [cm-1] = (3230 (w), 2929 (w), 1740 (m), 1669 (s), 1456 (m), 1364 (m) 1230 (m), 1098 (w), 745 (m), 622 (w).

MS: MS (ESI, 60 eV): m/z (%) = 324.15 (80) [M+]

Optical rotation: $[\alpha]_D^{25}$ = 1 (c 0.70, DMSO); Literature: 18 (*c* 3.28, H_2O)[367]

Melting point: 202.6 °C

7.2.2.5 cWA

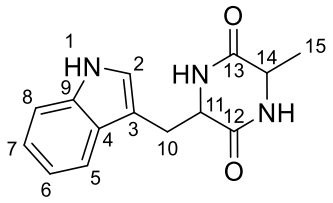

LL-cWA **216**

The product was obtained in a 62% yield (1.53 mmol, 393 mg) using the established DKP synthesis protocol.

^{1}H NMR (600 MHz, DMSO-d6) δ [ppm] = 10.87 (s, 1H, NH), 8.01 – 7.98 (m, 1H, NH), 7.90 – 7.86 (m, 1H, NH), 7.53 (d, $^{3}J_{5,6}$ = 7.9 Hz, 1H, 5-H), 7.27 (d, $^{3}J_{8,7}$ = 8.1 Hz, 1H, 8-H), 7.04 – 6.97 (m, 2H, 2-H + 6-H), 6.91 (dd, $^{3}J_{7,6+8}$ = 7.5 Hz, 1H, 7-H), 4.10 – 4.05 (m, 1H, 11-H), 3.59 – 3.52 (m, 1H, 14-H), 3.21 (dd, $^{3}J_{10b,10a}$ = 14.4 Hz, $^{3}J_{10b,11}$ =4.1 Hz, 1H, 10-H_b), 2.98 (dd, $^{3}J_{10a,10b}$ = 14.5 Hz, $^{3}J_{10a,11}$ =4.6 Hz, 1H, 10-H_a), 0.38 (d, $^{3}J_{15,14}$ = 6.9 Hz, 3H, 15-H).

^{13}C NMR (151 MHz, DMSO-d6) δ [ppm] = 167.73 (C-13), 166.75 (C-12), 135.79 (C-4), 127.80 (C-9), 124.56 (C-2), 120.80 (C-6), 118.98 (C-5), 118.38 (C-7), 111.10 (C-8), 108.50 (C-3), 55.40 (C-11), 49.78 (C-14), 28.84 (C-10), 19.55 (C-15).

IR: IR (ATR): ṽ [cm-1] = 3410 (w), 3187 (w), 3049 (w), 2919 (w), 1656 (s), 1454 (m), 1324 (m), 1094 (w), 826 (m), 742 (s), 504 (m).

MS: MS (ESI, 60 eV): m/z (%) = 258.12 (80) [M+]

Optical rotation: $[\alpha]_D^{25}$ = - 17 (*c* 0.22, DMSO)

Melting point: 284.0 °C; Literature: 289 °C[368]

7.2.2.6 cWV

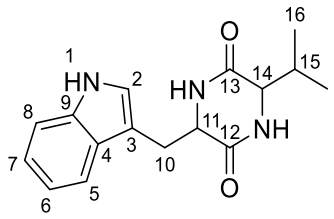

LL-cWV **244**

The product was obtained in a 80% yield (0.77 mmol, 220 mg) using the established DKP synthesis protocol.

^{1}H NMR (600 MHz, DMSO-d6) δ [ppm] = 10.83 (s, 1H, NH), 7.99 (s, 1H, NH), 7.87 (s, 1H, NH), 7.58 (d, $^{3}J_{5,6}$ = 7.9 Hz, 1H, 5-H), 7.27 (d, $^{3}J_{8,7}$ = 8.1 Hz, 1H, 8-H), 7.07 – 7.04 (m, 1H, 2-H), 7.00 (d, $^{3}J_{6,7}$ = 7.5 Hz, 1H, 6-H), 6.92 (dd, $^{3}J_{7,6+8}$ = 7.5 Hz, 1H, 7-H), 4.15 – 4.10 (m, 1H, 11-H), 3.49 – 3.45 (m, 1H, 14-H), 3.20 (dd, $^{3}J_{10b,10a}$ = 14.4 Hz, $^{3}J_{10b,11}$ =4.1 Hz, 1H, 10-H$_b$), 3.05 (dd, $^{3}J_{10a,10b}$ = 14.5 Hz, $^{3}J_{10a,11}$ =4.6 Hz, 1H, 10-H$_a$), 1.67 – 1.58 (m, 1H, 15-H), 0.58 (d, $^{3}J_{16a,15}$ = 7.0 Hz, 3H, 16-H$_a$), 0.15 (d, $^{3}J_{16b,15}$ = 6.8 Hz, 3H, 16-H$_b$).

^{13}C NMR (151 MHz, DMSO-d6) δ [ppm] = 167.36 (C-13), 166.29 (C-12), 136.02 (C-4), 127.94 (C-9), 124.49 (C-2), 120.67 (C-6), 118.91 (C-5), 118.18 (C-7), 111.01 (C-8), 108.84 (C-3), 59.29 (C-14), 55.18 (C-11), 31.10 (C-15), 28.75 (C-10), 18.33 (C-16a), 16.11 (C-16b).

IR: IR (ATR): ṽ [cm-1] = 3325 (w), 3187 (w), 2953 (w), 2919 (w), 1736 (m), 1661 (s), 1462 (m), 1339 (w), 1224 (w), 1102 (w), 849 (w), 741 (m), 548 (m).

MS: MS (ESI, 60 eV): m/z (%) = 286.16 (80) [M+]

Optical rotation: $[\alpha]_D^{25}$ = - 26 (*c* 0.30, DMSO); Literature: - 65 (*c* 0.11, MeOH)[369]

Melting point: 291.4 °C; Literature: 294 °C[369]

7.2.2.7 cWL

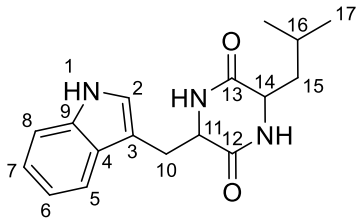

LL-cWL **245**

The product was obtained in a 77% yield (0.87 mmol, 260 mg) using the established DKP synthesis protocol.

^{1}H NMR (600 MHz, DMSO-d6) δ [ppm] = 10.95 – 10.92 (m, 1H, NH), 8.08 – 8.05 (m, 1H, NH), 7.98 – 7.94 (m, 1H, NH), 7.55 (d, $^{3}J_{5,6}$ = 7.9 Hz, 1H, 5-H), 7.30 (d, $^{3}J_{8,7}$ = 8.1 Hz, 1H, 8-H), 7.05 – 6.99 (m, 1H, 2-H, 6-H), 6.92 (dd, $^{3}J_{7,6+8}$ = 7.4 Hz, 1H, 7-H), 4.11 – 4.06 (m, 1H, 11-H), 3.42 – 3.37 (m, 1H, 14-H), 3.26 (dd, $^{3}J_{10b,10a}$ = 14.4 Hz, $^{3}J_{10b,11}$ =4.0 Hz, 1H, 10-H_b),), 2.98 (dd, $^{3}J_{10a,10b}$ = 14.5 Hz, $^{3}J_{10a,11}$ =4.7 Hz, 1H, 10-H_a), 1.25 – 1.15 (m, 1H, 16-H), 0.67 – 0.59 (m, 1H, 15-H_b), 0.52 (d, $^{3}J_{17b,16}$ = 6.5 Hz, 3H, 17-H_b), 0.42 (d, $^{3}J_{17a,16}$ = 6.6 Hz, 3H, 17-H_a), 0.01 – -0.06 (m, 1H, 15a).

^{13}C NMR (151 MHz, DMSO-d6) δ [ppm] = 167.48 (C-13), 167.11 (C-12), 135.93 (C-4), 127.80 (C-9), 124.65 (C-2), 120.76 (C-6), 119.01 (C-5), 118.34 (C-7), 111.12 (C-8), 108.51 (C-3), 55.54 (C-14), 52.37 (C-11), 43.69 (C-15), 29.12 (C-10), 22.87 (C-16), 22.69 (C-17a), 21.28 (C-17b).

IR: IR (ATR): ṽ [cm-1] = 3325 (w), 3192 (w), 2956 (w), 1661 (s), 1457 (m), 1327 (w), 1231 (w), 1093 (w), 1011 (w), 741 (m), 458 (w).

MS: MS (ESI, 60 eV): m/z (%) = 300.17 (80) [M+]

Optical rotation: $[\alpha]_D^{25}$ = - 7 (c 0.30, DMSO); Literature: - 2.6 (*c* 0.15, MeOH)[370]

Melting point: 247.0 °C

7.2.3 Synthesis of *C3*-methylated cWW references

The cWW (1.0 equiv) was dissolved in dry THF (0.5 mmol·mL^{-1}) in an oven-dried Schlenk flask under argon atmosphere at room temperature. Afterward, *t*-BuOK (3.0 equiv) was added and the reaction mixture was stirred at room temperature. 30 min later, Et_3B (1 M in THF, 5.0 equiv) was added dropwise to the reaction mixture, and stirring continued for another 30 min. Methyl iodide (4.0 equiv) was added and the reaction was heated to 40 °C for 48 h. For quenching, NaOH solution was added to an end concentration of 500 mM. The aqueous phase was extracted with S27 ethyl acetate (3x 25 mL). The merged organic phases were washed with brine and dried over $MgSO_4$. The solvent was removed under reduced pressure. The crude product was purified via column chromatography on silica using ethyl acetate as eluent. Starting from 90 mg (0.24 mmol) a 19 mg single methylated (0.05 mmol, 30%) and 10 mg (0.02 mmol) double methylated product were obtained.

Single *C3*-methylated LL-cWW **168a**

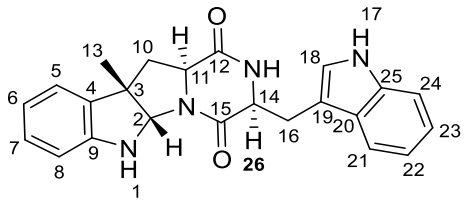

^{1}H NMR (600 MHz, $CDCl_3$) δ [ppm] = 8.35 (s, 1H, NH), 7.56 (d, $^3J_{24,23}$ = 8.0 Hz, 1H, 24-H), 7.36 (d, $^3J_{21,22}$ = 8.2 Hz, 1H, 21-H), 7.24 – 7.18 (m, 1H, Ar-H), 7.16 – 7.06 (m, 4H, Ar-H), 6.78 (t, *J* = 7.4, 1H, Ar-H), 6.63 (d, $^3J_{5,6}$ = 7.4 Hz, 1H, 5-H), 5.89 (s, 1H, NH), 5.26 (s, 1H, 2-H), 5.13 (s, 1H, NH), 4.30 (dd, $^3J_{14,16a}$ = 10.6 Hz, $^3J_{14,16b}$ = 3.8 Hz, 1H, 14-H), 3.95 (dd, $^3J_{11,10a}$ = 11.3 Hz, $^3J_{11,10b}$ = 6.1 Hz, 1H, 11-H), 3.67 (dd, $^2J_{16b,16a}$ = 15.2 Hz, $^3J_{16b,14}$ 3.8 Hz, 1H, 16-H_b), 3.03 (dd, $^2J_{16a,16b}$ = 15.0 Hz, $^3J_{16a,14}$ = 10.6 Hz, 1H, 16-H_a), 2.65 (dd, $^2J_{10b,10a}$ = 12.7 Hz, $^3J_{10b,11}$ = 6.1 Hz, 1H, 10-H_b), 2.03 (dd, $^2J_{10a,10b}$ = 12.7 Hz, $^3J_{10a,11}$ = 11.3 Hz, 1H, 10-H_a), 1.37 (s, 3H, 13-H).

^{13}C NMR (151 MHz, $CDCl_3$) δ [ppm] = 169.01 (C-15), 166.21 (C-12), 148.61 (C-9), 136.69 (C-25), 132.27 (C-4), 128.83 (C-18), 126.80 (C-20), 123.64 (C-18), 122.91, 122.88, 120.13, 119.71 (C-Ar), 118.67 (C-24), 111.68 (C-21), 109.57 (C-19), 109.52 (C-8), 81.57 (C-2), 59.16 (C-11), 54.88 (C-14), 51.71 (C-3), 40.93 (C-10), 27.33 (C-16), 24.47 (C-13).

IR: IR (ATR): ṽ [cm^{-1}] = 3316 (m), 1664 (vs), 1457 (s), 1321 (m), 1216 (w), 1097 (w), 1062 (w), 745 (s).

MS: MS (ESI, 60 eV): m/z (%) = 387.18 [M+]

Optical rotation: $[\alpha]_D^{20}$ = -140 (c 1.0, MeOH)

Single *C3*-methylated DD-cWW **168b**

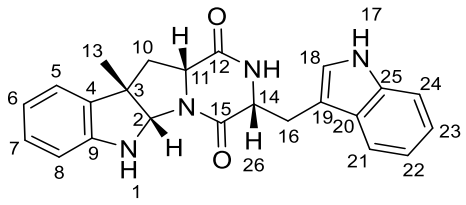

^{1}H NMR (600 MHz, $CDCl_3$) δ [ppm] = 8.26 (s, 1H, NH), 7.58 (d, $^3J_{24,23}$ = 7.9 Hz, 1H, 24-H), 7.33 (d, $^3J_{21,22}$ = 8.2 Hz, 1H, 21-H), 7.24 – 7.18 (m, 1H, Ar-H), 7.15 – 7.07 (m, 3H, Ar-H), 7.02 – 6.98 (m, H, NH), 6.78 (t, *J* = 7.5 Hz, 1H, Ar-H), 6.61 (d, $^3J_{5,6}$ = 7.7 Hz, 1H, 5-H), 5.95 (s, 1H, NH), 5.41 (d, $^3J_{2,NH}$ = 3.1 Hz, 1H, 2-H), 4.37 (dd, $^3J_{14,16a}$ = 11.0 Hz, $^3J_{14,16b}$ = 3.8 Hz, 1H, 14-H), 4.35 – 4.30 (m, 1H, 11-H), 3.72 (dd, $^2J_{16b,16a}$ = 15.0 Hz, $^3J_{16b,14}$ = 3.7 Hz, 1H, 16-H$_b$), 2.98 (dd, $^2J_{16a,16b}$ = 15.1 Hz, $^3J_{16a,14}$ =11.0 Hz, 1H, 16-H$_a$), 2.36 (d, $^3J_{10,11}$ = 8.7 Hz, 2H, 10-H), 1.48 (s, 3H, 13-H).

^{13}C NMR (151 MHz, $CDCl_3$) δ [ppm] = 168.22 (C-15), 167.26 (C-12), 147.28 (C-9), 136.74 (C-25), 133.51 (C-4), 128.67 (C-18), 126.77 (C-20), 123.63, 122.83, 122.61, 120.06, 119.42 (C-Ar), 118.55 (C-24), 111.71 (C-21), 109.9´65 (C-19), 109.58 (C-5), 84.09 (C-2), 58.41 (C-14), 54.81 (C-11), 51.32 (C-3), 41.03 (C-10), 26.81 (C-16), 23.57 (C-13).

IR: IR (ATR): ṽ [cm^{-1}] = 3333 (m), 2925 (w), 1668 (vs), 1418 (s), 1343 (w), 1199 (m), 1101 (w) 745 (vs), 463 (w).

MS: MS (ESI, 60 eV): m/z (%) = 387.18 [M+]

Optical rotation: $[\alpha]_D^{20}$ = -46 (*c* 1.0, MeOH)

The analytical data are consistent with the literature.

Double *C3*-methylated LL -cWW **240**

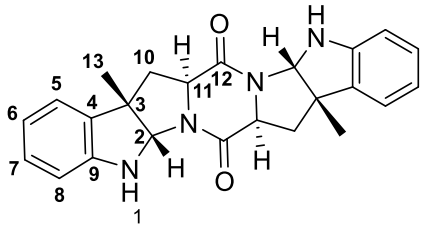

^{1}H NMR (600 MHz, $CDCl_3$) δ [ppm] = 7.05 (d, $^{3}J_{8.7}$ = 7.4 Hz, 1H, 8-H), 7.04 – 7.00 (m, 1H, 7-H), 6.74 (dd, $^{3}J_{6,5}$ = 7.4 Hz, $^{3}J_{6,7}$ = 7.4 Hz, 1H, 6-H), 6.52 (d, $^{3}J_{5,6}$ = 7.8 Hz, 1H, 5-H), 5.19 (s, 1H, 2-H), 5.04 (s, 1H, NH), 3.96 (dd, $^{3}J_{11,10b}$ = 11.0 Hz, $^{3}J_{11,10b}$ = 6.1 Hz, 1H, 11-H), 2.69 (dd, $^{2}J_{10b,10a}$ = 12.9 Hz, $^{3}J_{10b,11}$ = 6.2 Hz, 1H, 10-H_b), 2.27 (dd, $^{2}J_{10a,10b}$ = 12.9 Hz, $^{3}J_{10a,11}$ = 11.3 Hz, 1H, 10-H_a), 1.44 (s, 3H, 13-H).

^{13}C NMR (151 MHz, $CDCl_3$) δ [ppm] = 166.75 (C-12), 148.40 (C-9), 132.22 (C-4), 128.79 (C-7), 122.70 (C-8), 119.70 (C-6), 109.60 (C-5), 81.23 (C-2), 60.63 (C-11), 52.06 (C-3), 39.99 (C-10), 24.24 (C-13).

IR: IR (ATR): ṽ [cm^{-1}] = 3373 (m), 2960 (w), 1660 (vs), 1484 (m), 1424 (s), 1241 (w), 1165 (w), 1057 (w), 744 (s).

MS: MS (ESI, 60 eV): m/z (%) = 401.20 [M+]

Optical rotation: $[\alpha]_D^{20}$ = -704 (*c* 0.1, MeOH)

7.2.4 Synthesis brominated *C3*-methylated cWW derivatives

The brominated cWW substrates were subjected to methylation using immobilised SgMT (70 Vol%) under the conditions described in Section 7.1.17

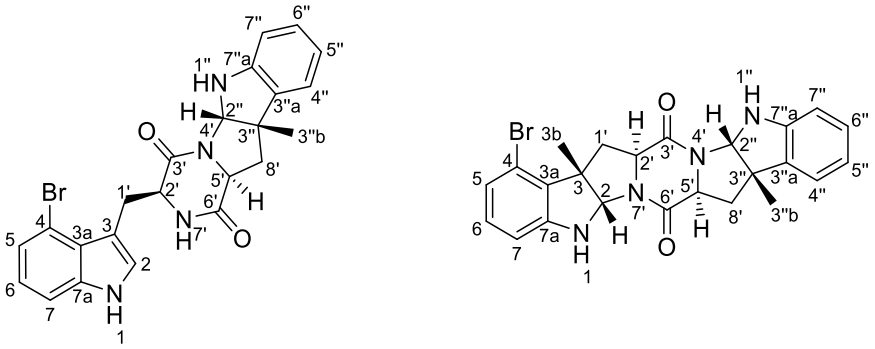

According to section 7.1.17, the monomethylated and dimethylated compound was yielded within one reaction utilizing 4-Br cWW (**274**) (100 mg, 0.22 mmol, 1.0 equiv.). The purification and product characterisation were conducted by Marcel Schatton.

Single *C3*-methylated 4-Br cWW **281** (56.5 mg, 0.12 mmol, 56%)

^{1}H NMR (600 MHz, $CDCl_3$) δ [ppm] = 8.53 (s, 1H), 7.38 – 7.27 (m, 2H, 2-H, 7-H), 7.16 – 7.07 (m, 3H, 5-H, 4‘‘-H, 6‘‘-H), 7.03 (t, $^{3}J_{6,5,4}$ = 7.9 Hz, 1H, 6-H), 6.79 (t, $^{3}J_{5‘‘,6‘‘,4‘‘}$ = 7.4 Hz, 1H, 5‘‘-H), 6.64 (d, $^{3}J_{7‘‘,6‘‘}$ = 7.9 Hz, 1H, 7‘‘-H), 5.80 (s, 1H, 7‘-H), 5.32 (s, 1H, 2‘‘-H), 5.14 (s, 1H, 1‘‘-H), 4.49 (d, $^{3}J_{2‘,1‘}$ = 8.5 Hz, 1H, 2‘-H), 4.20 (dd, $^{2}J_{1’,1‘}$ = 14.8, $^{3}J_{1’,2‘}$ = 3.5 Hz, 1H, 1’-H_a), 4.01 (dd, $^{3}J_{5‘,8‘}$ = 10.6 Hz, $^{3}J_{5‘,8‘}$ = 5.9 Hz, 1H, 5‘-H), 2.89 (dd, $^{2}J_{1’,1‘}$ = 14.8, $^{3}J_{1’,2‘}$ = 10.6 Hz, 1H, 1’-H_b), 2.73 (dd, $^{2}J_{8’,8‘}$ = 12.6 Hz, $^{3}J_{8’,5‘}$ = 6.2 Hz, 1H, 8’-H_a), 2.23 (dd, $^{2}J_{8’,8‘}$ = 12.0 Hz, $^{3}J_{8’,5‘}$ = 12.0 Hz, 1H, 8’-H_b), 1.46 (s, 3H, 3‘‘b-H).

^{13}C NMR (151 MHz, $CDCl_3$) δ [ppm] = 169.3 (C-6‘), 166.5 (C-3‘), 148.6 (C-7‘‘a), 138.2 (C-7a), 132.3 (C-3’’a), 128.9 (C-6’’), 125.7 (C-5), 125.1 (C-3a), 124.6 (C-2), 123.8 (C-6), 122.9 (C-4’’), 119.7 (C5’’), 114.1 (C-4), 111.1 (C-7), 110.7 (C-3), 109.7 (C-7’’), 81.7 (C-2’’), 59.3 (C-5’), 55.5 (C-2’), 51.7 (C-3’’), 40.8 (C-8’), 27.4 (C-1’), 24.5 (C-3’’b).

MS: MS (ESI, 60 eV): m/z (%) = 465.09 [M+]

IR: IR (ATR): $\tilde{\nu}$ [cm^{-1}] = 3341 (w), 3234 (br), 3052 (w), 1663 (vs), 1438 (s), 1190 (s), 1082 (s), 894 (m), 746 (w), 531 (w).

Optical rotation: $[\alpha]_D^{20}$ = -304.3° (c = 0.286, MeOH)

Double *C3*-methylated 4-Br cWW **282** (17.8 mg, 37 µmol, 17%)

^{1}H NMR (600 MHz, $CDCl_3$) δ [ppm] = 7.08 (dd, $^{3}J_{4'',5''}$ = 7.4 Hz, $^{4}J_{4'',6''}$ = 1.2 Hz, 1H, 4''-H), 7.03 (td, $^{3}J_{6'',5'',7''}$ = 7.6 Hz, $^{4}J_{6'',4''}$ = 1.2 Hz, 1H, 6''-H), 6.87 (t, $^{3}J_{6,4,7}$ = 7.8 Hz, 1H, 6-H), 6.83 (dd, $^{3}J_{5,6}$ = 7.9 Hz, $^{4}J_{5,7}$ = 1.0 Hz, 1H, 5-H), 6.76 (t, $^{3}J_{5'',4'',6''}$ = 7.4 Hz, 1H, 5''-H), 6.56 (d, $^{3}J_{7'',6''}$ = 7.7 Hz, 1H, 7''-H), 6.45 (dd, $^{3}J_{7,6}$ = 7.6, $^{4}J_{7,5}$ = 1.0 Hz, 1H, 7-H), 5.22 (s, 1H, 2''-H), 5.18 (s, 1H, 2-H), 4.06 (ddd, $^{3}J_{5',8'}$ = 11.6, $^{3}J_{5',8'}$ = 6.2, $^{3}J_{5',2''}$ = 2.0 Hz, 1H, 5'-H), 4.02 (ddd, $^{3}J_{2',1'}$ = 11.2, $^{3}J_{2',1'}$ = 6.2, $^{3}J_{2',2}$ = 1.9 Hz, 1H, 2'-H), 3.50 (dd, $^{2}J_{1',1'}$ = 13.5, $^{3}J_{1',2'}$ = 6.2 Hz, 1H, 1'-H_a), 2.71 (dd, $^{2}J_{8',8'}$ = 13.0, $^{3}J_{8',5'}$ = 6.2 Hz, 1H, 8'-H_a), 2.30 – 2.26 (m, 1H, 8'-H_b), 2.13 (dd, $^{2}J_{1',1'}$ = 13.5, $^{3}J_{1',2'}$ = 11.5 Hz, 1H, 1'-H_b), 1.57 (s, 3H, 3b-H), 1.45 (s, 3H, 3''b-H).

^{13}C NMR (151 MHz, $CDCl_3$) δ [ppm] = 166.9 (C-6'), 166.6 (C-3'), 150.4 (C-7a), 148.3 (C-7''a), 132.2 (C-3''a), 130.5 (C-6), 128.9 (C-6''), 128.6 (C-3a), 123.8 (C-5), 122.7 (C-4''), 119.8 (C-5''), 119.1 (C-4), 109.7 (C-7''), 108.6 (C-7), 81.6 (C-2), 81.3 (C-2''), 60.7 (C-5'), 60.6 (C-2'), 54.2 (C-3), 52.1 (C-3''), 39.9 (C-8'), 37.2 (C-1'), 24.2 (C-3''b), 21.7 (C-3b).

MS: MS (ESI, 60 eV): m/z (%) = 479.107 [M+]

IR: IR (ATR): $\tilde{\nu}$ [cm^{-1}] = 3193 (m), 3050 (br), 2857 (m), 1667 (s), 1456 (vs), 1243 (m) 1163 (m), 1095 (m), 1069 (m), 990 (s), 914 (m), 517 (m).

Optical rotation: $[\alpha]_D^{20}$ = -578.4° (c = 0.148, MeOH)

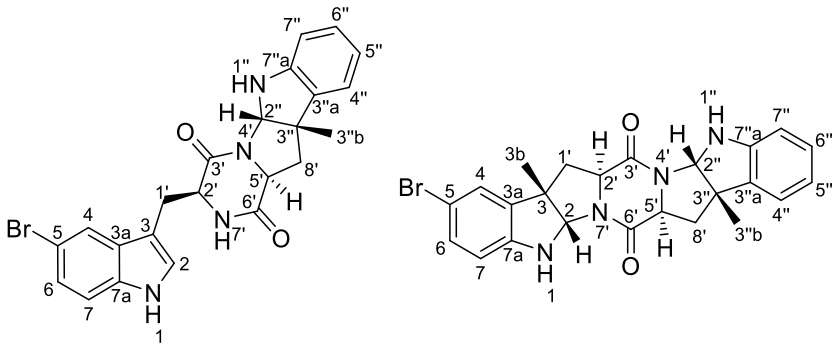

According to section 7.1.17, the monomethylated and dimethylated compound was yielded within one reaction utilizing 5-Br cWW (**258a**) (50 mg, 0.11 mmol, 1.0 equiv.). The purification and product characterisation were conducted by Marcel Schatton.

Single*C3*-methylated 5-Br cWW **264** (4 mg, 7.6 µmol, 6%)

^{1}H NMR (600 MHz, MeOD) δ [ppm] = 7.79 (d, $^{4}J_{4,6}$ = 1.9 Hz, 1H, 4-H), 7.31 (d, $^{3}J_{7,6}$ = 8.6 Hz, 1H, 7-H), 7.20 (dd, $^{3}J_{6,7}$ = 8.6 Hz, $^{4}J_{6,4}$ = 1.9 Hz, 1H, 6-H), 7.12 (s, 1H, 2-H), 6.96 (td, $^{3}J_{6'',5'',7''}$ = 7.6 Hz, $^{4}J_{6'',4''}$ = 1.2 Hz, 1H, 6''-H), 6.92 (d, $^{3}J_{4'',5''}$ = 7.4 Hz, 1H, 4''-H), 6.64 (t, $^{3}J_{5'',6'',4''}$ = 7.4 Hz, 1H, 5''-H), 6.52 (d, $^{3}J_{7'',6''}$ = 7.8 Hz, 1H, 7''-H), 4.92 (s, 1H, 2''-H), 4.36 (dd, $^{3}J_{2',1'}$ = 5.2, $^{3}J_{2',1'}$ = 2.8 Hz, 1H, 2'-H), 3.69 (ddd, $^{2}J_{5',8'}$ = 12.2 Hz, $^{3}J_{5',8'}$ = 5.2, $^{3}J_{5',2''}$ = 1.8 Hz, 1H, 5'-H), 3.50 (dd, $^{2}J_{1',1'}$ = 14.6 Hz, $^{3}J_{1',2'}$ = 3.5 Hz, 1H, 1'-H_b), 3.10 (dd, $^{2}J_{1',1'}$ = 14.6 Hz, $^{3}J_{1',2'}$ = 4.6 Hz, 1H, 1'-H_a), 2.11 (dd, $^{2}J_{8',8'}$ = 11.8 Hz, $^{3}J_{8',5'}$ = 5.2 Hz, 1H, 8'-H_a), 0.82 (s, 3H, 3''b-H), 0.51 (t, $J_{8',8',5'}$ = 12.0 Hz, 1H, 8'-H_b).

^{13}C NMR (151 MHz, MeOD) δ [ppm] = 169.6 (C-2'), 167.0 (C-6'), 150.9 (C-7''a), 136.4 (C-7a), 133.5 (C-3''a), 130.5 (C-3a), 129.5 (C-6''), 128.0 (C-2), 125.4 (C-6), 123.8 (C-4''), 122.8 (C-4), 120.1 (C-5''), 114.1 (C-7), 113.4 (C-5), 109.8 (C-7''), 108.8 (C-3), 82.4 (C-2''), 59.3 (C-5'), 57.4 (C-2'), 52.6 (C-3''), 43.6 (C-8'), 30.6 (C-1'), 25.0 (C-3''b).

MS: MS (ESI, 60 eV): m/z (%) = 465.091 [M+]

IR: IR (ATR): ṽ [cm^{-1}] = 3279 (br), 2924 (m), 2854 (m), 1661 (vs), 1609 (m), 1484 (m), 1455 (s), 1312 (m), 1214 (m), 1066 (s), 881 (m), 795 (m), 747 (s), 606 (m).

Optical rotation: $[\alpha]_D^{20}$ = -180 (c = 0.31, $CHCl_3$)

Double *C3*-methylated 5-Br cWW **267** (17.8 mg, 37 µmol, 17%)

^{1}H NMR (600 MHz, MeOD) δ [ppm] = 7.25 (d, $^{3}J_{4,6}$ = 2.0 Hz, 1H, 4-H), 7.12 – 7.08 (m, 2H, 4''-H, 6-H), 7.00 (t, $^{3}J_{6'',5'',7''}$ = 7.6 Hz, 1H, 6''-H), 6.71 (t, $^{3}J_{5'',4'',6''}$ = 7.4 Hz, 1H, 5''-H), 6.56 (d, $^{3}J_{7'',6''}$ = 7.8 Hz, 1H, 7''-H), 6.47 (d, $^{3}J_{7,6}$ = 8.3 Hz, 1H, 7-H), 5.23 (s, 1H, 2-H), 5.21 (s, 1H, 2''-H), 4.08 – 3.99 (m, 2H, 2'-H, 5'-H), 2.65 (app. dt, *J* = 13.4, 6.8 Hz, 2H, 1'-H, 8'-H), 2.28 – 2.19 (m, 2H, 1'-H, 8'-H), 1.42 (s, 3H, 3b-H/3''b-H), 1.41 (s, 3H, 3''b-H/3b-H).

^{13}C NMR (151 MHz, MeOD δ [ppm] = 168.1 (C-3'/6'), 168.0 (C-6'/3'), 150.3 (C-7''a), 149.7 (C-7a), 136.5 (C-3a), 133.9 (C-3''a), 132.3 (C-6), 129.6 (C-6''), 126.9 (C-4), 123.7 (C-4''), 120.3 (C-5''), 111.8 (C-7), 111.3 (C-5), 110.5 (C-7''), 82.5 (C-2/2''), 82.4 (C-2''/2), 61.4 (C-2'/5'), 61.3 (C-5'/2'), 53.1 (C-3/3''), 53.0 (C-3''/3), 41.6 (C-1'/8'), 41.5 (C-8'/1'), 25.0 (C-3b/3''b), 25.0 (C-3''b/3b).

MS: MS (ESI, 60 eV): m/z (%) = 479.107 [M+]

IR: IR (ATR): $\tilde{\nu}$ [cm^{-1}] = 3348 (br), 2971 (w), 2958 (m), 2925 (m), 2850 (w), 1661 (vs), 1600 (m), 1479 (s), 1427 (s), 1216 (m), 1190 (m), 1165 (m), 1057 (m), 813 (w), 753 (w).

Optical rotation: $[\alpha]_D^{20}$ = -494 (c = 0.174, $CHCl_3$)

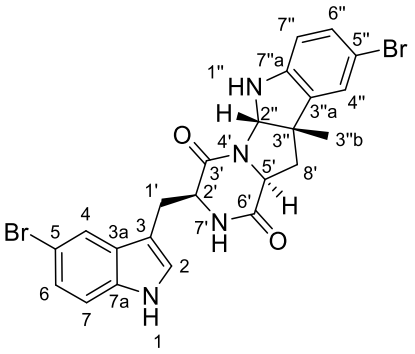

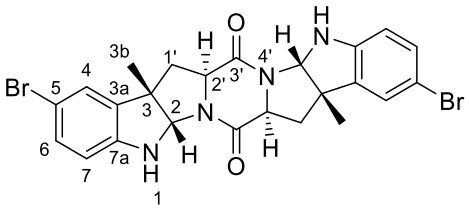

According to section 7.1.17, the monomethylated and dimethylated compound was yielded within one reaction utilizing 5,5'-Br cWW (**278**) (10 mg, 19 µmol, 1.0 equiv.). The purification and product characterisation were conducted by Marcel Schatton.

Single *C3*-methylated 5.5'-Br cWW **285** (5.5 mg, 10 µmol, 54%)

^{1}H NMR (600 MHz, MeOD) δ [ppm] = 7.78 (d, $^{3}J_{2,1}$ = 2.0 Hz, 1H, 2-H), 7.31 (d, $^{3}J_{7,6}$ = 8.6 Hz, 1H, 7-H), 7.20 (dd, $^{3}J_{6,7}$ = 8.6 Hz, $^{2}J_{6,4}$ = 2.0 Hz, 1H, 6-H), 7.12 (s, 1H, 4''-H), 7.08 – 7.05 (m, 2H, 4-H, 6''-H), 6.43 (d, $^{3}J_{7'',6''}$ = 9.0 Hz, 1H, 7''-H), 5.50 (s, 1H, NH), 4.46 – 4.31 (m, 1H, 5'-H), 3.72 (app. ddd, *J* = 12.2, 5.1 Hz, 1.8 Hz, 1H, 2'-H), 3.50 (dd, $^{2}J_{1',1'}$ = 14.6, $^{3}J_{1',2'}$ = 3.4 Hz, 1H, 1'-H_a), 3.10 (dd, $^{2}J_{1',1'}$ = 14.6, $^{3}J_{1',2'}$ = 4.6 Hz, 1H, 1'-H_b), 2.10 (dd, $^{2}J_{8'a,8'b}$ = 11.9, $^{3}J_{8'a,\ 5'}$ = 5.2 Hz, 1H, 8'-H_a), 0.81 (s, 3H, 3''b-H), 0.48 (dd, $^{2}J_{8'b,8'a}$= 12.1 Hz, $^{3}J_{8'b,5'}$ = 12.1 Hz, 1H, 8'-H_b).

^{13}C NMR (151 MHz, MeOD) δ [ppm] = 169.4 (C-3'), 166.9 (C-6'), 150.3 (C-7''a), 136.4 (C-7a), 136.1 (C-3''a), 132.2 (C-6''), 130.5 (C-3a), 128.0 (C-4''), 127.0 (C-4), 125.4 (C-6), 122.8 (C-2), 114.1 (C-7), 113.4 (C-5), 111.0 (C-7''), 110.9 (C-5''), 108.8 (C-3), 82.6 (C-2''), 59.3 (C-3''), 57.4 (C-5'), 52.7 (C-2'), 43.5 (C8'), 30.7 (C-1'), 24.9 (C-3''b).

MS: MS (ESI, 60 eV): m/z (%) = 545.000 [M+]

IR: IR (ATR): ṽ [cm^{-1}] = 2973 (br), 2921 (br), 1728 (vs), 1670 (w), 1446 (w), 1357 (s), 1232 (m), 2322 (s).

Optical rotation: $[\alpha]_D^{20}$ = -68.0 (c = 0.075, MeOH)

Double *C3*-methylated 5.5'-Br cWW **286** (2.6 mg, 4.8 µmol, 25%)

^{1}H NMR (600 MHz, MeOD) δ [ppm] = 7.09 (d, $^{4}J_{4,6}$ = 1.9 Hz, 2H, 4-H), 7.06 (dd, $^{3}J_{6,7}$ = 8.2, $^{4}J_{6,4}$ = 1.9 Hz, 2H, 6-H), 6.36 (d, $^{3}J_{7,6}$ = 8.2 Hz, 2H, 7-H), 5.12 (s, 2H, 2-H), 3.97 (dd, $^{3}J_{2',1'}$ = 10.4, $^{3}J_{2',1'}$ = 6.2 Hz, 2H, 2'-H), 2.60 (dd, $^{2}J_{1',1'}$ = 13.0, $^{3}J_{1',2'}$ = 6.2 Hz, 2H, 1'-H_a), 2.20 (dd, $^{2}J_{1',1'}$ = 13 Hz, $^{3}J_{1',2'}$ = 11.2 Hz, 2H, 1-H_a), 1.37 (s, 6H, 3b-H).

^{13}C NMR (151 MHz, $CDCl_3$) δ [ppm] = 166.6 (C-3'), 147.4 (C-7a), 134.7 (C-3a), 131.7 (C-6), 126.1 (C-4), 125.9 (C-7), 111.2 (C-5), 81.4 (C-2), 60.9 (C-2'), 52.3 (C-3), 39.8 (C-1'), 29.8 (C-3b).

MS: MS (ESI, 60 eV): m/z (%) = 559.0159 [M+]

IR: IR (ATR): $\tilde{\nu}$ [cm^{-1}] = 3348 (br), 2971 (w), 2958 (m), 2925 (m), 2850 (w), 1661 (vs), 1600 (m), 1479 (s), 1427 (s), 1216 (m), 1190 (m), 1165 (m), 1057 (m), 813 (w), 753 (w).

Optical rotation: $[\alpha]_D^{20}$ = -157 (c = 0.021, MeOH)

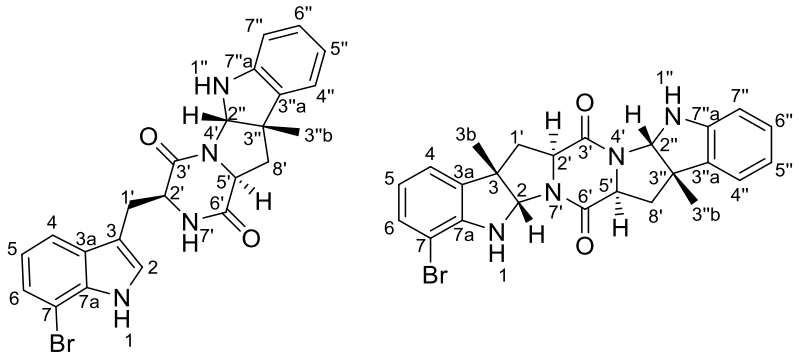

According to section 7.1.17, the monomethylated and dimethylated compound was yielded within one reaction utilizing 7-Br cWW (**276**) (100 mg, 0.22 mmol, 1.0 equiv.).

Single *C3*-methylated 7-Br cWW **283** (74 mg, 0.16 mmol, 72%.)

^{1}H NMR (600 MHz, MeOD) δ [ppm] = 8.36 (s, 1H, 1-H), 7.51 (d, $^{3}J_{4,5}$ = 7.9 Hz, 1H, 4-H), 7.38 (dd, $^{3}J_{6,5}$ = 7.6 Hz, $^{2}J_{6,4}$ = 0.8 Hz, 1H, 6-H), 7.17 (d, $^{3}J_{2,1}$ = 2.4 Hz, 1H, 2-H), 7.13 – 7.05 (m, 2H, 4‘‘-H, 7‘‘-H), 7.02 (t, $^{3}J_{5,6,4}$ = 7.8 Hz, 1H, 5-H), 6.78 (td, $^{3}J_{5‘‘,4‘‘,6‘‘}$ = 7.4 Hz, $^{2}J_{5‘‘,7‘‘}$ = 1.0 Hz, 1H, 5‘‘-H), 6.63 (dd, $^{3}J_{7‘‘,6‘‘}$ = 8.2 Hz, $^{2}J_{7‘‘,5‘‘}$ = 1.0 Hz, 1H, 7‘‘-H), 5.68 (s, 1H, 7‘-H), 5.25 (s, 1H, 2‘‘-H), 4.31 (ddd, $^{3}J_{2‘,1‘}$ = 10.2 Hz, $^{3}J_{2‘,1‘}$ = 3.7, $^{3}J_{2‘,7‘}$ = 1.7 Hz, 1H, 2‘-H), 3.97 (dd, $^{3}J_{5‘,8‘}$ = 11.4 Hz, $^{3}J_{5‘,8‘}$ = 6.1, 1H, 5‘-H), 3.65 (ddd, $^{2}J_{1’,1‘}$ = 15.1 Hz, $^{3}J_{1’,2‘}$ = 3.8 Hz, $^{4}J_{1’,2}$ = 1.0 Hz, 1H, 1’-H_b), 3.02 (dd, $^{2}J_{1’,1‘}$ = 15.1 Hz, $^{3}J_{1’,2‘}$ = 10.1 Hz, 1H, 1’-H_a), 2.67 (dd, $^{2}J_{8’,8‘}$ = 12.7 Hz, $^{3}J_{8’,5‘}$ = 6.1 Hz, 1H, 8’-H_b), 2.06 (dd, $^{2}J_{8’,8‘}$ = 12.7 Hz, $^{3}J_{8’,5‘}$ = 11.3 Hz, 1H, 8’-H_a), 1.40 (s, 3H, 3‘‘b-H).

^{13}C NMR (151 MHz, $CDCl_3$) δ [ppm] = 168.9 (C-6‘), 166.0 (C-3‘), 148.5 (C-7‘‘a), 135.4 (C-7a), 132.2 (C-3’’a), 128.9 (C-6’’), 128.0 (C-3a), 125.3 (C-6), 124.1 (C-2), 122.9 (C-4’’), 121.5 (C-5’), 119.8 (C-5’’), 117.9 (C-4), 111.1 (C-3), 109.6 (C-7’’), 105.3 (C-7), 81.6 (C-2), 59.2 (C-5’), 54.9 (C-2’), 51.8 (C-3’’), 40.9 (C-8’), 27.4 (C-1’), 24.5 (C-3’’b).

MS: MS (ESI, 60 eV): m/z (%) = 465.0918 [M+]

IR: IR (ATR): $\tilde{\nu}$ [cm^{-1}] = 3301 (br), 1978 (w), 2918 (w), 1734 (m), 1660 (vs), 1479 (m), 1465 (s), 1432 (s), 1358 (m), 1210 (s), 1102 (w), 786 (w), 746 (w).

Optical rotation: $[\alpha]_D^{20}$ = -176.8° (c = 0.203, MeOH)

Double *C3*-methylated 7-Br cWW **284** (3.1 mg, 6.4 µmol, 3%.)

^{1}H NMR (600 MHz, $CDCl_3$) δ [ppm] = 7.17 (dd, $^{3}J_{6,5}$ = 8.0 Hz, $^{4}J_{6,4}$ = 1.0 Hz, 1H, 6-H), 7.08 (dd, $^{3}J_{4'',5''}$ = 7.4 Hz, $^{3}J_{4'',6'}$ = 1.2 Hz, 1H, 4''-H), 7.02 (td, $^{3}J_{6'',5'',7''}$ = 7.6 Hz, $^{4}J_{6'',4''}$ = 1.2 Hz, 1H, 6''-H), 7.00 (dd, $^{3}J_{4,5}$ = 7.4 Hz, $^{4}J_{4,6}$ = 1.0 Hz, 1H, 4-H), 6.75 (t, $^{3}J_{5'',4'',6''}$ = 7.4 Hz, 1H, 5''-H), 6.63 (dd, $^{3}J_{5,6}$ = 7.9, $^{3}J_{5,4}$ = 7.4 Hz, 1H, 5-H), 6.54 (d, $^{3}J_{7'',6''}$ = 7.8 Hz, 1H, 6''-H), 5.27 (s, 1H, 2-H), 5.20 (s, 1H, 2''-H), 4.11 – 4.03 (m, 2H, 2'-H, 5'-H), 2.73 (dd, $^{2}J_{1',1'}$ = 12.9 Hz, $^{3}J_{1',2'}$ = 6.2 Hz, 1H, 1'-H_a), 2.69 (dd, $^{2}J_{8',8'}$ = 13.1 Hz, $^{3}J_{8',5'}$ = 6.2 Hz, 1H, 8'-H_a), 2.28 (m, 2H, 1'-H_b, 8'-H_b), 1.46 (s, 4H, 3b-H), 1.45 (s, 4H, 3''b-H).

^{13}C NMR (151 MHz, $CDCl_3$) δ [ppm] = 166.6 (C-3'), 166.6 (C-6'), 148.3 (C-7''a), 147.0 (C-7a), 133.5 (C-3a), 132.2 (C-3''a), 131.4 (C-6), 128.8 (C-6''), 122.8 (C-4''), 121.6 (C-4), 120.9 (C-5), 119.8 (C-5''), 109.7 (C-7''), 103.1 (C-7), 81.3 (C-2''), 80.2 (C-2), 60.7 (C-5'), 60.6 (C-2'), 53.4 (C-3), 52.1 (C-3''), 40.4 (C-1'), 40.0 (C-8'), 24.4 (C-3b), 24.2 (C-3''b).

MS: MS (ESI, 60 eV): m/z (%) = 479.1074 [M+]

IR: IR (ATR): $\tilde{\nu}$ [cm^{-1}] = 3361 (br), 2918 (m), 2857 (w), 1741 (vs), 1667 (s), 1432 (m), 1364 (s), 1351 (m), 1210 (s).

Optical rotation: $[\alpha]_D^{20}$ = -278.3° (c = 0.064, MeOH)

7.2.5 Synthesis *C3*- and *N*-methylated cWW

A preparative-scale reaction using the double *C3*-methylated LL-cWW **240** as substrate was performed with 25 mg of the substrate in 70 mL of pure lysate (see chapter 7.1.17 for preparation). After 40 hours at 40 °C with 4 mM SAM (**93**), a yield of 79% of the *N*-methylated product **287** was achieved.

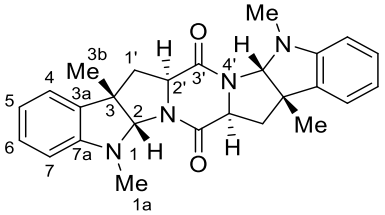

^{1}H NMR (600 MHz, $CDCl_3$) δ [ppm] = 7.09 (t, $^{3}J_{6,5,7}$ = 7.6 Hz, 2H, 6-H), 7.04 (d, $^{3}J_{4,5}$ = 7.3 Hz, 2H, 4-H), 6.70 (t, $^{3}J_{5,4,6}$ = 7.4 Hz, 2H, 5-H), 6.34 (d, $^{3}J_{7,6}$ = 7.8 Hz, 2H, 7-H), 5.44 (s, 2H, 2-H), 4.16 (dd, $^{3}J_{2',1'}$ = 11.0 Hz, $^{3}J_{2',1'}$ = 6.0 Hz, 2H, 2'-H), 2.97 (s, 6H, 1a-H), 2.70 (dd, $^{2}J_{1',1'}$ = 12.8 Hz, $^{3}J_{1',2'}$ = 5.9 Hz, 2H, 1'-H_b), 2.17 (dd, $^{2}J_{1',1'}$ = 11.9 Hz, $^{3}J_{1',2'}$ = 11.9 Hz, 2H, 1'-H_a), 1.47 (s, 6H, 3b-H).

^{13}C NMR (151 MHz, $CDCl_3$) δ [ppm] = 167.8 (C-3'), 151.6 (C-7a), 134.6 (C-3a), 129.7 (C-4), 123.3 (C-6), 119.3 (C-5), 107.1 (C-7), 88.1 (C-2), 61.2 (C-2'), 51.5 (C-3), 43.6 (C-1'), 33.3 (C-1a), 25.8 (C-3b).

MS: MS (ESI, 60 eV): m/z (%) =: 429.228 {M+]

Optical rotation: $[\alpha]_D^{20}$ = -437 (c = 0.200, MeOH).

7.2.6 Synthesis of benzodiazepinedione

Tryptophan **202** (500 mg, 2.47 mmol, 1.0 equiv.) and isatoic anhydride **252** (427.48 mg, 2.62 mmol, 1.06 equiv.) were solved in a 25 mL Schlenk flask in water. Triethylamine (0.345 mL, 2.47 mmol, 1.0 equiv.) was added and the reaction mixture was stirred at 21 °C for 5 h. The solvent was removed under reduced pressure before adding 6 mL of anhydrous acetic acid and heating the reaction to reflux for 5 h. The solvent was removed under reduced pressure and the residue was taken up in ethyl acetate and washed with 100 mL sodium hydrogen carbonate. After extraction with ethyl acetate, the combined organic phase was washed with brine and dried over $MgSO_4$. The solvent was removed under reduced pressure. The product **246** was recrystallised with ethyl acetate and pentane giving a white solid.[371]

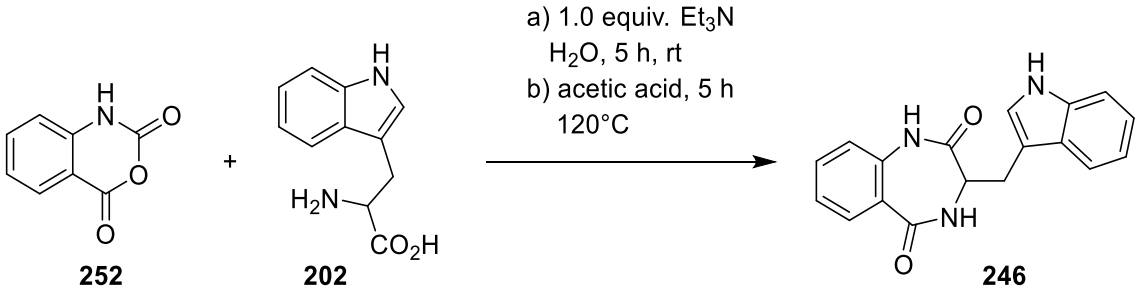

Figure 188: Synthesis of the benzodiazepinedione substrates.

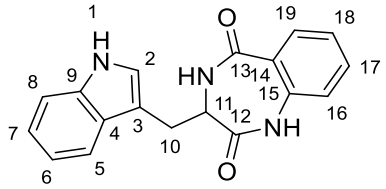

L-cWBenz **246a**

The product was obtained in a 31% yield (0.76 mmol, 231 mg) using the established benzodiazepinedione synthesis protocol.

^{1}H NMR (600 MHz, DMSO-d6) δ [ppm] = 10.86 – 10.82 (m, 1H, NH), 10.41 (s, 1H NH), 8.42 – 8.38 (m, 1H, NH), 7.62 (d, $^{3}J_{19,18}$ = 7.9, 1H, H-19), 7.50 – 7.44 (m, 2H, H-18 + 5-H), 7.29 (d, $^{3}J_{8,7}$ = 8.1 Hz, 1H, 8-H), 7.23 – 7.19 (m, 1H, 2-H), 7.15 (dd, $^{3}J_{17,16+18}$ = 7.5 Hz, 1H, 17-H), 7.08 (d, $^{3}J_{16,17}$ = 8.1 Hz, 1H, 16-H), 7.00 (dd, $^{3}J_{6,7+5}$ = 7.5 Hz, 1H, 6-H), 6.88 (d, $^{3}J_{7,8+9}$ = 7.4 Hz, 1H, 7-H), 3.85 (dd, $^{3}J_{11,10a}$ = 9.3 Hz, $^{3}J_{11,10b}$ = 5.6 Hz, 1H, 11-H), 3.21 (dd, $^{3}J_{10b,10a}$ = 14.9 Hz, $^{3}J_{10b,11}$ = 5.2 Hz, 1H, 10-H_b), 2.97 (dd, $^{3}J_{10a,10b}$ = 14.9 Hz, $^{3}J_{10a,11}$ = 9.4 Hz, 1H, 10-H_a)

^{13}C NMR (151 MHz, DMSO-d6) δ [ppm] = 171.55 (C-12), 167.60 (C-13), 136.80 (C-14), 136.06 (C-4), 132.24 (C-18), 130.39 (C-19), 126.96 (C-9), 126.24 (C-15), 124.32 (C-2), 123.90 (C-17), 120.97 (C-16), 120.93 (C-7), 118.34 (C-5), 118.25 (C-7), 111.40 (C-8), 109.65 (C-3), 52.79 (C.11), 23.54 (C-10).

IR: IR (ATR): $\tilde{\nu}$ [cm^{-1}] = 3272 (w), 3019 (w), 2973 (w), 1736 (s), 1646 (m), 1439 (w), 1366 (m), 1217 (m), 741 (w), 527 (w).

MS: MS (ESI, 60 eV): m/z (%) = 306.12 (80) [M^{+}]

Optical rotation: $[\alpha]_D^{25}$= 193 (c 0.26, DMSO*)*

Melting point: 247.4 °C

The analytical data are consistent with the literature.[371, 372]

D-cWBenz **246b**

The product was obtained in a 33% yield (0.78 mmol, 249 mg) using the established benzodiazepinedione synthesis protocol.

^{1}H NMR (600 MHz, DMSO-d6) δ [ppm] = 10.85 – 10.82 (m, 1H, NH), 10.41 (s, 1H NH), 8.42 – 8.38 (m, 1H, NH), 7.62 (d, $^{3}J_{19,18}$ = 7.8, 1H, H-19), 7.49 – 7.43 (m, 2H, H-18 + 5-H), 7.29 (d, $^{3}J_{8,7}$ = 8.1 Hz, 1H, 8-H), 7.23 – 7.19 (m, 1H, 2-H), 7.14 (dd, $^{3}J_{17,16+18}$ = 7.6 Hz, 1H, 17-H), 7.07 (d, $^{3}J_{16,17}$ = 8.1 Hz, 1H, 16-H), 7.00 (dd, $^{3}J_{6,7+5}$ = 7.5 Hz, 1H, 6-H), 6.87 (d, $^{3}J_{7,8+9}$ = 7.5 Hz, 1H, 7-H), 3.85 (dd, $^{3}J_{11,10a}$ = 9.3 Hz, $^{3}J_{11,10b}$ = 5.6 Hz, 1H, 11-H), 3.20 (dd, $^{3}J_{10b,10a}$ = 15.0 Hz, $^{3}J_{10b,11}$ = 5.2 Hz, 1H, 10-H_b), 2.97 (dd, $^{3}J_{10a,10b}$ = 14.9 Hz, $^{3}J_{10a,11}$ = 9.4 Hz, 1H, 10-H_a)

^{13}C NMR (151 MHz, DMSO-d6) δ [ppm] = 171.56 (C-12), 167.62 (C-13), 136.80 (C-14), 136.06 (C-4), 132.25 (C-18), 130.39 (C-19), 126.97 (C-9), 126.24 (C-15), 124.33 (C-2), 123.91 (C-17), 120.98 (C-16), 120.94 (C-7), 118.35 (C-5), 118.26 (C-7), 111.41 (C-8), 109.66 (C-3), 52.80 (C.11), 23.55 (C-10).

IR: IR (ATR): $\tilde{\nu}$ [cm^{-1}] = 3263 (w), 3066 (w), 2919 (w), 1738 (m), 1647 (s), 1480 (m), 1402 (m), 1365 (m), 1228 (m), 742 (m), 529 (w).

MS: MS (ESI, 60 eV): m/z (%) = 306.12 (80) [M^{+}]

Optical rotation: $[\alpha]_D^{25}$= -195 (c 0.29, DMSO*)*

Melting point: 250.0 °C

7.2.7 Synthesis of melatonin derivatives

1-(5-Methoxy-3a-methyl-3,3a,8,8a-tetrahydropyrrolo[2,3-b]indol-1(2*H*)-yl)ethan-1-one **228**

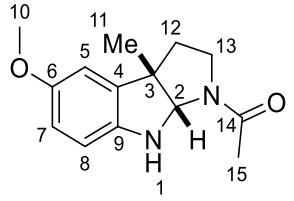

Melatonin (**227**) (1.0 equiv.) was dissolved in dry THF (0.5 mmol·mL^{-1}) in an oven-dried Schlenk flask under inert atmosphere. Tert-BuOK (3.0 equiv.) was added at room temperature. After 30 min, Et_3B (1 M in THF, 5.0 equiv.) was added dropwise. After 30 min, methyl iodide (4.0 equiv.) was added and the reaction was heated to 40 °C for 20 h. TLC was used to confirm full conversion of the starting material. NaOH solution was added (end concentration of 500 mM) to stop the reaction. The aqueous phase was extracted with ethyl acetate (3x 25 mL). The organic phase was washed afterwards with brine and dried over $MgSO_4$. The solvent was removed by rotary evaporation. For purification, a column chromatography on silica with ethyl acetate as eluent was performed yielding in a white solid product (84%).[136]

^{1}H NMR (600 MHz, $CDCl_3$) δ [ppm] = 6.68 (d, $^3J_{8,7}$ = 2.5 Hz, 1H, 8-H), 6.64 (dd, $^4J_{7,.5}$ = 8.4, $^3J_{7,.8}$ = 2.6 Hz, 1H, 7-H), 6.52 (d, $^4J_{5,7}$ = 8.4 Hz, 1H, 5-H), 5.15 (s, 1H, NH), 5.02 (s, 1H, 2-H), 3.75 (s, 3H, 10-H), 3.61 – 3.54 (m, 1H), 3.26 – 3.18 (m, 1H), 2.32 – 2.26 (m, 1H), 2.14 – 2.06 (m, 1H, 13-H_b), 3.26 – 3.18 (m, 1H, 13-H_a), 2.32 – 2.26 (m, 1H, 12-H_b), 2.14 – 2.06 (m, 1H, 12-H_a), 2.00 (s, 3H, 15-H), 1.40 (s, 3H, 11-H).

^{13}C NMR (151 MHz, $CDCl_3$) δ [ppm] = 170.30 (C-14), 153.78 (C-6), 142.87 (C-9), 134.84 (C-4), 112.95 (C-7), 110.05 (C-8), 109.76 (C-5), 82.70 (C-2), 56.13 (C-10), 52.78 (C-3), 47.50 (C-13), 37.22 (C-12), 24.18 (C-15), 22.81 (C-11).

IR: IR (ATR): ṽ [cm-1] = 3328, 2962, 2870, 1633, 1488, 1435, 1275, 1198, 1061, 1030, 862, 809, 679, 618, 460.

MS: MS (ESI, 60 eV): m/z (%) = 247.14 [M+]

Melting point: 111.5 °C

1-(5-Methoxy-3a-(3-methylbut-2-en-1-yl)-3,3a,8,8a-tetrahydropyrrolo[2,3-b]indol-1(2*H*)-yl)ethan-1-one **229**

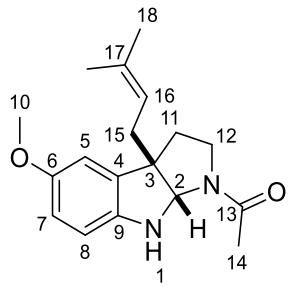

Melatonin (**227**) (100 mg, 0.43 mmol, 1.0 equiv.) was dissolved in dry THF (0.5 mmol·mL^{-1}) in an oven-dried Schlenk flask under inert atmosphere. tert-BuOK (1.3 mL, 1.29 mmol, 3.0 equiv.) was added at room temperature. After 30 min, Et_3B (1 M in THF, 2.1 mL, 2.15 mmol, 5.0 equiv.) was added dropwise. After 30 min, prenyl bromide (4.0 equiv.) was added and the reaction was heated to 40 °C for 20 h. TLC was used to confirm full conversion of the starting material. NaOH solution was added (end concentration of 500 mM) to stop the reaction. The aqueous phase was extracted with ethyl acetate (3x 25 mL). The organic phase was washed afterwards with brine and dried over $MgSO_4$. The solvent was removed by rotary evaporation. For purification, a column chromatography on silica with ethyl acetate as eluent was performed yielding in a pink solid product (106 mg, 0.35 mmol, 82%).[136]

^{1}H NMR (600 MHz, $CDCl_3$) δ [ppm] = 6.67 (d, $^3J_{8,7}$ = 2.5 Hz, 1H, 8-H), 6.64 (dd, $^4J_{7,.5}$ = 8.3, $^3J_{7,.8}$ = 2.6 Hz, 1H, 7-H), 6.51 (d, $^4J_{5,7}$ = 8.3 Hz, 1H, 5-H), 5.19 (s, 1H, 2-H), 5.18 – 5.14 (m, 1H, 16-H), 5.01 (s, 1H, NH), 3.75 (s, 3H, 10-H), 3.59 – 3.53 (m, 1H, 12-H_a), 3.23 – 3.15 (m, 1H, 12-H_b), 2.43 – 2.30 (m, 2H, 15-H), 2.22 – 2.13 (m, 2H, 11-H), 1.99 (s, 3H, 14-H), 1.71 (d, $^3J_{19,18}$ = 1.4 Hz, 3H, 18-H_a), 1.53 (d, $^3J_{18,19}$ = 1.4 Hz, 3H, 18-H_b).

^{13}C NMR (151 MHz, $CDCl_3$) δ [ppm] = 170.26 (C-13), 153.53 (C-6), 143.37 (C-9), 135.40 (C-17), 133.78 (C-4), 119.14 (C-16), 113.07 (C-7), 110.41 (C-8), 109.94 (C-5), 80.55 (C-2), 56.91 (C-10), 47.34 (C-12), 35.43 (C-15), 34.38 (C-11), 26.14 (C-18a), 22.85 (C-14), 18.09 (C-18b).

IR: IR (ATR): ṽ [cm-1] = 3343, 2931, 2878, 1633, 1488, 1282, 1030, 855, 809, 618.

MS: MS (ESI, 60 eV): m/z (%) = 301.19 [M+]

Melting point: 84.5 °C

tert-Butyl 3-(2-acetamidoethyl)-5-methoxy-1*H*-indole-1-carboxylate **231**

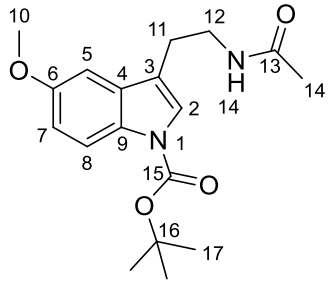

Melatonin (**227**) (250 mg, 1.08 mmol, 1.0 equiv.) was dissolved in dry acetonitrile in an oven-dried Schlenk flask under inert atmosphere. DMAP (5.2 mg, 0.04 mmol, 0.04 equiv.) and di-tert-butyl dicarbonate (305 mg, 1.40 mmol, 1.3 equiv.) were added to the reaction mixture. The reaction mixture was stirred at 25 °C for 16 h. After full conversion, the solvent was removed by rotary evaporation. The crude product was further purified by column chromatography using ethyl acetate as eluent yielding in a white solid (286 mg, 0.86 mmol, 80%).[373]

^{1}H NMR (600 MHz, $CDCl_3$) δ [ppm] = 8.00 (s, 1H, 7-H), 7.39 (s, 1H, 2-H), 7.01 – 6.98 (m, 1H, 5-H), 6.96 – 6.91 (m, 1H, 8-H), 5.55 (s, 1H, NH), 3.87 (s, 3H, 10-H), 3.61 – 3.55 (m, 2H, 12-H), 2.91 – 2.85 (m, 2H, 11-H), 1.96 (s, 3H, 14-H), 1.66 (s, 9H, 17-H).

^{13}C NMR (151 MHz, $CDCl_3$) δ [ppm] = 170.25 (C-13), 156.06 (C-15), 149,59 (C-6), 131.35 (C-4), 123.91 (C-2), 117.61 (C-3), 116.25 (C-7), 113.34 (C-8), 101.78 (C-5), 83.66 (C-16), 55.92 (C-10), 39.28 (C-12), 28.39 (C-17), 25.29 (C-11), 23.55 (C-14).

IR: IR (ATR): ṽ [cm-1] = 3290, 2977, 2939, 1733, 1658, 1542, 1488, 1381, 1275, 1259, 1160, 1084, 847, 481.

MS: MS (ESI, 60 eV): m/z (%) = 333.18 [M+]

Melting point: 132.2 °C; Literature: 133 °C[374]

Tert-butyl-1-acetyl-3a-bromo-5-methoxy-2,3,3a,8a-tetrahydropyrrolo[2,3-b]indole-8(1*H*)-carboxylate **232**

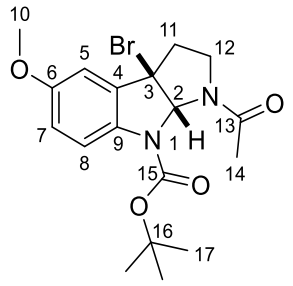

To the solution of Boc-protected melatonin **231** (250 mg, 0.75 mmol, 1 equiv.) in MeCN, KBr (90 mg, 0.75 mmol, 1 equiv.) and oxone (463 mg, 0.75 mmol, 1 equiv.) were added at room temperature. The reaction mixture was stirred for 4 h. After full conversion, saturated sodium thiosulfate aqueous solution was added and extracted with EtOAc three times. The combined organic phases were washed with brine and dried over magnesium sulfate. The organic phase was concentrated by rotary evaporation. The crude product was purified by silica gel column chromatography using ethyl acetate as eluent yielding in a white solid (302 mg, 0.73 mmol, 98%).[375]

^{1}H NMR (600 MHz, $CDCl_3$) δ [ppm] = 7.36 (s, 1H, 5-H), 6.90 – 6.84 (m, 2H, 7-H and 8-H), 6.34 (s, 1H, 2-H), 4.08 – 4.00 (m, 1H, 11-H_b), 3.81 (s, 3H, 10-H), 2.84 – 2.78 (m, 1H, 12-H_b), 2.77 – 2.73 (m, 1H, 11-H_a), 2.70 – 2.63 (m, 1H, 12-H_a), 2.33 (s, 3H, 14-H), 1.57 (s, 12H, 17-H).

^{13}C NMR (151 MHz, $CDCl_3$) δ [ppm] = 170.71 (C-13), 157.47 (C-6), 153.05 (C-15), 135.11 (C-9), 134.25 (C-4), 119.65 (C-5), 116.62 (C-8), 108.41 (C-7), 85.43 (C-2), 83.09 (C-16), 62.73 (C-3), 55.93 (C-10), 45.25 (C-11), 40.24 (C-12), 28.36 (C-17), 21.19 (C-14).

C-15

IR: IR (ATR): ṽ [cm-1] = 2977, 2931, 1710, 1664, 1488, 1397, 1320, 1282, 1152, 1076, 1038, 1015, 855, 778, 595.

MS: MS (ESI, 60 eV): m/z (%) = 411.09 [M+]

Melting point: 112.6 °C

1-(3a-bromo-5-methoxy-3,3a,8,8a-tetrahydropyrrolo[2,3-b]indol-1(2*H*)-yl)ethan-1-one **233**

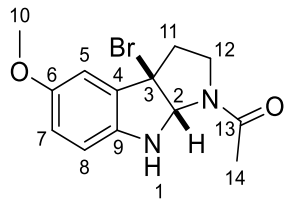

HCl in diethyl ether (1.0 M solution, 4.4 mL, 4.46 mmol, 7.0 equiv.) was added to the Boc-protected Bromo HPI **232** (262 mg, 0.64 mmol, 1.0 equiv.). The solution was stirred over night. After full conversion, ethyl acetate and water (1:1) were added. The aqueous phase was extracted with ethyl acetate (3 times). The organic phase was washed afterwards with brine and dried over $MgSO_4$. The solvent was removed by rotary evaporation. For purification, a column chromatography on silica with ethyl acetate as eluent was performed yielding in a colourless oil product (177 mg, 0.57 mmol, 89%).

^{1}H NMR (600 MHz, $CDCl_3$) δ [ppm] = 8.08 (s, 1H, NH), 7.18 (d, $^{4}J_{5,7}$ = 8.6 Hz, 1H, 5-H), 6.96 (d, $^{3}J_{8,7}$ = 2.4 Hz, 1H, 8-H), 6.85 (dd, $^{4}J_{7,5}$ = 8.8, $^{3}J_{7,8}$ = 2.5 Hz, 1H, 7-H), 5.52 (s, 1H, 2-H), 3.85 (s, 3H, 10-H), 3.57 – 3.49 (m, 2H, 12-H), 2.95 – 2.89 (m, 2H, 11-H), 1.93 (s, 3H, 14-H).

^{13}C NMR (151 MHz, $CDCl_3$) δ [ppm] = 170.31 (C-13), 154.78 (C-6), 129.60 (C-9), 128.24 (C-4), 121.86 (C-3), 112.63 (C-7), 111.59 (C-5), 109.26, 100.36 (C-7), 56.03 (C-10), 39.50 (C-12), 23.60 (C-11), 23.57 (C-14).

IR: IR (ATR): ṽ [cm-1] = 3267, 2931, 1656, 1549, 1481, 1435, 1358, 1297, 2113, 1183, 1068, 0115, 801, 610, 473.

MS: MS (ESI, 60 eV): m/z (%) = 311.04 [M+]

1-(3a-hydroxy-5-methoxy-3,3a,8,8a-tetrahydropyrrolo[2,3-b]indol-1(2*H*)-yl)ethan-1-one **230**

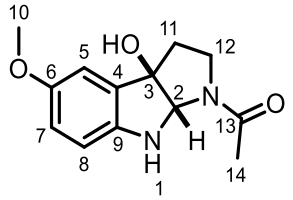

Bromo HPI **233** (100 mg, 0.24 mmol, 1 equiv.) was solved in a mixture solvent of acetonitrile and water (3:1). Ag_2SO_4 (151 mg, 0.49 mmol, 2 equiv.) was added to the mixture. After 2 h, the solid was filtered off. The solvent acetonitrile was removed by rotary evaporation. The residual water was extracted with ethyl acetate (3 times). Afterwards, the organic phase was dried over $MgSO_4$. The solvent was removed by rotary evaporation yielding in a crude white solid product .[376] HCl in diethyl ether (1.0 M solution, 7 equiv.) was added to the crude product. The solution was stirred over night. After full conversion, ethyl acetate and water (1:1) were added. The aqueous phase was extracted with ethyl acetate (3 times). The organic phase was washed afterwards with brine and dried over $MgSO_4$. The solvent was removed by rotary evaporation. For purification, a column chromatography on silica with ethyl acetate as eluent was performed yielding in a colourless oil (32 mg, 0.13 mmol, 63%).

^{1}H NMR (600 MHz, $CDCl_3$) δ [ppm] = 6.87 (d, $^3J_{8,7}$ = 2.6 Hz, 1H, 8-H), 6.73 (dd, $^4J_{7,.5}$ = 8.5, $^3J_{7,.8}$ = 2.6 Hz, 1H, 7-H), 6.53 (d, $^4J_{5,7}$ = 8.5 Hz, 1H, 5-H), 5.27 (s, 1H, 2-H), 3.74 (d, *J* = 3.0 Hz, 3H, 10-H), 3.70 – 3.63 (m, 1H, 12-H_a), 3.32 – 3.25 (m, 1H 12-H_b), 2.49 – 2.41 (m, 1H, 11-H_a), 2.40 – 2.34 (m, 1H, 11-H_b),1.95 (s, 3H, 14-H).

^{13}C NMR (151 MHz, $CDCl_3$) δ [ppm] = 170.87 (C-13), 153.92 (C-6), 143.29 (C-9), 130.79 (C-4), 116.35 (C-7), 111.42 (C-8), 109.49 (C-5), 82.60 (C-2), 56.14 (C-10), 47.18 (C-12), 36.76 (C-11), 22.14 (C-14).

IR: IR (ATR): ṽ [cm-1] = 3351, 2916, 2855, 1740, 1618, 1496, 1465, 1313, 1282, 1221, 1198, 1061, 1030, 870, 809, 717, 418.

MS: MS (ESI, 60 eV): m/z (%) = 249.12 [M+]

7.3 Language editing

To ensure clarity and correctness in English usage, AI-based language assistance tools (ChatGPT, OpenAI; DeepL Translator) were employed during the writing and editing phases. All scientific content was written and verified independently by the author.

8. APPENDIX

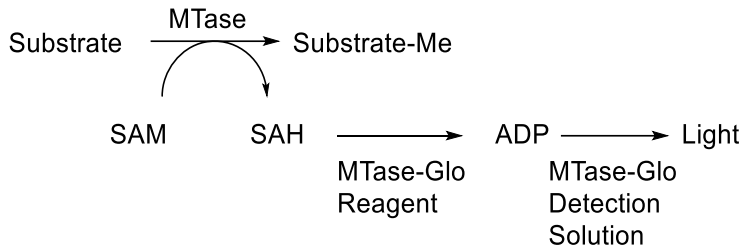

Figure S 1: MTase-Glo™ Methyltransferase Assay.

8.1 HPI based assay

Wild type PsmD from Streptomyces albulus

MQGQPHQDAGMPEPYAATADVYDRLVAYAIAQWGESPRPRMADFIEQAWKARGQ
RVRRVLELCCGTGLMTEELVRRGYEVTAVDRSETMLALAKKRVGGAADFRQIELPA
PLPGDTDAVVCTAAAFNYQSSAHSLGETLHAVATVLPAGATFVFDIETAALLKGHW
GNRMWAADEGDLAFIWNFTSQPDTTYCDVHYTQFTRSEAGPDTYTGTREVHRLYA
FDHDTVRAQARAAGFARAEVFDNYTERPATDATHYETWFLTRDESLEHHHHHH

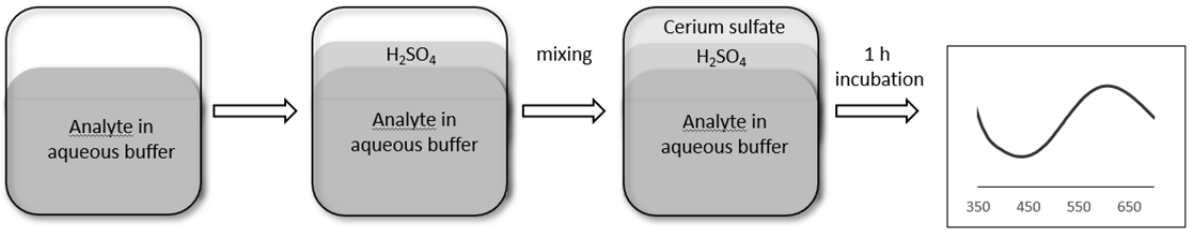

Figure S 2: General optimised procedure for the HPI assay.

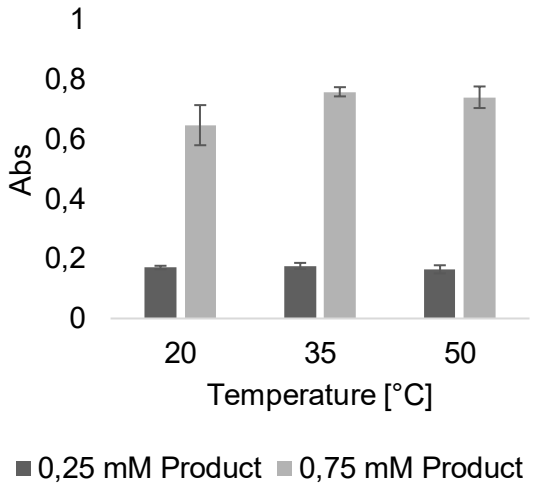

Figure S 3: Optimisation of the HPI assay. Temperature optimisation of acid concentration or cerium sulfate concentration for 0.25 mM and 0.75 mM HPI **228**.

Table S 1: Result of the design of experiment approach varying the acid and cerium sulfate concentration for 0.25 mM of *C3*-methylated melatonin **228**.

Sulphuric acid 1M [µl]	**Cerium sulfate (50 mM) [µL]**	**Absorption (608 nm)**
1,62	2,50	0,095
1,62	2,50	0,107
2,00	4,00	0,144
2,00	1,00	0,070
2,00	4,00	0,075
2,00	1,00	0,069
4,00	4,28	0,147
4,00	0,72	0,134
4,00	4,28	0,038
4,00	2,50	0,192
4,00	2,50	0,194
4,00	2,50	0,193
4,00	0,72	0,146
6,00	4,00	0,107
6,00	1,00	0,192
6,00	4,00	0,113
6,00	1,00	0,189
6,38	2,50	0,144
6,38	2,50	0,162

Table S 2: Result of the design of experiment approach varying the acid and cerium sulfate concentration for 0.27 mM of *C3*-methylated melatonin **228**.

Sulphuric acid 1M [µl]	**Cerium sulfate (50 mM) [µL]**	**Absorption (608 nm)**
2,00	8,00	0,260
8,57	5,00	0,675
5,00	1,43	0,410
2,00	2,00	0,088
8,00	2,00	0,570
8,00	8,00	0,402
5,00	8,57	0,580
1,43	5,00	0,150
1,43	5,00	0,164
5,00	5,00	0,816
2,00	8,00	0,265
8,00	2,00	0,580
8,00	8,00	0,434
5,00	5,00	0,771
2,00	2,00	0,105
5,00	8,57	0,443
5,00	1,43	0,409
5,00	5,00	0,780
8,57	5,00	0,551

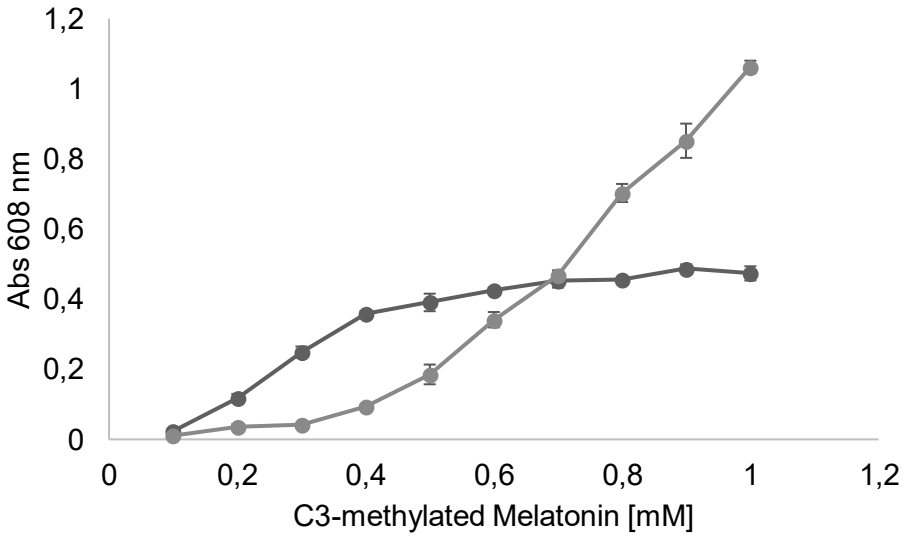

Figure S 4: Calibration of *C3*-methylated melatonin **228**with the small concentration conditions (22.5 mM sulphuric acid and 0.5 mM cerium sulfate; Blue) and the high concentration conditions (30.0 mM sulphuric acid and 1.25 mM cerium sulfate; Grey).

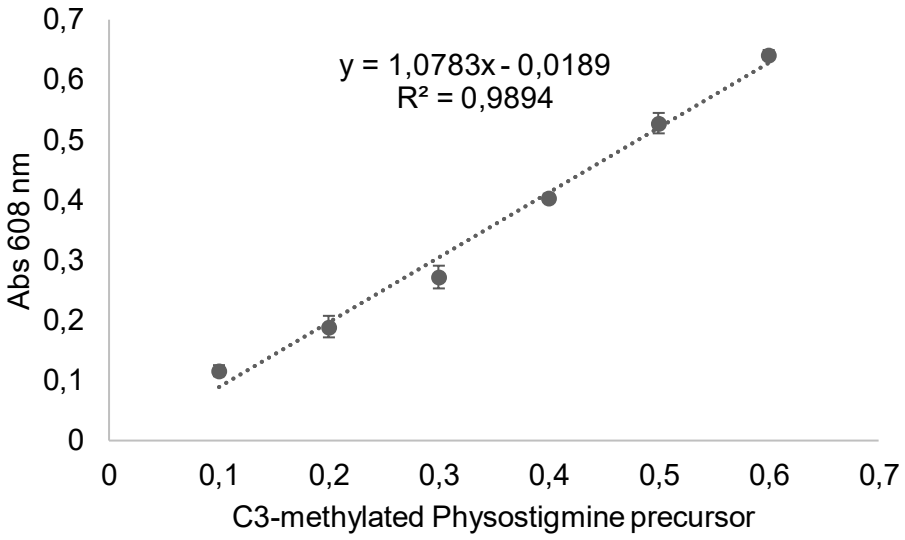

Figure S 5: Calibration of physostigmine precursor **149** (*C3*-methylated). Assay conditions: 30.0 mM sulphuric acid and 1.25 mM cerium sulfate.

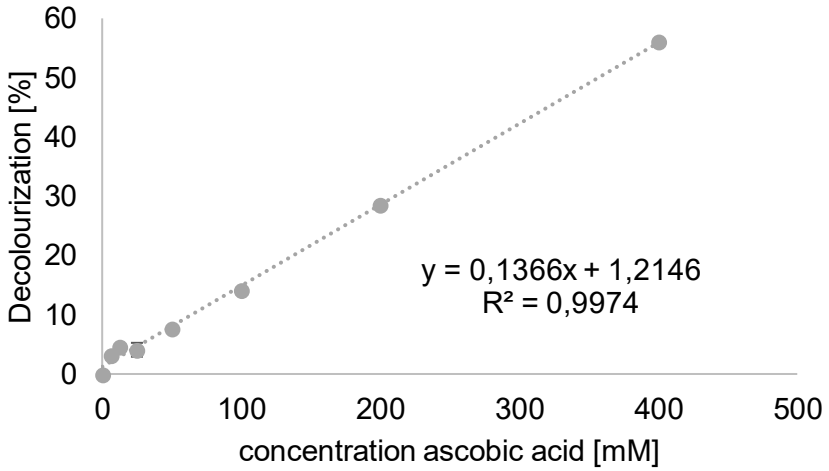

Figure S 6: Calibration of the ABTS Assay.

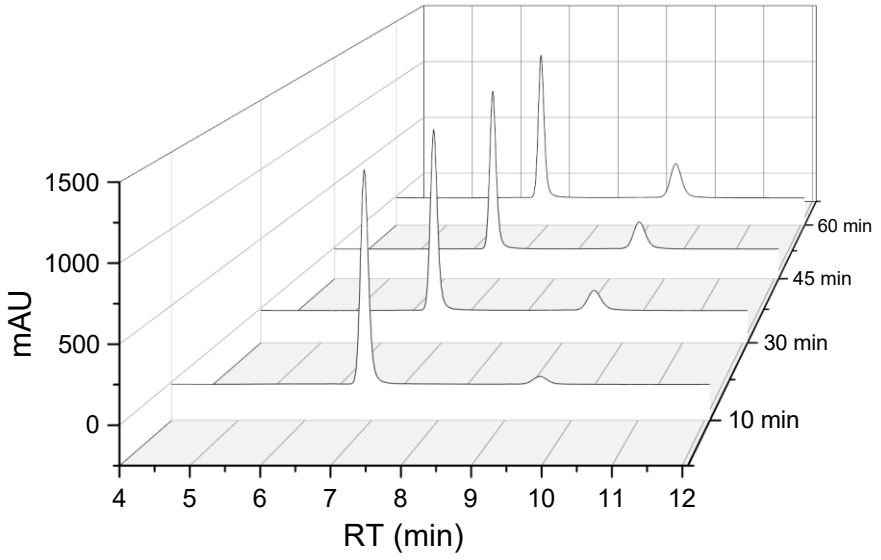

Figure S 7: RP-HPLC chromatograms showing the evolution of the substrate **148** (RT 6.5 min) and product **149** (RT 9.2 min) concentration in time during the enzymatic methylation catalysed by PsmD_Sa. Figure by Diana Amariei.

8.2 DKP *C3*-indole MTases

Sequences, which were used for modelling using RobettaFold from the BakerLab:[317]

>StspM1

MSSETATPADPYTNLADSYDRLAEWAVTCQKESPRDRVADFLQTFWQSQQRPVR
TVLEICCGTGLMLGELARRGYAVTGLDRSAAMLERARRRLGEETTLIHAALPHIPAE
AGPFDAVVSAAGGLNYLPEEQISATFAAVARALPAGGTFTFDVFGRGFFRKFFDSS
APRVMALELDDIAYIWTFTASPEAPFVDMAYTQFTPAPAADGGEPPFLRTRDLHRYY
PLPHTTVRRLAAEHGFTDTKAYDNYSTDPSGPDSLYDTWTMVRSSS

>SgMT

MSSQTVTPDPYGNLAESYDRLAQWAIDQQQESPRDRVGDFLQTFWQSQDRPVRT
VLEICCGTGLMLAELARRGYVVTGLDRSAAMLEQARARMGGKTTLIRAELPDIPAPA
GEFDAVVSAAGGLNYLSESQISATFGAVARLLPAGGTFTFDVFGQGFYAKFFDPSA
PRVMALELDDISYIWTFTKPAEAPFVDMSYTQFSPASRAVDGEPAFIRTRDLHRYYP
LPHATVLRLAAEHGFTDARAHDNYSSDPSGPHTLYDTWTMVRTGS

>SaMT

MAEWAVTCQEESPRDRVADFLQTFWQSQQRPVRTVLEICCGTGLMLGELARRGY
AVTGLDRSAAMLERARRRLGEETTLIHSALPQIPAEAGPFDAVVSAAGGLNYLPGEQ
ISATFAAVARALPAGGTFTFDVFGRGFFRKFFDSSAPRVMALELDDIAYIWTFTASPE
APFVDMAYTQFTPAPAADGGEPPFLRTRDLHRYYPLPHTTVHRLAAEHGFTDTKAY
DNYSTDPSGPDSLYD

TWTMVRSSS

>SeMT

MTVDVPVSSDPYANLAASYDRLVDWVISEQEETPRERMGDYIESFWRDQPRPVHK
VLEICCGTGLMLGDLQRRGYQVSGLDRSAAMLEQARNRLGTGVELVRAELPEIPLH
AGFDAVISAANGLTYLPGTGFGETLAAVARLLPPGGTFVFDLYGHGFFERFYDSAEP
RVLAVELEDVSYIWTFTAPPSRAHFDVVHSQFLRTPDAEAGTYTRTRELHRFHEHT
HTSVRRLAAEAGFSSAEVHDNWTSRPSTPESMYDTWTLTRGV

>NozMT

MTAPATAPHDHPQPYATIADSYDRLLDWSSRHWDESPRTRVGDFLDTLWAGRAEP
VRTVIELCCGTGAVLEELAERGYTVAGLDRSAPMLEQARARLGPAVDLVHSELPDIP
ARATYDALISVGTGLNYLASPDDLARTLESMARTVRPGGPVVFDLLSVRMLTVDAVE
GFSQRPIVEFDDSSFFWTYEHNVAEGHCDLTYTRFQRCPGTSEELFTRTRELHRIH
LRERDLVERLAREAGFTDIAVYDNYAHRPASAETQYEVWTMVAPS

>NOZB-CYIM

MITVDFSLFPVGPGDRVLDLGCGGGRHAFEAYRRGADVVAFDQNTADLADVATMF
AAMRAEGEAPAGTEAETVKGDALDMPFDDGSFNRVIAAEIFEHLPHDTAAMAELYR
VLRPGGIAAVTVPSFLPERLCWALSEDYHTAEGGHVRIYTRAELQAKLKATGFVIGP
HHRAHALHAPYWWLKCAVGTDDDAHPAVKAYHRMLVWDMLQAPPATRITEKALNP
LIGKSVVVYVRKPLRAGPA

>MtMT

MLDLGCGGGRHAFEVYRRGSDVVAFDQNENDLADVATMFAAMRAEGEAPHDASA
ETVKGDALDMPFEDASFDRVIAAEIFEHIPHDTAAMAELYRVLKPGGIAAVTVPSWLP
ERICWALSEEYHTNEGGHIRIYTRAELEAKLKATGFEIGPHHHAHALHSPYWWIKCA
VGTGDDDHPLVRAYHRLLVWDILKAPKATRVTERLLNPLIGKSVVVYLRKPTGAGNT
E

>ThMT

MITVDFTLFPVGPGNRVLDLGCGGGRHAFEAYRRGADVVAFDQNENDLASVSAMF
AAMRAEGEAPASATAETVRGDALAMPFEDGSFDRVIAAEIMEHIPHDTAAMAELHR
VLTPGGIAVVTVPSWLPERVCWALSEEYHTNEGGHIRIYTRAELEAKLKATGFRIGP
HHHAHALHSPYWWLKCAVGTDNDTHPLVRAYHNLLVWDMMKAPRVTRLAERALN
PLIGKSVVVYLRKPRRGGDTG

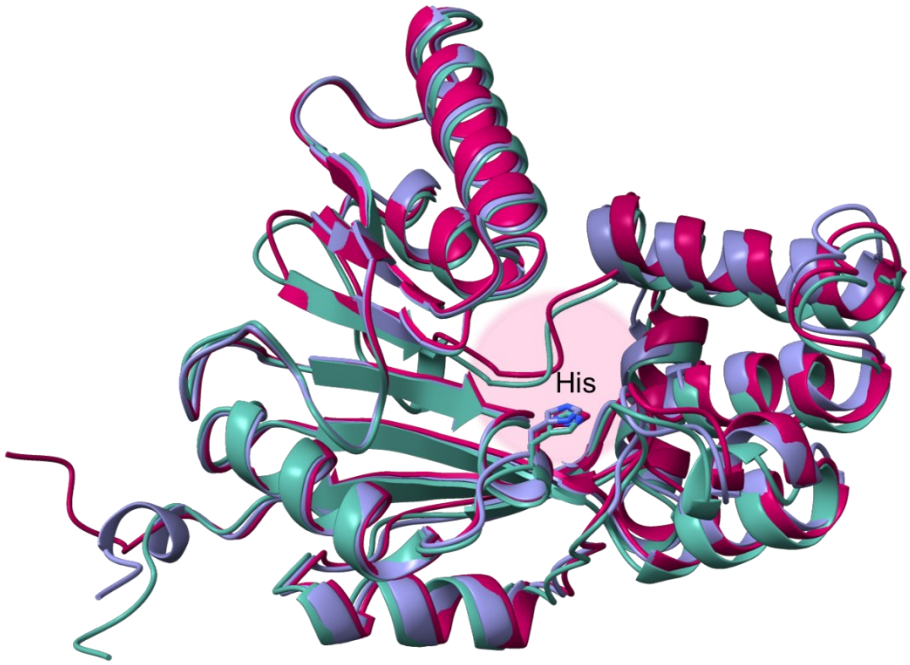

Figure S 8: Structures of NozB-CYIM (green), MtMT (violet) and ThMT (red) generated using RobettaFold. The active site is highlighted in pink, the histidine, that replaces the tyrosine of the catalytic triade of the group one MTases is shown.

8.3 StspM1

Gene Sequence:

MSSETATPADPYTNLADSYDRLAEWAVTCQKESPRDRVADFLQTFWQSQQRPVR
TVLEICCGTGLMLGELARRGYAVTGLDRSAAMLERARRRLGEETTLIHAALPHIPAE
AGPFDAVVSAAGGLNYLPEEQISATFAAVARALPAGGTFTFDVFGRGFFRKFFDSS
APRVMALELDDIAYIWTFTASPEAPFVDMAYTQFTPAPAADGGEPPFLRTRDLHRYY
PLPHTTVRRLAAEHGFTDTKAYDNYSTDPSGPDSLYDTWTMVRSSSLEHHHHHH

Table S 3: Results of SEC. Ve = elution volume, Vt=column volume (120 mL), Kav = partition coefficient (proportion of pores available to the molecule)

Protein	MW [kDa]	Ve [mL]	Kav =(Ve-V0)/(Vt-V0)
Blue Dextran : V0	2000	47,81	-
Alpha -Amylase	200	66,95	0,265
Cytochrome C	12,4	101,94	0,750
ADH	150	70,48	0,314
Carbonic anhydrase	29	86,31	0,533
BSA	66	77,43	0,410
StspM1		78,41	0,424

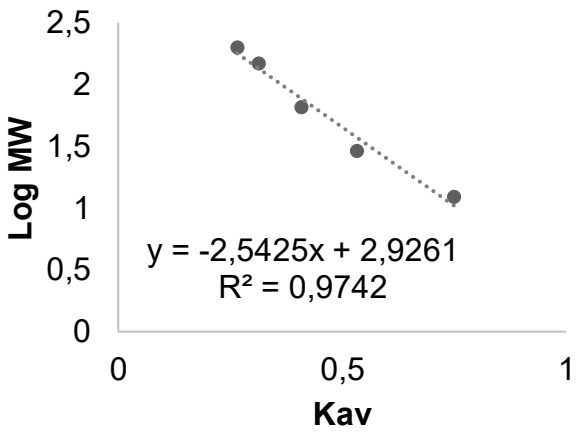

Figure S 9: Size exclusion chromatography calibration. Proteins: blue dextran, α-amylase, cytochrome C, alcohol dehydrogenase, BSA and carbonic anhydrase. Kav = partition coefficient (proportion of pores available to the molecule) Kav = (Ve-V0)/(Vt-Ve)

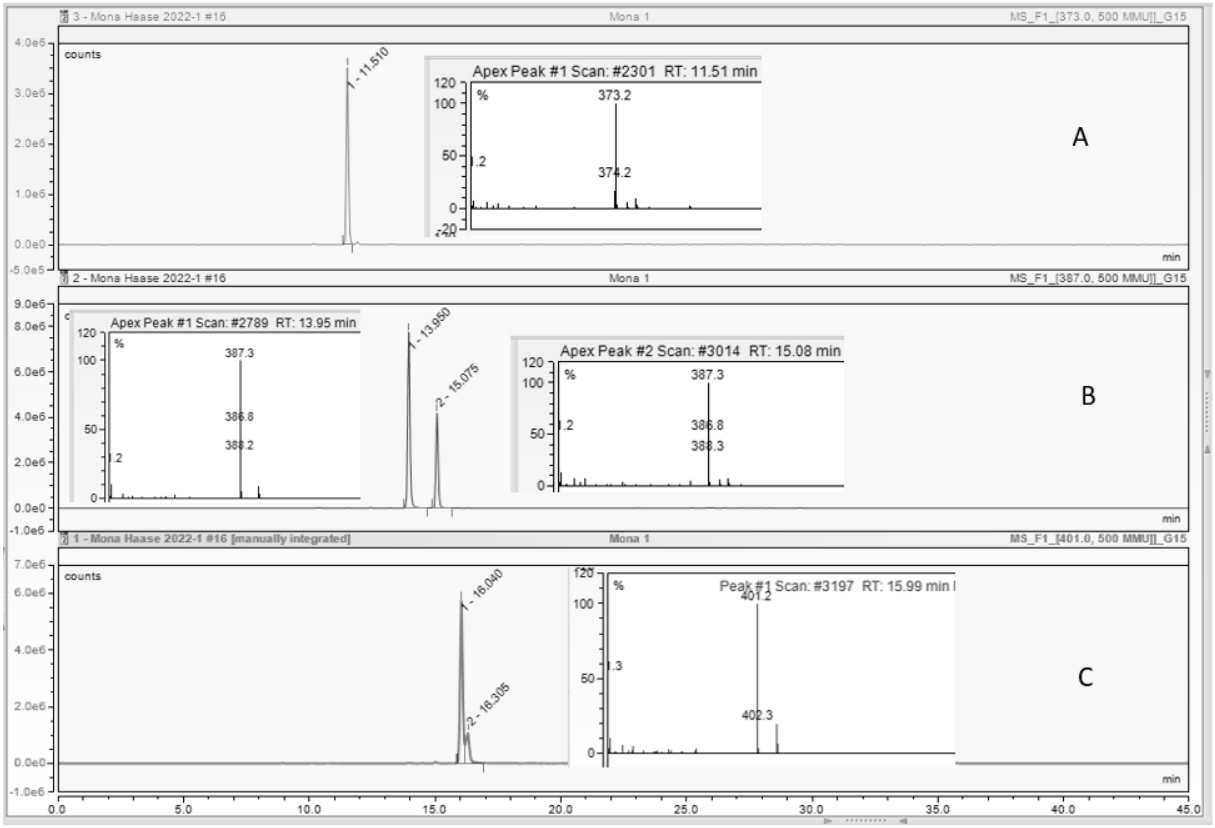

Figure S 10: Extracted chromatograms of references measured with HPLC/MS. A: **3** substrate, B: single methylated diastereomers **168**, C: double methylated product **240**.

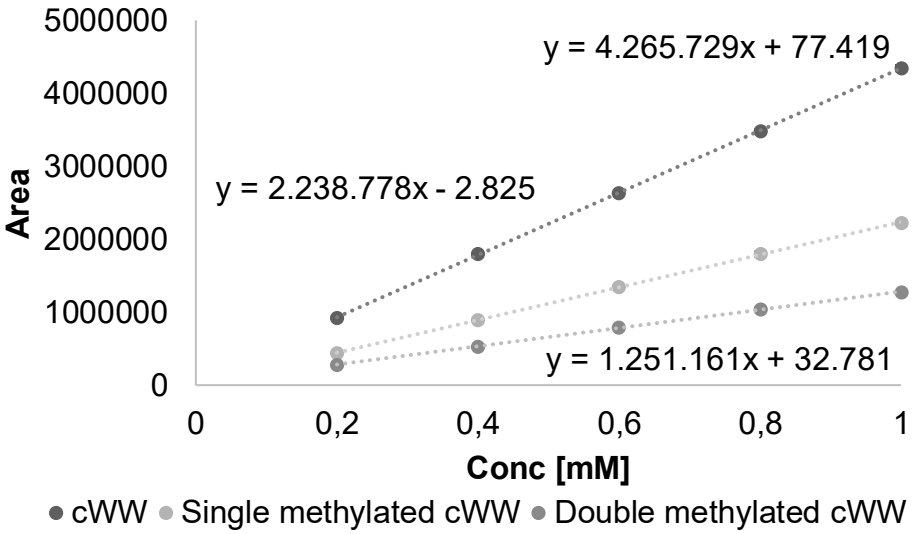

Figure S 11: HPLC calibration of LL-cWW **3a**, single methylated LL-cWW **168a** and double methylated LL-cWW **240**.

Table S 4: Conversion of cWW substrates **3** under initial conditions and with an exchanged buffer. Initial conditions: pH 7.5, 50 mM Tris, 100 mM NaCl, 1 mM SAM (**93**), 1 mM cWW **3**, 40 µM stspM1, 120 min, 30 °C; optimised conditions: pH 7.5, 50 mM KPi, 1 mM SAM (**93**), 1 mM cWW **3**, 40 µM StspM1, 120 min, 40 °C; negative control: pH 7.5, 50 mM KPi, 1 mM SAM (**93**), 1 mM cWW **3**, 120 min, 40 °C. Conversions have been analysed via RP-HPLC.

Conditions	Substrate	Remaining substrate (Rt = 11.5 min)	single methylated product (Rt_{LL} = 13.9 min, Rt_{DD}= 15.1 min)	double methylated product (RtLL = 16.0 min)	Rel. Conversion
Li et al. conditions	LL-cWW	89%	10%	1%	11%
	DD-cWW	95%	5%	-	5%
	LD-cWW	100%	-	-	-
optimised conditions	LL-cWW	54%	46%	3%	43%
	DD-cWW	80%	20%	-	20%
	LD-cWW	100%	-	-	-
Negative control	LL-cWW	100%	-	-	-
	DD-cWW	100%	-	-	-

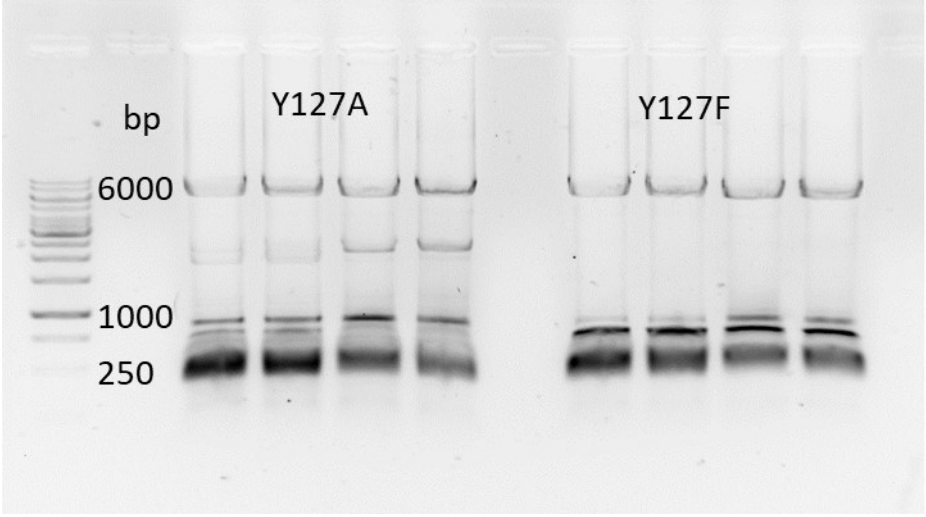

Figure S 12: Agarose gel of the mutated genetic constructs Y127A and Y127F of StspM1.

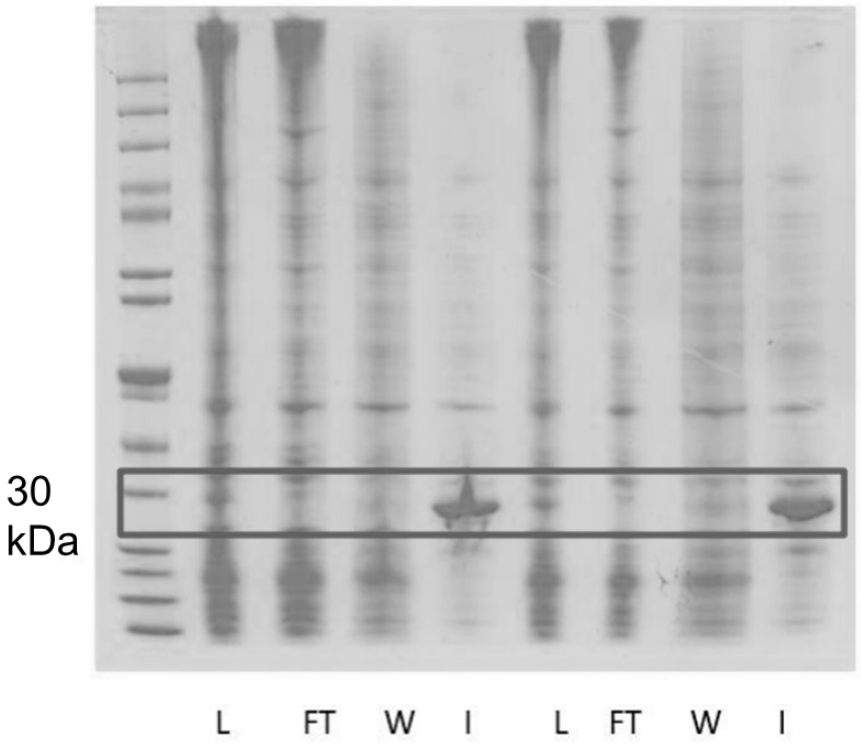

Figure S 13: SDS gel of the immobilisation of the Y127A (left) and Y127F (right). As standard the Page Ruler unstained protein ladder (0.02 – 0.05 µg/µL) has been used. L = lysate, FT = flow through, W = washing fraction, I = immobilisation fraction.

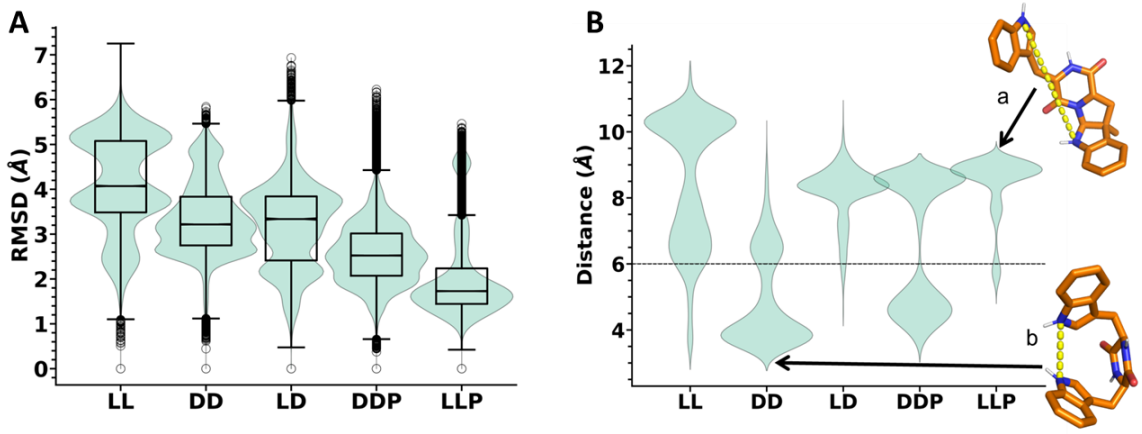

Figure S 14: A: Distribution of the cWW **3** RMSD (heavy atoms) over 7 replicas of 200 ns of MD simulation. The central boxplot line shows the median value. LL, DD, LD respectively refer to the unmethylated LL-cWW **3a**, DD-cWW **3b**, and LD-cWW **3c**. DDP and LLP respectively refer to the single methylated DD-cWW **168b** and LL-cWW **168a**. B: Distribution of the distance between the indole rings nitrogen atoms of the cWW **3a** over 7 replicas of 200 ns of MD simulation. LL, DD, LD respectively refer to the unmethylated LL-cWW **3a**, DD-cWW **3a**, and LD-cWW **3c**. DDP and LLP respectively refer to the single methylated DD-cWW and LL-cWW. A "stretched" conformation of the single methylated LL-cWW **3a** (a) and a "boat-like" conformation of the unmethylated DD-cWW substrate **3b** (b) are shown in comparison. The dashed line illustrates the distance measured and the black arrows points on the corresponding distance values. The black line at 6 Å is a crude distance threshold to separate these two classes of conformations. Figure by Benoit David.

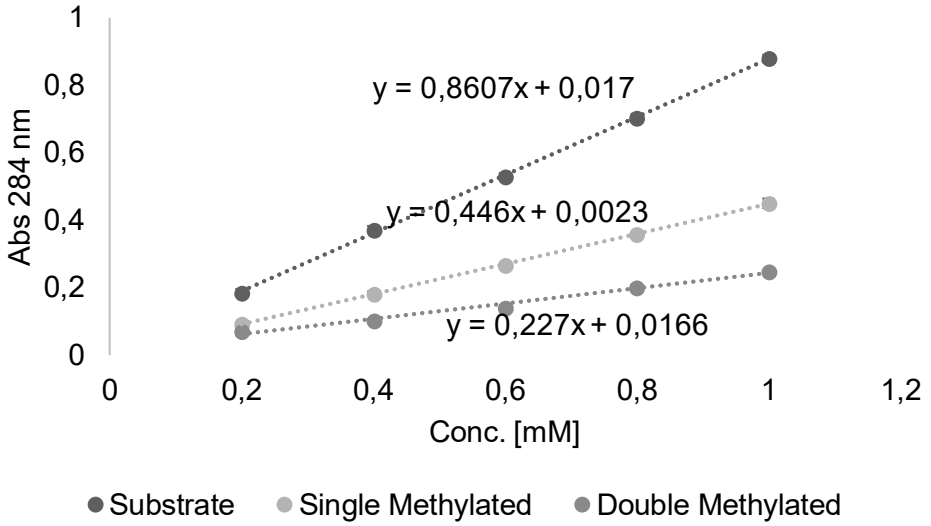

Figure S 15: Determination of extinction coefficient of LL-cWW **3a**, single methylated LL-cWW **168a** and double methylated LL-cWW **240**. The extinction coefficient of the substrate 7a is 8607 M^{-1} cm^{-1}, of the single methylated product 14 4460 M^{-1} cm^{-1} and of the double methylated product 15 2270 M^{-1} cm^{-1}.

Table S 5: Reaction of LL-cWW **3a** under in vitro assay conditions with 80% StspM1 lysate and 20% HMT Lysate. Retention times: 11.45 min (substrate), 13.65 min (single methylated product), 15.16 min (double methylated product).

Time [h]	Substrate	Single methylated	Double methylated
0,5	85%	16%	0%
1	41%	36%	22%
3	26%	41%	33%
24	0%	1%	99%

Table S 6: Conditions and results of the design of experiment approach. The Design Expert 12 (12.0.7.0) was used to create the conditions. Two additional negative controls (35 and 36) were measured. Reactions were performed under in vitro assay conditions.

	Factor 1	**Factor 2**	**Factor 3**	**Response**
Run	Lysate amount StspM1	Lysate amount HMT	MeI equiv.	conv (24h)
	µL	µL	equiv.	%
1	485	105	15	95
2	316	161	4	69
3	485	105	1	17
4	485	200	8	92
5	654	49	4	26
6	485	105	8	72
7	485	105	15	92
8	485	105	8	73
9	316	49	12	64
10	485	200	8	95
11	654	161	4	57
12	200	105	8	56
13	654	161	4	56
14	316	161	12	77
15	316	49	4	61
16	770	105	8	38
17	485	105	8	66
18	485	105	8	71
19	654	49	12	72
20	654	49	12	64
21	485	105	8	82
22	485	105	8	72
23	654	161	12	95
24	770	105	8	63
25	316	161	4	60
26	654	49	4	27
27	485	10	8	9
28	485	10	8	10
29	316	49	12	56
30	316	161	12	76
31	316	49	4	24
32	654	161	12	93
33	485	105	1	14
34	200	105	8	55
35	0	0	10	0
36	0	0	0	0

Table S 7: Calculated conditions for an experiment with a maximal conversion and a minimum amount of StspM1 Lysate. The Design Expert 12 (12.0.7.0) was used to calculate the conditions from the data of the design of experiment.

Factor	Calculated amount
Lysate amount [µL] STSP_M1 (minimum)	337,28
Lysate amount [µL] HMT (in range)	161,49
MeI equiv. (in range)	12,16

Table S 8: Validation of the predicted conversions for an experiment with the calculated conditions for an experiment with a maximal conversion and a minimum amount of StspM1 Lysate. The Design Expert 12 (12.0.7.0) was used to calculate the conditions. Reactions were performed under in vitro assay conditions.

	Factor 1	**Factor 2**	**Factor 3**	**Response**
Run	Lysate amount StspM1	Lysate amount HMT	MeI equiv.	conv (24h)
	µL	µL	equiv.	%
1	337	161	12	90
2	337	161	12	89
3	337	161	12	95
4	337	161	12	96

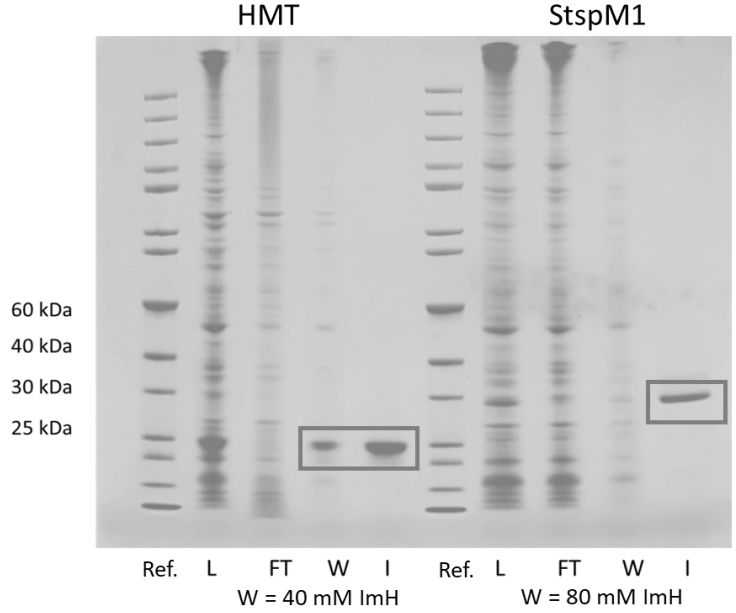

Figure S 16: SDS gel of the immobilisation of the HMT (24.617 kDa, left) and StspM1 (30.879 kDa, right). As standard the Page Ruler unstained protein ladder (0.02 – 0.05 µg/µL) has been used. For the lysate and flow through 2 µL sample have been diluted in 10 µL water before applying to the gel; the other samples were applied undiluted. L = lysate, FT = flow through, W = washing fraction, I = immobilisation fraction.

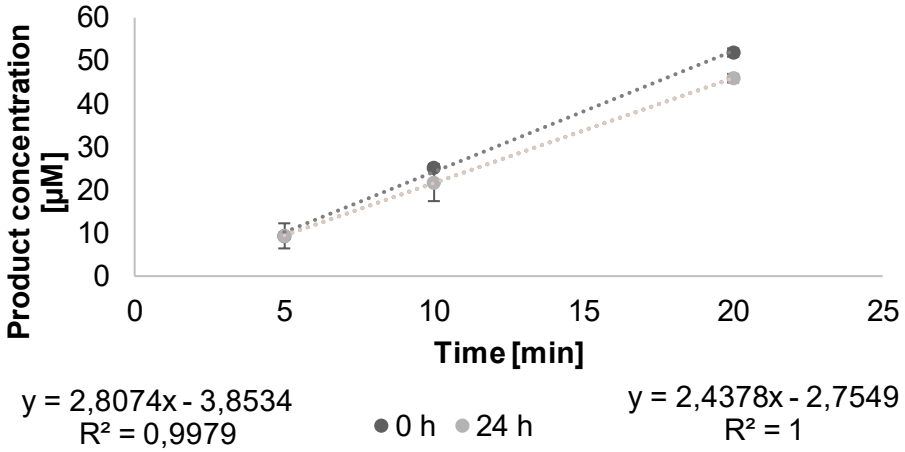

Figure S 17: Activity of StspM1 (immobilised from Lysate) after 0 h and 24 h incubation at 40 °C and 700 rpm. Reaction was performed under in vitro assay conditions with 40% immobilised lysate and an additional 1 mM SAM (**93**) in triplicates. Beads activity (0 h): 7.0 mU/mL; Beads activity (24 h): 6.1 mU/mL.

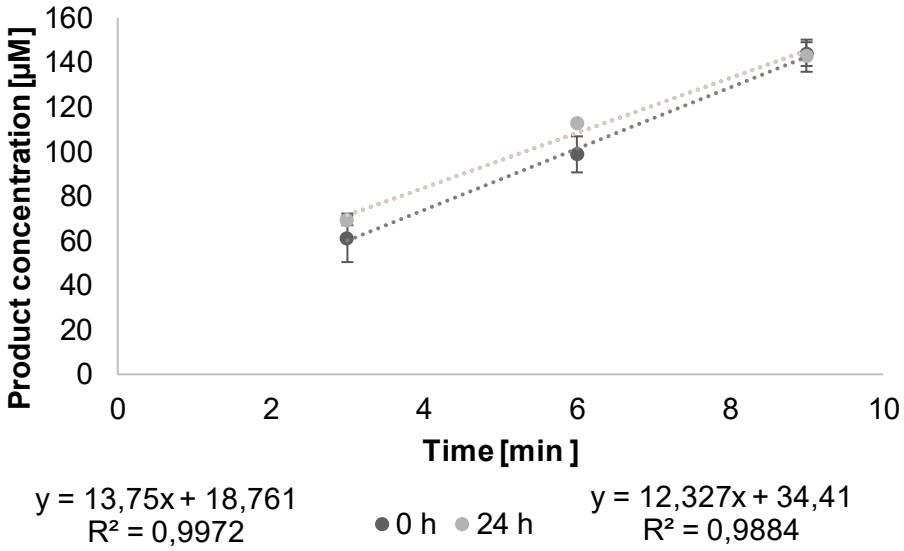

Figure S 18: Activity of HMT (immobilised from Lysate) after 0 h and 24 h incubation at 40 °C and 700 rpm. Reaction was performed under in vitro assay conditions with 3% immobilised lysate and additional 5 mM MeI. Beads activity (0 h) in triplicates: 0.46 U/mL; Beads activity (24 h): 0.41 U/mL.

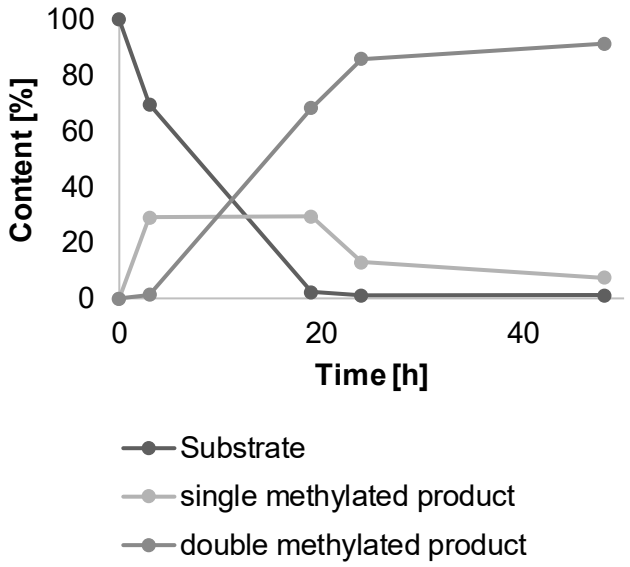

Figure S 19: Conversion of LL-cWW **3a** at different time points (monitored via HPLC). Reactions were carried out under preparative scale reaction conditions (immobilised enzyme).

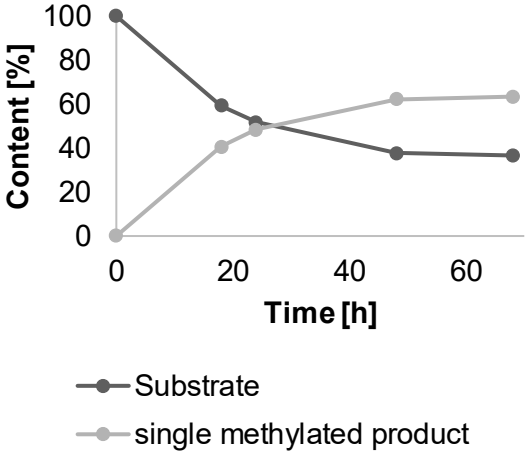

Figure S 20: Conversion of DD-cWW **3b** at different time points (monitored via HPLC). Reactions were carried out under preparative scale reaction conditions (immobilised enzyme) with a doubled enzyme load.

8.4 SgMT

N-terminal His-tagged:

MGSSHHHHHHSSGLVPRGSHMSSQTVTPDPYGNLAESYDRLAQWAIDQQQESPR
DRVGDFLQTFWQSQDRPVRTVLEICCGTGLMLAELARRGYVVTGLDRSAAMLEQA
RARMGGKTTLIRAELPDIPAPAGEFDAVVSAAGGLNYLSESQISATFGAVARLLPAG
GTFTFDVFGQGFYAKFFDPSAPRVMALELDDISYIWTFTKPAEAPFVDMSYTQFSPA
SRAVDGEPAFIRTRDLHRYYPLPHATVLRLAAEHGFTDARAHDNYSSDPSGPHTLY
DTWTMVRTGSLE

C-terminal His-tagged:

MGHMSSQTVTPDPYGNLAESYDRLAQWAIDQQQESPRDRVGDFLQTFWQSQDRP
VRTVLEICCGTGLMLAELARRGYVVTGLDRSAAMLEQARARMGGKTTLIRAELPDIP
APAGEFDAVVSAAGGLNYLSESQISATFGAVARLLPAGGTFTFDVFGQGFYAKFFD
PSAPRVMALELDDISYIWTFTKPAEAPFVDMSYTQFSPASRAVDGEPAFIRTRDLHR
YYPLPHATVLRLAAEHGFTDARAHDNYSSDPSGPHTLYDTWTMVRTGSLEHHHHH
H

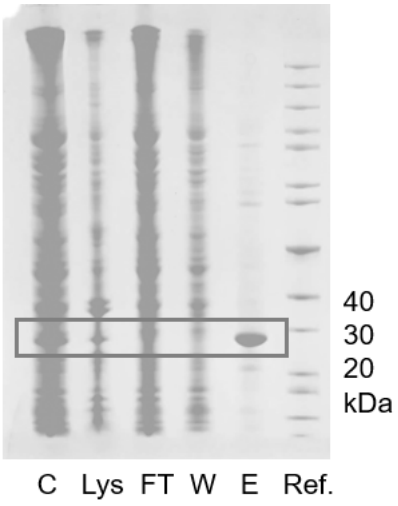

Figure S 21: SDS-PAGE of the purification of C-terminal His-tagged SgMT. Ref. = Unstained Protein Standard, Broad Range (10-200 kDa), New England Biolabs. The lysed cells were centrifuged leading to the pellet (P) and lysate (Lys) fraction. The lysate was applied to the column (FT) before the washing buffer (40 mM ImH) was applied. The protein was eluted with the elution buffer containing 160 mM ImH. The band at 30 kDa is highlighted.

Table S 9: X-ray data collection and refinement statistics. Values in parentheses refer to the highest-resolution shell.

Specimen	SgMT
PDB code	9GDJ
Data collection statistics	
Beamline	ESRF ID23-1
Detector	EIGER2 CdTe 16M
Wavelength [Å]	0.8856
Space group	P 4_1 2_1 2
Unit cell parameters	
a, b, c [Å]	123.9, 123.9, 126.4
α, β, γ [°]	90, 90, 90
Resolution range [Å]	37.43–1.47 (1.51–1.47)
No. reflections	166,186 (12,132)
Completeness [%]	100 (100)
Multiplicity	13.2 (13.2)
Mean I/σ(I)	11.7 (0.8)
$CC_{1/2}$ [%]	99.8 (34.7)
Refinement statistics	
No. of reflections used	166,176
R_{work}	0.147
R_{free}	0.175
RMS deviations from ideal	
Bonds [Å]	0.005
Angles [°]	0.740
Mean B [Å^2] (no. of atoms)	
Protein	30.4 (6816)
Ligands	54.0 (316)
Water	41.6 (815)
Ramachandran statistics	
Favoured	98.7
Allowed	1.3
Outliers	0.0
Unusual rotamers [%]	0.9

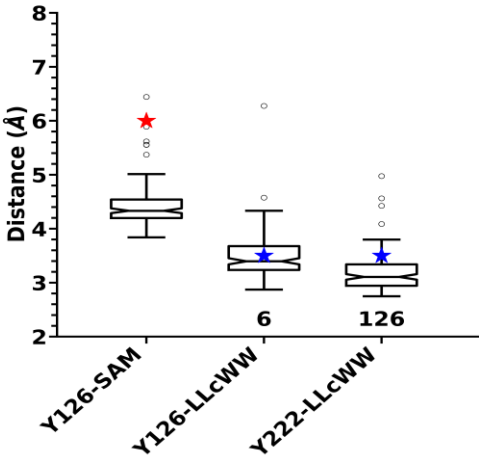

Figure S 22: Relevant distances measured in MD simulations. Only snapshots for which the LL-cWW **3a** reactive carbon is within 4 Å of the SAM (**93**) reactive methyl group were considered for the analysis. Y126-SAM: distance distribution between the Y126 hydroxyl group and the sulphur atom of the SAM (**93**) cofactor. Red star: maximum Y126-SAM distance value measured in the crystal structures of five MTases sharing a similar fold (PDB IDs 7ZKH, 1WZN, 1Y8C, 3D2L, 3BX0). Y126-LLcWW: distance distribution between the Y126 hydroxyl group and the nitrogen atom of the substrate reactive indole. Y222-LLcWW: distance distribution between the Y222 hydroxyl group and the nitrogen atom of the substrate reactive indole. Blue stars: maximum Y126-LLcWW / Y222-LLcWW distance value, below which a hydrogen bond can be formed. The number of hydrogen bonds formed between the corresponding Y126 and Y222 hydroxyl group and the reactive indole nitrogen atom of the substrate are indicated below the respective boxplots. Figure by Benoit David.

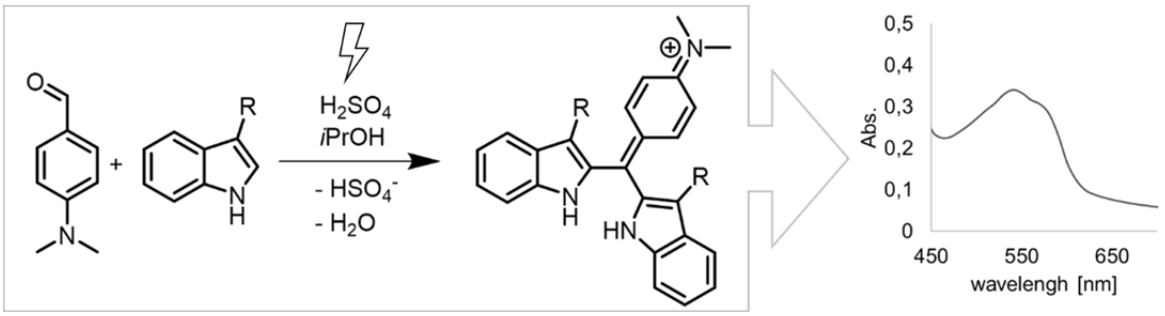

Figure S 23: Reaction scheme showing the light induced reaction between the indole derivative and *para*-dimethylaminobenzaldehyde (DMAB), and the putative colourful product.

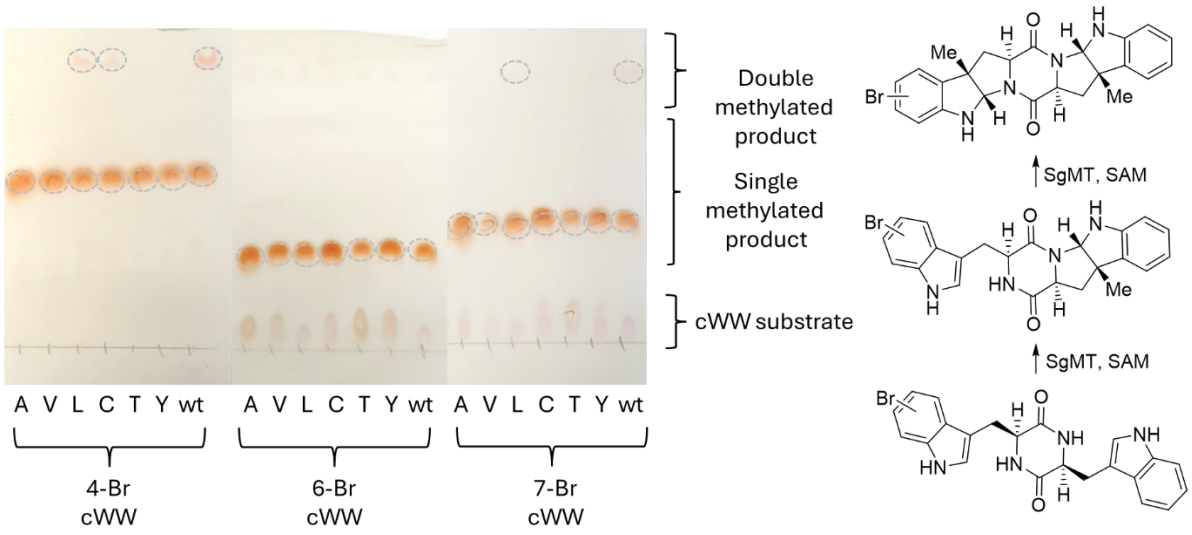

Figure S 24: TLC stained with cerium molybdenum stain for detection of the HPI containing products. Small-scale reactions were performed under the same conditions as on the automated platform with the mutants F184A, F184L, F184V, F184C, F184T, F184Y and the wild type.

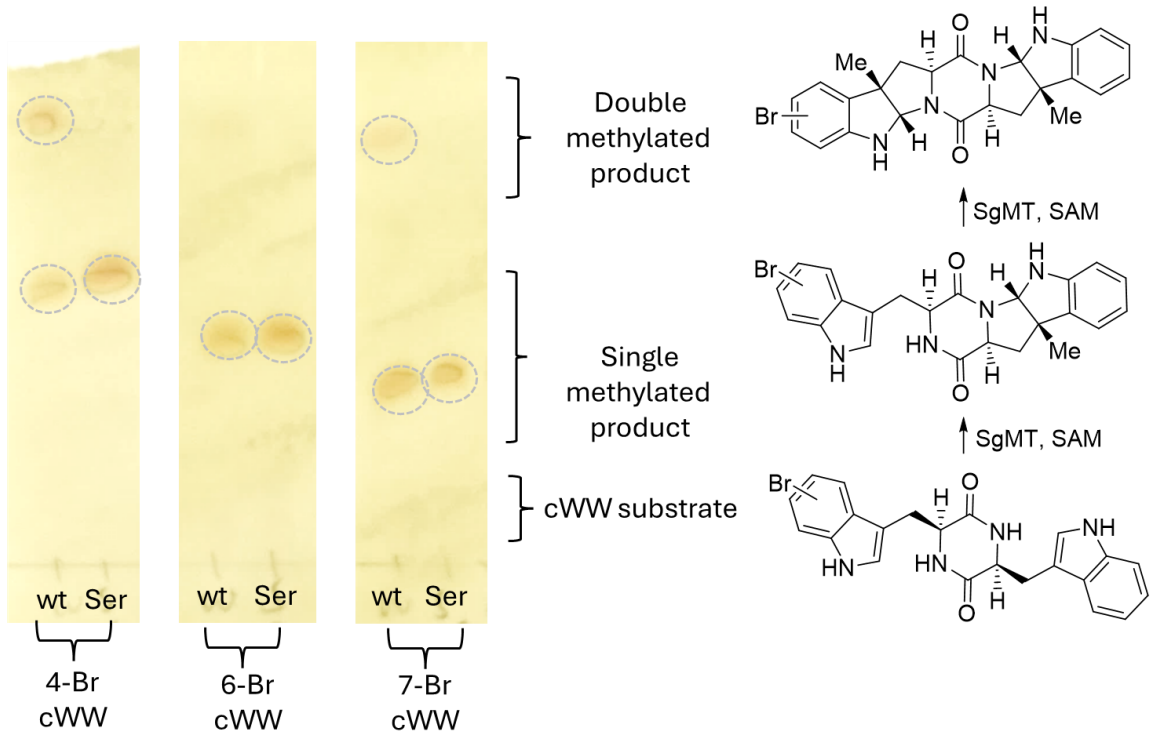

Figure S 25: TLC stained with cerium molybdenum stain for detection of the HPI containing products. Small-scale reactions were performed under the same conditions as on the automated platform with the mutants N125S and the wild type.

Table S 10: Layout of the 96 well plate format for the mutagenesis study: 66 variants were tested plus two negative (empty vector) and two positive controls (wt).

<>	1	2	3	4	5	6	7	8	9
A	1	9	17	25	33	41	49	57	65
B	2	10	18	26	34	42	50	58	66
C	3	11	19	27	35	43	51	59	Positive
D	4	12	20	28	36	44	52	60	Positive
E	5	13	21	29	37	45	53	61	Negative
F	6	14	22	30	38	46	54	62	Negative
G	7	15	23	31	39	47	55	63	
H	8	16	24	32	40	48	56	64	

Table S 11: 5-Br cWW **258a**: Results of the mutagenesis study for position N125. The indole assay was used to form the colourimetric product, which was measured via absorption at 540 nm.

<>	1	2	3	4	5	6	7	8	9
A	0,340	0,324	0,323	0,321	0,320	0,308	0,315	0,313	0,337
B	0,316	0,332	0,322	0,314	0,324	0,348	0,323	0,326	0,346
C	0,266	0,329	0,257	0,319	0,313	0,267	0,300	0,315	0,196
D	0,331	0,341	0,302	0,322	0,325	0,303	0,316	0,301	0,195
E	0,416	0,327	0,289	0,312	0,203	0,291	0,315	0,326	0,325
F	0,355	0,367	0,319	0,322	0,327	0,314	0,234	0,295	0,328
G	0,330	0,329	0,327	0,331	0,324	0,312	0,299	0,316	
H	0,339	0,338	0,338	0,204	0,334	0,328	0,308	0,313	

Table S 12: 5-Br cWW **258a**: Results of the mutagenesis study for position W182. The indole assay was used to form the colourimetric product, which was measured via absorption at 540 nm.

<>	1	2	3	4	5	6	7	8	9
A	0,334	0,343	0,345	0,297	0,325	0,301	0,321	0,281	0,313
B	0,329	0,329	0,350	0,306	0,296	0,296	0,258	0,282	0,316
C	0,346	0,297	0,316	0,329	0,312	0,313	0,292	0,261	0,183
D	0,346	0,346	0,348	0,308	0,298	0,294	0,317	0,267	0,181
E	0,348	0,299	0,315	0,284	0,296	0,293	0,332	0,285	0,325
F	0,362	0,323	0,307	0,351	0,304	0,309	0,361	0,302	0,350
G	0,363	0,316	0,321	0,290	0,321	0,315	0,343	0,304	
H	0,341	0,344	0,358	0,304	0,294	0,324	0,319	0,291	

Table S 13: 4-Br cWW **274**: Results of the mutagenesis study for position N125. The indole assay was used to form the colourimetric product, which was measured via absorption at 540 nm.

<>	1	2	3	4	5	6	7	8	9
A	0,381	0,389	0,357	0,377	0,354	0,406	0,370	0,363	0,325
B	0,255	0,372	0,373	0,396	0,350	0,492	0,391	0,377	0,359
C	0,194	0,391	0,209	0,377	0,388	0,230	0,374	0,361	0,201
D	0,367	0,382	0,329	0,357	0,364	0,376	0,373	0,284	0,214
E	0,468	0,380	0,208	0,375	0,202	0,211	0,377	0,357	0,378
F	0,393	0,463	0,373	0,359	0,389	0,339	0,196	0,298	0,314
G	0,366	0,370	0,411	0,387	0,313	0,366	0,348	0,366	
H	0,386	0,372	0,384	0,190	0,268	0,340	0,355	0,350	

Table S 14: 6-Br cWW **275**: Results of the mutagenesis study for position N125. The indole assay was used to form the colourimetric product, which was measured via absorption at 540 nm.

<>	1	2	3	4	5	6	7	8	9
A	0,260	0,266	0,264	0,269	0,254	0,257	0,266	0,262	0,265
B	0,281	0,274	0,253	0,260	0,268	0,271	0,267	0,256	0,268
C	0,254	0,274	0,245	0,282	0,268	0,256	0,272	0,261	0,232
D	0,289	0,279	0,264	0,271	0,276	0,257	0,271	0,260	0,199
E	0,308	0,274	0,273	0,272	0,223	0,256	0,253	0,274	0,271
F	0,290	0,291	0,276	0,276	0,274	0,269	0,223	0,253	0,274
G	0,285	0,271	0,250	0,275	0,259	0,273	0,272	0,252	
H	0,257	0,269	0,268	0,215	0,263	0,274	0,261	0,250	

Table S 15: 7-Br cWW **276**: Results of the mutagenesis study for position N125. The indole assay was used to form the colourimetric product, which was measured via absorption at 540 nm.

<>	1	2	3	4	5	6	7	8	9
A	0,266	0,274	0,257	0,267	0,260	0,270	0,269	0,262	0,26
B	0,275	0,261	0,249	0,263	0,261	0,273	0,263	0,271	0,27
C	0,244	0,275	0,251	0,268	0,266	0,255	0,264	0,254	0,21
D	0,271	0,277	0,269	0,266	0,271	0,268	0,272	0,259	0,21
E	0,264	0,271	0,252	0,270	0,201	0,250	0,273	0,270	0,27
F	0,284	0,271	0,261	0,244	0,256	0,271	0,218	0,249	0,27
G	0,261	0,265	0,216	0,237	0,255	0,256	0,250	0,254	
H	0,208	0,254	0,253	0,206	0,239	0,251	0,246	0,228	

Table S 16: 4-Br cWW **274**: Results of the mutagenesis study for position F184. The indole assay was used to form the colourimetric product, which was measured via absorption at 540 nm.

<>	1	2	3	4	5	6	7	8	9
A	0,175	0,251	0,163	0,354	0,181	0,176	0,188	0,180	0,207
B	0,172	0,276	0,214	0,178	0,162	0,236	0,260	0,260	0,347
C	0,364	0,265	0,265	0,261	0,176	0,254	0,219	0,245	0,167
D	0,313	0,278	0,287	0,228	0,348	0,252	0,216	0,243	0,157
E	0,296	0,250	0,274	0,186	0,153	0,235	0,264	0,226	0,397
F	0,170	0,151	0,267	0,172	0,274	0,280	0,297	0,170	0,419
G	0,276	0,270	0,150	0,217	0,174	0,256	0,281	0,254	
H	0,154	0,223	0,211	0,255	0,173	0,316	0,259	0,242	

Table S 17: 6-Br cWW **275**: Results of the mutagenesis study for position F184. The indole assay was used to form the colourimetric product, which was measured via absorption at 540 nm.

<>	1	2	3	4	5	6	7	8	9
A	0,165	0,186	0,156	0,169	0,150	0,146	0,153	0,169	0,17
B	0,134	0,178	0,168	0,147	0,161	0,168	0,174	0,165	0,18
C	0,208	0,194	0,199	0,190	0,186	0,186	0,177	0,178	0,18
D	0,199	0,192	0,170	0,160	0,179	0,165	0,153	0,161	0,18
E	0,155	0,188	0,184	0,158	0,150	0,164	0,168	0,155	0,23
F	0,176	0,147	0,176	0,168	0,160	0,178	0,175	0,149	0,22
G	0,217	0,204	0,167	0,179	0,185	0,174	0,183	0,177	
H	0,202	0,183	0,183	0,161	0,150	0,179	0,154	0,160	

Table S 18: 7-Br cWW **276**: Results of the mutagenesis study for position F184. The indole assay was used to form the colourimetric product, which was measured via absorption at 540 nm.

<>	1	2	3	4	5	6	7	8	9
A	0,179	0,292	0,186	0,264	0,191	0,181	0,205	0,198	0,268
B	0,175	0,327	0,253	0,183	0,199	0,226	0,232	0,223	0,268
C	0,290	0,282	0,257	0,236	0,183	0,234	0,228	0,215	0,252
D	0,274	0,254	0,249	0,231	0,233	0,235	0,212	0,220	0,243
E	0,279	(2,497)	0,256	0,206	0,183	0,233	0,226	0,224	(2,663)
F	0,253	0,295	0,251	0,222	0,238	0,255	0,233	0,190	0,281
G	0,240	0,401	0,196	0,226	0,213	0,224	0,243	0,238	
H	0,230	(1,901)	0,239	0,240	0,191	0,273	0,229	0,235	

Table S 19: 4-Br cWW **274**: Results of the mutagenesis study for position W182. The indole assay was used to form the colourimetric product, which was measured via absorption at 540 nm.

<>	1	2	3	4	5	6	7	8	9
A	0,338	0,345	0,403	0,341	0,397	0,400	0,431	0,444	0,397
B	0,343	0,355	0,424	0,396	0,400	0,414	0,362	0,400	0,419
C	0,333	0,388	0,401	0,432	0,410	0,436	0,282	0,390	0,167
D	0,377	0,390	0,435	0,417	0,416	0,231	0,411	0,368	0,157
E	0,366	0,367	0,416	0,366	0,387	0,317	0,395	0,370	0,496
F	0,372	0,262	0,419	0,417	0,414	0,403	0,415	0,403	0,520
G	0,376	0,288	0,429	0,315	0,422	0,386	0,419	0,396	
H	0,336	0,277	0,446	0,376	0,236	0,406	0,382	0,333	

Table S 20: 6-Br cWW **275**: Results of the mutagenesis study for position W182. The indole assay was used to form the colriometric product, which was measured via absorption at 540 nm.

<>	1	2	3	4	5	6	7	8	9
A	0,260	0,217	0,261	0,257	0,262	0,277	0,252	0,244	0,306
B	0,252	0,234	0,237	0,233	0,244	0,246	0,225	0,245	0,279
C	0,254	0,233	0,224	0,248	0,249	0,246	0,250	0,231	0,210
D	0,204	0,270	0,237	0,240	0,238	0,260	0,257	0,255	0,243
E	0,276	0,264	0,230	0,266	0,232	0,237	0,262	0,268	0,288
F	0,293	0,299	0,231	0,236	0,240	0,238	0,248	0,257	0,306
G	0,276	(1,895)	0,242	0,234	0,227	0,240	0,250	0,281	
H	0,220	0,208	0,229	0,228	0,241	0,271	0,282	0,276	

Table S 21: 7-Br cWW **276**: Results of the mutagenesis study for position W182. The indole assay was used to form the colourimetric product, which was measured via absorption at 540 nm.

<>	1	2	3	4	5	6	7	8	9
A	0,239	0,224	0,219	0,201	0,205	0,219	0,221	0,210	0,270
B	0,226	0,222	0,215	0,205	0,203	0,217	0,203	0,205	0,239
C	0,235	0,262	0,222	0,208	0,218	0,212	0,229	0,227	0,158
D	0,238	0,220	0,208	0,202	0,213	0,208	0,198	0,231	0,163
E	0,219	(1,604)	0,209	0,204	0,203	0,209	0,213	0,214	0,252
F	0,242	0,208	0,224	0,203	0,213	0,211	0,210	0,210	0,258
G	0,239	0,249	0,214	0,200	0,197	0,203	0,211	0,227	
H	0,233	0,222	0,232	0,204	0,218	0,210	0,210	0,220	

Table S 22: Sequenced mutants of the F184 library.

Position	AS
A1	Ala
A3	Leu
A5	Leu
A6	Ala
B1	Cys
B4	Cys
C5	Thr
E5	Val
F2	Tyr
F8	Leu
G3	Tyr
H1	Thr
H5	Leu

Table S 23: Sequenced mutants of the F184 library.

Position	AS
H4	Ser
F7	Ser
E5	Ser

8.5 SeMT and SaMT

SeMT *C*-terminal His-tagged:

MGHMTVDVPVSSDPYANLAASYDRLVDWVISEQEETPRERMGDYIESFWRDQPRP
VHKVLEICCGTGLMLGDLQRRGYQVSGLDRSAAMLEQARNRLGTGVELVRAELPEI
PLHAGFDAVISAANGLTYLPGTGFGETLAAVARLLPPGGTFVFDLYGHGFFERFYDS
AEPRVLAVELEDVSYIWTFTAPPSRAHFDVVHSQFLRTPDAEAGTYTRTRELHRFH
EHTHTSVRRLAAEAGFSSAEVHDNWTSRPSTPESMYDTWTLTRGVLEHHHHHH*

SeMT *N*-terminal His-tagged:

MGSSHHHHHHSSGLVPRGSHMTVDVPVSSDPYANLAASYDRLVDWVISEQEETPR
ERMGDYIESFWRDQPRPVHKVLEICCGTGLMLGDLQRRGYQVSGLDRSAAMLEQA
RNRLGTGVELVRAELPEIPLHAGFDAVISAANGLTYLPGTGFGETLAAVARLLPPGG
TFVFDLYGHGFFERFYDSAEPRVLAVELEDVSYIWTFTAPPSRAHFDVVHSQFLRTP
DAEAGTYTRTRELHRFHEHTHTSVRRLAAEAGFSSAEVHDNWTSRPSTPESMYDT
WTLTRGVLE

SaMT SeMT *N*-terminal His-tagged:

MGSSHHHHHHSSGLVPRGSHMAEWAVTCQEESPRDRVADFLQTFWQSQQRPVR
TVLEICCGTGLMLGELARRGYAVTGLDRSAAMLERARRRLGEETTLIHSALPQIPAE
AGPFDAVVSAAGGLNYLPGEQISATFAAVARALPAGGTFTFDVFGRGFFRKFFDSS
APRVMALELDDIAYIWTFTASPEAPFVDMAYTQFTPAPAADGGEPPFLRTRDLHRYY
PLPHTTVHRLAAEHGFTDTKAYDNYSTDPSGPDSLYDTWTMVRSSSLE

SaMT *C*-terminal His-tagged:

MGHMAEWAVTCQEESPRDRVADFLQTFWQSQQRPVRTVLEICCGTGLMLGELAR
RGYAVTGLDRSAAMLERARRRLGEETTLIHSALPQIPAEAGPFDAVVSAAGGLNYLP
GEQISATFAAVARALPAGGTFTFDVFGRGFFRKFFDSSAPRVMALELDDIAYIWTFT
ASPEAPFVDMAYTQFTPAPAADGGEPPFLRTRDLHRYYPLPHTTVHRLAAEHGFTD
TKAYDNYSTDPSGPDSLYDTWTMVRSSSLEHHHHHH

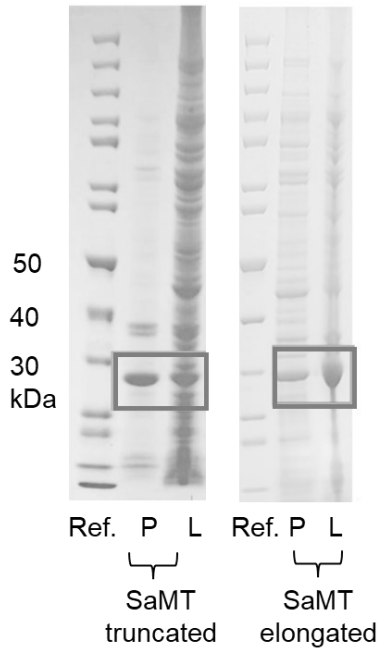

Figure S 26: SDS-Gel of the truncated and elongated C-terminal His-tagged SaMT. The cells were lysed and the pellet (P) and lysate (L) fractions were applied to the gel. The band at 30 kDa is highlighted. Ref. = Unstained Protein Standard, Broad Range (10-200 kDa), New England Biolabs.

Figure S 27: Sequences of SeMT, SgMT and StspM1. The nine mutation positions are highlighted in red, the 10th mutation position in green.

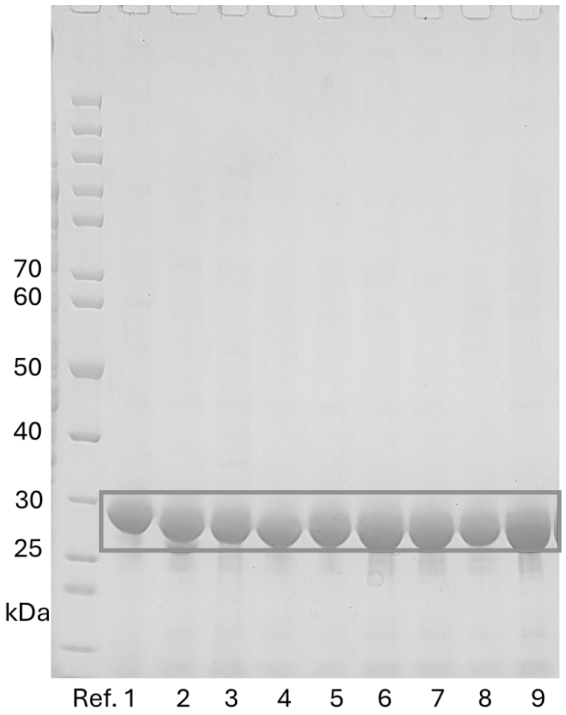

Figure S 28: SDS gel of purified SeMT variants: Wt (1), 10x mutant (2), 10x mutant with reversed mutation of V23A+V26A (3), N122G+T125N (4), G131Q (5), Y154F (6), V195M+H197Y (7), E216D (8) or F220Y (9).

Table S 24: Data collection and refinement statistics. Values in parentheses refer to the highest-resolution shell.

Specimen	SeMT
PDB code	9ICZ
Data collection statistics	
Beamline	ESRF ID30B
Detector	EIGER2 Si 9M
Wavelength [Å]	0.873
Space group	C 2 2 2_1
Unit cell parameters	
a, b, c [Å]	153.0, 213.0, 48.2
α, β, γ [°]	90, 90, 90
Resolution range [Å]	62.12–1.58 (1.62–1.58)
No. reflections	106,524 (7,866)
Completeness [%]	98.4 (99.2)
Multiplicity	4.2 (4.3)
Mean I/σ(I)	11.4 (0.6)
$CC_{1/2}$ [%]	99.9 (30.6)
Refinement statistics	
No. of reflections used	106,441
R_{work}	0.173
R_{free}	0.193
RMS deviations from ideal	
Bonds [Å]	0.006
Angles [°]	0.760
Mean B [$Å^2$] (no. of atoms)	
Protein	38.7 (4948)
Ligands	51.0 (137)
Water	46.5 (668)
Ramachandran statistics [%]	
Favoured	97.7
Allowed	2.3
Outliers	0.0
Unusual rotamers [%]	0.8

8.6 NozB-CYIM

NozB-CYIM *C*-terminal His-Tag

MITVDFSLFPVGPGDRVLDLGCGGGRHAFEAYRRGADVVAFDQNTADLADVATMF
AAMRAEGEAPAGTEAETVKGDALDMPFDDGSFNRVIAAEIFEHLPHDTAAMAELYR
VLRPGGIAAVTVPSFLPERLCWALSEDYHTAEGGHVRIYTRAELQAKLKATGFVIGP
HHRAHALHAPYWWLKCAVGTDDDAHPAVKAYHRMLVWDMLQAPPATRITEKALNP
LIGKSVVVYVRKPLRAGPALEHHHHHH

MtMT *N*-terminal His-tagged:
MGSSHHHHHHSSGLVPRGSHMITVDFSLFPVGPGHRVLDLGCGGGRHAFEVYRR
GSDVVAFDQNENDLADVATMFAAMRAEGEAPHDASAETVKGDALDMPFEDASFD
RVIAAEIFEHIPHDTAAMAELYRVLKPGGIAAVTVPSWLPERICWALSEEYHTNEGGH
IRIYTRAELEAKLKATGFEIGPHHHAHALHSPYWWIKCAVGTGDDDHPLVRAYHRLL
VWDILKAPKATRVTERLLNPLIGKSVVVYLRKPTGAGNTELE

MtMT *C*-terminal His-tagged:

MGHMITVDFSLFPVGPGHRVLDLGCGGGRHAFEVYRRGSDVVAFDQNENDLADVA
TMFAAMRAEGEAPHDASAETVKGDALDMPFEDASFDRVIAAEIFEHIPHDTAAMAEL
YRVLKPGGIAAVTVPSWLPERICWALSEEYHTNEGGHIRIYTRAELEAKLKATGFEIG
PHHHAHALHSPYWWIKCAVGTGDDDHPLVRAYHRLLVWDILKAPKATRVTERLLNP
LIGKSVVVYLRKPTGAGNTELEHHHHHH

ThMT *N*-terminal His-tagged:
MGSSHHHHHHSSGLVPRGSHMITVDFTLFPVGPGNRVLDLGCGGGRHAFEAYRR
GADVVAFDQNENDLASVSAMFAAMRAEGEAPASATAETVRGDALAMPFEDGSFDR
VIAAEIMEHIPHDTAAMAELHRVLTPGGIAVVTVPSWLPERVCWALSEEYHTNEGGH
IRIYTRAELEAKLKATGFRIGPHHHAHALHSPYWWLKCAVGTDNDTHPLVRAYHNLL
VWDMMKAPRVTRLAERALNPLIGKSVVVYLRKPRRGGDTGLE

ThMT *C*-terminal His-tagged:

MGHMITVDFTLFPVGPGNRVLDLGCGGGRHAFEAYRRGADVVAFDQNENDLASVS
AMFAAMRAEGEAPASATAETVRGDALAMPFEDGSFDRVIAAEIMEHIPHDTAAMAE
LHRVLTPGGIAVVTVPSWLPERVCWALSEEYHTNEGGHIRIYTRAELEAKLKATGFRI
GPHHHAHALHSPYWWLKCAVGTDNDTHPLVRAYHNLLVWDMMKAPRVTRLAERA
LNPLIGKSVVVYLRKPRRGGDTGLEHHHHHH

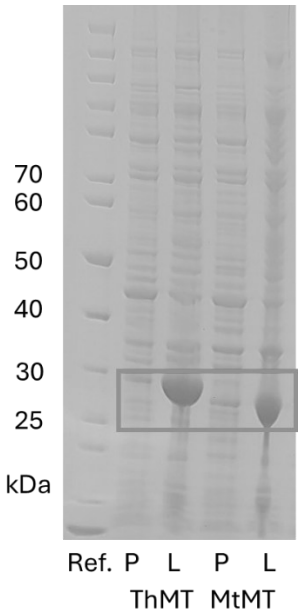

Figure S 29: SDS-Gel of ThMT and MtMT. The cells were lysed and the pellet (P) and lysate (L) fractions were applied to the gel. The band at 30 kDa is highlighted. Ref. = Unstained Protein Standard, Broad Range (10-200 kDa), New England Biolabs.

8.7 Studies towards the biosynthesis of lansai B like natural products

SgCDPS

MRYVPNGLGPGTYCSVPAHMEFSIEPMTENCYSVCQRREHVVLGVSPGNSFFKVPLLTDLI
RWLSREFARLDIVVPDVELSTTFTSLGYPPGRAARKALAEVNAVRNRVVRAWQALG
GPRPCDGLHLMSDLVDRSRYRTARAACEKALREDETLRVTCREASRVVLRARRPG
SEPTAEAVEQAMRYLLAELPFFIASADIFDVPSSLCFYHRPLPLAELVFSGRTVLKPG
PQQGYALVRPVAPPAGPAAQRAVPDT

StspCDPS

MTENCASVCERREHVVVGVSPGNSFFRVPLLADLIHWLNSRFARMDIIVPDAELAPT
FMALGYSPERAAGKARGEVNAVRNRIVRAWESLGGPRPGDGLHLMSELVDRPQYL
TARRRCEKALAVDGNLRTACQNASRTVLLARRPEKEPTAREIEQGMRYLLAELPFF
VASADIFGVPSSLCFYHRPLPLAALIFSGRTVLKPTLRQAYALIRPTGLPHSREHGKA
GHVSSETATPADPYTNLADSYDRLAEWAVTCQKESPRDRVADFLQTFWQSQQRP
VRTVLEICCGTGVGIPMFFCATVARLP

SgMT2

MVSSPDRNPTVSHHYARWADAFVGLRGTRAMHAGYYTGAGDTATIADAADRLVRL
AGRQLGLGPGHHLLDIGCGTGQPAVLLAEETGCRVAGVDASRDMLELGRCQAAGS
VAADRISFHHSDATKLPFPDRSFDRALMIEVVSHVPDTAEDGKQAAFAEAARCLRP
DGLLALVDMTAPSAAAAERRNWMDDVPSVHLTTRQRLLELLVAAGLEVRDVTDISP
HVRHGGRRTQEVFDDHRQELAAALGSGTVERMARLVGQVAEAYENLGYLMVTAR
VRLEHHHHHH

StspM2

MEHQDEPERRAIARYYERGAEAFAALRGTRAMHAGYYTGAEDPATIAESTDRLVRL
AGQRLGLGSGHHLLDIGCGAGQPALLLAEETGCSVTAVDASAGMVAAGRRLAAGS
AAGDRISFHHADAAQLPFPGRSFDRALMLEVASHLPDTARDGKQAAFAEAARCLKR
GGLLALVDMVEPPVAPGAGTLMGEVPSVHLSTRNRLEELLAAVGFDVLDVTDISEH
TRYSAQRNRAAFENRRQELAAAFGADTVRRIALLLGQLAEADASLGYVTVIARAGH
MHHHHHH

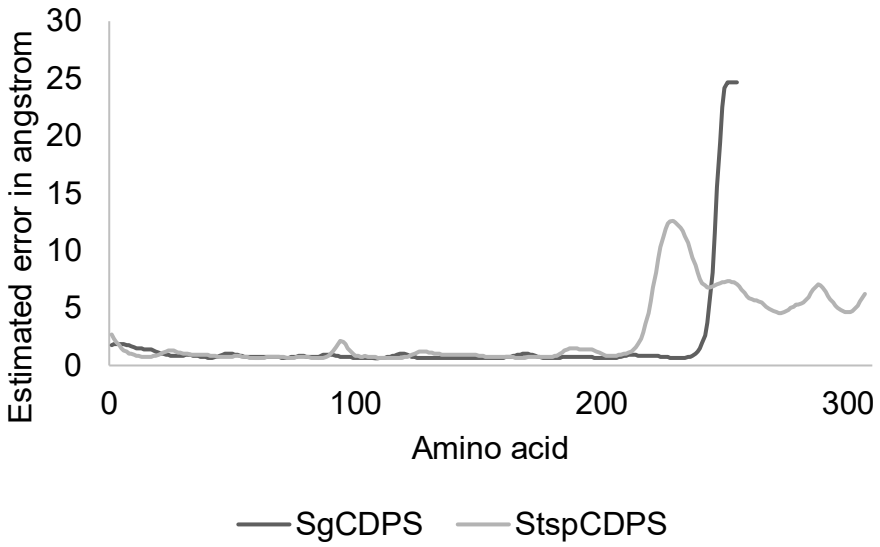

Figure S 30: Estimated errors in angstrom for each residue in the structural models of SgCDPS and StspCDPS.

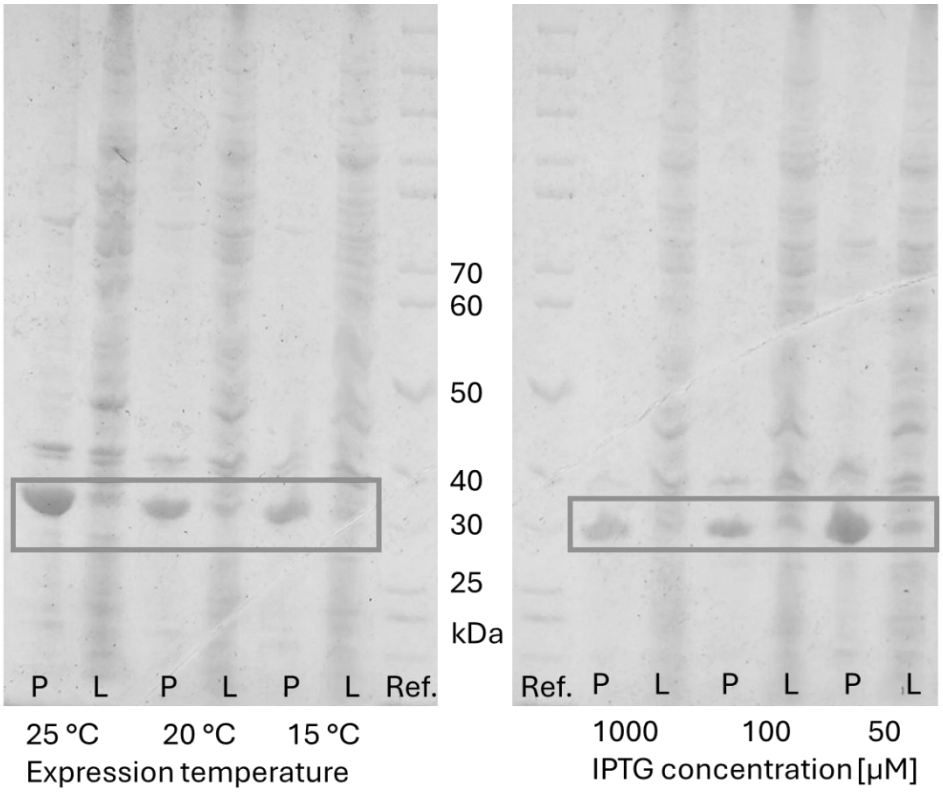

Figure S 31: SDS-gel of the expression study for StspM2 (30 kDa). The expression temperature was varied at 15, 20, and 25 °C while maintaining the IPTG induction concentration at 100 µM. Additionally, IPTG concentrations were tested at 50, 100, and 1000 µM, with the temperature held constant at 20 °C. After cell lysis, both the lysate (L) and pellet fraction (P) were applied to the gel. Ref. = Unstained Protein Standard, Broad Range (10-200 kDa), New England Biolabs.

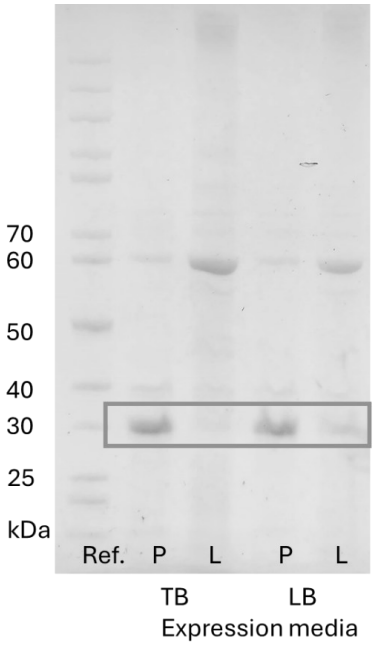

Figure S 32: SDS-gel of the expression study for StspM2 (30 kDa). The expression was carried out in the E. coli Arctic express strain in TB or LB media. After cell lysis, both the lysate (L) and pellet fraction (P) were applied to the gel. Ref. = Unstained Protein Standard, Broad Range (10-200 kDa), New England Biolabs.

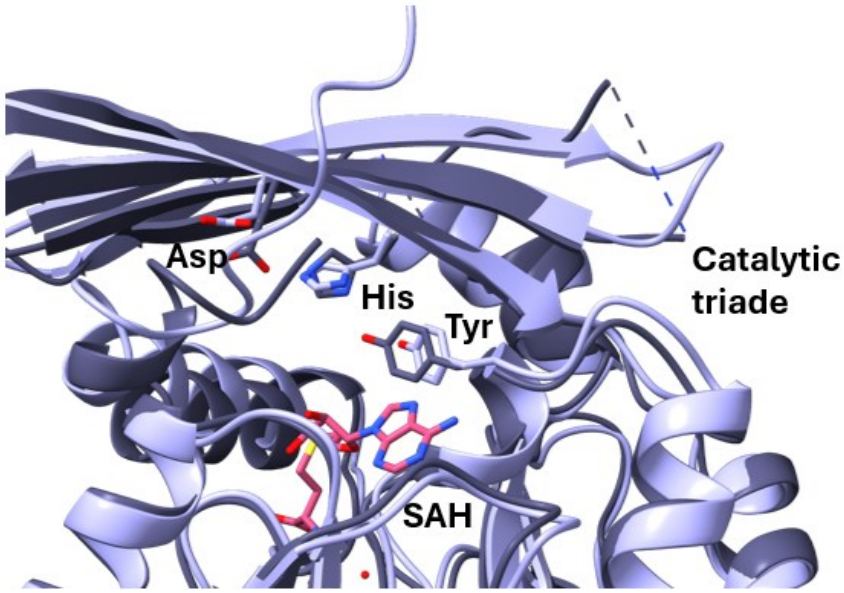

Figure S 33: Catalytic side of PsmC (dark blue) and NozMT (light violet) – both enzymes contain a catalytic triade positioned like in SgMT and StspM1.

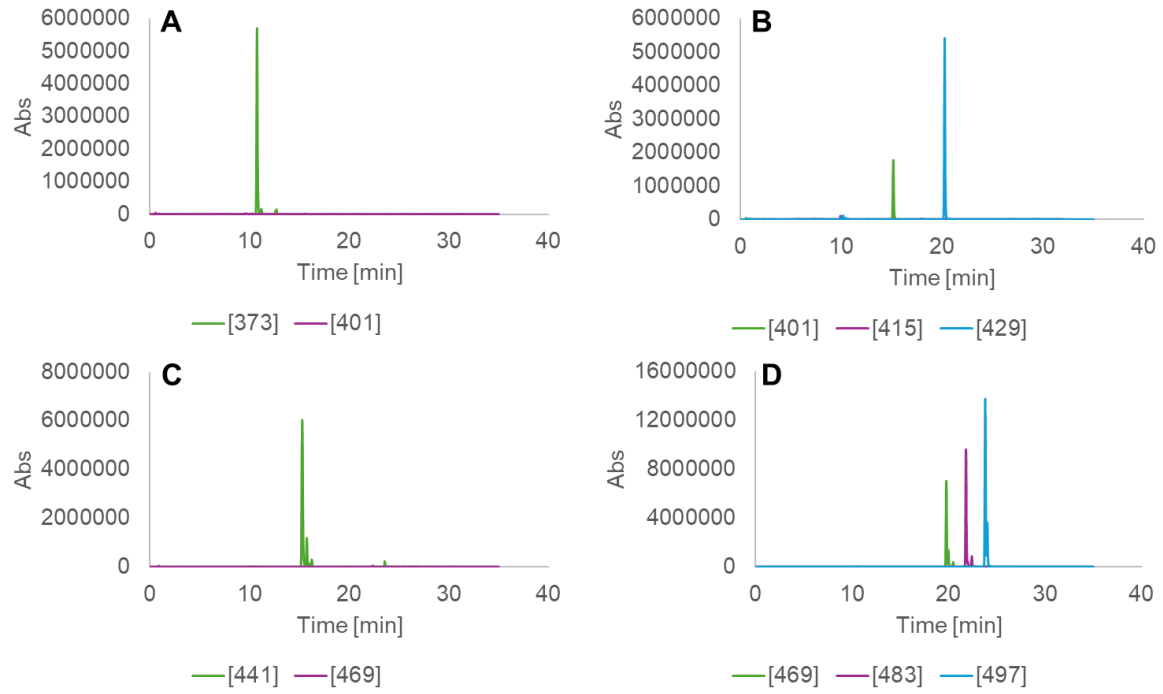

Figure S 34: Activity test of SgM2 with the cWW **7** [A], the double *C3*-methylated **240** [B], the *C5*-prenylated cWW **261a** [C] and the double *C3*-methylated+*C5*-prenylated cWW **269** [D] measured with the LC-MS.

SgPT

MHHHHHHMTAAIDQTGLRADFAACTAFMRRRGAVVYAMPRMLLPPDRRPYCDAV
QAFTIYADKLIDDPRVPVADRRRRYQDYSRAVLALLETGDPDRWDGPRSPEDTVGR
HLARAFAHFTRVWDVPPESVRRLLDTMAGDAEATEYPTFADLDQYIRGTGVPYIHW
INALLGRRAHTSEVAREKAAAAIFGLALTDNLQDLAEDLTAGRLCLPVEDLRAFGLDR
DDLARAVREWRMPGPVRDLVRFEADRAYRYLEQADGWWRTADPVARELPRQYV
RLTLHTLRRTVGAEYDLFAPRRRARLTWGARACAGFALGYGRARVRWSARLPDRR
PRPASN

StspPT

MAMSSAIDRAGLRDDYIACKDFMRRCGPVVYLMPRMLLPPDRRPYCDAVQAFTIHA
DRLIDDPHVPAADRVTRYQDYSRAVLTLLEGADPDPWGSAPASREEAVGRQLARA
FAHFTRVWEVPCDSVRTLLENMAGDAHASEYPAFTDLERYVRGTGVPYILWLNALL
GPAAHNGEEAREQAAAAIFALQLTDNLSDLEEDLTAGRLCLPLEDLKTFGLKCGDLE
RAVRERRTTEPVRELVRFEAERVRRYVEEAEGWWRAADPVARELPRQYVRMTLH
TLRKTVGSRYDLFAPRRTARLAWASRMGAGFALGCTRASVRRFGTPRGRRRPRPA
PRHMHHHHHH

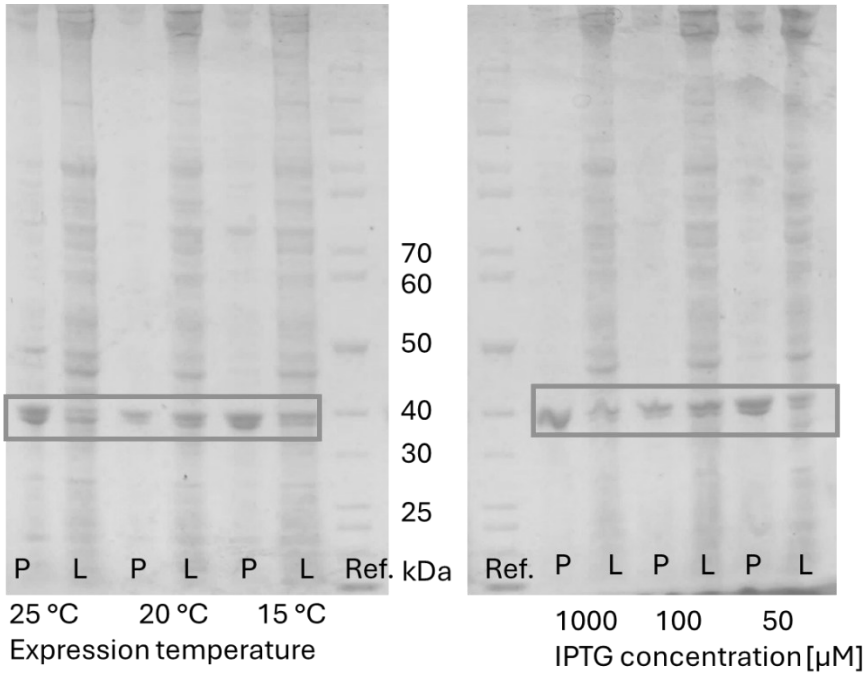

Figure S 35: SDS-gel of the expression study for StspPT (38 kDa). The expression temperature was varied at 15, 20, and 25 °C while maintaining the IPTG induction concentration at 100 µM. Additionally, IPTG concentrations were tested at 50, 100, and 1000 µM, with the temperature held constant at 20 °C. After cell lysis, both the lysate (L) and pellet fraction (P) were applied to the gel. Ref. = Unstained Protein Standard, Broad Range (10-200 kDa), New England Biolabs.

Figure S 36: Structures of SgPT (blue) and a SQS (pink, PDB: 7WGH). The C-terminus is highlighted.

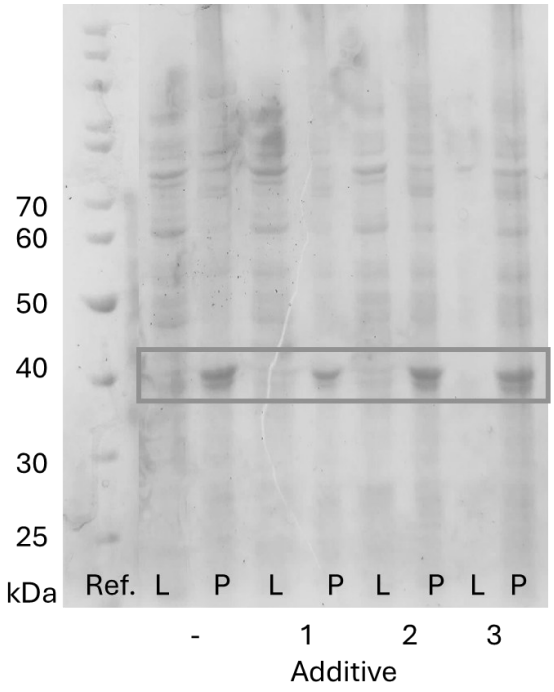

Figure S 37: SDS-gel of the expression study for StspPT (38 kDa). During the cell lysis either 5 mM MgCl (additive 1) or 1% w/v CHAPS (additive 2) or 0.75 mM trehalose (additive 3) were added to the lysis buffer. After cell lysis, both the lysate (L) and pellet fraction (P) were applied to the gel. Ref. = Unstained Protein Standard, Broad Range (10-200 kDa), New England Biolabs.

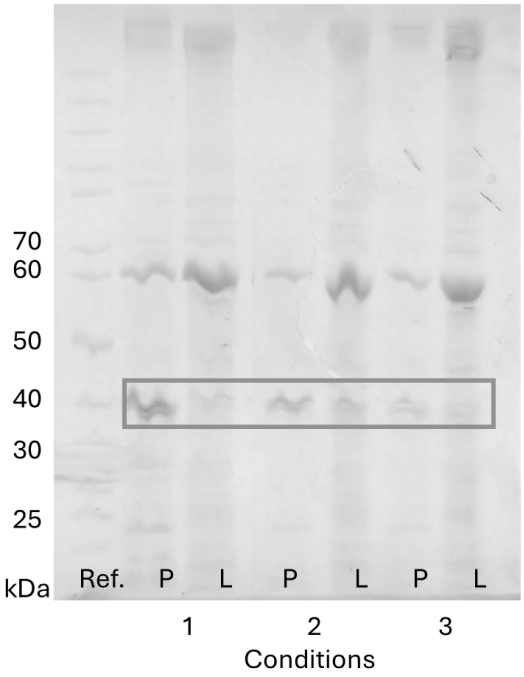

Figure S 38: SDS-gel of the expression study for StspPT (38 kDa). The expression was carried out in the E. coli Arctic express strain in TB (condition 1) or LB media with antibiotic (condition 2) or without (condition 3). After cell lysis, both the lysate (L) and pellet fraction (P) were applied to the gel. Ref. = Unstained Protein Standard, Broad Range (10-200 kDa), New England Biolabs.

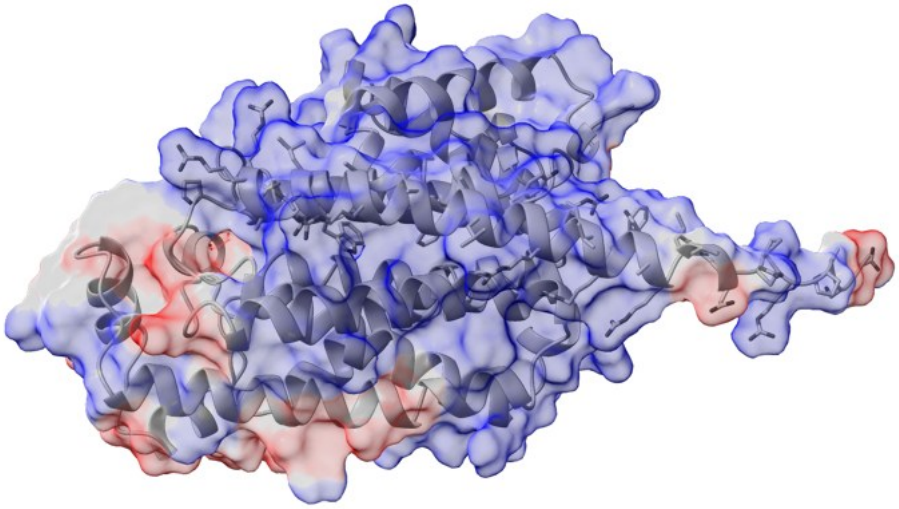

Figure S 39: Structure of SgPT with a polarity-surface. basic amino acids are highlighted in blue, acidic amino acids in red.

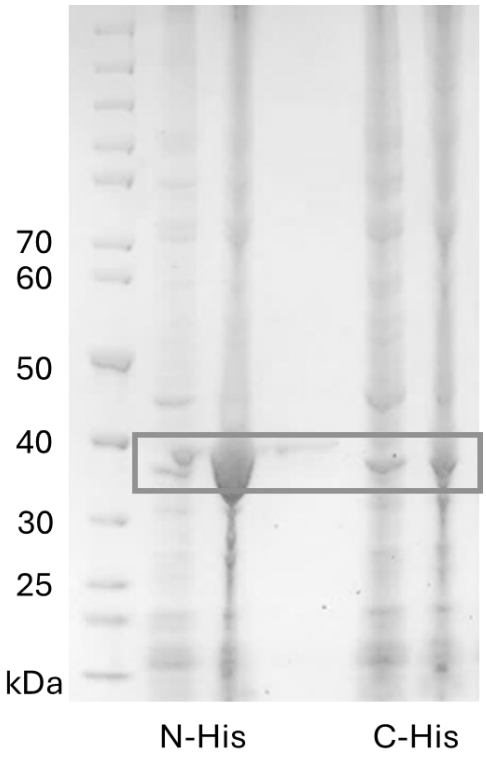

Figure S 40: SDS-gel of StspPT (38 kDa) with a *N*-terminal or a C-terminal His-Tag. After cell lysis, both the lysate (L) and pellet fraction (P) were applied to the gel. Ref. = Unstained Protein Standard, Broad Range (10-200 kDa), New England Biolabs.

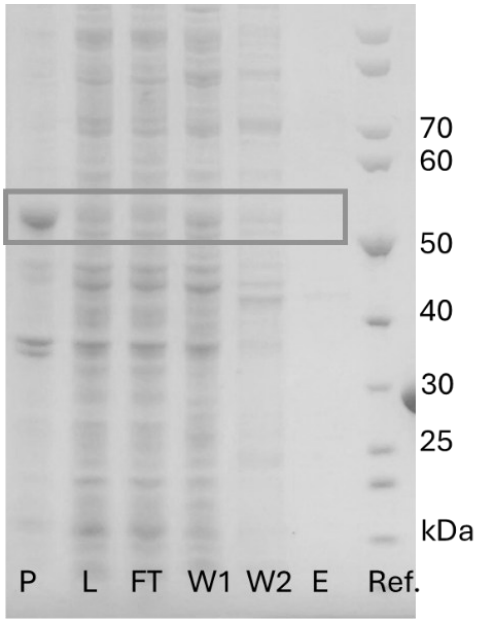

Figure S 41: SDS-gel of the purification of StspPT with the solubility Trx-Tag (55 kDa) using a Ni-NTA column. After cell lysis, both the lysate (L) and pellet fraction (P) were applied to the gel. The Ni-NTA column loaded with the cleared lysate (FT = flow through; lysate after passing the column) and washed with buffers containing various concentrations of imidazole - 40 mM (W1), 80 mM (W2), 250 mM (E). Ref. = Unstained Protein Standard, Broad Range (10-200 kDa), New England Biolabs.

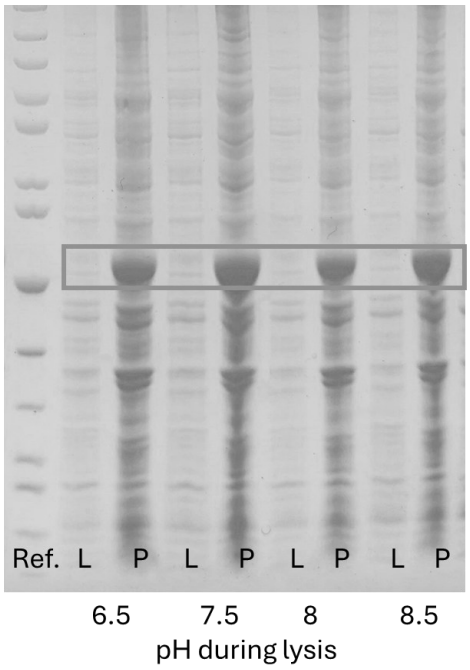

Figure S 42: SDS-gel of StspPT with the solubility Trx-Tag (55 kDa). After cell lysis, both the lysate (L) and pellet fraction (P) were applied to the gel. The lysis was carried out at different pH values (6.5, 7.5, 8.0, 8.5). Ref. = Unstained Protein Standard, Broad Range (10-200 kDa), New England Biolabs.

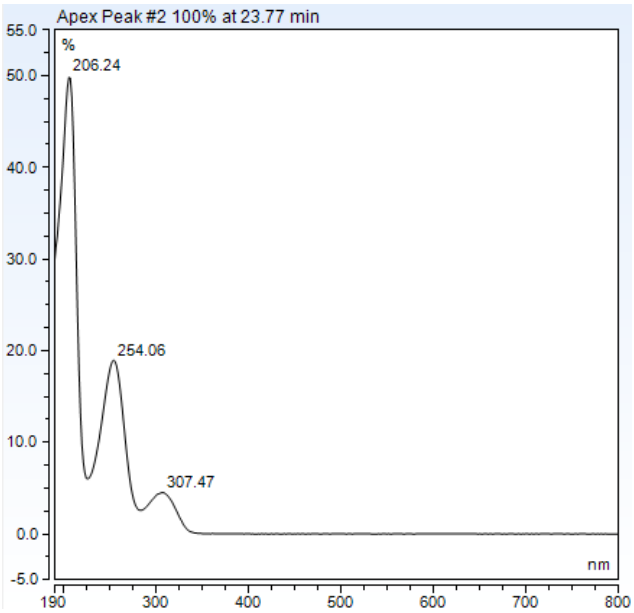

Figure S 43: UV-Vis spectrum of the product formed in the prenylation reaction of the *N*- and *C3*-methylated cWW (lansai B) with SgPT.

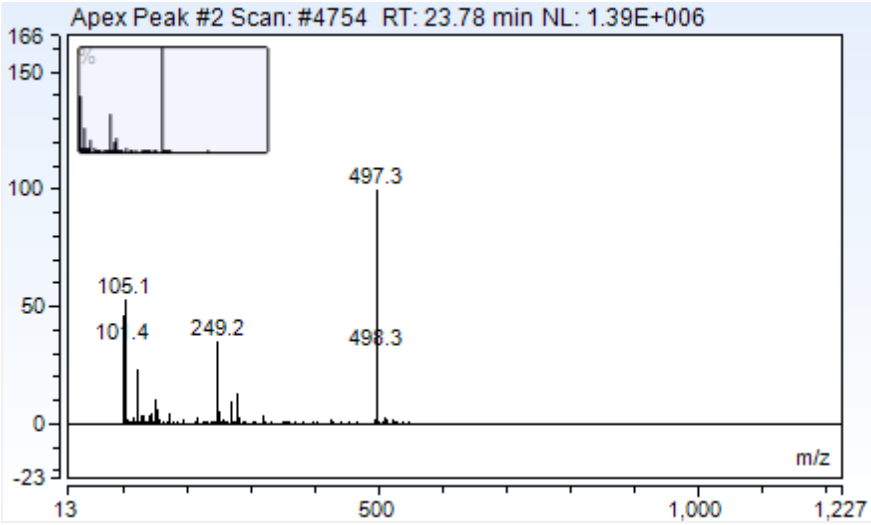

Figure S 44: MS spectrum of the product formed in the prenylation reaction of the *N*- and *C3*-methylated cWW (lansai B) with SgPT.

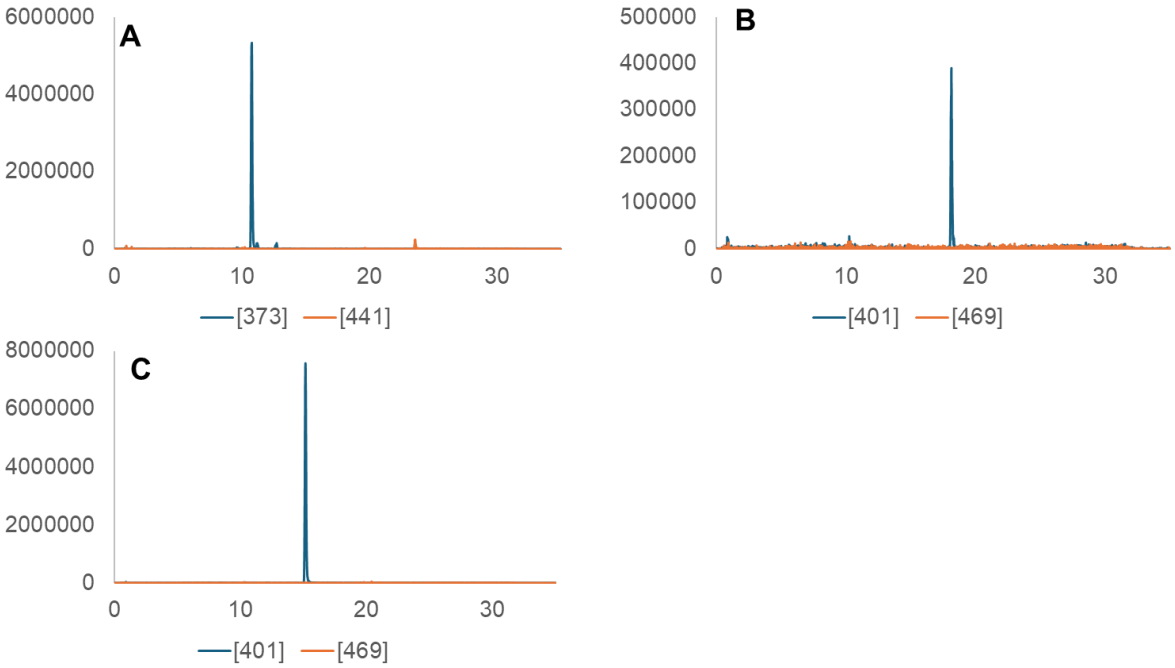

Figure S 45: Activity of SgPT with the cWW **3a** [A], the double *N*-methylated **292** [B] and the *C3*-methylated cWW **240** [C] as substrates measured with the LC-MS.

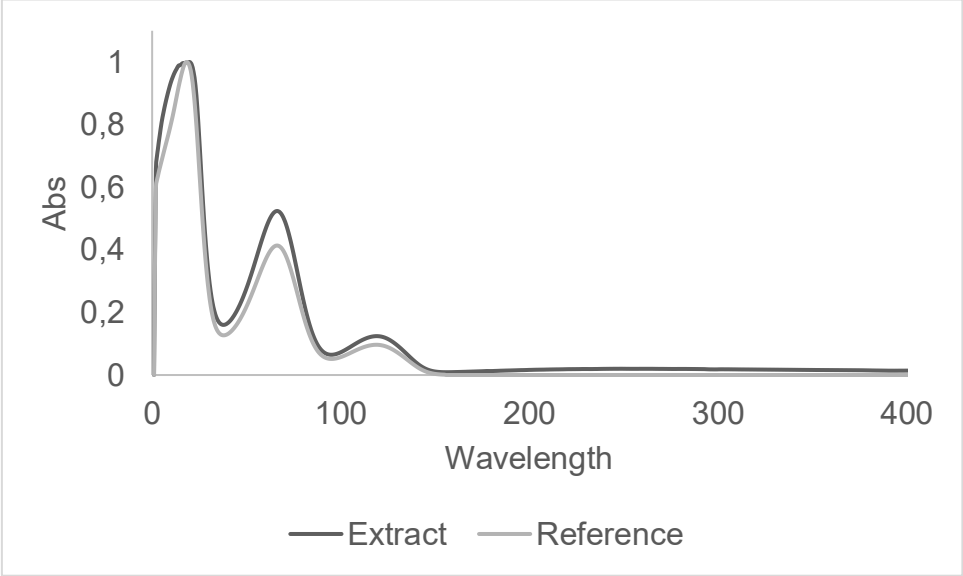

Figure S 46: UV-Vis spectrum of lansai B (**5**): The chemically synthesised reference in shown in orange, the extracted lansai B in blue.

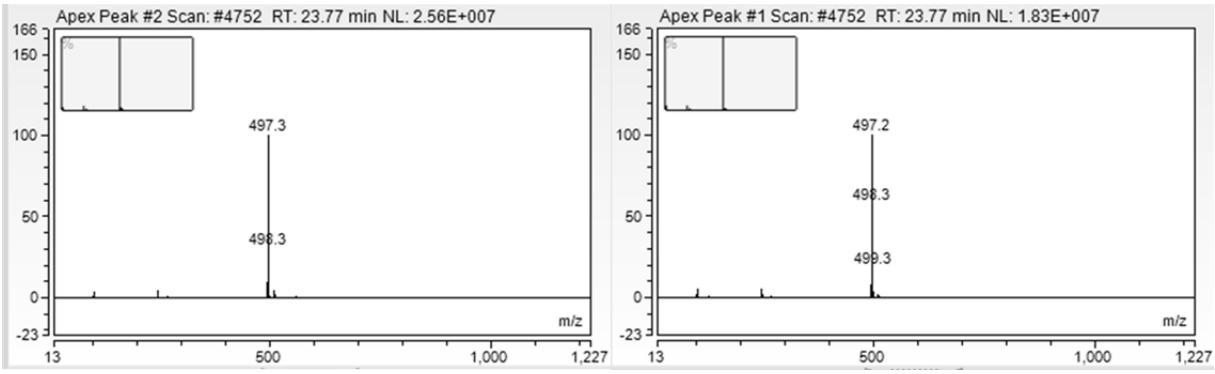

Figure S 47: MS spectra of lansai B (**5**): The chemically synthesised reference in shown on the left, the extracted lansai B right.

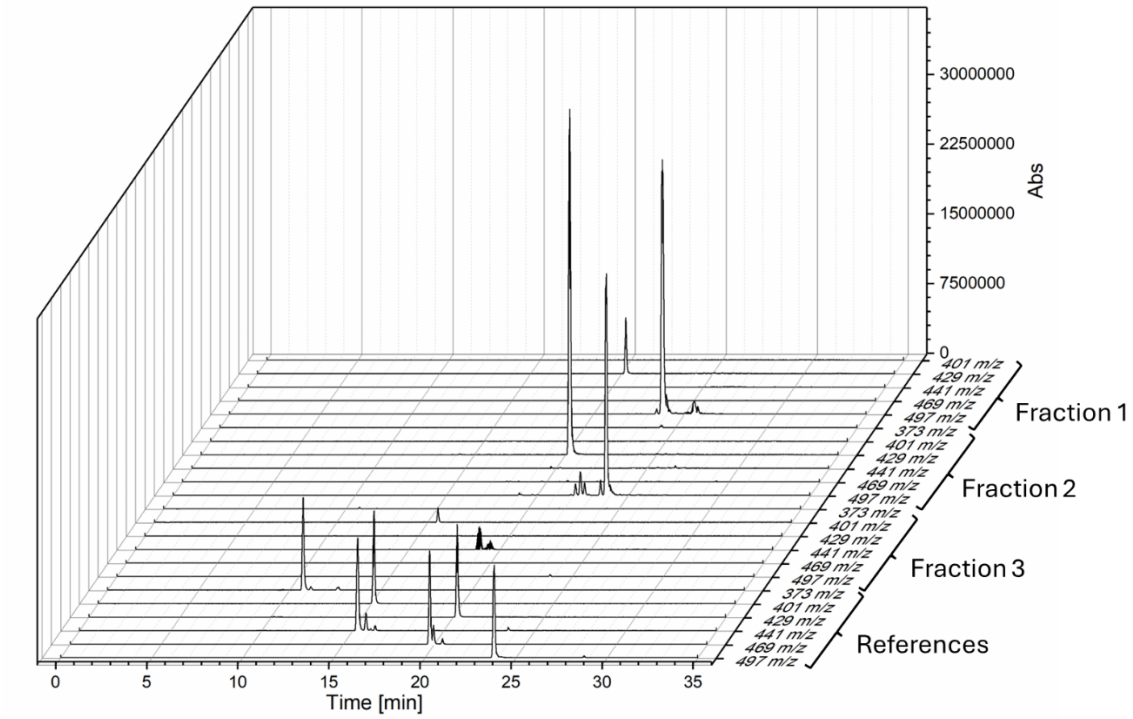

Figure S 48: LC-MS traces of all potential intermediates of the biosynthesis of lansai B in the extracted fractions 1-3 and the chemically synthesised references.

8.8 Outlook

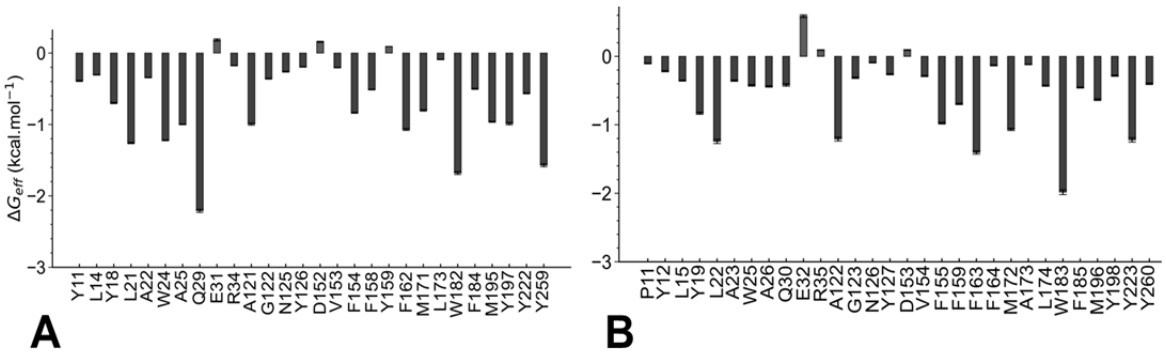

Figure S 49: MM-GBSA effective free-energy per residue for SgMT (A) and StspM1 (B). Calculations for SgMT and StspM1 were done using LL-cWW **3a** as ligand for both enzymes. The averages and standard errors were calculated over eight simulation replicas (200 ns each). Blue and red bars indicate positive versus negative contributions to the binding effective energy, respectively. Figure by Benoit David.

Table S 25: Result of the alkylation experiments using SgMT and AcHMT with the corresponding alkyldonor allyl iodide, prenyl bromide and ethyl iodide.

	Retention time [min]	**Relative peak area [%]**	**m/z**
Allyl	11,4	68	373
	15,2	26	413
	18,9	6	453
Prenyl	11,4	97	373
	15,7	3	441
Ethyl	11,4	100	373

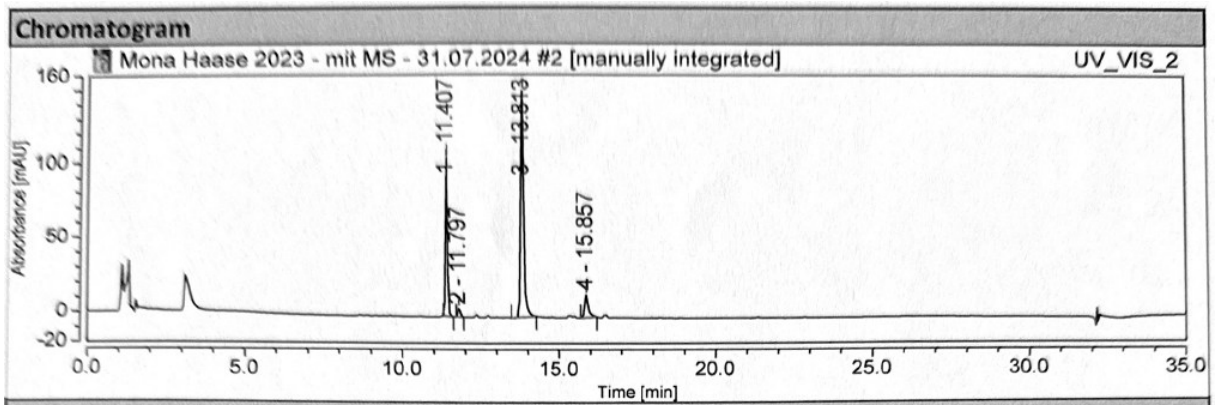

Figure S 50: LC-MS chromatogram of the alkylation experiments with SgMT. The absorption was measured at 284 nm. Methyl iodide was used as alkyl-donor.

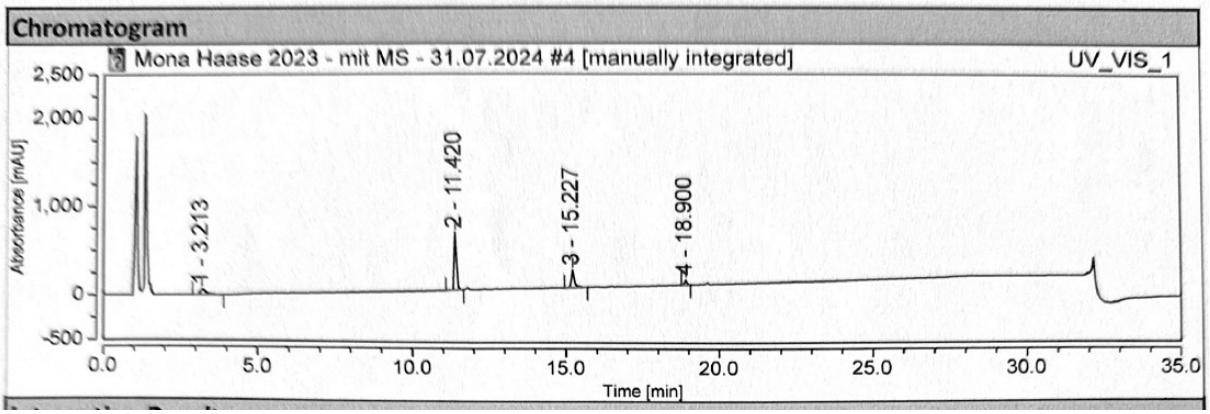

Figure S 51: LC-MS chromatogram of the alkylation experiments with SgMT. The absorption was measured at 284 nm. Allyl iodide was used as alkyl-donor.

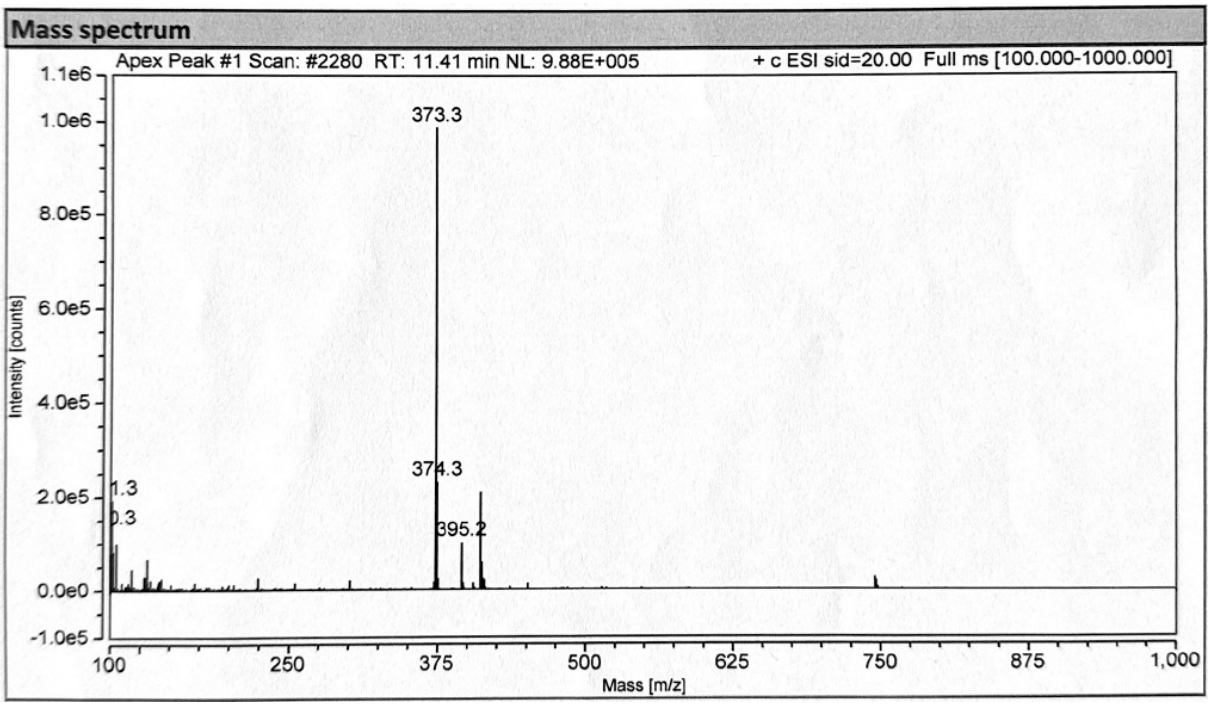

Figure S 52: Mass spectrum of the compound eluting at 11.4 min in the alkylation experiment with SgMT using allyl iodide as alkyl donor.

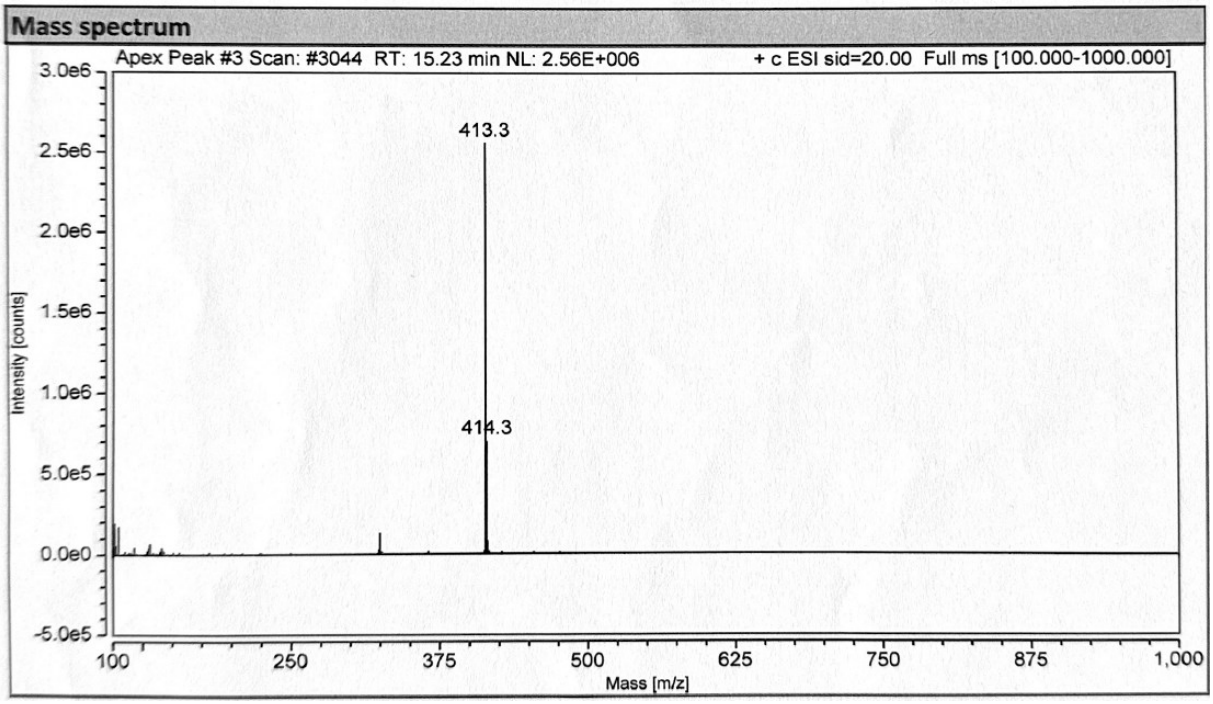

Figure S 53: Mass spectrum of the compound eluting at 15.2 min in the alkylation experiment with SgMT using allyl iodide as alkyl donor.

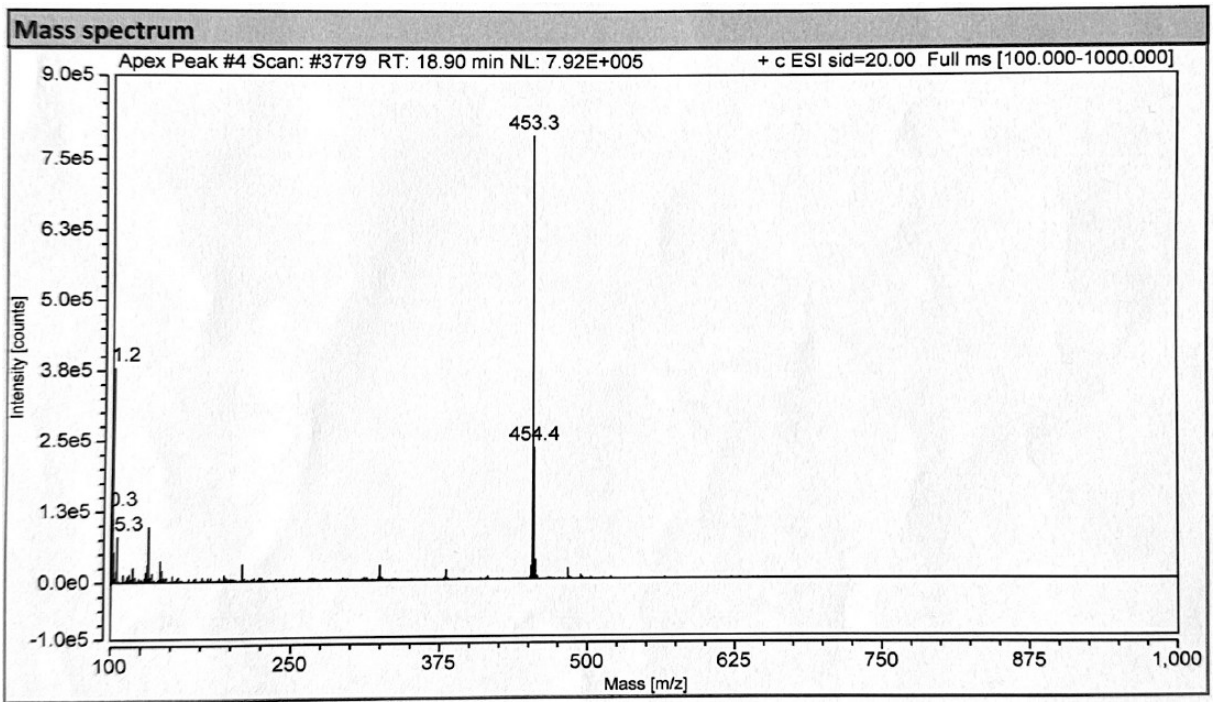

Figure S 54: Mass spectrum of the compound eluting at 18.9 min in the alkylation experiment with SgMT using allyl iodide as alkyl donor.

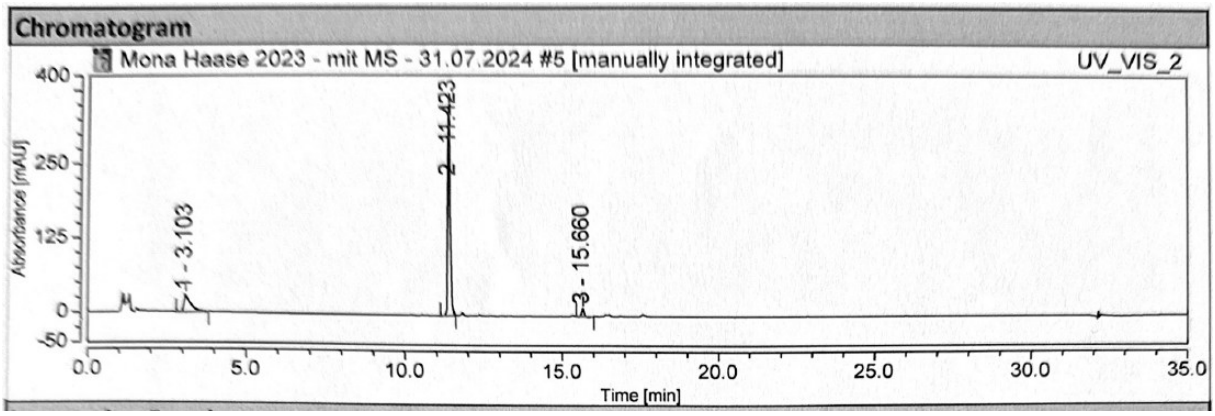

Figure S 55: LC-MS chromatogram of the alkylation experiments with SgMT. The absorption was measured at 284 nm. Prenyl bromide was used as alkyl-donor.

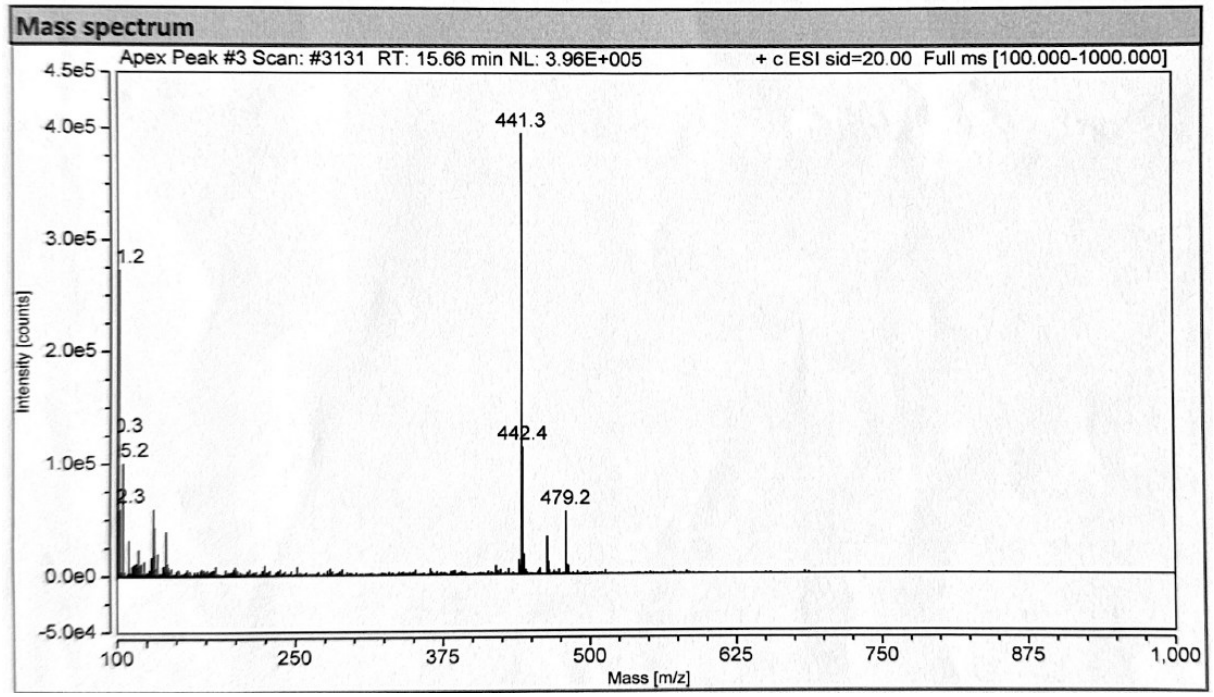

Figure S 56: Mass spectrum of the compound eluting at 15.7 min in the alkylation experiment with SgMT using prenyl bromide as alkyl donor.

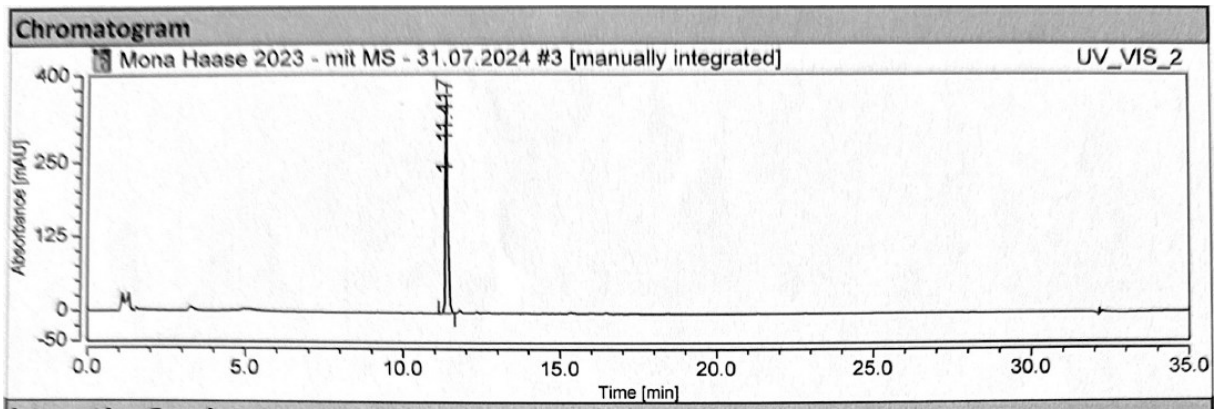

Figure S 57: LC-MS chromatogram of the alkylation experiments with SgMT. The absorption was measured at 284 nm. Ethyl iodide was used as alkyl-donor.

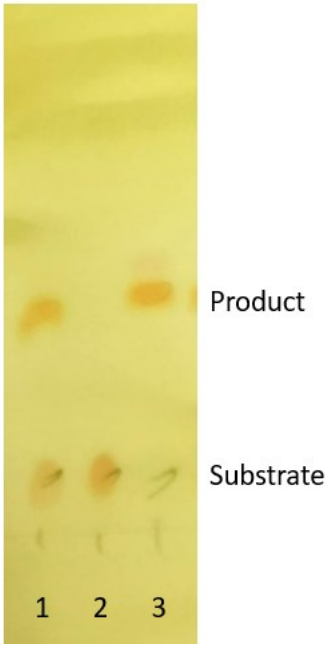

Figure S 58: TLC colored with Moly-Dip of the allylation reaction with SgMT. 1: Conditions by Diana Amariei (pre-incubation of AcHMT, SAH (**94**) and allyl iodide before adding SgMT and the cWW **3a**), B: negative control (condition of Diana Amariei without HMT), C: direct recycling conditions.

8.10 Plasmids

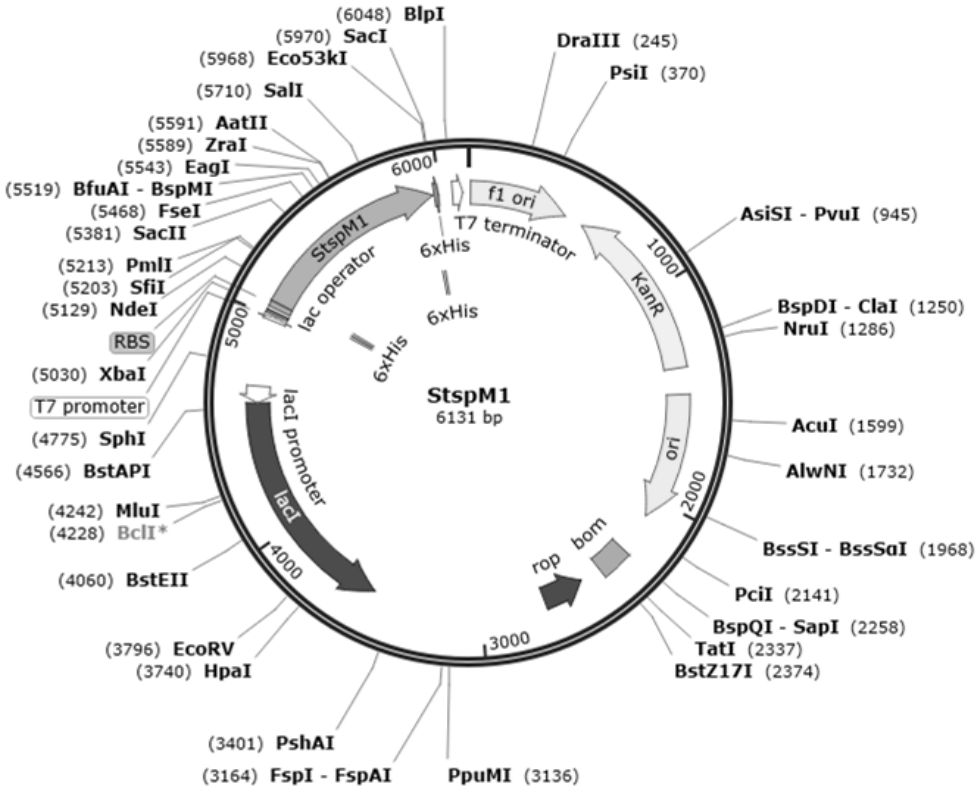

Figure 189: Plasmid card of the pet28a(+) vector containing the gene of StspM1.

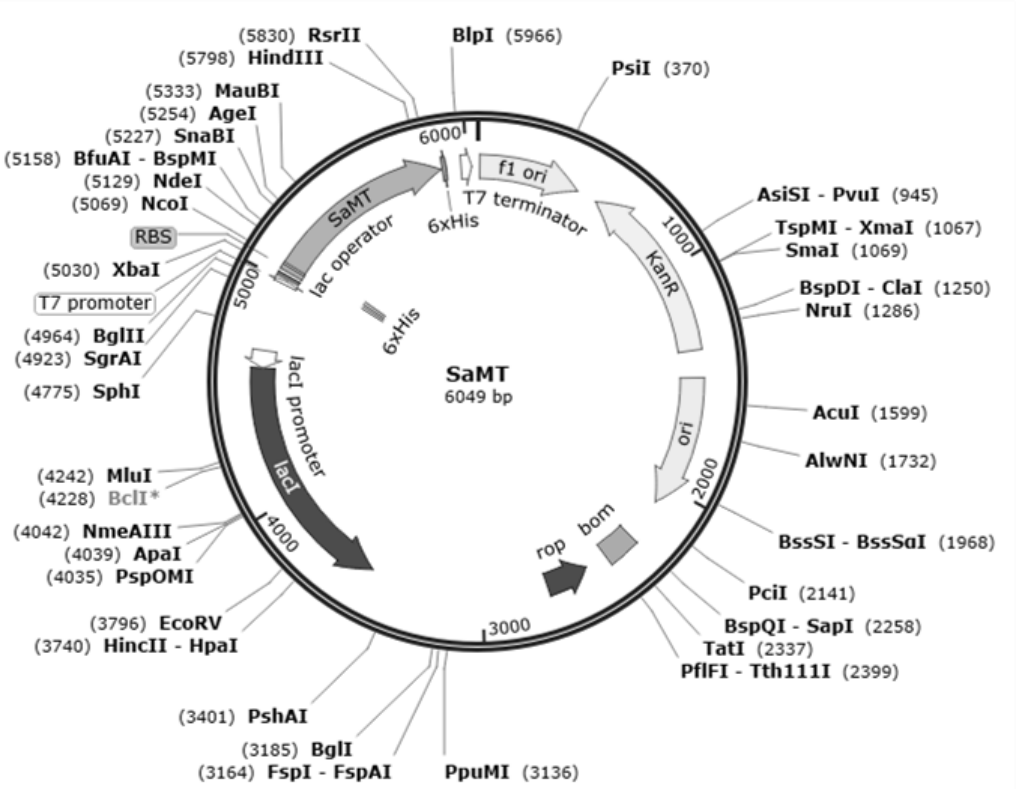

Figure 190: Plasmid card of the pet28a(+) vector containing the gene of SaMT.

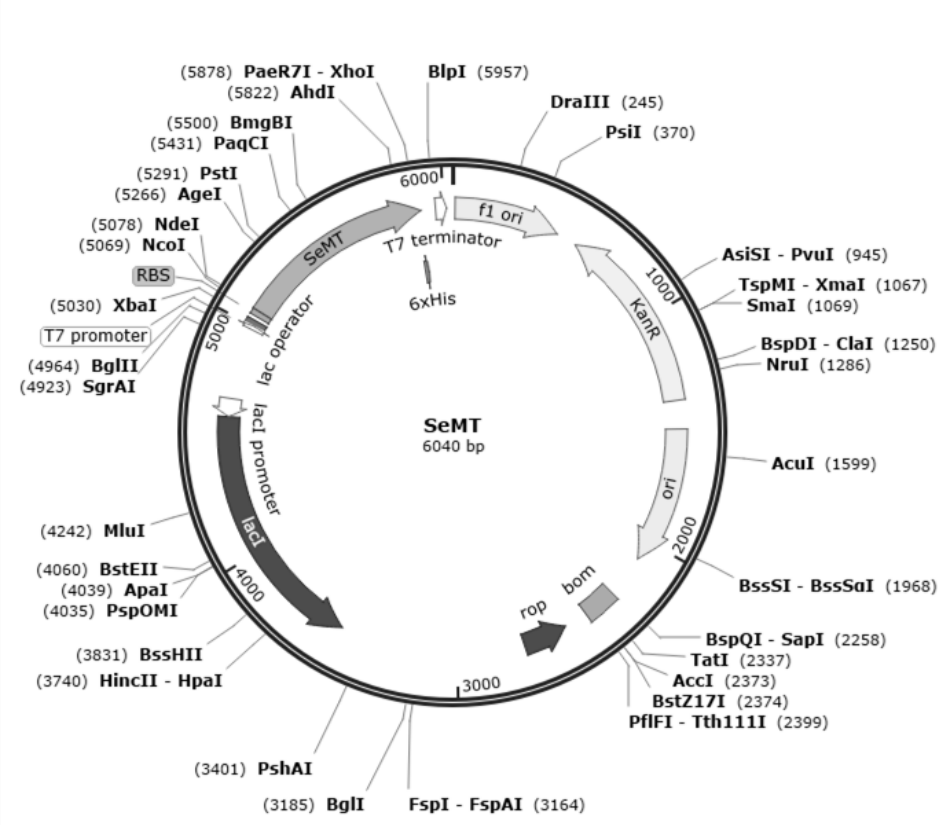

Figure 191: Plasmid card of the pet28a(+) vector containing the gene of SeMT.

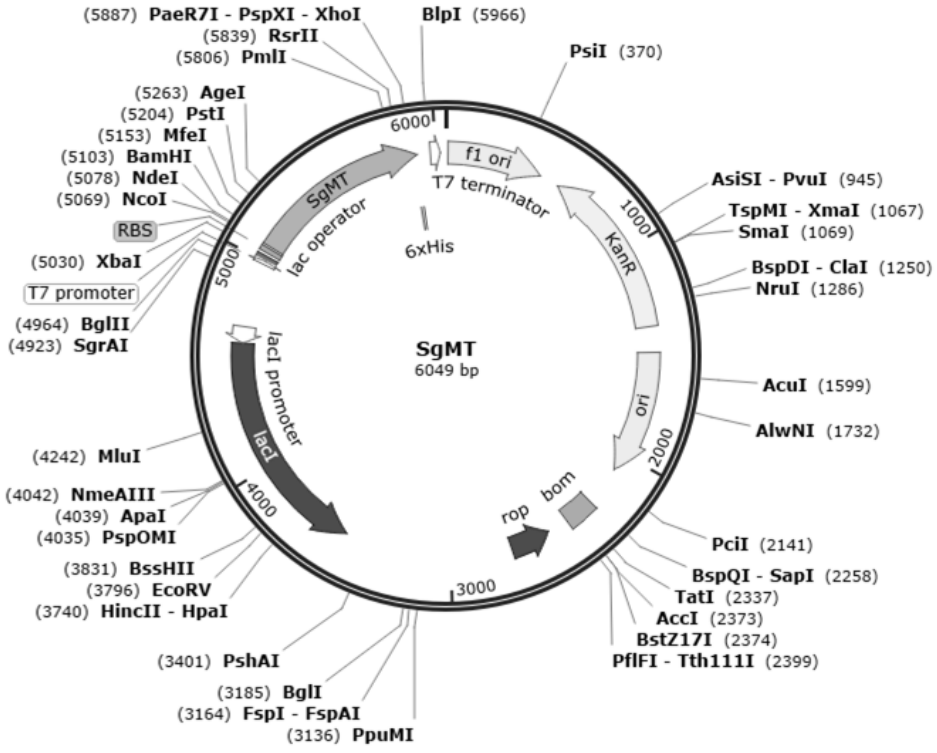

Figure 192: Plasmid card of the pet28a(+) vector containing the gene of SgMT.

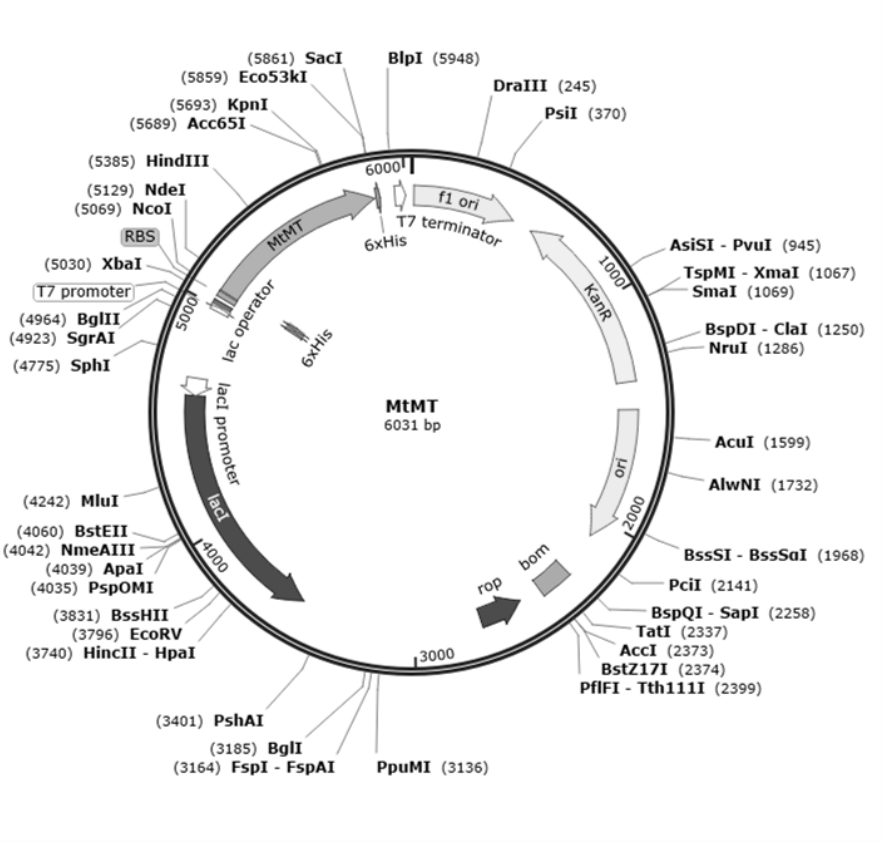

Figure 193: Plasmid card of the pet28a(+) vector containing the gene of MtMT.

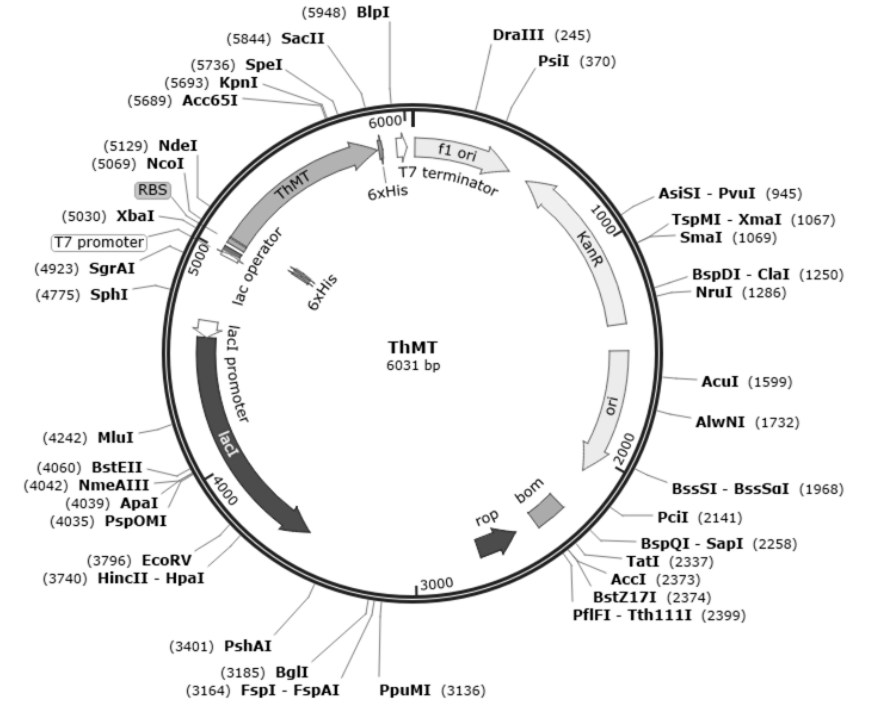

Figure 194: Plasmid card of the pet28a(+) vector containing the gene of ThMT.

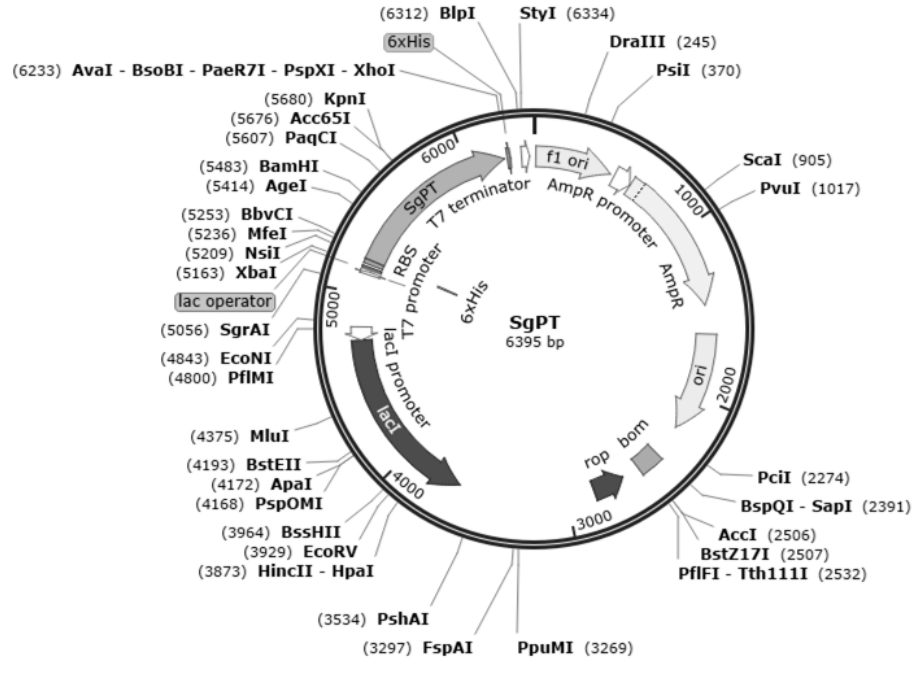

Figure 195: Plasmid card of the pet28a(+) vector containing the gene of SgPT.

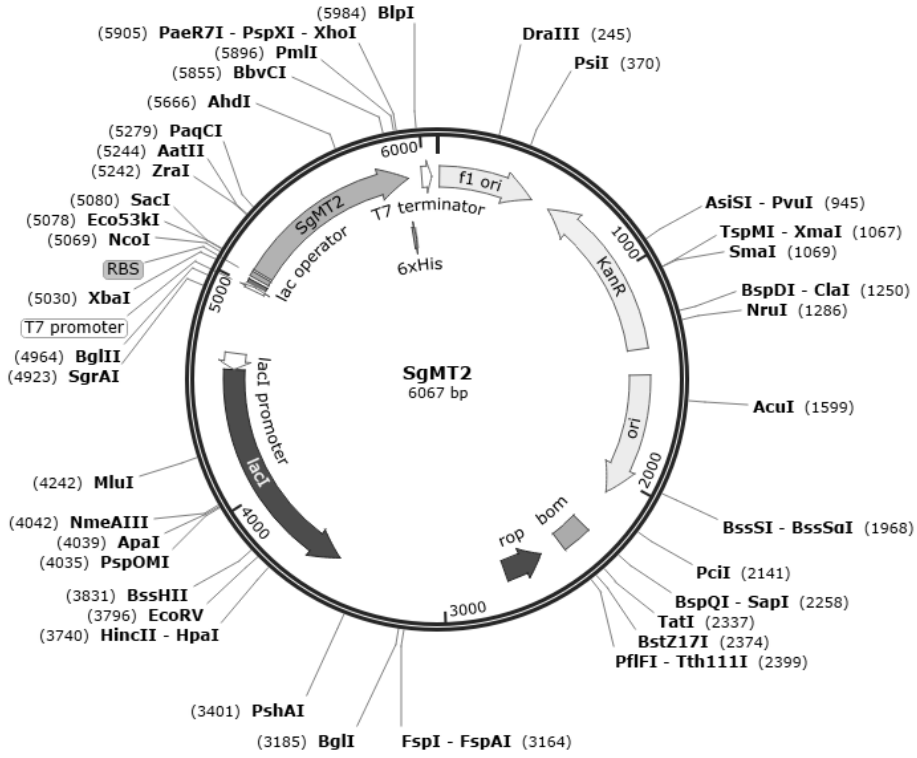

Figure 196: Plasmid card of the pet28a(+) vector containing the gene of SgMT2.

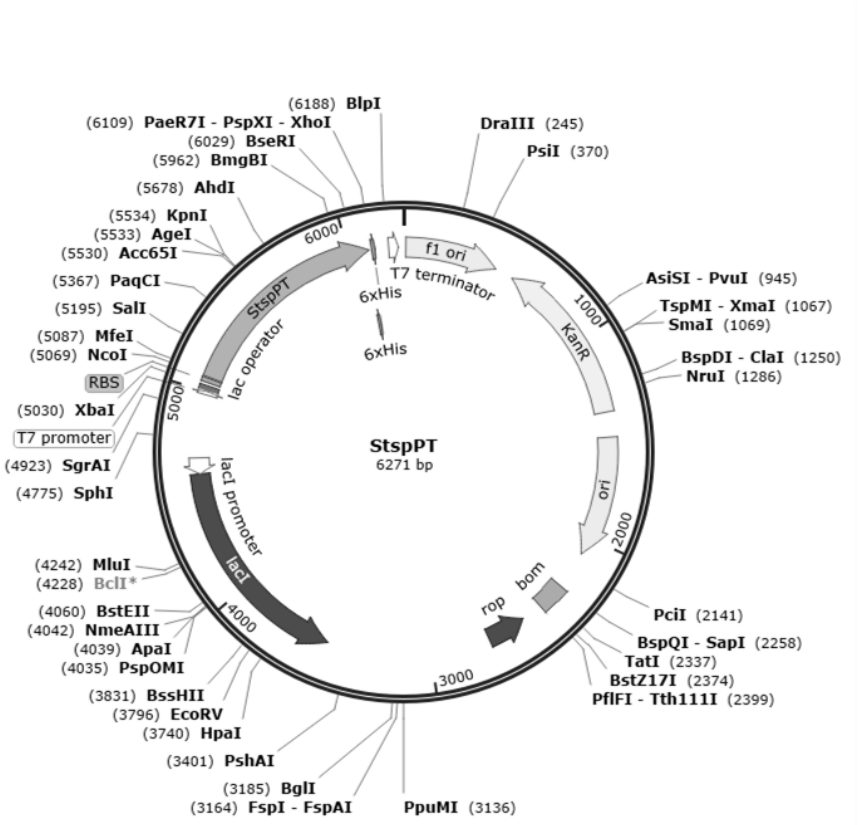

Figure 197: Plasmid card of the pet28a(+) vector containing the gene of StspPT.

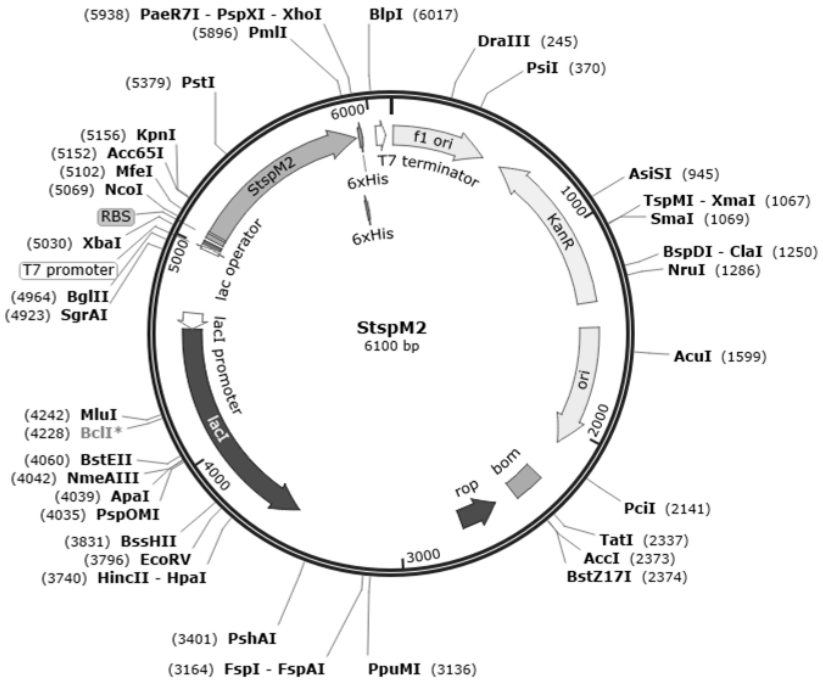

Figure 198: Plasmid card of the pet28a(+) vector containing the gene of StspM2.

8.11 NMR-Spectra

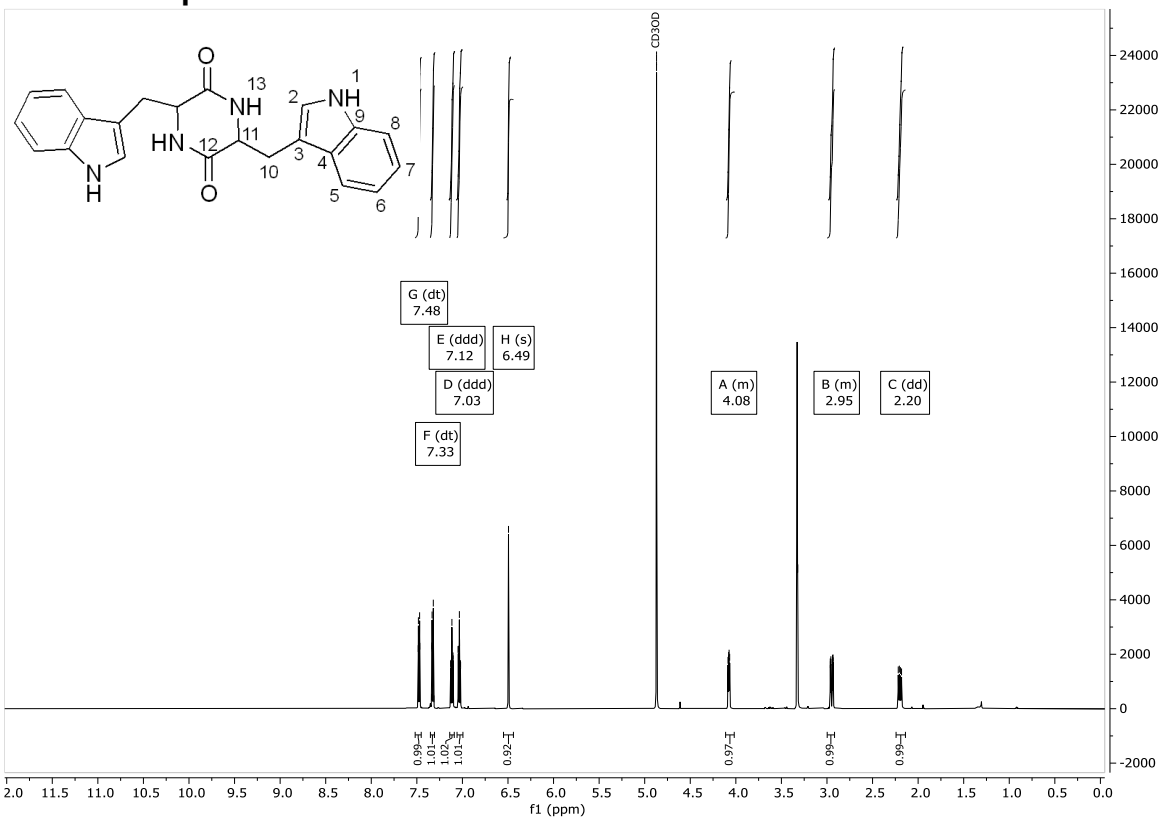

Figure 199: ^{1}H-NMR spectrum of LL-cWW **3a** in MeOD (600 MHz).

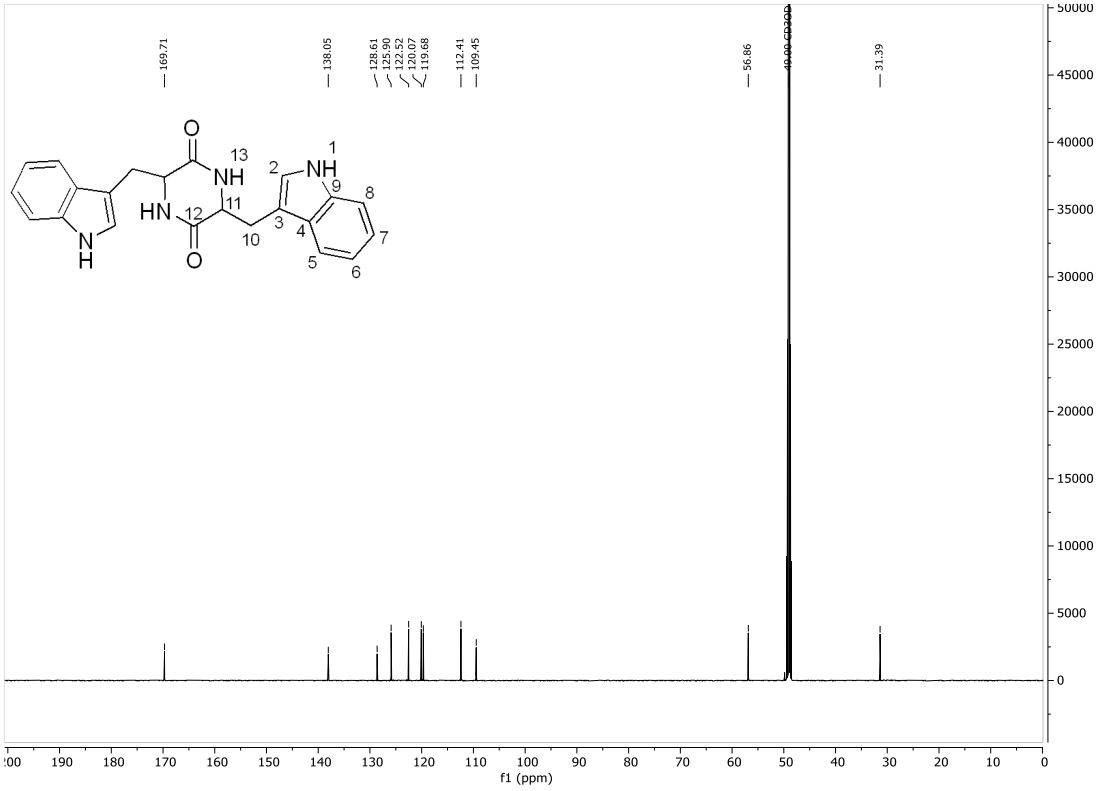

Figure 200: ^{13}C-NMR spectrum of LL-cWW **3a** in MeOD (151 MHz).

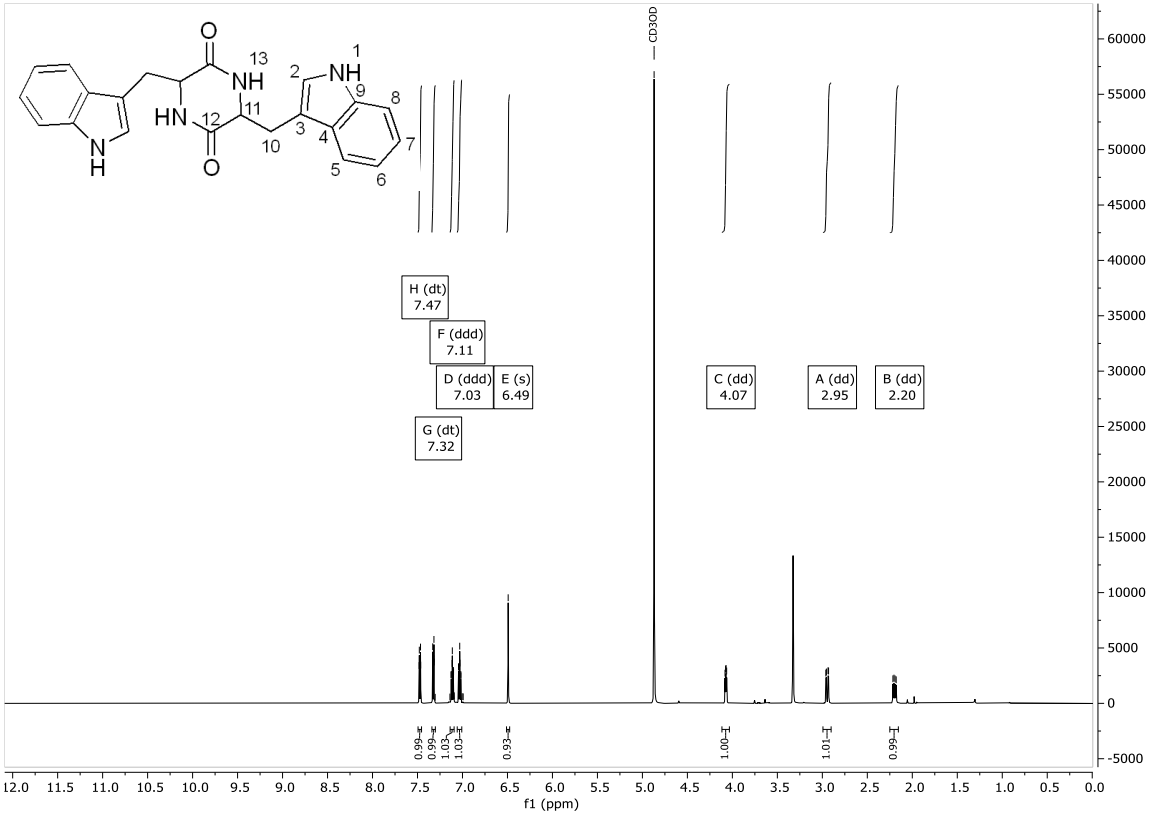

Figure 201: ^{1}H-NMR spectrum of DD-cWW **3b** in MeOD (600 MHz).

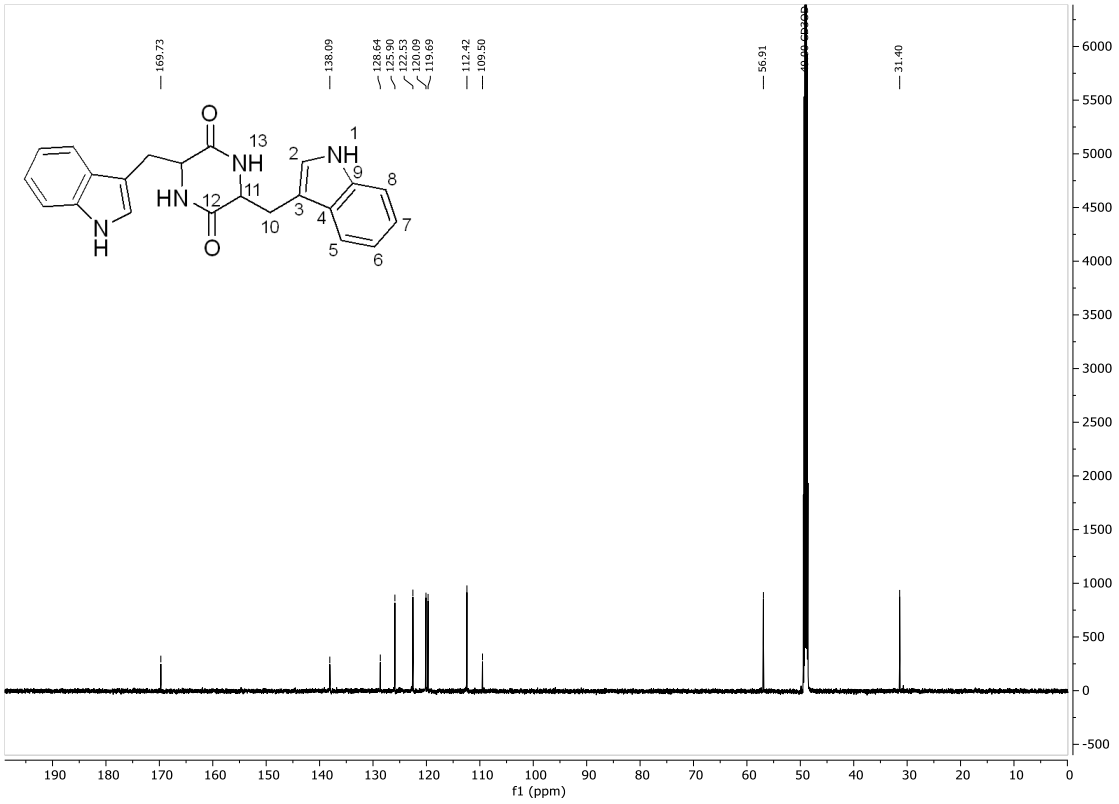

Figure 202: ^{13}C-NMR spectrum of DD-cWW **3b** in MeOD (151 MHz).

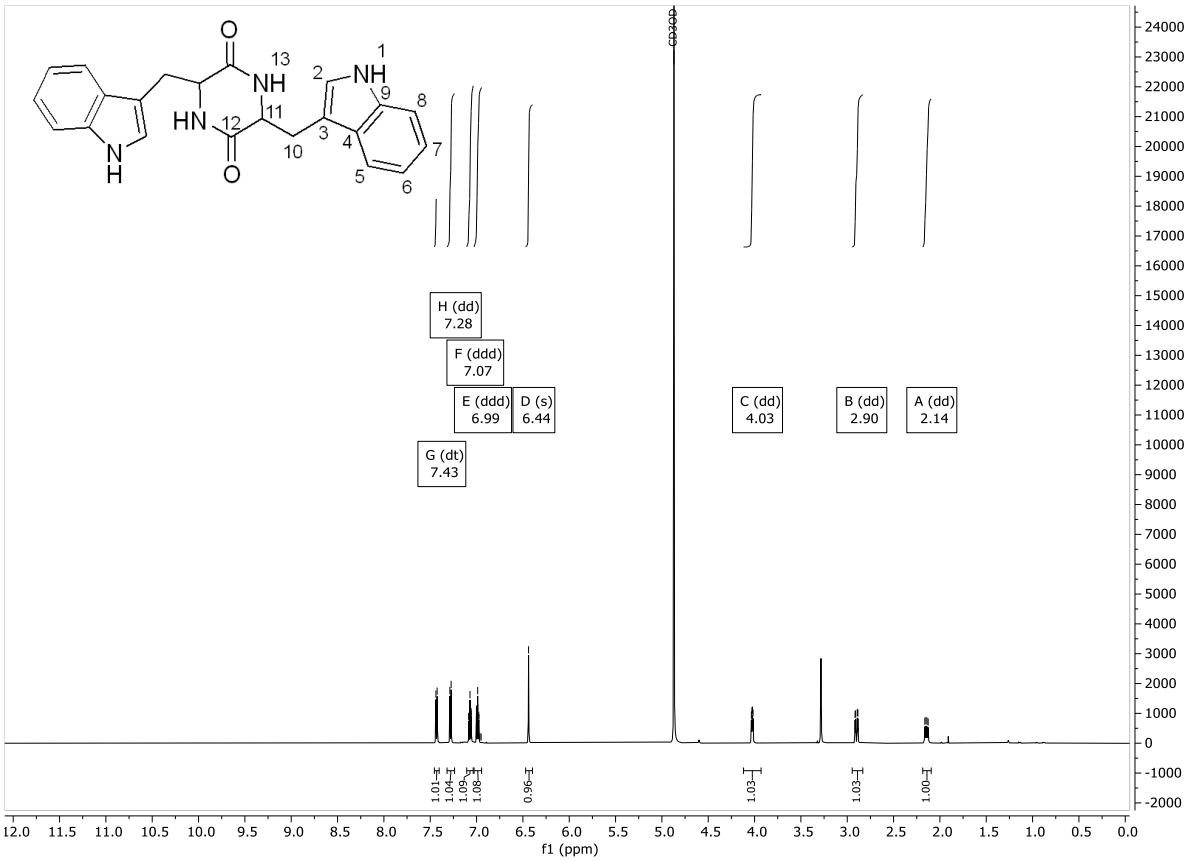

Figure 203: ^{1}H-NMR spectrum of LD-cWW **3c** in MeOD (600 MHz).

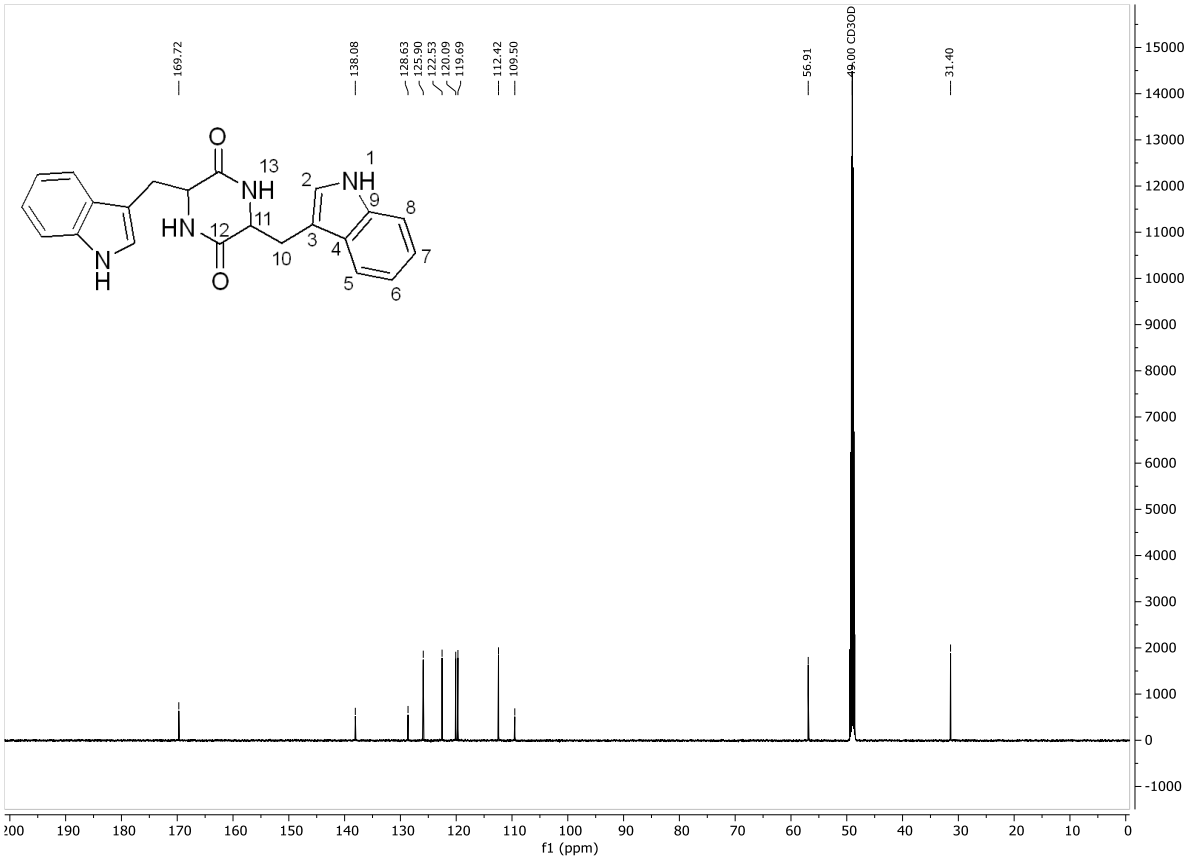

Figure 204: ^{13}C-NMR spectrum of LD-cWW **3c** in MeOD (151 MHz).

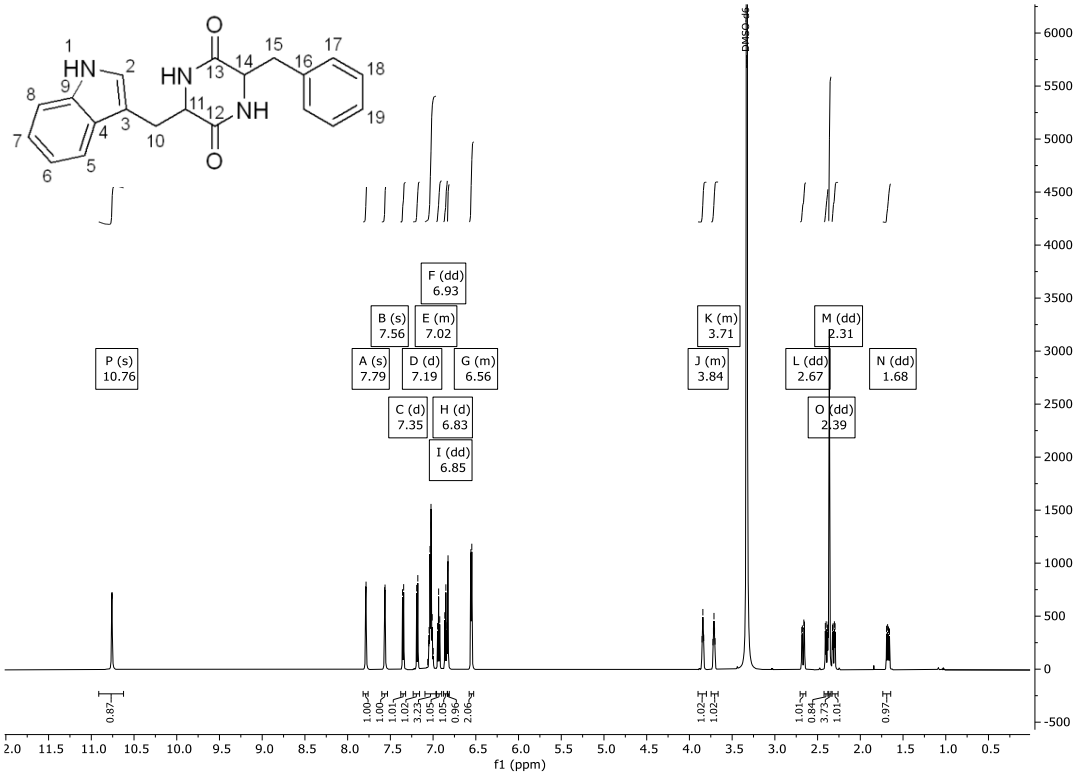

Figure 205: ^{1}H-NMR spectrum of LL-cWF **242a** in DMSO-d6 (600 MHz).

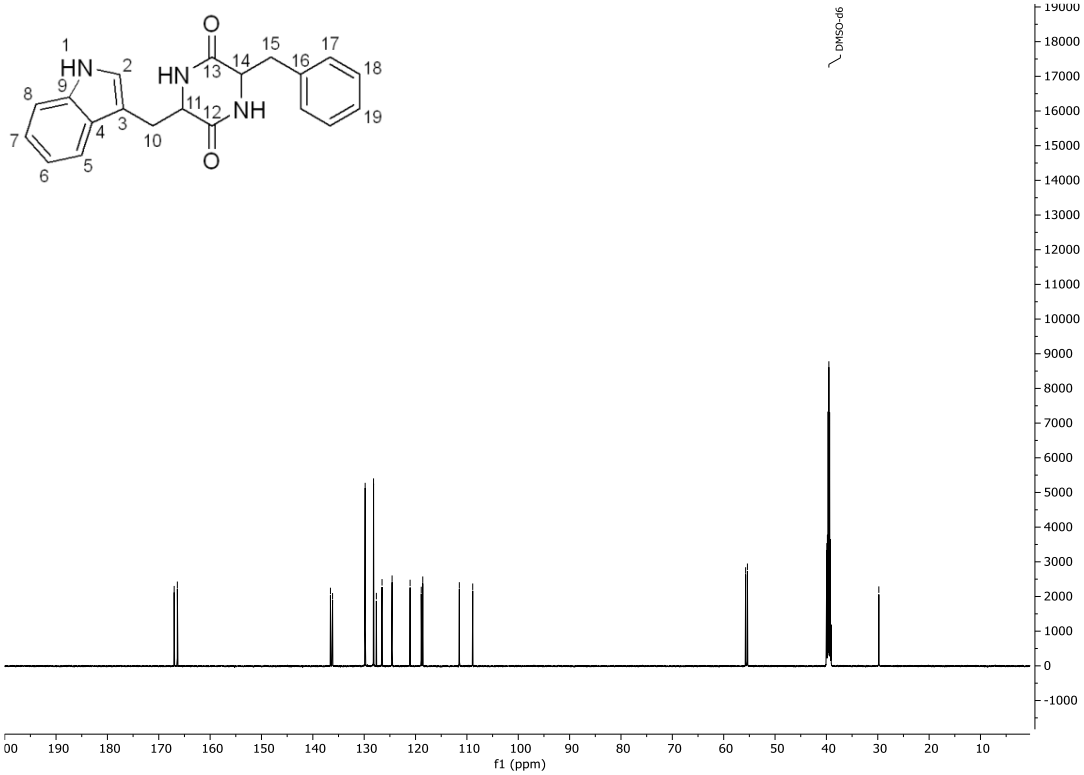

Figure 206: ^{13}C-NMR spectrum of LL-cWF **242a** in DMSO-d6 (151 MHz).

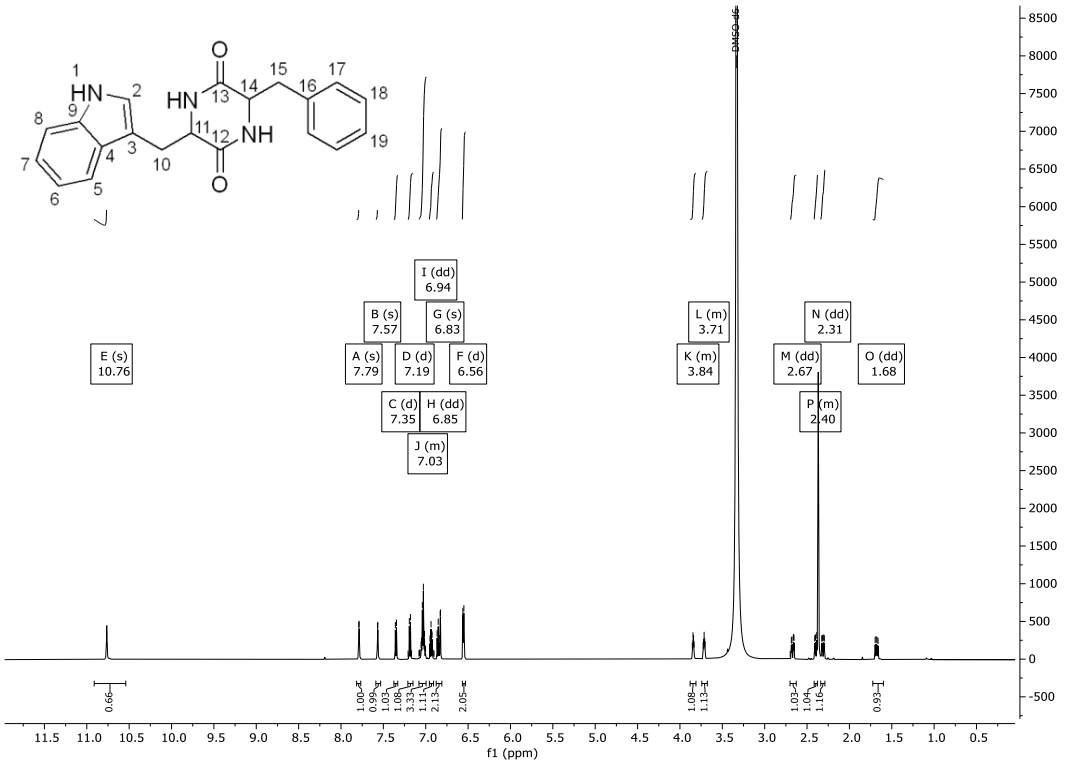

Figure 207: ^{1}H-NMR spectrum of DD-cWF **242b** in DMSO-d6 (600 MHz).

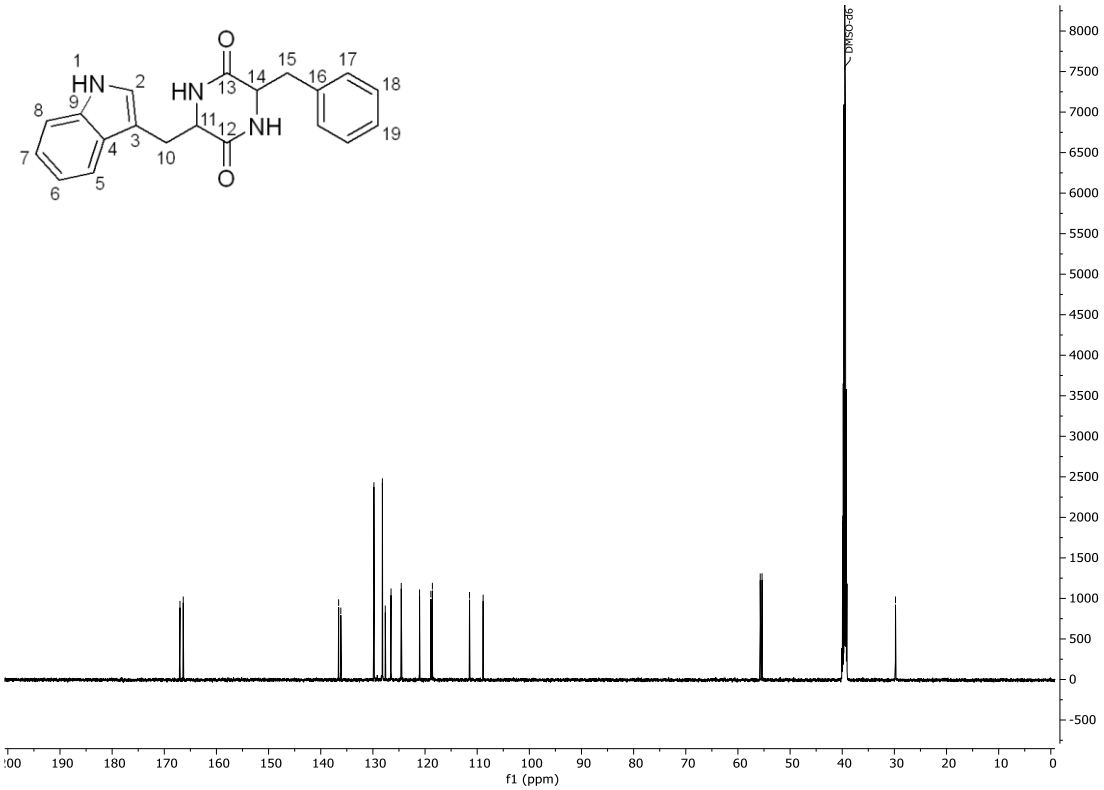

Figure 208: ^{13}C-NMR spectrum of DD-cWF **242b** in DMSO-d6 (151 MHz).

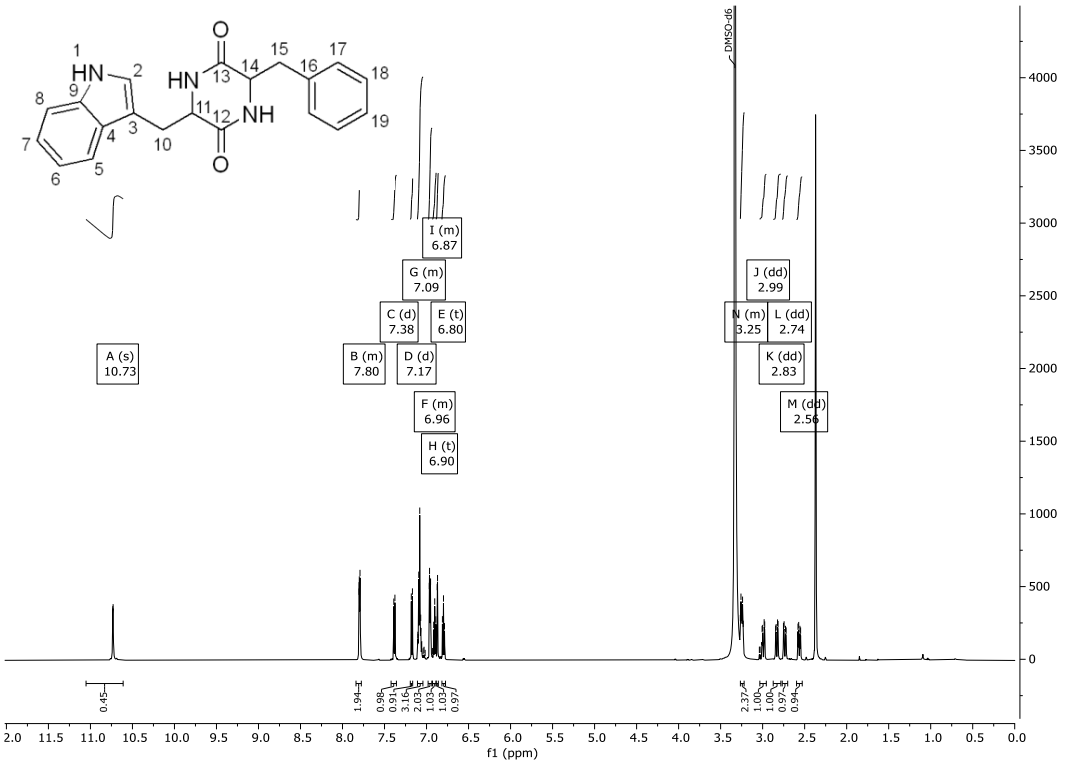

Figure 209: ^{1}H-NMR spectrum of LD-cWF **242c** in DMSO-d6 (600 MHz).

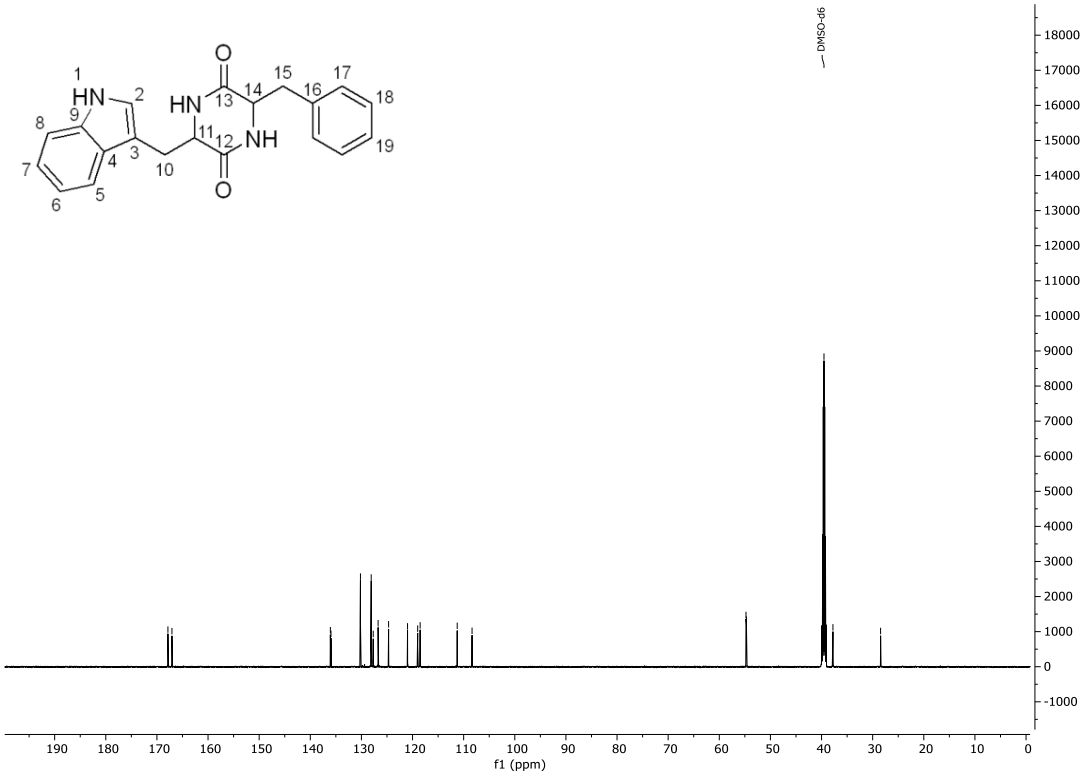

Figure 210: ^{13}C-NMR spectrum of LD-cWF **242c** in DMSO-d6 (151 MHz).

Figure 211: ^{1}H-NMR spectrum of DL-cWF **242d** in DMSO-d6 (600 MHz).

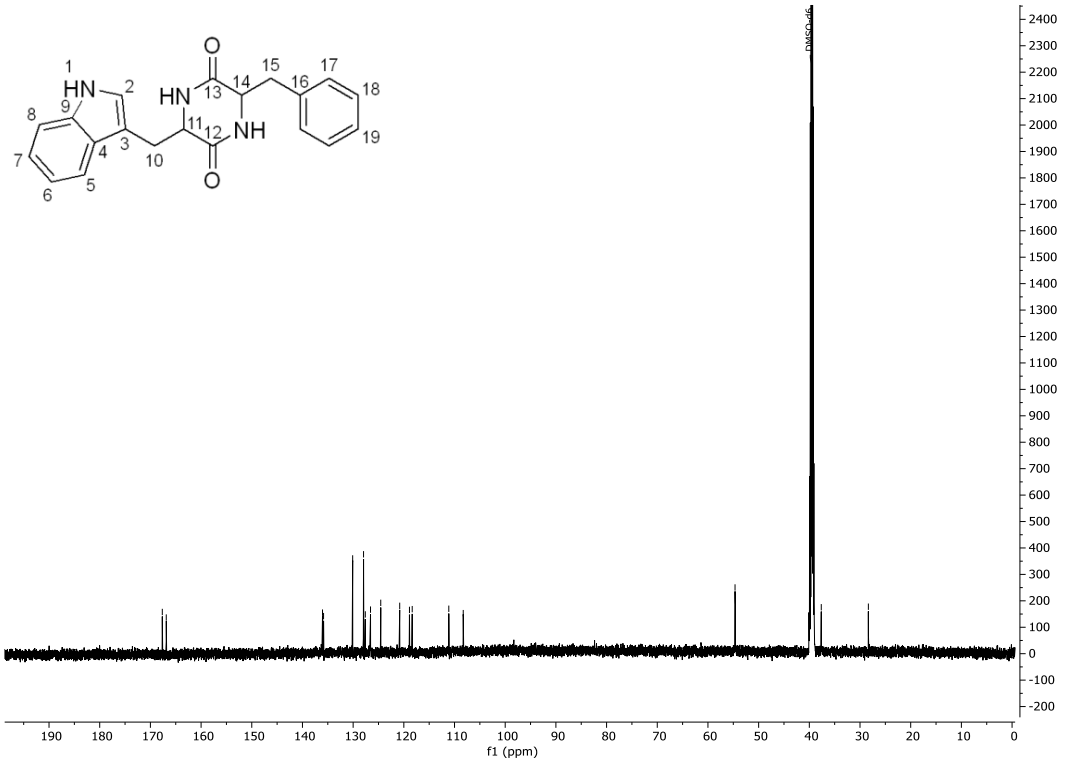

Figure 212: ^{13}C-NMR spectrum of DL-cWF **242d** in DMSO-d6 (151 MHz).

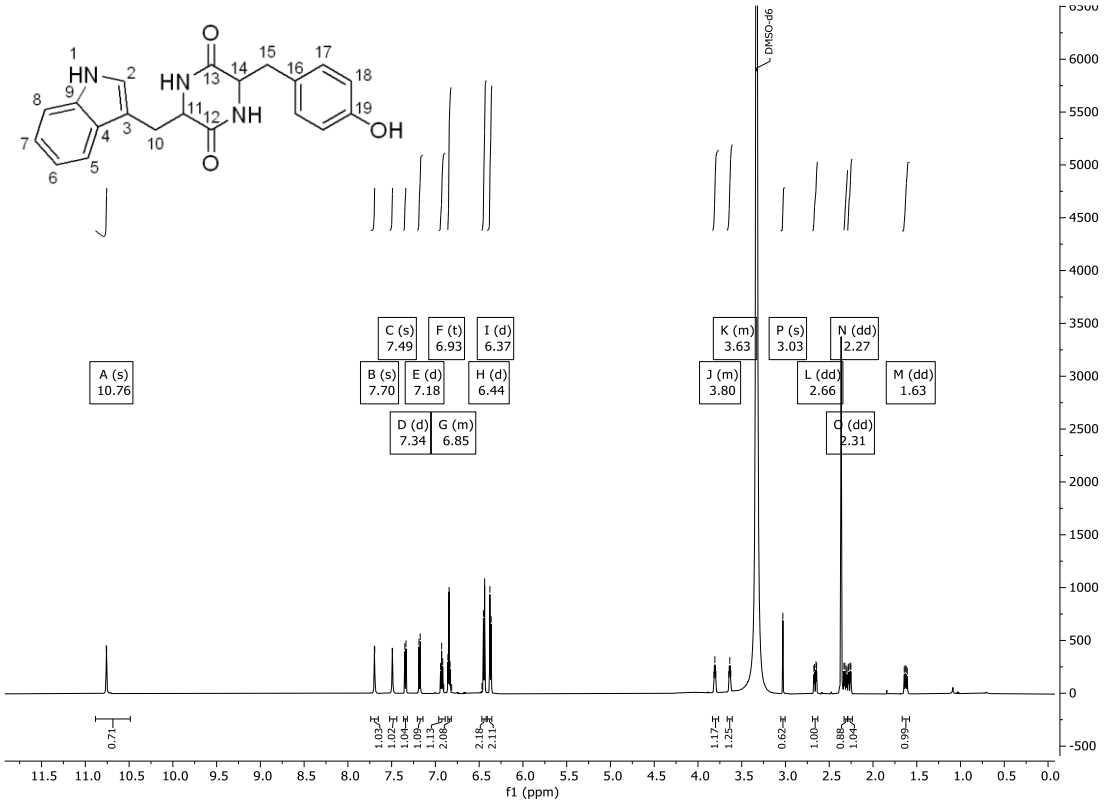

Figure 213: ^{1}H-NMR spectrum of LL-cWY **241a** in DMSO-d6 (600 MHz).

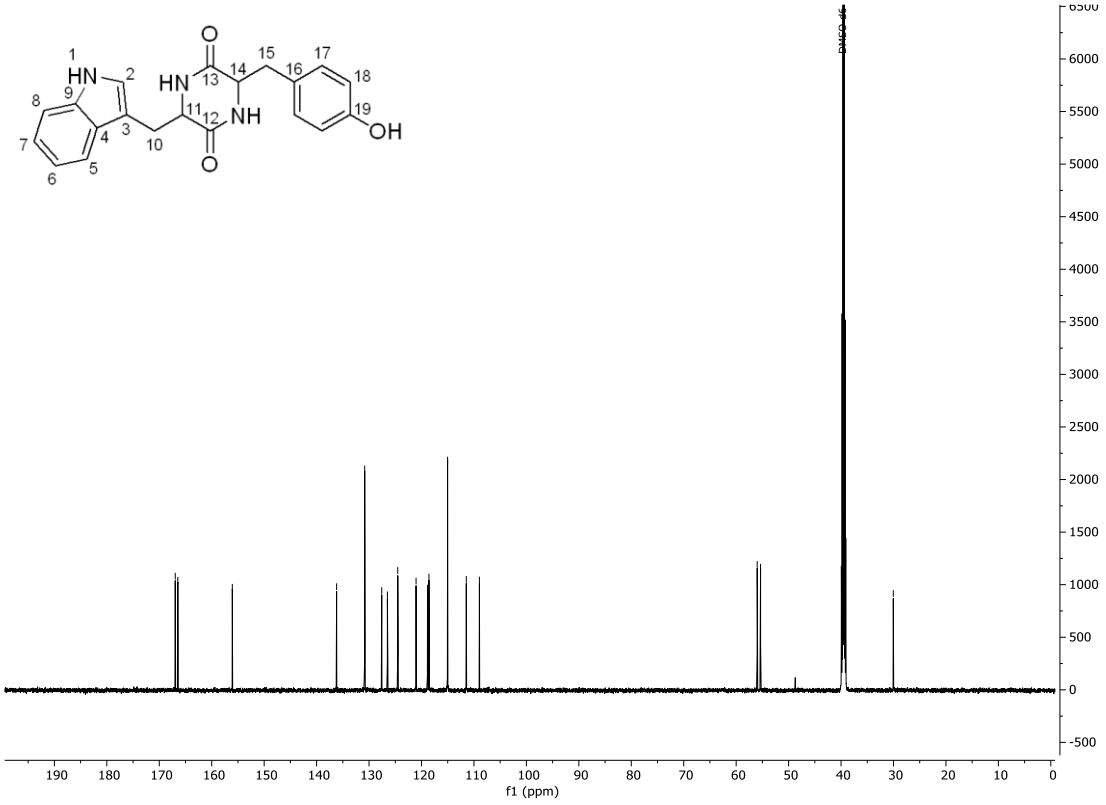

Figure 214: ^{13}C-NMR spectrum of LL-cWY **241a** in DMSO-d6 (151 MHz).

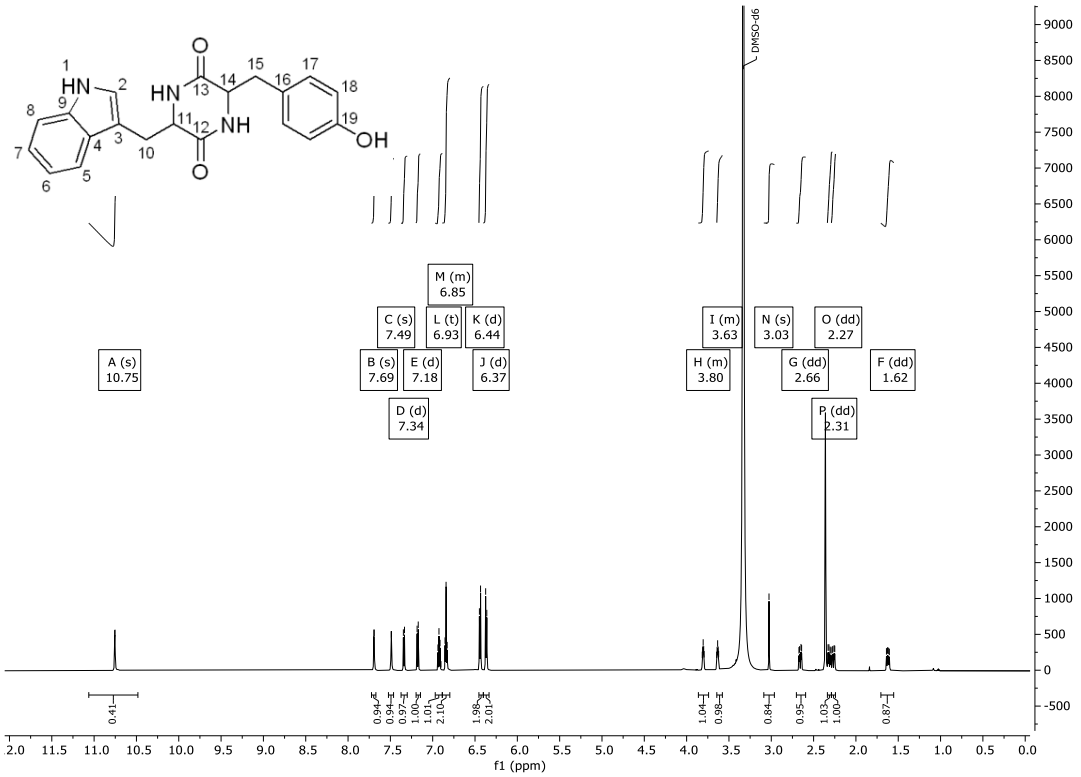

Figure 215: ^{1}H-NMR spectrum of DD-cWY **241b** in DMSO-d6 (600 MHz).

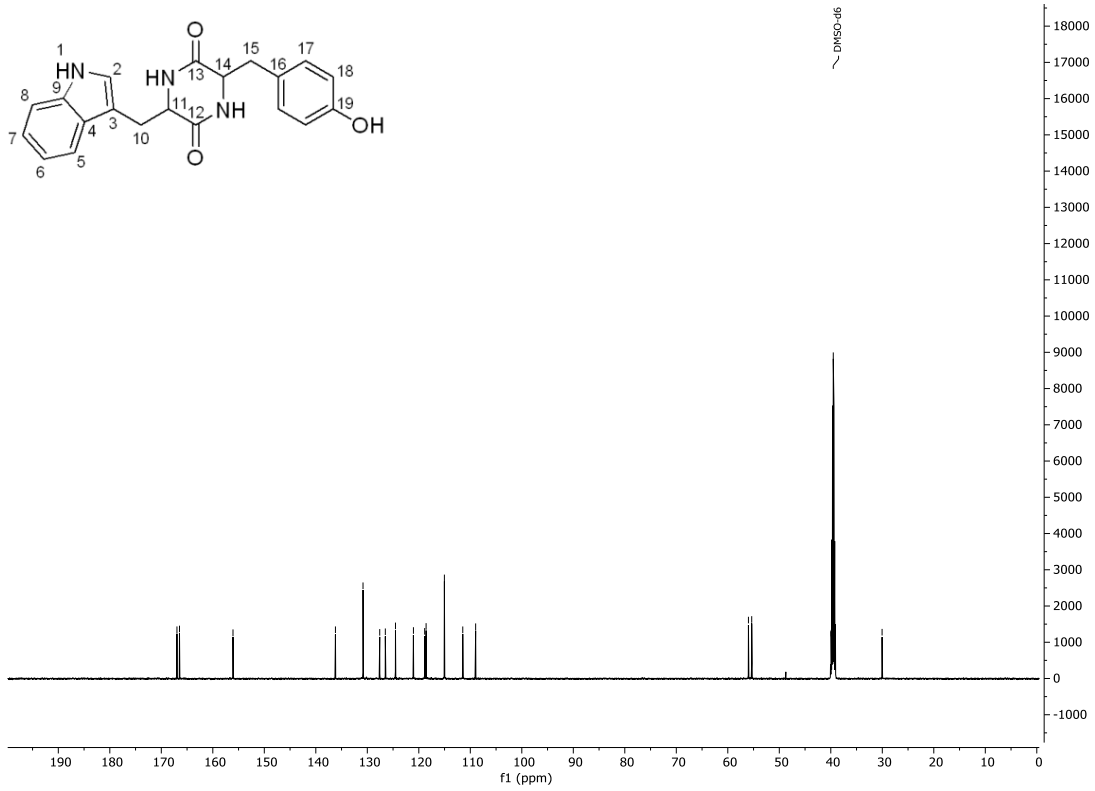

Figure 216: ^{13}C-NMR spectrum of DD-cWY **241b** in DMSO-d6 (151 MHz).

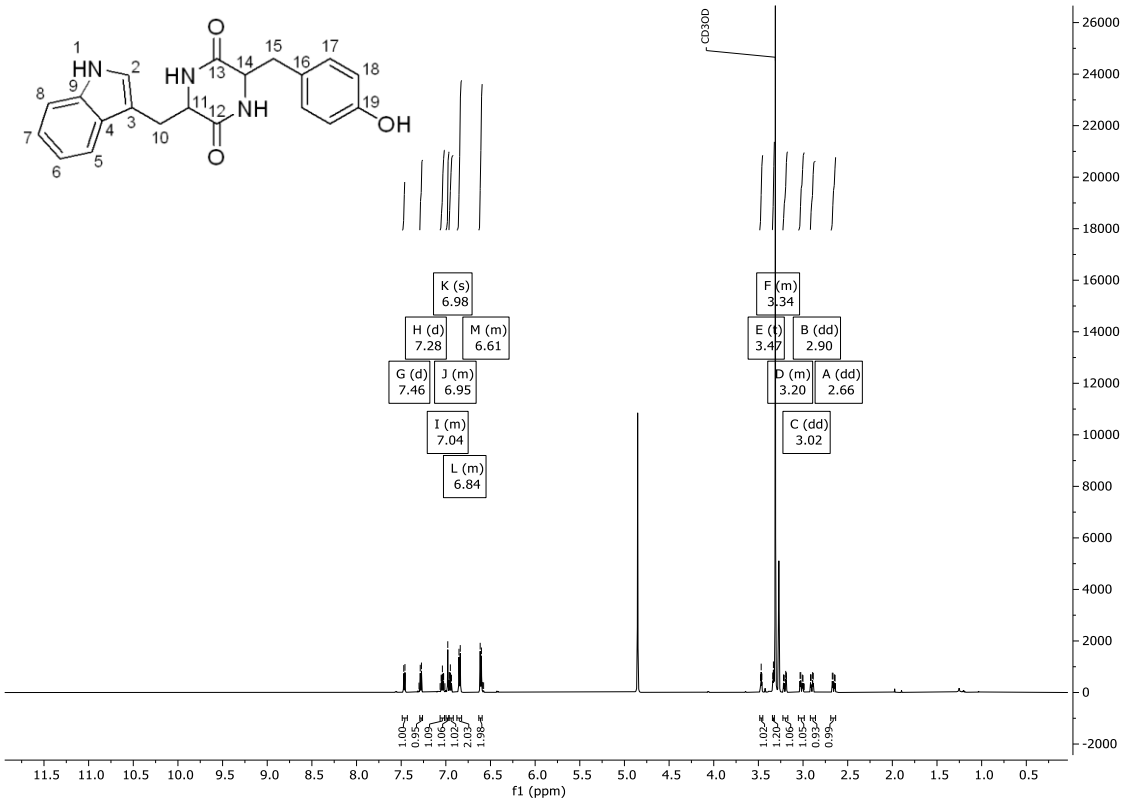

Figure 217: ^{1}H-NMR spectrum of LD-cWY **241c** in MeOD (600 MHz).

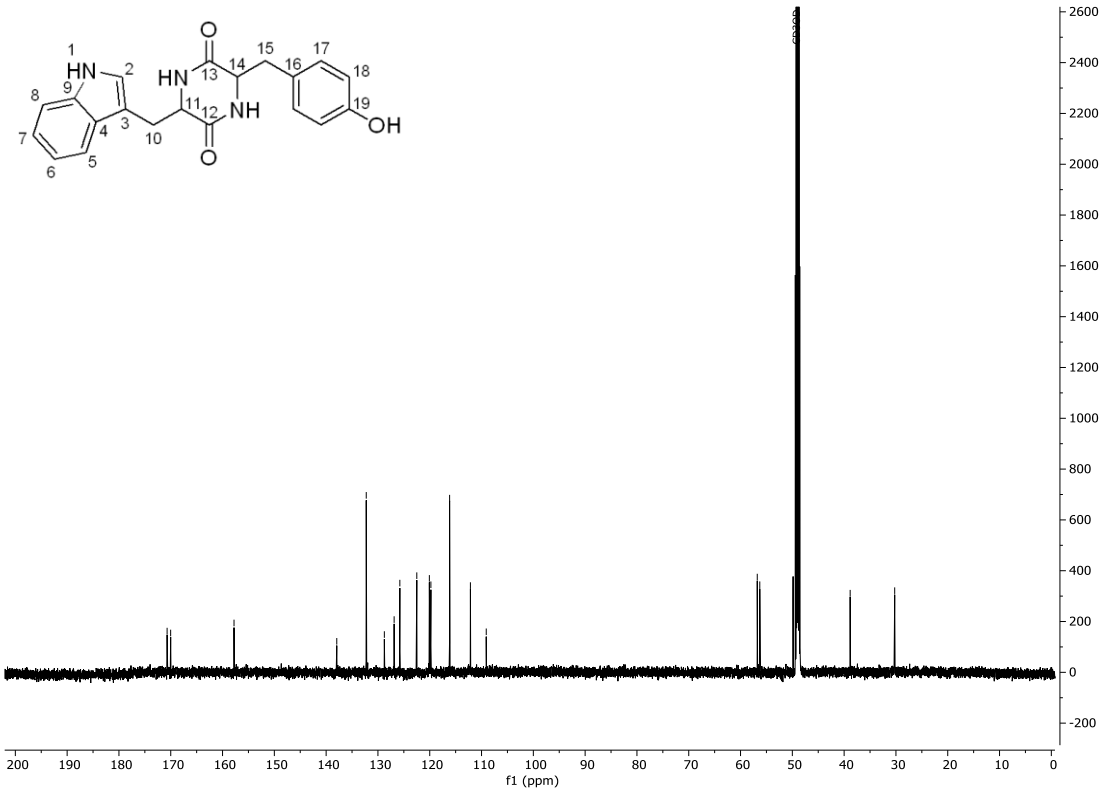

Figure 218: ^{13}C-NMR spectrum of LD-cWY **241c** in DMSO-d6 (151 MHz).

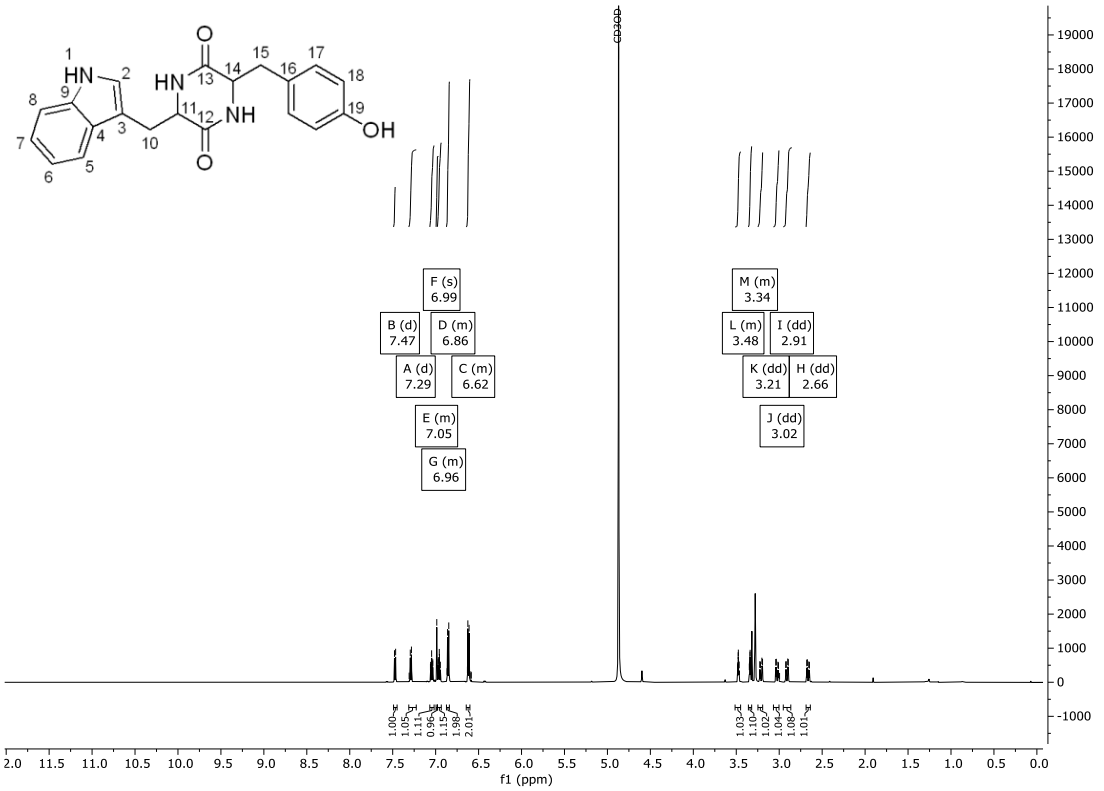

Figure 219: ^{1}H-NMR spectrum of DL-cWY **241d** in MeOD (600 MHz).

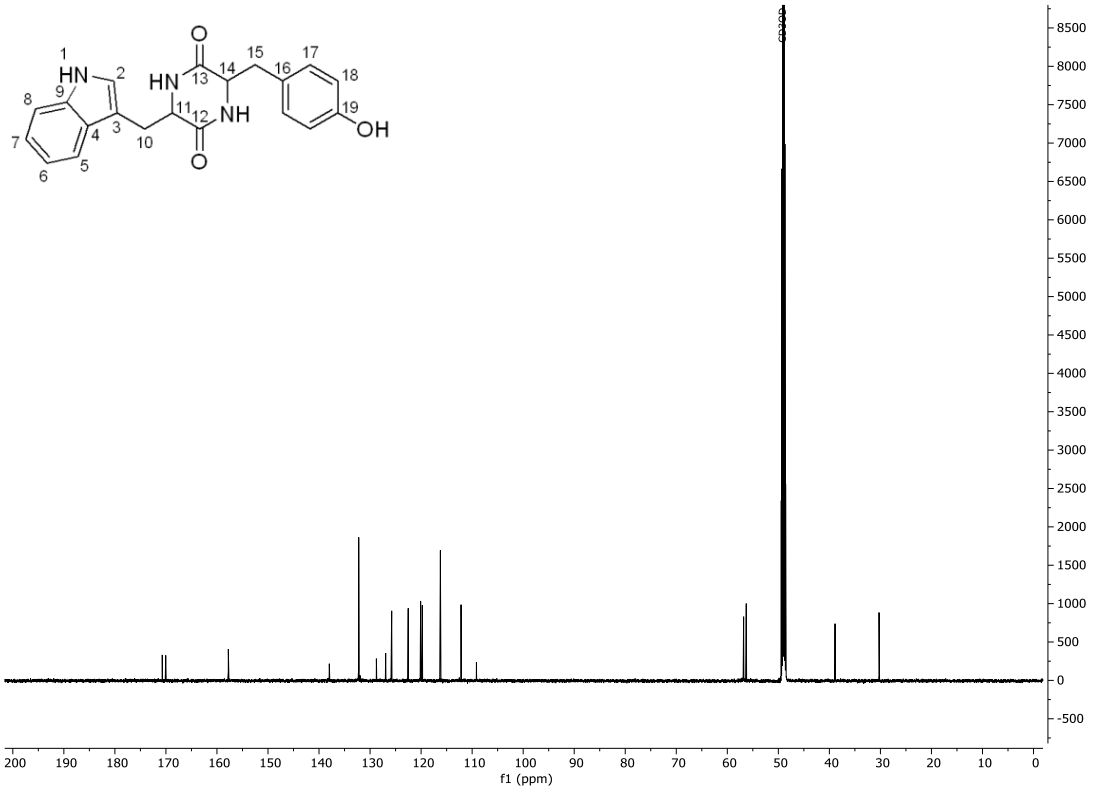

Figure 220: ^{13}C-NMR spectrum of DL-cWY **241d** in DMSO-d6 (151 MHz).

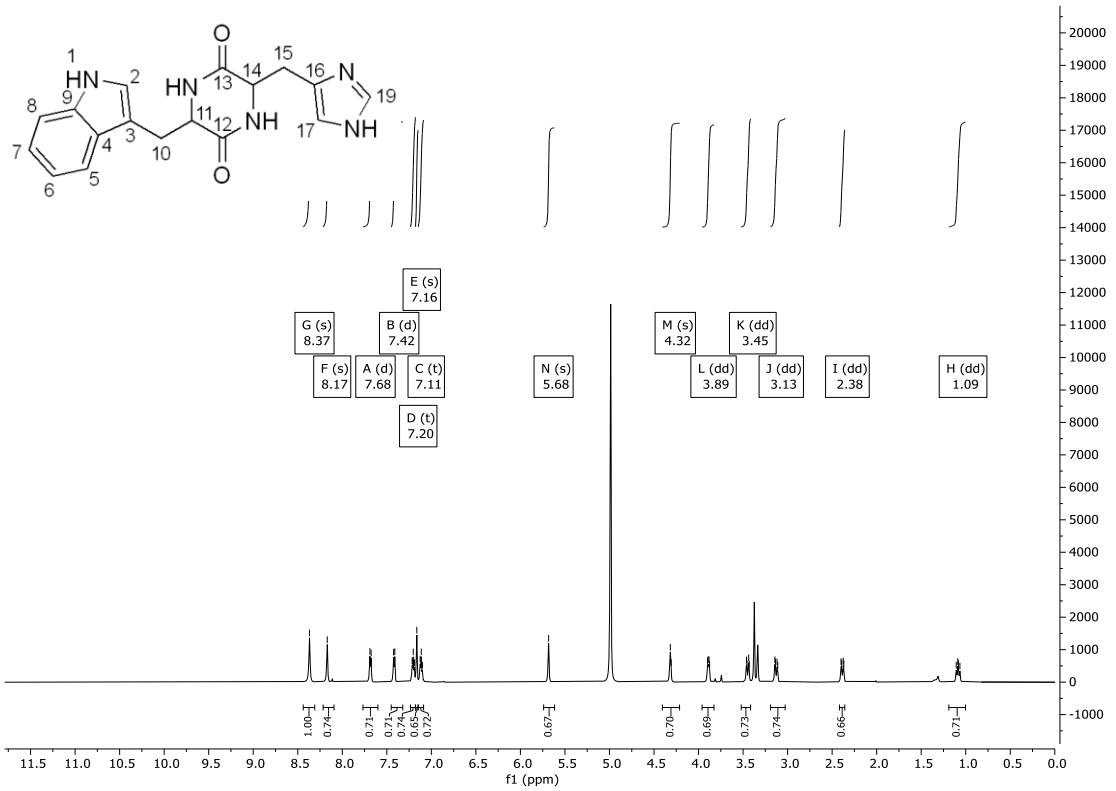

Figure 221: ^{1}H-NMR spectrum of LL-cWH **243a** in MeOD (600 MHz).

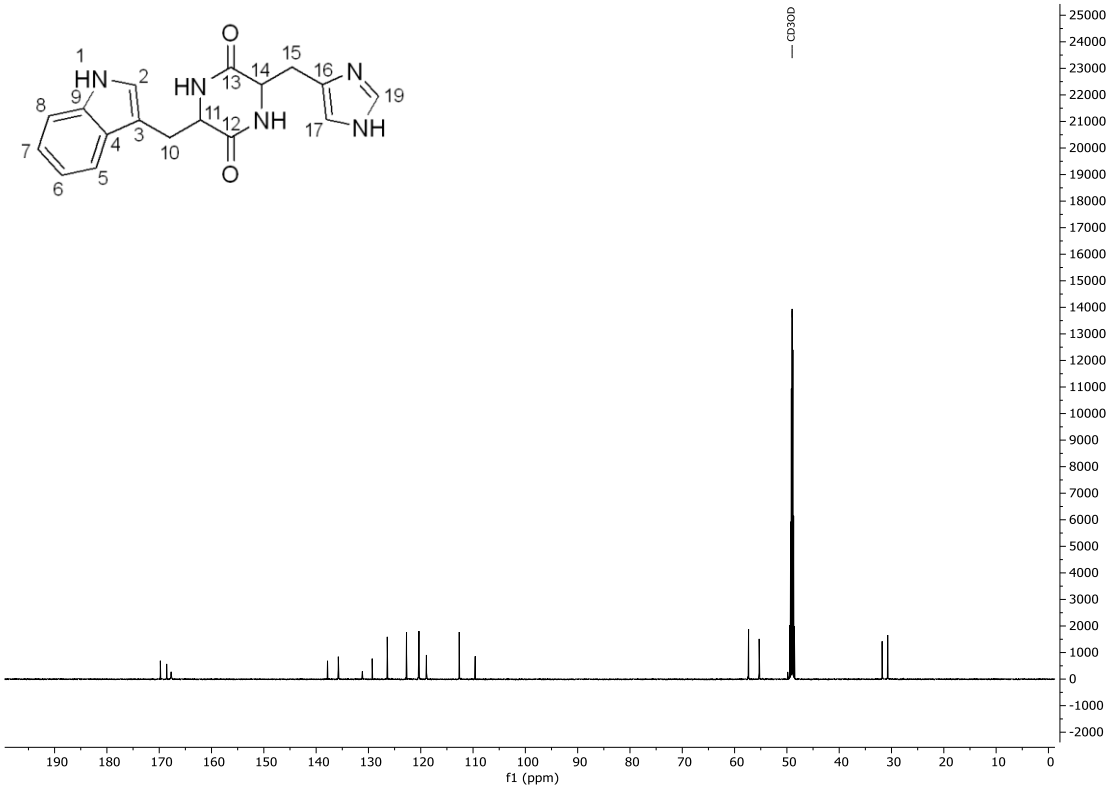

Figure 222: ^{13}C-NMR spectrum of LL-cWH **243a** in MeOD (151 MHz).

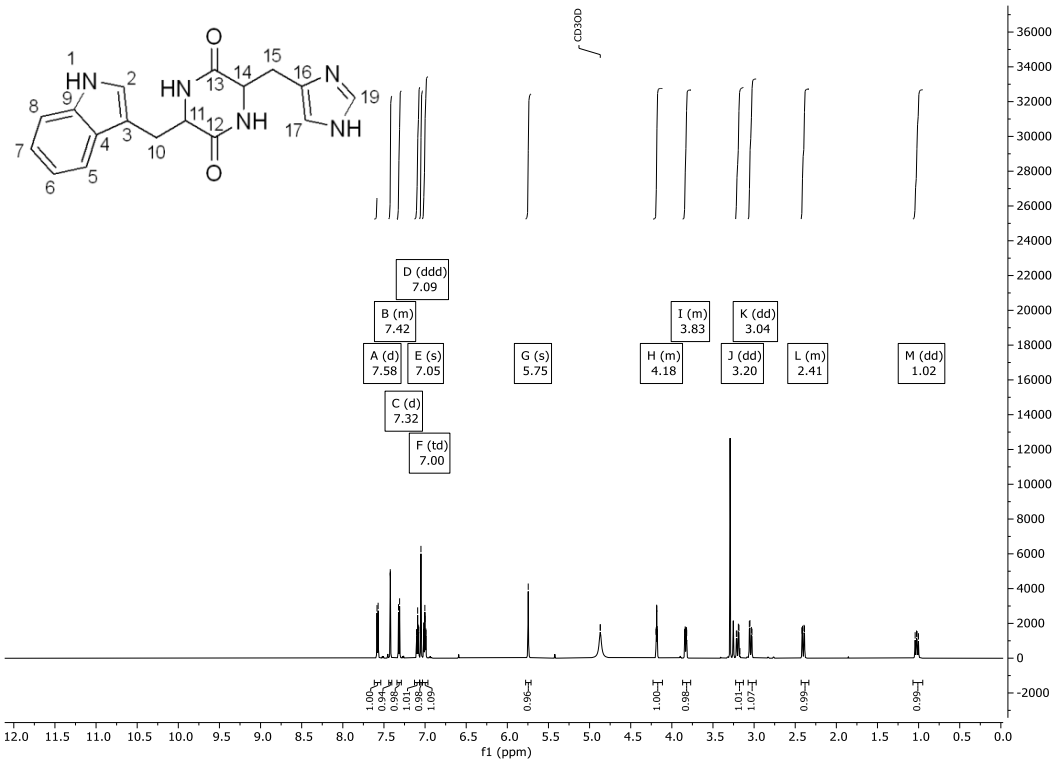

Figure 223: ^{1}H-NMR spectrum of DD-cWH **243b** in MeOD (600 MHz).

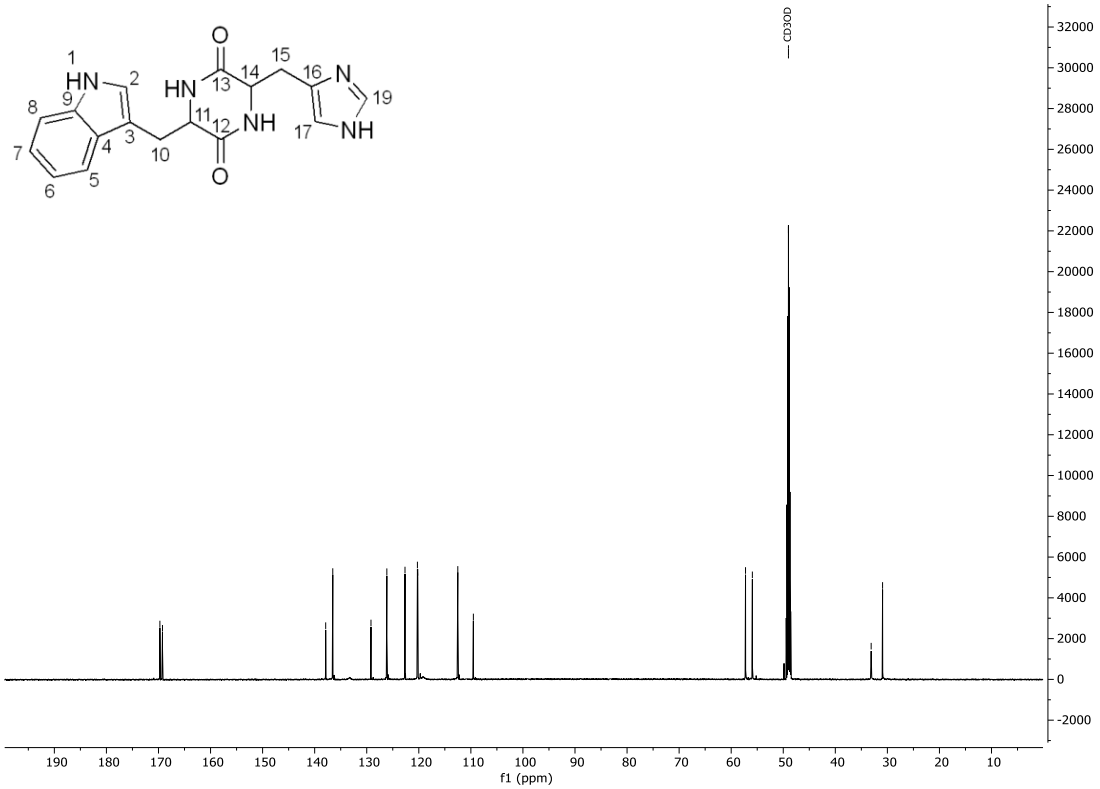

Figure 224: ^{13}C-NMR spectrum of DD-cWH **243b** in MeOD (151 MHz).

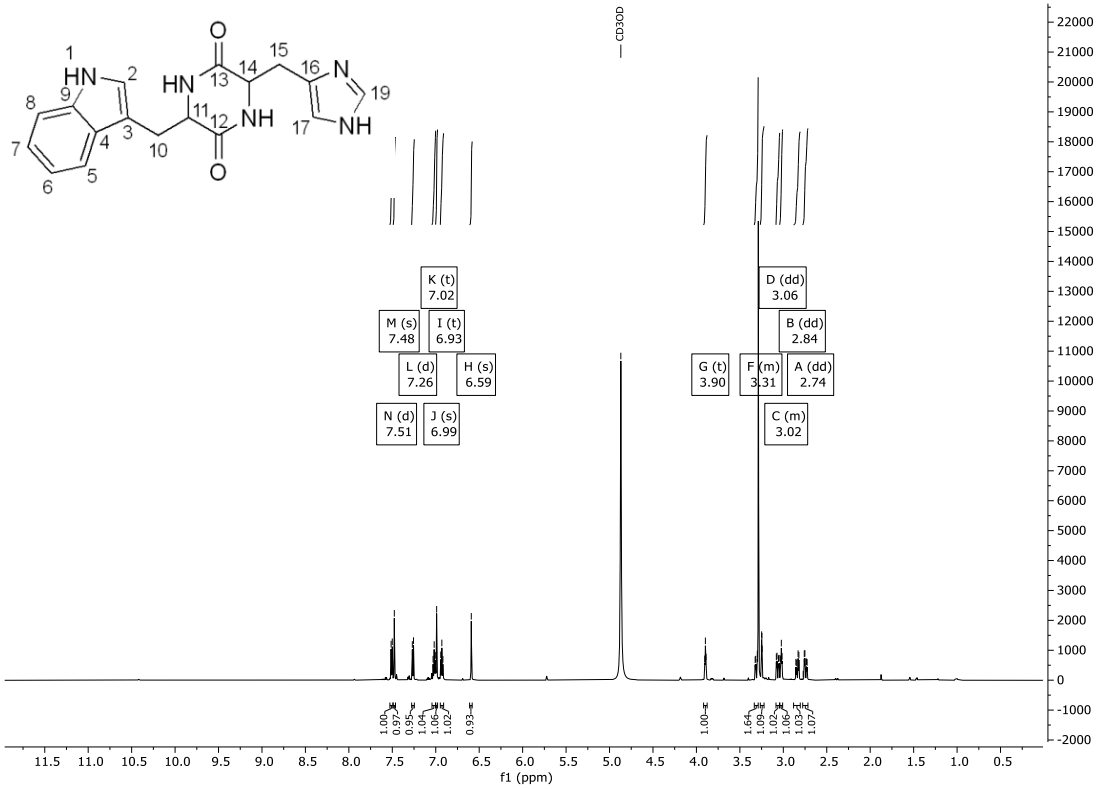

Figure 225: ^{1}H-NMR spectrum of LD-cWH **243c** in MeOD (600 MHz).

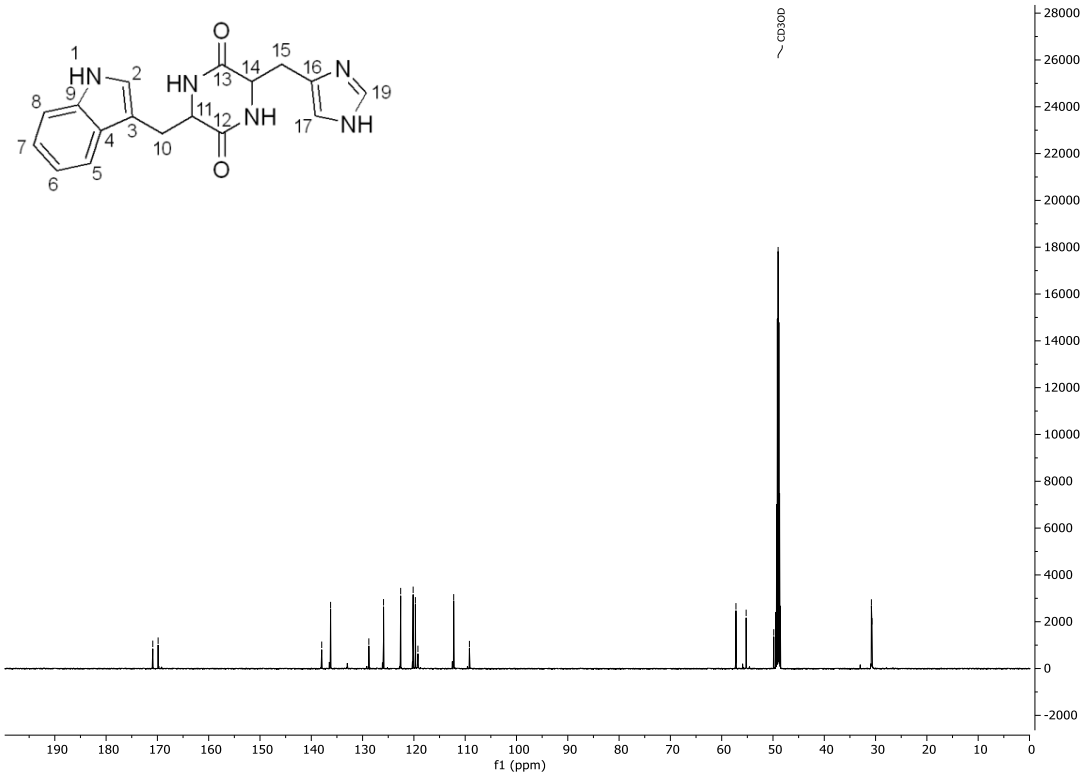

Figure 226: ^{13}C-NMR spectrum of LD-cWH **243c** in MeOD (151 MHz).

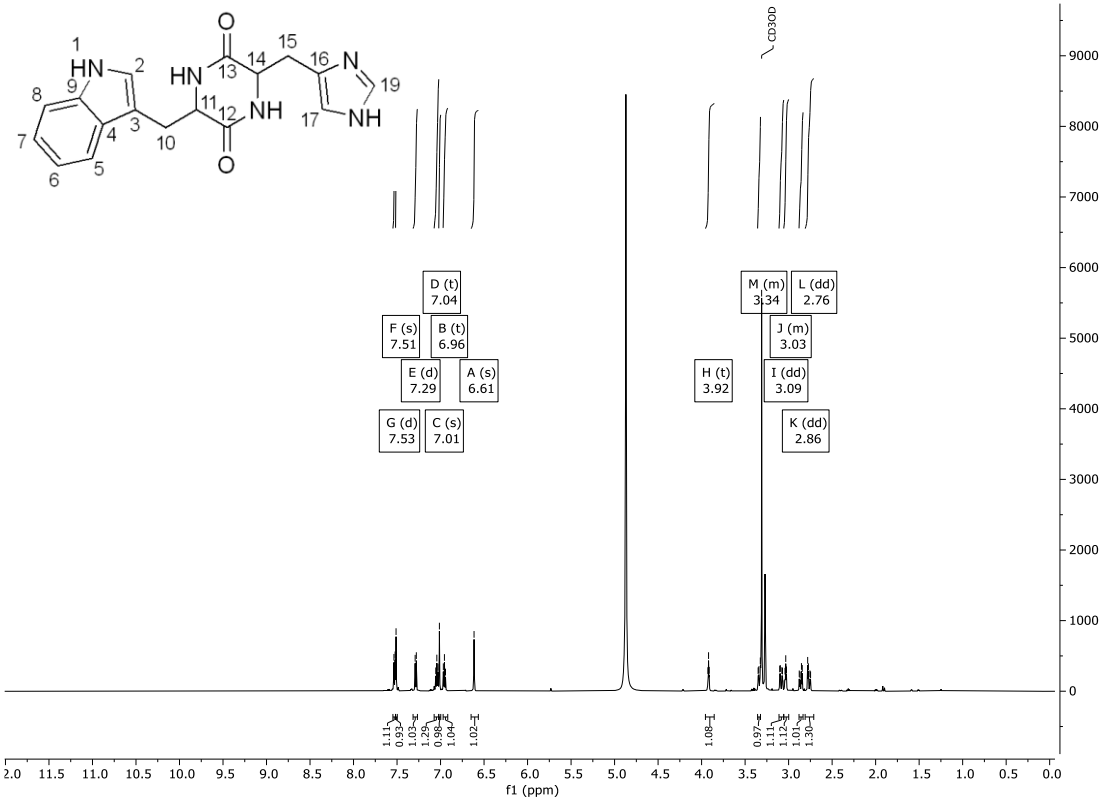

Figure 227: ^{1}H-NMR spectrum of DL-cWH **243d** in MeOD (600 MHz).

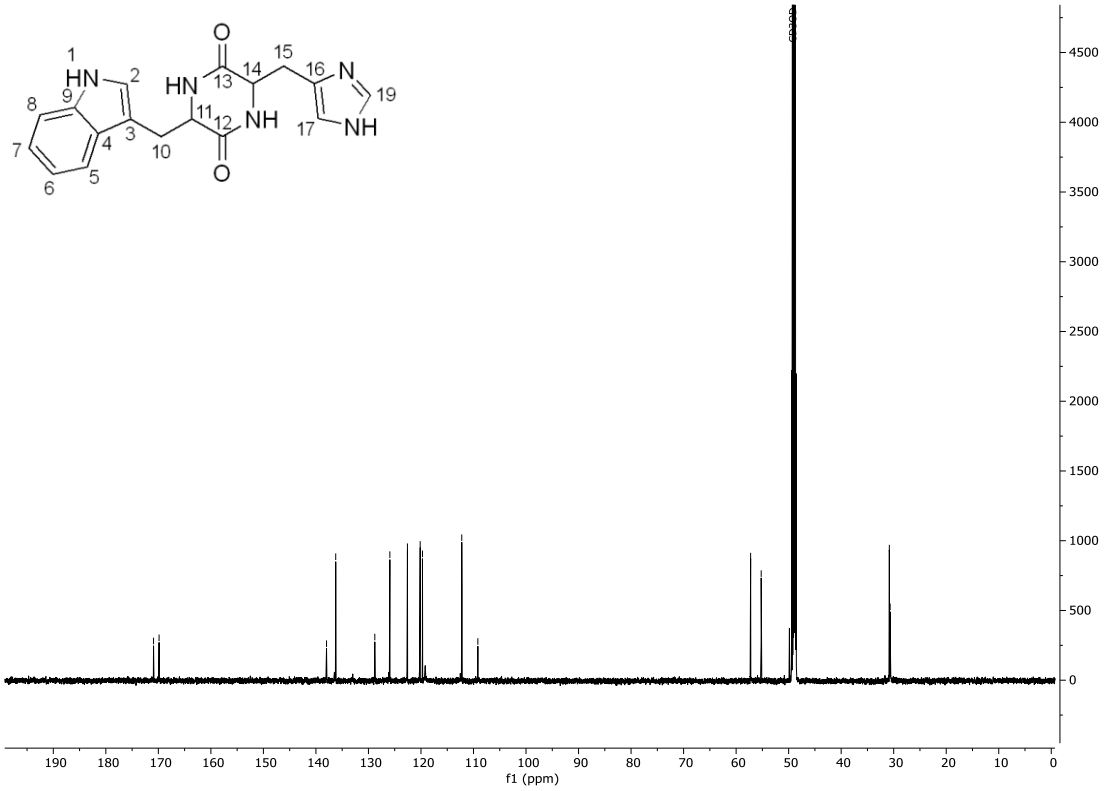

Figure 228: ^{13}C-NMR spectrum of DL-cWH **243d** in MeOD (151 MHz).

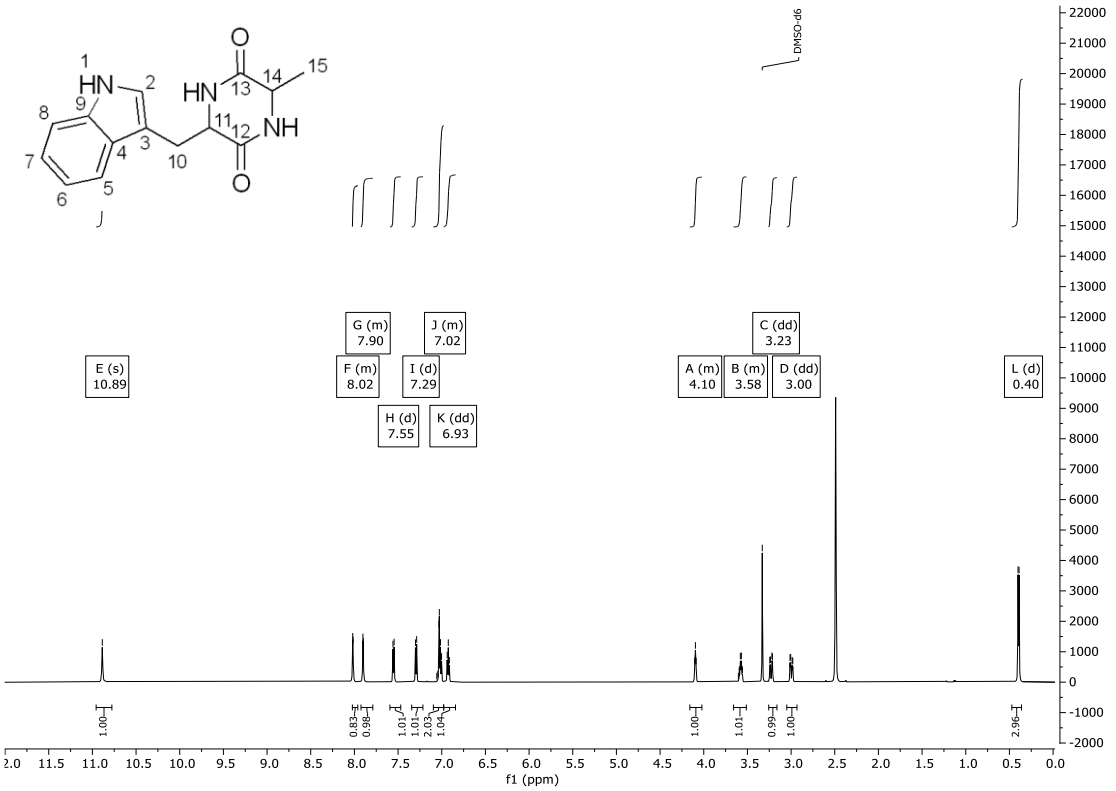

Figure 229: ^{1}H-NMR spectrum of LL-cWA **216** in DMSO-d6 (600 MHz).

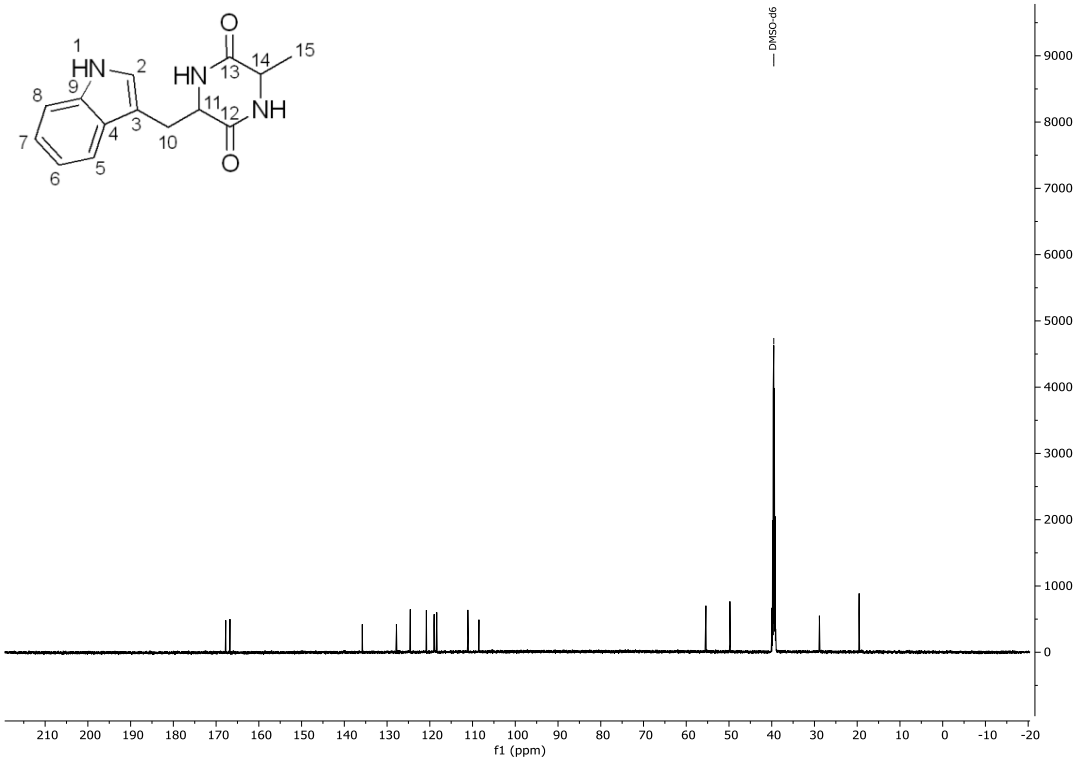

Figure 230: ^{13}C-NMR spectrum of LL-cWA **216** in DMSO-d6 (151 MHz).

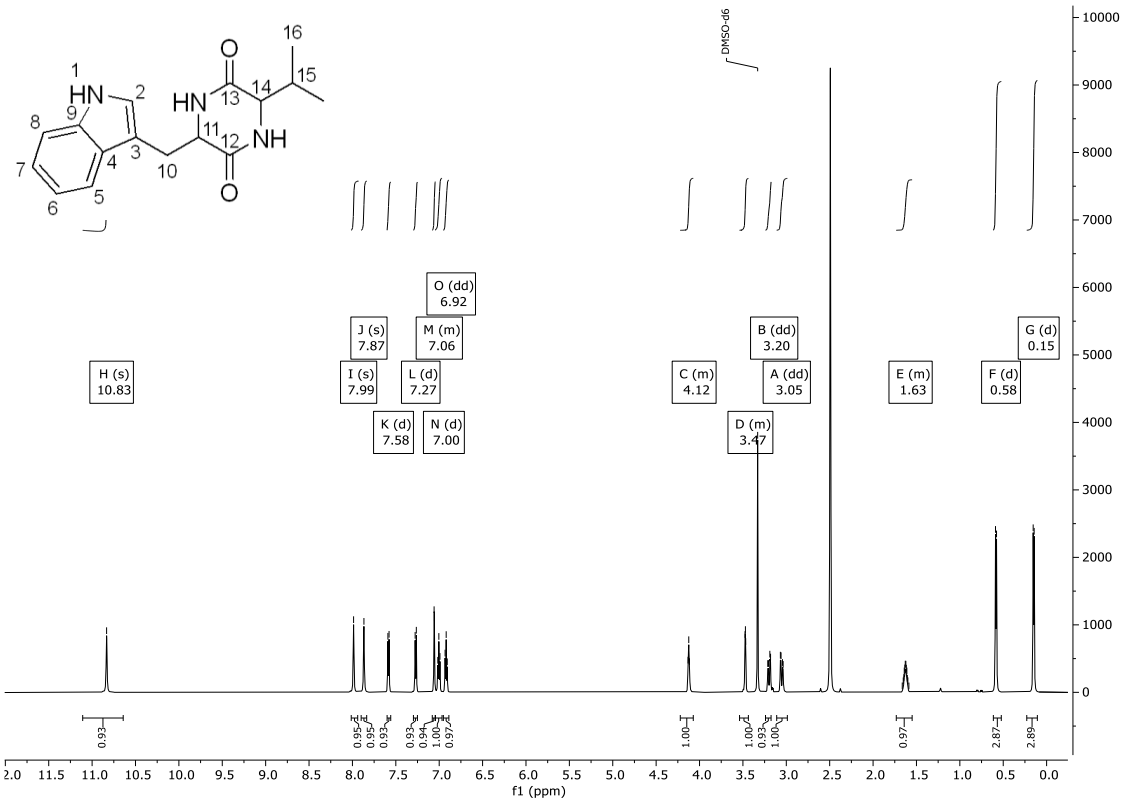

Figure 231: ^{1}H-NMR spectrum of LL-cWV **244** in DMSO-d6 (600 MHz).

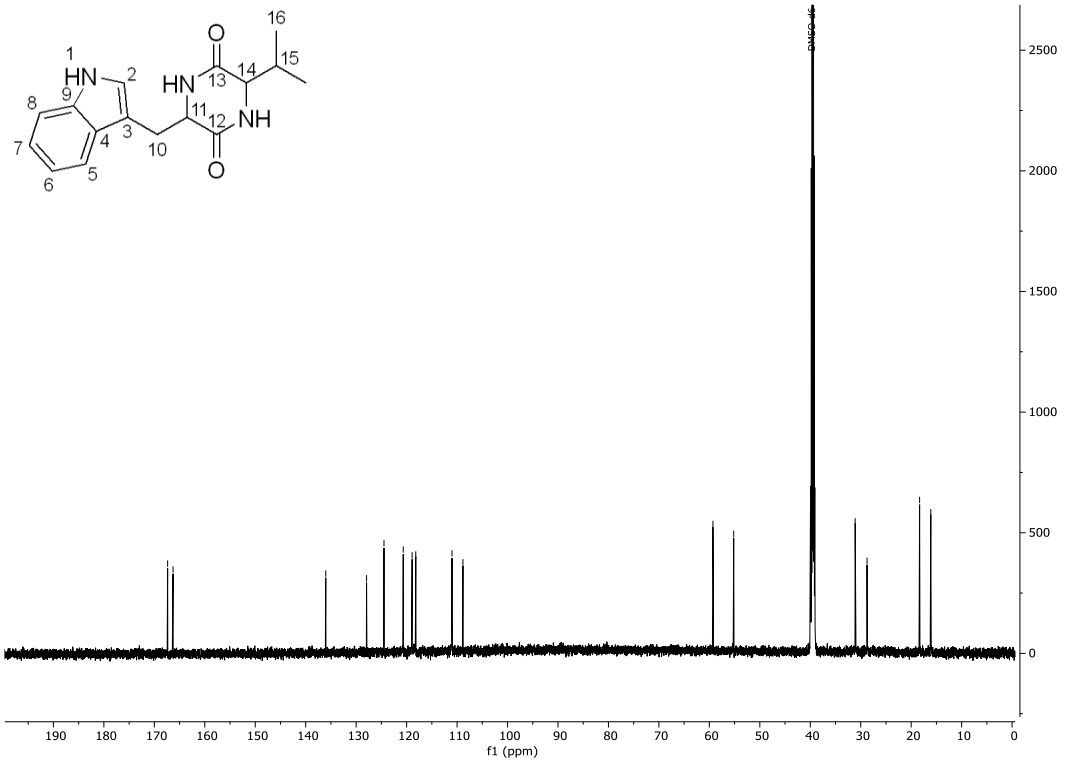

Figure 232: ^{13}C-NMR spectrum of LL-cWV **244** in DMSO-d6 (151 MHz).

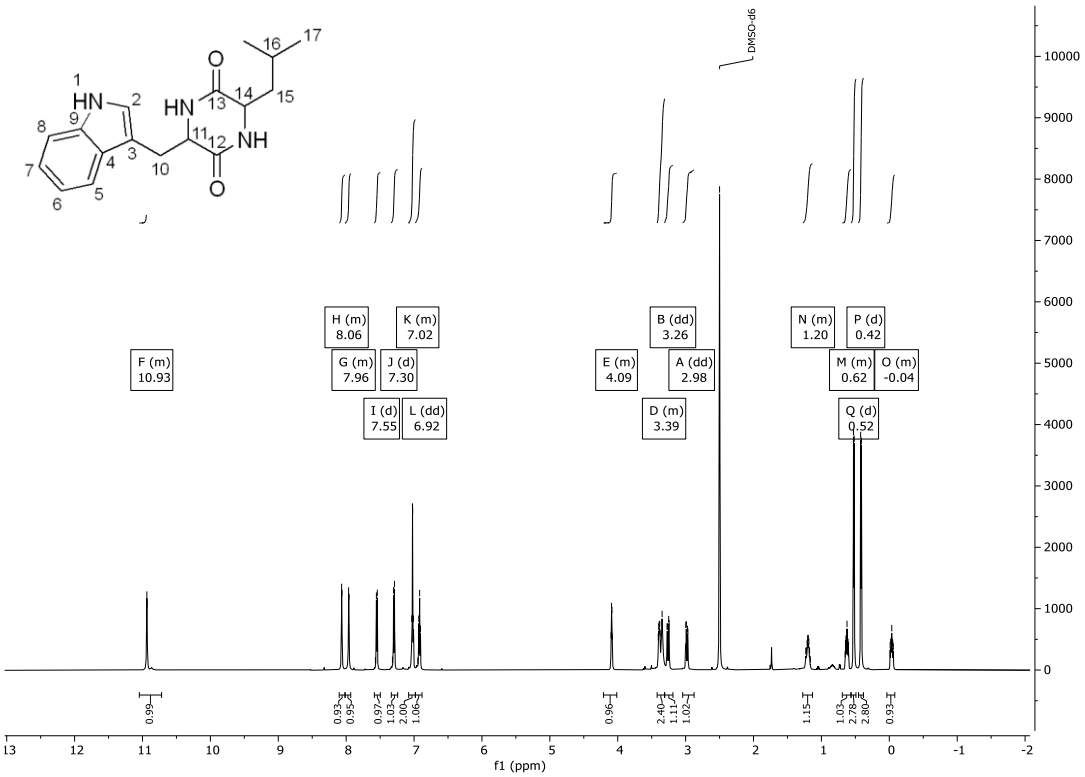

Figure 233: ^{1}H-NMR spectrum of LL-cWL **245** in DMSO-d6 (600 MHz).

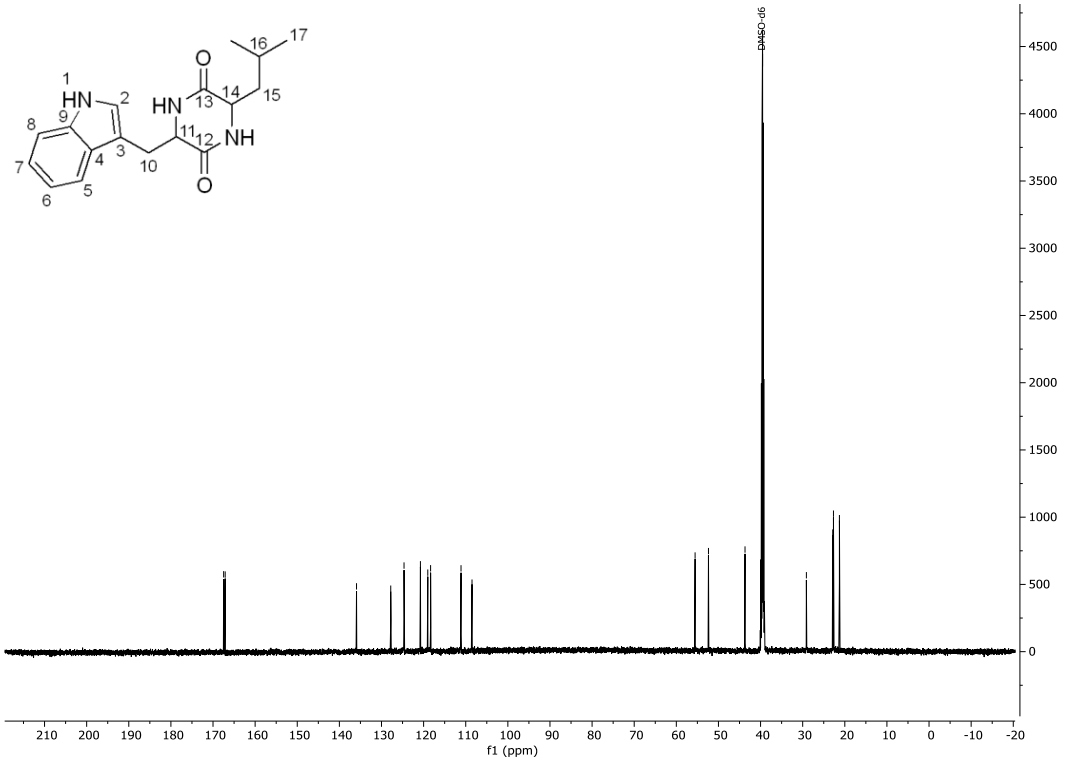

Figure 234: ^{13}C-NMR spectrum of LL-cWL **245** in DMSO-d6 (151 MHz).

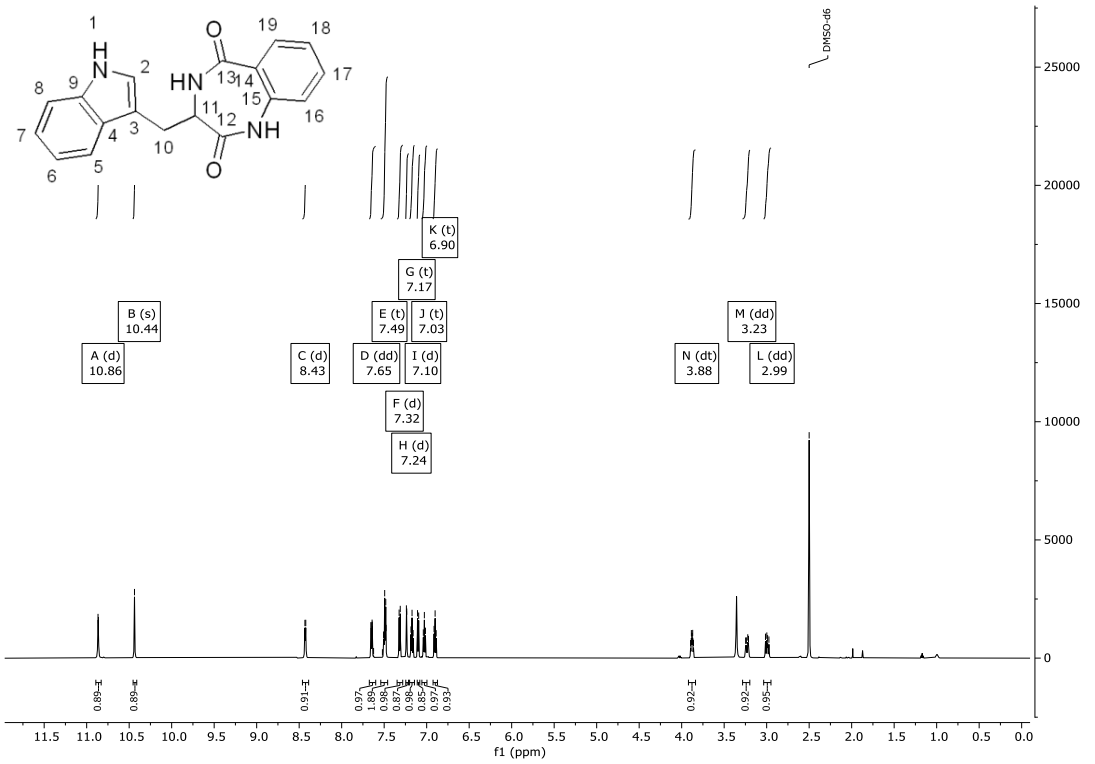

Figure 235: ^{1}H-NMR spectrum of L-cWBenz **246a** in DMSO-d6 (600 MHz).

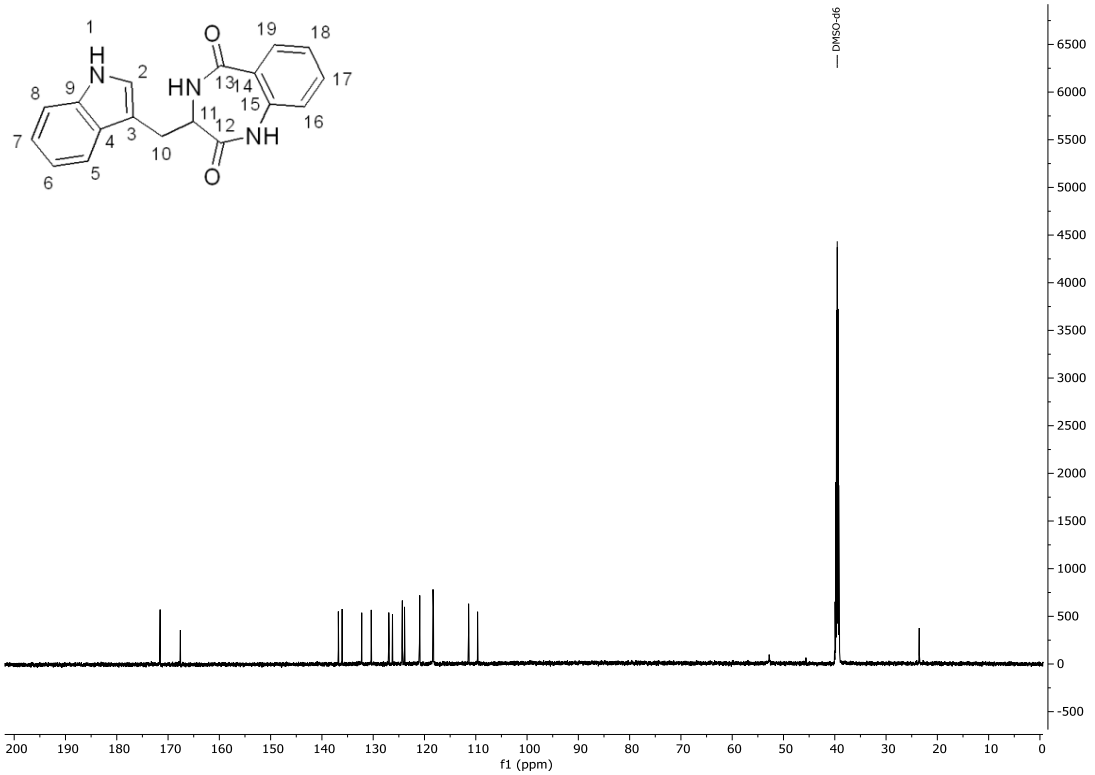

Figure 236: ^{13}C-NMR spectrum of L-cWBenz **246a** in DMSO-d6 (151 MHz).

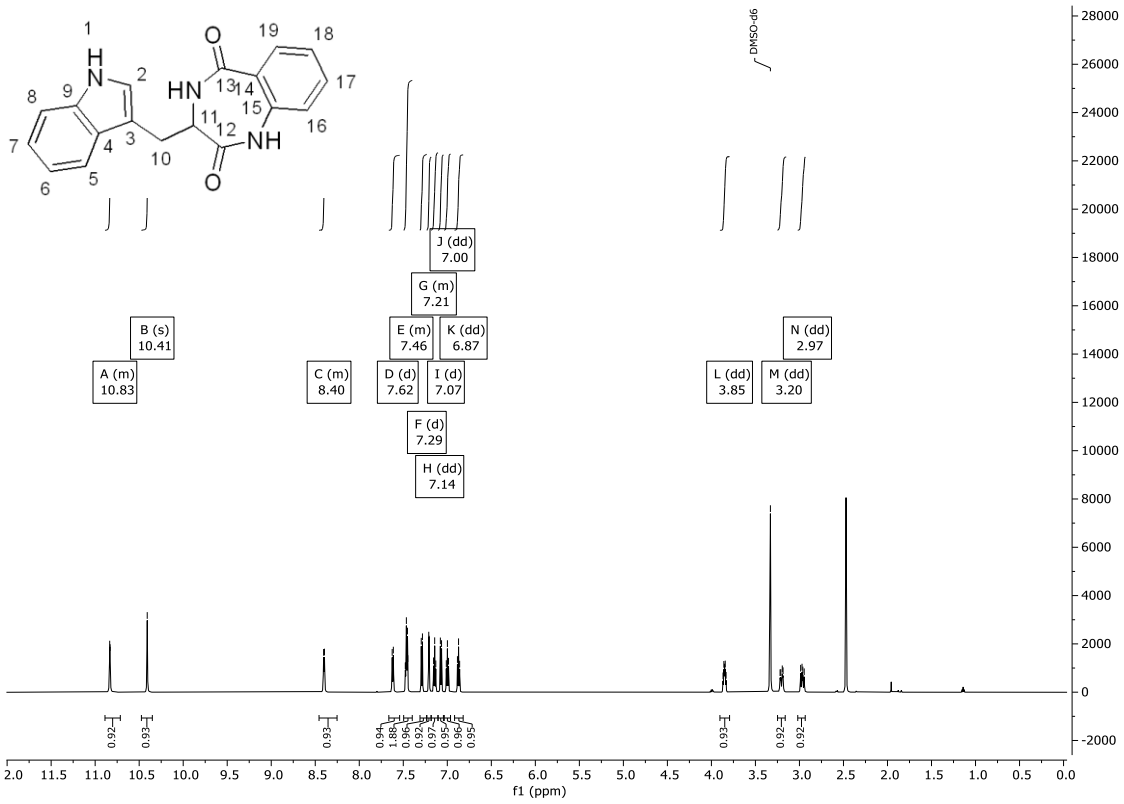

Figure 237: ^{1}H-NMR spectrum of D-cWBenz **246b** in DMSO-d6 (600 MHz).

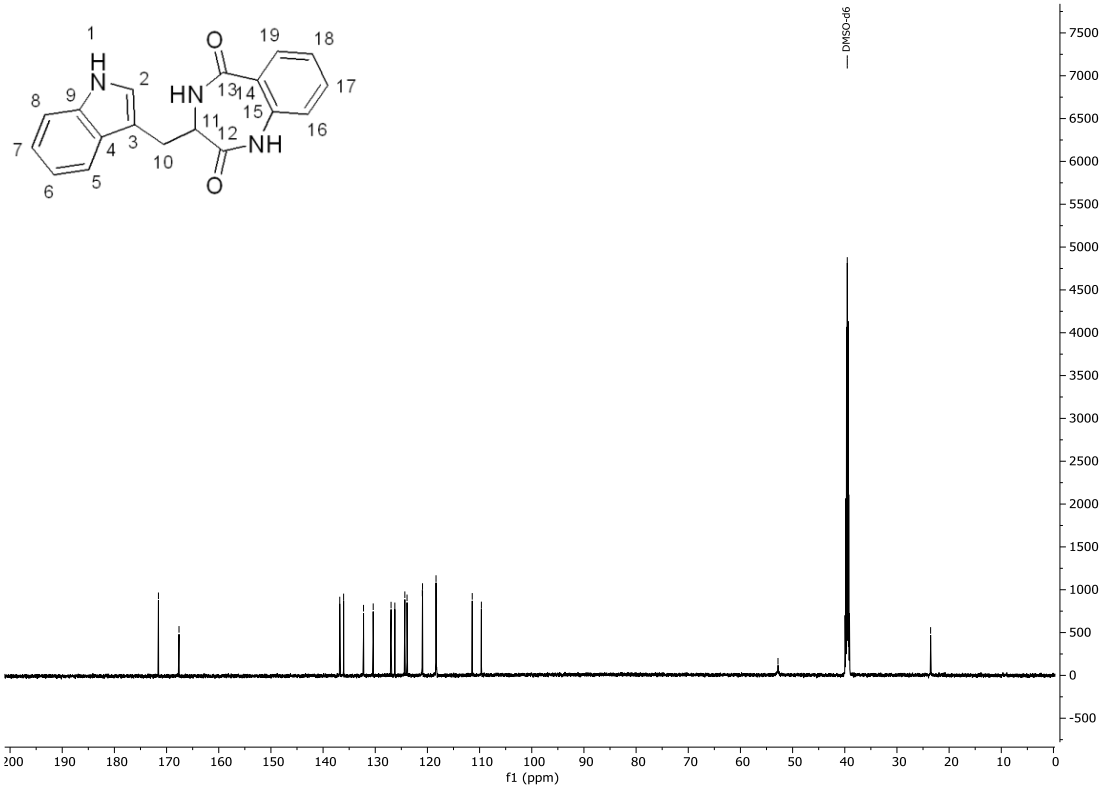

Figure 238: ^{13}C-NMR spectrum of D-cWBenz **246b** in DMSO-d6 (151 MHz).

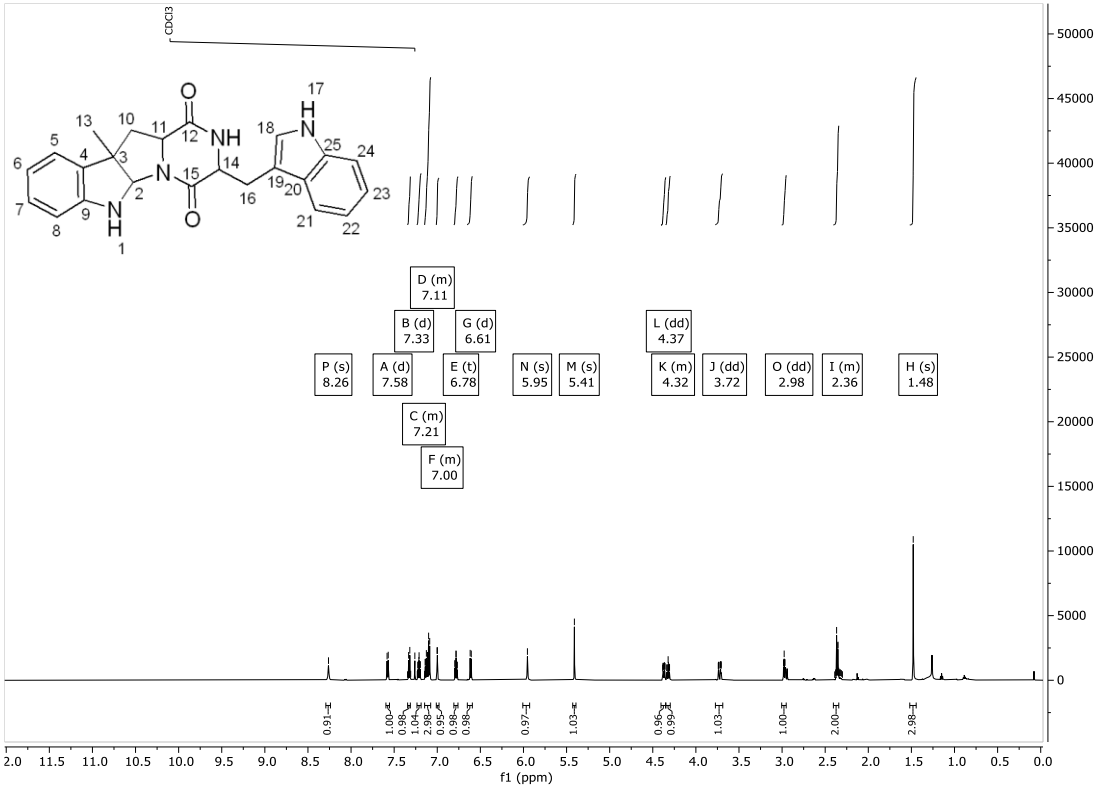

Figure 239: ^{1}H-NMR spectrum of single methylated DD-cWW **168b** in $CDCl_3$ (600 MHz).

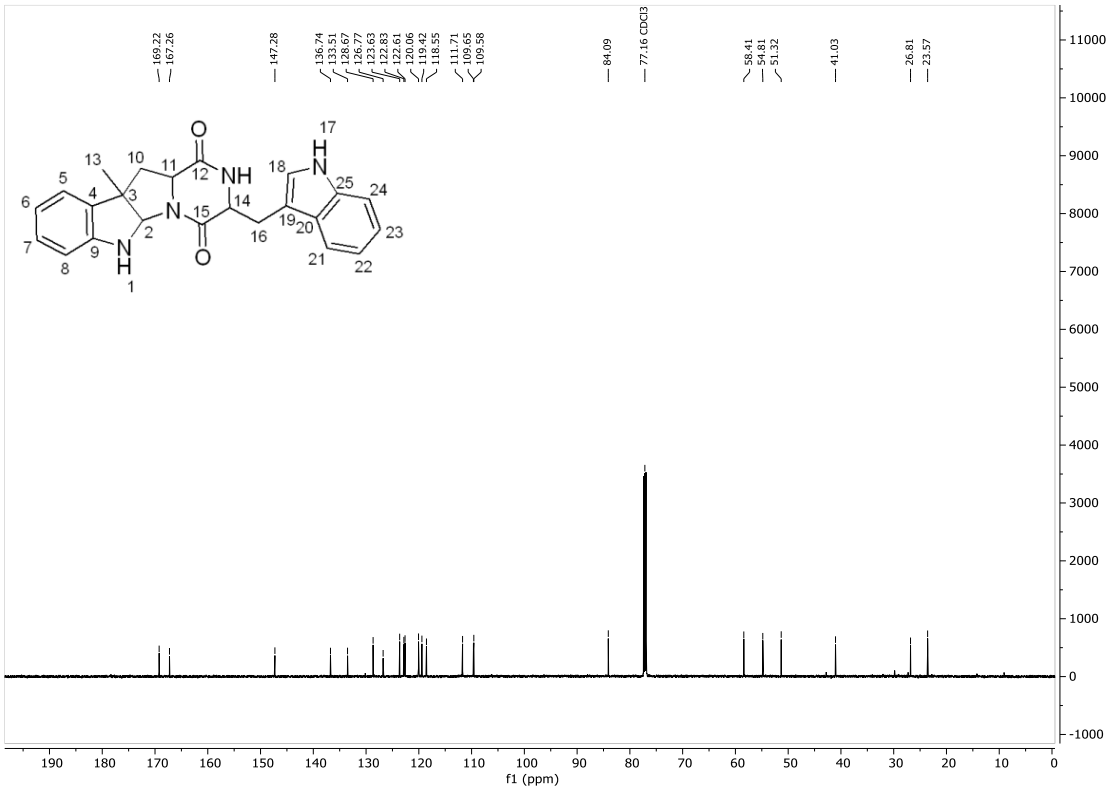

Figure 240: ^{13}C-NMR spectrum of single methylated DD-cWW **168b** in $CDCl_3$ (151 MHz)

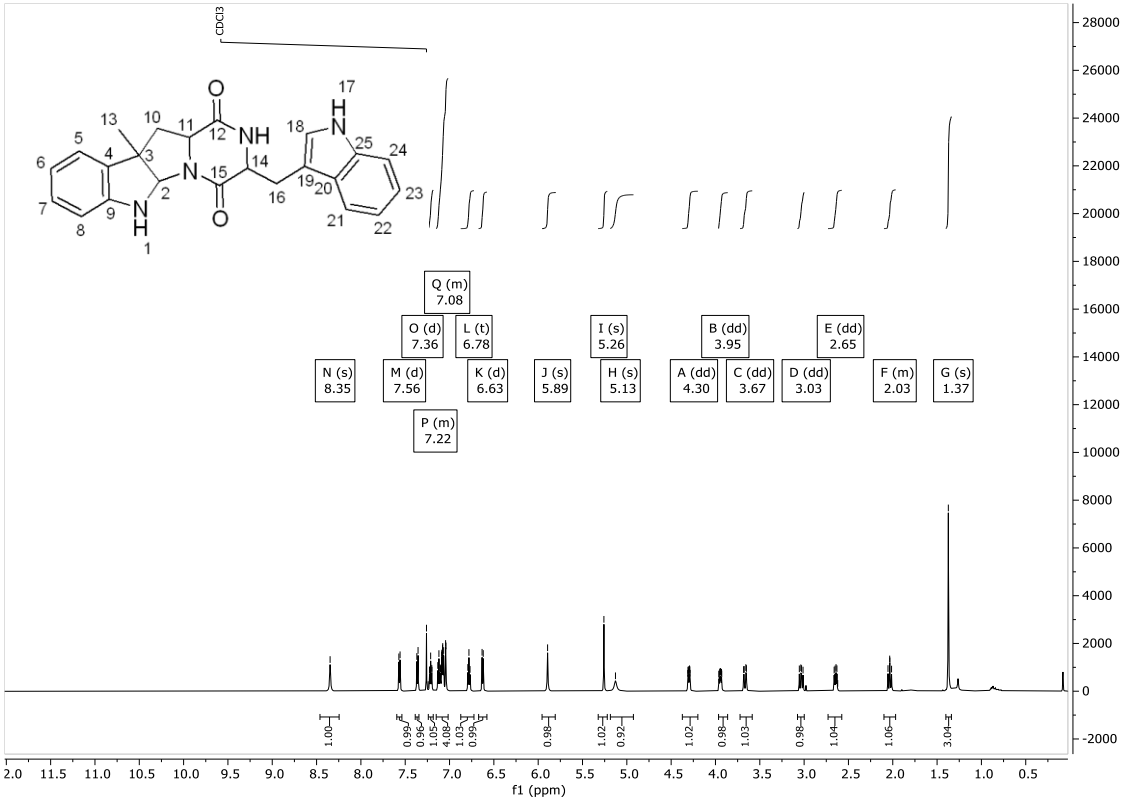

Figure 241: ^{1}H-NMR spectrum of single methylated LL-cWW **168a** in $CDCl_3$ (600 MHz).

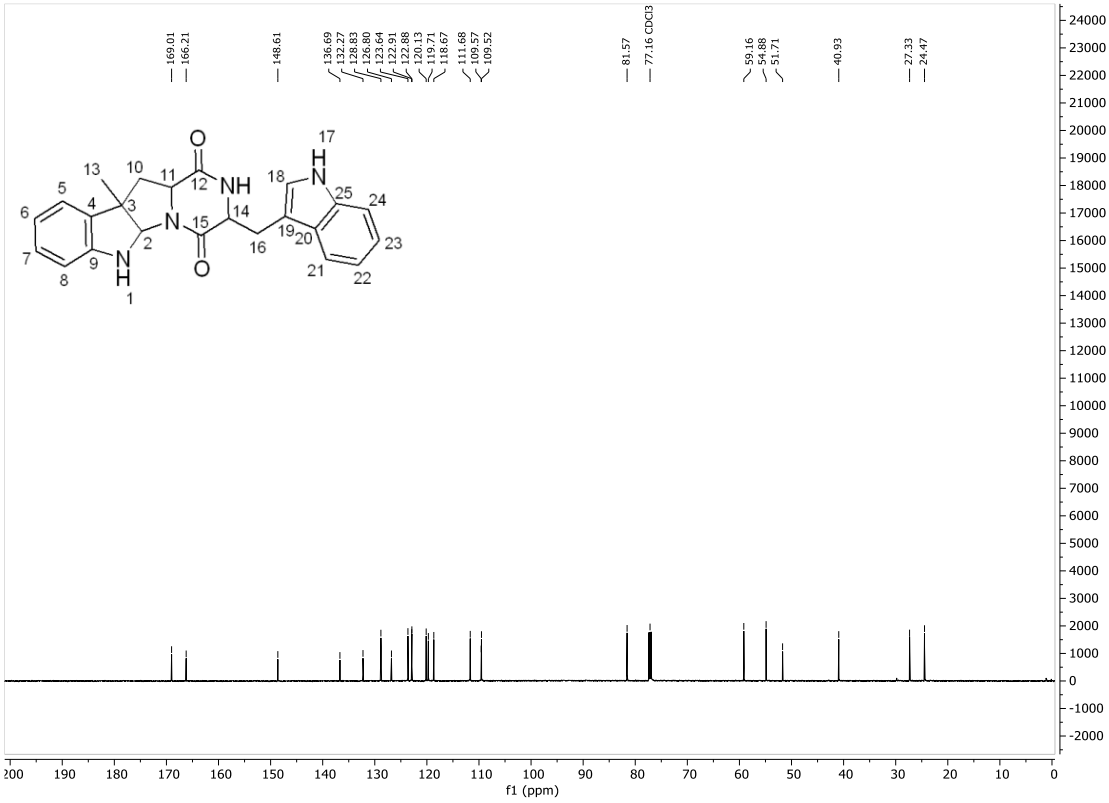

Figure 242: ^{13}C-NMR spectrum of single methylated LL-cWW **168a** in $CDCl_3$ (151 MHz).

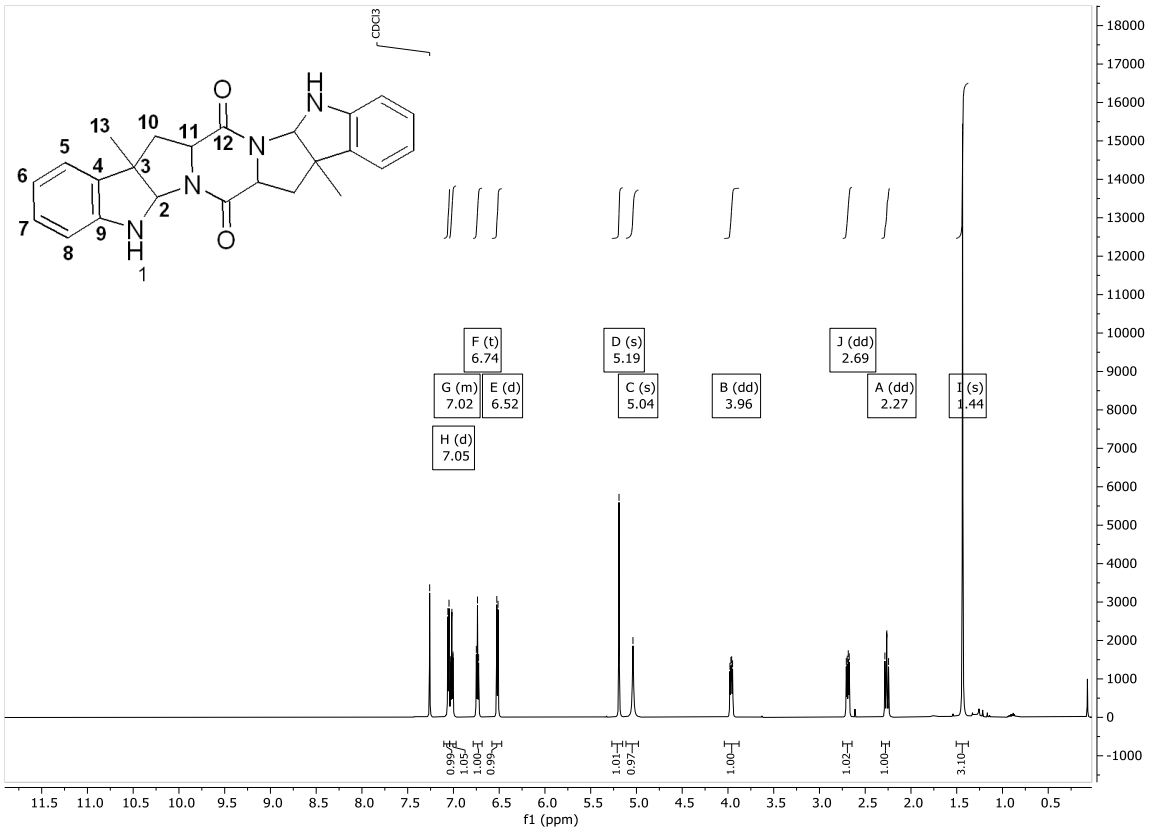

Figure 243: ^{1}H-NMR spectrum of double methylated LL-cWW **240** in $CDCl_3$ (600 MHz).

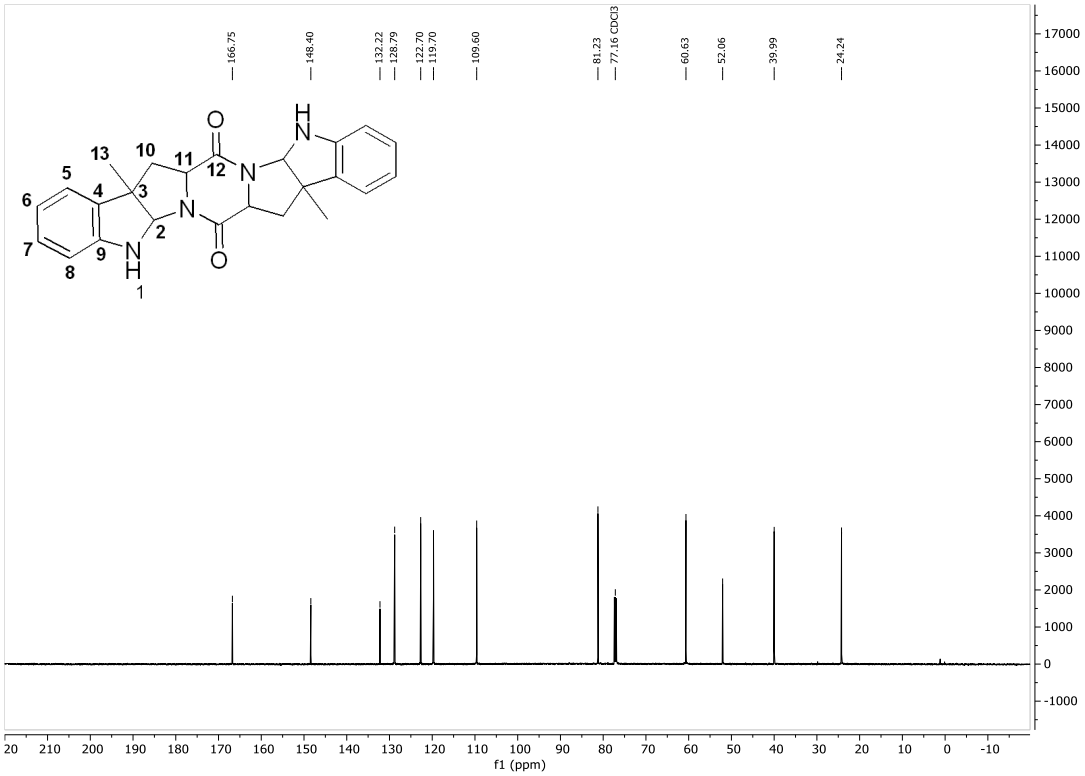

Figure 244: ^{13}C-NMR spectrum of double methylated LL-cWW **240** in $CDCl_3$ (151 MHz).

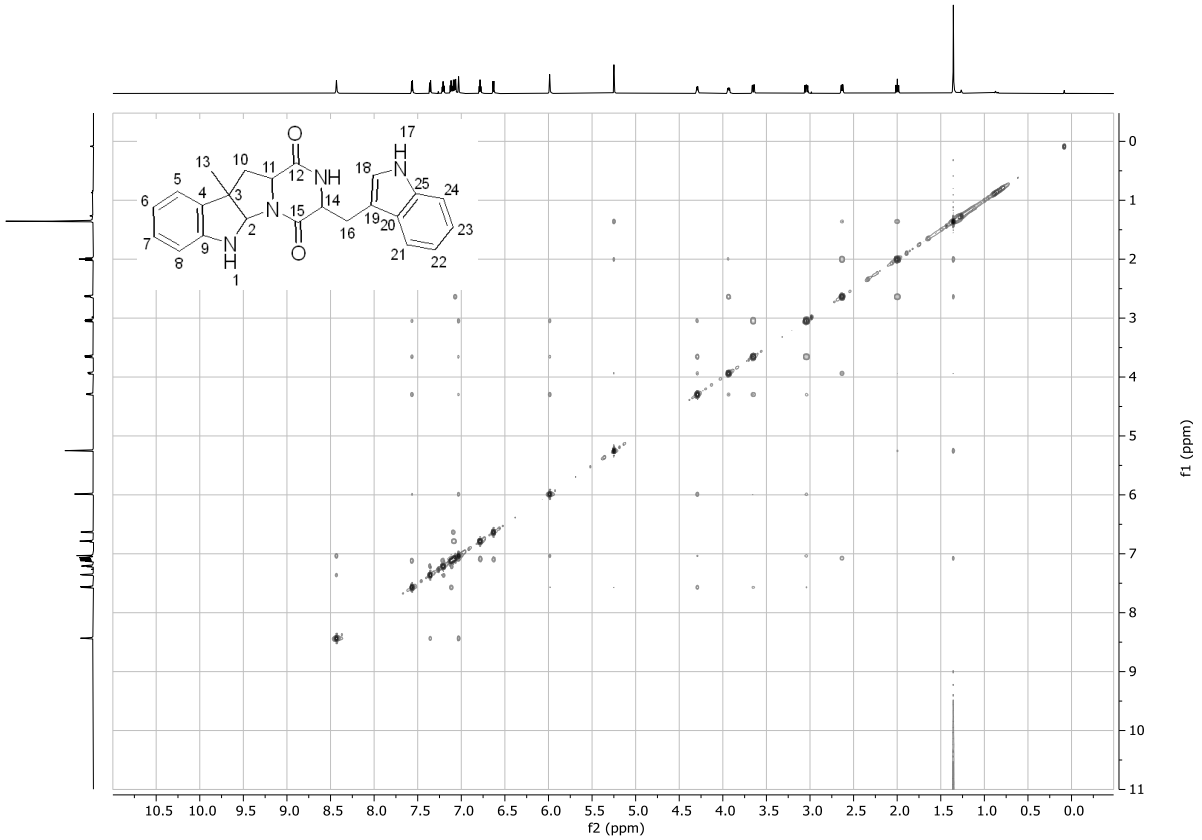

Figure 245: ROESY-spectrum of single methylated LL-cWW **168a** in $CDCl_3$ (750 MHz).

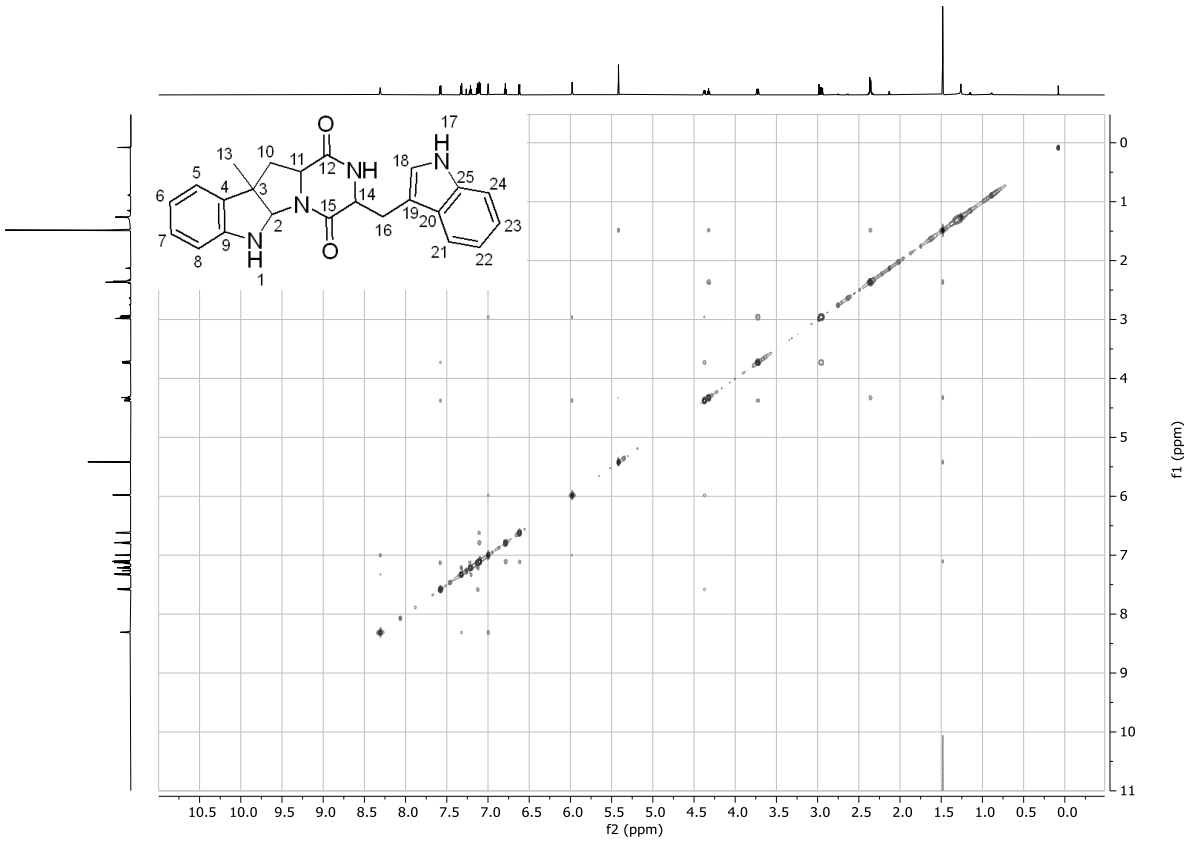

Figure 246: ROESY-spectrum of single methylated DD-cWW **168b** in $CDCl_3$ (750 MHz).

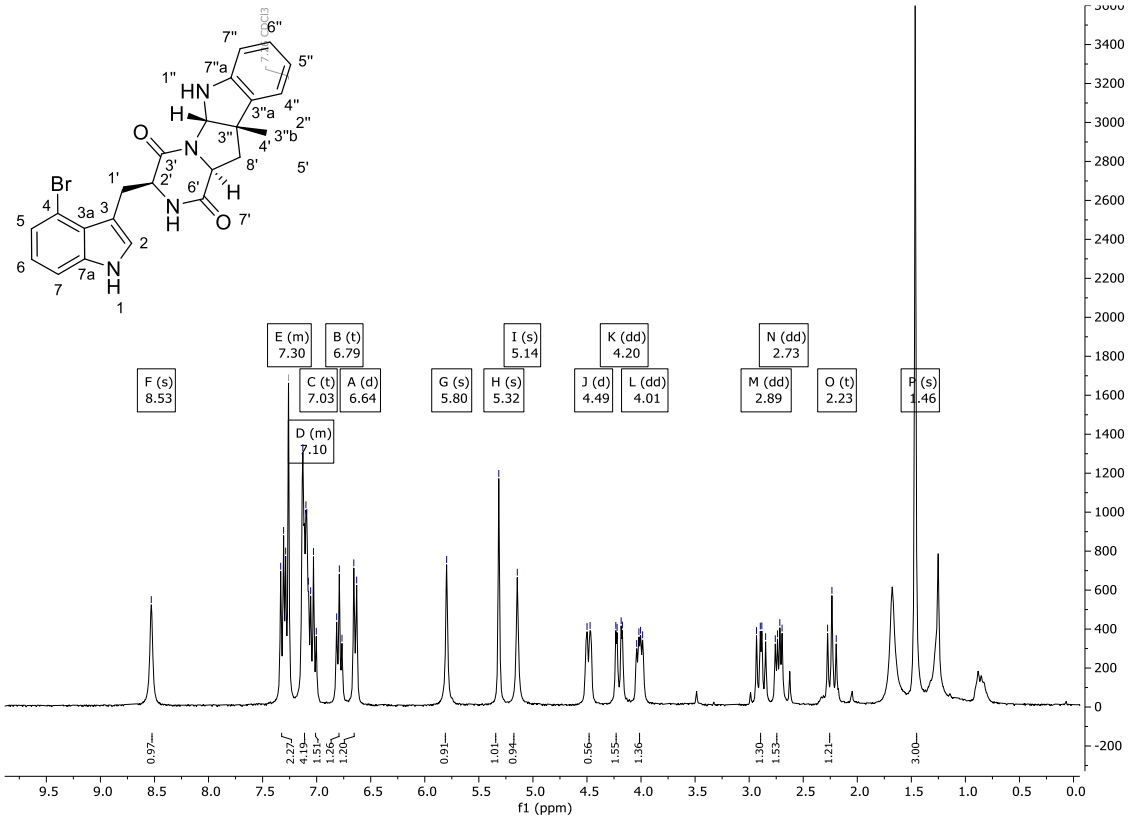

Figure 247: ^{1}H-NMR spectrum of **281** in $CDCl_3$ (600 MHz).

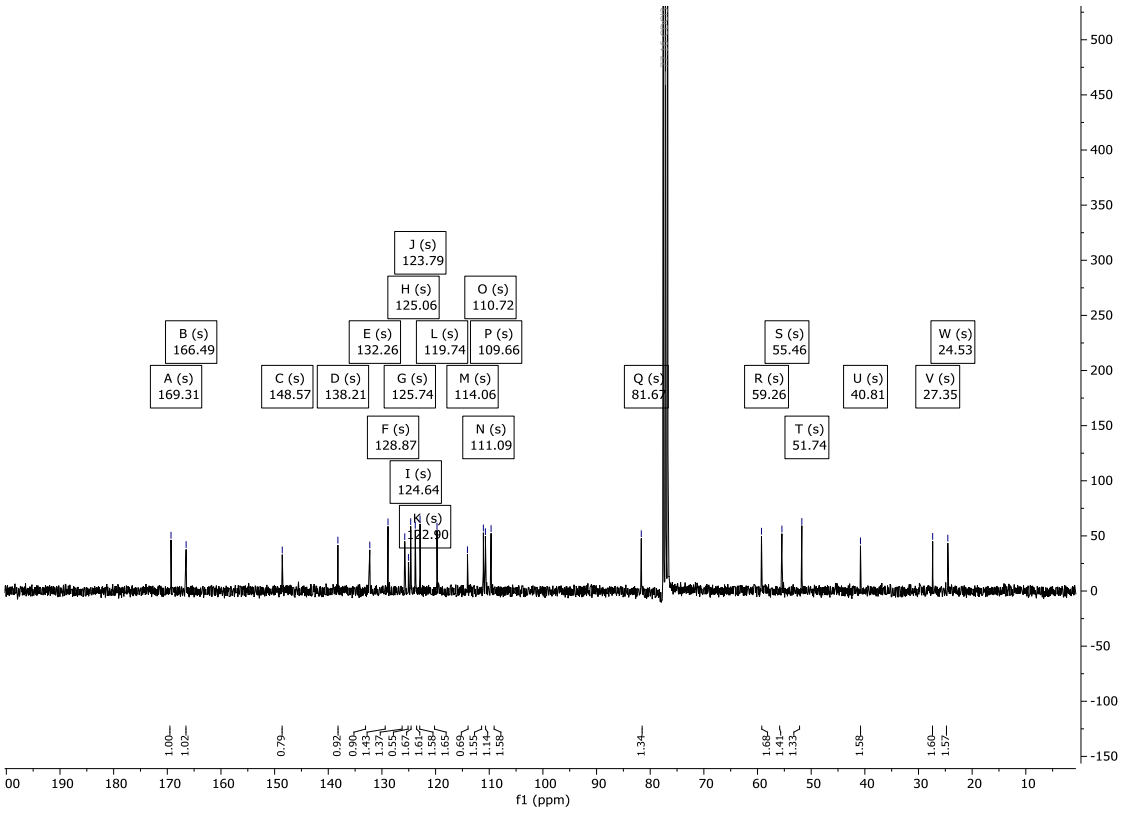

Figure 248: ^{13}C-NMR spectrum of **281** in $CDCl_3$ (151 MHz).

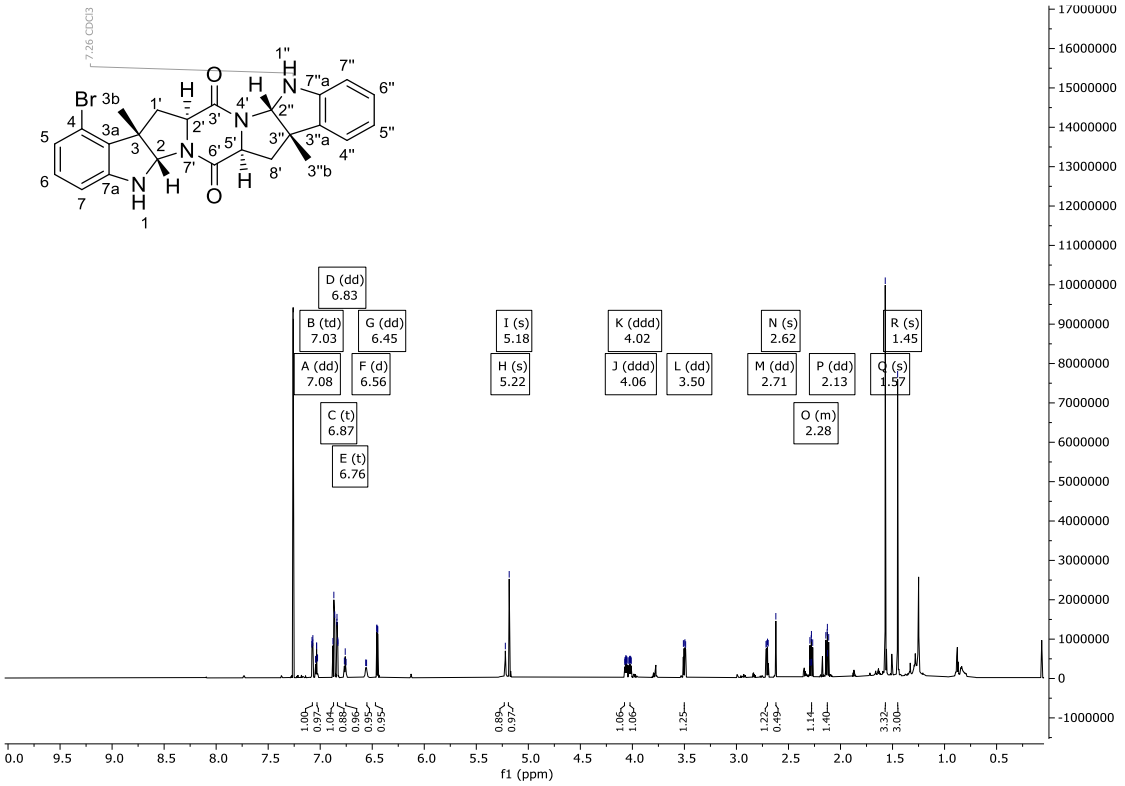

Figure 249: ^{1}H-NMR spectrum of **282** in $CDCl_3$ (600 MHz).

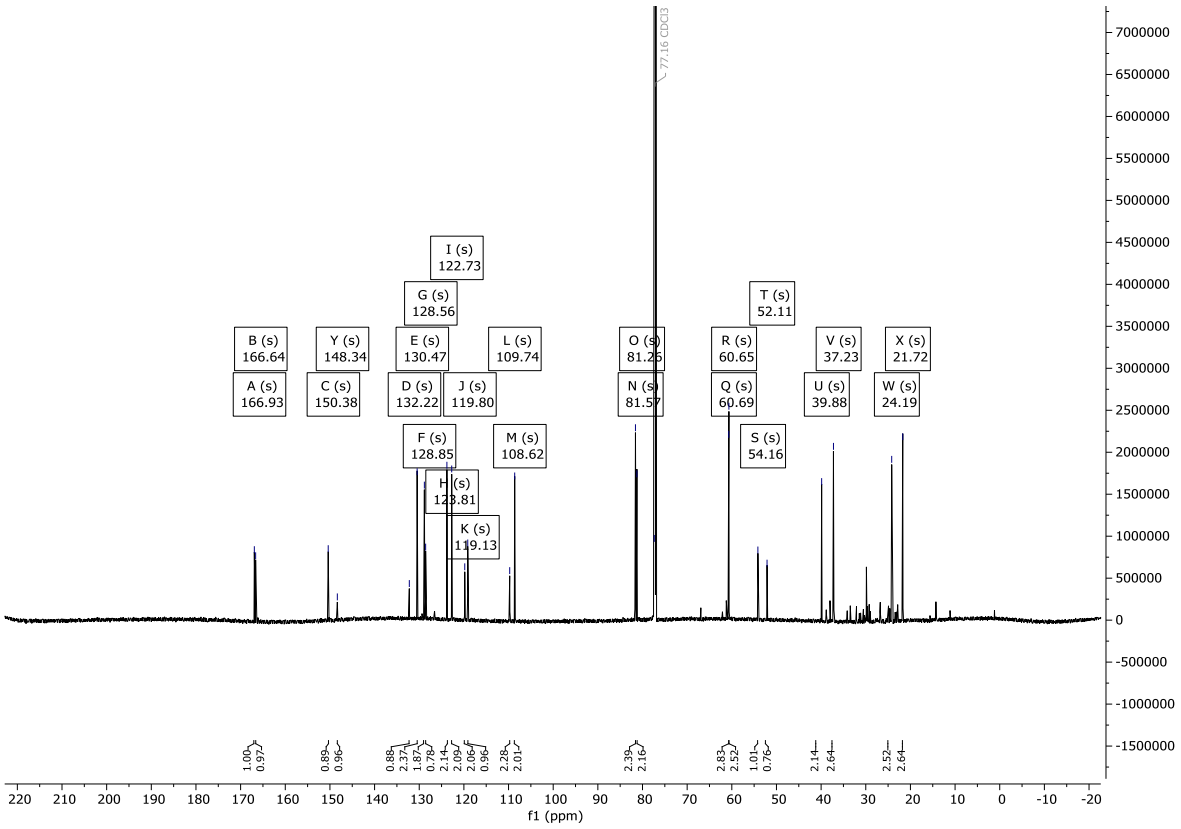

Figure 250: ^{13}C-NMR spectrum of **282** in $CDCl_3$ (151 MHz).

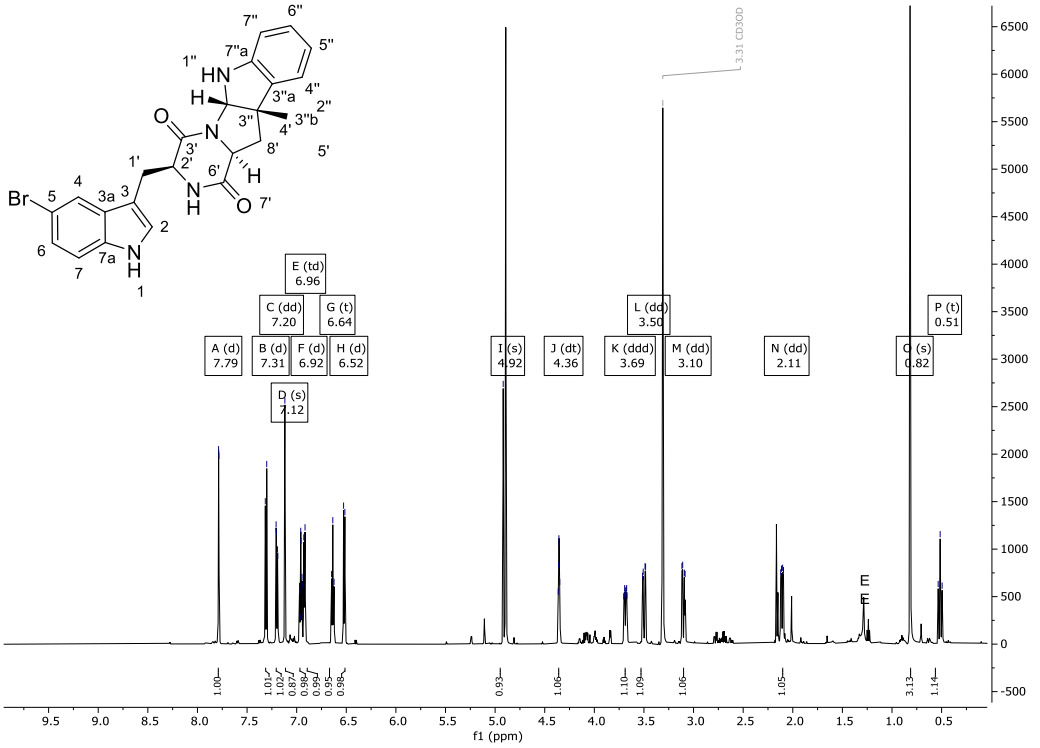

Figure 251: ^{1}H-NMR spectrum of **264** in $CDCl_3$ (600 MHz).

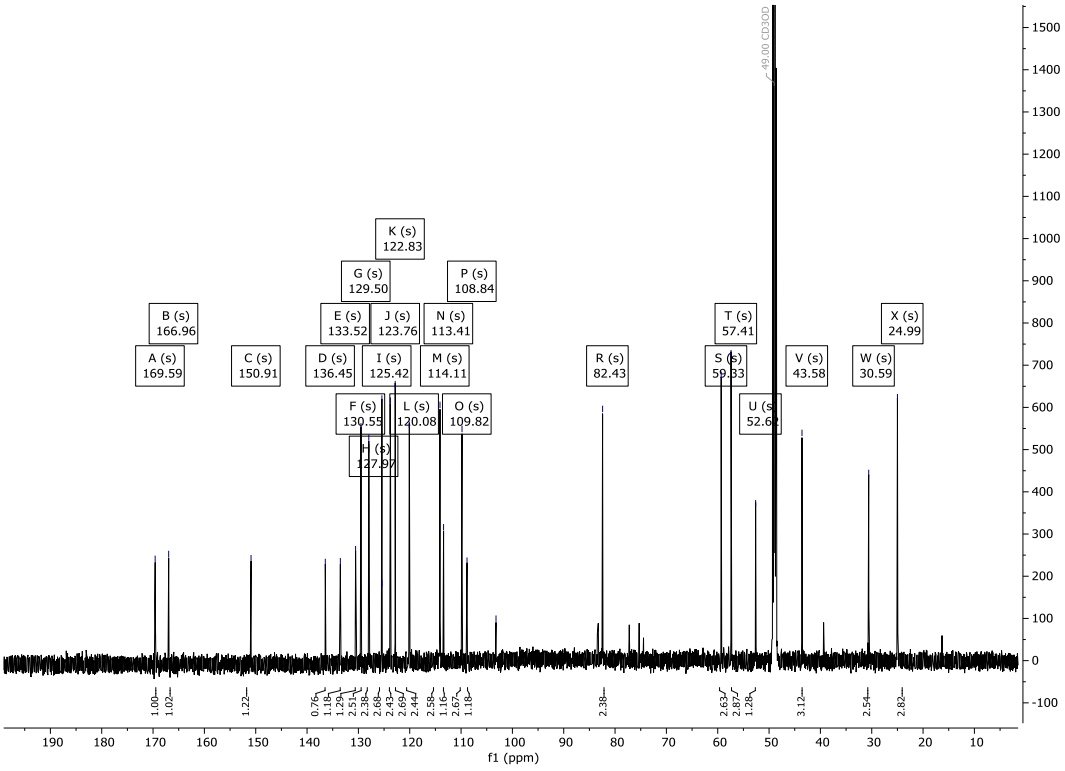

Figure 252: ^{13}C-NMR spectrum of **264** in $CDCl_3$ (151 MHz).

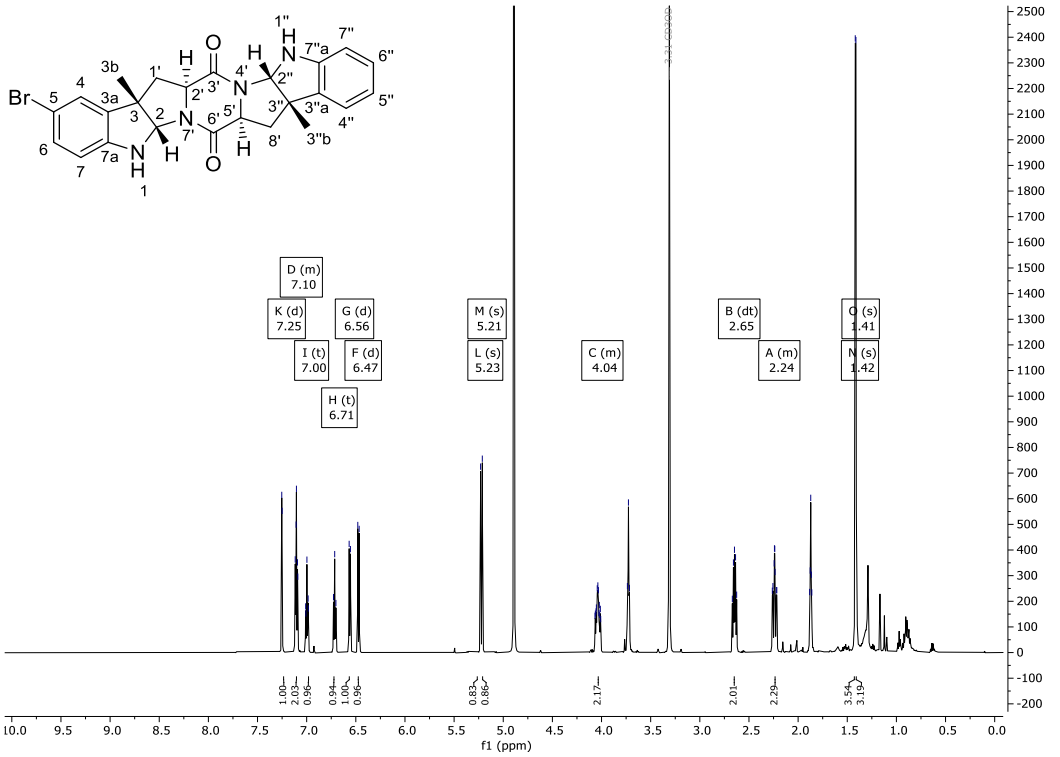

Figure 253: ^{1}H-NMR spectrum of **267** in $CDCl_3$ (600 MHz).

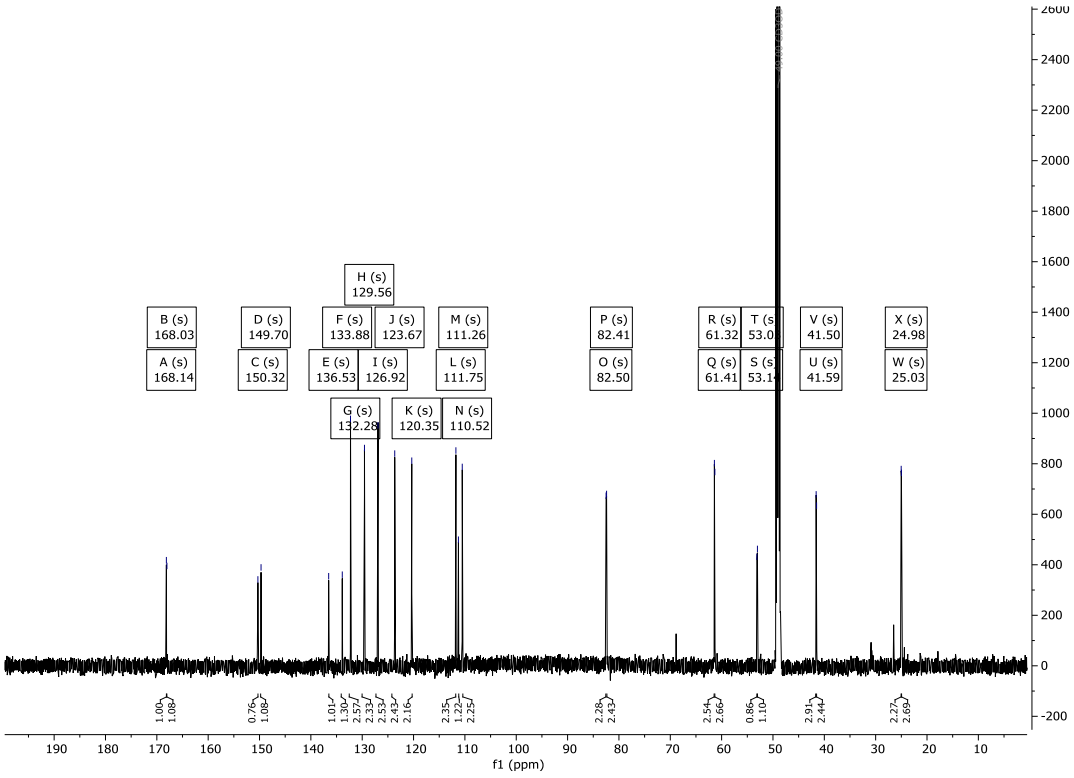

Figure 254: ^{13}C-NMR spectrum of **264** in $CDCl_3$ (151 MHz).

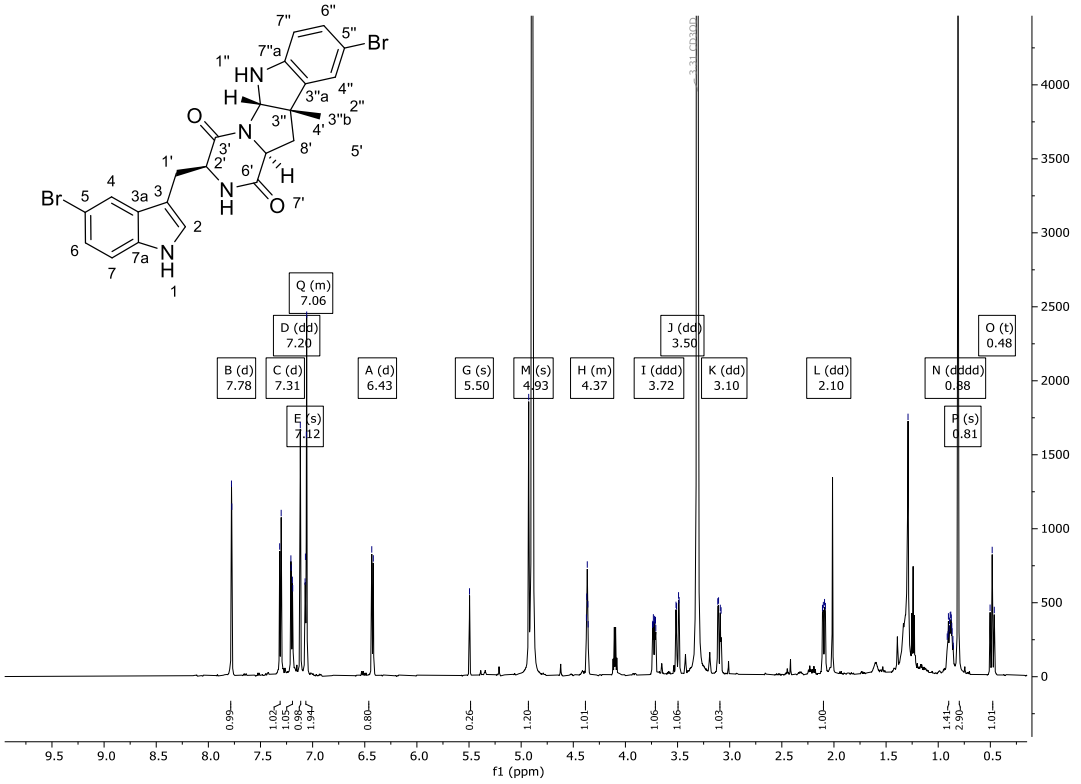

Figure 255: ^{1}H-NMR spectrum of **285** in $CDCl_3$ (600 MHz).

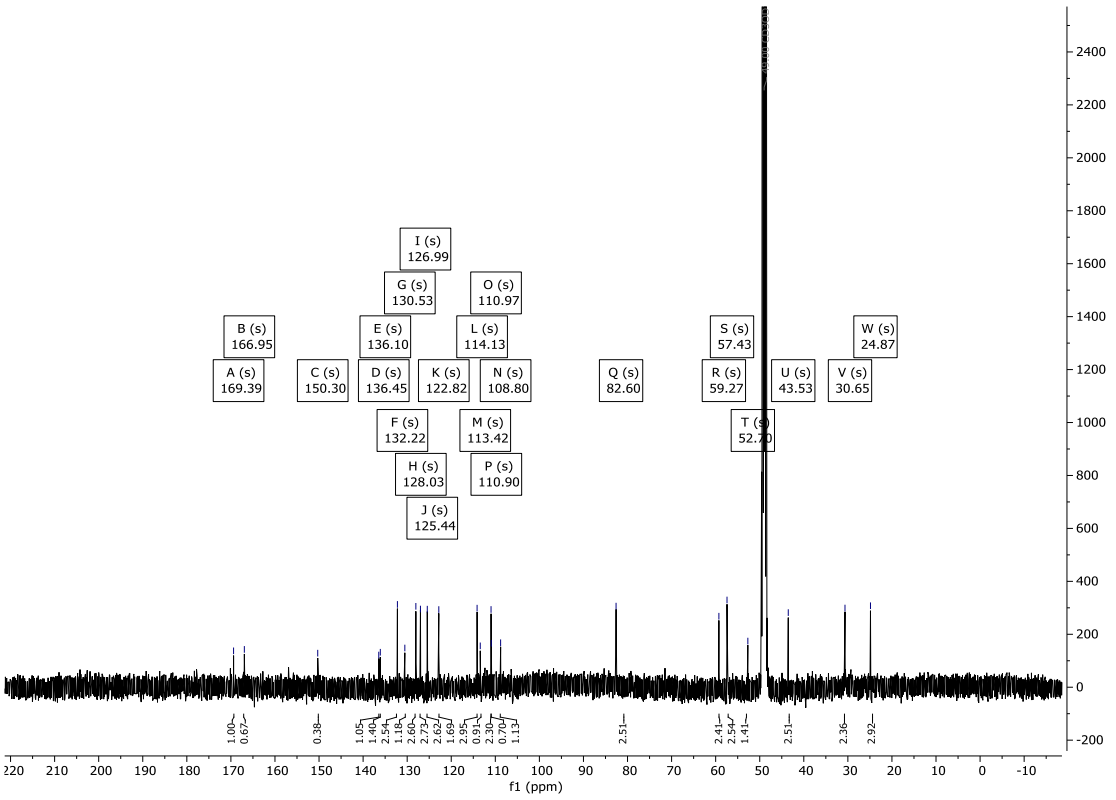

Figure 256: ^{13}C-NMR spectrum of **285** in $CDCl_3$ (151 MHz).

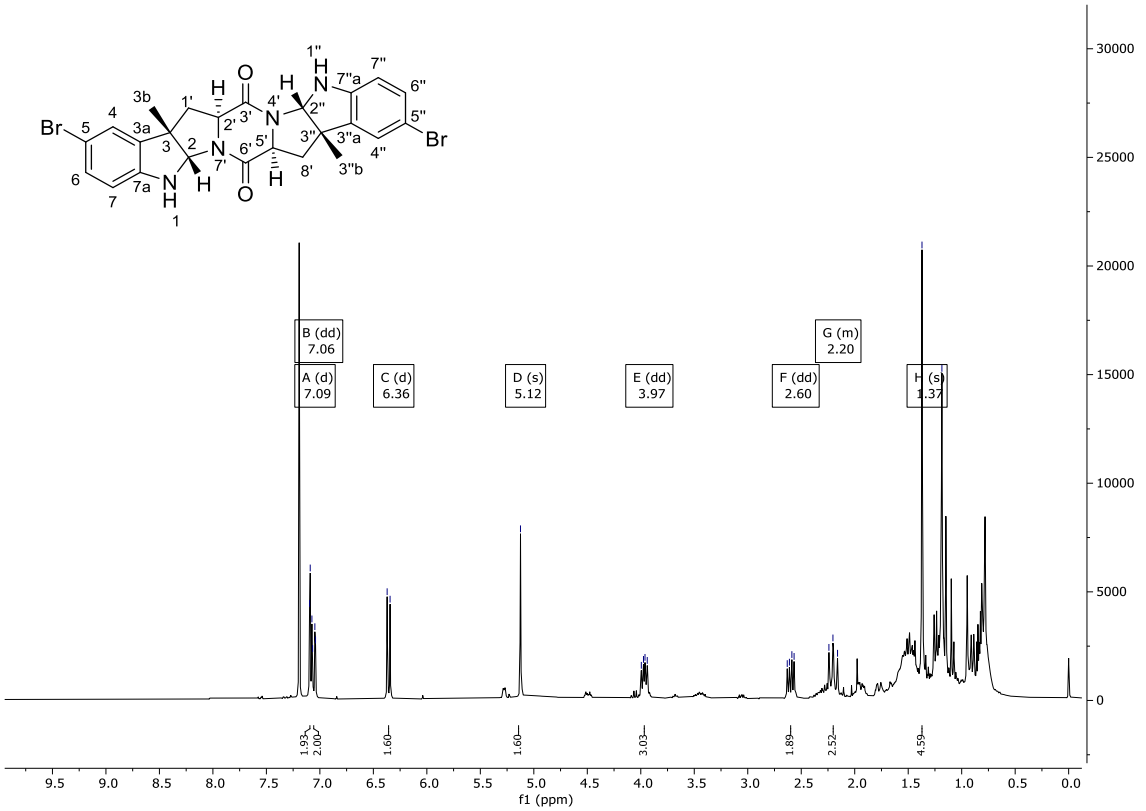

Figure 257: ^{1}H-NMR spectrum of **286** in $CDCl_3$ (600 MHz).

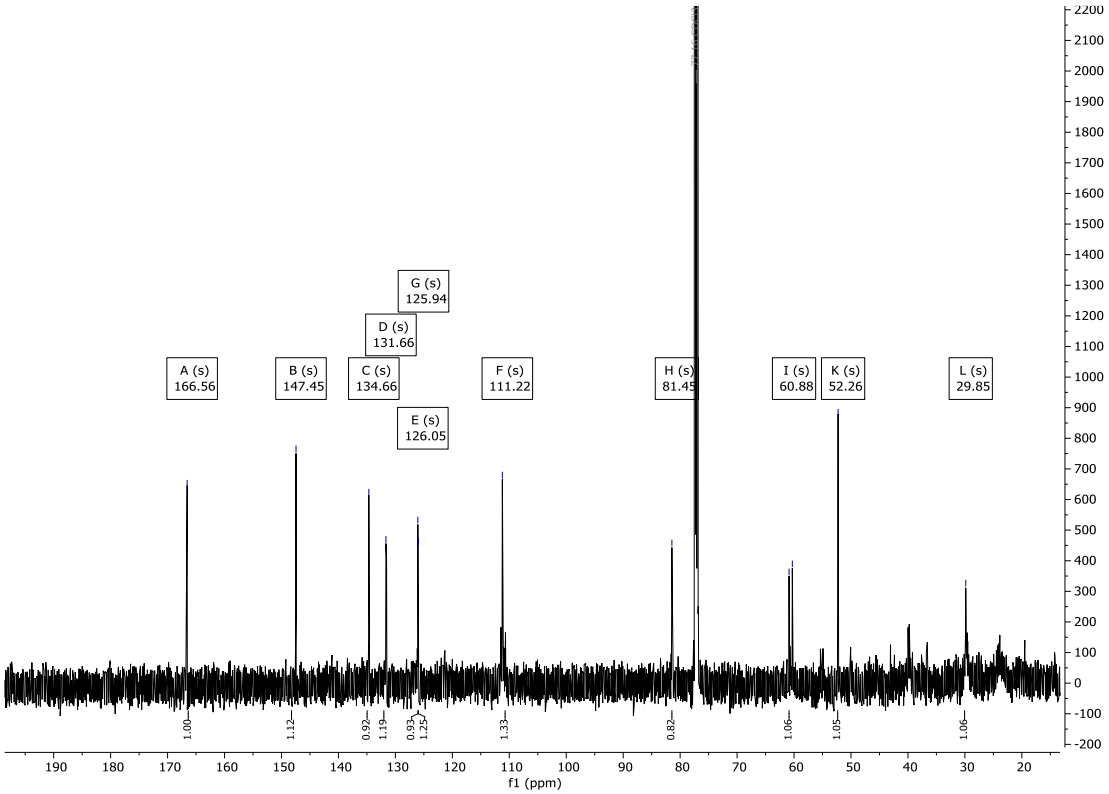

Figure 258: ^{13}C-NMR spectrum of **286** in $CDCl_3$ (151 MHz).

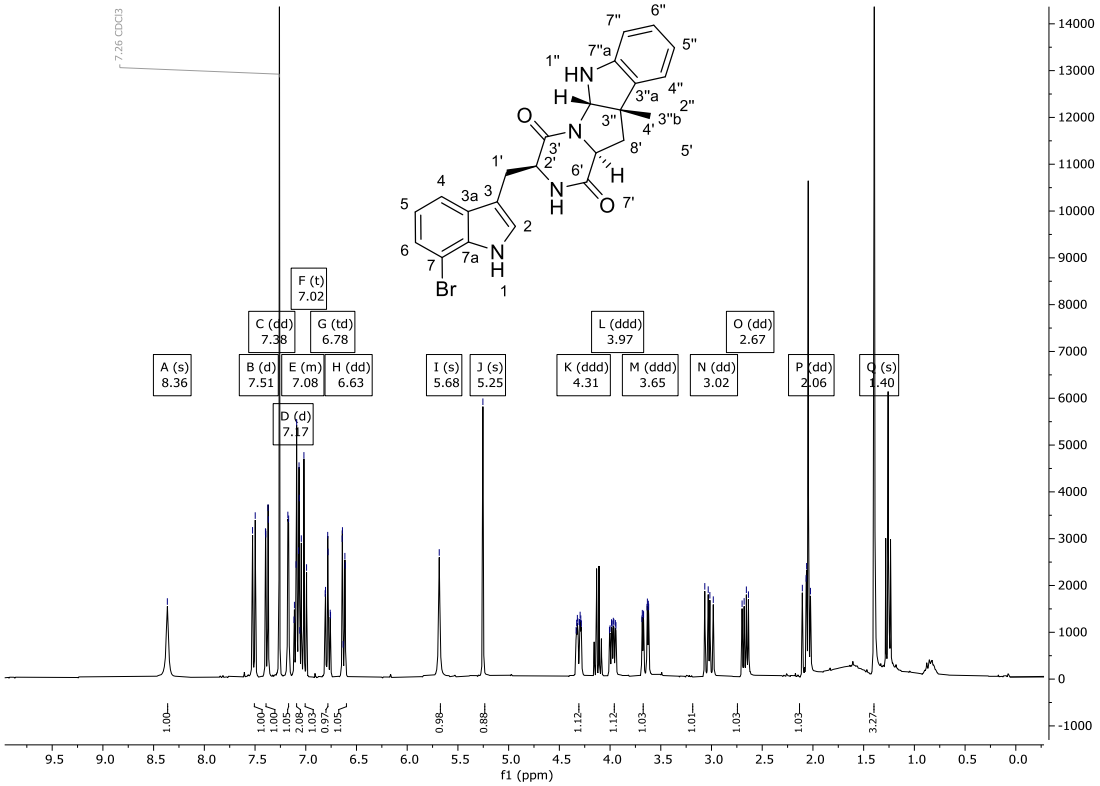

Figure 259: ^{1}H-NMR spectrum of **283** in $CDCl_3$ (600 MHz).

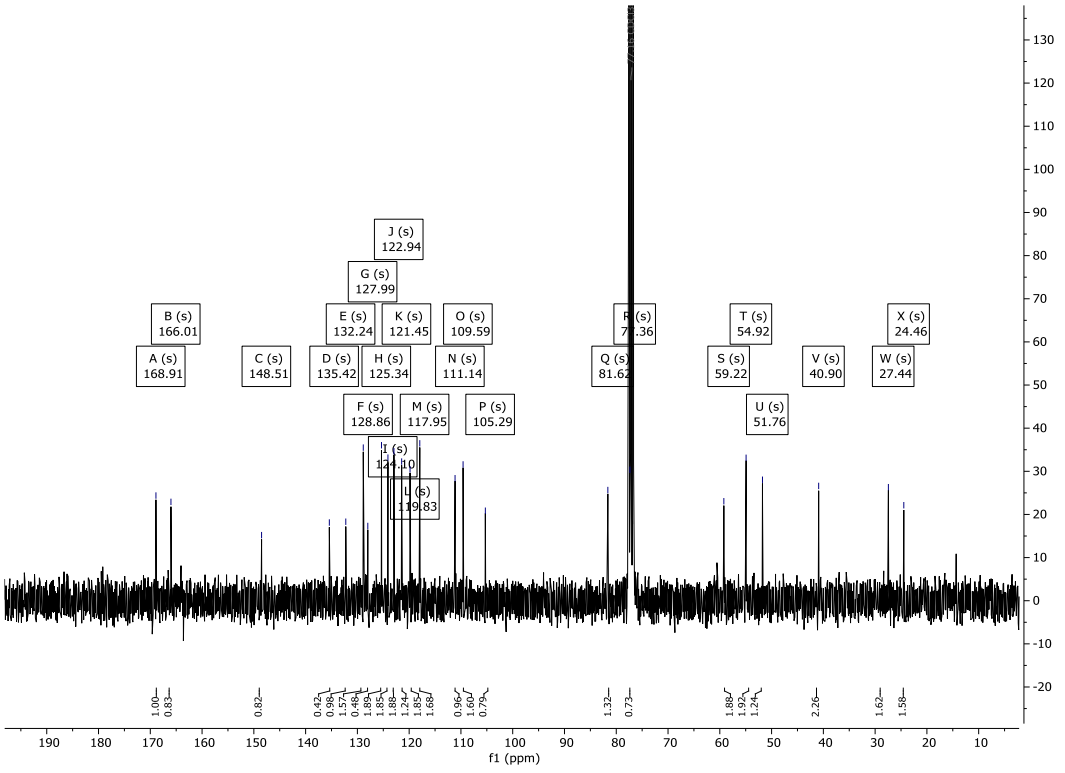

Figure 260: ^{13}C-NMR spectrum of **283** in $CDCl_3$ (151 MHz).

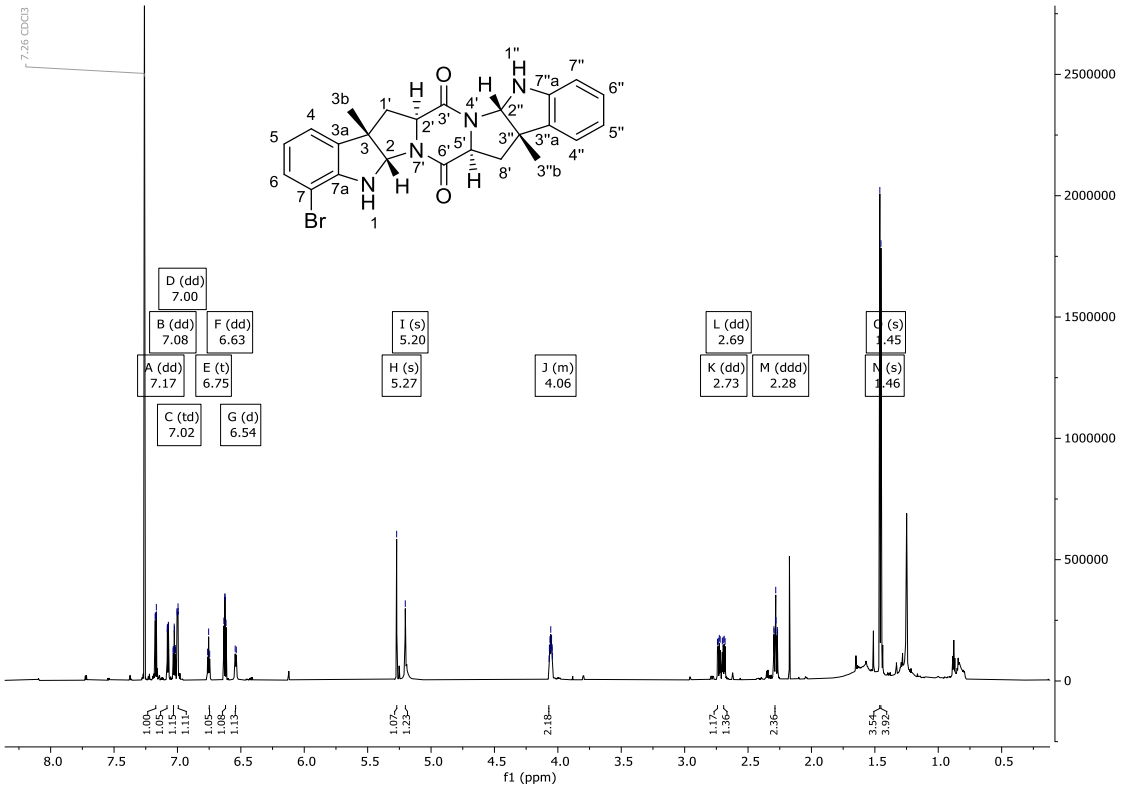

Figure 261: ^{1}H-NMR spectrum of **284** in $CDCl_3$ (600 MHz).

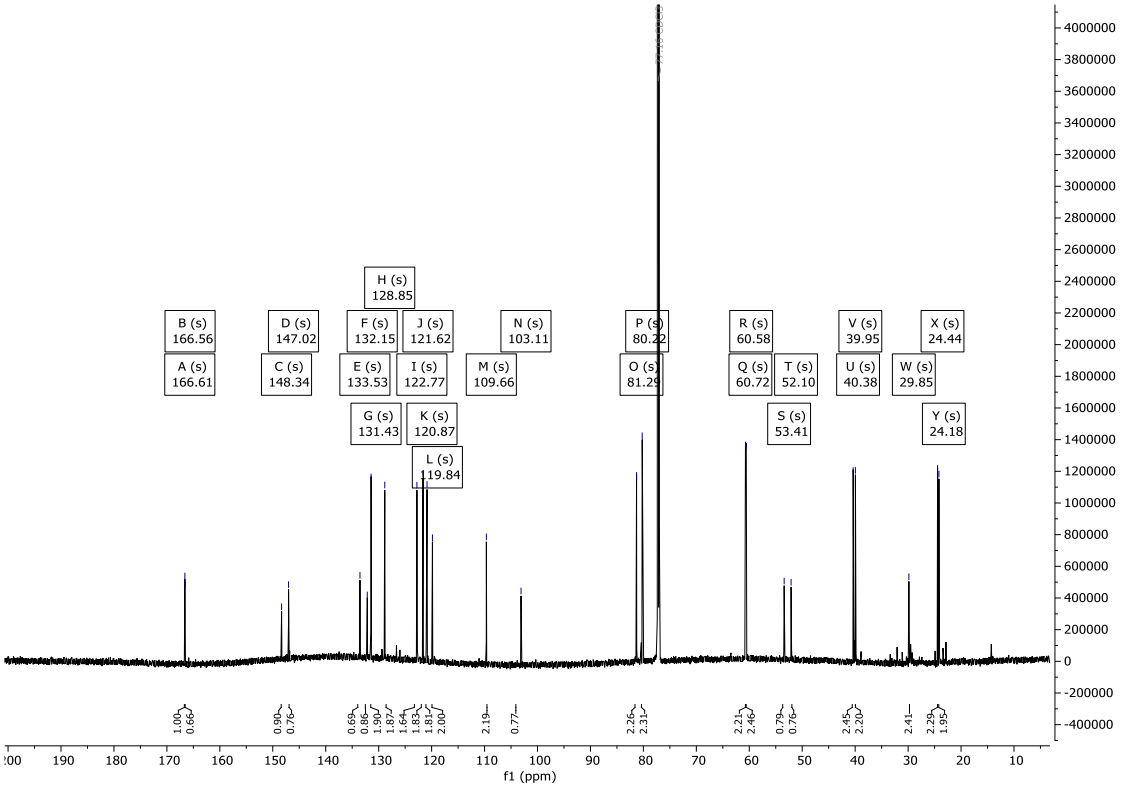

Figure 262: ^{13}C-NMR spectrum of **284** in $CDCl_3$ (151 MHz).

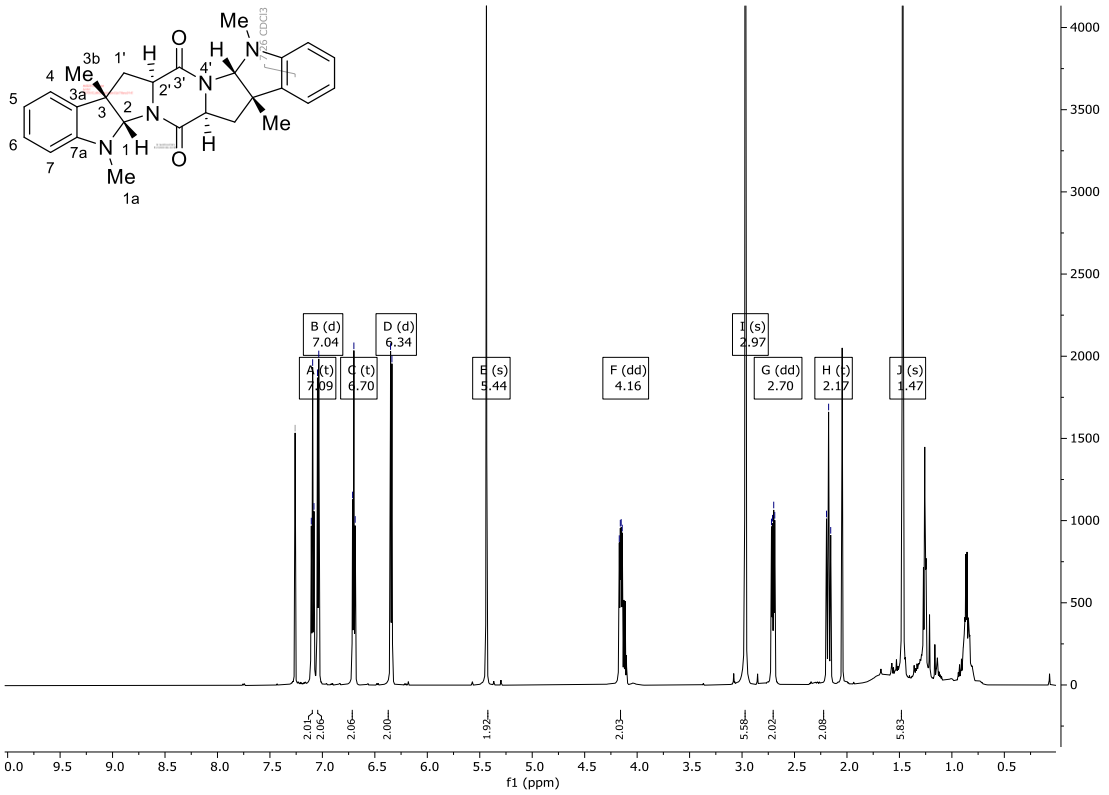

Figure 263: ^{1}H-NMR spectrum of **287** in $CDCl_3$ (600 MHz).

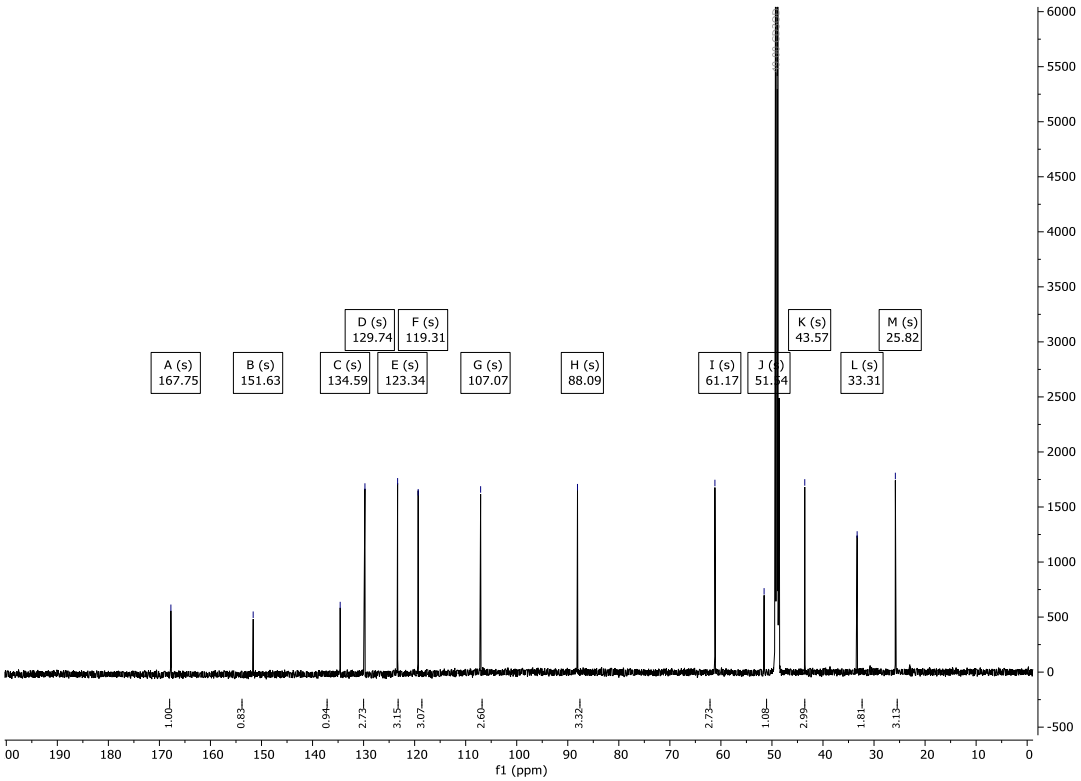

Figure 264: ^{13}C-NMR spectrum of **287** in $CDCl_3$ (151 MHz).

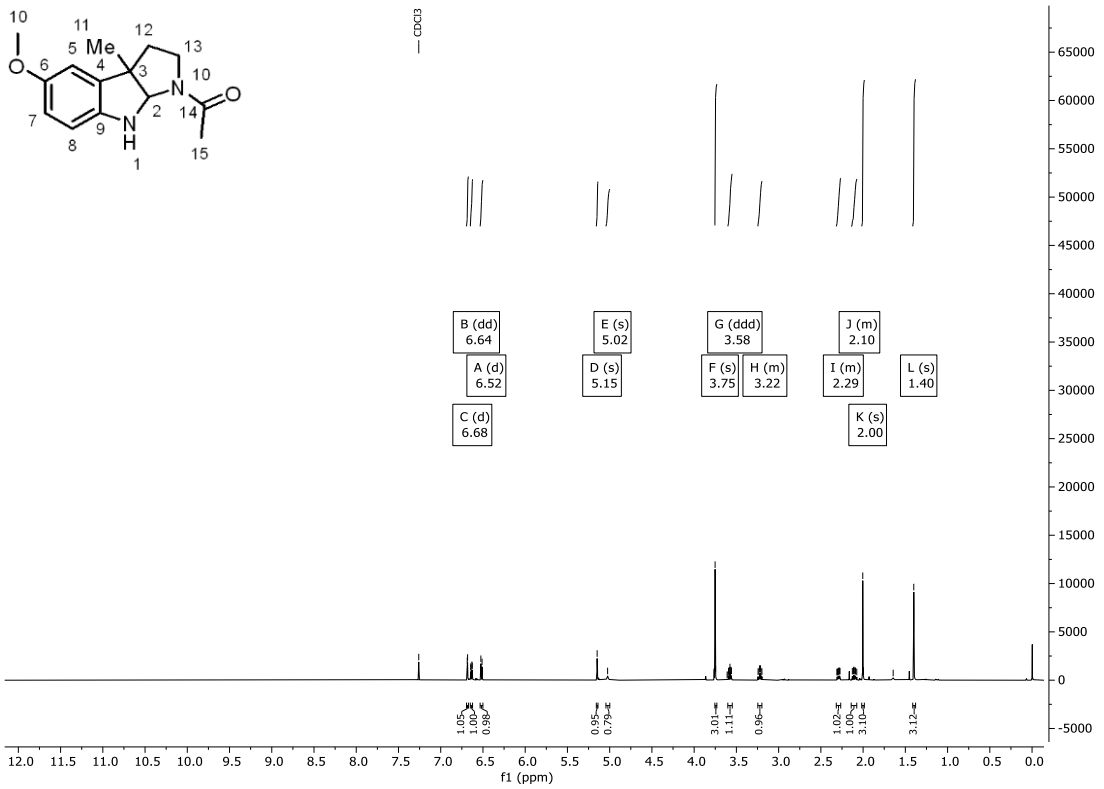

Figure 265: ^{1}H-NMR spectrum of **228** in $CDCl_3$ (600 MHz).

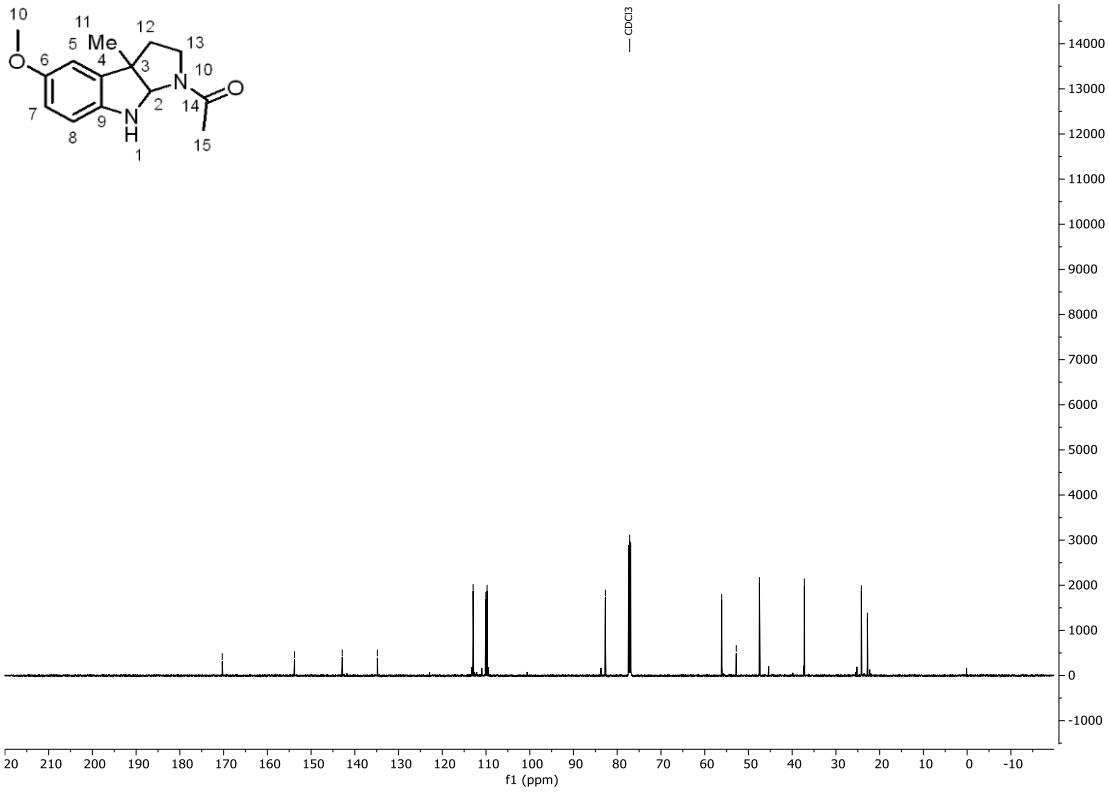

Figure 266: ^{13}C-NMR spectrum of **228** in $CDCl_3$ (151 MHz).

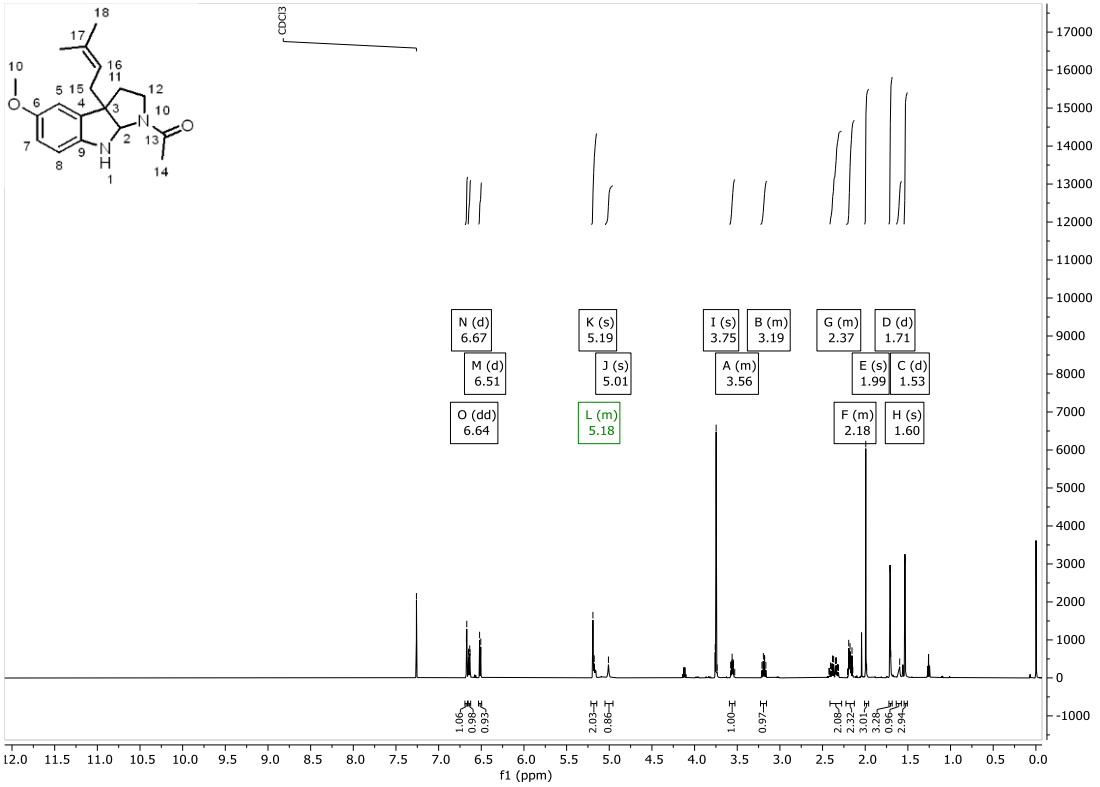

Figure 267: ^{1}H-NMR spectrum of **229** in $CDCl_3$ (600 MHz).

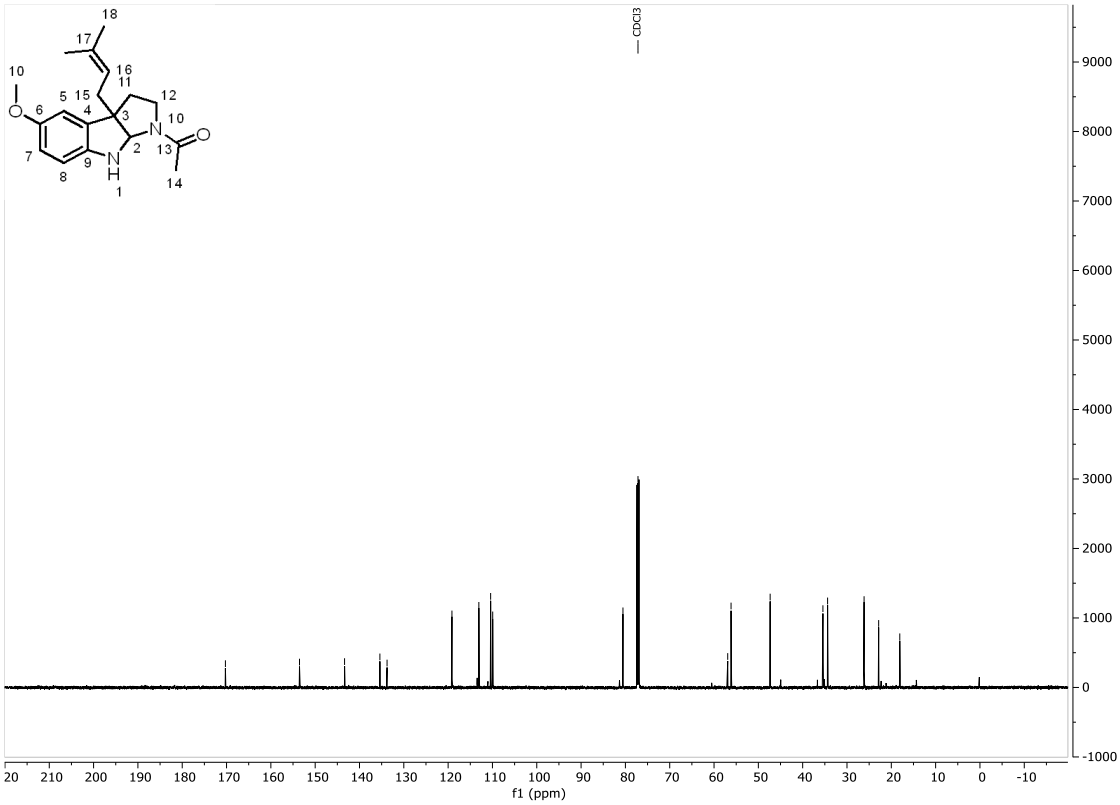

Figure 268: ^{13}C-NMR spectrum of **229** in $CDCl_3$ (151 MHz).

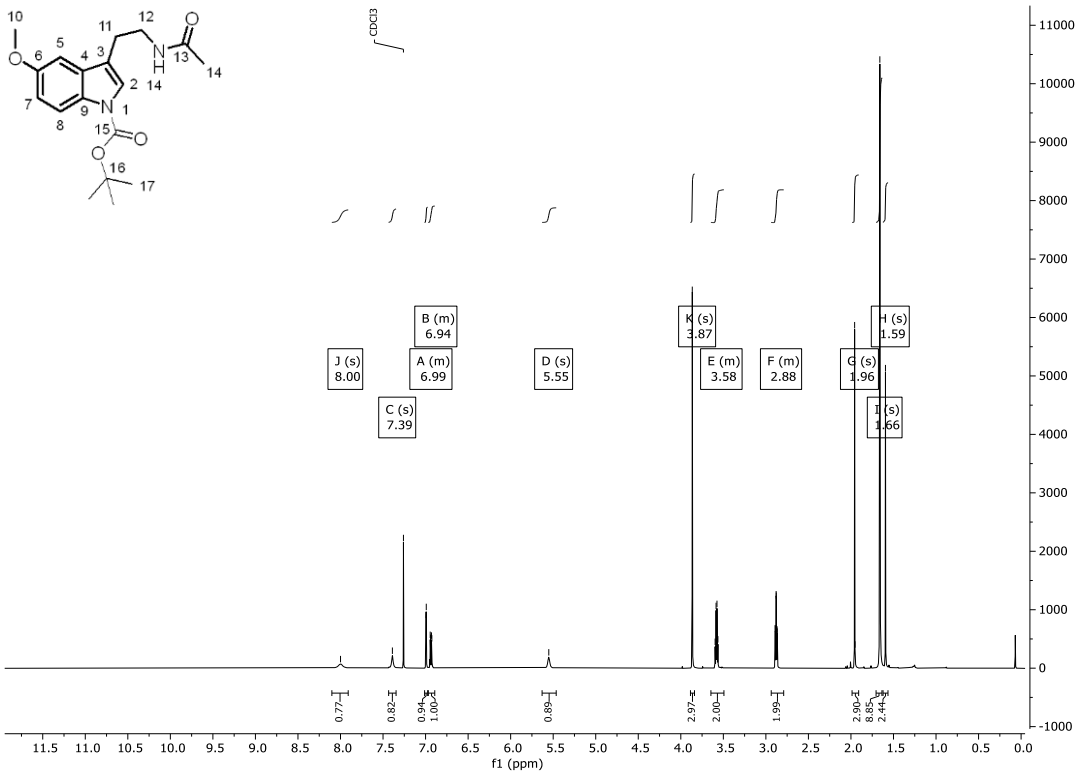

Figure 269: ^{1}H-NMR spectrum of **231** in $CDCl_3$ (600 MHz).

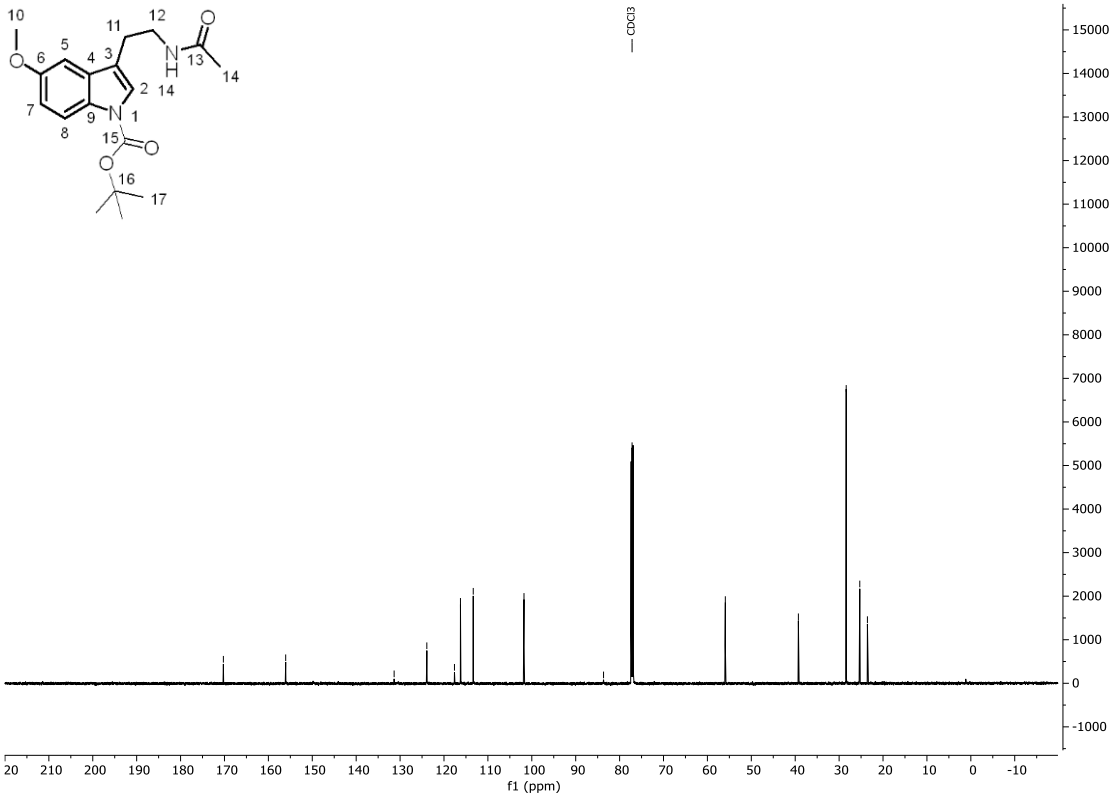

Figure 270: ^{13}C-NMR spectrum of **231** in $CDCl_3$ (151 MHz).

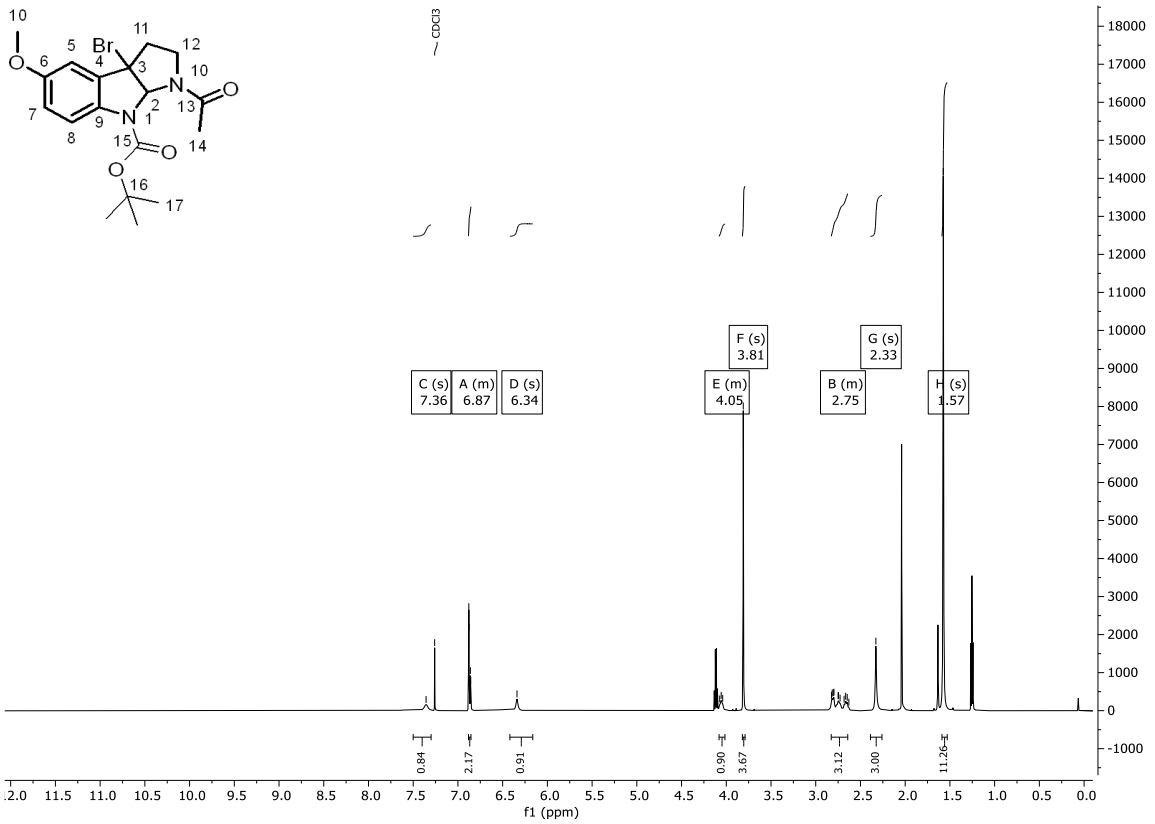

Figure 271: ^{1}H-NMR spectrum of **232** in $CDCl_3$ (600 MHz).

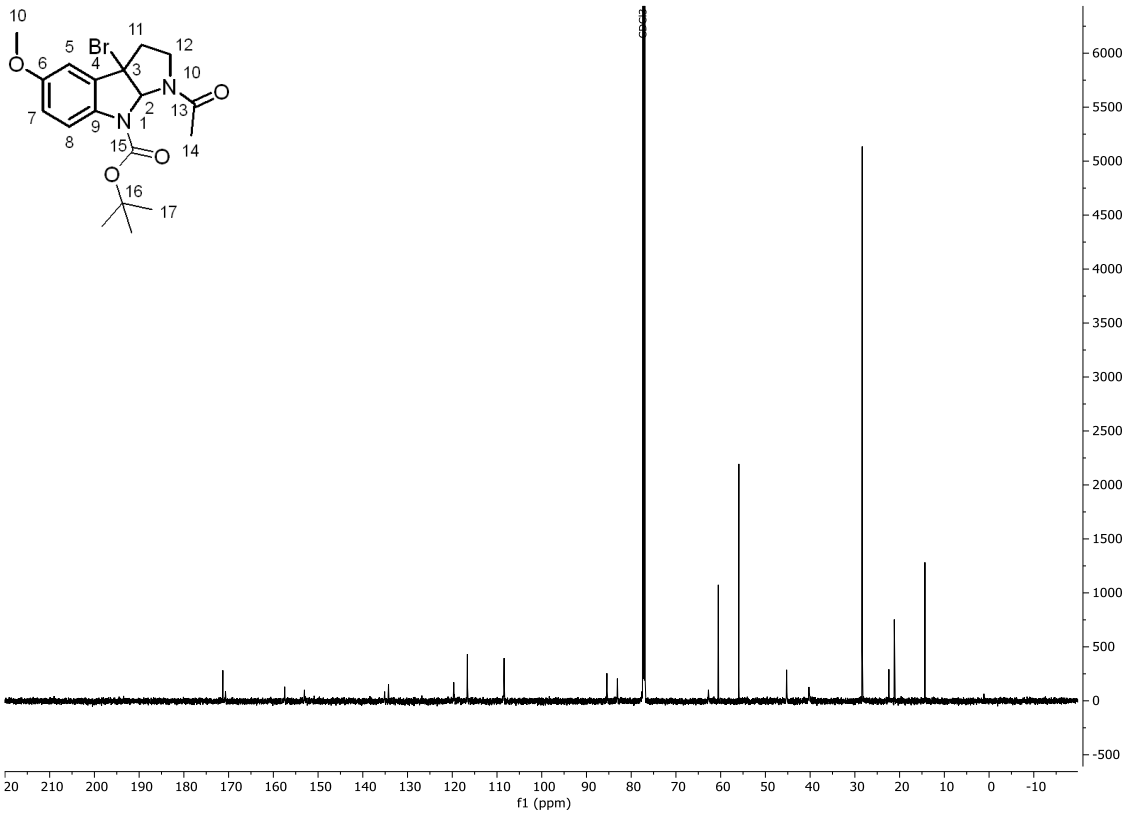

Figure 272: ^{13}C-NMR spectrum of **232** in $CDCl_3$ (151 MHz).

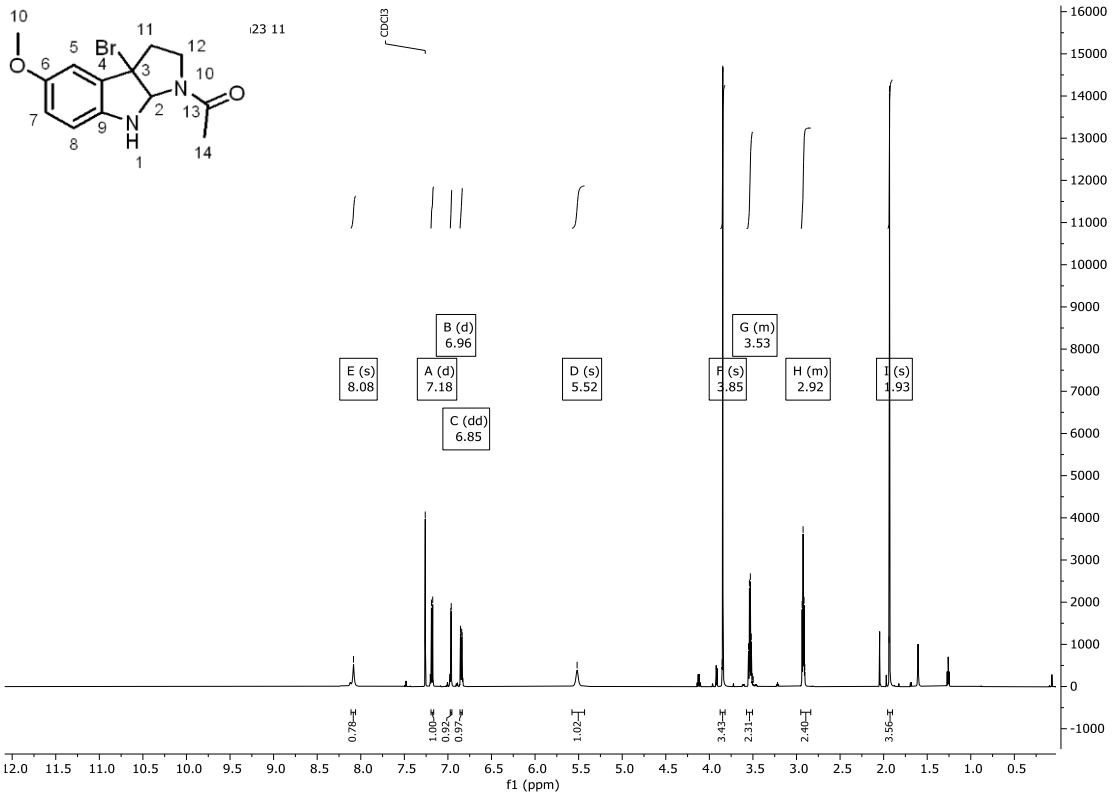

Figure 273: ^{1}H-NMR spectrum of **233** in $CDCl_3$ (600 MHz).

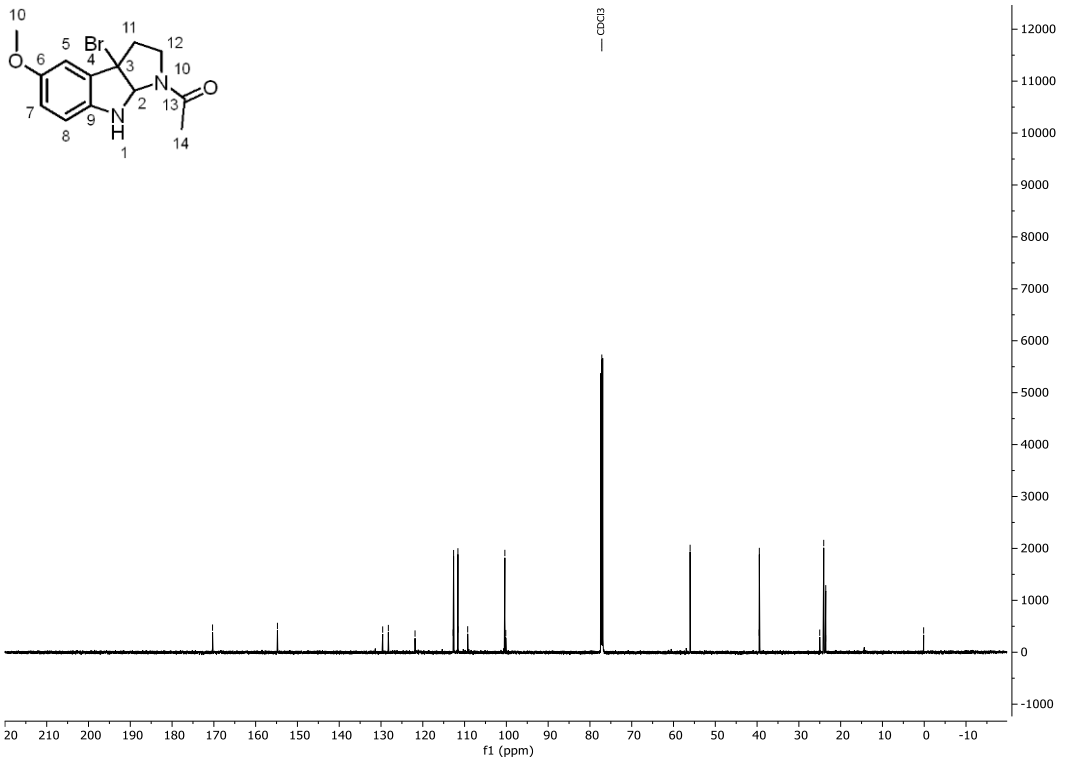

Figure 274: ^{13}C-NMR spectrum of **233** in $CDCl_3$ (151 MHz).

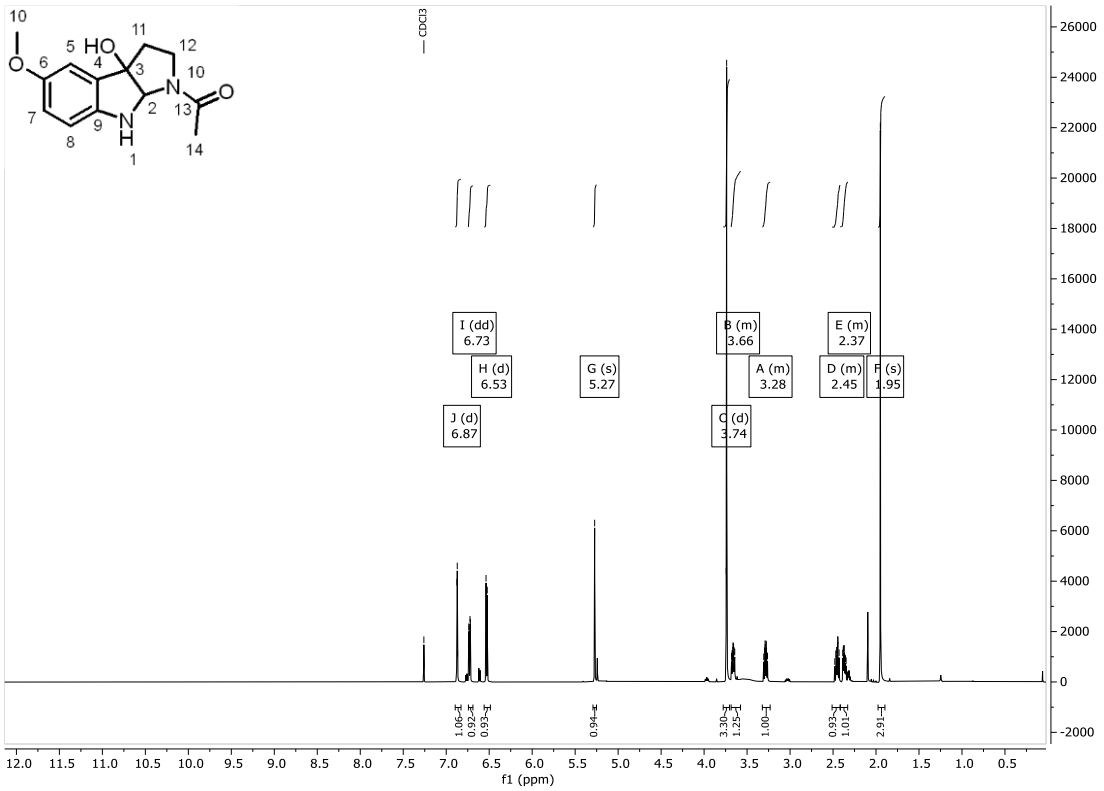

Figure 275: ^{1}H-NMR spectrum of **230** in $CDCl_3$ (600 MHz).

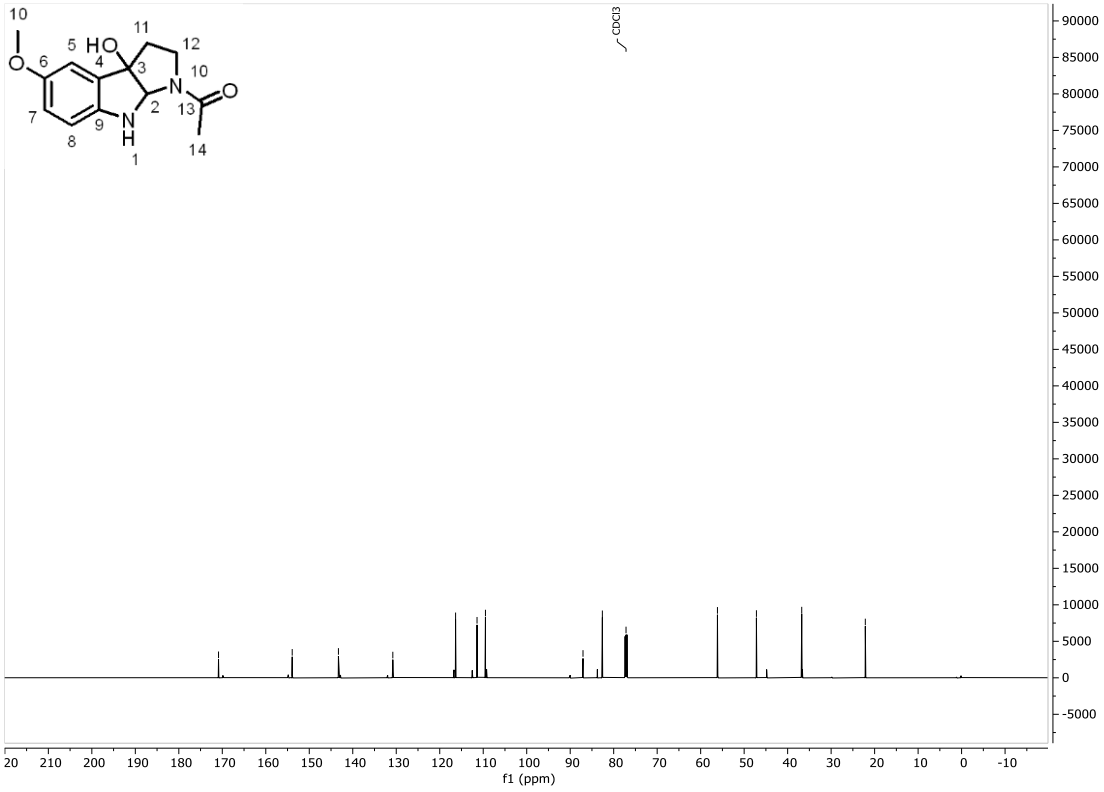

Figure 276: ^{13}C-NMR spectrum of **230** in $CDCl_3$ (151 MHz).

9. STRUCTURE REGISTER

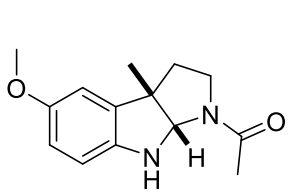

228

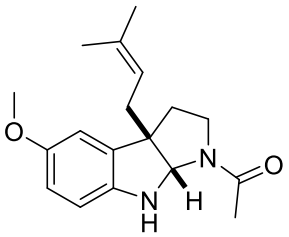

229

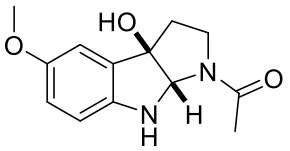

230

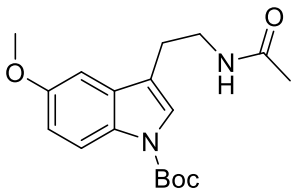

231

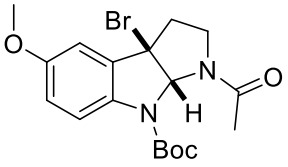

232

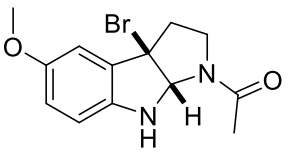

233

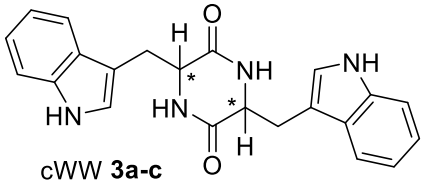

cWW **3a-c**

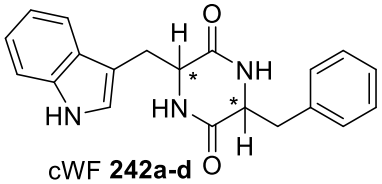

cWF **242a-d**

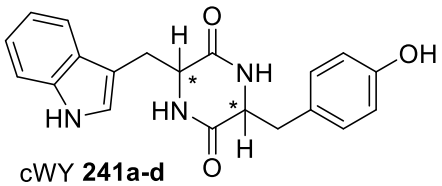

cWY **241a-d**

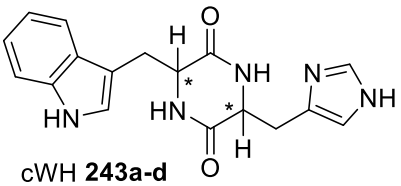

cWH **243a-d**

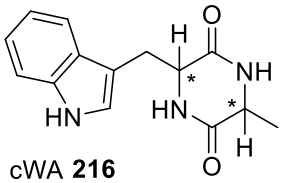

cWA **216**

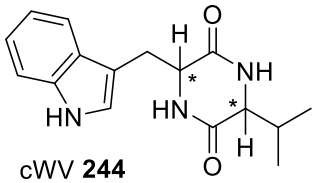

cWV **244**

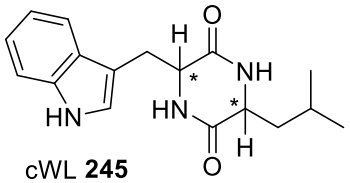

cWL **245**

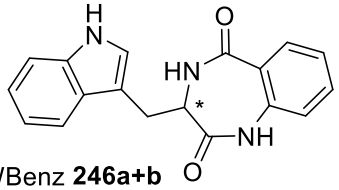

cWBenz **246a+b**

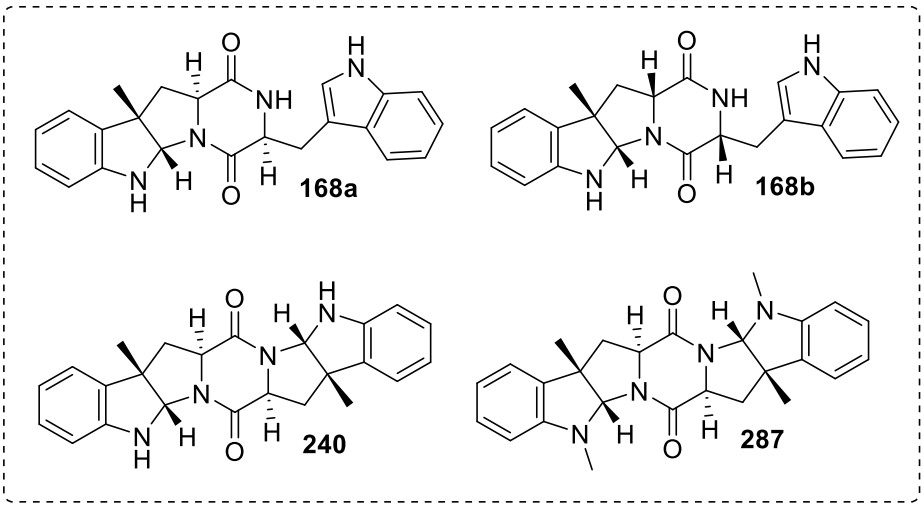
168a
168b
240
287

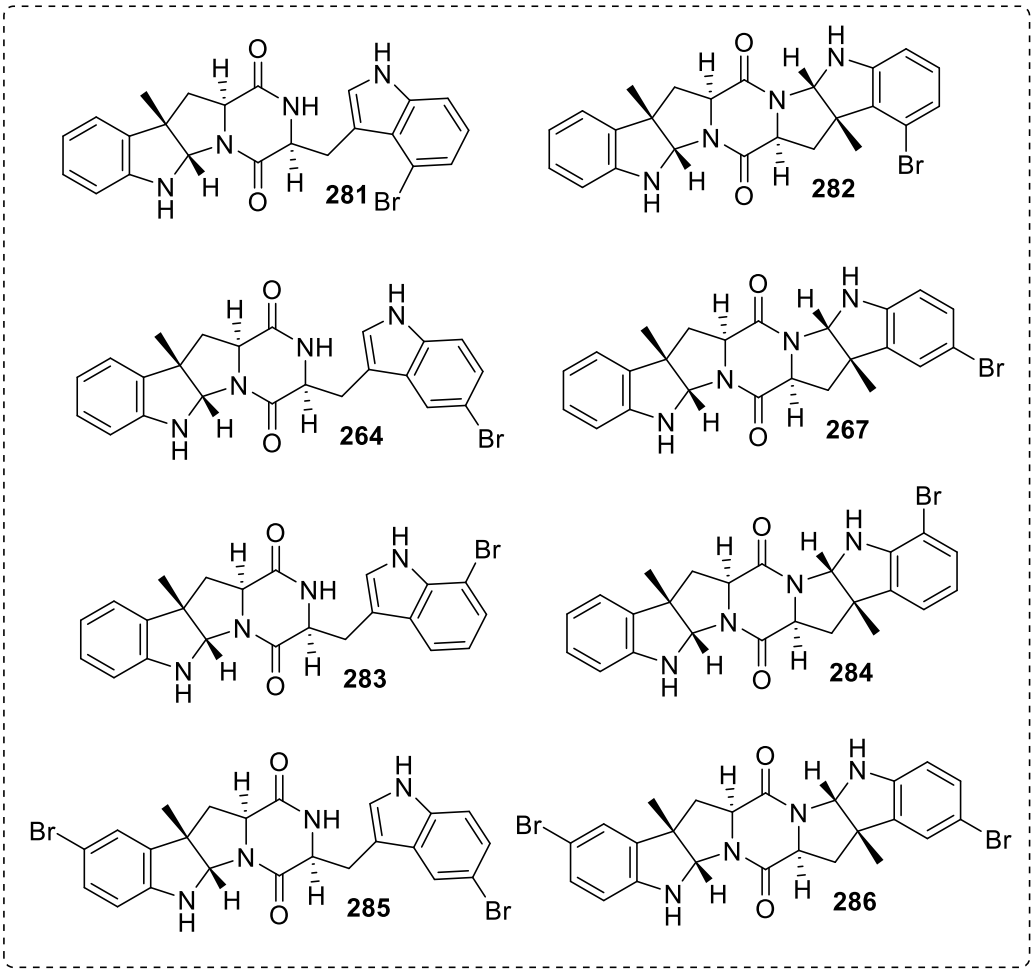
281
282
264
267
283
284
285
286

10. ACKNOWLEDGEMENTS

Am Ende dieser Arbeit möchte ich die Gelegenheit nutzen, mich bei den Menschen zu bedanken, die mich auf meinem Weg begleitet und unterstützt haben.

Mein besonderer Dank gilt dir, Jörg, für deine stets offene Tür, deine konstruktiven Rückmeldungen und die vertrauensvolle Zusammenarbeit. Deine Unterstützung und deine Bereitschaft, meine Ideen zu diskutieren und zu fördern, haben maßgeblich zum Gelingen dieser Arbeit beigetragen. Ich bin sehr froh, mich für die Promotion an deinem zweiten Zuhause – dem IBOC – entschieden zu haben. Die Begeisterung und Hingabe, mit der du deine Doktorandinnen und Doktoranden begleitest, sind wirklich außergewöhnlich. Einen Chef zu haben, der fachlich so kompetent und zugleich menschlich, nahbar und humorvoll ist, war für mich ein großes Glück und echtes Privileg.

Ebenso danke ich meinem Gutachter, Prof. Dr. Gohlke für ihre Zeit, ihr wertvolles Feedback und ihre Bereitschaft, meine Arbeit zu begutachten.

Ein herzliches Dankeschön geht an meine Kooperationspartner Dr. Benoit David und Prof. Dr. Holger Gohlke. Die produktive Zusammenarbeit und die spannenden gemeinsamen Projekte waren für diese Arbeit von großer Bedeutung. Besonders bedanken möchte ich mich außerdem bei Prof. Dr. Oliver Weiergräber für die erfolgreiche Kooperation und die stets verlässliche Kommunikation. Mir hat die Arbeit im Kristallisationslabor viel Freude bereitet und ich bin dankbar für all deine Ideen und wertvollen Beträge. Vielen Dank auch an Julia und Prof. Dr. Stephan Noack für die spannende Zusammenarbeit im Rahmen des AutoBioTech Projektes.

Ein großer Dank gilt ebenfalls den Festangestellten, die mich im Laufe der Promotion bei den alltäglichen Aufgaben unterstützt haben. Danke an Birgit - ohne dich würde das IBOC nicht so gut laufen, wie es gerade der Fall ist. Danke an Tom für die spannenden Diskussionen und Beiträge in den Seminaren. Danke an Irene und Andreas, die mir bei der Erstellung meines Titelbildes geholfen haben. Mein größter Dank gilt Bea – ich bewundere immer wieder mit welch einer Begeisterung und Neugier du deine Arbeit erledigst. Du bist mir wirklich eine sehr große Hilfe gewesen und durch deine sympathische und hilfsbereite Art war es für mich immer eine Freude, mit dir zusammen zu arbeiten.

Meinen weiteren Kolleginnen und Kollegen möchte ich herzlich für den inspirierenden fachlichen Austausch, die angenehme Arbeitsatmosphäre und das gemeinsame Durchstehen von Höhen und Tiefen im Forschungsalltag danken. Eure Unterstützung, Diskussionen und der Humor im Labor haben den Weg deutlich erleichtert.

Ein herzliches Dankeschön geht an das Team *Methylution* – Diana, Ben und Lisa. Ohne euch wäre die Zeit im Labor nur halb so schön gewesen. Danke für eure Unterstützung, eure wertvollen Tipps und für all die gemeinsamen Teepausen.

Teresa, dank dir habe ich mich vom ersten Moment am IBOC willkommen und wohlgefühlt. Unsere Gespräche im Auto oder auf Spaziergängen zum Seecasino waren für mich oft wie kleine Therapiesitzungen – ich habe mich selten so schnell verstanden gefühlt. Danke auch an Marvin, der nicht nur meine Arbeit korrigiert hat, sondern auch immer mit mehr oder weniger wertvollen Kommentaren glänzt. Danke auch an Moritz, Bene und Lisa für all die Sushi-Dates und Tanzeinlagen bei Siggi.

Ein besonderer Dank gilt auch Vicky und Cornelius. Gerade im letzten Jahr meiner Promotion seid ihr mir sehr ans Herz gewachsen. Ich habe selten so oft Tränen gelacht wie mit euch. Und auch wenn ihr beide manchmal daran zweifelt – *Ihr reicht halt auch immer!* Vielen Dank für all die getrunkenen Aperols und Weine, vielen Dank für den Tequila und das Dosenbier. In diesem Zusammenhang auch vielen Dank an die Malle-Gang! Danke auch an Marisa, Stina und Simon für die Motivation – nicht nur beim Sport. Simon, bereits als Masterstudent hast du mich überzeugt – aber du bist ein noch besserer Doktorand geworden und ich bin froh, dass du an unserem Thema weiter arbeitest. Ein herzlicher Dank gilt auch allen Studierenden – insbesondere Elias – die an diesem Thema mitgewirkt und wertvolle Beiträge geleistet haben.

Außerdem möchte ich mich herzlich bei Mella und Marcel bedanken. Wir haben uns am ersten Tag meines Studiums kennengelernt – und seitdem so ziemlich jedes Praktikum gemeinsam durchgestanden. Ich bin wirklich froh, dass wir diesen Weg zusammen gegangen sind.

Ein großes Dankeschön geht auch an Anja und Alex, die ich während meiner Zeit bei Jan Deska in Helsinki kennenlernen durfte. Danke für die schöne gemeinsame Zeit, eure Unterstützung und den tollen Austausch – in und außerhalb des Labors.

Meinen Freundinnen und Freunden danke ich von Herzen für ihre Freundschaft, ihr Verständnis und ihre Geduld in Zeiten, in denen ich wenig Zeit und Kopf für andere Dinge hatte. Ihr habt mich immer wieder daran erinnert, wie wichtig es ist, auch abseits des Labors das Leben zu genießen, durchzuatmen und den Blick für das Wesentliche nicht zu verlieren.

Ein großes Dankeschön gilt Sven, der mir in all den Jahren des Studiums und der Promotion mit großer Geduld, Verständnis und Liebe zur Seite gestanden hat. Du bist nicht nur mein Ruhepol, sondern auch mein größter Unterstützer in schwierigen Momenten. Du hast mir zugehört – bei jedem Vortrag, bei jeder Idee, bei jedem Frust. Ohne dich an meiner Seite hätte ich viele Herausforderungen nicht so gut bewältigt. Danke – für einfach alles!

Ein besonderer Dank gilt meiner Familie – vor allem meinen Eltern – für ihre unerschütterliche Unterstützung, ihren Rückhalt und ihr Vertrauen in mich.

Mama, du bist mein größtes Vorbild. Deine Stärke, deine Freundlichkeit und dein unermüdlicher Glaube an mich haben mir schon so oft gezeigt, dass ich alles schaffen kann, was ich mir vornehme. Mit dir an meiner Seite war ich nie allein.

Papa, du fehlst. Ich hätte so gerne mit dir gemeinsam diesen Moment erlebt – das Ende der Promotion. Und auch wenn du nicht mehr da bist, weiß ich: Du wärst überglücklich gewesen. Wahrscheinlich wärst du vor Stolz geplatzt, hättest es aber wie immer still und mit einem warmen Lächeln gezeigt. Diese Arbeit ist nicht nur das Ergebnis jahrelanger Forschung – sie ist auch dein Verdienst.

Und deshalb ist sie dir gewidmet.

11. EXPLANATION

Ich versichere an Eides statt, dass die Dissertation von mir selbständig und ohne unzulässige fremde Hilfe unter Beachtung der „Grundsätze zur Sicherung guter wissenschaftlicher Praxis an der Heinrich-Heine-Universität Düsseldorf“ erstellt worden ist. Die vorliegende Dissertation wurde ausschließlich an der Mathematisch-Naturwissenschaftlichen Fakultät der Heinrich-Heine-Universität Düsseldorf vorgelegt. Es wurde zuvor kein weiterer Promotionsversuch unternommen.

Mona Haase

12. LITERATURE

[1] A. Zhang, A. L. Demain, in *Natural Products and Drug Discovery*, Humana Press, **2005**, pp. 3-29.

[2] D. A. Dias, S. Urban, U. Roessner, *Metabolites* **2012**, *2*, 303-336; 'A historical overview of natural products in drug discovery', 10.3390/metabo2020303.

[3] D. J. Newman, G. M. Cragg, K. M. Snader, *Nat. Prod. Rep.* **2000**, *17*, 215-234; 'The influence of natural products upon drug discovery', 10.1039/A902202C.

[4] M. R. Montinari, S. Minelli, R. De Caterina, *Vasc. Pharmacol.* **2019**, *113*, 1-8; 'The first 3500 years of aspirin history from its roots - A concise summary', 10.1016/j.vph.2018.10.008.

[5] H. Leroux, *J. Chem. Med.* **1830**, *6*, 341; 'Découverte de la salicine'.

[6] O. Kayser, in *Von den Molukken zu Molekülen: Wie Naturstoffe Geschichte schreiben*, Springer, **2024**, pp. 77-128.

[7] F. von Heyden, *Die Salicylsäure und ihre Unwendung in der Medicin, der Technik und im Hause*, Barth, **1876**.

[8] H. Dreser, *Pflügers Arch.* **1899**, *76*, 306-318; 'Pharmakologisches über Aspirin (Acetylsalicylsäure)', 10.1007/BF01662127.

[9] G. Schwedt, *Einführung in die pharmazeutische Chemie: an Beispielen aus der Hausapotheke*, Springer Spektum, **2019**.

[10] P. Ding, Y. Ding, *Trends Plant Sci.* **2020**, *25*, 549-565; 'Stories of salicylic acid: a plant defense hormone', 10.1016/j.tplants.2020.01.004.

[11] K. Schrör, in *Acetylsalicylsäure im Kardiovaskulären System*, **1996**, pp. 3-11.

[12] R. M. Botting, *Pharmacol. Rep.* **2010**, *62*, 518-525; 'Vane's discovery of the mechanism of action of aspirin changed our understanding of its clinical pharmacology', 10.1016/S1734-1140(10)70308-X.

[13] S. Ferreira, S. Moncada, J. Vane, *Nat. New Biol.* **1971**, *231*, 237-239; 'Indomethacin and aspirin abolish prostaglandin release from the spleen', 10.1038/newbio231237a0.

[14] J. R. Hanson, *Natural products: the secondary metabolites, Vol. 17*, Royal Society of Chemistry, **2003**.

[15] V. L. Challinor, H. B. Bode, *Ann. N. Y. Acad. Sci.* **2015**, *1354*, 82-97; 'Bioactive natural products from novel microbial sources', 10.1111/nyas.12954.

[16] D. Jakubczyk, F. Dussart, *Molecules* **2020**, *25*, 911; 'Selected fungal natural products with antimicrobial properties', 10.3390/molecules25040911.

[17] A. G. Atanasov, B. Waltenberger, E.-M. Pferschy-Wenzig, T. Linder, C. Wawrosch, P. Uhrin, V. Temml, L. Wang, S. Schwaiger, E. H. Heiss, J. M. Rollinger, D. Schuster, J. M. Breuss, V. Bochkov, M. D. Mihovilovic, B. Kopp, R. Bauer, V. M. Dirsch, H. Stuppner, *Biotechnol. Adv.* **2015**, *33*, 1582-1614; 'Discovery and resupply of pharmacologically active plant-derived natural products: A review', 10.1016/j.biotechadv.2015.08.001.

[18] D. J. Newman, G. M. Cragg, *J. Nat. Prod.* **2020**, *83*, 770-803; 'Natural products as sources of new drugs over the nearly four decades from 01/1981 to 09/2019', 10.1021/acs.jnatprod.9b01285.

[19] A. Fleming, *Br. J. Exp. Pathol.* **1929**, *10*, 226; 'On the antibacterial action of cultures of a penicillium, with special reference to their use in the isolation of B. influenzae'.

[20] D. D. Baker, M. Chu, U. Oza, V. Rajgarhia, *Nat. Prod. Rep.* **2007**, *24*, 1225-1244; 'The value of natural products to future pharmaceutical discovery', 10.1039/B602241N.

[21] F. Von Nussbaum, M. Brands, B. Hinzen, S. Weigand, D. Häbich, *Angew. Chem., Int. Ed.* **2006**, *45*, 5072-5129; 'Antibacterial natural products in medicinal chemistry - exodus or revival?', 10.1002/anie.200600350.

[22] D. G. Corley, R. C. Durley, *J. Nat. Prod.* **1994**, *57*, 1484-1490; 'Strategies for database dereplication of natural products', 10.1021/np50113a002.

[23] S. M. Colegate, R. J. Molyneux, *Bioactive natural products: detection, isolation, and structural determination*, CRC press, **2007**.

[24] U. Roessner, A. Nahid, B. Chapman, A. Hunter, M. Bellgard, in *Comprehensive Biotechnology (Second Edition)*, Academic Press, **2011**, pp. 447-459.

[25] A. H. Banday, N. ul Azha, R. Farooq, S. A. Sheikh, M. A. Ganie, M. N. Parray, H. Mushtaq, I. Hameed, M. A. Lone, *Phytochem. Lett.* **2024**, *59*, 124-135; 'Exploring the potential of marine natural products in drug development: A comprehensive review', 10.1016/j.phytol.2024.01.001.

[26] A. R. Carroll, B. R. Copp, T. Grkovic, R. A. Keyzers, M. R. Prinsep, *Nat. Prod. Rep.* **2024**, *41*, 162-207; 'Marine natural products', 10.1039/D3NP00061C.

[27] E. Montuori, C. A. Hyde, F. Crea, J. Golding, C. Lauritano, *Int. J. Mol. Sci.* **2023**, *24*, 1435; 'Marine Natural products with activities against prostate Cancer: recent discoveries', 10.3390/ijms24021435.

[28] C. F. Stratton, D. J. Newman, D. S. Tan, *Bioorg. Med. Chem. Lett.* **2015**, *25*, 4802-4807; 'Cheminformatic comparison of approved drugs from natural product versus synthetic origins', 10.1016/j.bmcl.2015.07.014.
[29] F. E. Koehn, G. T. Carter, *Nat. Rev. Drug Discov.* **2005**, *4*, 206-220; 'The evolving role of natural products in drug discovery', 10.1038/nrd1657.
[30] Z. Guo, *Acta Pharm. Sin.* **2017**, *7*, 119-136; 'The modification of natural products for medical use', 10.1016/j.apsb.2016.06.003.
[31] W. Z. Shou, *J. Pharm. Anal.* **2020**, *10*, 201-208; 'Current status and future directions of high-throughput ADME screening in drug discovery', 10.1016/j.jpha.2020.05.004.
[32] M. D. Shultz, *J. Med. Chem.* **2018**, *62*, 1701-1714; 'Two decades under the influence of the rule of five and the changing properties of approved oral drugs: miniperspective', 10.1021/acs.jmedchem.8b00686.
[33] C. A. Lipinski, F. Lombardo, B. W. Dominy, P. J. Feeney, *Adv. Drug Deliv. Rev.* **2012**, *64*, 4-17; 'Experimental and computational approaches to estimate solubility and permeability in drug discovery and development settings', 10.1016/j.addr.2012.09.019.
[34] M. P. Pollastri, *Curr. Protoc. Pharmacol.* **2010**, *49*, 9.12. 11-19.12. 18; 'Overview on the Rule of Five', 10.1002/widm.1231.
[35] C. Sohrabi, Z. Alsafi, N. O'neill, M. Khan, A. Kerwan, A. Al-Jabir, C. Iosifidis, R. Agha, *Int. J. Surg.* **2020**, *76*, 71-76; 'World Health Organization declares global emergency: A review of the 2019 novel coronavirus (COVID-19)', 10.1016/j.ijsu.2020.02.034.
[36] D.-h. Zhang, K.-l. Wu, X. Zhang, S.-q. Deng, B. Peng, *J. Integr. Med.* **2020**, *18*, 152-158; 'In silico screening of Chinese herbal medicines with the potential to directly inhibit 2019 novel coronavirus', 10.1016/j.joim.2020.02.005.
[37] A. L. Hopkins, G. M. Keserü, P. D. Leeson, D. C. Rees, C. H. Reynolds, *Nat. Rev. Drug Discov.* **2014**, *13*, 105-121; 'The role of ligand efficiency metrics in drug discovery', 10.1038/nrd4163.
[38] B. Liu, J. Zhou, *J. Comput. Chem.* **2005**, *26*, 484-490; 'SARS-CoV protease inhibitors design using virtual screening method from natural products libraries', 10.1002/jcc.20186.
[39] S.-Q. Wang, Q.-S. Du, K. Zhao, A.-X. Li, D.-Q. Wei, K.-C. Chou, *Amino Acids* **2007**, *33*, 129-135; 'Virtual screening for finding natural inhibitor against cathepsin-L for SARS therapy', 10.1007/s00726-006-0403-1.

[40] J. S. Mani, J. B. Johnson, J. C. Steel, D. A. Broszczak, P. M. Neilsen, K. B. Walsh, M. Naiker, *Virus Res.* **2020**, *284*, 197989; 'Natural product-derived phytochemicals as potential agents against coronaviruses: A review', 10.1016/j.virusres.2020.197989.
[41] L. Pinzi, G. Rastelli, *Int. J. Mol. Sci.* **2019**, *20*, 4331; 'Molecular docking: shifting paradigms in drug discovery', 10.3390/ijms20184331.
[42] M. Kontoyianni, *Meth. Mol. Biol.* **2017**, 255-266; 'Docking and virtual screening in drug discovery', 10.1007/978-1-4939-7201-2_18.
[43] X.-Y. Meng, H.-X. Zhang, M. Mezei, M. Cui, *Curr. Comput.-Aided Drug Des.* **2011**, *7*, 146-157; 'Molecular docking: a powerful approach for structure-based drug discovery', 10.2174/157340911795677602.
[44] P. Ruiz-Sanchis, S. A. Savina, F. Albericio, M. Alvarez, *Chem. Eur. J.* **2011**, *17*, 1388-1408; 'Structure, Bioactivity and Synthesis of Natural Products with Hexahydropyrrolo[2, 3-b]indole', 10.1002/chem.201001451.
[45] A. D. Borthwick, *Chem. Rev.* **2012**, *112*, 3641-3716; '2, 5-Diketopiperazines: synthesis, reactions, medicinal chemistry, and bioactive natural products', 10.1021/cr200398y.
[46] T. Amador, L. Verotta, D. Nunes, E. Elisabetsky, *Planta Med.* **2000**, *66*, 770-772; 'Antinociceptive profile of hodgkinsine', 10.1055/s-2000-9604.
[47] G.-J. Mei, W. L. Koay, C. X. A. Tan, Y. Lu, *Chem. Soc. Rev.* **2021**, *50*, 5985-6012; 'Catalytic asymmetric preparation of pyrroloindolines: strategies and applications to total synthesis', 10.1039/D0CS00530D.
[48] L. M. Repka, S. E. Reisman, *J. Org. Chem.* **2013**, *78*, 12314-12320; 'Recent developments in the catalytic, asymmetric construction of pyrroloindolines bearing all-carbon quaternary stereocenters', 10.1021/jo4017953.
[49] J. E. Spangler, H. M. Davies, *J. Am. Chem. Soc.* **2013**, *135*, 6802-6805; 'Catalytic asymmetric synthesis of pyrroloindolines via a rhodium (II)-catalyzed annulation of indoles', 10.1021/ja4025337.
[50] Z. Zhang, J. C. Antilla, *Angew. Chem. Int. Ed.* **2012**, *47*, 11778-11782; 'Enantioselective Construction of Pyrroloindolines Catalyzed by Chiral Phosphoric Acids: Total Synthesis of (−)-Debromoflustramine B', 10.1002/anie.201203553.
[51] B. M. Trost, J. Quancard, *J. Am. Chem. Soc.* **2006**, *128*, 6314-6315; 'Palladium-catalyzed enantioselective C-3 allylation of 3-substituted-1 H-indoles using trialkylboranes', 10.1021/ja0608139.

[52] P. Tuntiwachwuttikul, T. Taechowisan, A. Wanbanjob, S. Thadaniti, W. C. Taylor, *Tetrahedron* **2008**, *64*, 7583-7586; 'Lansai A–D, secondary metabolites from Streptomyces sp. SUC1', 10.1016/j.tet.2008.05.104.

[53] H. Wang, S. E. Reisman, *Angew. Chem., Int. Ed.* **2014**, *53*, 6206-6210; 'Enantioselective Total Synthesis of (−)-Lansai B and (+)-Nocardioazines A and B', 10.1002/anie.201402571.

[54] R. Raju, A. M. Piggott, X.-C. Huang, R. J. Capon, *Org. Lett.* **2011**, *13*, 2770-2773; 'Nocardioazines: A novel bridged diketopiperazine scaffold from a marine-derived bacterium inhibits P-glycoprotein', 10.1021/ol200904v.

[55] M. Wang, X. Feng, L. Cai, Z. Xu, T. Ye, *ChemComm* **2012**, *48*, 4344-4346; 'Total synthesis and absolute configuration of nocardioazine B', 10.1039/C2CC31025B.

[56] T. M. Khopade, K. Ajayan, D. M. Vincent, A. L. Lane, R. Viswanathan, *J. Org. Chem.* **2022**, *87*, 11519-11533; 'Biomimetic total synthesis of (+)-nocardioazine B and analogs', 10.1021/acs.joc.2c01120.

[57] X. Shen, J. Zhao, Y. Xi, W. Chen, Y. Zhou, X. Yang, H. Zhang, *J. Org. Chem.* **2018**, *83*, 14507-14517; 'Enantioselective Total Synthesis of (+)-Nocardioazine B', 10.1021/acs.joc.8b02329.

[58] G. Deletti, S. D. Green, C. Weber, K. N. Patterson, S. S. Joshi, T. M. Khopade, M. Coban, J. Veek-Wilson, T. R. Caulfield, R. L. Viswanathan, Amy L., *Nat. Commun.* **2023**, *14*, 2558; 'Unveiling an indole alkaloid diketopiperazine biosynthetic pathway that features a unique stereoisomerase and multifunctional methyltransferase', 10.1038/s41467-023-38168-3.

[59] C. Sun, W. Tian, Z. Lin, X. Qu, *Nat. Prod. Rep.* **2022**, *39*, 1721-1765; 'Biosynthesis of pyrroloindoline-containing natural products', 10.1039/D2NP00030J.

[60] C. Prasad, *Peptides* **1995**, *16*, 151-164; 'Bioactive cyclic dipeptides', 10.1016/0196-9781(94)00017-Z.

[61] M. B. Martins, I. Carvalho, *Tetrahedron* **2007**, *63*, 9923-9932; 'Diketopiperazines: biological activity and synthesis', 10.1016/j.tet.2007.04.105.

[62] S. Hirano, S. Ichikawa, A. Matsuda, *Bioorg. Med. Chem. Lett.* **2008**, *16*, 428-436; 'Design and synthesis of diketopiperazine and acyclic analogs related to the caprazamycins and liposidomycins as potential antibacterial agents', 10.1016/j.bmc.2007.09.022.

[63] R. R. King, L. A. Calhoun, *Phytochem.* **2009**, *70*, 833-841; 'The thaxtomin phytotoxins: sources, synthesis, biosynthesis, biotransformation and biological activity', 10.1016/j.phytochem.2009.04.013.

[64] H. Izumida, M. Nishijima, T. Takadera, A. M. Nomoto, H. Sano, *J. Antibiot.* **1996**, *49*, 829-831; 'The effect of chitinase inhibitors, cyclo (Arg-Pro) against cell separation of Saccharomyces cerevisiae and the morphological change of Candida albicans', 10.7164/antibiotics.49.829.

[65] E. Van der Merwe, D. Huang, D. Peterson, G. Kilian, P. Milne, M. Van de Venter, C. Frost, *Peptides* **2008**, *29*, 1305-1311; 'The synthesis and anticancer activity of selected diketopiperazines', 10.1016/j.peptides.2008.03.010.

[66] S. Zhao, K. S. Smith, A. M. Deveau, C. M. Dieckhaus, M. A. Johnson, T. L. Macdonald, J. M. Cook, *J. Med. Chem.* **2002**, *45*, 1559-1562; 'Biological activity of the tryprostatins and their diastereomers on human carcinoma cell lines', 10.1021/jm0155953.

[67] S. Sinha, R. Srivastava, E. De Clercq, R. K. Singh, *Nucleos. Nucleot. Nucl.* **2004**, *23*, 1815-1824; 'Synthesis and antiviral properties of arabino and ribonucleosides of 1, 3-dideazaadenine, 4-nitro-1, 3-dideazaadenine and diketopiperazine', 10.1081/NCN-200040614.

[68] S. Nakajima, K. Watashi, H. Ohashi, S. Kamisuki, J. Izaguirre-Carbonell, A. T.-J. Kwon, H. Suzuki, M. Kataoka, S. Tsukuda, M. Okada, *J. Virol.* **2016**, *90*, 9058-9074; 'Fungus-derived neoechinulin B as a novel antagonist of liver X receptor, identified by chemical genetics using a hepatitis C virus cell culture system', 10.1128/jvi.00856-16.

[69] A. Minelli, S. Grottelli, A. Mierla, F. Pinnen, I. Cacciatore, I. Bellezza, *Int. J. Biochem. Cell Biol.* **2012**, *44*, 525-535; 'Cyclo (His-Pro) exerts anti-inflammatory effects by modulating NF-κB and Nrf2 signalling', 10.1016/j.biocel.2011.12.006.

[70] L. Adler-Abramovich, D. Aronov, P. Beker, M. Yevnin, S. Stempler, L. Buzhansky, G. Rosenman, E. Gazit, *Nat. Nanotechnol.* **2009**, *4*, 849-854; 'Self-assembled arrays of peptide nanotubes by vapour deposition', 10.1038/nnano.2009.298.

[71] Z. Xie, A. Zhang, L. Ye, X. Wang, Z.-g. Feng, *J. Mater. Chem.* **2009**, *19*, 6100-6102; 'Shear-assisted hydrogels based on self-assembly of cyclic dipeptide derivatives', 10.1039/B912020C

[72] S. Manchineella, T. Govindaraju, *ChemPlusChem* **2017**, *82*, 88-106; 'Molecular self-assembly of cyclic dipeptide derivatives and their applications', 10.1002/cplu.201600450.

[73] J. D. Hirst, B. J. Persson, *J. Phys. Chem. A* **1998**, *102*, 7519-7524; 'Ab initio calculations of the vibrational and electronic spectra of diketopiperazine', 10.1021/jp982423h.

[74] C.-B. Cui, H. Kakeya, G. Okada, R. Onose, M. Ubukata, I. Takahashi, K. Isono, H. Osada, *J. Antibiot.* **1995**, *48*, 1382-1384; 'Tryprostatins A and B, novel mammalian cell cycle inhibitors produced by Aspergillus fumigatus', 10.7164/antibiotics.48.1382.

[75] K. Kanoh, S. Kohno, T. Asari, T. Harada, J. Katada, M. Muramatsu, H. Kawashima, H. Sekiya, I. Uno, *BMCL* **1997**, *7*, 2847-2852; '(−)-Phenylahistin: a new mammalian cell cycle inhibitor produced by Aspergillus ustus', 10.1016/S0960-894X(97)10104-4.

[76] K. Kanoh, S. Kohno, J. Katada, Y. Hayashi, M. Muramatsu, I. Uno, *Biosci. Biotechnol. Biochem.* **1999**, *63*, 1130-1133; 'Antitumor activity of phenylahistin in vitro and in vivo', 10.1271/bbb.63.1130.

[77] D. Tian, X. Gou, J. Jia, J. Wei, M. Zheng, W. Ding, H. Bi, B. Wu, J. Tang, *Fitoterapia* **2022**, *156*, 105095; 'New diketopiperazine alkaloid and polyketides from marine-derived fungus Penicillium sp. TW58-16 with antibacterial activity against Helicobacter pylori', 10.1016/j.fitote.2021.105095.

[78] N. Shimazaki, I. Shima, M. Okamoto, K. Yoshida, K. Hemmi, M. Hashimoto, in *Platelet-Activating Factor and Structurally Related Alkyl Ehter Lipids*, AOCS Publishing, **1992**, pp. 223-226.

[79] A. Kohler, *Justus Liebigs Ann. Chem.* **1865**, *134*, 367-372; 'Ueber eine neue Verwandlung des Leucins'.

[80] T. Curtius, F. Goebel, *J. Prakt. Chem* **1888**, *37*, 173-181; 'Ueber Glycinanhydrid und seine Verbindungen'.

[81] P. M. Fischer, *J. Pept. Sci.* **2003**, *9*, 9-35; 'Diketopiperazines in peptide and combinatorial chemistry', 10.1002/psc.446.

[82] J. Peng, D. L. Clive, *J. Org. Chem.* **2009**, *74*, 513-519; 'Asymmetric synthesis of the ABC-ring system of the antitumor antibiotic MPC1001', 10.1021/jo802344t.

[83] K. M. Depew, S. P. Marsden, D. Zatorska, A. Zatorski, W. G. Bornmann, S. J. Danishefsky, *J. Am. Chem. Soc.* **1999**, *121*, 11953-11963; 'Total synthesis of 5-N-acetylardeemin and amauromine: Practical routes to potential MDR reversal agents', 10.1021/ja991558d.

[84] S. D. Bull, S. G. Davies, W. O. Moss, *Tetrahedron: Asymmetr.* **1998**, *9*, 321-327; 'Practical synthesis of Schöllkopf's bis-lactim ether chiral auxiliary:(3S)-3,6-dihydro-2,5-dimethoxy-3-isopropyl-pyrazine', 10.1016/S0957-4166(97)00623-X.

[85] J. R. Cochrane, J. M. White, U. Wille, C. A. Hutton, *Org. Lett.* **2012**, *14*, 2402-2405; 'Total synthesis of mycocyclosin', 10.1021/ol300831t.

[86] M. Tullberg, M. Grøtli, K. Luthman, *Tetrahedron* **2006**, *62*, 7484-7491; 'Efficient synthesis of 2,5-diketopiperazines using microwave assisted heating', 10.1016/j.tet.2006.05.010.

[87] N. Alqahtani, S. K. Porwal, E. D. James, D. M. Bis, J. A. Karty, A. L. Lane, R. Viswanathan, *Org. Biomol. Chem.* **2015**, *13*, 7177-7192; 'Synergism between genome sequencing, tandem mass spectrometry and bio-inspired synthesis reveals insights into nocardioazine B biogenesis', 10.1039/C5OB00537J.
[88] I. Ugi, in *Angew. Chem., Int. Ed., Vol. 71*, **1959**, pp. 373-388.
[89] R. W. Armstrong, A. P. Combs, P. A. Tempest, S. D. Brown, T. A. Keating, *Acc. Chem. Res.* **1996**, *29*, 123-131; 'Multiple-component condensation strategies for combinatorial library synthesis', 10.1021/ar9502083.
[90] C. Hulme, V. Gore, *Curr. Med. Chem.* **2003**, *10*, 51-80; '"Multi-component reactions: emerging chemistry in drug discovery" 'from xylocain to crixivan", 10.2174/0929867033368600.
[91] A. Hazra, P. Paira, P. Palit, S. Banerjee, N. B. Mondal, N. P. Sahu, *J. Chem. Res.* **2007**, *2007*, 381-383; 'Synthesis of symmetrically 1,4-disubstituted piperazine-2,5-diones: a new class of antileishmanial agents', 10.3184/030823407X228254.
[92] S. S. Ramesh, R. Gattu, S. Ramesh, *Asian J. Org. Chem.* **2024**, *13*, e202300594; 'Pyrroloindoles as Therapeutically Invaluable Agents: A Review on their Diverse Synthetic Methodologies', 10.1002/ajoc.202300594.
[93] C. R. Isham, J. D. Tibodeau, W. Jin, R. Xu, M. M. Timm, K. C. Bible, *Blood* **2007**, *109*, 2579-2588; 'Chaetocin: a promising new antimyeloma agent with in vitro and in vivo activity mediated via imposition of oxidative stress', 10.1182/blood-2006-07-027326.
[94] S. Li, J. M. Finefield, J. D. Sunderhaus, T. J. McAfoos, R. M. Williams, D. H. Sherman, *J. Am. Chem. Soc.* **2012**, *134*, 788-791; 'Biochemical characterization of NotB as an FAD-dependent oxidase in the biosynthesis of notoamide indole alkaloids', 10.1021/ja2093212.
[95] Y. Ye, L. Du, X. Zhang, S. A. Newmister, M. McCauley, J. V. Alegre-Requena, W. Zhang, S. Mu, A. Minami, A. E. Fraley, M. L. Adrover-Castellano, N. A. Carney, V. V. Shende, F. Qi, H. Oikawa, H. Kato, S. Tsukamoto, R. S. Paton, R. M. Williams, D. H. Sherman, S. Li, *Nat. Catal.* **2020**, *3*, 497-506; 'Fungal-derived brevianamide assembly by a stereoselective semipinacolase', 10.1038/s41929-020-0454-9.
[96] C. Y. Lai, I. W. Lo, R. T. Hewage, Y. C. Chen, C. T. Chen, C. F. Lee, S. Lin, M. C. Tang, H. C. Lin, *Angew. Chem. Int. Ed.* **2017**, *129*, 9606-9610; 'Biosynthesis of complex indole alkaloids: elucidation of the concise pathway of okaramines', 10.1002/ange.201705501.

[97] D. G. Fujimori, S. Hrvatin, C. S. Neumann, M. Strieker, M. A. Marahiel, C. T. Walsh, *Proc. Natl. Acad. Sci.* **2007**, *104*, 16498-16503; 'Cloning and characterization of the biosynthetic gene cluster for kutznerides', 10.1073/pnas.0708242104.

[98] Z. Guo, P. Li, G. Chen, C. Li, Z. Cao, Y. Zhang, J. Ren, H. Xiang, S. Lin, J. Ju, *J. Am. Chem. Soc.* **2018**, *140*, 18009-18015; 'Design and biosynthesis of dimeric alboflavusins with biaryl linkages via regiospecific C–C bond coupling', 10.1021/jacs.8b10136.

[99] D. A. Amariei, N. Pozhydaieva, B. David, P. Schneider, T. Classen, H. Gohlke, O. H. Weiergräber, J. Pietruszka, *ACS Catal.* **2022**, *12*, 14130-14139; 'Enzymatic C3-Methylation of Indoles Using Methyltransferase PsmD─ Crystal Structure, Catalytic Mechanism, and Preparative Applications', 10.1021/acscatal.2c04240.

[100] M. Haase, B. David, B. Paschold, T. Classen, P. Schneider, N. Pozhydaieva, H. Gohlke, J. Pietruszka, *ACS Catal.* **2023**, *14*, 227-236; 'Application of the C3-Methyltransferase StspM1 for the Synthesis of the Natural Pyrroloindole Motif', 10.1021/acscatal.3c04952.

[101] W.-B. Yin, J. Cheng, S.-M. Li, *Org. Biomol. Chem.* **2009**, *7*, 2202-2207; 'Stereospecific synthesis of aszonalenins by using two recombinant prenyltransferases', 10.1039/B902413A.

[102] L. Zheng, P. Mai, A. Fan, S.-M. Li, *Org. Biomol. Chem.* **2018**, *16*, 6688-6694; 'Switching a regular tryptophan C4-prenyltransferase to a reverse tryptophan-containing cyclic dipeptide C3-prenyltransferase by sequential site-directed mutagenesis', 10.1039/C8OB01735B.

[103] J. Liu, Y. Yang, L. Harken, S.-M. Li, *J. Nat. Prod.* **2021**, *84*, 3100-3109; 'Elucidation of the streptoazine biosynthetic pathway in Streptomyces aurantiacus reveals the presence of a promiscuous prenyltransferase/cyclase', 10.1021/acs.jnatprod.1c00844.

[104] C.-Y. Gan, Y.-Y. Low, N. F. Thomas, T.-S. Kam, *J. Nat. Prod.* **2013**, *76*, 957-964; 'Rhazinilam–leuconolam–leuconoxine alkaloids from Leuconotis griffithii', 10.1021/np400214y.

[105] W.-M. Zhong, J.-F. Wang, X.-F. Shi, X.-Y. Wei, Y.-C. Chen, Q. Zeng, Y. Xiang, X.-Y. Chen, X.-P. Tian, Z.-H. Xiao, W.-M. Zhang, F.-Z. Wang, S. Zhang, *Mar. Drugs* **2018**, *16*, 136; 'Eurotiumins A–E, five new alkaloids from the marine-derived fungus Eurotium sp. SCSIO F452', 10.3390/md16040136.

[106] R. S. Chang, V. J. Lotti, R. L. Monaghan, J. Birnbaum, E. O. Stapley, M. Goetz, G. Albers-Schoenberg, A. A. Patchett, J. M. Liesch, O. D. S. Hensens, James P, *Science* **1985**, *230*, 177-179; 'A potent nonpeptide cholecystokinin antagonist selective for peripheral tissues isolated from Aspergillus alliaceus', 10.1126/science.2994227.
[107] L. A. Wessjohann, J. Keim, B. Weigel, M. Dippe, *Curr. Opin. Chem. Biol.* **2013**, *17*, 229-235; 'Alkylating enzymes', 10.1016/j.cbpa.2013.02.016.
[108] P. d. S. M. Pinheiro, L. S. Franco, C. A. M. Fraga, *Pharmaceuticals* **2023**, *16*, 1157; 'The Magic Methyl and Its Tricks in Drug Discovery and Development', 10.3390/ph16081157.
[109] R. P. Granacher, R. J. Baldessarini, *Clin. Neuropharmacol.* **1976**, *1*, 63-80; 'The usefulness of physostigmine in neurology and psychiatry'.
[110] P. Schneider, B. Henßen, B. Paschold, B. P. Chapple, M. Schatton, F. P. Seebeck, T. Classen, J. Pietruszka, *Angew. Chem. Int. Ed.* **2021**, *60*, 23412-23418; 'Biocatalytic C3-Indole Methylation—A Useful Tool for the Natural-Product-Inspired Stereoselective Synthesis of Pyrroloindoles', 10.1002/anie.202107619.
[111] W.-B. Yin, A. Grundmann, J. Cheng, S.-M. Li, *J. Biol. Chem.* **2009**, *284*, 100-109; 'Acetylaszonalenin biosynthesis in Neosartorya fischeri: Identification of the biosynthetic gene cluster by genomic mining and functional proof of the genes by biochemical investigation', 10.1074/jbc.M807606200.
[112] S.-L. Wang, H.-F. Yu, Y.-L. Xu, T. Tian, Z.-J. Zhan, W.-G. Shan, Y.-M. Ying, *Chem. Nat. Compd.* **2020**, *56*, 780-782; 'Identification of aszonalenin derivatives as α-glucosidase inhibitors from Neosartorya fischeri NRRL 181', 10.1007/s10600-020-03149-1.
[113] J.-Y. Dong, H.-P. He, Y.-M. Shen, K.-Q. Zhang, *J. Nat. Prod.* **2005**, *68*, 1510-1513; 'Nematicidal Epipolysulfanyldioxopiperazines from Gliocladium roseum', 10.1021/np0502241.
[114] J. Liu, X. Xie, S.-M. Li, *ChemComm* **2020**, *56*, 11042-11045; 'Increasing cytochrome P450 enzyme diversity by identification of two distinct cyclodipeptide dimerases', 10.1039/D0CC04772D.
[115] J. Xu, Q. Hu, W. Ding, P. Wang, Y. Di, *Nat. Prod. Res.* **2018**, *32*, 815-820; 'New asymmetrical bispyrrolidinoindoline diketopiperazines from the marine fungus Aspergillus sp. DX4H', 10.1080/14786419.2017.1363752.
[116] X. Zhang, L. Han, S.-L. You, *Chem. Sci.* **2014**, *5*, 1059-1063; 'Ir-catalyzed intermolecular asymmetric allylic dearomatization reaction of indoles', 10.1039/C3SC53019A.

[117] Y. Liu, H. Du, *Org. Lett.* **2013**, *15*, 740-743; 'Pd-catalyzed asymmetric allylic alkylations of 3-substituted indoles using chiral P/olefin ligands', 10.1021/ol3032736.
[118] M. E. Kieffer, L. M. Repka, S. E. Reisman, *J. Am. Chem. Soc.* **2012**, *134*, 5131-5137; 'Enantioselective synthesis of tryptophan derivatives by a tandem Friedel–Crafts conjugate addition/asymmetric protonation reaction', 10.1021/ja209390d.
[119] P. Dauban, G. Malik, *Angew. Chem., Int. Ed.* **2009**, *48*, 9026-9029; 'A masked 1, 3-dipole revealed from aziridines', 10.1002/anie.200904941.
[120] H. Tian, F. Peng, P. Zhang, H. Yang, H. Fu, *Org. Lett.* **2019**, *21*, 8501-8505; 'Highly enantioselective iridium-catalyzed cascade double allylation strategy: synthesis of pyrrolidinoindolines with an all-carbon quaternary stereocenter', 10.1021/acs.orglett.9b03382.
[121] J. R. Wolstenhulme, A. Cavell, M. Gredičak, R. W. Driver, M. D. Smith, *Chem. Commun.* **2014**, *50*, 13585-13588; 'A cation-directed two-component cascade approach to enantioenriched pyrroloindolines'.
[122] H. Cheng, R. Zhang, S. Yang, M. Wang, X. Zeng, L. Xie, C. Xie, J. Wu, G. Zhong, *Adv. Synth. Catal.* **2016**, *358*, 970-976; 'Assembly of Enantioenriched cis-3a,8a-Hexahydropyrrolo [2,3-b] indole Scaffolds by Silver (I)-Catalyzed Asymmetric Domino Reaction of Isocyanoacetates in the Presence of Cinchona-Derived Chiral Phosphorus Ligands', 10.1002/adsc.201500538.
[123] J. Zheng, L. Lin, L. Dai, Q. Tang, X. Liu, X. Feng, *Angew. Chem., Int. Ed.* **2017**, *56*, 13107-13111; 'Nickel-Catalyzed Conjugate Addition of Silyl Ketene Imines to In Situ Generated Indol-2-ones: Highly Enantioselective Construction of Vicinal All-Carbon Quaternary Stereocenters'.
[124] W. Kong, Q. Wang, J. Zhu, *J. Am. Chem. Soc.* **2015**, *137*, 16028-16031; 'Palladium-catalyzed enantioselective domino heck/intermolecular C–H bond functionalization: Development and application to the synthesis of (+)-esermethole', 10.1021/jacs.5b11625.
[125] J. M. Müller, C. B. W. Stark, *Angew. Chem. Int. Ed.* **2016**, *55*, 4798-4802; 'Diastereodivergent Reverse Prenylation of Indole and Tryptophan Derivatives: Total Synthesis of Amauromine, Novoamauromine, and epi-Amauromine', 10.1002/anie.201509468.
[126] E. Harnack, L. Witkowski, *Arch. Exp. Pathol. Pharmakol.* **1876**, *5*, 401-454; 'Pharmakologische Untersuchungen über das Physostigmin und Calabarin', 10.1007/BF01976905.

[127] P. L. Julian, J. Pikl, *J. Am. Chem. Soc.* **1935**, *57*, 755-757; 'Studies in the indole series. V. The complete synthesis of physostigmine (eserine)'.
[128] A. Steven, L. E. Overman, *Angew. Chem. Int. Ed.* **2007**, *46*, 5488-5508; 'Total Synthesis of Complex Cyclotryptamine Alkaloids: Stereocontrolled Construction of Quaternary Carbon Stereocenters', 10.1002/anie.200700612.
[129] L. E. Overman, Y. Shin, *Org. Lett.* **2007**, *9*, 339-341; 'Enantioselective Total Synthesis of (+)-Gliocladin C', 10.1021/ol062801y.
[130] S. K. A. Saleh, A. Hazra, M. S. Singh, S. Hajra, *J. Org. Chem.* **2022**, *87*, 8656-8671; 'Selective C3-Allylation and Formal [3+2]-Annulation of Spiro-Aziridine Oxindoles: Synthesis of 5′-Substituted Spiro[pyrrolidine-3,3′-oxindoles] and Coerulescine', 10.1021/acs.joc.2c00863.
[131] W. Wang, F. Zhang, Y. Liu, X. Feng, *Angewandte Chemie International Edition* **2022**, *61*, e202208837; 'Diastereo- and Enantioselective Construction of Vicinal All-Carbon Quaternary Stereocenters via Iridium/Europium Bimetallic Catalysis', 10.1002/anie.202208837.
[132] A. Ashimori, T. Matsuura, L. E. Overman, D. J. Poon, *J. Org. Chem.* **1993**, *58*, 6949-6951; 'Catalytic asymmetric synthesis of either enantiomer of physostigmine. Formation of quaternary carbon centers with high enantioselection by intramolecular Heck reactions of (Z)-2-butenanilides', 10.1021/jo00077a005.
[133] B. M. Trost, Y. Zhang, *J. Am. Chem. Soc.* **2006**, *128*, 4590-4591; 'Molybdenum-Catalyzed Asymmetric Allylation of 3-Alkyloxindoles: Application to the Formal Total Synthesis of (−)-Physostigmine', 10.1021/ja060560j.
[134] H. Yoon, A. D. Marchese, M. Lautens, *J. Am. Chem. Soc.* **2018**, *140*, 10950-10954; 'Carboiodination Catalyzed by Nickel', 10.1021/jacs.8b06966.
[135] A. D. Marchese, M. Wollenburg, B. Mirabi, X. Abel-Snape, A. Whyte, F. Glorius, M. Lautens, *ACS Catal.* **2020**, *10*, 4780-4785; 'Nickel-Catalyzed Enantioselective Carbamoyl Iodination: A Surrogate for Carbamoyl Iodides', 10.1021/acscatal.0c00841.
[136] J. C. Yi, C. Liu, L. X. Dai, S. L. You, *Chem. Asian J.* **2017**, *12*, 2975-2979; 'Synthesis of C3-Methyl-Substituted Pyrroloindolines and Furoindolines via Cascade Dearomatization of Indole Derivatives with Methyl Iodide', 10.1002/asia.201701151.

[137] H. Duan, M. Zhang, Z. Chen, X. Wang, F. Xiao, W. Li, *Bioorg. Chem.* **2025**, *160*, 108448; 'Unveiling a pyrroloindoline diketopiperazine biosynthetic pathway featuring a phytoene-synthase-like family prenyltransferase with distinct regioselectivity', 10.1016/j.bioorg.2025.108448.
[138] A. Minelli, I. Bellezza, S. Grottelli, F. Galli, *Amino Acids* **2008**, *35*, 283-289; 'Focus on cyclo (His-Pro): history and perspectives as antioxidant peptide', 10.1007/s00726-007-0629-6.
[139] C. Prasad, A. Peterkofsky, *JBC* **1976**, *251*, 3229-3234; 'Demonstration of pyroglutamylpeptidase and amidase activities toward thyrotropin-releasing hormone in hamster hypothalamus extracts', 10.1016/S0021-9258(17)33427-0.
[140] T. Mizuma, S. Masubuchi, S. Awazu, *J. Pharm. Pharmacol.* **1997**, *49*, 1067-1071; 'Intestinal absorption of stable cyclic glycylphenylalanine: comparison with the linear form', 10.1111/j.2042-7158.1997.tb06043.x.
[141] S.-M. Li, *Nat. Prod. Rep.* **2010**, *27*, 57-78; 'Prenylated indole derivatives from fungi: structure diversity, biological activities, biosynthesis and chemoenzymatic synthesis', 10.1039/B909987P.
[142] W. Xu, D. J. Gavia, Y. Tang, *Nat. Prod. Rep.* **2014**, *31*, 1474-1487; 'Biosynthesis of fungal indole alkaloids', 10.1039/C4NP00073K.
[143] M. Gondry, L. Sauguet, P. Belin, R. Thai, R. Amouroux, C. Tellier, K. Tuphile, M. Jacquet, S. Braud, M. Courçon, C. Masson, S. Dubois, S. Lautru, A. Lecoq, S.-i. Hashimoto, R. Genet, J.-L. Pernodet, *Nat. Chem. Biol.* **2009**, *5*, 414-420; 'Cyclodipeptide synthases are a family of tRNA-dependent peptide bond–forming enzymes', 10.1038/nchembio.175.
[144] S. Lautru, M. Gondry, R. Genet, J.-L. Pernodet, *Chem. Biol.* **2002**, *9*, 1355-1364; 'The Albonoursin Gene Cluster of *S. noursei*: Biosynthesis of Diketopiperazine Metabolites Independent of Nonribosomal Peptide Synthetases', 10.1016/S1074-5521(02)00285-5.
[145] K. Fukushima, K. Yazawa, T. Arai, *J. Antibiot.* **1973**, *26*, 175-176; 'Biological activities of albonoursin', 10.7164/antibiotics.26.175.
[146] P. Belin, M. Moutiez, S. Lautru, J. Seguin, J.-L. Pernodet, M. Gondry, *Nat. Prod. Rep.* **2012**, *29*, 961-979; 'The nonribosomal synthesis of diketopiperazines in tRNA-dependent cyclodipeptide synthase pathways', 10.1039/C2NP20010D.
[147] L. Bonnefond, T. Arai, Y. Sakaguchi, T. Suzuki, R. Ishitani, O. Nureki, *Proc. Natl. Acad. Sci.* **2011**, *108*, 3912-3917; 'Structural basis for nonribosomal peptide synthesis by an aminoacyl-tRNA synthetase paralog', 10.1073/pnas.1019480108.

[148] M. W. Vetting, S. S. Hegde, J. S. Blanchard, *Nat. Chem. Biol.* **2010**, *6*, 797-799; 'The structure and mechanism of the Mycobacterium tuberculosis cyclodityrosine synthetase', 10.1038/nchembio.440.
[149] L. Sauguet, M. Moutiez, Y. Li, P. Belin, J. Seguin, M.-H. Le Du, R. Thai, C. Masson, M. Fonvielle, J.-L. Pernodet, J.-B. Charbonnier, M. Gondry, *Nucleic Acids Res.* **2011**, *39*, 4475-4489; 'Cyclodipeptide synthases, a family of class-I aminoacyl-tRNA synthetase-like enzymes involved in non-ribosomal peptide synthesis', 10.1093/nar/gkr027.
[150] M. Moutiez, E. Schmitt, J. Seguin, R. Thai, E. Favry, P. Belin, Y. Mechulam, M. Gondry, *Nat. Commun.* **2014**, *5*, 5141; 'Unravelling the mechanism of non-ribosomal peptide synthesis by cyclodipeptide synthases', 10.1038/ncomms6141.
[151] I. B. Jacques, M. Moutiez, J. Witwinowski, E. Darbon, C. Martel, J. Seguin, E. Favry, R. Thai, A. Lecoq, S. Dubois, J.-L. Pernodet, M. Gondry, P. Belin, *Nat. Chem. Biol.* **2015**, *11*, 721-727; 'Analysis of 51 cyclodipeptide synthases reveals the basis for substrate specificity', 10.1038/nchembio.1868.
[152] M. Gondry, I. B. Jacques, R. Thai, M. Babin, N. Canu, J. Seguin, P. Belin, J.-L. Pernodet, M. Moutiez, *Front. microbiol.* **2018**, *9*, 46; 'A comprehensive overview of the cyclodipeptide synthase family enriched with the characterization of 32 new enzymes', 10.3389/fmicb.2018.00046.
[153] D. M. Gardiner, A. J. Cozijnsen, L. M. Wilson, M. S. C. Pedras, B. J. Howlett, *Mol. Microbiol.* **2004**, *53*, 1307-1318; 'The sirodesmin biosynthetic gene cluster of the plant pathogenic fungus Leptosphaeria maculans', 10.1111/j.1365-2958.2004.04215.x.
[154] R. Loria, D. R. D. Bignell, S. Moll, J. C. Huguet-Tapia, M. V. Joshi, E. G. Johnson, R. F. Seipke, D. M. Gibson, *Antonie van Leeuwenhoek* **2008**, *94*, 3-10; 'Thaxtomin biosynthesis: the path to plant pathogenicity in the genus Streptomyces', 10.1007/s10482-008-9240-4.
[155] A. Yaron, F. Naider, S. Scharpe, *Crit. Rev. Biochem. Mol. Biol.* **1993**, *28*, 31-81; 'Proline-dependent structural and biological properties of peptides and proteins', 10.3109/10409239309082572.
[156] R. M. Williams, R. J. Cox, *Acc. Chem. Res.* **2003**, *36*, 127-139; 'Paraherquamides, brevianamides, and asperparalines: laboratory synthesis and biosynthesis. An interim report', 10.1021/ar020229e.
[157] Z. Li, S. Mukamel, *J. Phys. Chem. A* **2007**, *111*, 11579-11583; 'First-principles simulation of amide and aromatic side chain ultraviolet spectroscopy of a cyclic dipeptide', 10.1021/jp075515s.

[158] T. J. Qazi, Z. Quan, A. Mir, H. Qing, *Mol. Neurobiol.* **2018**, *55*, 1026-1044; 'Epigenetics in Alzheimer's disease: perspective of DNA methylation', 10.1007/s12035-016-0357-6.
[159] E. R. Satterwhite, K. D. Mansfield, *Interdiscip. Rev. RNA* **2022**, *13*, e1681; 'RNA methyltransferase METTL16: Targets and function', 10.1002/wrna.1681.
[160] Y. Chen, X. Shao, X. Zhao, Y. Ji, X. Liu, P. Li, M. Zhang, Q. Wang, *Biomed. Pharmacother.* **2021**, *144*, 112252; 'Targeting protein arginine methyltransferase 5 in cancers: Roles, inhibitors and mechanisms', 10.1016/j.biopha.2021.112252.
[161] D. Chen, H. Ma, H. Hong, S. S. Koh, S.-M. Huang, B. T. Schurter, D. W. Aswad, M. R. Stallcup, *Science* **1999**, *284*, 2174-2177; 'Regulation of transcription by a protein methyltransferase', 10.1126/science.284.5423.2174.
[162] C. Zubieta, J. R. Ross, P. Koscheski, Y. Yang, E. Pichersky, J. P. Noel, *Plant Cell* **2003**, *15*, 1704-1716; 'Structural basis for substrate recognition in the salicylic acid carboxyl methyltransferase family', 10.1105/tpc.014548.
[163] I. d. A. A. Batista, L. A. Helguero, *Signal Transduct. Target. Ther.* **2018**, *3*, 19; 'Biological processes and signal transduction pathways regulated by the protein methyltransferase SETD7 and their significance in cancer', 10.1038/s41392-018-0017-6.
[164] M. R. Bennett, S. A. Shepherd, V. A. Cronin, J. Micklefield, *Curr. Opin. Chem. Biol.* **2017**, *37*, 97-106; 'Recent advances in methyltransferase biocatalysis', 10.1016/j.cbpa.2017.01.020.
[165] D. K. Liscombe, G. V. Louie, J. P. Noel, *Nat. Prod. Rep.* **2012**, *29*, 1238-1250; 'Architectures, mechanisms and molecular evolution of natural product methyltransferases', 10.1039/C2NP20029E.
[166] N. A. McGrath, M. Brichacek, J. T. Njardarson, *J. Chem. Educ.* **2010**, *87*, 1348-1349; 'A graphical journey of innovative organic architectures that have improved our lives', 10.1021/ed1003806.
[167] C. G. Wermuth, *The practice of medicinal chemistry*, Academic Press, **2011**.
[168] B. Testa, P.-A. Carrupt, P. Gaillard, F. Billois, P. Weber, *Pharm. Res.* **1996**, *13*, 335-343; 'Lipophilicity in molecular modeling', 10.1023/A:1016024005429.
[169] A. Mälkiä, L. Murtomäki, A. Urtti, K. Kontturi, *Eur. J. Pharm. Sci.* **2004**, *23*, 13-47; 'Drug permeation in biomembranes: in vitro and in silico prediction and influence of physicochemical properties', 10.1016/j.ejps.2004.05.009.

[170] U. Fagerholm, *Pharm. Res.* **2008**, *25*, 625-638; 'The role of permeability in drug ADME/PK, interactions and toxicity—presentation of a permeability-based classification system (PCS) for prediction of ADME/PK in humans', 10.1007/s11095-007-9397-y.
[171] P. Ginnings, R. Baum, *J. Am. Chem. Soc.* **1937**, *59*, 1111-1113; 'Aqueous solubilities of the isomeric pentanols'.
[172] E. J. Barreiro, A. E. Kümmerle, C. A. Fraga, *Chem. Rev.* **2011**, *111*, 5215-5246; 'The methylation effect in medicinal chemistry', 10.1021/cr200060g.
[173] C. S. Leung, S. S. Leung, J. Tirado-Rives, W. L. Jorgensen, *J. Med. Chem.* **2012**, *55*, 4489-4500; 'Methyl effects on protein–ligand binding', 10.1021/jm3003697.
[174] K. A. Brameld, B. Kuhn, D. C. Reuter, M. Stahl, *J. Chem. Inf. Model.* **2008**, *48*, 1-24; 'Small molecule conformational preferences derived from crystal structure data. A medicinal chemistry focused analysis', 10.1021/ci7002494.
[175] M. Donaldson, J. H. Goodchild, *Gen. Dent.* **2018**, *1*; 'Lidocaine turns 70: the evolution of dental local anesthesia'.
[176] M. Redman, *Anesth. Pain. Med.* **2011**, *1*, 95; 'Cocaine: what is the crack? A brief history of the use of cocaine as an anesthetic', 10.5812%2Fkowsar.22287523.1890.
[177] Y. A. Ruetsch, T. Boni, A. Borgeat, *Curr. Top. Med. Chem.* **2001**, *1*, 175-182; 'From cocaine to ropivacaine: the history of local anesthetic drugs', 10.2174/1568026013395335.
[178] R. Karnina, S. K. Arif, M. Hatta, A. Bukhari, *Ann. med. surg.* **2021**, *69*, 102733; 'Molecular mechanisms of lidocaine', 10.1016/j.amsu.2021.102733.
[179] T. D. Penning, J. J. Talley, S. R. Bertenshaw, J. S. Carter, P. W. Collins, S. Docter, M. J. Graneto, L. F. Lee, J. W. Malecha, J. M. Miyashiro, *J. Med. Chem.* **1997**, *40*, 1347-1365; 'Synthesis and biological evaluation of the 1,5-diarylpyrazole class of cyclooxygenase-2 inhibitors: identification of 4-[5-(4-methylphenyl)-3-(trifluoromethyl)-1H-pyrazol-1-yl] benzenesulfonamide (SC-58635, celecoxib)', 10.1021/jm960803q.
[180] L. Gong, C. F. Thorn, M. M. Bertagnolli, T. Grosser, R. B. Altman, T. E. Klein, *Pharmacogenet. genom.* **2012**, *22*, 310-318; 'Celecoxib pathways: pharmacokinetics and pharmacodynamics', 10.1097/FPC.0b013e32834f94cb.
[181] B. Meunier, S. P. De Visser, S. Shaik, *Chem. Rev.* **2004**, *104*, 3947-3980; 'Mechanism of oxidation reactions catalyzed by cytochrome P450 enzymes', 10.1021/cr020443g.

[182] H. Schönherr, T. Cernak, *Angew. Chem., Int. Ed.* **2013**, *52*, 12256-12267; 'Profound Methyl Effects in Drug Discovery and a Call for New C-H Methylation Reactions', 10.1002/anie.201303207.
[183] K. W. Kuntz, J. E. Campbell, H. Keilhack, R. M. Pollock, S. K. Knutson, M. Porter-Scott, V. M. Richon, C. J. Sneeringer, T. J. Wigle, C. J. Allain, *J. Med. Chem.* **2016**, *59*, 1556-1564; 'The importance of being me: magic methyls, methyltransferase inhibitors, and the discovery of tazemetostat', 10.1021/acs.jmedchem.5b01501.
[184] K. Raynor, H. Kong, Y. Chen, K. Yasuda, L. Yu, G. I. Bell, T. Reisine, *Mol. Pharmacol.* **1994**, *45*, 330-334; 'Pharmacological characterization of the cloned kappa-, delta-, and mu-opioid receptors', 10.1016/S0026-895X(25)09932-8.
[185] J. W. Miller, *J. Pharmacol. Exp. Ther.* **1954**, *112*, 191-196; 'The effect of N-demethylation on certain pharmacologic actions of morphine, codeine, and meperidine in the mouse', 10.1016/S0022-3565(25)11314-1.
[186] B. E. Kane, B. Svensson, D. M. Ferguson, *AAPS J.* **2006**, *8*, 126-137; 'Molecular recognition of opioid receptor ligands', 10.1208/aapsj080115.
[187] M. F. Lockett, M. Davis, *J. Pharm. Pharmacol.* **1958**, *10*, 80-85; 'The analgesic action of normorphine administered intracisternally to mice', 10.1111/j.2042-7158.1958.tb10276.x.
[188] C. Mignat, U. Wille, A. Ziegler, *Life Sci.* **1995**, *56*, 793-799; 'Affinity profiles of morphine, codeine, dihydrocodeine and their glucuronides at opioid receptor subtypes', 10.1016/0024-3205(95)00010-4.
[189] J. v. Braun, *Ber. Dtsch. Chem. Ges.* **1914**, *47*, 2312-2330; 'Untersuchungen über Morphium-Alkaloide', 10.1002/cber.191404702149.
[190] B. F. Faris, L. Small, *J. Org. Chem.* **1936**, *1*, 194-208; 'Ethers and hetero-ethers of morphine and its isomers', 10.1021/jo01231a010.
[191] E. Abdelraheem, B. Thair, R. F. Varela, E. Jockmann, D. Popadić, H. C. Hailes, J. M. Ward, A. M. Iribarren, E. S. Lewkowicz, J. N. Andexer, P.-L. Hagedoorn, U. Hanefeld, *ChemBioChem* **2022**, *23*, e202200212; 'Methyltransferases: functions and applications', 10.1002/cbic.202200212.
[192] A. W. Struck, M. L. Thompson, L. S. Wong, J. Micklefield, *ChemBioChem* **2012**, *13*, 2642-2655; 'S-adenosyl-methionine-dependent methyltransferases: highly versatile enzymes in biocatalysis, biosynthesis and other biotechnological applications', 10.1002/cbic.201200556.
[193] W.-H. Shin, D. Kihara, *Methods Mol. Biol.* **2019**, 1-13; '55 Years of the Rossmann fold', 10.1007/978-1-4939-9161-7_1.

[194] B. P. S. Chouhan, S. Maimaiti, M. Gade, P. Laurino, *Biochem.* **2018**, *58*, 166-170; 'Rossmann-fold methyltransferases: taking a “β-Turn” around their cofactor, S-adenosylmethionine', 10.1021/acs.biochem.8b00994.
[195] R. M. Kagan, S. Clarke, *Arch. Biochem. Biophys.* **1994**, *310*, 417-427; 'Widespread occurrence of three sequence motifs in diverse S-adenosylmethionine-dependent methyltransferases suggests a common structure for these enzymes', 10.1006/abbi.1994.1187.
[196] C. Zubieta, X.-Z. He, R. A. Dixon, J. P. Noel, *Nat. Struct. Biol.* **2001**, *8*, 271-279; 'Structures of two natural product methyltransferases reveal the basis for substrate specificity in plant O-methyltransferases', 10.1038/85029.
[197] P. Z. Kozbial, A. R. Mushegian, *BMC Struct. Biol.* **2005**, *5*, 1-26; 'Natural history of S-adenosylmethionine-binding proteins', 10.1186/1472-6807-5-19.
[198] S. Klimašauskas, E. Weinhold, *Trends Biotechnol.* **2007**, *25*, 99-104; 'A new tool for biotechnology: AdoMet-dependent methyltransferases', 10.1016/j.tibtech.2007.01.006.
[199] J. T. Jarrett, S. Huang, R. G. Matthews, *Biochem.* **1998**, *37*, 5372-5382; 'Methionine synthase exists in two distinct conformations that differ in reactivity toward methyltetrahydrofolate, adenosylmethionine, and flavodoxin', 10.1021/bi9730893.
[200] M. M. Dixon, S. Huang, R. G. Matthews, M. Ludwig, *Structure* **1996**, *4*, 1263-1275; 'The structure of the C-terminal domain of methionine synthase: presenting S-adenosylmethionine for reductive methylation of B12', 10.1016/S0969-2126(96)00135-9.
[201] H. L. Schubert, K. S. Wilson, E. Raux, S. C. Woodcock, M. J. Warren, *Nat. Struct. Biol.* **1998**, *5*, 585-592; 'The X-ray structure of a cobalamin biosynthetic enzyme, cobalt-precorrin-4 methyltransferase', 10.1038/846.
[202] E. Raux, H. L. Schubert, S. C. Woodcock, K. S. Wilson, M. J. Warren, *Eur. J. Biochem.* **1998**, *254*, 341-346; 'Cobalamin (vitamin B12) biosynthesis: Cloning, expression and crystallisation of the Bacillus megaterium S-adenosyl-l-methionine-dependent cobalt-precorrin-4 transmethylase CbiF', 10.1046/j.1432-1327.1998.2540341.x.
[203] A. Krishnamohan, J. E. Jackman, *Biochemistry* **2018**, *58*, 336-345; 'A family divided: distinct structural and mechanistic features of the SpoU-TrmD (SPOUT) methyltransferase superfamily', 10.1021/acs.biochem.8b01047.

[204] K. Lim, H. Zhang, A. Tempczyk, W. Krajewski, N. Bonander, J. Toedt, A. Howard, E. Eisenstein, O. Herzberg, *Proteins Struct. Funct. Bioinf.* **2003**, *51*, 56-67; 'Structure of the YibK methyltransferase from Haemophilus influenzae (HI0766): a cofactor bound at a site formed by a knot', 10.1002/prot.10323.

[205] R.-J. Liu, M. Zhou, Z.-P. Fang, M. Wang, X.-L. Zhou, E.-D. Wang, *Nucleic Acids Res.* **2013**, *41*, 7828-7842; 'The tRNA recognition mechanism of the minimalist SPOUT methyltransferase, TrmL', 10.1093/nar/gkt568.

[206] B. Xiao, C. Jing, J. R. Wilson, P. A. Walker, N. Vasisht, G. Kelly, S. Howell, I. A. Taylor, G. M. Blackburn, S. J. Gamblin, *Nature* **2003**, *421*, 652-656; 'Structure and catalytic mechanism of the human histone methyltransferase SET7/9', 10.1038/nature01378.

[207] C. Qian, M.-M. Zhou, *Cell. Mol. Life Sci.* **2006**, *63*, 2755-2763; 'SET domain protein lysine methyltransferases: Structure, specificity and catalysis', 10.1007/s00018-006-6274-5.

[208] H. Song, A. J. Burton, S. L. Shirran, J. Fahrig-Kamarauskaitė, H. Kaspar, T. W. Muir, M. Künzler, J. H. Naismith, *Angew. Chem. Int. Ed.* **2021**, *60*, 14319-14323; 'Engineering of a Peptide α-N-Methyltransferase to Methylate Non-Proteinogenic Amino Acids', 10.1002/anie.202100818.

[209] R. J. Connett, N. Kirshner, *J. Biol. Chem.* **1970**, *245*, 329-334; 'Purification and properties of bovine phenylethanolamine N-methyltransferase', 10.1016/S0021-9258(18)63396-4.

[210] E. Vitaku, D. T. Smith, J. T. Njardarson, *J. Med. Chem.* **2014**, *57*, 10257-10274; 'Analysis of the structural diversity, substitution patterns, and frequency of nitrogen heterocycles among US FDA approved pharmaceuticals: miniperspective', 10.1021/jm501100b.

[211] C. T. Walsh, *Tetrahedron Lett.* **2015**, *56*, 3075-3081; 'Nature loves nitrogen heterocycles', 10.1016/j.tetlet.2014.11.046.

[212] M. M. Heravi, V. Zadsirjan, *RSC Adv.* **2020**, *10*, 44247-44311; 'Prescribed drugs containing nitrogen heterocycles: an overview', 10.1039/D0RA09198G.

[213] M. I. Wilde, A. Markham, *Drugs* **1996**, *52*, 773-794; 'Ondansetron: a review of its pharmacology and preliminary clinical findings in novel applications', 10.2165/00003495-199652050-00010.

[214] X. Deyi, W. Linxiu, P. Shuqiu, *Fundam. Appl. Toxicol.* **1981**, *1*, 217-221; 'The inhibition and protection of cholinesterase by physostigmine and pyridostigmine against soman poisoning in vivo', 10.1016/S0272-0590(81)80061-9.

[215] A. D. Strelnik, A. S. Petukhov, I. V. Zueva, V. V. Zobov, K. A. Petrov, E. E. Nikolsky, K. V. Balakin, S. O. Bachurin, Y. G. Shtyrlin, *Bioorg. Med. Chem. Lett.* **2016**, *26*, 4092-4094; 'Novel potent pyridoxine-based inhibitors of AChE and BChE, structural analogs of pyridostigmine, with improved in vivo safety profile', 10.1016/j.bmcl.2016.06.070.

[216] M. F. Marmor, R. Kessler, *Surv. Ophthalmol.* **1999**, *44*, 153-162; 'Sildenafil (Viagra) and ophthalmology', 10.1016/S0039-6257(99)00079-X.

[217] J. Weber, P. L. McCormack, *CNS drugs* **2009**, *23*, 781-792; 'Asenapine', 10.2165/11200860-000000000-00000.

[218] D. C. Blakemore, L. Castro, I. Churcher, D. C. Rees, A. W. Thomas, D. M. Wilson, A. Wood, *Nat. Chem.* **2018**, *10*, 383-394; 'Organic synthesis provides opportunities to transform drug discovery', 10.1038/s41557-018-0021-z.

[219] Y. Chen, *Chem. Eur. J.* **2019**, *25*, 3405-3439; 'Recent advances in methylation: a guide for selecting methylation reagents', 10.1002/chem.201803642.

[220] L. L. Bengel, B. Aberle, A. N. Egler-Kemmerer, S. Kienzle, B. Hauer, S. C. Hammer, *Angew. Chem. Int. Ed.* **2021**, *60*, 5554-5560; 'Engineered Enzymes Enable Selective N-Alkylation of Pyrazoles With Simple Haloalkanes', 10.1002/anie.202014239.

[221] F. Ospina, K. H. Schülke, J. Soler, A. Klein, B. Prosenc, M. Garcia-Borràs, S. C. Hammer, *Angew. Chem. Int. Ed.* **2022**, *61*, e202213056; 'Selective Biocatalytic N-Methylation of Unsaturated Heterocycles', 10.1002/anie.202213056.

[222] O. Khersonsky, R. Lipsh, Z. Avizemer, Y. Ashani, M. Goldsmith, H. Leader, O. Dym, S. Rogotner, D. L. Trudeau, J. Prilusky, P. Amengual-Rigo, V. Guallar, D. S. Tawfik, S. J. Fleishman, *Mol. Cell* **2018**, *72*, 178-186. e175; 'Automated design of efficient and functionally diverse enzyme repertoires', 10.1016/j.molcel.2018.08.033.

[223] Y. Zhang, T. Yao, Y. Jiang, H. Li, W. Yuan, W. Li, *Appl. Environ. Microbiol.* **2021**, *87*, e02525-02520; 'Deciphering a cyclodipeptide synthase pathway encoding prenylated indole alkaloids in streptomyces leeuwenhoekii', 10.1128/AEM.02525-20.

[224] T. Yao, J. Liu, E. Jin, Z. Liu, H. Li, Q. Che, T. Zhu, D. Li, W. Li, *iScience* **2020**, *23*; 'Expanding the Structural Diversity of Drimentines by Exploring the Promiscuity of Two N-methyltransferases', 10.1016/j.isci.2020.101323.

[225] J. Liu, T. Ng, Z. Rui, O. Ad, W. Zhang, *Angew. Chem. Int. Ed.* **2014**, *53*, 136-139; 'Unusual Acetylation-Dependent Reaction Cascade in the Biosynthesis of the Pyrroloindole Drug Physostigmine', 10.1002/anie.201308069.
[226] T. Wlodarski, J. Kutner, J. Towpik, L. Knizewski, L. Rychlewski, A. Kudlicki, M. Rowicka, A. Dziembowski, K. Ginalski, *PloS One* **2011**, *6*, e23168; 'Comprehensive structural and substrate specificity classification of the Saccharomyces cerevisiae methyltransferome', 10.1371/journal.pone.0023168.
[227] Y. Zou, Q. Fang, H. Yin, Z. Liang, D. Kong, L. Bai, Z. Deng, S. Lin, *Angew. Chem. Int. Ed.* **2013**, *125*, 13189-13193; 'Stereospecific Biosynthesis of β-Methyltryptophan from L-Tryptophan Features a Stereochemical Switch', 10.1002/ange.201306255.
[228] Y. T. Huang, S. Y. Lyu, P. H. Chuang, N. S. Hsu, Y. S. Li, H. C. Chan, C. J. Huang, Y. C. Liu, C. J. Wu, W. B. L. Yang, Tsung-Lin, *ChemBioChem* **2009**, *10*, 2480-2487; 'In vitro characterization of enzymes involved in the synthesis of nonproteinogenic residue (2S, 3S)-β-methylphenylalanine in glycopeptide antibiotic mannopeptimycin', 10.1002/cbic.200900351.
[229] C. Mahlert, F. Kopp, J. Thirlway, J. Micklefield, M. A. Marahiel, *J. Am. Chem. Soc.* **2007**, *129*, 12011-12018; 'Stereospecific enzymatic transformation of α-ketoglutarate to (2 s, 3 r)-3-methyl glutamate during acidic lipopeptide biosynthesis', 10.1021/ja074427i.
[230] T. Pavkov-Keller, K. Steiner, M. Faber, M. Tengg, H. Schwab, M. Gruber-Khadjawi, K. Gruber, *PLoS One* **2017**, *12*, e0171056; 'Crystal structure and catalytic mechanism of CouO, a versatile C-methyltransferase from Streptomyces rishiriensis', 10.1371/journal.pone.0171056.
[231] S.-C. Chen, C.-H. Huang, S.-J. Lai, J.-S. Liu, P.-K. Fu, S.-T. Tseng, C. S. Yang, M.-C. Lai, T.-P. Ko, Y. Chen, *Sci. Rep.* **2015**, *5*, 10100; 'Structure and mechanism of an antibiotics-synthesizing 3-hydroxykynurenine C-methyltransferase', 10.1038/srep10100.
[232] M. C. Lemfack, W. Brandt, K. Krüger, A. Gurowietz, J. Djifack, J.-P. Jung, M. Hopf, H. Noack, B. Junker, S. P. von Reuß, Birgit, *Sci. Rep.* **2021**, *11*, 3182; 'Reaction mechanism of the farnesyl pyrophosphate C-methyltransferase towards the biosynthesis of pre-sodorifen pyrophosphate by Serratia plymuthica 4Rx13', 10.1038/s41598-021-82521-9.
[233] F. Zhao, Y. Moriwaki, T. Noguchi, K. Shimizu, T. Kuzuyama, T. Terada, *Biochem.* **2024**, *63*, 806-814; 'QM/MM Study of the Catalytic Mechanism and Substrate Specificity of the Aromatic Substrate C-Methyltransferase Fur6', 10.1021/acs.biochem.3c00556.

[234] H. Stecher, M. Tengg, B. J. Ueberbacher, P. Remler, H. Schwab, H. Griengl, M. Gruber-Khadjawi, *Angew. Chem. Int. Ed.* **2009**, *48*, 9546-9548; 'Biocatalytic Friedel–Crafts Alkylation Using Non-natural Cofactors', 10.1002/anie.200905095.
[235] H. Li, Y. Qiu, C. Guo, M. Han, Y. Zhou, Y. Feng, S. Luo, Y. Tong, G. Zheng, S. Zhu, *Chem. Commun.* **2019**, *55*, 8390-8393; 'Pyrroloindoline cyclization in tryptophan-containing cyclodipeptides mediated by an unprecedented indole C3 methyltransferase from Streptomyces sp. HPH0547', 10.1039/C9CC03745D.
[236] Sigma-Aldrich, Sigma-Aldrich, **2024**.
[237] S. Mordhorst, J. N. Andexer, *Nat. Prod. Rep.* **2020**, *37*, 1316-1333; 'Round, round we go–strategies for enzymatic cofactor regeneration', 10.1039/D0NP00004C.
[238] S. Mordhorst, J. Siegrist, M. Müller, M. Richter, J. N. Andexer, *Angew. Chem. Int. Ed.* **2017**, *56*, 4037-4041; 'Catalytic alkylation using a cyclic S-adenosylmethionine regeneration system', 10.1002/anie.201611038.
[239] C. Liao, F. P. Seebeck, *Nat. Catal.* **2019**, *2*, 696-701; 'S-adenosylhomocysteine as a methyl transfer catalyst in biocatalytic methylation reactions', 10.1038/s41929-019-0300-0.
[240] M. Fontecave, M. Atta, E. Mulliez, *Trends Biochem. Sci.* **2004**, *29*, 243-249; 'S-adenosylmethionine: nothing goes to waste', 10.1016/j.tibs.2004.03.007.
[241] S. C. Lu, *Int. J. Biochem. Cell Biol.* **2000**, *32*, 391-395; 'S-adenosylmethionine', 10.1016/S1357-2725(99)00139-9.
[242] G. D. Markham, E. Hafner, C. W. Tabor, H. Tabor, *J. Biol. Chem.* **1980**, *255*, 9082-9092; 'S-Adenosylmethionine synthetase from Escherichia coli', 10.1016/S0021-9258(19)70530-4.
[243] J. Siegrist, S. Aschwanden, S. Mordhorst, L. Thöny-Meyer, M. Richter, J. N. Andexer, *ChemBioChem* **2015**, *16*, 2576-2579; 'Regiocomplementary O-Methylation of Catechols by Using Three-Enzyme Cascades', 10.1002/cbic.201500410.
[244] C. Sommer-Kamann, A. Fries, S. Mordhorst, J. N. Andexer, M. Müller, *Angew. Chem. Int. Ed.* **2017**, *129*, 4091-4094; 'Asymmetric C-Alkylation by the S-Adenosylmethionine-Dependent Methyltransferase SgvM', 10.1002/ange.201609375.
[245] T. D. Huber, F. Wang, S. Singh, B. R. Johnson, J. Zhang, M. Sunkara, S. G. Van Lanen, A. J. Morris, G. N. Phillips Jr, J. S. Thorson, *ACS Chem. Biol.* **2016**, *11*, 2484-2491; 'Functional AdoMet isosteres resistant to classical AdoMet degradation pathways', 10.1021/acschembio.6b00348.

[246] D. Popadić, D. Mhaindarkar, M. H. D. Thai, H. C. Hailes, S. Mordhorst, J. N. Andexer, *RSC Chem. Biol.* **2021**, *2*, 883-891; 'A bicyclic S-adenosylmethionine regeneration system applicable with different nucleosides or nucleotides as cofactor building blocks', 10.1039/D1CB00033K.
[247] A. S. Eustáquio, F. Pojer, J. P. Noel, B. S. Moore, *Nat. Chem. Biol.* **2008**, *4*, 69-74; 'Discovery and characterization of a marine bacterial SAM-dependent chlorinase', 10.1038/nchembio.2007.56.
[248] J. M. Lipson, M. Thomsen, B. S. Moore, R. P. Clausen, J. J. La Clair, M. D. Burkart, *ChemBioChem* **2013**, *14*, 950; 'A Tandem Chemoenzymatic Methylation via S-Adenosyl-l-methionine', 10.1002/cbic.201300221.
[249] H. Deng, S. L. Cobb, A. R. McEwan, R. P. McGlinchey, J. H. Naismith, D. O'Hagan, D. A. Robinson, J. B. Spencer, *Angew. Chem. Int. Ed.* **2006**, *45*, 759; 'The fluorinase from Streptomyces cattleya is also a chlorinase', 10.1002/anie.200503582.
[250] J. Micklefield, *Nat. Catal.* **2019**, *2*, 644-645; 'Streamlined recycling of S-adenosylmethionine', 10.1038/s41929-019-0323-6.
[251] C. Liao, F. P. Seebeck, *Angew. Chem. Int. Ed.* **2020**, *59*, 7184-7187; 'Asymmetric β-Methylation of l-and d-α-Amino Acids by a Self-Contained Enzyme Cascade', 10.1002/anie.201916025.
[252] S. Ju, K. P. Kuzelka, R. Guo, B. Krohn-Hansen, J. Wu, S. K. Nair, Y. Yang, *Nat. Commun.* **2023**, *14*, 5704; 'A biocatalytic platform for asymmetric alkylation of α-keto acids by mining and engineering of methyltransferases', 10.1038/s41467-023-40980-w.
[253] M. T. Salinger, D. Castellano Garrido, E. D. Lamming, J. M. Ward, T. S. Moody, J. W. Jeffries, H. C. Hailes, *ChemCatChem* **2024**, e202400492; 'An Alternative Cascade for the Selective Methylation of Catechols and Tetrahydroisoquinolines by O-Methyltransferases', 10.1002/cctc.202400492.
[254] X. Wen, F. Leisinger, V. Leopold, F. P. Seebeck, *Angew. Chem. Int. Ed.* **2022**, *134*, e202208746; 'Synthetic Reagents for Enzyme-Catalyzed Methylation', 10.1002/ange.202208746.
[255] K. H. Schülke, F. Ospina, K. Hörnschemeyer, S. Gergel, S. C. Hammer, *ChemBioChem* **2022**, *23*, e202100632; 'Substrate Profiling of Anion Methyltransferases for Promiscuous Synthesis of S-Adenosylmethionine Analogs from Haloalkanes', 10.1002/cbic.202100632.
[256] Q. Tang, C. W. Grathwol, A. S. Aslan-Üzel, S. Wu, A. Link, I. V. Pavlidis, C. P. Badenhorst, U. T. Bornscheuer, *Angew. Chem. Int. Ed.* **2021**, *60*, 1524-1527; 'Directed evolution of a halide methyltransferase enables biocatalytic synthesis of diverse SAM analogs', 10.1002/anie.202013871.

[257] Q. Tang, I. V. Pavlidis, C. P. Badenhorst, U. T. Bornscheuer, *ChemBioChem* **2021**, *22*, 2584-2590; 'From natural methylation to versatile alkylations using halide methyltransferases', 10.1002/cbic.202100153.
[258] I. R. Bothwell, M. Luo, *Org. Lett.* **2014**, *16*, 3056-3059; 'Large-scale, protection-free synthesis of Se-adenosyl-L-selenomethionine analogues and their application as cofactor surrogates of methyltransferases', 10.1021/ol501169y.
[259] A. Y. Rudenko, S. Mariasina, P. Sergiev, V. Polshakov, *Mol. Biol.* **2022**, *56*, 229-250; 'Analogs of S-adenosyl-l-methionine in studies of methyltransferases', 10.1134/S002689332202011X.
[260] S. Singh, J. Zhang, T. D. Huber, M. Sunkara, K. Hurley, R. D. Goff, G. Wang, W. Zhang, C. Liu, J. Rohr, *Angew. Chem. Int. Ed.* **2014**, *53*, 3965-3969; 'Facile chemoenzymatic strategies for the synthesis and utilization of S-adenosyl-L-methionine analogues', 10.1002/anie.201308272.
[261] F. Wang, S. Singh, J. Zhang, T. D. Huber, K. E. Helmich, M. Sunkara, K. A. Hurley, R. D. Goff, C. A. Bingman, A. J. Morris, J. S. P. J. Thorson, George N, *FFEBS J.* **2014**, *281*, 4224-4239; 'Understanding molecular recognition of promiscuity of thermophilic methionine adenosyltransferase sMAT from Sulfolobus solfataricus', 10.1111/febs.12784.
[262] J. Peng, C. Liao, C. Bauer, F. P. Seebeck, *Angew. Chem. Int. Ed.* **2021**, *60*, 27178-27183; 'Fluorinated S-Adenosylmethionine as a Reagent for Enzyme-Catalyzed Fluoromethylation', 10.1002/anie.202108802.
[263] L. Hunter, *Beilstein J. Org. Chem.* **2010**, *6*, 38; 'The C–F bond as a conformational tool in organic and biological chemistry', 10.3762/bjoc.6.38.
[264] A. Postigo, *Late-stage fluorination of bioactive molecules and biologically-relevant substrates*, Elsevier, **2018**.
[265] W. Wang, H. Zhao, N. Yu, F. Chen, M. Dong, *ACS Catal.* **2023**, *13*, 13729-13734; 'Stable S-Adenosylmethionine Analogue for Enzymatic Fluoromethylation', 10.1021/acscatal.3c03313.
[266] J. R. Matos, C.-H. Wong, *Bioorg. Chem.* **1987**, *15*, 71-80; 'S-adenosylmethionine: Stability and stabilization', 10.1016/0045-2068(87)90008-3.
[267] J. Winkelblech, A. Fan, S.-M. Li, *Appl. Microbiol. Biotechnol.* **2015**, *99*, 7379-7397; 'Prenyltransferases as key enzymes in primary and secondary metabolism', 10.1007/s00253-015-6811-y.
[268] R. Mukai, *Biosci. Biotechnol. Biochem.* **2018**, *82*, 207-215; 'Prenylation enhances the biological activity of dietary flavonoids by altering their bioavailability', 10.1080/09168451.2017.1415750.

[269] K. Yazaki, K. Sasaki, Y. Tsurumaru, *Phytochem.* **2009**, *70*, 1739-1745; 'Prenylation of aromatic compounds, a key diversification of plant secondary metabolites', 10.1016/j.phytochem.2009.08.023.
[270] T. An, X. Feng, C. Li, *J. Agric. Food Chem.* **2023**, *71*, 2211-2233; 'Prenylation: a critical step for biomanufacturing of prenylated aromatic natural products', 10.1021/acs.jafc.2c07287.
[271] H.-M. Wang, L. Zhang, J. Liu, Z.-L. Yang, H.-Y. Zhao, Y. Yang, D. Shen, K. Lu, Z.-C. Fan, Q.-W. Yao, *Eur. J. Med. Chem.* **2015**, *92*, 439-448; 'Synthesis and anti-cancer activity evaluation of novel prenylated and geranylated chalcone natural products and their analogs', 10.1016/j.ejmech.2015.01.007.
[272] L. Heide, *Curr. Opin. Chem. Biol.* **2009**, *13*, 171-179; 'Prenyl transfer to aromatic substrates: genetics and enzymology', 10.1016/j.cbpa.2009.02.020.
[273] H. Y. Chang, T. H. Cheng, A. H. J. Wang, *IUBMB life* **2021**, *73*, 40-63; 'Structure, catalysis, and inhibition mechanism of prenyltransferase', 10.1002/iub.2418.
[274] W. Li, *Trends Biochem. Sci.* **2016**, *41*, 356-370; 'Bringing bioactive compounds into membranes: the UbiA superfamily of intramembrane aromatic prenyltransferases', 10.1016/j.tibs.2016.01.007.
[275] W. Cheng, W. Li, *Science* **2014**, *343*, 878-881; 'Structural insights into ubiquinone biosynthesis in membranes', 10.1126/science.1246774.
[276] I. Young, R. Leppik, J. Hamilton, F. Gibson, *J. Bacteriol.* **1972**, *110*, 18-25; 'Biochemical and genetic studies on ubiquinone biosynthesis in Escherichia coli K-12: 4-hydroxybenzoate octaprenyltransferase', 10.1128/jb.110.1.18-25.1972.
[277] H. Huang, E. J. Levin, S. Liu, Y. Bai, S. W. Lockless, M. Zhou, *PLoS Biol.* **2014**, *12*, e1001911; 'Structure of a membrane-embedded prenyltransferase homologous to UBIAD1', 10.1371/journal.pbio.1001911.
[278] T. Mori, *J. Nat. Med.* **2020**, *74*, 501-512; 'Enzymatic studies on aromatic prenyltransferases', 10.1007/s11418-020-01393-x.
[279] F. Pojer, S.-M. Li, L. Heide, *Microbiology* **2002**, *148*, 3901-3911; 'Molecular cloning and sequence analysis of the clorobiocin biosynthetic gene cluster: new insights into the biosynthesis of aminocoumarin antibiotics', 10.1099/00221287-148-12-3901.
[280] F. Pojer, E. Wemakor, B. Kammerer, H. Chen, C. T. Walsh, S.-M. Li, L. Heide, *Proc. Natl. Acad. Sci.* **2003**, *100*, 2316-2321; 'CloQ, a prenyltransferase involved in clorobiocin biosynthesis', 10.1073/pnas.0337708100.

[281] T. Kuzuyama, J. P. Noel, S. B. Richard, *Nature* **2005**, *435*, 983-987; 'Structural basis for the promiscuous biosynthetic prenylation of aromatic natural products', 10.1038/nature03668.
[282] H.-F. Tsai, H. Wang, J. C. Gebler, C. D. Poulter, C. L. Schardl, *Biochem. Biophys. Res. Commun.* **1995**, *216*, 119-125; 'The Claviceps purpurea gene encoding dimethylallyltryptophan synthase, the committed step for ergot alkaloid biosynthesis', 10.1006/bbrc.1995.2599.
[283] I. A. Unsold, S.-M. Li, *Microbiol.* **2005**, *151*, 1499-1505; 'Overproduction, purification and characterization of FgaPT2, a dimethylallyltryptophan synthase from Aspergillus fumigatus', 10.1099/mic.0.27759-0.
[284] C. M. Coyle, D. G. Panaccione, *Applied and Environmental Microbiology* **2005**, *71*, 3112-3118; 'An Ergot Alkaloid Biosynthesis Gene and Clustered Hypothetical Genes from Aspergillus fumigatus', 10.1128/AEM.71.6.3112-3118.2005.
[285] X. Yu, S.-M. Li, in *Methods Enzymol., Vol. 516*, Elsevier, **2012**, pp. 259-278.
[286] E. T. Miller, O. V. Tsodikov, S. Garneau-Tsodikova, *Nat. Prod. Rep.* **2023**; 'Structural insights into the diverse prenylating capabilities of DMATS prenyltransferases', 10.1039/D3NP00036B.
[287] R. Nagata, H. Suemune, M. Kobayashi, T. Shinada, K. Shin-ya, M. Nishiyama, T. Hino, Y. Sato, T. Kuzuyama, S. Nagano, *Angew. Chem. Int. Ed.* **2022**, *134*, e202117430; 'Structural Basis for the Prenylation Reaction of Carbazole-Containing Natural Products Catalyzed by Squalene Synthase-Like Enzymes', 10.1002/ange.202117430.
[288] M. Kobayashi, T. Tomita, K. Shin-ya, M. Nishiyama, T. Kuzuyama, *Angew. Chem. Int. Ed.* **2019**, *58*, 13349-13353; 'An unprecedented cyclization mechanism in the biosynthesis of carbazole alkaloids in streptomyces', 10.1002/anie.201906864.
[289] R. Chen, B. Gao, X. Liu, F. Ruan, Y. Zhang, J. Lou, K. Feng, C. Wunsch, S.-M. Li, J. S. Dai, Fei, *Nat. Chem. Biol.* **2017**, *13*, 226-234; 'Molecular insights into the enzyme promiscuity of an aromatic prenyltransferase', 10.1038/nchembio.2263.
[290] A. Grundmann, S.-M. Li, *Microbiol.* **2005**, *151*, 2199-2207; 'Overproduction, purification and characterization of FtmPT1, a brevianamide F prenyltransferase from Aspergillus fumigatus', 10.1099/mic.0.27962-0.
[291] H. Zou, X. Zheng, S.-M. Li, *J. Nat. Prod.* **2009**, *72*, 44-52; 'Substrate promiscuity of the cyclic dipeptide prenyltransferases from Aspergillus fumigatus', 10.1021/np800501m.

[292] M. Jost, G. Zocher, S. Tarcz, M. Matuschek, X. Xie, S.-M. Li, T. Stehle, *J. Am. Chem. Soc.* **2010**, *132*, 17849-17858; 'Structure−function analysis of an enzymatic prenyl transfer reaction identifies a reaction chamber with modifiable specificity', 10.1021/ja106817c.
[293] X. Yu, G. Zocher, X. Xie, M. Liebhold, S. Schütz, T. Stehle, S.-M. Li, *Chem. Biol.* **2013**, *20*, 1492-1501; 'Catalytic mechanism of stereospecific formation of cis-configured prenylated pyrroloindoline diketopiperazines by indole prenyltransferases', 10.1016/j.chembiol.2013.10.007.
[294] J. M. Schuller, G. Zocher, M. Liebhold, X. Xie, M. Stahl, S.-M. Li, T. Stehle, *J. Mol. Biol.* **2012**, *422*, 87-99; 'Structure and catalytic mechanism of a cyclic dipeptide prenyltransferase with broad substrate promiscuity', 10.1016/j.jmb.2012.05.033.
[295] W. B. Yin, H. L. Ruan, L. Westrich, A. Grundmann, S. M. Li, *ChemBioChem* **2007**, *8*, 1154-1161; 'CdpNPT, an N-Prenyltransferase from Aspergillus fumigatus: Overproduction, Purification and Biochemical Characterisation', 10.1002/cbic.200700079.
[296] H.-X. Zou, X.-L. Xie, U. Linne, X.-D. Zheng, S.-M. Li, *Org. Biomol. Chem.* **2010**, *8*, 3037-3044; 'Simultaneous C7-and N1-prenylation of cyclo-L-Trp-L-Trp catalyzed by a prenyltransferase from Aspergillus oryzae', 10.1039/c002850a.
[297] X. Yu, Y. Liu, X. Xie, X.-D. Zheng, S.-M. Li, *J. Biol. Chem.* **2012**, *287*, 1371-1380; 'Biochemical characterization of indole prenyltransferases: filling the last gap of prenylation positions by a 5-dimethylallyltryptophan synthase from Aspergillus clavatus', 10.1074/jbc.M111.317982.
[298] C. Wunsch, H.-X. Zou, U. Linne, S.-M. Li, *Appl. Microbiol. Biotechnol.* **2015**, *99*, 1719-1730; 'C7-prenylation of tryptophanyl and O-prenylation of tyrosyl residues in dipeptides by an Aspergillus terreus prenyltransferase', 10.1007/s00253-014-5999-6.
[299] N. Steffan, S.-M. Li, *Arch. Microbiol.* **2009**, *191*, 461-466; 'Increasing structure diversity of prenylated diketopiperazine derivatives by using a 4-dimethylallyltryptophan synthase', 10.1007/s00203-009-0467-x.
[300] X. Liu, C. T. Walsh, *Biochem.* **2009**, *48*, 11032-11044; 'Characterization of cyclo-Acetoacetyl-l-Tryptophan Dimethylallyltransferase in Cyclopiazonic Acid Biosynthesis: Substrate Promiscuity and Site Directed Mutagenesis Studies', 10.1021/bi901597j.

[301] J. Nies, S.-M. Li, *ACS Chem. Biol.* **2021**, *16*, 185-192; 'Prenylation and Dehydrogenation of a C2-Reversely Prenylated Diketopiperazine as a Branching Point in the Biosynthesis of Echinulin Family Alkaloids in Aspergillus ruber', 10.1021/acschembio.0c00874.
[302] T. Yao, J. Liu, Z. Liu, T. Li, H. Li, Q. Che, T. Zhu, D. Li, Q. Gu, W. Li, *Nat. Commun.* **2018**, *9*, 4091; 'Genome mining of cyclodipeptide synthases unravels unusual tRNA-dependent diketopiperazine-terpene biosynthetic machinery', 10.1038/s41467-018-06411-x.
[303] J. J. L. Malit, C. Wu, X. Tian, W. Liu, D. Huang, H. H. Y. Sung, L.-L. Liu, I. D. Williams, P.-Y. Qian, *Org. Lett.* **2022**, *24*, 2967-2972; 'Griseocazines: Neuroprotective Multiprenylated Cyclodipeptides Identified through Targeted Genome Mining', 10.1021/acs.orglett.2c00745.
[304] U. T. Bornscheuer, G. W. Huisman, R. J. Kazlauskas, S. Lutz, J. C. Moore, K. Robins, *Nature* **2012**, *485*, 185-194; 'Engineering the third wave of biocatalysis', 10.1038/nature11117.
[305] N. J. Turner, *Nat. Chem. Biol.* **2009**, *5*, 567-573; 'Directed evolution drives the next generation of biocatalysts', 10.1038/nchembio.203.
[306] F. H. Arnold, *Angew. Chem. Int. Ed.* **2018**, *57*, 4143-4148; 'Directed Evolution: Bringing New Chemistry to Life', 10.1002/anie.201708408.
[307] J. M. Stoddard, L. Nguyen, H. Mata-Chavez, K. Nguyen, *Chem. Commun.* **2007**, 1240-1241; 'TLC plates as a convenient platform for solvent-free reactions', 10.1039/B616311D.
[308] K. H. Asressu, Q. Zhang, *Eur. J. Lipid Sci. Technol.* **2023**, *125*, 2200096; 'Detection and Semi-Quantification of Lipids on High-Performance Thin-Layer Chromatography Plate Using Ceric Ammonium Molybdate Staining', 10.1002/ejlt.202200096.
[309] S. Suljić, J. Pietruszka, D. Worgull, *Adv. Synth. Catal.* **2015**, *357*, 1822-1830; 'Asymmetric Bio- and Organocatalytic Cascade Reaction – Laccase and Secondary Amine-Catalyzed α-Arylation of Aldehydes', 10.1002/adsc.201500183.
[310] L. Cai, *Curr. Protoc. Essent. Lab. Tech.* **2014**, *8*, 6.3.1-6.3.18; 'Thin Layer Chromatography', 10.1002/9780470089941.et0603s08.
[311] K. A. Gschneidner, J.-C. G. Bunzli, V. K. Pecharsky, *Handbook on the physics and chemistry of rare earths, Vol. 34*, Elsevier, **2005**.
[312] S. Burstein, *Anal. Chem.* **1953**, *25*, 422-424; 'Reduction of Phosphomolybdic Acid by Compounds Possessing Conjugated Double Bonds', 10.1021/ac60075a012.

[313] R. Re, N. Pellegrini, A. Proteggente, A. Pannala, M. Yang, C. Rice-Evans, *Free Radical Biol. Med.* **1999**, *26*, 1231-1237; 'Antioxidant activity applying an improved ABTS radical cation decolorization assay', 10.1016/S0891-5849(98)00315-3.
[314] A. L. Hensley, A. R. Colley, A. E. Ross, *Anal. Chem.* **2018**, *90*, 8642-8650; 'Real-Time Detection of Melatonin Using Fast-Scan Cyclic Voltammetry', 10.1021/acs.analchem.8b01976.
[315] X. Ma, J. R. Idle, K. W. Krausz, D.-X. Tan, L. Ceraulo, F. J. Gonzalez, *J. Pineal Res.* **2006**, *40*, 343-349; 'Urinary metabolites and antioxidant products of exogenous melatonin in the mouse', 10.1111/j.1600-079X.2006.00321.x.
[316] D.-X. Tan, L. C. Manchester, M. P. Terron, L. J. Flores, R. J. Reiter, *J. Pineal Res.* **2007**, *42*, 28-42; 'One molecule, many derivatives: A never-ending interaction of melatonin with reactive oxygen and nitrogen species?', 10.1111/j.1600-079X.2006.00407.x.
[317] M. Baek, F. DiMaio, I. Anishchenko, J. Dauparas, S. Ovchinnikov, G. R. Lee, J. Wang, Q. Cong, L. N. Kinch, R. D. Schaeffer, C. Millán, H. Park, C. Adams, C. R. Glassman, A. DeGiovanni, J. H. Pereira, A. V. Rodrigues, A. A. van Dijk, A. C. Ebrecht, D. J. Opperman, T. Sagmeister, C. Buhlheller, T. Pavkov-Keller, M. K. Rathinaswamy, U. Dalwadi, C. K. Yip, J. E. Burke, K. C. Garcia, N. V. Grishin, P. D. Adams, R. J. Read, D. Baker, *Science* **2021**, *373*, 871-876; 'Accurate prediction of protein structures and interactions using a three-track neural network', doi:10.1126/science.abj8754.
[318] B. Bha, D. M. Harrison, *Tetrahedron* **1993**, *49*, 10655-10662; 'The synthesis of (-)-dihydroaszonalenin from L-tryptophan; the relative and absolute configuration of aszonalenin', 10.1016/S0040-4020(01)81555-6.
[319] N. Pozhydaieva, Master Thesis, Heinrich Heine University Düsseldorf **2020**.
[320] M. Baek, T. Park, L. Heo, C. Park, C. Seok, *Nucleic Acids Res.* **2017**, *45*, W320-W324; 'GalaxyHomomer: a web server for protein homo-oligomer structure prediction from a monomer sequence or structure', 10.1093/nar/gkx246.
[321] R. A. Friesner, J. L. Banks, R. B. Murphy, T. A. Halgren, J. J. Klicic, D. T. Mainz, M. P. Repasky, E. H. Knoll, M. Shelley, J. K. Perry, D. E. Shaw, P. Francis, P. S. Shenkin, *J. Med. Chem.* **2004**, *47*, 1739-1749; 'Glide: A New Approach for Rapid, Accurate Docking and Scoring. 1. Method and Assessment of Docking Accuracy', 10.1021/jm0306430.

[322] T. A. Halgren, R. B. Murphy, R. A. Friesner, H. S. Beard, L. L. Frye, W. T. Pollard, J. L. Banks, *J. Med. Chem.* **2004**, *47*, 1750-1759; 'Glide: A New Approach for Rapid, Accurate Docking and Scoring. 2. Enrichment Factors in Database Screening', 10.1021/jm030644s.
[323] J. Jumper, R. Evans, A. Pritzel, T. Green, M. Figurnov, O. Ronneberger, K. Tunyasuvunakool, R. Bates, A. Žídek, A. Potapenko, A. Bridgland, C. Meyer, S. A. A. Kohl, A. J. Ballard, A. Cowie, B. Romera-Paredes, S. Nikolov, R. Jain, J. Adler, T. Back, S. Petersen, D. Reiman, E. Clancy, M. Zielinski, M. Steinegger, M. Pacholska, T. Berghammer, S. Bodenstein, D. Silver, O. Vinyals, A. W. Senior, K. Kavukcuoglu, P. Kohli, D. Hassabis, *Nature* **2021**, *596*, 583-589; 'Highly accurate protein structure prediction with AlphaFold', 10.1038/s41586-021-03819-2.
[324] M. Mirdita, K. Schütze, Y. Moriwaki, L. Heo, S. Ovchinnikov, M. Steinegger, *Nat. Methods* **2022**, *19*, 679-682; 'ColabFold: making protein folding accessible to all', 10.1038/s41592-022-01488-1.
[325] M. Schatton, Indolderivate in der Synthese von naturstoffinspirierte Wirkstoffen, Dissertation, Heinrich Heine University Düsseldorf **2025**.
[326] T. M. Rosch, J. Tenhaef, T. Stoltmann, T. Redeker, D. Kösters, N. Hollmann, K. Krumbach, W. Wiechert, M. Bott, S. Matamouros, J. Marienhagen, S. Noack, *ACS Synth. Biol.* **2024**, *13*, 2227-2237; 'AutoBioTech─A Versatile Biofoundry for Automated Strain Engineering', 10.1021/acssynbio.4c00298.
[327] S. Kille, C. G. Acevedo-Rocha, L. P. Parra, Z.-G. Zhang, D. J. Opperman, M. T. Reetz, J. P. Acevedo, *ACS Synth. Biol.* **2013**, *2*, 83-92; 'Reducing Codon Redundancy and Screening Effort of Combinatorial Protein Libraries Created by Saturation Mutagenesis', 10.1021/sb300037w.
[328] D. A. Amariei, M. Haase, M. K. T. Klischan, M. Wäscher, J. Pietruszka, *ChemCatChem* **2024**, *16*, e202400052; 'High-Throughput Colorimetric Detection and Quantification of Indoles and Pyrroloindoles for Enzymatic Activity Determination', 10.1002/cctc.202400052.
[329] D. A. Amariei, J. Tenhaef, T. Classen, B. David, T. M. Rosch, H. Gohlke, S. Noack, J. Pietruszka, *Catal. Sci. Technol.* **2024**, *14*, 6298-6306; 'Directed evolution of C-methyltransferase PsmD for enantioselective pyrroloindole derivative production', 10.1039/D4CY00657G.
[330] D. K. Romney, J. Murciano-Calles, J. E. Wehrmüller, F. H. Arnold, *J. Am. Chem. Soc.* **2017**, *139*, 10769-10776; 'Unlocking Reactivity of TrpB: A General Biocatalytic Platform for Synthesis of Tryptophan Analogues', 10.1021/jacs.7b05007.

[331] A. R. Buller, S. Brinkmann-Chen, D. K. Romney, M. Herger, J. Murciano-Calles, F. H. Arnold, *Proc. Nati. Acad. Sci.* **2015**, *112*, 14599-14604; 'Directed evolution of the tryptophan synthase β-subunit for stand-alone function recapitulates allosteric activation', 10.1073/pnas.1516401112.

[332] L.-L. Yang, S.-K. Tang, Y.-Q. Zhang, X.-Y. Zhi, D. Wang, L.-H. Xu, W.-J. Li, *Int. J. Syst. Evol. Microbiol.* **2008**, *58*, 1821-1825; 'Thermobifida halotolerans sp. nov., isolated from a salt mine sample, and emended description of the genus Thermobifida', 10.1099/ijs.0.65732-0.

[333] X.-P. Tian, S.-K. Tang, J.-D. Dong, Y.-Q. Zhang, L.-H. Xu, S. Zhang, W.-J. Li, *Int. J. Syst. Evol. Microbiol.* **2009**, *59*, 948-952; 'Marinactinospora thermotolerans gen. nov., sp. nov., a marine actinomycete isolated from a sediment in the northern South China Sea', 10.1099/ijs.0.005231-0.

[334] F. Zhang, J.-J. Chen, W.-Z. Ren, G.-X. Nie, H. Ming, S.-K. Tang, W.-J. Li, *Bioresour. Technol.* **2011**, *102*, 10143-10146; 'Cloning, expression and characterization of an alkaline thermostable GH9 endoglucanase from Thermobifida halotolerans YIM 90462T', 10.1016/j.biortech.2011.08.019.

[335] F. Zhang, J.-J. Chen, W.-Z. Ren, L.-B. Lin, Y. Zhou, X.-Y. Zhi, S.-K. Tang, W.-J. Li, *J. Ind. Microbiol. Biotechnol.* **2012**, *39*, 1109-1116; 'Cloning, expression, and characterization of an alkaline thermostable GH11 xylanase from Thermobifida halotolerans YIM 90462T', 10.1007/s10295-012-1119-8.

[336] Y.-R. Yin, W.-D. Xian, M.-X. Han, E.-M. Zhou, L. Liu, D. H. M. Alkhalifah, W. N. Hozzein, M. Xiao, W.-J. Li, *Antonie van Leeuwenhoek* **2019**, *112*, 339-350; 'Expression and characterisation of a pH and salt tolerant, thermostable and xylose tolerant recombinant GH43 β-xylosidase from Thermobifida halotolerans YIM 90462T for promoting hemicellulose degradation', 10.1007/s10482-018-1161-2.

[337] D. Jiang, Z. Min, J. Leng, H. Niu, Y. Chen, D. Liu, C. Zhu, M. Li, W. Zhuang, H. Ying, *Chin. J. Chem. Eng.* **2023**, *53*, 56-62; 'Characterization of two halophilic adenylate cyclases from Thermobifida halotolerans and Haloactinopolyspora alba', 10.1016/j.cjche.2022.01.020.

[338] S. Huang, Somayah S. Elsayed, M. Lv, J. Tabudravu, Mostafa E. Rateb, R. Gyampoh, K. Kyeremeh, R. Ebel, M. Jaspars, Z. Deng, Y. Yu, H. Deng, *Chem. Biol.* **2015**, *22*, 1633-1642; 'Biosynthesis of Neocarazostatin A Reveals the Sequential Carbazole Prenylation and Hydroxylation in the Tailoring Steps', 10.1016/j.chembiol.2015.10.012.

[339] T. R. Tansey, I. Shechter, *Biochim. Biophys. Acta, Mol. Cell Biol. Lipids* **2000**, *1529*, 49-62; 'Structure and regulation of mammalian squalene synthase', 10.1016/S1388-1981(00)00137-2.
[340] P. Banerjee, J. B. Joo, J. T. Buse, G. Dawson, *Chem. Phys. Lipids* **1995**, *77*, 65-78; 'Differential solubilization of lipids along with membrane proteins by different classes of detergents', 10.1016/0009-3084(95)02455-R.
[341] D. J. Leibly, T. N. Nguyen, L. T. Kao, S. N. Hewitt, L. K. Barrett, W. C. Van Voorhis, *PLoS One* **2012**, *7*, e52482; 'Stabilizing Additives Added during Cell Lysis Aid in the Solubilization of Recombinant Proteins', 10.1371/journal.pone.0052482.
[342] L. Song, C. D. Poulter, *Proc. Nati. Acad. Sci.* **1994**, *91*, 3044-3048; 'Yeast farnesyl-diphosphate synthase: site-directed mutagenesis of residues in highly conserved prenyltransferase domains I and II', 10.1073/pnas.91.8.3044.
[343] D. Esposito, D. K. Chatterjee, *Curr. Opin. Biotechnol.* **2006**, *17*, 353-358; 'Enhancement of soluble protein expression through the use of fusion tags', 10.1016/j.copbio.2006.06.003.
[344] E. R. LaVallie, Z. Lu, E. A. Diblasio-Smith, L. A. Collins-Racie, J. M. McCoy, in *Methods Enzymol., Vol. 326*, Academic Press, **2000**, pp. 322-340.
[345] P. Sivalingam, K. Hong, J. Pote, K. Prabakar, *Int. J. Mircobiol.* **2019**, *2019*, 5283948; 'Extreme environment Streptomyces: potential sources for new antibacterial and anticancer drug leads?', 10.1155/2019/5283948.
[346] J. Bérdy, *J. Antibiot.* **2012**, *65*, 385-395; 'Thoughts and facts about antibiotics: Where we are now and where we are heading', 10.1038/ja.2012.27.
[347] D. A. Amariei, **2025**.
[348] B. Metin, *Fermentation* **2023**, *9*, 836; 'Penicillium roqueforti Secondary Metabolites: Biosynthetic Pathways, Gene Clusters, and Bioactivities'.
[349] H.-F. Tu, X. Zhang, C. Zheng, M. Zhu, S.-L. You, *Nat. Catal.* **2018**, *1*, 601-608; 'Enantioselective dearomative prenylation of indole derivatives', 10.1038/s41929-018-0111-8.
[350] N. Lall, C. J. Henley-Smith, M. N. De Canha, C. B. Oosthuizen, D. Berrington, *Int. J. Microbiol.* **2013**, *2013*, 420601; 'Viability Reagent, PrestoBlue, in Comparison with Other Available Reagents, Utilized in Cytotoxicity and Antimicrobial Assays', 10.1155/2013/420601.
[351] E. Potapskyi, K. Kustrzyńska, D. Łażewski, P. Skupin-Mrugalska, R. Lesyk, M. Wierzchowski, *J. Med. Sci.* **2024**, *93*, e1128-e1128; 'Introducing bromine in the molecular structure as a good strategy to the drug design', 10.20883/medical.e1128.

[352] Z. Xu, Z. Yang, Y. Liu, Y. Lu, K. Chen, W. Zhu, *J. Chem. Inf. Model.* **2014**, *54*, 69-78; 'Halogen Bond: Its Role beyond Drug–Target Binding Affinity for Drug Discovery and Development', 10.1021/ci400539q.
[353] B. R. Smith, C. M. Eastman, J. T. Njardarson, *J. Med. Chem.* **2014**, *57*, 9764-9773; 'Beyond C, H, O, and N! Analysis of the elemental composition of US FDA approved drug architectures: Miniperspective', 10.1021/jm501105n.
[354] C. R. Whitlock, M. P. Cava, *Tetrahedron Lett.* **1994**, *35*, 371-374; 'A total synthesis of dragmacidin B', 10.1016/0040-4039(94)85056-9.
[355] S. Kohmoto, Y. Kashman, O. J. McConnell, K. L. Rinehart Jr, A. Wright, F. Koehn, *J. Org. Chem.* **1988**, *53*, 3116-3118; 'Dragmacidin, a new cytotoxic bis (indole) alkaloid from a deep water marine sponge, Dragmacidon sp', 10.1021/jo00248a040.
[356] H. Sun, K. Sun, J. Sun, *Molecules* **2023**, *28*, 2204; 'Recent Advances of Marine Natural Indole Products in Chemical and Biological Aspects'.
[357] D. Mariya Vincent, H. Mostafa, A. Suneer, S. Radha Krishnan, M. Ong, Y. Itahana, K. Itahana, R. Viswanathan, *Chem. Eur. J.* **2024**, *30*, e202401782; 'Development of Natural-Product-Inspired ABCB1 Inhibitors Through Regioselective Tryptophan C3-Benzylation', 10.1002/chem.202401782.
[358] J. Y. P. Koh, Y. Itahana, A. Krah, H. Mostafa, M. Ong, S. Iwamura, D. M. Vincent, S. Radha Krishnan, W. Ye, P. W. C. Yim, T. M. Khopade, K. Chen, P. S. Kong, L.-F. Wang, R. W. Bates, Y. Kimura, R. Viswanathan, P. J. Bond, K. Itahana, *Commun. Chem.* **2024**, *7*, 158; 'Exploring bat-inspired cyclic tryptophan diketopiperazines as ABCB1 Inhibitors', 10.1038/s42004-024-01225-z.
[359] W.-B. Yin, X.-L. Xie, M. Matuschek, S.-M. Li, *Org. Biomol. Chem.* **2010**, *8*, 1133-1141; 'Reconstruction of pyrrolo[2,3-b]indoles carrying an α-configured reverse C3-dimethylallyl moiety by using recombinant enzymes', 10.1039/B922440H.
[360] J. G. Marblestone, S. C. Edavettal, Y. Lim, P. Lim, X. Zuo, T. R. Butt, *Protein Sci.* **2006**, *15*, 182-189; 'Comparison of SUMO fusion technology with traditional gene fusion systems: Enhanced expression and solubility with SUMO', 10.1110/ps.051812706.
[361] Y. Shen, L. Zhang, M. Yang, T. Shi, Y. Li, L. Li, Y. Yu, H. Deng, H.-W. Lin, Y. Zhou, *ACS Chem. Biol.* **2023**, *18*, 123-133; 'Switching Prenyl Donor Specificities in Squalene Synthase-Like Aromatic Prenyltransferases from Bacterial Carbazole Alkaloid Biosynthesis', 10.1021/acschembio.2c00756.

[362] E. De Bernardez Clark, *Curr. Opin. Biotechnol.* **1998**, *9*, 157-163; 'Refolding of recombinant proteins', 10.1016/S0958-1669(98)80109-2.
[363] S. M. Singh, A. K. Panda, *J. Biosci. Bioeng.* **2005**, *99*, 303-310; 'Solubilization and refolding of bacterial inclusion body proteins', 10.1263/jbb.99.303.
[364] I. Cacciatore, A. Cocco, M. Costa, M. Fontana, G. Lucente, L. Pecci, F. Pinnen, *Amino Acids* **2005**, *28*, 77-83; 'Biochemical properties of new synthetic carnosine analogues containing the residue of 2,3-diaminopropionic acid: the effect of N-acetylation', 10.1007/s00726-004-0142-0.
[365] C. Pérez-Balado, Á. R. de Lera, *Org. Biomol. Chem.* **2010**, *8*, 5179-5186; 'Concise total synthesis and structural revision of (+)-pestalazine B', 10.1039/C0OB00531B.
[366] S. Nishanth Kumar, C. Mohandas, B. Nambisan, *Peptides* **2014**, *53*, 48-58; 'Purification, structural elucidation and bioactivity of tryptophan containing diketopiperazines, from Comamonas testosteroni associated with a rhabditid entomopathogenic nematode against major human-pathogenic bacteria', 10.1016/j.peptides.2013.09.019.
[367] K. Ouchaou, F. Maire, O. Salo, H. Ali, T. Hankemeier, G. A. van der Marel, D. V. Filippov, R. A. L. Bovenberg, R. J. Vreeken, A. J. M. Driessen, H. S. Overkleeft, *ChemBioChem* **2015**, *16*, 915-923; 'A Mutasynthesis Approach with a Penicillium chrysogenum ΔroqA Strain Yields New Roquefortine D Analogues', 10.1002/cbic.201402686.
[368] B. N. S. Ningsih, V. Rukachaisirikul, S. Phongpaichit, S. Preedanon, J. Sakayaroj, C. Muanprasat, *Nat. Prod. Res.* **2023**, *37*, 2311-2318; 'A nonadride derivative from the marine-derived fungus Aspergillus chevalieri PSU-AMF79', 10.1080/14786419.2022.2039651.
[369] M. S. C. Pedras, K. C. Smith, J. L. Taylor, *Phytochemistry* **1998**, *49*, 1575-1577; 'Production of 2,5-dioxopiperazine by a new isolate type of the blackleg fungus Phoma lingam', 10.1016/S0031-9422(98)00271-4.
[370] T. Furukawa, T. Akutagawa, H. Funatani, T. Uchida, Y. Hotta, M. Niwa, Y. Takaya, *Bioorgan. Med. Chem.* **2012**, *20*, 2002-2009; 'Cyclic dipeptides exhibit potency for scavenging radicals', 10.1016/j.bmc.2012.01.050.
[371] P.-Q. Huang, Y. Wang, S.-P. Luo, H. Geng, Y.-P. Ruan, A.-E. Wang, *Tetrahedron Lett.* **2015**, *56*, 1255-1258; 'Procedure - economical enantioselective total syntheses of asperlicins C and E', 10.1016/j.tetlet.2015.01.084.

[372] S. M. Anil, R. Shobith, K. R. Kiran, T. R. Swaroop, N. Mallesha, M. P. Sadashiva, *New J. Chem.* **2019**, *43*, 182-187; 'Facile synthesis of 1,4-benzodiazepine-2,5-diones and quinazolinones from amino acids as anti-tubercular agents', 10.1039/C8NJ04936J.
[373] H.-C. Hsu, D.-R. Hou, *Tetrahedron Lett.* **2009**, *50*, 7169-7171; 'Reduction of 1-pyrrolyl and 1-indolyl carbamates to hemiaminals', 10.1016/j.tetlet.2009.10.025.
[374] V. Leclerc, S. Yous, P. Delagrange, J. A. Boutin, P. Renard, D. Lesieur, *J. Med. Chem.* **2002**, *45*, 1853-1859; 'Synthesis of Nitroindole Derivatives with High Affinity and Selectivity for Melatoninergic Binding Sites MT3', 10.1021/jm011053+.
[375] J. Xu, R. Tong, *Green Chem.* **2017**, *19*, 2952-2956; 'An environmentally friendly protocol for oxidative halocyclization of tryptamine and tryptophol derivatives', 10.1039/C7GC01341H.
[376] X.-W. Li, T.-X. Si, Y.-P. Liu, M.-Z. Wang, A. S. C. Chan, *Org. Biomol. Chem.* **2020**, *18*, 3848-3852; 'Divergent syntheses of okaramines C, J, L, and S–U', 10.1039/D0OB00587H.